

NANOPARTICULATE MATERIALS

NANOPARTICULATE MATERIALS

Synthesis, Characterization,
and Processing

KATHY LU

Materials Science and Engineering,
Virginia Tech, Blacksburg, VA

 **WILEY**

A JOHN WILEY & SONS, INC., PUBLICATION

Copyright © 2013 by John Wiley & Sons, Inc. All rights reserved

Published by John Wiley & Sons, Inc., Hoboken, New Jersey
Published simultaneously in Canada

No part of this publication may be reproduced, stored in a retrieval system, or transmitted in any form or by any means, electronic, mechanical, photocopying, recording, scanning, or otherwise, except as permitted under Section 107 or 108 of the 1976 United States Copyright Act, without either the prior written permission of the Publisher, or authorization through payment of the appropriate per-copy fee to the Copyright Clearance Center, Inc., 222 Rosewood Drive, Danvers, MA 01923, (978) 750-8400, fax (978) 750-4470, or on the web at www.copyright.com. Requests to the Publisher for permission should be addressed to the Permissions Department, John Wiley & Sons, Inc., 111 River Street, Hoboken, NJ 07030, (201) 748-6011, fax (201) 748-6008, or online at <http://www.wiley.com/go/permission>.

Limit of Liability/Disclaimer of Warranty: While the publisher and author have used their best efforts in preparing this book, they make no representations or warranties with respect to the accuracy or completeness of the contents of this book and specifically disclaim any implied warranties of merchantability or fitness for a particular purpose. No warranty may be created or extended by sales representatives or written sales materials. The advice and strategies contained herein may not be suitable for your situation. You should consult with a professional where appropriate. Neither the publisher nor author shall be liable for any loss of profit or any other commercial damages, including but not limited to special, incidental, consequential, or other damages.

For general information on our other products and services or for technical support, please contact our Customer Care Department within the United States at (800) 762-2974, outside the United States at (317) 572-3993 or fax (317) 572-4002.

Wiley also publishes its books in a variety of electronic formats. Some content that appears in print may not be available in electronic formats. For more information about Wiley products, visit our web site at www.wiley.com.

Library of Congress Cataloging-in-Publication Data:

Lu, Kathy.

Nanoparticulate materials : synthesis, characterization, and processing / Kathy Lu.
pages cm

Includes bibliographical references and index.

ISBN 978-1-118-29142-9 (cloth)

1. Nanoparticles. 2. Nanostructured materials. I. Title.

TA418.78.L825 2012

620.1'15—dc23

2012025733

Printed in the United States of America

ISBN: 9781118291429

10 9 8 7 6 5 4 3 2 1

To Jim, Maggie, and Aron.

CONTENTS

| | |
|--------------------------------------|-------------|
| PREFACE | xv |
| LIST OF SYMBOLS | xvii |
| LIST OF ABBREVIATIONS | xxv |
| ABOUT THE AUTHOR | xxix |
| 1 INTRODUCTION | 1 |
| 1.1 Overview | 1 |
| 1.2 Nanoparticle-Based Materials | 2 |
| 1.3 Unique Characteristics | 3 |
| 1.3.1 Surface Behaviors | 4 |
| 1.3.2 Vapor Pressure and Solubility | 5 |
| 1.3.3 Size-Dependent Characteristics | 6 |
| 1.4 Properties | 7 |
| 1.4.1 Chemical | 7 |
| 1.4.2 Mechanical | 9 |
| 1.4.3 Electrical | 10 |
| 1.4.4 Magnetic | 11 |
| 1.4.5 Optical | 12 |
| 1.4.6 Biological | 13 |

| | | |
|----------|---|-----------|
| 1.5 | Key Scientific and Technical Challenges | 14 |
| 1.5.1 | Synthesis | 14 |
| 1.5.2 | Characterization | 14 |
| 1.5.3 | Superstructure Assembly | 14 |
| 1.5.4 | Bulk Processing | 15 |
| 1.5.5 | Large-Scale Production | 15 |
| 1.5.6 | Modeling and Simulation | 15 |
| 1.6 | Applications | 16 |
| 1.7 | Processing Overview | 18 |
| 1.8 | Summary | 21 |
| | Questions | 21 |
| | References | 21 |
| 2 | NANOPARTICLE SYNTHESIS | 24 |
| 2.1 | Introduction | 24 |
| 2.2 | Theory | 25 |
| 2.2.1 | Nucleation | 26 |
| 2.2.1.1 | Homogeneous Nucleation | 26 |
| 2.2.1.2 | Heterogeneous Nucleation | 27 |
| 2.2.2 | Growth | 28 |
| 2.3 | Gas-Phase Nanoparticle Synthesis | 32 |
| 2.3.1 | Gas–Gas Reaction | 32 |
| 2.3.1.1 | Physical Vapor Synthesis | 32 |
| 2.3.1.2 | Chemical Vapor Synthesis | 39 |
| 2.3.1.3 | Laser Ablation | 43 |
| 2.3.2 | Gas–Liquid Reaction | 49 |
| 2.3.3 | Gas–Solid Reaction | 51 |
| 2.4 | Liquid Nanoparticle Synthesis | 53 |
| 2.4.1 | Fundamental Method | 53 |
| 2.4.1.1 | Precipitation | 53 |
| 2.4.1.2 | Metal Salt Reduction | 58 |
| 2.4.1.3 | Hydrolysis | 61 |
| 2.4.1.4 | Solvothermal Synthesis | 65 |
| 2.4.1.5 | Cryochemical Synthesis | 70 |
| 2.4.2 | Confinement Method | 72 |
| 2.4.2.1 | Spray Pyrolysis | 72 |
| 2.4.2.2 | Solventless Synthesis | 76 |
| 2.4.3 | Composite Nanoparticle Synthesis | 78 |

| | | |
|----------|---------------------------------------|------------|
| 2.4.3.1 | Core/Shell Structure | 78 |
| 2.4.3.2 | Electroless Deposition | 83 |
| 2.4.3.3 | Templating | 83 |
| 2.4.3.4 | Bio-Based Synthesis | 85 |
| 2.4.4 | Field-Assisted Nanoparticle Synthesis | 88 |
| 2.4.4.1 | Micelle Synthesis | 89 |
| 2.4.4.2 | Laser-Assisted Synthesis | 92 |
| 2.4.4.3 | Plasma-Assisted Synthesis | 94 |
| 2.4.4.4 | Microwave-Assisted Synthesis | 95 |
| 2.4.4.5 | Sonication-Assisted Synthesis | 97 |
| 2.4.4.6 | Radiation-Assisted Synthesis | 100 |
| 2.4.4.7 | Electric Field-Assisted Synthesis | 101 |
| 2.5 | Solid Nanoparticle Synthesis | 102 |
| 2.5.1 | Milling | 102 |
| 2.5.2 | Reactions between Solids | 107 |
| 2.6 | Summary | 109 |
| | Questions | 115 |
| | References | 116 |
| 3 | NANOPARTICLE CHARACTERIZATION | 128 |
| 3.1 | Introduction | 128 |
| 3.2 | Size, Shape, and Morphology | 130 |
| 3.2.1 | Microscopy | 130 |
| 3.2.1.1 | Scanning Electron Microscopy | 130 |
| 3.2.1.2 | Transmission Electron Microscopy | 132 |
| 3.2.1.3 | Scanning Probe Microscopy | 133 |
| 3.2.2 | Dynamic Light Scattering | 135 |
| 3.2.3 | X-ray Diffraction Line Broadening | 138 |
| 3.2.4 | Small-Angle Scattering | 140 |
| 3.2.5 | Optical Spectroscopy | 144 |
| 3.3 | Energetics and Global Thermodynamics | 144 |
| 3.4 | Surface Area | 146 |
| 3.5 | Porosity and Pore Size | 148 |
| 3.5.1 | Electron Imaging | 148 |
| 3.5.2 | Gas Adsorption | 149 |
| 3.6 | Structure | 150 |
| 3.6.1 | Surface Structure | 151 |
| 3.6.1.1 | Low-Energy Electron Diffraction | 151 |

| | | |
|----------|---|------------|
| 3.6.1.2 | Atomic Force Microscopy | 152 |
| 3.6.1.3 | Scanning Tunneling Microscopy | 153 |
| 3.6.2 | Bulk Structure | 155 |
| 3.6.2.1 | X-ray Diffraction | 155 |
| 3.6.2.2 | Electron Diffraction | 156 |
| 3.6.2.3 | Neutron Diffraction | 160 |
| 3.7 | Composition | 161 |
| 3.7.1 | Surface Composition | 161 |
| 3.7.1.1 | Auger Electron Spectroscopy | 161 |
| 3.7.1.2 | X-ray Photoelectron Spectroscopy | 164 |
| 3.7.1.3 | Secondary Ion Mass Spectroscopy | 165 |
| 3.7.2 | Bulk Composition | 168 |
| 3.7.2.1 | Optical Atomic Spectroscopy | 168 |
| 3.7.2.2 | X-ray Fluorescence Spectroscopy | 170 |
| 3.7.2.3 | Energy Dispersive X-ray Analysis | 171 |
| 3.7.2.4 | Electron Energy Loss Spectroscopy | 174 |
| 3.7.2.5 | Fourier Transform Infrared Spectroscopy | 176 |
| 3.7.2.6 | Ultraviolet-Visible Absorption Spectroscopy | 178 |
| 3.7.2.7 | Raman Spectroscopy | 181 |
| 3.8 | Needs in Nanoscale Characterization | 183 |
| 3.9 | Summary | 184 |
| | Questions | 189 |
| | References | 189 |
| 4 | NANOPARTICLE-BASED SUPERSTRUCTURES | 195 |
| 4.1 | Introduction | 195 |
| 4.2 | Top-Down Processes | 196 |
| 4.2.1 | Photolithography | 197 |
| 4.2.2 | Electron Beam Lithography | 206 |
| 4.2.3 | Ion Beam Lithography | 212 |
| 4.2.4 | Other Top-Down Processes | 215 |
| 4.3 | Bottom-Up Processes | 217 |
| 4.3.1 | Nondirectional Interactions | 220 |
| 4.3.1.1 | van der Waals Forces | 220 |
| 4.3.1.2 | Dipole Moments | 222 |
| 4.3.1.3 | Electrostatic Interactions | 223 |
| 4.3.2 | Directional Interactions | 225 |
| 4.3.2.1 | Covalent Bonding | 225 |
| 4.3.2.2 | Hydrogen Bonding | 227 |

| | | |
|-------|--------------------------------|-----|
| 4.3.3 | Field-Assisted Assembly | 229 |
| 4.3.4 | Capillary Forces | 230 |
| 4.3.5 | Other Approaches | 236 |
| 4.4 | Hybrid | 236 |
| 4.4.1 | Functionalized Interactions | 236 |
| 4.4.2 | Nonfunctionalized Interactions | 241 |
| 4.5 | Templating | 242 |
| 4.5.1 | Natural Template | 243 |
| 4.5.2 | Synthetic Template | 245 |
| 4.6 | Three-Dimensional Assembly | 252 |
| 4.7 | Summary | 256 |
| | Questions | 256 |
| | References | 257 |

5 NANOPARTICLE-BASED MATERIAL SHAPING 263

| | | |
|---------|-------------------------------|-----|
| 5.1 | Introduction | 263 |
| 5.2 | Dry Forming Techniques | 264 |
| 5.2.1 | Uniaxial Compaction | 264 |
| 5.2.2 | Cold Isostatic Pressing | 266 |
| 5.2.3 | Superhigh Pressure Compaction | 268 |
| 5.2.4 | Dynamic Compaction | 270 |
| 5.3 | Semidry Forming Techniques | 272 |
| 5.3.1 | Molding | 273 |
| 5.3.1.1 | Powder Injection Molding | 273 |
| 5.3.1.2 | Micromolding | 274 |
| 5.3.2 | Extrusion | 277 |
| 5.3.2.1 | Microextrusion | 277 |
| 5.3.2.2 | Electrospinning | 279 |
| 5.4 | Wet Forming Techniques | 282 |
| 5.4.1 | Colloidal Suspension | 282 |
| 5.4.2 | Pressure Casting | 288 |
| 5.4.2.1 | Slip Casting | 288 |
| 5.4.2.2 | Uniaxial Pressure Casting | 289 |
| 5.4.2.3 | Spin Casting | 290 |
| 5.4.3 | Tape Casting | 291 |
| 5.4.4 | Freeze Casting | 293 |
| 5.4.5 | Gel Casting | 297 |
| 5.4.6 | Electrophoretic Deposition | 300 |

| | | |
|----------|--|------------|
| 5.5 | Digital Processing Techniques | 304 |
| 5.5.1 | Direct Writing | 304 |
| 5.5.1.1 | Robocasting | 304 |
| 5.5.1.2 | Omnidirectional Printing | 307 |
| 5.5.2 | Stereolithography | 307 |
| 5.5.3 | Ink-Jet Printing | 312 |
| 5.6 | Bio-Derived Processes | 313 |
| 5.6.1 | Bioactive Materials | 313 |
| 5.6.2 | Biomimetic Materials | 314 |
| 5.7 | Summary | 316 |
| | Questions | 319 |
| | References | 320 |
| 6 | SINTERING | 329 |
| 6.1 | Introduction | 329 |
| 6.2 | Theories | 330 |
| 6.2.1 | Sintering Stages | 330 |
| 6.2.2 | Shrinkage | 330 |
| 6.2.3 | Grain Growth | 332 |
| 6.3 | Characteristics of Nanoparticle Sintering | 334 |
| 6.3.1 | Designer Systems | 334 |
| 6.3.2 | Particle Size Distribution and Packing Characteristics | 335 |
| 6.3.3 | Complex Systems | 336 |
| 6.3.4 | Phase Transformation | 337 |
| 6.3.5 | Lower Sintering Temperature | 337 |
| 6.3.6 | Larger Sintering Driving Force | 339 |
| 6.4 | Porous Nanoparticle Material Sintering | 341 |
| 6.4.1 | Partial Sintering | 342 |
| 6.4.2 | Pore Forming Sintering | 346 |
| 6.4.3 | Template-Directed Sintering | 349 |
| 6.4.4 | Special Sintering Processes | 351 |
| 6.4.4.1 | Microwave Sintering | 351 |
| 6.4.4.2 | Electrical Sintering | 356 |
| 6.4.4.3 | Laser Sintering | 358 |
| 6.5 | Dense Nanoparticle-Based Material Sintering | 359 |
| 6.5.1 | Free Sintering | 359 |
| 6.5.1.1 | Customized Nanoparticle Systems | 359 |
| 6.5.1.2 | Customized Sintering Cycles | 363 |
| 6.5.1.3 | Remarks on Free Sintering | 367 |

| | | |
|----------|---|------------|
| 6.5.2 | Pressure Sintering | 368 |
| 6.5.2.1 | Hot Pressing | 368 |
| 6.5.2.2 | Hot Isostatic Pressing | 373 |
| 6.5.2.3 | Sinter Forging | 375 |
| 6.5.2.4 | Pressure Spark Plasma Sintering | 376 |
| 6.5.2.5 | Other Sintering Techniques | 382 |
| 6.6 | Summary | 383 |
| | Questions | 384 |
| | References | 385 |
| 7 | MANUFACTURING ISSUES AND EMERGING AREAS | 394 |
| 7.1 | Introduction | 394 |
| 7.2 | Defects and Measurement | 396 |
| 7.2.1 | Defects | 396 |
| 7.2.1.1 | Defect Nature | 396 |
| 7.2.1.2 | Defect Size | 397 |
| 7.2.1.3 | Defect Density | 397 |
| 7.2.2 | Measurement | 398 |
| 7.2.2.1 | Composition | 399 |
| 7.2.2.2 | Structure | 399 |
| 7.2.2.3 | Surface and Interface | 399 |
| 7.3 | Process and Quality Control | 401 |
| 7.4 | Modeling and Simulation | 402 |
| 7.5 | Environmental and Health Concerns | 407 |
| 7.5.1 | Environmental Concerns | 407 |
| 7.5.2 | Health Concerns | 409 |
| 7.6 | Summary | 412 |
| | Questions | 413 |
| | References | 413 |
| | APPENDIX 1 EXPLANATION OF UNFAMILIAR NOMENCLATURES | 415 |
| | APPENDIX 2 PREFIXES IN THE INTERNATIONAL SYSTEM OF UNITS | 425 |
| | INDEX | 427 |

PREFACE

This book specifically focuses on nanoparticle-based materials. It is intended to provide a more detailed look in this subfield of nanomaterials. On the one hand, it is intended to move beyond the broad, introductory stage of most books on nanomaterials and gives readers an in-depth coverage of this more specialized area. On the other hand, the book provides a transition between conventional particulate materials and nanoparticle-based materials so that the readers can view the existing and new fields in a continuous manner. The book is organized in the chronological order of nanoparticle material processing so that it can easily be used as a textbook.

I am aware that, in various places, the book does not provide detailed theoretical discussion of specific processes or the enabling techniques. This decision is based on the fact that many fundamental theories and equations have been well explained in other books and this book would be too long for the readers who mainly seek a comprehensive treatment of nanoparticle-based materials. The nanomaterials using nanoparticles as minor additives and polymer-based nanoparticle materials have purposely been omitted. I have tried my best to use a large number of representative images from the literature with the belief that seeing is believing.

This book is intended to provide comprehensive coverage for the readers involved in the nanoparticle-based material field. Upper-level undergraduates, graduate students, and professionals who are active in or curious about the fundamentals and advances in this area should find this book useful. I hope this book provides deeper understanding and knowledge in this fascinating and wide-ranging discipline. Each chapter can be used separately or in conjunction with one another. Questions are provided at the end of each chapter for pondering.

This book would not have been possible without all the encouragement and support from my colleagues, friends, students, and family. It is impossible to list every one of them. Specifically, I would like to acknowledge Professor Randall German for igniting my idea of writing this book. The reviewers' efforts for this book have been extremely helpful and I am thankful for their input. My graduate and undergraduate students, especially Wenle Li, Bo Chen, Yongxuan Liang, Zhenbo Xia, Kevin Penyak, Margaret Anderson, Kelly Ramsburg, and Matt McCarley, helped me with the many details of the manuscript. I would like to thank my family for giving me the time and encouragement for completing this effort. Final thanks go to Anita Lekhwani at Wiley who helped bring this book to fruition.

KATHY LU

LIST OF SYMBOLS

| | |
|--------------------------------|---|
| α_e : | diffusion coefficient due to an electric field |
| α_{GB} : | grain boundary diffusion coefficient |
| α_{HIP} : | diffusion coefficient due to hot isostatic pressing stress |
| α_{HP} : | diffusion coefficient due to hot pressing stress |
| α_{SPS} : | diffusion coefficient due to spark plasma sintering stress |
| α_V : | volume diffusion coefficient |
| β : | a geometric factor that depends on the shape of a particle (for a spherical particle, the value is 3) |
| γ : | specific surface energy |
| γ_{GB} : | grain boundary energy |
| γ_{GV} : | particle-pore interfacial energy |
| γ_{L-V} : | surface tension of liquid–solid interface |
| γ_{S-L} : | solid–liquid interfacial energy |
| γ_{S-V} : | solid–vapor interfacial energy |
| γ_V : | volume energy |
| ΔC_V : | difference in vacancy concentration |
| ΔG : | free energy change during the formation of a spherical nucleus |
| ΔG_c : | free energy barrier against nucleation |
| ΔG_c^{het} : | activation energy for heterogeneous nucleation |
| $\Delta G_{T \rightarrow S}$: | free energy change per unit volume when new nuclei are formed from liquid |

| | |
|-------------------------|---|
| ΔG_t : | activation free energy for transfer of a “structural unit” from liquid to a nucleus (kinetic barrier) |
| $\Delta\mu$: | chemical potential difference |
| δ : | polymer adsorption layer thickness |
| ε : | absorbicity |
| ε_m : | static dielectric constant of a medium |
| ε_0 : | permittivity of free space (8.85×10^{-12} farads m^{-1}) |
| ε_{pw} : | depth of a potential well |
| ε''_{eff} : | effective dielectric loss (dissipation) factor (unitless) |
| η : | viscosity of a liquid |
| η_0 : | viscosity of a suspension medium (in most cases, water) |
| η_r : | relative viscosity |
| θ : | diffraction angle (in radian) of considered diffraction peak |
| θ_{min} : | angle at which the first minimum occurs, measured from the direction of incoming light, in radians |
| κ : | curvature of a surface |
| $1/\kappa$: | Debye length |
| λ : | mean free path length for a particle/cluster in a gas |
| λ_e : | wavelength of electrons |
| λ_L : | wavelength of light |
| λ_N : | wavelength of incident neutron beam |
| λ_X : | wavelength of X-ray beam |
| μ_{flat} : | chemical potential on a flat surface |
| μ_{curv} : | chemical potential on a particle surface |
| ν : | Poisson’s ratio |
| ν_M : | molecular volume of dispersing medium |
| ν_s : | volume per molecule in a solid |
| ν_X : | frequency of X-ray photons used |
| ρ : | density |
| ρ' : | driving force of sintering |
| ρ_{rel} : | relative density |
| ρ_t : | nanoparticle theoretical density |
| ΣH : | vector sum of mean curvature H of the grain boundaries in a compact |
| σ_0 : | a material constant representing the starting stress for dislocation movement |
| σ_A : | cross-section area of an adsorbate molecule |
| $\sigma_{L,J}(r)$: | finite distance at which the interparticle potential is zero ($u_{L,J}(r) = 0$) |
| σ_y : | yield strength |
| φ : | contact angle |

| | |
|---|---|
| ϕ : | particle solids loading |
| ϕ_{eff} : | effective solids loading |
| ϕ_{max} : | maximum solids loading (~ 0.64) |
| ϕ' : | stress intensification factor due to particle–particle neck geometry |
| χ : | Flory–Huggins parameter |
| Ω : | atomic volume |
| ω : | angular frequency |
| ω_s : | scattering angle |
| $\frac{d\rho}{\rho dr}$: | chemical potential difference between atoms per formula unit on a flat surface and on a particle surface of curvature H |
| $\frac{dG}{dt}$: | overall grain growth rate |
| $\left. \frac{dG}{dt} \right _{\text{E-C}}$: | grain growth rate through evaporation–condensation mechanism |
| $\left. \frac{dG}{dt} \right _s$: | grain growth rate from surface diffusion mechanism |
| $\left. \frac{dG}{dt} \right _V$: | grain growth rate due to volume diffusion coarsening |
| $\left. \frac{dV}{dt} \right _{\text{GB}}$: | overall absolute volumetric change rate by grain boundary diffusion $dV/dt _{\text{GB}}$ |
| $\left. \frac{dV}{dt} \right _{\text{GB},2}$: | absolute volumetric change rate due to grain boundary diffusion for two grains |
| $\left. \frac{dV}{dt} \right _V$: | volumetric change rate due to volume diffusion densification |
| $\frac{dV}{V dt}$: | total absolute shrinkage rate for a sintering body |
| $\left. \frac{dV}{V dt} \right _{\text{d,HIP}}$: | densification rate during hot isostatic pressing |
| $\left. \frac{dV}{V dt} \right _{\text{d,HP}}$: | densification rate during hot pressing |
| $\left. \frac{dV}{V dt} \right _{\text{d,SPS}}$: | densification rate during spark plasma sintering |
| \vec{Q} : | scattering vector during neutron scattering |
| A : | volumetric grain boundary area |
| A_{GB} : | total grain boundary area |
| $A_{\text{GB},2}$: | grain boundary area between two grains |
| A' : | absorbance |
| a : | structural unit size |
| a' and b' : | constants |
| a_1 and a_2 : | particle radii |
| a_p : | nanoparticle size |
| B : | full width at half maximum intensity of a diffraction peak |
| b : | path length |
| C : | bulk concentration of growing species in a solution |
| C' : | system and temperature related constant |
| C_d : | cured depth of a polymer layer |

xx LIST OF SYMBOLS

| | |
|---------------------|---|
| C_E : | a system-related constant under an applied electrical field |
| C_{HIP} : | a system-related constant determined by hot isostatic pressing stress and temperature |
| C_{HP} : | a system-related constant determined by hot pressing stress and temperature |
| C_s : | saturation concentration |
| C_{SPS} : | a system-related constant under spark plasma sintering stress |
| C_{ss} : | supersaturated concentration |
| C_v : | vacancy concentration for a surface with curvature |
| C_{v0} : | vacancy concentration for a flat surface |
| c : | a constant |
| c_a : | concentration of absorbing species |
| D_{diff} : | diffusion coefficient |
| D_G : | diameter of atoms or molecules of gas species |
| D_{hkl} : | crystallite size |
| D_p : | particle size |
| $D_{penetration}$: | penetration depth from the Beer–Lambert law |
| d : | tip-sample distance in scanning tunneling microscope |
| d_A : | diameter of an aperture |
| da : | area element at grain–grain-pore triple junctions |
| E : | electrical field |
| E_a : | acceleration voltage (energy in eV) |
| $E_{binding}$: | binding energy of photoelectrons |
| E_c : | critical energy density below which polymerization will not proceed |
| $E_{elastic}(h)$: | elastic interaction energy |
| $E_{kinetic}$: | kinetic energy of ejected photoelectrons |
| E_{max} : | peak value of exposure ($J\ m^{-2}$) of a laser beam with Gaussian distribution of energy |
| $E_{mix}(h)$: | mixing interaction energy |
| E_{rms} : | root-mean-square of internal electric field (volts m^{-1}) |
| e : | electron charge ($1.6 \times 10^{-19}\ C$) |
| F : | Faraday’s constant |
| f : | microwave frequency in hertz |
| G : | grain size |
| G_0 : | initial grain size |
| g : | a constant in the unit of length |
| H : | mean curvature |
| H_{rms} : | root-mean-square of a magnetic field ($A\ m^{-1}$) |
| h : | Planck constant ($6.626 \times 10^{-34}\ J\ s$) |

| | |
|------------------------|---|
| I : | steady state homogenous volume nucleation rate |
| I_{het} : | maximum heterogeneous nucleation rate |
| I_t : | tunneling current in scanning tunneling microscope |
| J : | growing species flux through a spherical shell of radius x |
| J_N : | nucleation rate during inert gas condensation |
| j : | diffusion flux |
| K : | a thermally activated parameter that includes grain boundary mobility |
| K_{E-C} : | a constant representing grain boundary mobility due to evaporation–condensation diffusion mechanism |
| K_{mo} : | a constant |
| K_{mt} : | a constant |
| K_r : | a constant that obeys the Arrhenius relation |
| K_S : | a constant representing grain surface mobility due to surface diffusion mechanism |
| K_V : | a constant representing grain surface mobility due to volume diffusion coarsening mechanism |
| k : | Boltzmann’s constant ($1.3806 \times 10^{-23} \text{ m}^2 \text{ kg s}^{-2} \text{ K}^{-1}$) |
| k_σ : | a constant |
| L : | distance between particle surfaces |
| L_A : | adsorbed layer thickness |
| L_N : | dimension of inhomogeneity during neutron scattering |
| L_w : | cured line width |
| M_w : | molecular weight |
| m : | electron mass ($9.11 \times 10^{-31} \text{ kg}$) |
| N : | coordination number |
| N_A : | Avogadro’s number ($6.023 \times 10^{23} \text{ mol}^{-1}$) |
| N_f : | number of structural unit (formula) per unit volume of a solution |
| N_g : | number of gas atoms or molecules per unit volume |
| N_s : | structural units in contact with nucleating surface per unit volume for heterogeneous nucleation |
| n : | a constant representing the intrinsic viscosity of a suspension |
| n_i : | ionic concentration |
| n_p : | particle number density |
| P : | vapor pressure at a specific given condition |
| P_a : | ambient pressure |
| P_{applied} : | applied pressure during sintering |
| P_{curv} : | partial pressure on a particle/grain surface |
| P_f : | nucleus formation probability |
| P_{flat} : | partial pressure of a flat particle/grain surface |

| | |
|----------------------|---|
| P_0 : | equilibrium pressure on a flat surface |
| p : | gas pressure over a meniscus with radius r_m |
| p_A : | gas pressure applied during gas adsorption measurement |
| p_S : | saturation pressure of adsorbed gas at testing temperature |
| $p_{S,L}$: | saturation pressure of a liquid on a plane surface |
| R : | gas constant |
| R_1 and R_2 : | principal radii of a curvature |
| r : | particle/nucleus radius (assumed spherical shape) |
| r_1, r_2 : | principal curvatures at grain–grain–pore triple junctions |
| r_{a-a} : | interparticle/atom separation distance |
| r_c : | critical nucleus radius |
| r_m : | pore radius |
| r_0 : | initial particle radius |
| r_p : | average pore radius |
| r_c^{het} : | critical nucleus size for heterogeneous nucleation |
| S_∞ : | solubility when a particle size is very large that the particle surface can be considered flat |
| S : | supersaturation of a vapor phase in inert gas condensation |
| S_{E-C} : | a constant representing intrinsic material properties at a given temperature |
| S_d : | solubility for a given particle of radius r |
| S_s : | a system-related constant |
| S_{sch} : | Scherrer constant (~ 0.9) |
| S_T : | total surface area |
| S_V : | a system-related constant |
| S_w : | specific surface area ($\text{m}^2 \text{g}^{-1}$) |
| T : | absolute temperature |
| T_b : | boiling point of gas used |
| T_m : | melting temperature |
| t : | nanoparticle growth time |
| U_{DLVO} : | interaction potential between particles |
| $u_{L,j}(r)$: | interparticle potential |
| V : | volume of gas adsorbed per unit mass of nanoparticles (cm^3/g) at relative pressure $\frac{p}{p_0}$ |
| V_{ads} : | volume of adsorbed gas |
| V_f : | average volume fraction of polymeric molecules in an adsorbed layer |
| V_{gm} : | volume of gas required to form a monolayer per unit mass of nanoparticles ($\text{cm}^3 \text{g}^{-1}$) |
| V_L : | molar volume of a liquid |

| | |
|--------------------------|---|
| V_{Lads} : | molar volume of liquid adsorbate |
| V_{m} : | nucleus molar volume |
| V_0 : | molar volume of gas at standard temperature and pressure (22.4 L mol ⁻¹) |
| V_{P} : | pore volume |
| W : | work function of a spectrometer |
| $W_{\text{microwave}}$: | rate of energy absorption during microwave sintering |
| W_0 : | Gaussian half-width of a laser beam |
| W_{S} : | weight of a measured sample |
| X : | grain–grain contact neck size |
| Z_1^* and Z_2^* : | charges on particles |
| z : | effective charge on diffusing species |

LIST OF ABBREVIATIONS

| | |
|--------------|--|
| 11-MUA: | mercaptoundecanoic acid |
| 3DOM: | three-dimensionally ordered macroporous material |
| 4NP: | 4-nitrophenol |
| AA: | atomic absorption |
| acac: | acetylacetonate |
| AE: | atomic emission |
| AES: | Auger electron spectroscopy |
| AFM: | atomic force microscopy |
| APTES: | aminopropyltriethoxysilane |
| BET: | Brunauer–Emmett–Teller |
| BMI: | 1- <i>n</i> -butyl-3-methylimidazolium |
| CAD: | computer-aided design |
| CHAp: | carbonated hydroxyapatite |
| CNT: | carbon nanotube |
| CVS: | chemical vapor synthesis |
| DLS: | dynamic light scattering |
| DLVO theory: | Derjaguin–Landau–Verwey–Overbeek theory |
| DT: | decanethiol |
| EDS: | energy dispersive X-ray spectroscopy |
| EELS: | electron energy-loss spectroscopy |
| EPD: | electrophoretic deposition |

| | |
|------------|---|
| FGM: | functionally graded |
| FIB: | focused ion beam lithography |
| FT-IR: | Fourier transform infrared spectroscopy |
| FWHM: | full-width at half-maximum |
| HA: | hydroxyapatite |
| HNA: | 2-hydroxo-1-naphthaldehyde |
| ITO: | indium-doped tin oxide |
| LB: | Langmuir–Blodgett |
| LED: | light-emitting diodes |
| LEED: | low energy electron diffraction |
| LS: | Langmuir–Schaefer |
| LSCF: | $\text{La}_{0.6}\text{Sr}_{0.4}\text{Co}_{0.2}\text{Fe}_{0.8}\text{O}_{3-\delta}$ |
| LSM: | $\text{La}_{0.8}\text{Sr}_{0.2}\text{MnO}_{3-\delta}$ |
| MD: | molecular dynamics |
| MHA: | 16-mercaptohexadecanoic acid |
| MMA: | methyl methacrylate |
| MUA: | 11-mercaptoundecanoic acid |
| ODS: | <i>n</i> -octadecyltriethoxysilane |
| PAA: | poly(acrylic acid) |
| PCS: | photo correlation spectroscopy |
| PDMS: | polydimethylsiloxane |
| PDMS-g-PA: | poly(dimethylsiloxane)-graft-polyacrylate |
| PEG: | poly(ethylene glycol) |
| PEI: | polyethylenimine |
| PLLA: | poly(L-lactide) |
| PMMA: | poly(methyl methacrylate) |
| PS: | polystyrene |
| PTAA: | poly(3-thiophene acetic acid) |
| PVA: | poly(vinyl alcohol) |
| PVP: | poly(vinyl pyrrolidone) |
| QDS: | quantum dots |
| SAMS: | self-assembled monolayers |
| SANS: | small-angle neutron scattering |
| SAXS: | small-angle X-ray scattering |
| SDS: | sodium dodecyl sulfate |
| SEM: | scanning electron microscope |
| SIMS: | secondary ion mass spectroscopy (ion emission) |
| SPM: | scanning probe microscope |

| | |
|----------------------|---|
| STM: | scanning tunneling microscope |
| TBP: | tri-butyl-phosphine, $C_{12}H_{27}P$ |
| TEM: | transmission electron microscope |
| TEOS: | tetraethoxysilane |
| TEOS: | tetraethyl orthosilicate |
| TMOS: | tetramethylorthosilicate |
| TOPO: | trioctylphosphine oxide |
| UV-vis spectroscopy: | ultraviolet-visible absorption spectroscopy |
| vdW: | van der Waals |
| XFS: | X-ray fluorescence spectroscopy |
| XRD: | X-ray diffraction |

ABOUT THE AUTHOR

Kathy Lu is a Professor in Materials Science and Engineering of Virginia Tech. She received her PhD and MS degrees from Ohio State University and BS from Tianjin University. Before joining Virginia Tech, she held positions at Penn State University and Energizer, Inc. She has authored about 100 papers and three book chapters, edited four books, and taught materials science courses from the undergraduate to graduate levels. She has been honored with several awards including Friedrich Wilhelm Bessel Research Award from Alexander von Humboldt Foundation (2011), Karl Schwartzwalder-PACE Award from American Ceramic Society (2008), and Ralph E. Powe Junior Faculty Award from Oak Ridge Associated Universities (2005).

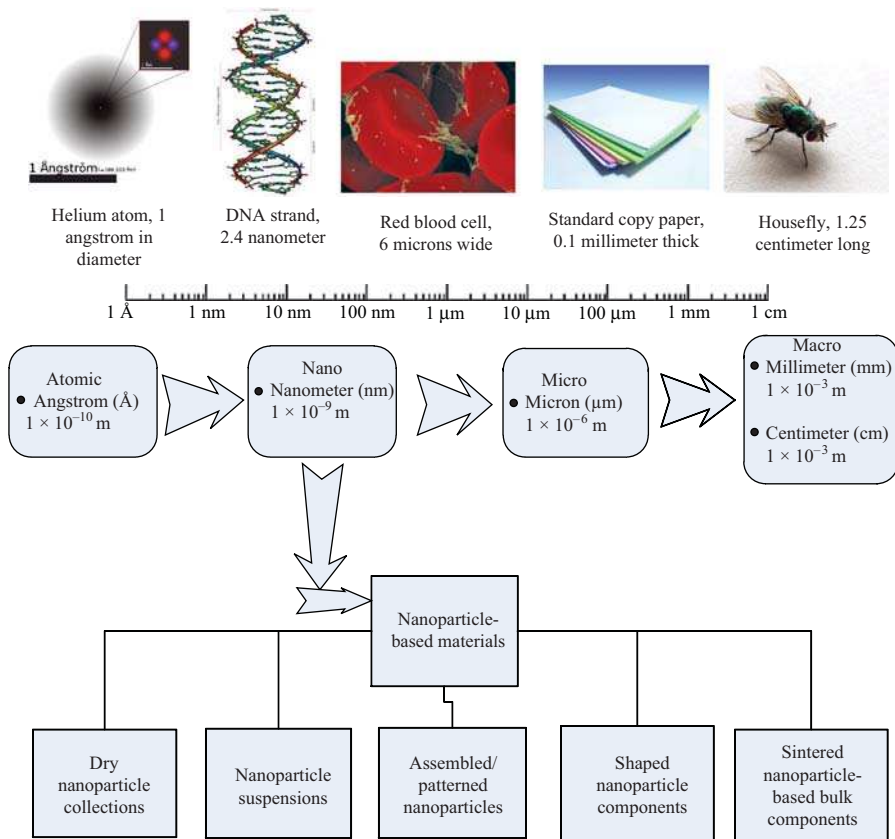


FIGURE 1.2 Illustration of species, scales, and formats of nanoparticle-based materials.



FIGURE 1.7 Examples of consumer products that can use nanoparticles as antibacterial agents.

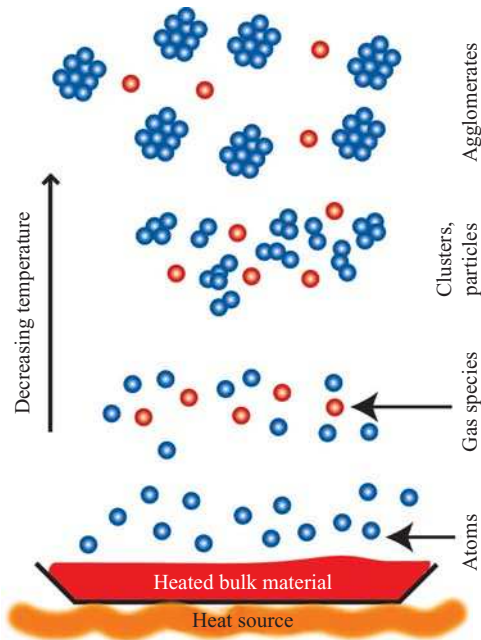


FIGURE 2.3 Illustration of the inert gas condensation process.

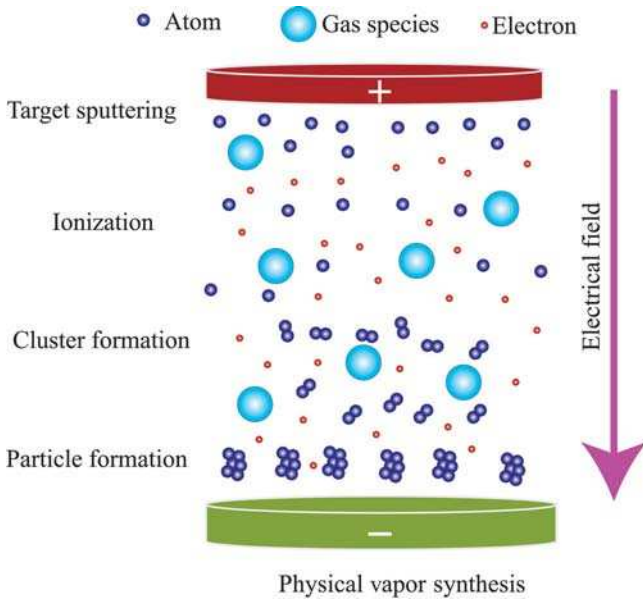


FIGURE 2.5 An illustration of physical vapor deposition process.

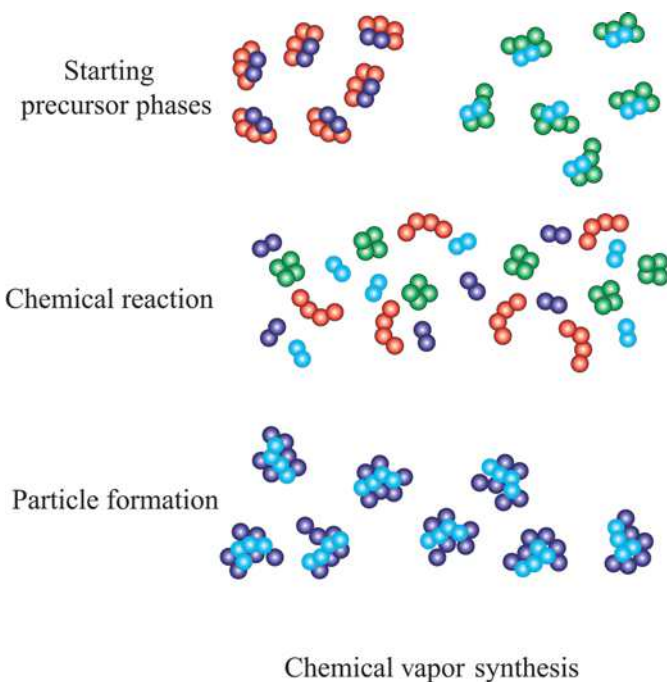


FIGURE 2.8 Illustration of chemical vapor synthesis process.

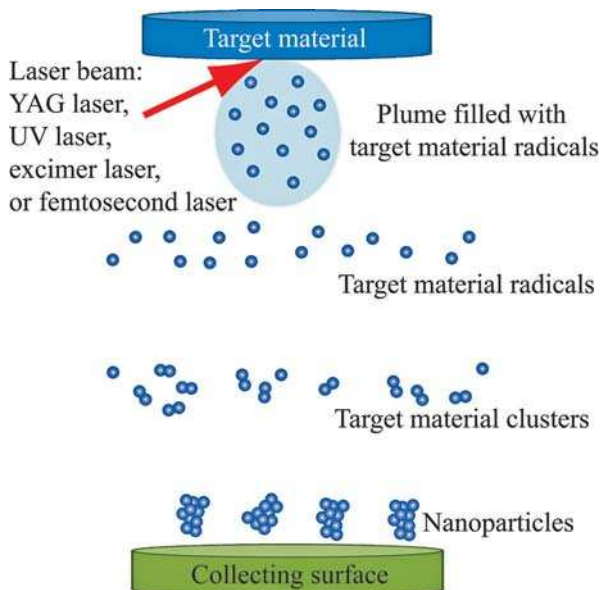


FIGURE 2.9 Illustration of laser ablation process.

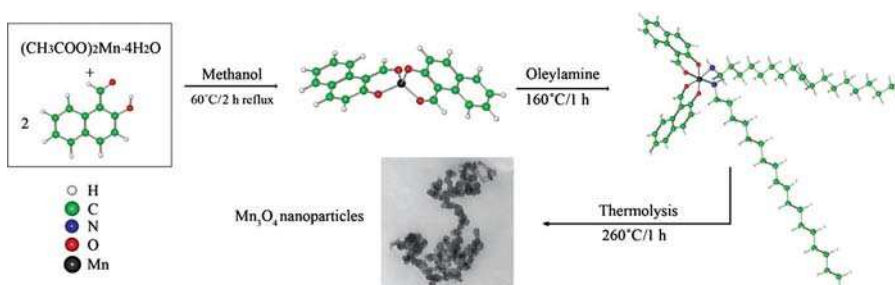


FIGURE 2.21 Schematic diagram illustrating the formation of Mn_3O_4 nanoparticles [66]. (Reprinted with permission from Davar F, Salavati-Niasari M, Mir N, Saberyan K, Monemzadeh M, Ahmadi E. Thermal decomposition route for synthesis of Mn_3O_4 nanoparticles in presence of a novel precursor. Polyhedron 2010;29:1747–1753, Copyright 2010, Elsevier.)

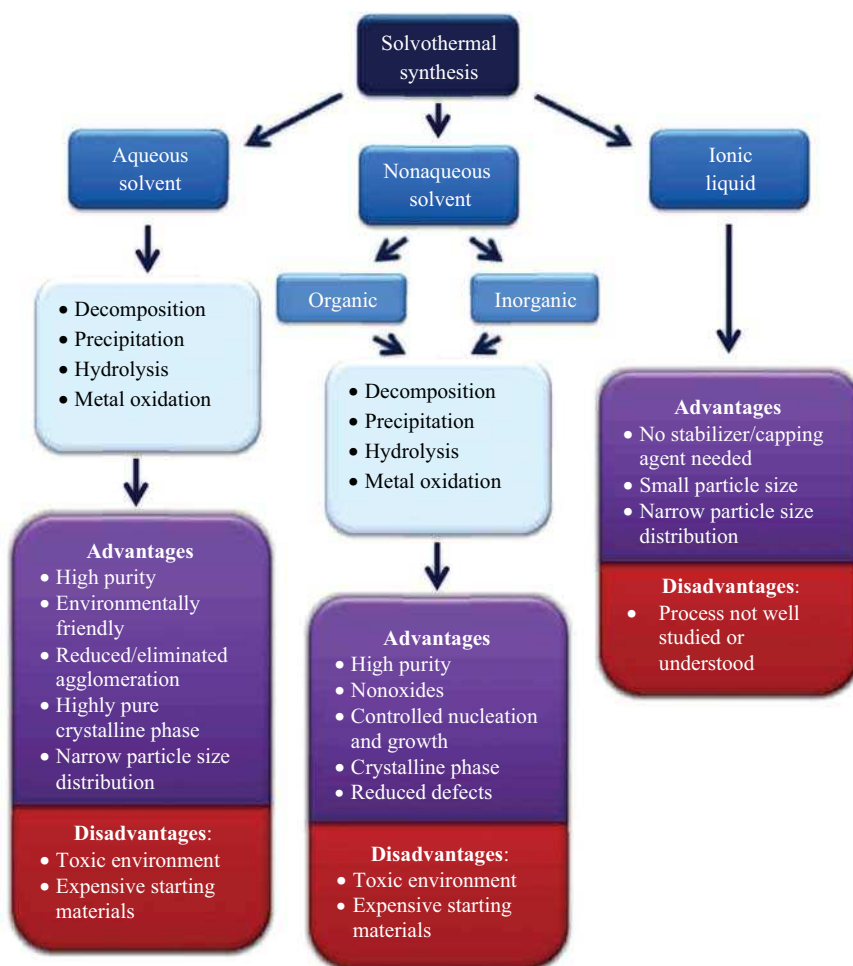


FIGURE 2.23 Solvothermal synthesis approaches and characteristics.

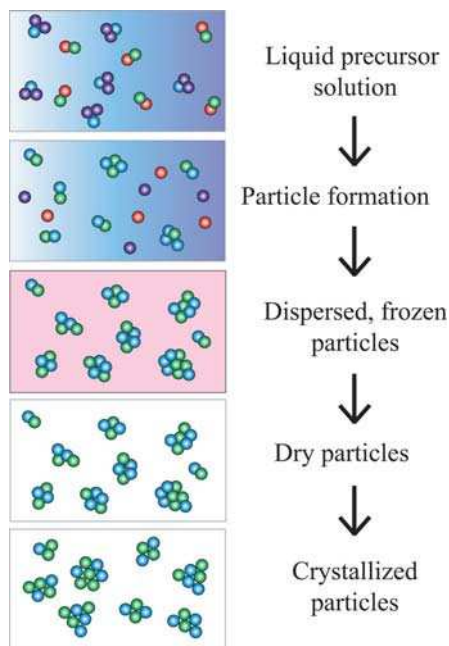


FIGURE 2.25 Illustration of the cryochemical synthesis process.

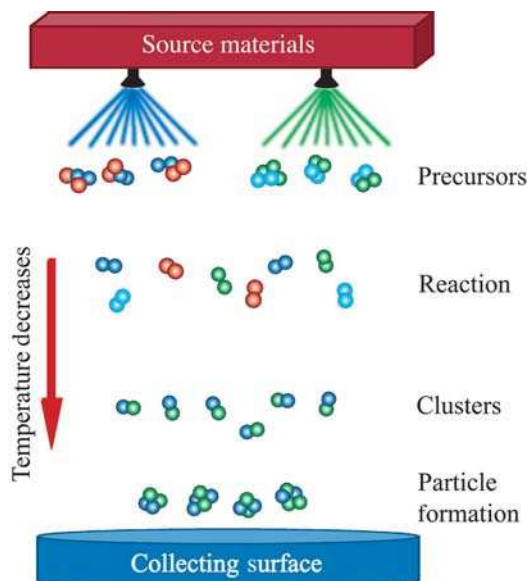


FIGURE 2.26 Illustration of the spray pyrolysis process.

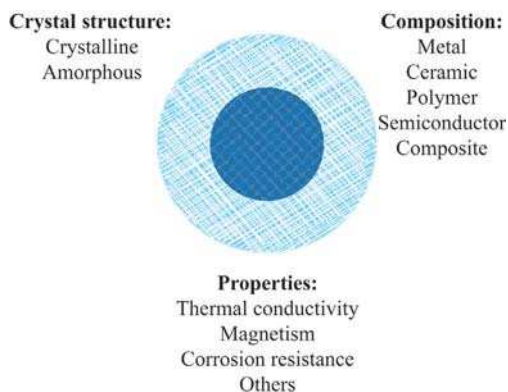


FIGURE 2.29 Illustration of different crystal structure, composition, and properties for core/shell particles.

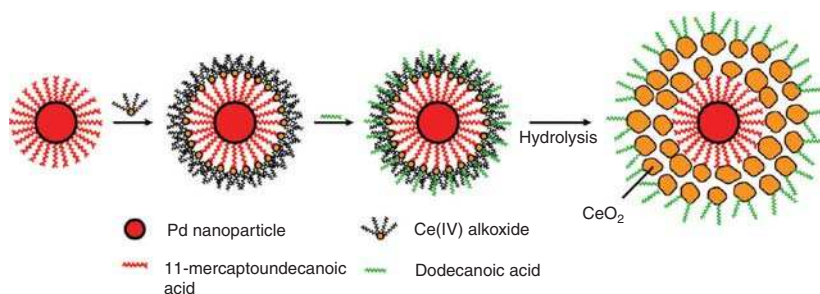


FIGURE 2.30 Schematic representation of the procedure used to obtain dispersible Pd@CeO₂ core-shell nanostructures [136]. (Reprinted with permission from Cargnello M, Wieder NL, Montini T, Gorte RJ, Fornasiero P. Synthesis of dispersible Pd@CeO₂ core-shell nanostructures by self-assembly. *J Am Chem Soc* 2010;132:1402–1409, Copyright 2010, American Chemical Society.)

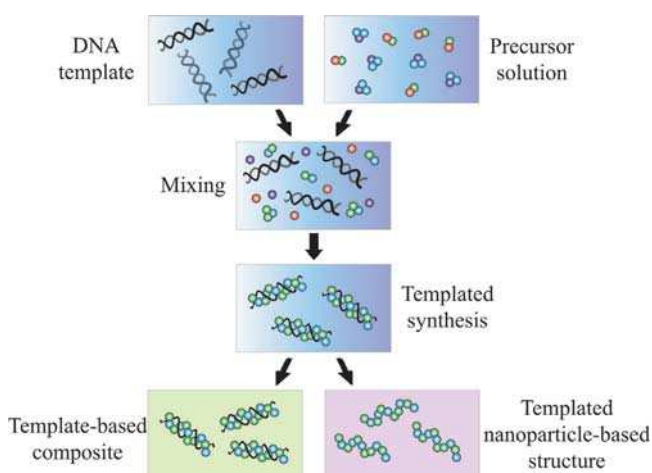
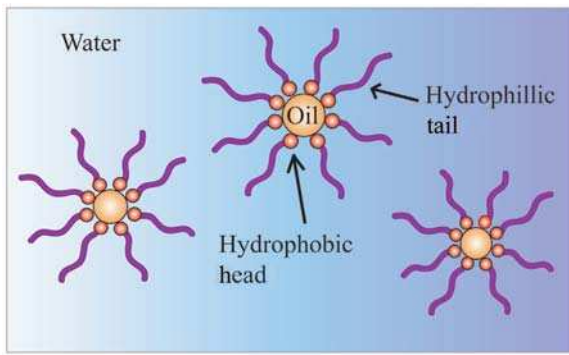
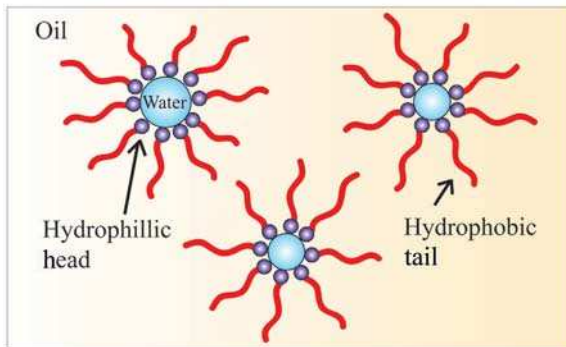


FIGURE 2.34 Illustration of biomimetic synthesis of nanoparticle composite structures or nanoparticle-based assemblies.



Micelles



Reverse micelles

FIGURE 2.38 Micelle and reverse micelle structures.

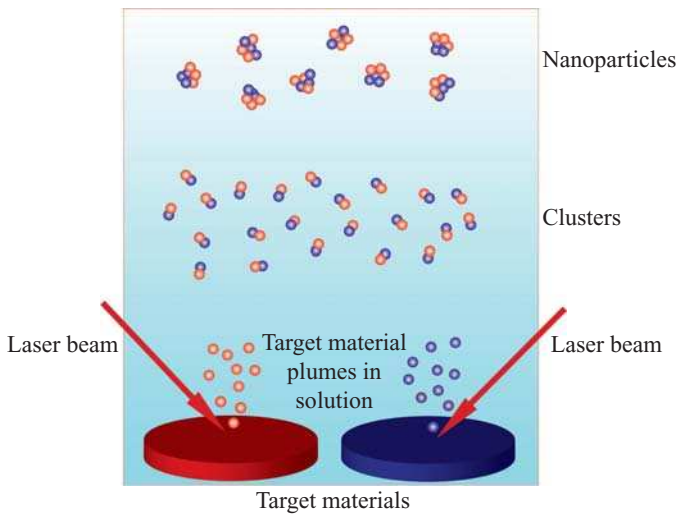


FIGURE 2.40 Illustration of laser-assisted nanoparticle synthesis.

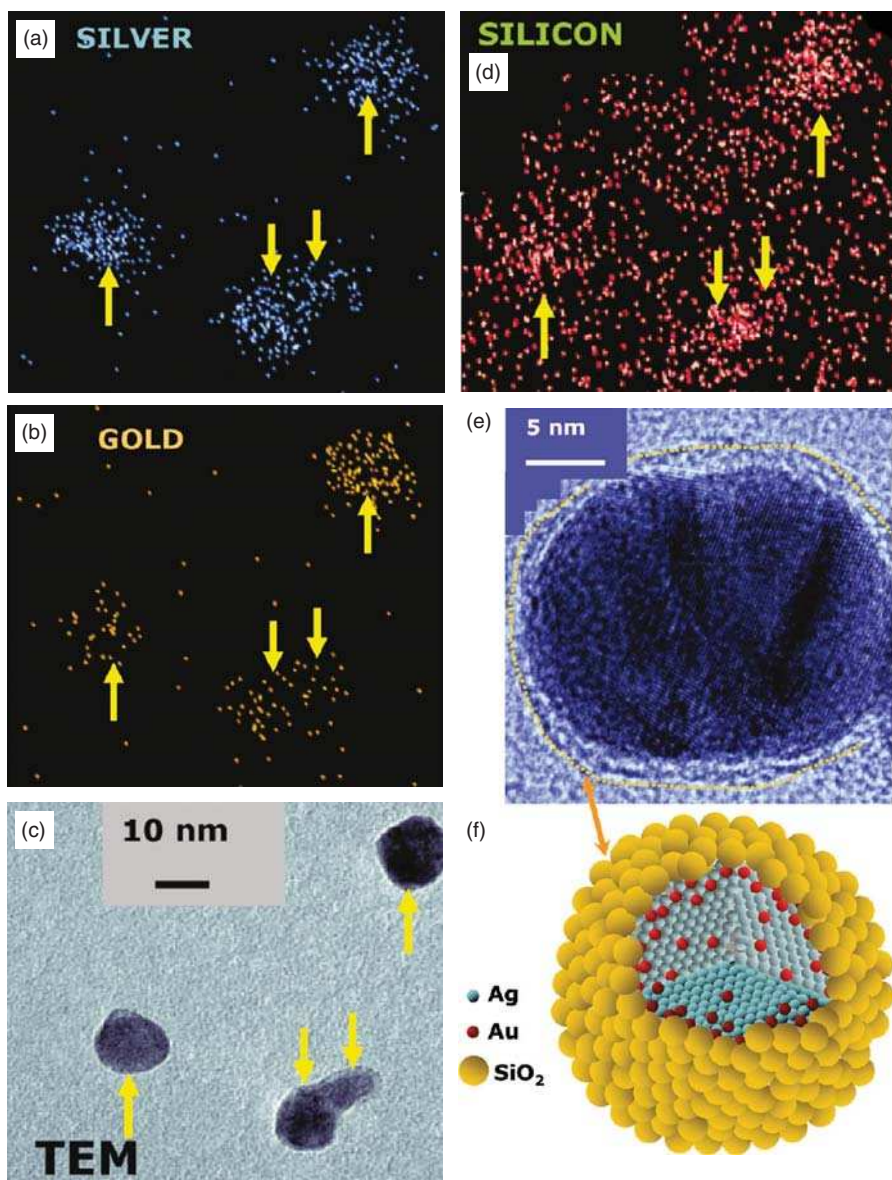


FIGURE 2.41 Energy-dispersive spectroscopy chemical mapping of silver–gold alloy nanoparticles demonstrates the presence of (a) silver and (b) gold in the four nanoparticles marked by arrows and observed in (c) transmission electron image. (d) Other than silver and gold, the energy-dispersive spectroscopy–high-resolution image also reveals the presence of silicon. The limit of the shell is indicated by a dotted line in (e) transmission electron image and illustrated in panel (f) [172]. (Reprinted with permission from Jimenez E, Abderrafi K, Abargues R, Valdes JL, Martinez-Pastor JP. Laser-ablation-induced synthesis of SiO₂-capped noble metal nanoparticles in a single step. *Langmuir* 2010;26:7458–7463, Copyright 2010, American Chemical Society.)

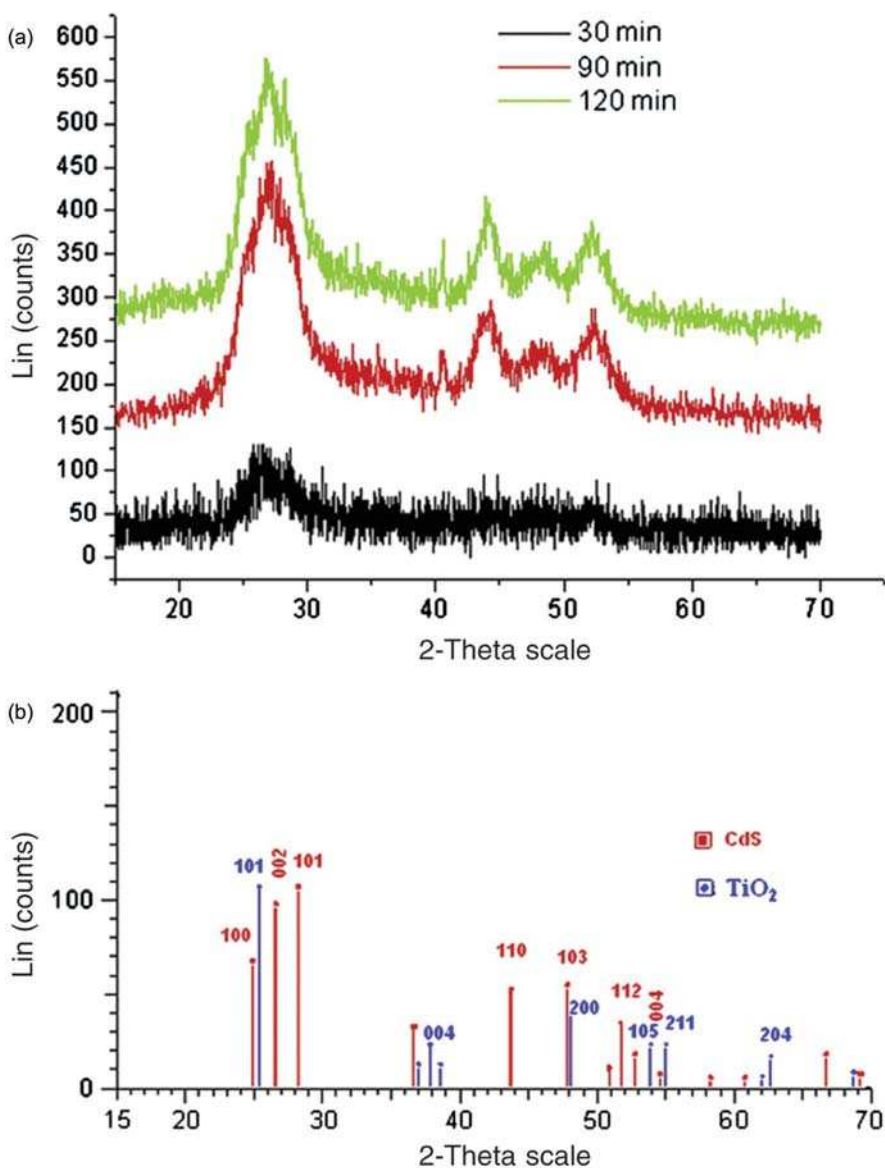


FIGURE 2.44 X-ray diffraction patterns of the prepared CdS/TiO₂ composite at different sonication times (mole ratio = 2.5) [184]. (Reprinted with permission from Ghows N, Entezari MH. Fast and easy synthesis of core-shell nanocrystal (CdS/TiO₂) at low temperature by microemulsion under ultrasound. *Ultrason Sonochem* 2011;18:629–634, Copyright 2011, Elsevier.)

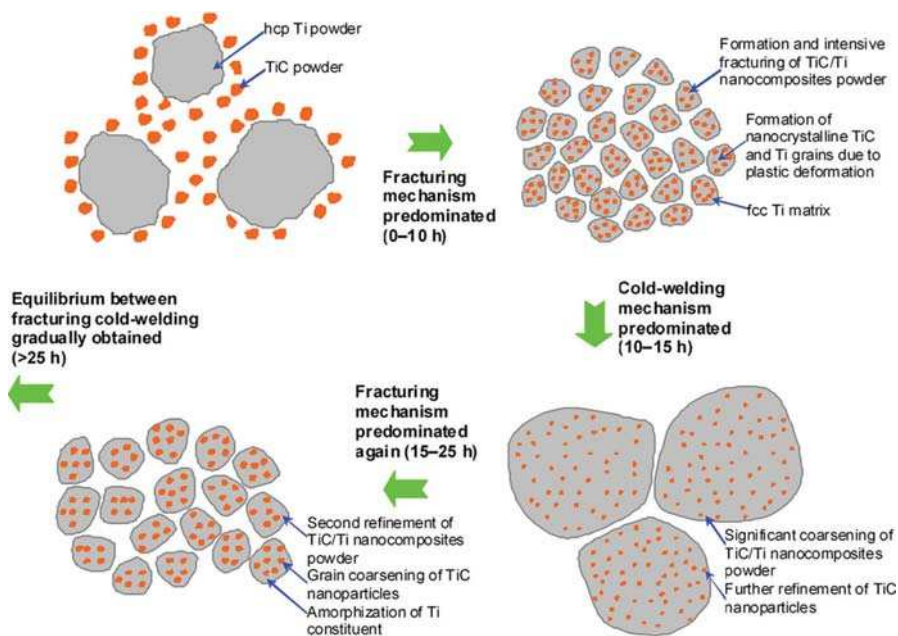


FIGURE 2.46 Schematic diagram of the structural development during milling of TiC/Ti nanocomposite powder [209]. (Reprinted with permission from Gu D, Meiners W, Hagedorn Y-C, Wissenbach K, Poprawe R. Structural evolution and formation mechanisms of TiC/Ti nanocomposites prepared by high-energy mechanical alloying. *J Phys D: Appl Phys* 2010;43:135402-1-1, IOP Publishing, Inc.)

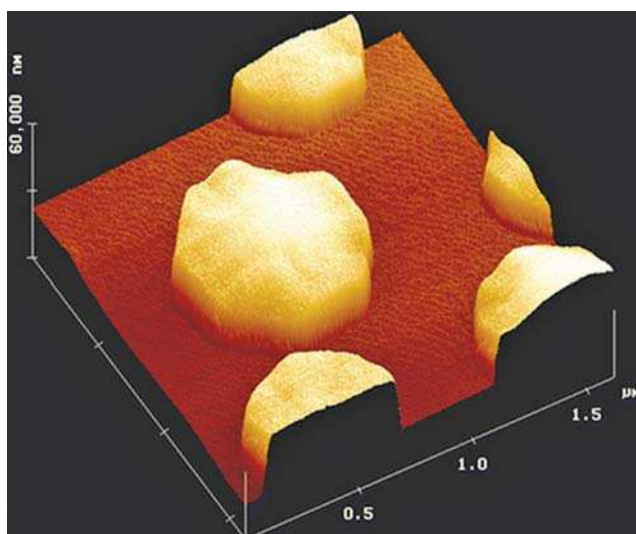


FIGURE 3.3 Atomic force microscopy image of Cu_2O nanodots formed on a SrTiO_3 substrate [5]. (Reprinted with permission from Baer DR, Gaspar DJ, Nachimuthu P, Techane SD, Castner DG. Application of surface chemical analysis tools for characterization of nanoparticles. *Anal Bioanal Chem* 2010;396:983–1002, Springer Science + Business Media, Fig. 6.)

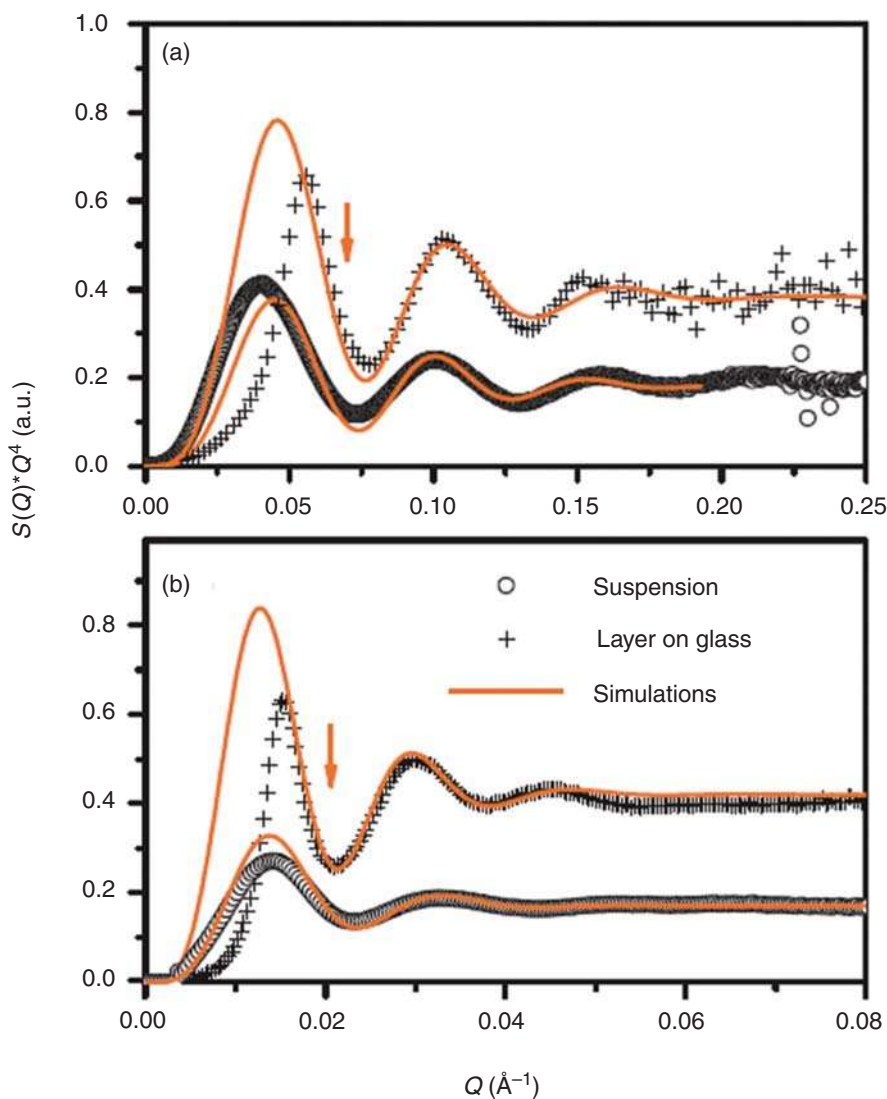


FIGURE 3.7 Small-angle X-ray scattering data from a gold particle suspension (circles) and the corresponding layer (crosses) on a glass surface together with a calculation of the sphere form factor (full lines). The x -axis is the scattering vector and the y -axis is the scattering intensity. In (a), the curves for the smaller particles (11.6 nm) are shown, while in (b), the SAXS from larger particles (39.2 nm) is depicted. The arrows mark the position of a structure factor maximum, when a close packing of particles is assumed. In both cases, the observed maximum is shifted to smaller scattering vectors [18]. (Reprinted with permission from Ciesia F, Plech A. Gold nanoparticle membranes as large-area surface monolayers. *J Colloid Interface Sci* 2010;346:1–7, Copyright 2010, Elsevier.)

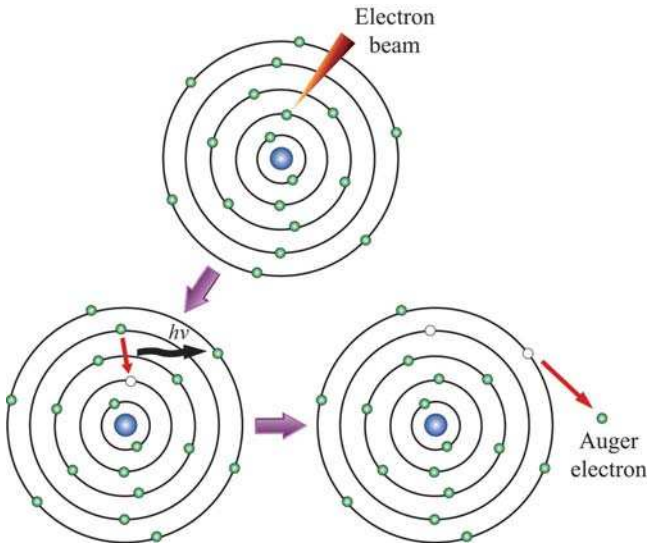


FIGURE 3.14 Auger electron generation process.

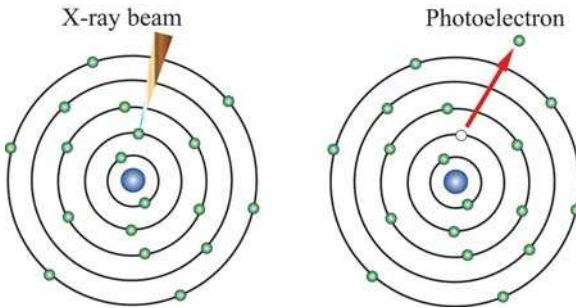


FIGURE 3.16 X-ray photoelectron generation process.

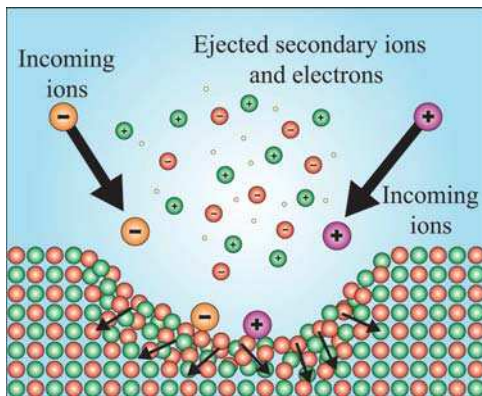


FIGURE 3.18 Ion bombardment process during secondary ion mass spectroscopy.

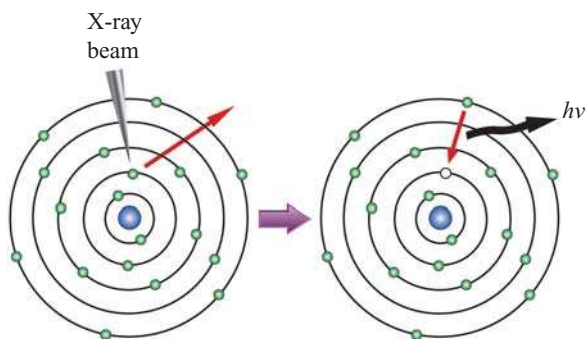


FIGURE 3.19 X-ray fluorescence spectroscopy working mechanism.

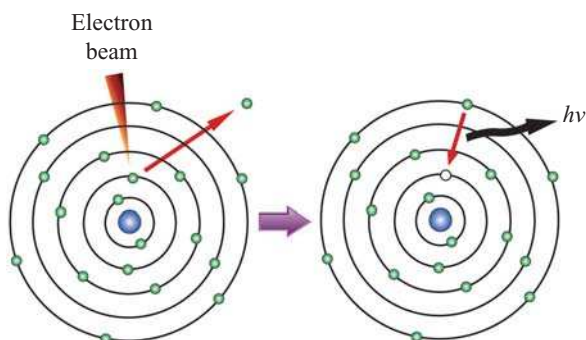


FIGURE 3.20 Energy dispersive spectroscopy working mechanism.

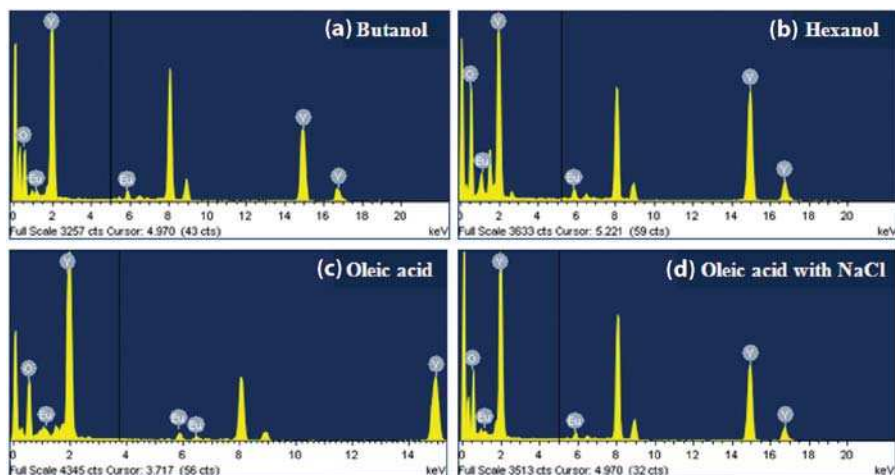


FIGURE 3.21 EDS spectra of annealed $\text{Y}_2\text{O}_3:\text{Eu}^{3+}$ nanoparticles prepared with (a) butanol, (b) hexanol, (c) oleic acid, and (d) oleic acid as surfactants [77]. (Reprinted with permission from Jadhav AP, Kim CW, Cha HG, Pawar AU, Jadhav NA, Pal U, Kang YS. Effect of different surfactants on the size control and optical properties of $\text{Y}_2\text{O}_3:\text{Eu}^{3+}$ nanoparticles prepared by coprecipitation method. *J Phys Chem C* 2009;113:13600–13604, Copyright 2009, American Chemical Society.)

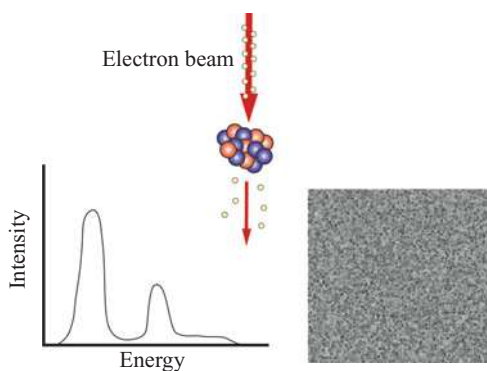


FIGURE 3.22 Electron energy loss spectroscopy illustration.

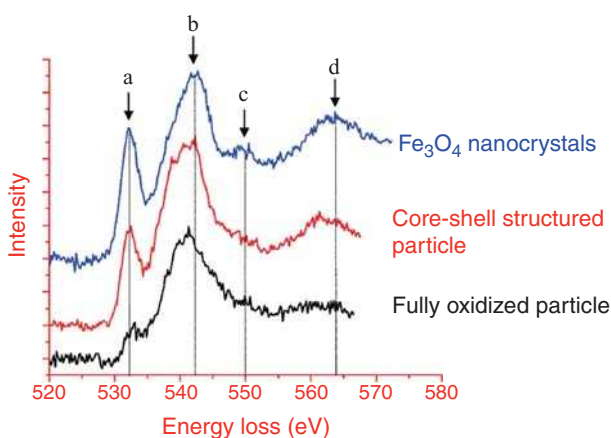


FIGURE 3.23 Comparison of EELS spectra (around 530 eV) collected on standard Fe_3O_4 nanoparticles, core/shell structured iron nanoparticles, and fully oxidized nanoparticles (no iron core at the center). To exclude the uncertainty for the absolute energy-loss scale, the prepeak is aligned at 532 eV, and, for clarity, each spectrum is vertically shifted [80]. (Reprinted with permission from Wang C, Baer DR, Amonette JE, Engelhard MH, Antony J, Qiang Y. Morphology and electronic structure of the oxide shell on the surface of iron nanoparticles. *J Am Chem Soc* 2009;131:8824–8832, Copyright 2009, American Chemical Society.)

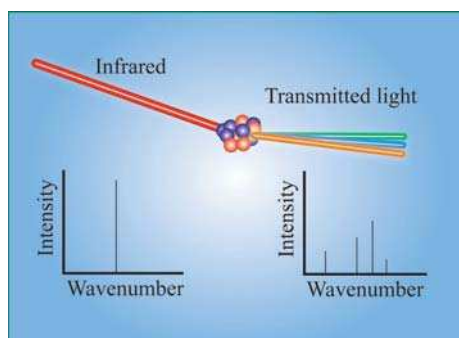


FIGURE 3.24 FT-IR characterization process.

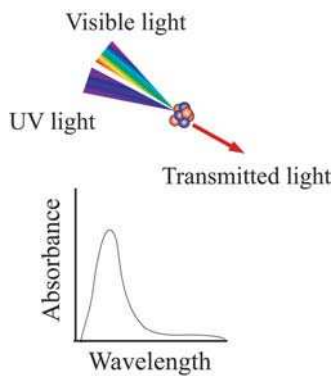


FIGURE 3.26 UV-vis spectroscopy illustration.

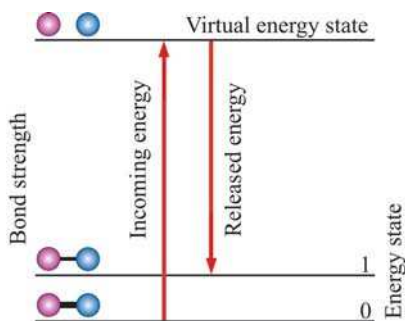


FIGURE 3.28 Different energy states during Raman spectroscopy.

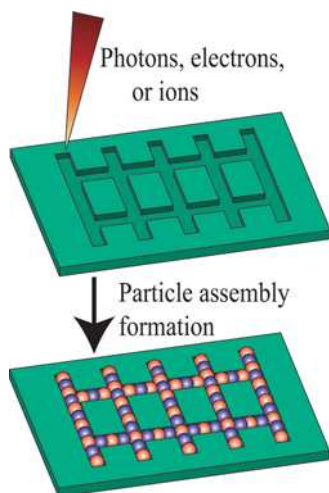


FIGURE 4.1 Top-down process of creating superstructures.

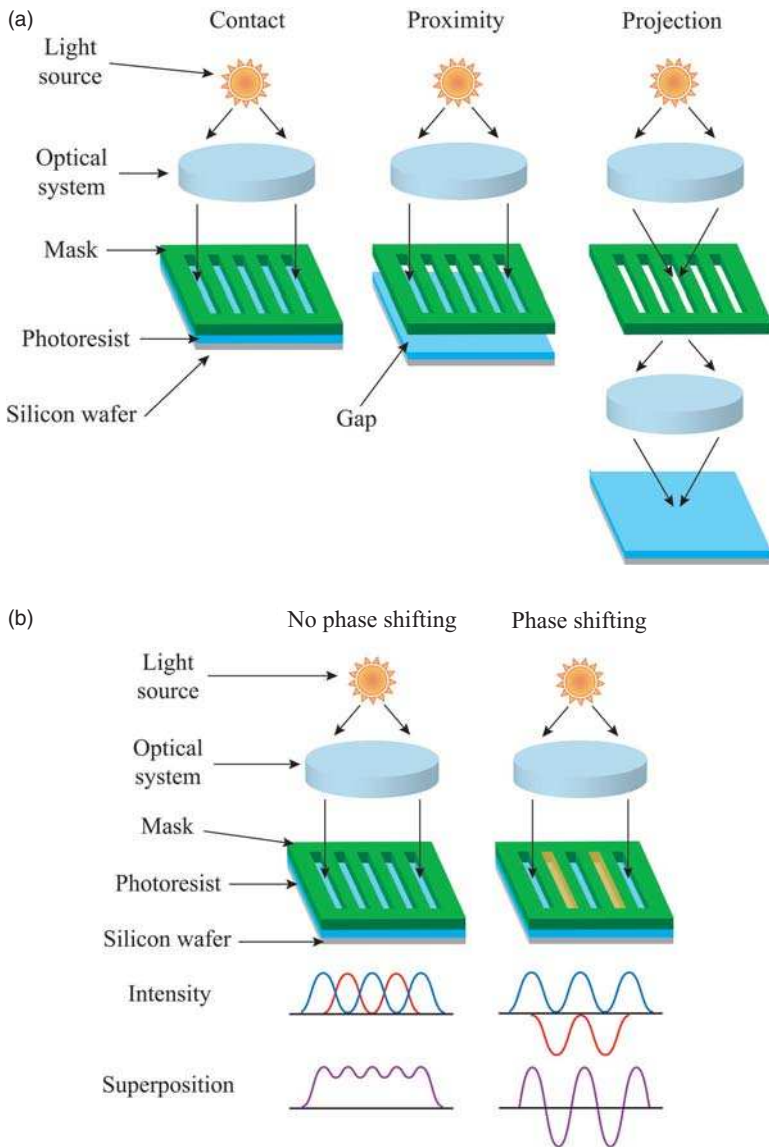


FIGURE 4.2 Photolithography process: (a) contact, proximity, and projection methods, (b) phase shifting photolithography.

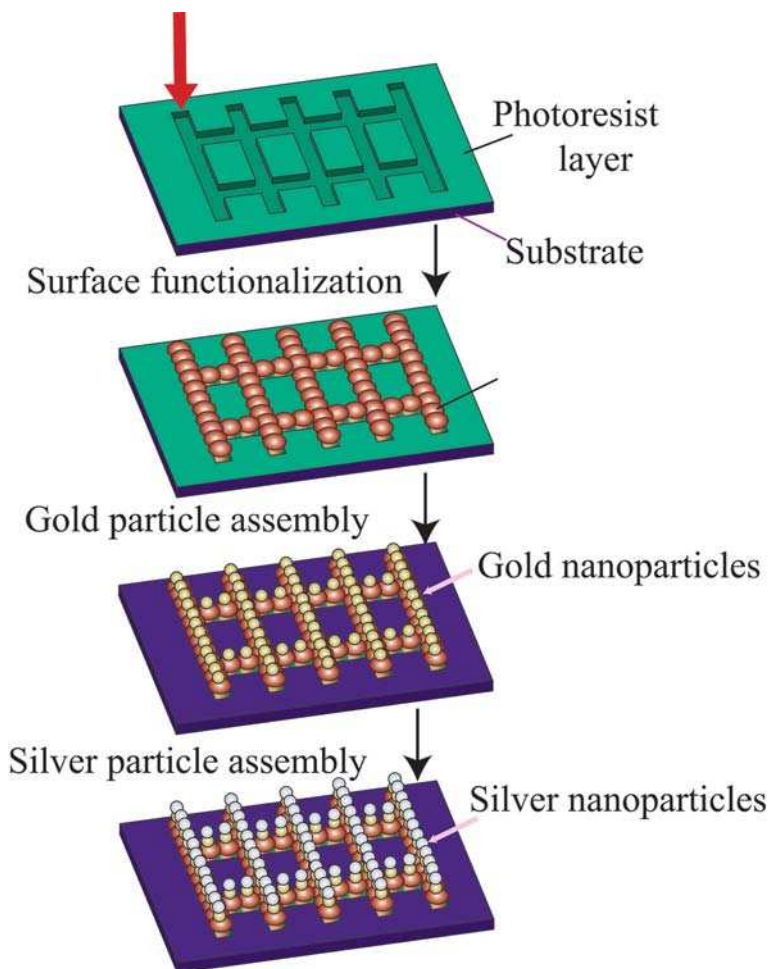


FIGURE 4.3 Silver-gold micropatterns via photolithography.

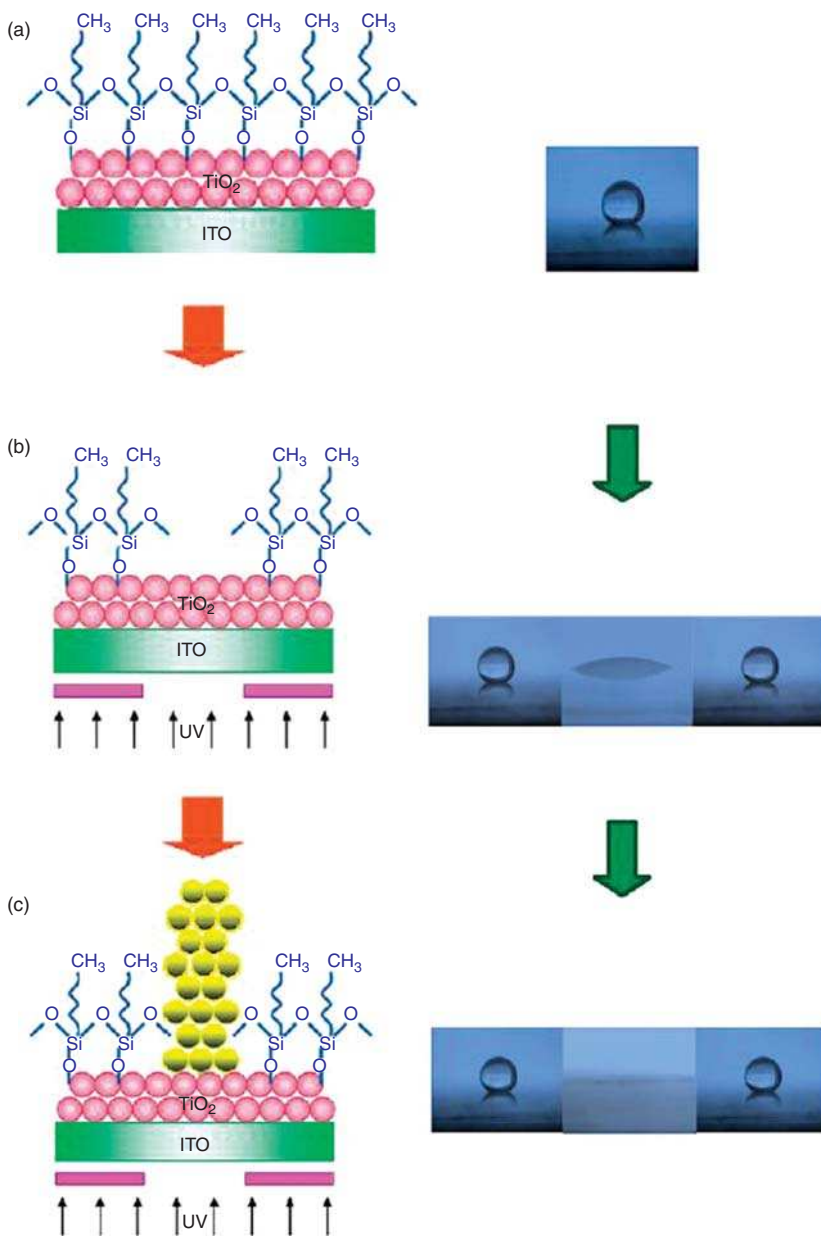


FIGURE 4.5 Fabrication procedure of microelectrode arrays: (a) superhydrophobic ODS-modified TiO_2 film, (b) TiO_2 nanoparticle-based microelectrode arrays after photolithography with a photomask, and (c) metal nanoparticle-based microelectrode arrays after site-selective photocatalytic deposition of metal nanoparticles [5]. (Reprinted with permission from Li X, Tian Y, Xia P, Luo Y, Rui Q. Fabrication of TiO_2 and metal nanoparticle-microelectrode arrays by photolithography and site-selective photocatalytic deposition. *Anal Chem* 2009;81:8249–8255. Copyright 2009, American Chemical Society.)

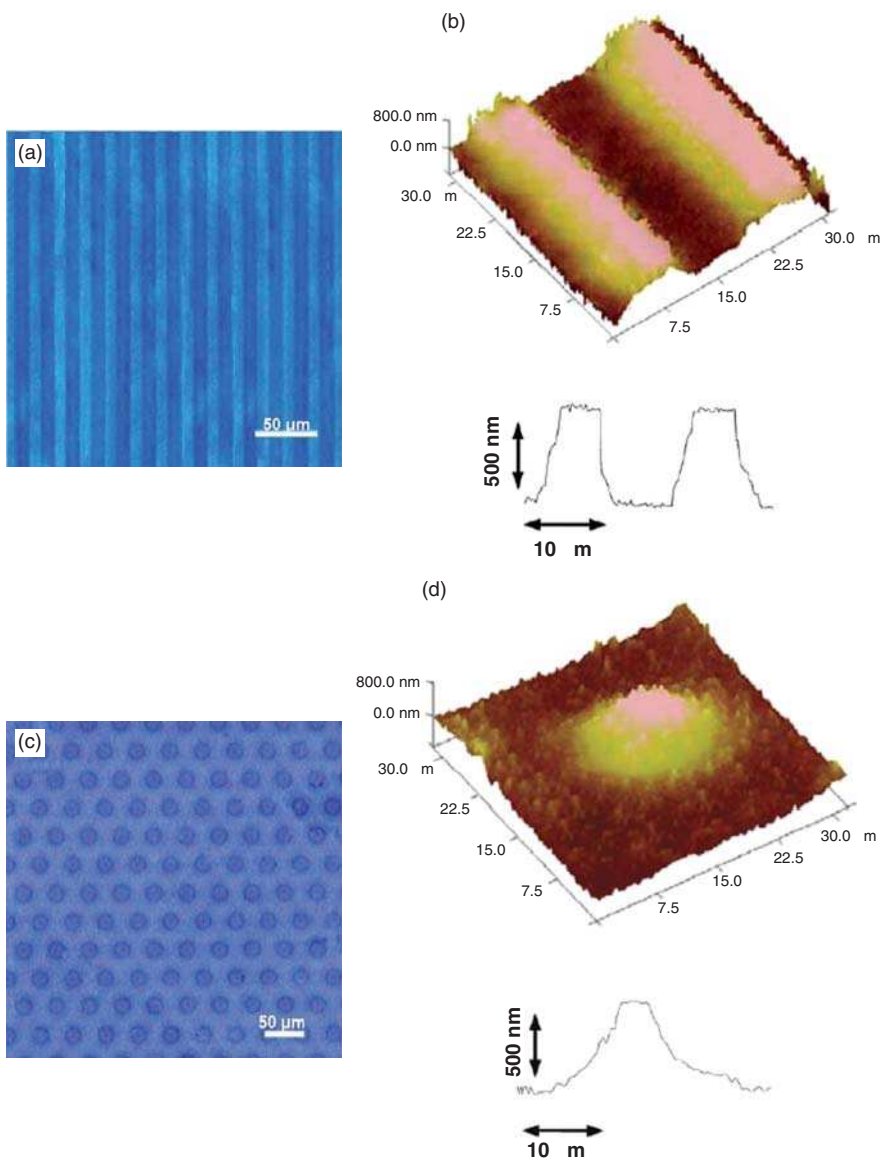


FIGURE 4.7 (a, c) Microscopic images and (b, d) AFM images of elevated gold nanoparticle-based microarray electrodes (a, b) with 10 μm bandwidth and (c, d) with 6 μm disk radius [5]. (Reprinted with permission from Li X, Tian Y, Xia P, Luo Y, Rui Q. Fabrication of TiO_2 and metal nanoparticle-microelectrode arrays by photolithography and site-selective photocatalytic deposition. *Anal Chem* 2009;81:8249–8255, Copyright 2009, American Chemical Society.)

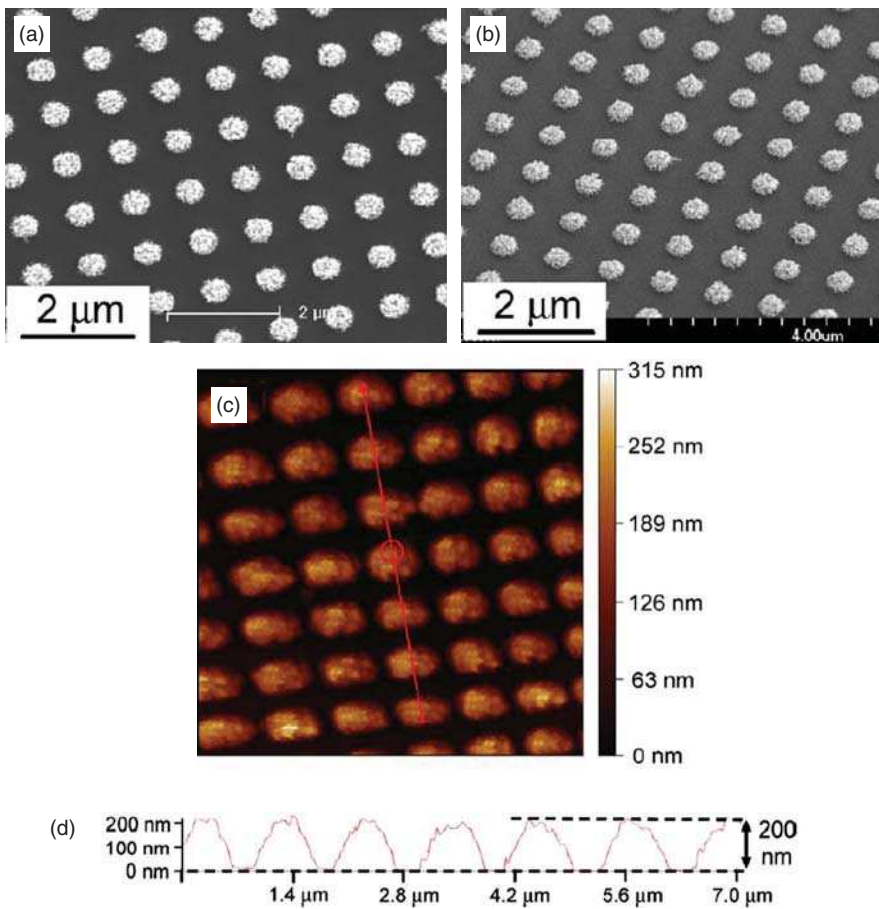


FIGURE 4.11 Scanning electron images of gold nanoparticles (average diameter 13.8 nm) deposited for 60 minutes onto a silicon substrate patterned with circular dots of 500 nm in diameter: (a) top view, (b) 45° tilted view, (c) atomic force microscope image, and (d) height analysis of the image of (c) [13]. (Reprinted with permission from Kawabata S, Naono Y, Taguchi Y, Huh SH, Nakajima A. Designable formation of metal nanoparticle array with the deposition of negatively charged nanoparticles. *Appl Surf Sci* 2007;253:6690–6696, Copyright 2007, Elsevier.)

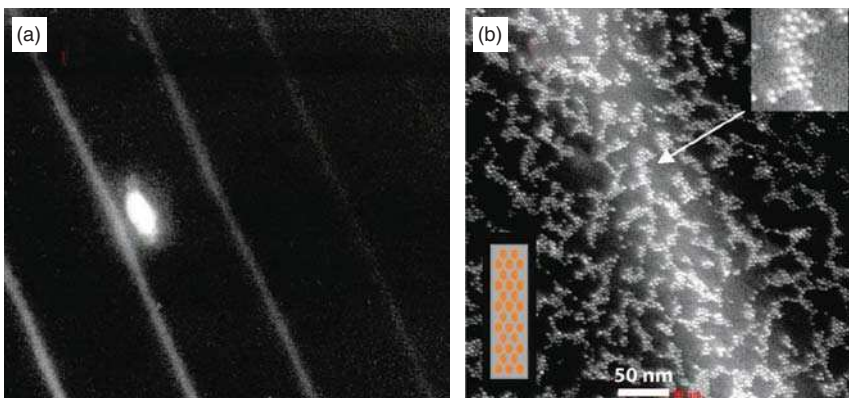


FIGURE 4.12 Scanning transmission electron images of (a) nanowires created by direct electron-beam writing in a submonolayer nanoparticle film (beam energy of 7 keV) and (b) a nanowire at high resolution together with a scheme depicting the network of discrete nanoparticles interconnected by a carbon matrix [15]. (Reprinted with permission from Plaza JL, Chen Y, Jacke S, Palmer RE. Nanoparticle arrays patterned by electron-beam writing: structure, composition, and electrical properties. *Langmuir* 2005;21:1556–1559, Copyright 2005, American Chemical Society.)

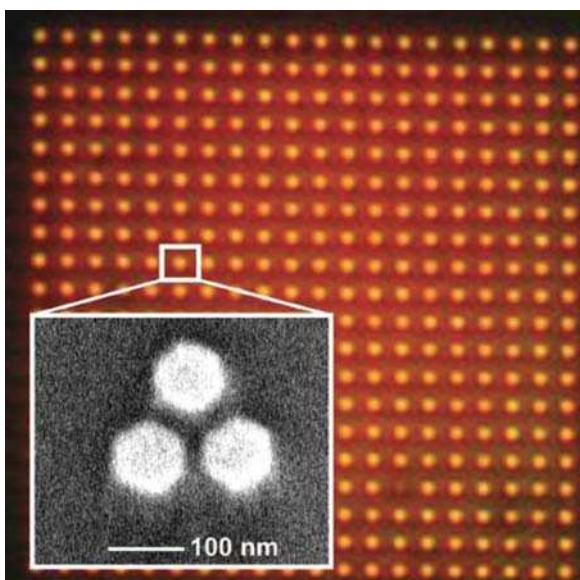


FIGURE 4.13 An array of silver nanoparticle trimers on glass in immersion oil. Each dot corresponds to one individual trimer composed of silver particles with 100 nm diameter and 25 nm height. The nanoparticles have an edge-to-edge distance of 20 nm, while the lattice constant of the array is 1 μm . The inset shows a scanning electron image of one representative silver nanoparticle trimer [17]. (Reprinted with permission from Alegret J, Rindzevicius T, Pakizeh T, Alaverdyan Y, Gunnarsson L, Kall M. Plasmonic properties of silver trimers with trigonal symmetry fabricated by electron-beam lithography. *J Phys Chem C* 2008;112:14313–14317, Copyright 2008, American Chemical Society.)

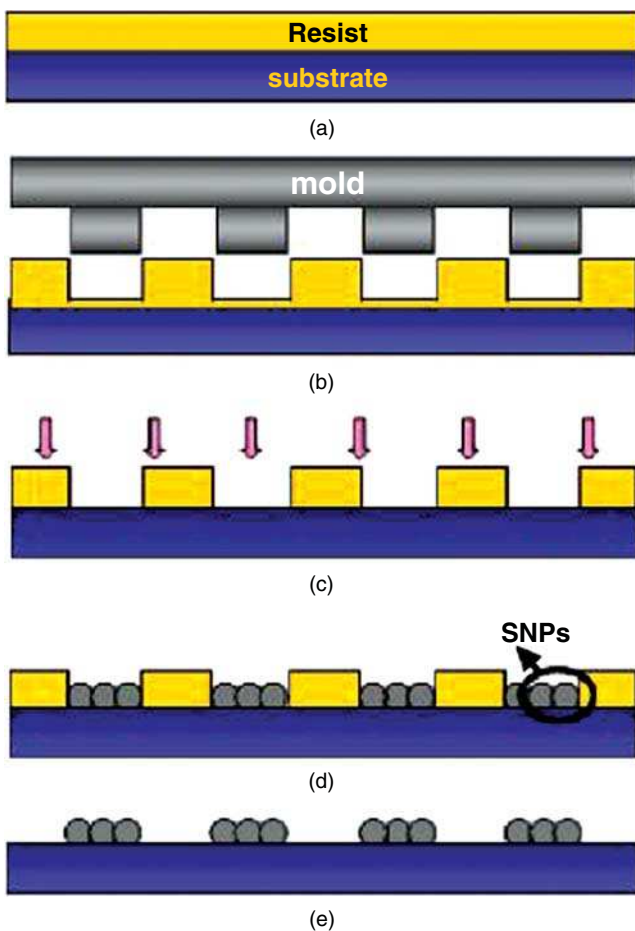


FIGURE 4.17 Schematic illustration of the procedure for fabricating arrays of silver nanoparticles (SNPs). (a) Spin-coating resists polymer onto an indium-doped SnO_2 substrate, (b) imprinting, (c) reactive-ion etching process, (d) electrochemical deposition of silver nanoparticles, and (e) "lift-off" of the resist layer [24]. (Reprinted with permission from Yang B, Lu N, Huang C, Qi D, Shi G, Xu H, Chen X, Dong B, Song W, Zhao B, Chi L. Electrochemical deposition of silver nanoparticle arrays with tunable density. *Langmuir* 2009;25:55–58, Copyright 2009, American Chemical Society.)

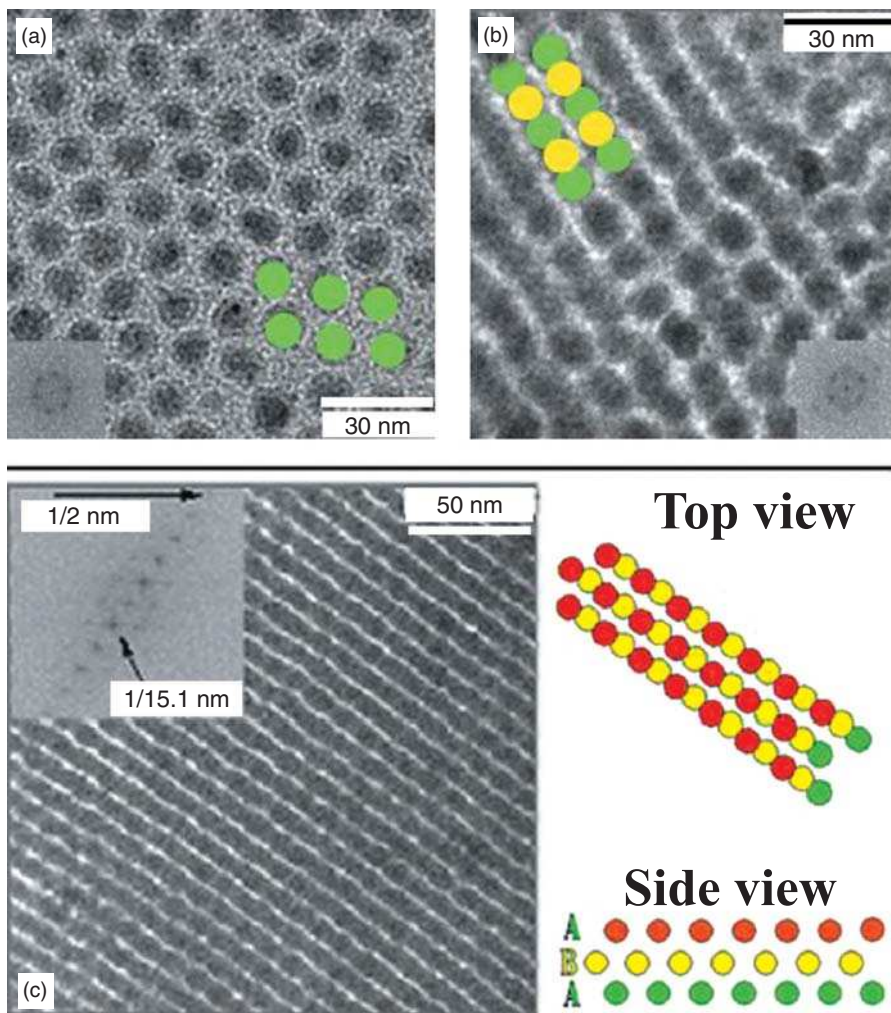


FIGURE 4.22 Transmission electron images of ordered cobalt particles with external applied magnetic fields of (a) 0.8 T, (b) 1.5 T, and (c) 6 T. The schematic diagrams are a guide to understanding the structure of the presented superstructure images [42] (Reproduced with permission from Hilgendorff M, Tesche B, Giersig M. *Aust J Chem* 2001;54(8): 497–510, Copyright CSRIO 2001. Published by CSRIO PUBLISHING, Collingwood, Victoria, Australia – <http://www.publish.csiro.au/nid/51/paper/CH01119.htm>).

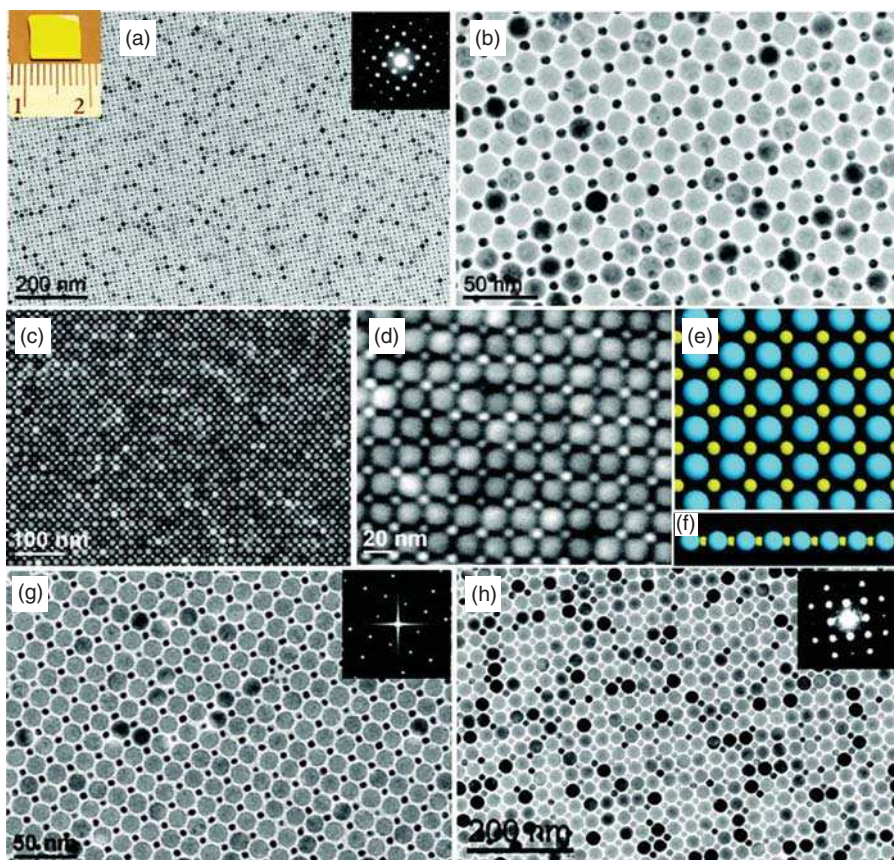


FIGURE 4.30 (a) Transmission electron image and selected area electron diffraction pattern (upper right inset) of an AB-type binary superlattice monolayer self-assembled from 16.5 nm Fe_3O_4 and 6.4 nm Au nanoparticles. The upper left inset shows a photograph of a SiO_2/Si wafer coated with a typical AB-type binary superlattice monolayer membrane. (b) High-magnification transmission electron image of the AB-type binary superlattice monolayer. High-resolution scanning electron images of an AB-type binary superlattice monolayer monolayer at low (c) and high (d) magnifications, respectively. Structural models of the AB-type binary superlattice monolayer from top (e) and side (f) views, respectively. (g) Transmission electron image and Fourier transform (inset) of an AB-type binary superlattice monolayer self-assembled from 16.5 nm Fe_3O_4 and 5.5 nm FePt nanoparticles. (h) Transmission electron image and selected area electron diffraction pattern (inset) of an AB-type binary superlattice monolayer consisting of 28.9 nm $\text{NaFY}_4:\text{Yb/Er}$ and 13.4 nm Fe_3O_4 nanoparticles [65]. (Reprinted with permission from Dong A, Ye X, Chen J, Murray CB. Two-dimensional binary and ternary nanocrystal superlattices: the case of monolayers and bilayers. *Nano Lett* 2011;11:1804–1809, Copyright 2011, American Chemical Society.)

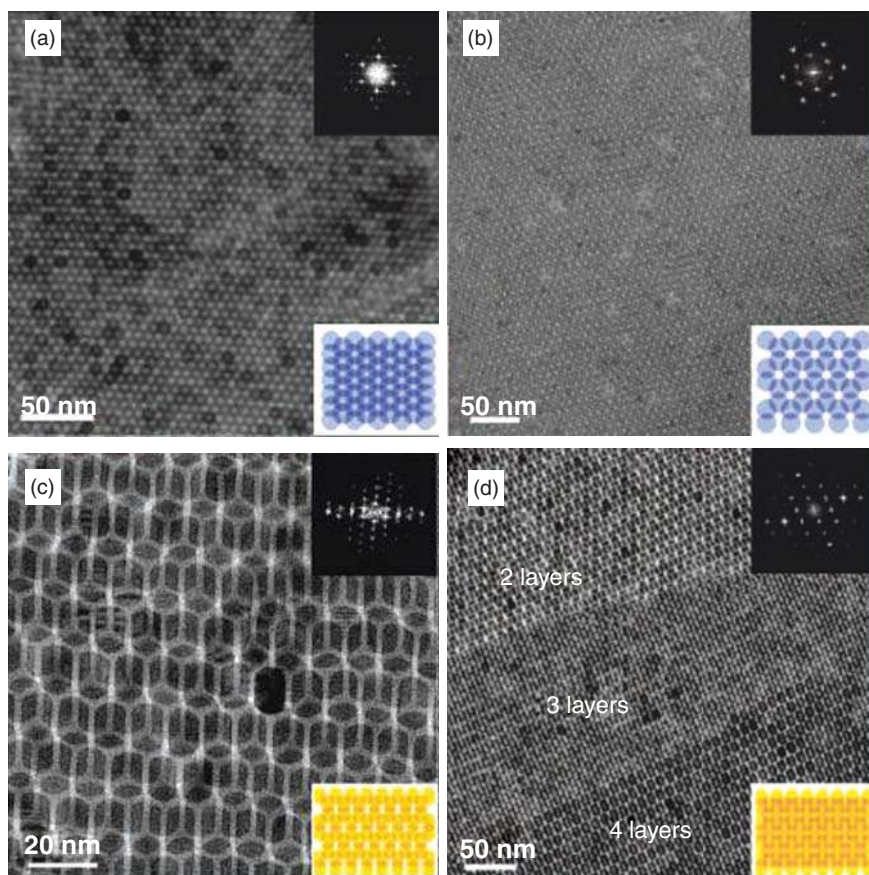


FIGURE 4.31 Transmission electron images of Cu_2S nanoparticle assemblies: (a) face-centered cubic-packed spherical nanoparticles, (b) hexagonal close-packed spherical nanoparticles, (c) two layers of close-packed elongated nanoparticles, and (d) multilayers of elongated nanoparticles. The top insets are the corresponding Fourier transform patterns, and the bottom insets are the schemes of the stacking of nanoparticles [66]. (Reprinted with permission from Zhuang Z, Peng Q, Zhang B, Li Y. Controllable synthesis of Cu_2S nanocrystals and their assembly into a superlattice. *J Am Chem Soc* 2008;130:10482–10483, Copyright 2008, American Chemical Society.)

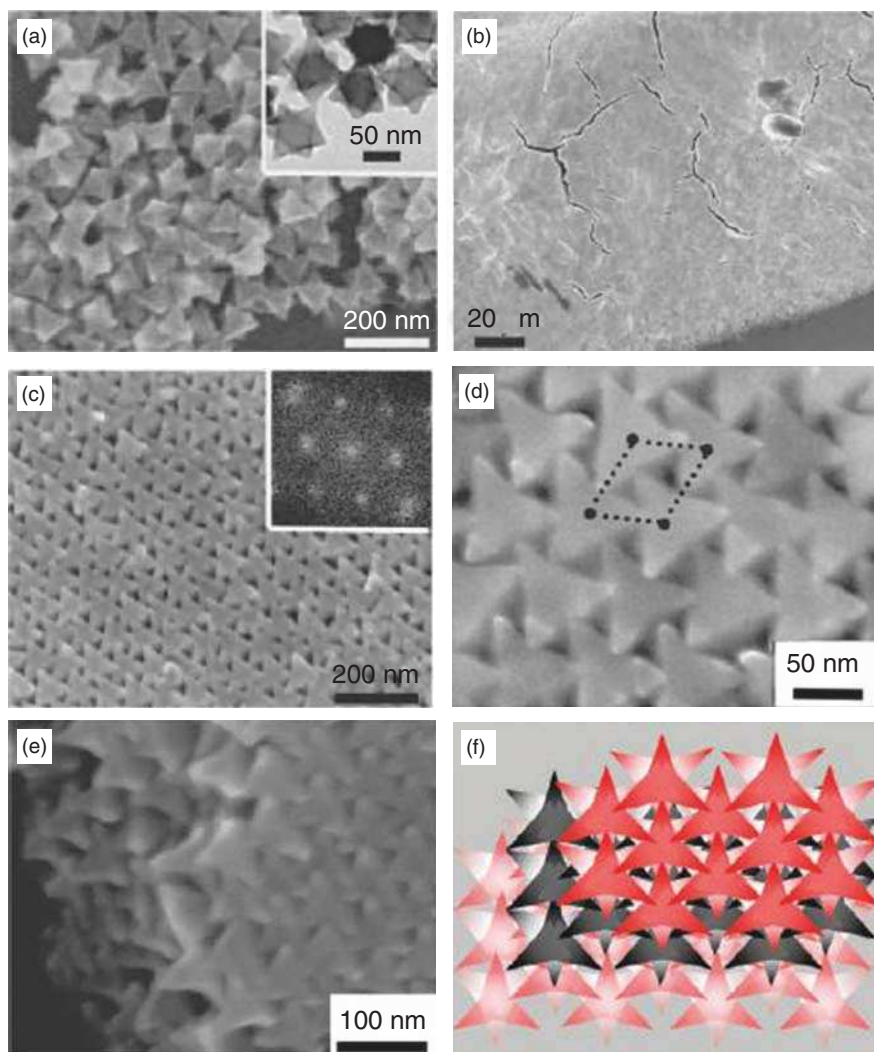


FIGURE 4.41 Scanning electron images of (a) PbS nanostars and (b–e) their three-dimensional hexagonal close-packed assemblies obtained by drop coating. (f) Schematic illustration of the three-dimensional hexagonal close-packed structures of six-horn stars. Inset in (a) is a transmission electron image of PbS nanostars, and the inset in (c) is the corresponding Fourier transform [106]. (Reprinted with permission from Huang T, Zhao Q, Xiao J, Qi L. Controllable self-assembly of PbS nanostars into ordered structures: close-packed arrays and patterned arrays. *ACS Nano* 2010;4:4707–4716, Copyright 2010, American Chemical Society.)



FIGURE 5.3 Cu/ α -Al₂O₃ bulk sample under three levels of explosion pressure [34]. (Reprinted with permission from Zhao Z, Li X-J, Tao G. Manufacturing nano-alumina particle-reinforced copper alloy by explosive compaction. *J Alloys Compd* 2009;478:237–239, Copyright 2009, Elsevier.)

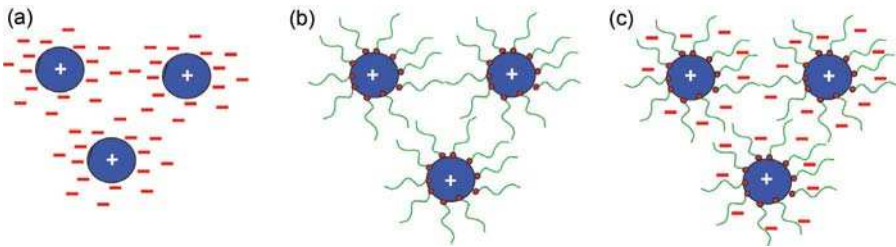


FIGURE 5.10 Different mechanisms of nanoparticle interaction and stabilization: (a) electrostatic stabilization, (b) steric stabilization, and (c) electrosteric stabilization.

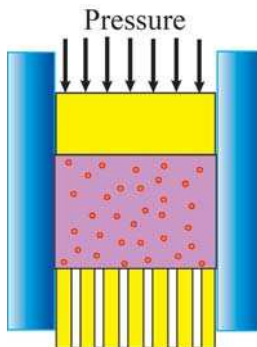


FIGURE 5.11 Uniaxial pressure casting setup illustration.

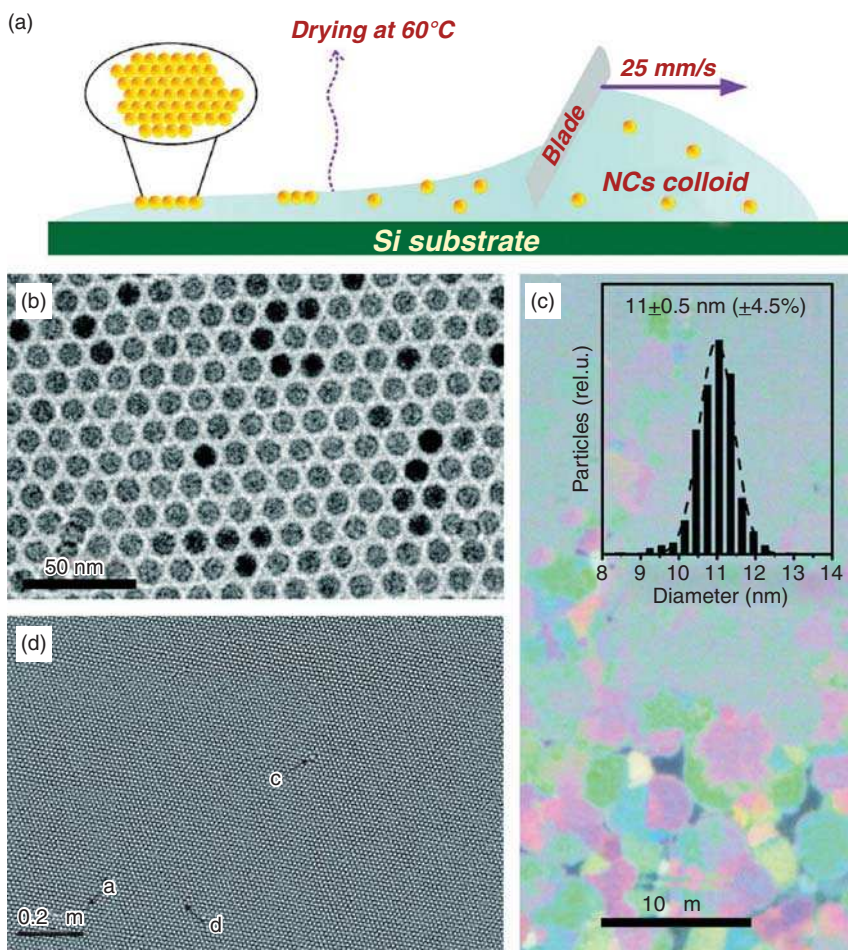


FIGURE 5.13 (a) Sketch of the tape casting process in which nanoparticles assemble at the liquid–air interface. (b) Transmission electron image of $\text{Fe}_x\text{O}/\text{CoFe}_2\text{O}_4$ nanoparticles of 11 nm size. (c) Optical microscope image of the nanoparticle film exhibiting separate islands only at the border of the substrate. The inset shows the size distribution of the 11 nm $\text{Fe}_x\text{O}/\text{CoFe}_2\text{O}_4$ nanoparticles used. (d) Background flattened scanning electron image of the 11 nm $\text{Fe}_x\text{O}/\text{CoFe}_2\text{O}_4$ nanoparticles deposited by doctor blade casting on a Pt-covered silicon substrate. The labeled arrows indicate point defects in the nanoparticle superlattice [91]. (Reprinted with permission from Bodnarchuk M, Kovalenko MV, Pichler S, Fritz-Popovski G, Hesser G, Heiss W. Large-area ordered superlattices from magnetic wustite/cobalt ferrite core/shell nanocrystals by doctor blade casting. *ACS Nano* 2010;4:423–431, Copyright 2010, American Chemical Society.)

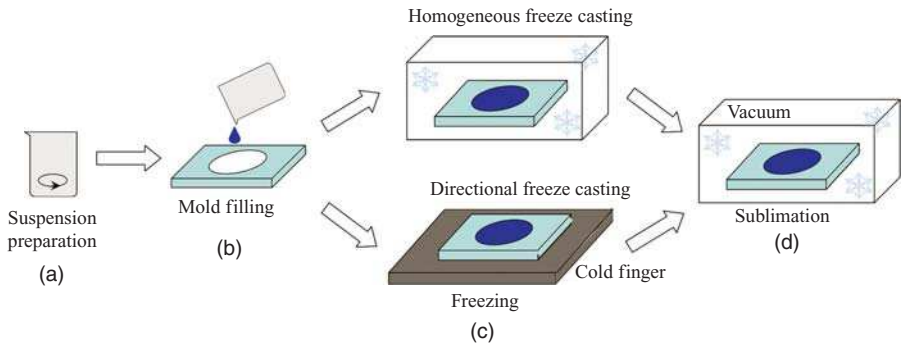


FIGURE 5.14 Illustration of the freeze casting process [99]. (Reprinted with permission from Li W, Lu K, Walz JY. Freeze casting of porous materials—a review of critical factors in microstructure evolution. *Int Mater Rev* 2012;57:37–60, www.maney.co.uk/journals/imr, Maney Publishing.)

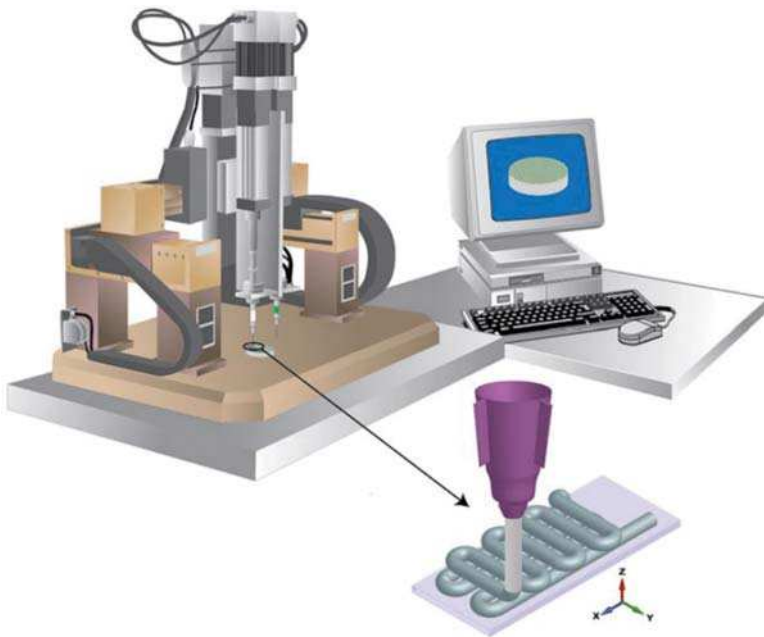


FIGURE 5.21 A schematic representation of the robocasting process. A suspension is extruded through a thin nozzle to build a part layer-by-layer following a computer design [161]. (Reprinted with permission from Munch E, Franco J, Deville S, Hunger P, Saiz E, Tomsia AP. Porous ceramic scaffolds with complex architectures. *JOM* 2008;60:54–58, Springer Science + Business Media, Fig. 1.)

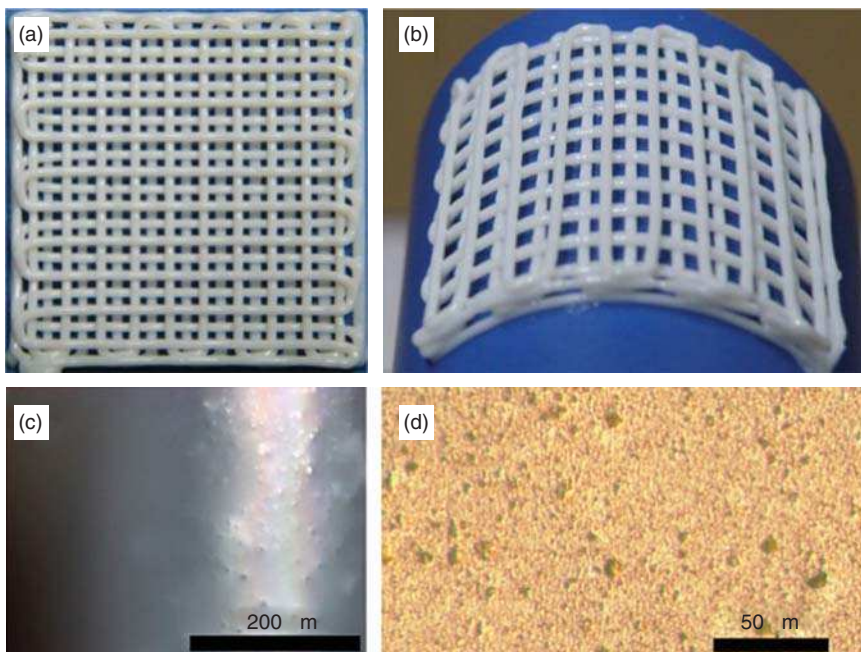


FIGURE 5.24 Images of assembled structures on different scales: (a) a four-layer scaffold piled by perpendicular rods with $500\ \mu\text{m}$ diameter and $2\ \text{mm}$ interrod distance in a $20\ \text{mm} \times 20\ \text{mm}$ square, (b) bending of the formed structure, (c) agglomeration of nanoparticles at the rod's surface, and (d) magnified image of the nanoparticle-doped ink [166]. (Reprinted with permission from Cai K, Sun J, Li Q, Wang R, Li B, Zhou J. Direct-writing construction of layered meshes from nanoparticle-vaseline composite inks: rheological properties and structures. *Appl Phys A* 2011;102:501–507, Fig. 6.)

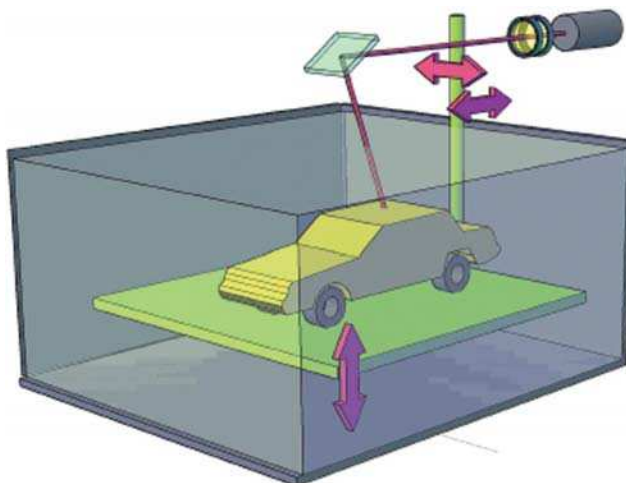


FIGURE 5.25 Schematic representation of the stereolithography process.

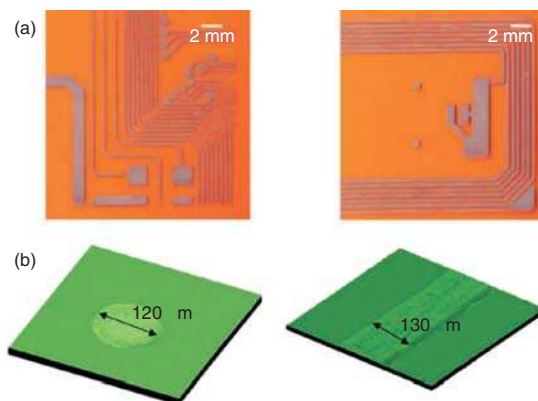


FIGURE 5.27 (a) Conductive patterns ink-jet printed on polyimide substrates using copper nanoparticles and (b) confocal images of a single ink droplet after drying and a single printed line [173]. (Reprinted with permission from Jeong S, Woo K, Kim D, Lim S, Kim JS, Shin H, Xia Y, Moon J. Controlling the thickness of the surface oxide layer on Cu nanoparticles for the fabrication of conductive structures by ink-jet printing. *Adv Funct Mater* 2008;18:679–686, John Wiley & Sons.)

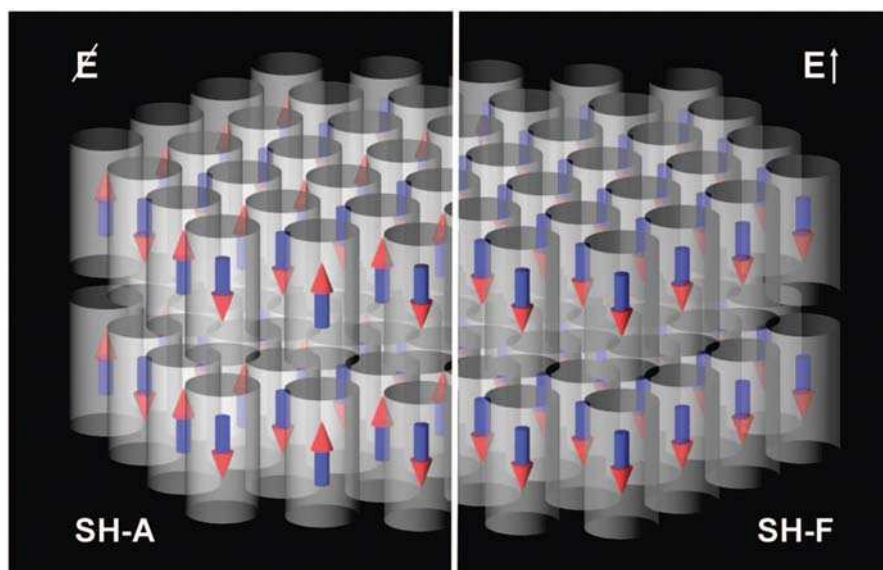


FIGURE 7.4 (left) Nanorods in the bilayer cluster with a hexagonal symmetry formed on the substrate. The nanorod dipoles are vertically oriented in the antiferroelectric order, which provides the lowest possible energy. (right) Nanorods in a bilayer cluster with a hexagonal symmetry that are formed perpendicularly to the substrate in the presence of the electric field. The nanorod dipoles are oriented in the ferroelectric order antiparallel to the field [7]. (Reprinted with permission from Titov AV, Kral P. Modeling the self-assembly of colloidal nanorod superlattices. *Nano Lett* 2008;8:3605–3612, Copyright 2008, American Chemical Society.)

CHAPTER 1

INTRODUCTION

1.1 OVERVIEW

Nanoscale science and technology have become an indispensable part of technological advancement in modern day society. Many books have been written on the subject [1–3]. Nanomaterial understanding, advancement, and development are an important part of this active area, since nanomaterials are the fundamental building blocks of nanoscale devices, modules, and instruments. Historically, materials development has been the cornerstone of human civilization and nanomaterials are no exceptions. It is reasonable to say that nanomaterials are the cornerstone of nanoscale science and engineering. Because of this importance, extensive research on nanomaterials is ongoing all over the globe and a few books have emerged on this topic [4–6]. However, most of these books are introductory in nature and cover a wide spectrum of nanomaterial topics. There is a lack of specific books that focus on nanomaterial fundamental understanding, research, and development even though this is much needed.

Nanomaterial research is multidisciplinary in nature and spans physics, chemistry, biology, and engineering. In this vast field, a long studied and still evolving topic is nanoparticle-based materials (shown in Fig. 1.1). Even though nanoparticle synthesis is one of the earliest and most mature fields in the nanotechnology area, there is a lack of methodic discussion of nanoparticle synthesis, nanostructure construction, and processing of nanoparticle-based bulk materials. Thousands of research papers have been written on nanoparticle-related technical issues. Nanoparticle synthesis, characterization, assembly, and processing

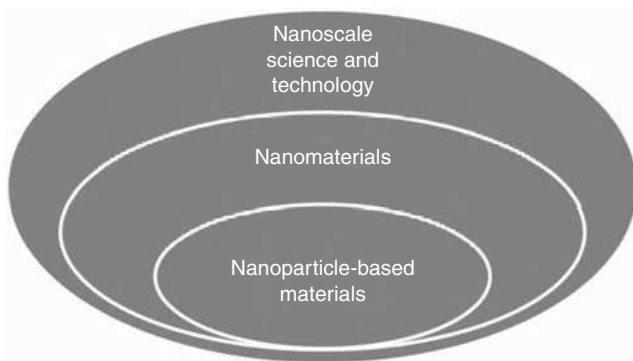


FIGURE 1.1 Relationships of the involving nanofields.

have greatly advanced. Many industries are actively engaged in the research and development of nanoparticle-based materials and products. However, there is no dedicated book on this important and exciting, yet challenging, topic. In light of this, it is highly desired to examine this specific subject in a comprehensive manner and provide a systematic treatment of this field to the people who are either active in the field or are interested in understanding more about the field. A more advanced and nanoparticle-focused book that moves beyond the introduction stage is in great demand and this book aims to serve this purpose.

1.2 NANOPARTICLE-BASED MATERIALS

Dimension-wise, atoms and molecules are in the range of angstroms to nanometers; bulk materials are in the hundreds of microns and greater. In between these two ranges exist a special group of materials that can be grouped as particles, which can be further divided into micron to submicron particles and nanoparticles. For the micron to submicron level particles, extensive studies have been conducted; many excellent books have been written related to the synthesis, processing, and application of micron-sized particles [7, 8]. Because of this, the treatment of this topic is omitted in this book. Nanoparticle-based materials, on the other hand, involve making, evaluating, and processing entities that are up to three orders of magnitude smaller than micron-sized particles. This group of materials often exhibits exciting properties, and the corresponding length scale bridges the gap between individual atoms/molecules and bulk components; thus, they are the focus of this book.

To understand nanoparticle-based materials, it is conducive to first provide a proper definition of a nanoparticle itself. A nanoparticle can be defined as any microscopic particle <100 nanometers (nm) in size and behaves as a whole unit in terms of its transport, functional, and structural properties and its interaction with other species and its environment. The term “nanoparticle” might be new,

but nanoparticles themselves had been in existence long before the word was coined. For example, medieval church windows had gold and silver nanoparticles dispersed in a glass matrix to produce different beautiful colors while also purifying the air. The color production was accomplished by the size-dependent absorption of visible light by the metal nanoparticles. In addition, when the metal nanoparticles were energized by the sun, they were able to destroy airborne pollutants, like volatile organic chemicals, which may often come from the paint in the building.

Since an atom generally has $\sim 1 \text{ \AA}$ size, a cluster of 1 nm radius would consist of ~ 25 atoms and most of the atoms would be on the surface. Compared to some large molecules with hundreds or thousands of atoms, such as many polymer molecules, a nanoparticle might be much smaller. The nanosize by itself does not warrant unique nanomaterial behaviors or exciting properties. What makes nanoparticles such an interesting and unique material category is that their size is smaller than the critical dimensions that characterize many physical phenomena, such as thermal diffusion length, light wavelength, and electron mean free path. When a dimension is less than these critical lengths, new physics or chemistry is likely to occur, such as catalytic properties or quantum effects. The intent of this book is to provide a treatment of nanoparticle-based synthesis, characterization, and processing issues that have the potential to offer improved or unique performance traits. Diminishing in size alone does not warrant special treatment of the topic.

Nanoparticle-based systems, structures, and materials are particulate collections with either one dimension of the individual entity or the basic constituent size at $< 100 \text{ nm}$. In this broad sense, nanoparticle-based materials can come in many different forms, such as loose dry powders, nanoparticle suspensions, engineered nanoparticle architectures, or sintered nanograin-based bulk components. From a different perspective, nanoparticle materials can be metals, oxides, semiconductors, or polymers. For this book, polymer-based nanomaterials will not be discussed extensively since many of the corresponding processing issues are very different from those of metals, oxides, and semiconductors and deserve a separate treatment. Metals, oxides, and semiconductors, on the other hand, share many similarities in synthesis, assembly, and bulk processing and will be covered in this book. With this understanding, the nanoparticle-based materials to be discussed can be composed of one species or multiple species. When multiple species are involved, the resulting materials are called nanoparticle-based composites. Figure 1.2 shows species, scales, and formats of nanoparticle-based materials.

1.3 UNIQUE CHARACTERISTICS

The unique length range of nanoparticle-based materials bridging atomic to micron dimensions is reflected in many of their characteristics. This includes surface behaviors, vapor pressure, solubility, and size-dependent characteristics.

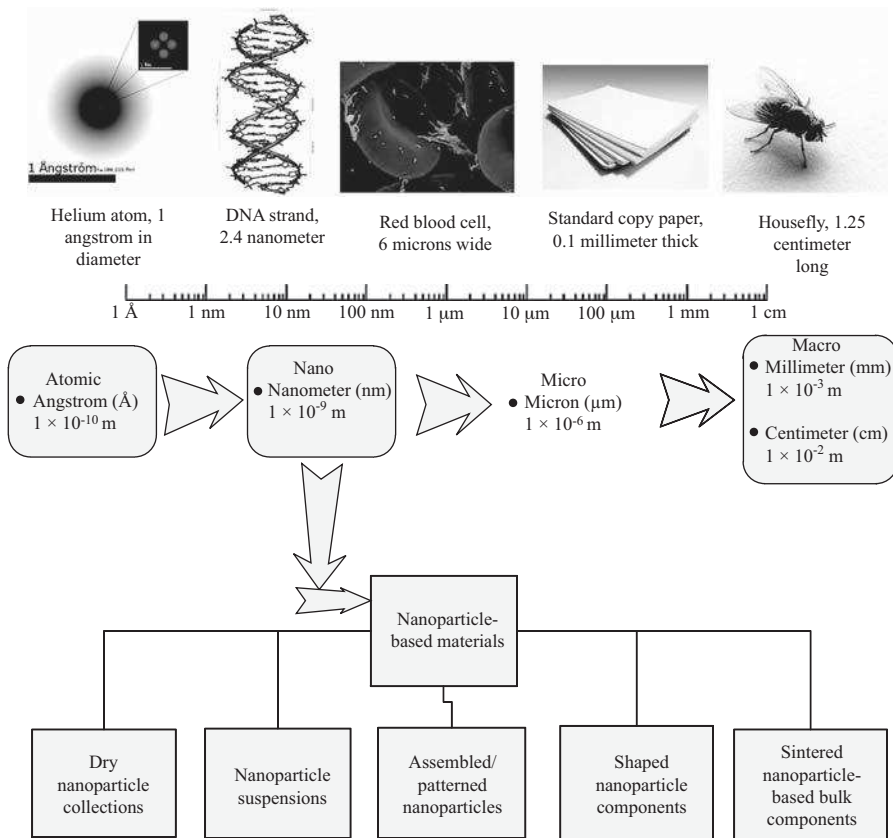


FIGURE 1.2 Illustration of species, scales, and formats of nanoparticle-based materials. (For a color version of this figure, see the color plate section.)

1.3.1 Surface Behaviors

One of the most distinct characteristics of nanoparticle-based materials is the large surface/interface energy available for consumption. Figure 1.3 shows that specific surface area and surface species content increase with particle size decrease. For example, for a gram of TiO_2 particles, the specific surface area increases from $1.41 \text{ m}^2 \text{ g}^{-1}$ to $281.69 \text{ m}^2 \text{ g}^{-1}$ and the percent of surface species increases from 0.18 vol% to 36 vol% when the particle size decreases from 100 μm to 5 nm . Along with the very large specific surface area, nanoparticle-based materials exhibit extremely high surface activity. This explains why nanoparticles are excellent candidates for antibacterial agents, sensors, and catalysts. However, nanoparticles can also undesirably adsorb or react with species in the environment. If nothing else, nanoparticles have a high tendency for agglomeration at a dry state. For liquid-based processes, nanoparticle flocculation is common. Nanoparticle dispersion presents great challenges because of agglomeration or hydrodynamic

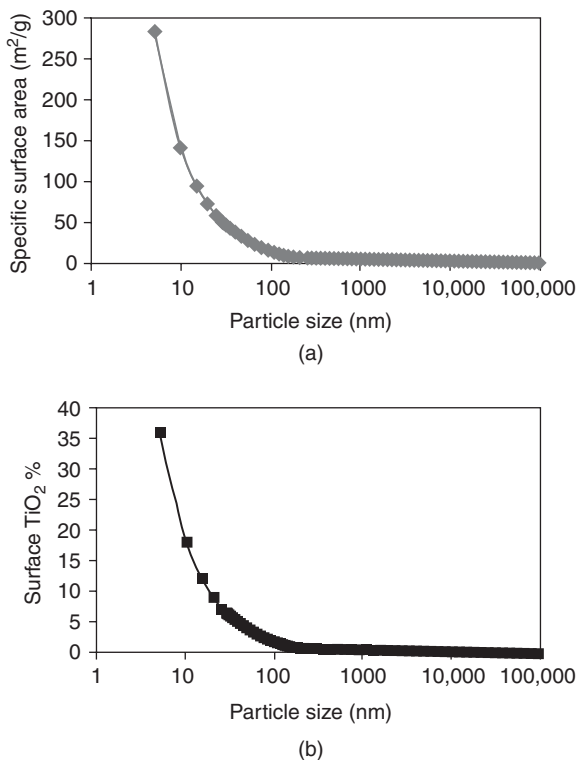


FIGURE 1.3 Specific surface area change (a) and volume percent change of surface species (b) with particle size for 1 g of TiO_2 particles.

size (a hypothetical hard sphere that diffuses with the same speed as the particle under examination, apparent size of the dynamic hydrated/solvated particle) of particles, especially when high solids loading is desired. For nanoparticle-based synthetic structures, such as those created by patterning or assembly, nanoparticles may not remain stable for the designed life cycle; the carefully constructed patterns and arrangements may be destroyed easily by the high surface energy or minor external perturbation. During nanoparticle-based bulk material forming, agglomeration-induced inhomogeneous microstructures are undesirable but hard to control. During sintering, the high surface energy of the nanoparticles has the potential to enable the material to be sintered at relatively low temperatures. However, extensive coarsening is also more likely to occur. If any agglomerates are present or created during shaping, sintering defects can easily result.

1.3.2 Vapor Pressure and Solubility

The second unique characteristic of nanoparticle materials is high vapor pressure and increased solubility. This is especially the case when individual nanoparticles

are considered. The fundamental cause is the increased fraction of the species residing on the particle surface (Fig. 1.3b). Since surface atoms are only partially bonded to the interior of particles, they behave more freely and can separate from the particles under certain circumstances; the nanoparticle surface atomic structure is more amorphous compared to the crystalline core. In addition, small particles by nature have a higher surface vapor pressure based on the Kelvin equation:

$$\ln \frac{P}{P_0} = \frac{2\gamma\Omega}{kTr_{S-V}}, \quad (1.1)$$

where P_0 is the equilibrium pressure on a flat surface, P is the vapor pressure at a specific given condition, γ_{S-V} is the solid–vapor interfacial energy, Ω is the atomic volume of the species, k is Boltzmann constant, T is absolute temperature, and r is particle radius. Nanoparticles have smaller radius r compared to micron-sized particles and thus higher surface vapor pressure P at the same condition. When a sufficient amount of energy is available, nanoparticle species are more likely to vaporize.

The increased solubility of nanoparticles comes primarily from the more active surface species. The less bonded surface atoms are more likely to interact with or dissolve into the surroundings. In addition, the solubility of the particles increases with the particle size decrease based on [9]

$$\rho \frac{RT}{M_w} \ln \frac{S_d}{S_\infty} = \frac{2}{3} \beta \frac{\gamma_{S-L}}{r}, \quad (1.2)$$

where ρ is the density of the solid particle, R is gas constant, M_w is the molecular weight of the solid, S_d is the solubility for a given particle of radius r , S_∞ is the solubility when the particle size is so large that the particle surface can be considered flat, β is a geometric factor that depends on the shape of the particle (for a spherical particle, the value is 3) and, γ_{S-L} is the solid–liquid interfacial energy. Smaller nanoparticles mean higher solubility. Even though there is some debate about the applicability of Equations (1.1)–(1.2) to solid–liquid interfaces in consideration of the net negative interfacial tension between the solid and the solution, it has been widely used to understand the particle size effect on solubility and the results are generally consistent.

1.3.3 Size-Dependent Characteristics

Size-dependent characteristics manifest themselves when the size of an individual particle is sufficiently small. These include nanoparticle electronic structure, chemical reactivity, and self-assembly. For an atom on a nanoparticle surface, the coordination with the neighbors is imperfect and many bonds are not fulfilled. The remaining bonds of the less-coordinated surface atoms have the tendency to relax spontaneously. The electronic structure of a nanoparticle critically depends

on its size. The electronic energy levels are not continuous as in bulk materials, but discrete due to the confinement of the electron wave function. For an individual silver nanoparticle of 3 nm diameter, which contains ~ 1000 silver atoms, the energy gap between different energy levels is 5 ± 10 meV. Since the thermal energy at room temperature, kT , is ~ 25 meV, the particle would be metallic. At low temperatures, however, the energy gap may become comparable to kT , rendering the Ag nanoparticle nonmetallic. Because of the presence of the band gap in individual nanoparticles, properties such as electrical conductivity and magnetic susceptibility exhibit quantum size effects. The electronic absorption spectrum of metal nanoparticles in the visible region is dominated by the plasmon band. In colloids, surface plasmon excitations impart characteristic colors to the metal nanoparticles, the beautiful wine-red color of gold sols being well known.

The increased chemical activity of nanoparticles can be understood as follows. The surface area of nanoparticles increases markedly with their decrease in size. A small metal nanoparticle of 1 nm diameter would have 100% of its atoms on the surface; a nanoparticle of 10 nm diameter, on the other hand, would have only 15% of its atoms on the surface. Thus, a small nanoparticle with a high surface area would be expected to be more reactive. Furthermore, the electronic structure change arising due to the quantum confinement will also bestow unusual catalytic properties on these particles, completely different from those of the bulk.

Just as individual atoms aggregate to form crystals, nanoparticles themselves can act as building units to form particle superlattices when the sizes are properly controlled. For example, monodispersed nanoparticles suitably covered by ligands such as alkane thiols, when transferred to a flat substrate, can spontaneously assemble into two-dimensional superstructures [10].

1.4 PROPERTIES

Since this book is focused on nanoparticle synthesis, characterization, assembly, and processing, the improved or novel properties accompanying these new materials are not separately addressed in the following chapters. Instead, related material properties are included in the broad theme of processing and discussed when appropriate. In brief, they can be categorized as follows.

1.4.1 Chemical

Along with semiconductor nanoparticles, metal and metal oxide particles in the quantum size regime have drawn much interest because of their unique chemical properties for various potential applications such as nanoscale optoelectronic devices, chemical sensors, displays, photovoltaics, and nanobiosensors. As explained, when individual nanoparticles are considered or a multitude of nanoparticles are in a dispersed state, they possess high specific surface areas. This enables nanoparticle materials to exhibit high chemical activity. For gold nanoparticles

smaller than ~ 6 nm in diameter, a new oxygen species forms in gold nanoparticles, which is absent in larger particles and bulk gold crystals. This oxygen species is attributed to the subsurface oxygen, which has been suggested to play an important role in heterogeneous catalysis. With decreasing gold particle size, an increase in the number of under-coordinated atoms is also evidenced by a reduced splitting between $5d_{3/2}$ and $5d_{5/2}$ states and a band narrowing [11]. SnO_2 nanoparticles exhibit better sensitivity compared with bulk SnO_2 material, an n -type material used in humidity sensing [12]. A model for size-dependent melting temperature, Debye temperature, diffusion activation energy, and vacancy formation energy, has been proposed. It is found that the above properties have the same size dependency that is contributed by the essential effects of surface/volume atom ratio. Vacancy formation determined by the cohesive energy is the intrinsic factor that dominates the size-dependent chemical properties [13]. The catalytic activity of the samples with different gold nanoparticle loading, measured in the temperature range of 140 – 350°C , is presented in Figure 1.4 [14]. As can be seen, the sample with the highest gold loading ($5\text{Au}/\text{CeO}_2$) exhibits the highest CO conversion. The activity of the $3\text{Au}/\text{CeO}_2$ sample is slightly less than that of $5\text{Au}/\text{CeO}_2$. The activity of pure CeO_2 becomes significant only at temperatures above 300°C .

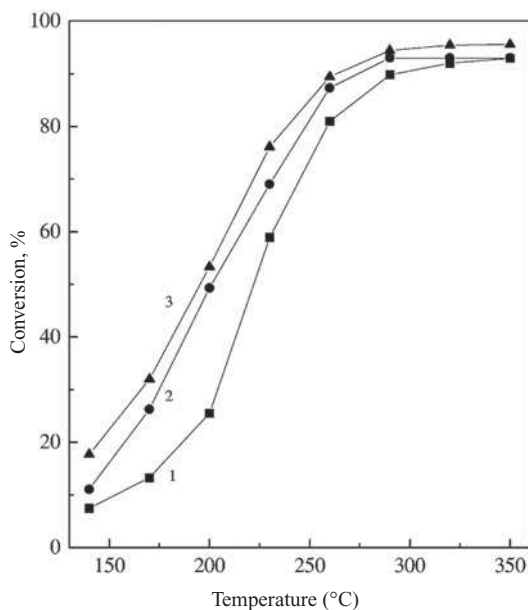


FIGURE 1.4 Effect of gold nanoparticle loading on the CO conversion: (1) $1\text{Au}/\text{CeO}_2$, (2) $3\text{Au}/\text{CeO}_2$, and (3) $5\text{Au}/\text{CeO}_2$ [14]. (Reprinted with permission from Andreeva D, Idakiev V, Tabakova T, Ilieva L, Falaras P, Bourlinos A, Travlos A. Low-temperature water-gas shift reaction over Au/CeO_2 catalysts. *Catal Today* 2002;72:51–57, Copyright 2002, Elsevier.)

1.4.2 Mechanical

Regarding different property improvements in nanostructured materials, mechanical properties are among the first ones that have motivated extensive research. For example, the grain size (G) effect on yield strength σ_y improvement has been described by the well-known Hall–Petch equation:

$$\sigma_y = \sigma_0 + \frac{k_\sigma}{\sqrt{G}}, \quad (1.3)$$

where σ_0 is a materials constant representing the starting stress for dislocation movement, k_σ is a constant. With the grain size G decrease, the yield strength σ_y increases remarkably, although it may be lower than the predicted value.

Since the interaction between dislocations and grain boundaries (the pile-up of dislocations and suppression of dislocation movement at the grain boundaries) is believed to be the main source for yield strength improvement, the Hall–Petch equation is mainly applicable to nanostructured metal materials, which have a substantial amount of dislocations. However, it has also been used to explain the strength improvement in nanostructured ceramic materials and the results fit the explanation. On the other hand, it is believed that the Hall–Petch equation does not always hold. Grain sliding may become dominant when the grain size decreases to <5 nm; the yield strength may decrease with further grain size decrease. So far, there has not been extensive studies or confirmation of such a trend; most of the studies focus on nanostructured materials with grain size >5 nm.

For nanostructured ceramic materials, an exciting property change is going from being brittle to being ductile at elevated temperatures. This is termed superplasticity and mainly attributed to the increased creep rate at elevated temperatures due to grain sliding. CaF_2 , TiO_2 [15], ZnO [16], ZrO_2 [17], and Si_3N_4 [18] have all been reported to exhibit superplasticity when the grain size is a couple of tens of nanometers or less. It also suggests that the yield strength decrease for very fine structured ceramics is related to superplasticity.

In addition to these fundamental material property changes, size effect alone can dramatically alter (mostly improve) the mechanical properties of composites. Submicron aluminum matrix embedded with Al_2O_3 nanoparticles is dispersed into a magnesium matrix. Compared with monolithic pure magnesium, the hierarchical composites exhibit significant and simultaneous enhancement of strengthening, hardening, and failure strain. The composition with 0.97 vol% aluminum and 0.66 vol% Al_2O_3 (Mg/0.97 Al–0.66 Al_2O_3) exhibits the best overall mechanical properties compared to monolithic magnesium, with an improvement of 96% in the 0.2% yield strength, 80% in the ultimate tensile strength, 42% in the failure strain, and 147% in the work of fracture [19]. ZrO_2 nanoparticle addition into a ceramic matrix also improves mechanical properties. The flexural strength and fracture toughness of Al_2O_3 –TiC–10 wt% ZrO_2 composite are $\sim 20\%$ higher than those of Al_2O_3 –TiC composite. This is mainly because the addition of ZrO_2

nanoparticles reduces the grain size of the matrix and improves the distribution of different phases [20].

1.4.3 Electrical

The effects of refined microstructures on electrical conductivity of nanoparticles and nanoparticle-based materials are complex, since conductivity may originate from distinctly different mechanisms. Electrical conduction in metals can be hindered by various electron scatterings, and the total resistivity of a metal is a combination of the contribution of individual and independent scattering, which includes thermal scattering, defect scattering, and surface scattering (including grain boundary scattering). Thermal scattering originates from electron collisions with vibrating atoms (phonons) displaced from their equilibrium lattice positions. Defect scattering can be divided into impurity scattering, lattice defect scattering, and grain boundary scattering. Increased perfection of nanoparticles and nanoparticle-based materials, such as reduced impurities, structural defects, and dislocations, would increase the electrical conductivity. However, the defect scattering makes a minor contribution to the total electrical resistivity at room temperature, and thus the reduction of defects has very small influence on the electrical resistivity, mostly unnoticeable experimentally. Surface scattering, on the other hand, plays a very important role in determining the total electrical resistivity of nanostructured materials. With decreased nanoparticle or grain sizes, the electrical conductivity decreases.

Another nanoscale-related electrical property is that the band gap in the electronic structure increases with decreasing species size. A metallic material can change from being conductive to being semiconducting, while a semiconductor can become insulating. Electrical transport properties of single-crystal bismuth nanowire arrays with different wire diameters (60–110 nm) embedded in a dielectric matrix have been measured over a wide range of temperatures (2.0–300 K) and magnetic fields (0–5.4 T). At low temperatures, wire boundary scattering is the dominant scattering process for carriers in the single-crystal bismuth nanowires, and the electrical resistance increases with the wire diameter [21]. In addition, silicon single-crystal nanowires with atomic straightness, a diameter ranging 14–35 nm, and a length of 1–10 μm , are insulators [22].

In addition to the intrinsic electric conductivity change with decrease in the size of the constituting species, the electrical properties of nanomaterials can be simply modified by using combinations of different species. Aluminum has been doped into ZnO nanoparticles by chemical vapor synthesis. Undoped ZnO and Al-doped ZnO (up to 7 mol% Al) nanoparticles exhibit ohmic conduction behavior in a hydrogen environment. In synthetic air, semiconductor transport behavior is observed for Al-doped ZnO and the optimum doping concentration is in the range of 7–8% [23]. $\text{SrZr}_x\text{Cu}_x\text{Fe}_{12-2x}\text{O}_{19}$ (where $x = 0.0\text{--}0.8$) hexaferrite nanoparticles are synthesized by chemical coprecipitation method. The particle size is in the range of 26–80 nm. Curie temperature (T_C) decreases with an increase in Zr–Cu. A significant increase in the room temperature resistivity

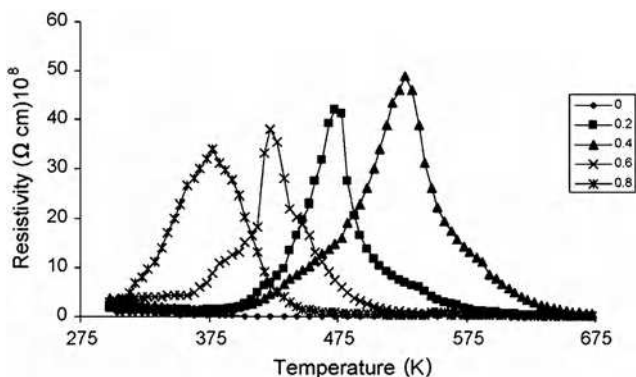


FIGURE 1.5 Variation in electrical resistivity with temperature for different $\text{SrZr}_x\text{Cu}_x\text{Fe}_{12-2x}\text{O}_{19}$ ($x = 0.0\text{--}0.8$) hexaferrite samples [24]. (Reprinted with permission from Iqbal MJ, Ashiq MN. Physical and electrical properties of Zr–Cu substituted strontium hexaferrite nanoparticles synthesized by coprecipitation method. *Chem Eng J* 2008;136:383–389, Copyright 2008, Elsevier.)

is noted with the addition of Zr–Cu up to $x \leq 0.4$. The temperature dependence of electrical resistivity (under direct current) is shown in Figure 1.5. The semiconductor–metal transition temperature (the resistivity peak temperature in Fig. 1.5) increases with the addition of dopant up to $x \leq 0.4$. Furthermore, the peak height of resistivity increases with Zr_xCu_x contents up to $x \leq 0.4$ but sharply decreases for $x > 0.4$. The initial resistivity increase with the temperature is indicative of the metallic behavior, and the following decrease in resistivity represents the semiconducting behavior [24].

1.4.4 Magnetic

The magnetic behavior of nanoparticles is of great interest from both fundamental understanding and technological application points of view. As the particle size decreases, finite-size and surface effects dominate the magnetic properties of nanoparticles; the magnetic behavior may strongly differ from that of conventional bulk materials. In particular, the magnetic properties of antiferromagnetic nanoparticles have received great attention because of their potential (due to the small intrinsic magnetic moment) for investigating surface effects and magnetization reversal by quantum tunneling [25]. The interaction between iron oxide (Fe_2O_3) nanoparticles and their sizes play a critical role in controlling their magnetic properties [26]. Anomalous magnetic properties, such as hysteresis, are observed in antiferromagnetic CoO nanoparticles from 10 to 80 nm (Fig. 1.6), compared to the correspondingly coarser grain materials. The coercive force increases as the particle size is reduced, but decreases when the size is < 20 nm. The magnetization also increases below 100 K for the nanoparticles [27]. Palladium nanoparticles (2 nm in diameter) containing magnetic iron atoms are prepared and

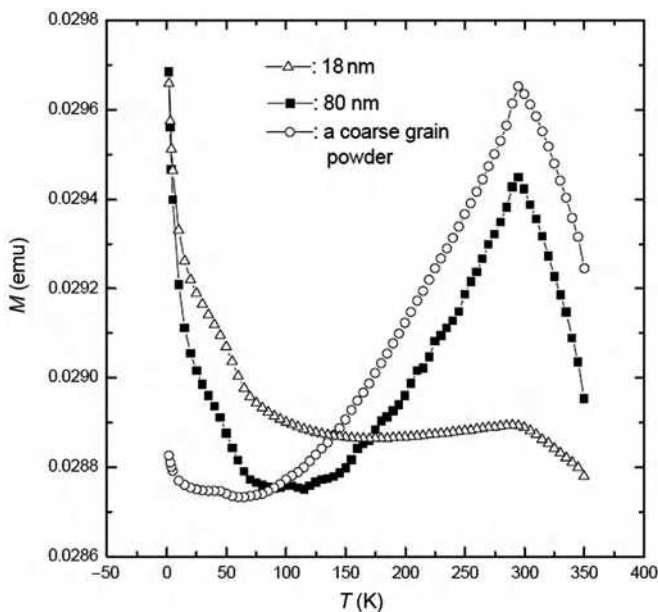


FIGURE 1.6 Temperature dependence of magnetization curves of coarse CoO powder and CoO nanoparticles with sizes of 18 and 80 nm from 1.9 to 350 K in a magnetic field of 10 kOe [27]. (Reprinted with permission from Zhang L, Xue D, Gao C. Temperature dependence of magnetization curves of coarse CoO powder and CoO nanoparticles with size of 18 and 80 nm from 1.9 to 350 K in magnetic field of 10 kOe. *J Magn Magn Mater* 2003;267:111–114, Copyright 2003, Elsevier.)

their magnetic properties are investigated. The magnetic moment of the particles is enhanced in the low iron concentration region and takes a maximum value of 7.6 μB per iron atom at the concentration in which each palladium nanoparticle contains one Fe atom on average. This large magnetic moment is explained in terms of the spin polarization on palladium atoms caused by the exchange enhancement mechanism. The magnetization curve shows that these Fe–Pd alloy nanoparticles exhibit superparamagnetic behavior, although no blocking behavior in the temperature dependence of the magnetic susceptibility is observed due to the small magnetic anisotropy of iron [28].

1.4.5 Optical

As particle size decreases to nanoscale, exciting optical properties may emerge. For example, gold particles of 5 nm size, which contain on the order of 105 atoms, absorb light strongly at 520 nm, whereas bulk gold is reflective at this wavelength. The intense light absorption and scattering that these particles exhibit are a result of plasmon excitation, a collective excitation of the conduction electrons. The

excitation wavelength depends on the shape and size of the nanoparticles. The larger the particles, the more important the higher-order modes are as light can no longer polarize the nanoparticles homogeneously. Therefore, the plasmon band blue shifts with decreasing particle size. At the same time, the plasmon bandwidth decreases with decreasing particle size. In many applications, the nanoparticle shape and size can be varied to optimize sensitivity and enhance the surface plasmon effect.

Semiconductor nanoparticles (quantum dots) exhibit unique optical properties because their electronic characteristics are closely related to the size and shape of individual particles. Small size quantum dots require more energy for excitation. Concurrently, more energy is released when excited small quantum dots return to their resting states. For example, higher frequencies of lights are emitted after the excitation of smaller quantum dots, resulting in a color shift from red to blue in the lights emitted.

For nanostructured ceramic materials, a prime application example relying on optical properties is transparent armor, which is optically transparent yet resistant to fragmentation and ballistic impacts. This class of materials can be used as protective visors, including riot control or explosive ordinance disposal actions, as well as vehicle protection from terrorist actions or other hostile conflicts. One example material is nanostructured spinel. If the particles are brought to a state of improved deagglomeration followed by a shaping procedure that ensures a high degree of homogeneity in the green bodies, spinel particle (~ 53 nm) samples (with specific surface area ~ 30 m² g⁻¹) can be sintered to transparency (as windows) at hot isostatic pressing temperatures $< 1300^\circ\text{C}$ without any doping additives [29].

1.4.6 Biological

Nanoparticles have many biological applications. The therapeutic use of gold can be traced back to the Chinese in 2500 BC. Red colloidal gold is still in use today in India in the form of Ayurvedic medicine for rejuvenation and revitalization under the name of Swarna Bhasma (“Swarna” meaning gold, “Bhasma” meaning ash) [30, 31]. Silver is widely used in wound dressing. Acticoat-7 is a dressing marketed by Smith and Newpew in United Kingdom. This dressing consists of polyethylene mesh coated with silver nanoparticles. A large amount of silver nanoparticles is provided to the wound initially, followed by a sustained release. Actisorb Silver 220 is another dressing containing silver nanoparticles marketed by Johnson & Johnson, New Brunswick, NJ, USA. In this formulation, silver nanoparticles are bound to charcoal dressing. Actisorb functions by adsorbing bacteria to the charcoal dressing where they are killed by the silver nanoparticles. Aquacel-Ag hydrofiber, marketed by Convatec, Skillman, NJ, USA, is a carboxymethylcellulose dressing impregnated with silver nanoparticles. It functions by slowly releasing silver ions upon hydration. Platinum nanoparticles are used in combination with multiwalled carbon nanotubes for fabricating sensitivity-enhanced electrochemical DNA biosensors, where carbon nanotubes promote

electron transfer reactions, and platinum nanoparticles provide high catalytic activities for chemical reactions. The sensitivity of the electrochemical DNA biosensors is remarkably improved [32].

1.5 KEY SCIENTIFIC AND TECHNICAL CHALLENGES

1.5.1 Synthesis

For nanoparticle synthesis, an amazing array of nanoparticles has been made in the lab. Even different nanoparticle morphologies of the same compositions have been achieved by controlling synthesis conditions. The challenge lies in producing nanoparticles consistently in large quantities such as kilograms or tons. Inhomogeneity in temperature, solution pH, or mixing of reactants in the synthesis system often contributes to the variation in particles (either in size, shape, or composition). However, synthesis at the level of grams or even hundreds of grams can barely sustain any realistic applications. This issue is even more acute for unique nanoparticle structures such as core/shell or functionalized particles.

1.5.2 Characterization

For the characterization of nanoparticles and nanoparticle-based materials, sophisticated equipment is available in different research centers or labs. The challenges in these settings are the long process time and the very small amount of materials involved. The statistical significance of these analyses needs to be carefully scrutinized. In the production setting, the slow speeds of measurement and data acquisition often mean compromised product quality and inadequate traceability of the problems to the root cause. There is a serious lack of instruments that provide real-time data from the nanoscale about nanoparticle synthesis, assembly, and processing and a lack of instrumentation for mapping chemical compositions and understanding the interfacial regions of nanoparticles. Among the above lacking areas, characterization and understanding of nanoparticles or nanoparticle-based material surfaces are relatively easy to address because they are accessible. The more challenging issue is analysis and description of interfacial structures and interactions, especially for the buried interfaces/interphases at the nanoscale. Often times, these interfaces at the nanoscale are dynamic or unstable and cannot be dissected or transferred to the sophisticated characterization facilities for evaluation. Nondestructive characterization techniques are highly needed but are lacking.

1.5.3 Superstructure Assembly

The interfacial interactions and the mechanisms involved also directly impact the ability to assemble and pattern nanoparticles. Since nanoparticle assembly and

patterning involve minute forces (van der Waals, electrostatic, hydrogen bonding, covalent) between nanoparticles, it is challenging to measure these forces, let alone controlling them. Current techniques are often insufficient in measuring these small forces, especially when the nanoparticle interaction involves liquid–vapor interfaces or liquid medium. Manipulation of nanoparticle arrangement is a science as well as an art. The technical precision is daunting and the process is tedious. However, this level of particle manipulation has the potential to revolutionize the way materials are made, and the range and nature of functionalities to which nanomaterials may be tailored, and should be vigorously pursued.

1.5.4 Bulk Processing

For forming and sintering, the most challenging issue is how to controllably and consistently create homogeneous or heterogeneous microstructures and maintain the nanoscale constituent size at each step while achieving the functionality and/or robustness of the designed products. Low-density particle packing or heterogeneous microstructure may be desired for the shaping process in contrast to the conventional forming process, which focuses on obtaining homogenous and dense microstructures. For the sintering process, obtaining stable but highly porous nanostructures, or fully densifying the sintered body while maintaining the sintered grains at <100 nm size, can be difficult to achieve.

1.5.5 Large-Scale Production

From a large-scale production point of view, the challenge for nanoparticle-based materials is how to incorporate nanoparticles into useful products. The most important questions are quality control, efficiency of the manufacturing process, and production cost. The encouraging news is that the new or improved properties accompanying nanomaterials often provide solutions to problems that cannot be solved with conventional materials. As a result, the incentive for developing nanoparticle-based materials is still strong and active research is still ongoing in this challenging but exciting field.

1.5.6 Modeling and Simulation

Computer modeling and simulation can save time and reduce cost in nanoparticle-based material advancement when properly used. However, the sophistication of modeling and simulation packages leaves much to be desired, especially when a large number of nanoparticles are involved and their arrangement and interaction are complex. There is a lack of tools to bridge time and length scales, a deficiency of fast methods for calculating a large number of nanoparticles to predict structures and properties of nanomaterials, and a lack of methods to integrate and analyze large datasets.

1.6 APPLICATIONS

Nanoparticles and nanoparticle-based materials have important applications in energy, electronics, photonics, magnetics, biomedical engineering, catalysis, transportation, health care, communications, and medicine. The related industries range from aerospace, automotive, chemical, pharmaceutical, food processing, to semiconductors. Nanoparticles can be used as they are, dispersed in a liquid, patterned into superstructures, or processed into bulk components with specifically desired properties. Current products include metals, oxides, and semiconductors, which are used as catalysts, pigments for paints, UV protectants for sunscreens, and coating materials for cutting tools. Additional products include filters, sorbents, membranes, and ion conductors.

Nanoparticles can be used as they are on a discrete basis. For example, palladium nanoparticles provide a high surface to volume ratio compared to macroscale palladium thin films used for hydrogen sensing. The increased percentage of active surface atoms detects molecular events more effectively and maximizes sensor signals. Socks can be impregnated with silver nanoparticles. The unique antimicrobial properties of silver nanoparticles have already been commercialized in wound dressings to prevent infection and speed healing. Fresh-smelling socks are a natural extension. They might seem rather mundane by comparison, but enduring freshness is a real benefit valued by consumers with significant market potentials. Antibacterial socks, offered by retailers including AgActive and Sharper Image, are being used by the military, which is always looking for ways to reduce the number of items soldiers need to pack. Hunters who want to mask their human scent also use them. Germany's Jack Wolfskin offers a jacket combining the antibacterial properties of silver nanoparticles with a waterproofing membrane. In home products like bedding, AgActive offers silver-impregnated, odor-resistant cotton sheets. Figure 1.7 shows some examples of consumer products that can use nanoparticles as antibacterial agents. ZnO nanoparticles are used in coatings to reduce UV exposure. Iron nanoparticles are emerging remediation to degrade recalcitrant chemicals by reductive processes to treat groundwater pollutants including trichloroethene, dichloroethene, and chloroform, just to name a few.

Most pollution from U.S. automobiles is emitted in the first 5 minutes after start-up. This is because Pt- or Pd-based catalysts currently used in automobile exhaust cleanup are inactive below about 200°C. Heterogeneous Au-based catalysts present a potential solution to this cold start-up problem. Their surfaces can be made with highly specific structural and chemical properties that vary on the nanometer scale, primarily with respect to particle size, particle structure, support, and promoters [33]. Gold nanoparticles dispersed across the surfaces of certain oxides are amazingly active and selective as catalysts for a variety of important reactions. There is intense interest in these catalysts for CO oxidation because they are active at room temperature. However, it should be pointed out that the low-temperature gold catalysts are totally inactive unless the particles are smaller than ~ 8 nm. Although gold nanoparticles have been perhaps the



FIGURE 1.7 Examples of consumer products that can use nanoparticles as antibacterial agents. (For a color version of this figure, see the color plate section.)

most widely studied catalyst system, the structure of the active sites remains elusive [34].

Nanofluids are stable suspensions of nanoparticles (metals, oxides, carbides, nitrides, or nanotubes) in a liquid (usually water or oil). In order to avoid coagulation, the particles must be coated with a surfactant/dispersant. The surfactant/dispersant should overcome the tendency of nanoparticles to form van der Waals force bonded clusters. The Brownian motion (random movement of particles suspended in a fluid) should be high enough to avoid the settlement of the nanoparticles. Typically, nanofluids contain up to 10 vol% nanoparticles and >10 vol% surfactant. Nanofluids have high heat capacity, good thermal conductivity, and high heat transfer coefficients compared to the base fluid. They can be used in engines, heat-treating operations, rubber manufacturing, etc. Figure 1.8 shows examples of nanoparticle suspensions that can be used as nanofluids.

Substantial progress has been made in the development of nanoparticle-based superstructures, which can lead to controllable size, composition, shape, and surface chemistry clusters. Quantum dot monolayers have been used in the design of light-emitting diodes (LED) [35], whereas quantum dot multilayers have been used for multicolored light-emitting films [36], biosensors [37], light-harvesting devices [38], photodetectors [39], and Förster resonant energy transfer sensing [40].

For nanostructured bulk materials, the applications include powertrains, lightweight construction, energy conversion, pollution sensing and reduction, interior cooling, wear reduction, surveillance control, and many more [41]. Porous composites have numerous applications as separation filters, catalyst supports, bio-implants, and sensors due to their controllable microstructures, high specific

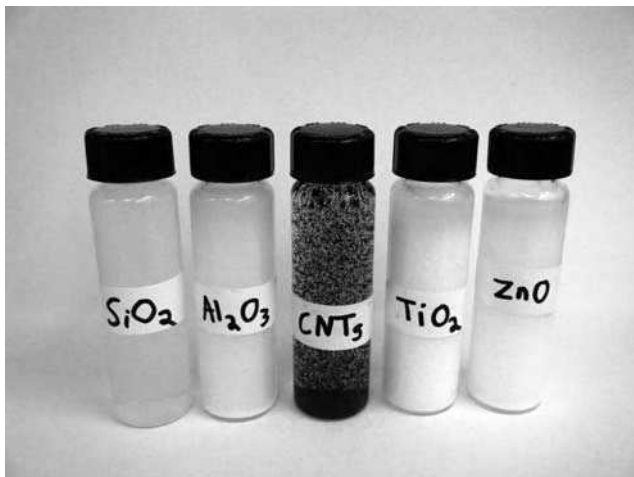


FIGURE 1.8 Examples of nanoparticle suspensions that can be used as nanofluids.

surface area, and desirable mechanical properties. Among different porous materials, those with interconnected pores are drawing more attention. Interconnected porous microstructures provide an open, three-dimensional network and thus high fluid permeability, resistance to chemical attack, and mechanical strength. Figure 1.9 shows partially sintered SiO₂ (from SiO₂ nanoparticles of 22 nm) and SiO₂–kaolinite composite with a large amount of porosities.

1.7 PROCESSING OVERVIEW

Nanoparticles and nanoparticle-based materials are complex systems in which the properties of the final products are influenced by a multitude of variables that

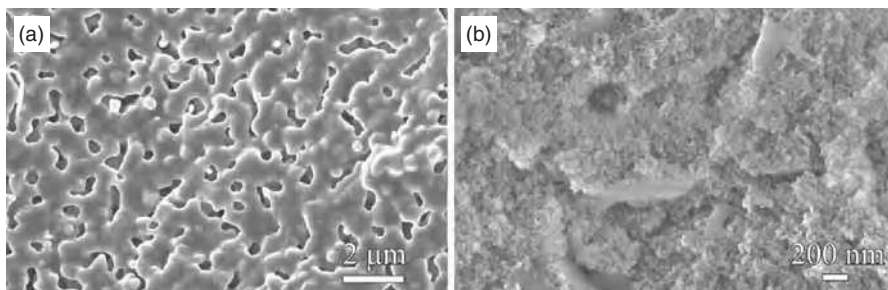


FIGURE 1.9 Partially sintered SiO₂ (from SiO₂ nanoparticles of 22 nm) (a) and SiO₂–kaolinite nanocomposite (b).

operate at different length scales. There is a lack of fundamental theoretical understanding of the important processing variables that influence the performance and properties. Sometimes it is even difficult to know what processing variables are important for a given performance requirement. This lack of understanding leads to nanomaterial processing practices based on trial-and-error efforts and inhibits the timely development and commercialization of these materials. This book is focused on these important processing issues. The discussion on nanoparticle-based materials is divided into seven chapters: (1) introduction, (2) nanoparticle synthesis, (3) nanoparticle characterization, (4) nanoparticle-based superstructures, (5) nanoparticle-based material shaping, (6) nanoparticle-based material sintering, and (7) manufacturing issues and emerging areas for nanoparticle-based materials. Figure 1.10 shows the interrelationship of the different chapters in this book.

In this introduction chapter, an overview of general nanoscale science and technology and nanomaterials is provided. Nanoparticle and nanoparticle-based materials are defined. These are followed by a discussion of the unique characteristics and properties of nanoparticle-based materials. The key scientific and technical barriers in this important field are analyzed, and the vast applications of nanoparticle-based materials are reviewed.

In the nanoparticle synthesis chapter, fundamental nucleation and particle growth theories are first reviewed, with a focus on homogeneous nucleation. The discussion of nanoparticle synthesis is divided into three general categories:

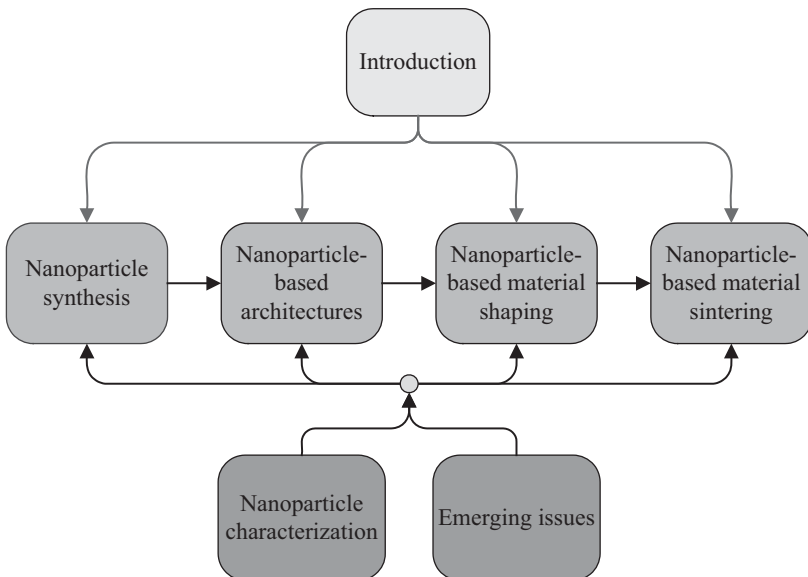


FIGURE 1.10 Interrelationship of the different chapters in this book.

gas phase, liquid phase, and solid phase. For each synthesis category, different subcategories are defined and discussed. Among these, liquid phase nanoparticle synthesis is the most widely studied because of its ability to overcome the agglomeration tendency of nanoparticles.

In the nanoparticle characterization chapter, the discussion evolves into the following categories: size, shape, and morphology; energetics and global thermodynamics; surface area; porosity and pore size measurement; structure characterization; and composition characterization. Many of the characterization techniques are extensions of conventional material analysis capabilities. However, new capabilities for an existing characterization technique may be developed and new issues might arise for the characterization of nanoparticles and nanoparticle-based materials.

In the nanoparticle-based superstructure chapter, the discussion is divided into top-down, bottom-up, and hybrid approaches followed by templating and three-dimensional assembly. The top-down processes discussed include photolithography, electron beam lithography, and ion beam lithography. For the bottom-up approach, the discussion is grouped based on the driving forces: van der Waals force, dipole moment, electrostatic or magnetic interaction, covalent bonding, hydrogen bonding, field-assisted assembly, and capillary force. The hybrid process includes functionalized interaction and nonfunctionalized interaction. The templating approaches involve natural and synthetic templates.

In the nanoparticle-based material shaping chapter, the discussion is divided based on the water content of a system: dry forming techniques, semidry forming techniques, and wet forming techniques, followed by special techniques such as digital processing techniques and bio-derived processes. The dry forming technique includes uniaxial compaction, cold isostatic processing, superhigh pressure compaction, and dynamic compaction. The semidry forming technique mainly includes molding and extrusion. The wet forming technique includes colloidal suspension, pressure casting, tape casting, freeze casting, gel casting, and electrophoretic deposition. The digital processing technique includes digital writing, stereolithography, and ink-jet printing. The bio-derived processing includes bioactive material-derived and biomimetic material-derived shaping.

In the nanoparticle-based material sintering chapter, sintering theories are discussed first, followed by an analysis of nanoparticle sintering characteristics. After that, the sintering discussion is divided into studies related to porous and dense materials. For the porous nanoparticle material sintering, it includes free sintering and special sintering techniques. For dense nanoparticle material sintering, the discussion concerns sintering cycles, nanoparticle size and packing, and diffusion rate. For pressure sintering, hot pressing, hot isostatic pressing, sinter forging, spark plasma sintering, and other niche sintering techniques are addressed.

The chapter on manufacturing issues and emerging areas in nanoparticles and nanoparticle-based materials is divided into defect measurement, process and quality control, modeling and simulation, and environmental and health concerns.

1.8 SUMMARY

In this chapter, the general scopes of nanoscale science and technology and nanomaterials are explained and nanoparticles and nanoparticle-based materials are defined in this broad scheme. These are followed by a discussion of the unique characteristics of nanoparticles and nanoparticle-based materials. Some of the exciting properties for nanoparticle-related materials are introduced. The key scientific and technical barriers in this important field are analyzed. The vast applications and future potentials of nanoparticle-based materials are reviewed. Lastly, the overall structure of the book is presented.

QUESTIONS

1. What is the interrelationship among nanotechnology, nanomaterials, and nanoparticle-based materials?
2. Design a concept tree related to the processing stages of nanoparticles and nanoparticle-based materials. Point out the technical challenges at each step.
3. Give three examples about the unique characteristics of nanoparticles or nanoparticle based materials and explain why?
4. From everyday life applications, give two examples about the enhanced properties that nanoparticle-based materials can offer. What are the potential hurdles for utilizing these materials?
5. Devise a flow chart showing the nanoparticle-based material processing steps.

REFERENCES

1. Rubahn H-G. *Basics of Nanotechnology*. 3rd ed. Weinheim, Germany: Wiley-VCH Verlag GmbH & Co. KGaA; 2008.
2. Poole CP Jr, Owens FJ. *Introduction to Nanotechnology*. Hoboken, NJ: John Wiley & Sons; 2003.
3. Di Ventra M, Evoy S, Heflin JR Jr. *Introduction to Nanoscale Science and Technology*. New York: Springer; 2004.
4. Cao G. *Nanostructures & Nanomaterials: Synthesis, Properties, and Applications*. London: Imperial College Press; 2004.
5. Vollath D. *Nanomaterials, An Introduction to Synthesis, Properties and Applications*. Weinheim, Germany: Wiley-VCH Verlag GmbH & Co. KGaA; 2008.
6. Edelstein AS, Cammarata RC. *Nanomaterials: Synthesis, Properties and Applications*. New York, NY: Taylor & Francis; 1996.
7. German RM. *Powder Metallurgy & Particulate Materials Processing*. Princeton, NJ: MPIF; 2005.
8. Rahaman MN. *Ceramic Processing*. New York, NY: Taylor & Francis; 2007.
9. Wu W, Nancollas GH. A new understanding of the relationship between solubility and particle size. *J Solution Chem* 1998;27:521–531.
10. Rao CNR, Kulkarni GU, Thomas PJ, Edwards PP. Size-dependent chemistry: properties of nanocrystals. *Chem Eur J* 2002;8:29–35.

11. Lim DC, Lopez-Salido I, Dietsche R, Bubek M, Kim YD. Electronic and chemical properties of supported Au nanoparticles. *Chem Phys* 2006;330:441–448.
12. Krishnakumar T, Jayaprakash R, Singh VN, Mehta BR, Phani AR. Synthesis and characterization of tin oxide nanoparticle for humidity sensor applications. *J Nano Res* 2008;4: 91–101.
13. Yang CC, Li S. Investigation of cohesive energy effects on size-dependent physical and chemical properties of nanocrystals. *Phys Rev B* 2007;75:165413 5pp.
14. Andreeva D, Idakiev V, Tabakova T, Ilieva L, Falaras P, Bourlinos A, Travlos A. Low-temperature water-gas shift reaction over Au/CeO₂ catalysts. *Catal Today* 2002;72: 51–57.
15. Karch J, Birringer R, Gleiter H. Ceramics ductile at low temperature. *Nature* 1987;330:556–558.
16. Mayo MJ, Siegel RW, Liao YX, Nix WD. Nanoindentation of nanocrystalline ZnO. *J Mater Res* 1992;7:973–979.
17. Wakai F, Sakaguchi S, Matsuno Y. Super-plasticity of yttria-stabilized tetragonal ZrO₂ poly-crystals. *Adv Ceram Mater* 1986;1:259–263.
18. Wakai F, Kondo N, Ogawa H, Nagano T, Tsurekawa S. Ceramics superplasticity: deforms mechanisms and microstructures. *Mater Charact* 1996;37:331–341.
19. Habibi MK, Joshi SP, Gupta M. Hierarchical magnesium nano-composites for enhanced mechanical response. *Acta Mater* 2010;58:6104–6114.
20. Donga Q, Tang Q, Li W. Al₂O₃-TiC-ZrO₂ nanocomposites fabricated by combustion synthesis followed by hot pressing. *Mater Sci Eng A* 2008;475:68–75.
21. Zhang ZB, Sun XZ, Dresselhaus MS, Ying JY, Heremans J. Electronic transport properties of single-crystal bismuth nanowire arrays. *Phys Rev B* 2000;61:4850–4861.
22. Chung S-W, Yu J-Y, Heath JR. Silicon nanowire devices. *Appl Phys Lett* 2000;76:2068–2070.
23. Hartner S, Ali M, Schulz C, Winterer M, Wiggers H. Electrical properties of aluminum-doped zinc oxide (AZO) nanoparticles synthesized by chemical vapor synthesis. *Nanotechnology* 2009;20:445701 8pp.
24. Iqbal MJ, Ashiq MN. Physical and electrical properties of Zr-Cu substituted strontium hexaferrite nanoparticles synthesized by co-precipitation method. *Chem Eng J* 2008;136: 383–389.
25. Mansillaa MV, Zyslera R, Fioranib D, Suber L. Annealing effects on magnetic properties of acicular hematite nanoparticles. *Phys B* 2002;320:206–209.
26. Alam S, Anand C, Logudurai R, Balasubramanian VV, Ariga K, Bose AC, Mori T, Srinivasu P, Vinu A. Comparative study on the magnetic properties of iron oxide nanoparticles loaded on mesoporous silica and carbon materials with different structure. *Micro-porous Mesoporous Mater* 2009;121:178–184.
27. Zhang L, Xue D, Gao C. Anomalous magnetic properties of antiferromagnetic CoO nanoparticles. *J Magn Magn Mater* 2003;267:111–114.
28. Ito Y, Miyazaki A, Valiyaveetil S, Enoki T. Magnetic properties of Fe-Pd alloy nanoparticles. *J Phys Chem C* 2010;114:11699–11702.
29. Krell A, Hutzler T, Klimke J, Potthoff A. Fine-grained transport spinel windows by the processing of different nanopowder. *J Am Ceram Soc* 2010;93:2656–2666.
30. Mahdihassan S. Colloidal gold as an alchemical preparation. *Janus* 1971;58:112–118.
31. Mahdihassan S. The tradition of alchemy in India. *Am J Chin Med* 1981;9:23–33.
32. Nagy JA, Meyers MS, Masse EM, Herzberg KT, Dvorak HF. Pathogenesis of ascites tumor growth: fibrinogen influx and fibrin accumulation in tissues lining the peritoneal cavity. *Cancer Res* 1995;55:369–375.

33. Johaneck V, Laurin M, Grant AW, Kasemo B, Henry CR, Libuda J. Fluctuations and bistabilities on catalyst nanoparticles. *Science* 2004;304:1639.
34. Campbell CT. The active site in nanoparticle gold catalysis (A perspective). *Science* 2004;306:234.
35. Coe S, Woo W, Bawendi M, Bulovic V. Electroluminescence from single monolayers of nanocrystals in molecular organic devices. *Nature* 2002;420:800–803.
36. Lin Y, Tseng W, Chang H. Using layer-by-layer assembly technique to fabricate multicolored-light-emitting films of CdSe@CdS and CdTe quantum dots. *Adv Mater* 2006;18:1381–1386.
37. Li X, Zhou Y, Zheng Z, Yue X, Dai Z, Liu S, Tang Z. Glucose biosensor based on nanocomposite films of CdTe quantum dots and glucose oxidase. *Langmuir* 2009;25: 6580–6586.
38. Rogach AL, Klar TA, Lupton JM, Meijerink A, Feldmann J. Energy transfer with semiconductor nanocrystals. *J Mater Chem* 2009;19:1208–1221.
39. Konstantatos G, Clifford J, Levina L, Sargent EH. Sensitive solution-processed visible-wavelength photodetectors. *Nat Photonics* 2007;1:531–534.
40. Gole A, Jana NR, Selvan ST, Ying JY. Langmuir-Blodgett thin films of quantum dots: synthesis, surface modification and fluorescence resonance energy transfer (FRET) studies. *Langmuir* 2008;24:8181–8186.
41. Presting H, König U. Future nanotechnology developments for automotive applications. *Mater Sci Eng C* 2003;23:737–741.

CHAPTER 2

NANOPARTICLE SYNTHESIS

2.1 INTRODUCTION

Nanoparticle synthesis involves the creation of nanoparticles from ions, atoms, or molecules. Different from conventional micron-sized particle synthesis, nanoparticle synthesis often involves careful design of nanoparticle atomic structure, composition, size, and even specific composition distribution. Synthesized nanoparticles generally range from <100 atoms to ~ 100 nm in size. Nanoparticle synthesis is the first necessary and fundamental step for the entire nanoparticle-based material field and plays pivotal roles in the continuous advancement of nanomaterials. In this chapter, nanoparticle synthesis discussion is divided into gas-, liquid-, and solid-based systems (Fig. 2.1). For each system, different synthesis methods are discussed based on the fundamental synthesis mechanisms. Gas-phase nanoparticle synthesis includes gas–gas reaction, gas–liquid reaction, and gas–solid reaction. Liquid-phase nanoparticle synthesis includes fundamental methods, confined methods, composite nanoparticle synthesis, and field-assisted nanoparticle synthesis. Solid-phase synthesis includes milling and reaction between solids. Besides discrete nanoparticle synthesis, there has been a growing trend in forming nanoparticles on a substrate or other supports. Since this family of nanoparticle synthesis is more or less a variation in heterogeneous nucleation and growth process, it will not be extensively covered. However, examples will be given for nanoparticles formed on the surfaces of existing core particles or on certain templates. These types of particles are categorized as composite nanoparticles and are included in the liquid-phase synthesis category.

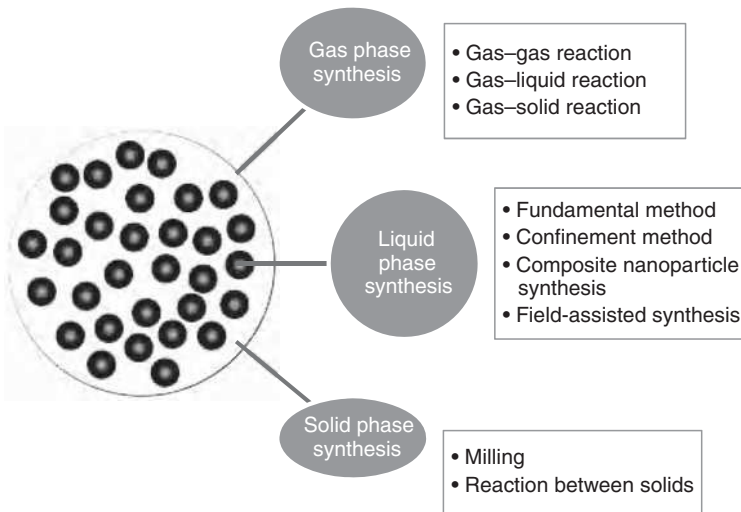


FIGURE 2.1 Nanoparticle synthesis methods.

Liquid-phase approach is dominant in nanoparticle synthesis. This is mainly because nanoparticles require careful nucleation and growth process control in order to obtain the required size and shape. After nanoparticles are obtained, huge surface areas are available; thus, diligent efforts are required for agglomeration prevention. Liquid provides more flexibility in controlling nanoparticle formation processes and a natural vehicle for nanoparticle dispersion and manipulation afterwards.

For certain specific nanoparticle synthesis needs, one technique may be more suitable than another. For example, nonaqueous solvothermal synthesis is mainly developed for nonoxide semiconductor nanoparticles and hydrolysis is mainly suited for oxide nanoparticles. Each synthesis approach has its strengths and deficiencies. For all the synthesis techniques, highly controllable processes and environmentally benign starting materials are universally desired. According to the specific needs and constraints of the applications on hand, there can be various modifications to the general systems discussed here.

2.2 THEORY

For nanoparticle synthesis, just as for micron-sized particle synthesis, there are two essential steps: nucleation and growth of nanoparticles. At the beginning of the nanoparticle formation process, the thermodynamic state of the system is very important for nucleation. Sometimes this can involve very short timescales, such as sub-picoseconds. After nuclei are formed and remain stable, nanoparticle growth needs to be carefully controlled in order to obtain targeted particle

size, shape, and distribution. An integrated understanding of nanoparticle growth across a variety of timescales, such as from femtoseconds to hours or even days, is needed. Thermodynamics is the fundamental science guiding the understanding in this area.

2.2.1 Nucleation

There are two types of nucleation: homogeneous and heterogeneous. In homogeneous nucleation, nuclei are formed in a completely uniform environment. In heterogeneous nucleation, nuclei are preferentially formed on some media such as existing particles or the walls of the container. Reactant addition mode, stirring rate, container surface condition, temperature uniformity, and many other factors can all affect the nucleation process.

2.2.1.1 Homogeneous Nucleation First, the nucleation process can be understood as follows using a liquid system as an example. For a given system, there are always thermodynamic fluctuations that will result in local changes from the equilibrium state. The local fluctuation of solution concentration generates the possibility of forming small nuclei—a new phase in the liquid that is composed of the intended new species. Whether the new phase remains stable or not depends on the chemical potentials of the old and new phases. When the initial bulk phase is unstable, for which the chemical potential is higher than that of the newly formed phase, the new phase will become stable and grow after some critical size is exceeded. For nucleation to occur, supersaturation of the solute is necessary. To achieve the desired supersaturation state, the solution can be oversaturated either by dissolving the solute at higher temperatures or by adding reactants to produce a supersaturated solution. In other words, the work of nucleus formation must be overcome for the process to proceed.

If a system is free from other preferential nucleation sites, such as container walls or other surfaces, homogeneous nucleation occurs when the precursor concentration increases to above the nucleation threshold. The free energy change during the formation of a spherical nucleus, ΔG , can be expressed as [1]

$$\Delta G = 4\pi r^2 \gamma + \frac{4}{3}\pi r^3 \Delta G_{1 \rightarrow s}, \quad (2.1)$$

where r is the radius of the nucleus, γ is the specific surface energy of the nucleus, and $\Delta G_{1 \rightarrow s}$ is the free energy change per unit volume when new nuclei are formed from the liquid, which is negative if nuclei form spontaneously. The first term represents the free energy change upon the formation of a new interface and contributes positively to the total free energy change. The second term is the volume term and represents the change in chemical potential of the matter comprising the nuclei. When the second term is positive, the nucleus formed is unstable and disappears spontaneously. In order for a stable nucleus to form, an

energy barrier needs to be overcome. This can be expressed as the maximum free energy change at critical nucleus radius r_c :

$$r_c = -\frac{2\gamma}{\Delta G_{l \rightarrow s}}. \quad (2.2)$$

The free energy change barrier that needs to be overcome, ΔG_c , is

$$\Delta G_c = \frac{16\pi\gamma^3}{3\Delta G_{l \rightarrow s}^2}, \quad (2.3)$$

$$\Delta G_{l \rightarrow s} = -\frac{kT}{\nu_s} \ln \frac{C_{ss}}{C_s}, \quad (2.4)$$

where k is Boltzmann's constant ($1.3806 \times 10^{-23} \text{ m}^2 \text{ kg s}^{-2} \text{ K}^{-1}$), T is absolute temperature, ν_s is the volume per molecule in the solid, C_{ss} is the supersaturated concentration of the ions in the solution, and C_s is the saturated concentration of the ions in the solution. When the nucleus size is smaller than r_c , the free energy increases with the particle size. The critical free energy change ΔG_c at critical size r_c has to be exceeded before the newly formed nucleus becomes stable. A stable nucleus is the smallest particle size that can be obtained. After this point, the free energy will decrease with the particle size, indicating a stable phase forming. With further free energy decrease, the particle keeps growing.

Assuming the nucleation process is thermodynamically favorable, the nucleus formation probability P_f can be expressed as

$$P_f = \exp\left(-\frac{\Delta G_t}{kT}\right), \quad (2.5)$$

where ΔG_t is the activation energy for transfer of a "structural unit" from the liquid to a nucleus (kinetic barrier). The steady-state homogeneous volume nucleation rate I can be written as

$$I = \frac{2N_f \cdot a \cdot (k \cdot T \cdot \gamma)^{1/2}}{h} \exp\left(\frac{-\Delta G_t}{kT}\right) \exp\left(\frac{-16\pi\gamma^3}{3\Delta G_{l \rightarrow s}^2}\right), \quad (2.6)$$

where N_f is the number of structural units (formula) per unit volume of the solution, a is the structural unit size, and h is Planck's constant. Equation (2.6) indicates that high supersaturation (high N) and low critical energy barrier (ΔG_c) favor nucleation.

2.2.1.2 Heterogeneous Nucleation When nuclei originate on the surface of foreign species, such as impurities, dispersed particles, or container walls,

heterogeneous formation of nuclei occurs. Heterogeneous nucleation on a foreign surface has a lower surface energy and a diminished thermodynamic barrier, which leads to a lower critical supersaturation. For heterogeneous nucleation on a planar surface, the critical nucleus size r_c^{het} and activation energy ΔG_c^{het} for heterogeneous nucleation are

$$r_c^{\text{het}} = \frac{2\gamma}{\Delta G_{1 \rightarrow s}} \cdot \frac{\sin^2 \varphi \cdot \cos \varphi + 2 \cos \varphi - 2}{2 - 3 \cos \varphi + \cos^3 \varphi}, \quad (2.7)$$

$$\Delta G_c^{\text{het}} = \frac{16\pi\gamma^3}{3(\Delta G_{1 \rightarrow s})^2} \cdot \frac{2 - 3 \cos \varphi + \cos^3 \varphi}{4}, \quad (2.8)$$

where φ is the contact angle of the new phase on the substrate. Depending on the value of φ , the second term in Equation (2.8) may vary from zero to unity.

For the heterogeneous nucleation rate, the number of structural units per volume N needs to be replaced by N_s , the structural units in contact with the nucleating surface per unit volume. Once the heterogeneous nucleation sites are used up, there are no more of them, limiting the maximum heterogeneous nucleation rate I_{het} to

$$I_{\text{het}} \cong \frac{N_s \cdot k \cdot T}{h} \exp\left(\frac{-\Delta G_t}{kT}\right) \exp\left(\frac{-16\pi\gamma^3}{3\Delta G_{1 \rightarrow s}^2}\right). \quad (2.9)$$

Although traditionally not quite desirable, heterogeneous nucleation has found new applications such as coating one type of particles with a layer of the second type of species. With the increasing interest in forming unique composition nanoparticles and templating, heterogeneous nucleation is being utilized in increasingly creative manners for novel materials and properties.

2.2.2 Growth

After stable nuclei are formed, nanoparticles can grow in three ways: homogeneous growth, Ostwald ripening, and aggregation. The ability to control the growth of nuclei determines if the obtained particles will be nano-sized or micron-sized and how wide the particle size distribution will be.

During homogeneous nanoparticle growth, nucleus size increases by molecular addition. Along with nucleus growth, solution supersaturation decreases. There are three discrete steps for nanoparticle growth: diffusion of the growing species from the solution to the nucleus surface, adsorption of the growing species onto the nucleus, and the incorporation of the growing species into the nucleus. Nanoparticle growth process can be diffusion-controlled or particle surface reaction controlled. If the growth is controlled by diffusion, concentration gradient and temperature distribution in the given system are important factors in determining the growth rate.

For homogeneous nanoparticle growth, diffusion-controlled growth is often encountered. No new nuclei form as long as the consumption of the precursor(s) by the growing nanoparticles is not exceeded by the rate of precursor addition. At this stage, smaller particles grow more quickly than larger ones because the free energy driving force is larger for smaller particles. As a result, the particle size distribution becomes smaller. This is called focusing in size. Nearly monodispersed size distribution can be obtained at this stage [2]. Assuming the growing nanoparticles have a spherical shape, the particle size distribution change can be understood from Fick's first law [3,4]:

$$J = 4\pi x^2 D_{\text{diff}} \frac{dC}{dx}, \quad (2.10)$$

where J is the growing species flux through a spherical shell of radius x . D_{diff} is the diffusion coefficient of the growing species, and C is the bulk concentration of the growing species in the solution. Assuming that the saturation concentration, C_s , is maintained at the particle surface and a steady-state diffusion exists in the solution:

$$J = 4\pi r D_{\text{diff}}(C - C_s), \quad (2.11)$$

$$\frac{dr}{dt} = \frac{JV_m}{4\pi r^2} = D_{\text{diff}}(C - C_s) \frac{V_m}{r}, \quad (2.12)$$

where V_m is the nucleus molar volume. In general, the average nanoparticle radius r can be estimated as a function of growth time, t :

$$r^2 = r_0^2 + K_r t, \quad (2.13)$$

where r_0 is the initial particle radius, and K_r is a constant that obeys the Arrhenius relation. In addition, from Equation (2.12), there is

$$\frac{\delta r}{\delta r_0} = \frac{r_0}{r}. \quad (2.14)$$

Thus,

$$\frac{\delta r}{r} = \left(\frac{r_0}{r}\right)^2 \frac{\delta r_0}{r_0}. \quad (2.15)$$

Equation (2.15) shows that the relative particle size distribution becomes narrower as the particles grow. This is why nanoparticle focusing in size can occur.

For surface reaction-controlled particle growth, the relative particle size distribution depends on whether the surface layers grow in a sequential (monolayer, slow reaction-controlled growth) or parallel (multilayer) manner. For monolayer

growth, the growth is limited by reaction(s) on particle surfaces; therefore, all nanoparticles will grow simultaneously:

$$\frac{dr}{dt} = K_{mo}r^2, \quad (2.16)$$

$$\frac{\delta r}{r} = \frac{r}{r_0} \frac{\delta r_0}{r_0}, \quad (2.17)$$

where K_{mo} is a constant. This means that the relative particle size distribution increases with particle growth. For multilayer growth,

$$\frac{dr}{dt} = K_{mt}, \quad (2.18)$$

$$\frac{\delta r}{r} = \frac{r_0}{r} \frac{\delta r_0}{r_0}, \quad (2.19)$$

where K_{mt} is a constant. This means that the relative particle size distribution decreases with particle growth, but to a lesser extent than the diffusion-controlled particle growth mode.

When the solute concentration drops below supersaturation level, many systems exhibit a distinct nanoparticle growth phase in which Ostwald ripening (a phenomenon in solid solutions or liquid suspensions that, over time, small particles dissolve and redeposit onto larger particles) occurs. Smaller particles dissolve because of their higher solubility and precipitate on the surface of larger particles, where the solubility is lower. A detailed mathematical description of Ostwald ripening was first developed by Lifshitz and Slyozov, and separately by Wagner. The combined model is referred to as LSW theory and can be found elsewhere [5,6]. At the Ostwald ripening stage of nanoparticle growth, it is very difficult to obtain monodispersed particles. If the process is extended for a long enough time to completely deplete the smaller particles, the average particle size increases and the desired nanoparticle size range can easily be exceeded. If the nanoparticle growth process is stopped at this Ostwald ripening stage, the particles will have a wide size distribution. From a different perspective, since high enough solubility of the solid phase is the necessary condition for Ostwald ripening, this approach is mostly only effective for narrowing the size distribution of semiconductor nanoparticles, at the expense of increasing average particle size. For metal nanoparticles, this method is less effective. For oxide nanoparticles, this method has almost no effect. In general, Ostwald ripening is undesirable and should be avoided, most effectively by eliminating the necessary thermodynamic condition(s), such as by suppressing the solubility of the nanoparticles. Nanoparticle growth can also be confined within a limited space to control the nanoparticle

growth kinetically and avoid Ostwald ripening. Such processes include micelle synthesis, spray pyrolysis, and templating, which will be discussed later.

Because of the large surface area and high surface energy available, nanoparticles can also grow through aggregation of small particles or unstable nuclei. Aggregation occurs by engulfing smaller particles onto the surfaces of large particle clusters; the growth rate is higher than that through molecular addition, but the process is not as controllable. More problematically, smaller nanoparticles or nuclei tend to aggregate with large particles more often than with the same size counterparts. This is because when the surface charge density is the same, the aggregation rate decreases exponentially. In addition, the barrier for aggregation increases with the particle size. This means that aggregation is a more dominant phenomenon for nanoparticles compared with their micron-sized counterparts. To prevent aggregation of nanoparticles, stabilizing agents can be used. When stabilizing agent molecules attach to nanoparticle surfaces [7], they sterically stabilize nanoparticles in the solution, mediate nanoparticle growth/aggregation, and passivate the electronic states of nanoparticle surfaces. In summary, overall nanoparticle nucleation and growth can be illustrated in Figure 2.2.

Particle size growth is a relatively well-discussed topic, under the assumption that particles are spherical and grow isotropically. This concept works well for amorphous particles. Many nanoparticles, however, are crystalline and the surface energies are different at different crystallographic orientations, which need to be considered during particle growth. Anisotropic particle growth is thermodynamically favored. This is also the basis for synthesizing nanobelts, nanoribbons, nanotubes, nanoprisms, etc. However, anisotropic nanoparticle growth is beyond the scope of this book and will not be covered. When the surface energies of different crystal planes are not drastically different, the isotropic assumption is acceptable and equiaxed particles can be made.

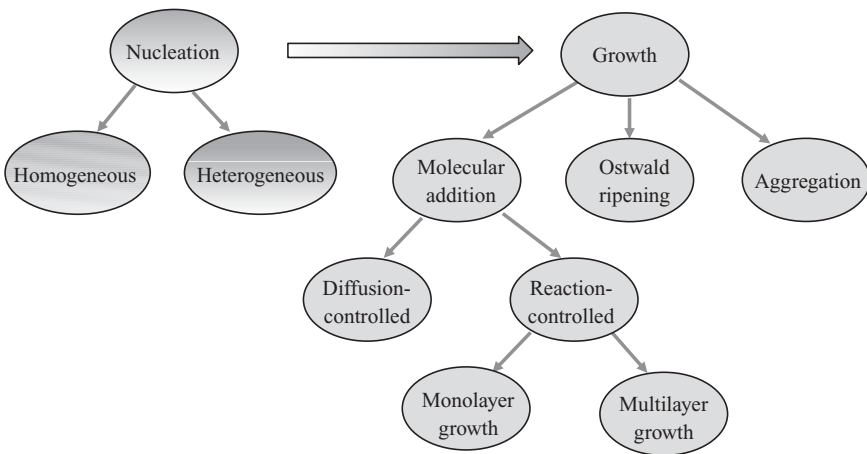


FIGURE 2.2 Nanoparticle nucleation and growth relationships.

2.3 GAS-PHASE NANOPARTICLE SYNTHESIS

In gas-phase synthesis, vapors of different starting materials react and condense to form nanoparticles. First, with the thermal fluctuation of the synthesis system, nucleation of two or three atoms or molecules occurs when the local vapor concentration is high. Second, atom or molecule level clusters collide, combine, and condense to form a stable nucleus/particle. This collision and condensation step is a stochastic process, and is ruled by the dynamics of the gas species. Colliding clusters or small particles may coagulate and grow until they reach a critical size, after which further growth of the particles becomes undesirable. The mean free path length λ for a particle/cluster in a gas is estimated by [8]

$$\lambda = \frac{4}{\sqrt{2}\pi N_g (D_G + D_p)^2}, \quad (2.20)$$

where D_p is the particle diameter, D_G is the diameter of the atoms or molecules of the gas species, and N_g is the number of gas atoms or molecules per unit volume. λ is inversely proportional to the density of gas molecules and the vapor pressure in the system.

As the processes of condensation and cluster collision are random by nature, the distribution of particle sizes obtained by gas-phase synthesis is relatively broad. Lowering synthesis temperature can reduce excessive cluster collision and decrease particle size distribution; but the minimum temperature must be able to sustain the vapor phase and cluster collision and reaction. This means that a reasonably high temperature must be sustained throughout the process. However, the high synthesis temperature often causes hard agglomerate formation because of nanoparticle sintering and solid bond formation. To overcome this problem, the synthesis system is sometimes quenched with an inert, cold gas directly after particle formation, or the particles are loaded with electrical charges of the same sign so that the particles repel each other and the agglomeration process is terminated.

2.3.1 Gas–Gas Reaction

2.3.1.1 Physical Vapor Synthesis **Inert gas condensation:** The earliest process for synthesizing nanoparticles in a gas phase is inert gas condensation, which applies thermal evaporation to a metal source within a vacuum chamber filled with a small amount of inert gas and the condensation of the metal vapor leads to metal nanoparticle formation. The inert gas is used to influence the collision frequency of the evaporating species. During the entire process, only the physical state of the species is altered. The condensation process includes nucleation, particle growth, and particle coagulation and coalescence. The process is illustratively shown in Figure 2.3.

The specific synthesis conditions dictate which of these processes will have a more significant role in the nanoparticle characteristics. For example, gold

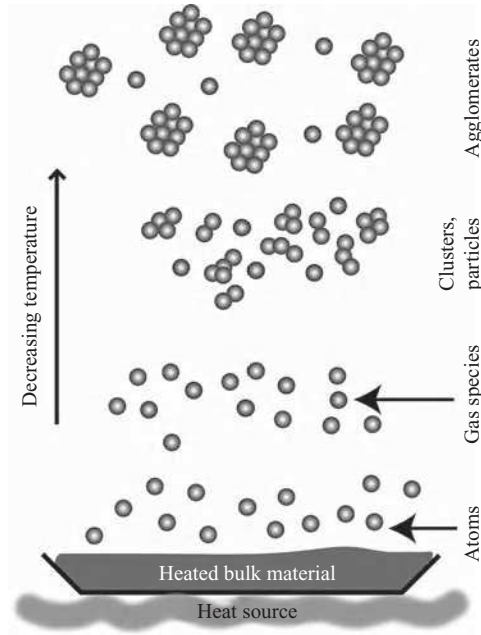


FIGURE 2.3 Illustration of the inert gas condensation process. (For a color version of this figure, see the color plate section.)

nanoparticles can be made by evaporating bulk gold in a boat at high temperatures. The atoms of gold vapor emanating from the boat collide with the atoms of the inert gas, rapidly losing energy with each collision. The collisions with other thermalized gold atoms lead to gold nanoparticle nucleation and formation. As long as the collision mean free path is very short, that is, in the order of 100 nm, the nucleation process proceeds homogeneously in the vapor phase. Helium is usually used as the inert gas as it has a high thermal conductivity. At a high supersaturation of the evaporating species, nucleation abruptly takes place, forming a very large number of extremely small primary particles. For steady-state cluster formation and distribution, the nucleation rate J_N depends on the supersaturation S of the metal vapor in the gas phase:

$$J_N \propto \exp\left(\frac{-\gamma^3}{\ln^2 S}\right), \quad (2.21)$$

where γ is the specific surface energy. The free energy barrier, ΔG_c , against nucleation is also a function of γ and S as follows:

$$\Delta G_c = \frac{16}{3}\pi \frac{\gamma^3}{(\rho RT \ln S)^2}, \quad (2.22)$$

where ρ is particle density, R is gas constant, and T is temperature.

The supersaturation of a metal vapor is related to the collision of the metal atoms with the gas atoms and the amount of undercooling, thus the nucleation process and the evaporation temperature of the metal source. Based on the temperature dependence of vapor pressures of various vaporizing species, it is possible to estimate the supersaturation in the gas phase at a given condition [9].

Once nucleation has taken place, the growth of nanoparticles is spontaneous and occurs within a thin layer above the surface of the evaporating source [9]. Particles experience collisions due to random motion and grow to larger sizes as additional material is deposited on the surfaces of the primary particles. Coalescence (joining, bonding, or welding of particles) is the dominant mechanism for particle growth [10]. Particles formed in the gas phase can travel by thermophoresis (a natural movement of nanoparticles in a decreasing temperature direction) to a cold finger where they are collected.

Inert gas condensation was pioneered by Gleiter, who synthesized iron nanoparticles that demonstrated properties different from their bulk counterparts [11]. Since then, the process has been improved and applied to different pure metals, alloys, oxides, and composites.

First, for metal species, silver nanoparticles are synthesized by inert gas condensation with flowing helium in the chamber. The example synthesis temperatures are 1123, 1273, and 1423 K and the helium pressures are 0.5, 1, 5, 50, and 100 torr, respectively [10]. Silver atoms evaporated from a tungsten boat rapidly lose their kinetic energy by collision with the helium atoms and transform from vapor phase to solid phase above the evaporation source. Near the evaporation source, where the temperature is high, homogeneous nucleation of primary particles in the gas phase takes place abruptly and proceeds at a high rate. These particles serve as a sink for additional vapors that quickly reduce the supersaturation and quench any additional nucleation. The particle size synthesized is fairly small and ranges from 9 to 32 nm, depending on the growth conditions. At lower evaporation temperature and inert gas pressure, the particle growth by collision is subdued, anisotropic specific surface energy for different crystallographic planes is minimized, and smaller particles are formed with a spherical shape. Also, particle coalescence and sintering are less likely and the synthesized particles have less agglomeration. Particle sizes range from 9 ± 1 to 24 ± 1 nm when the evaporation temperature is 1123 K and the helium pressures are 0.5, 1, 5, 50, and 100 torr for the silver nanoparticles. Figure 2.4a shows the image of silver nanoparticles synthesized at 1123 K and at a helium pressure of 0.5 torr (low temperature, low inert gas pressure). Size distribution of the silver nanoparticles is shown in Figure 2.4b. These particles are 9 nm in size and spherical in shape, have a narrow size distribution, and are necked with each other in a chain-like morphology. Figure 2.4c shows the transmission electron micrograph of silver nanoparticles synthesized at 1423 K and at a helium pressure of 0.5 torr, which have a much larger particle size and exhibit a greater amount of necking. Note that the magnifications of Figures 2.4a and c are the same. The substantial effect of temperature on the silver nanoparticle size is easy to see. Bismuth nanoparticles with an average diameter of 12–37 nm are synthesized by controlling the

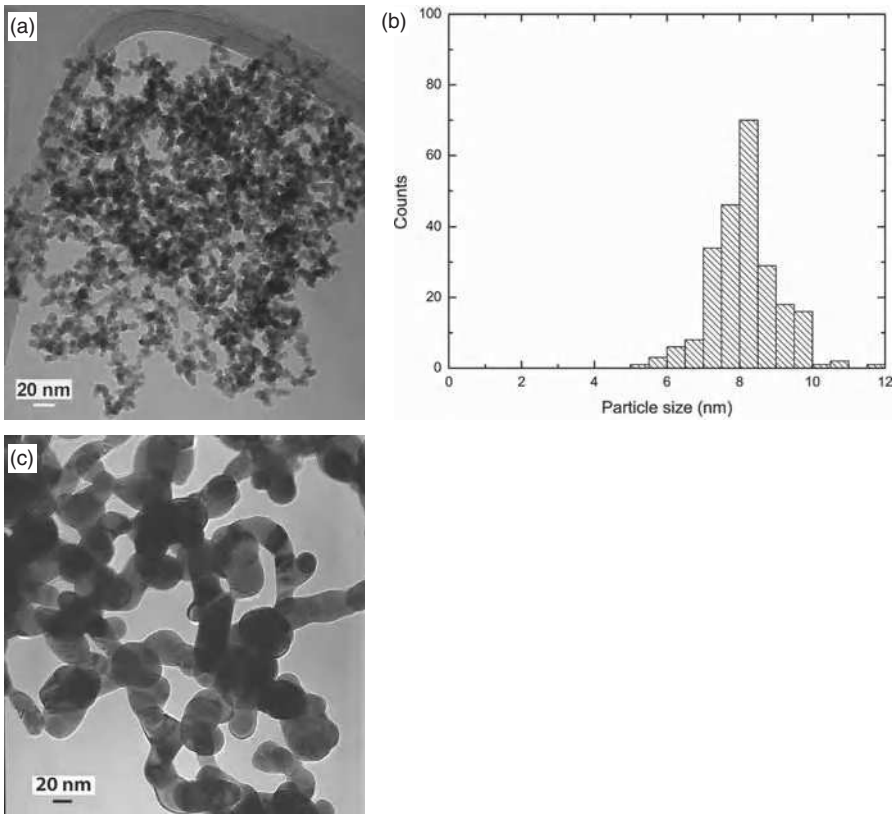


FIGURE 2.4 Transmission electron bright field images: (a) silver nanoparticles synthesized at an evaporation temperature of 1123 K and a helium pressure of 0.5 torr, (b) particle size distribution, and (c) silver nanoparticles synthesized at an evaporation temperature of 1423 K and a helium pressure of 0.5 torr. The scale bars are 20 nm [10]. (Reprinted with permission from Raffi M, Rumaiz AK, Hasan MM, Shah SI. Studies of the growth parameters for silver nanoparticle synthesis by inert gas condensation. *J Mater Res* 2007;22(12):3378–3384.)

quenching gas flow rate, carrier gas flow rate, and chamber pressure [12]. Narrow particle size distribution is obtained when these parameters are properly controlled. Increasing the carrier or quenching gas flow rates and decreasing the pressure decrease the product particle size. Particles directly deposited from the gas phase are similarly sized spheres and essentially nonagglomerated.

In addition to single element metallic nanoparticles, inert gas condensation can also be applied to alloys. The key is to control the evaporation and condensation rates of the source materials so that the desired stoichiometry is obtained. When properly done, atomic level alloying can be achieved. Au/Pd bimetallic nanoparticles are fabricated by inert gas condensation with a sputter. The starting material used is 50:50 Au/Pd alloy. By controlling both the atmosphere (Ar and He) in the condensation chamber (partial pressure $1\text{--}2 \times 10^{-1}$

torr) and the magnetron power (in the range of 32–130 W), Au/Pd nanoparticles with a high degree of monodispersity in size (1.1, 3.0, and 5.0 nm) are produced [13].

In order to produce monodispersed nanoparticles, two prerequisites must be satisfied for inert gas condensation [4]. First, the nucleation and growth stages must be separated distinctly. Since nuclei grow stochastically in the nucleation stage, a long nucleation stage leads to a broad size distribution. For monodispersed particle size formation, nucleation must be finished in the early stage of the particle formation process, and then only the initially formed nuclei should grow without further nucleation. Second, the aggregation/coalescence of the growing particles must be prohibited because it broadens the particle size distribution significantly. In general, quenching the system right after the nucleation to eliminate extended nucleation process and separating particles completely after a certain size are effective strategies.

While metal nanoparticle synthesis by inert gas condensation is more common, oxides such as AgO, WO₃, and SnO [14] nanoparticles are also produced by this method with different O₂ amounts, raw material feeding rates, and gas types and pressures. The effects of these parameters on the size, morphology, and specific surface area of the nanoparticles follow three general trends [15]. (i) With an increasing amount of O₂, smaller, more spherical, and less chain-like nanoparticles are more likely. This is because high oxygen amount leads to faster and more complete consumption of metal species. (ii) Low raw material feeding rate results in the formation of finer nanoparticles. At lower raw material feeding rate, due to the lower vapor pressure from the precursors, less collision and coalescence take place, the growth rate of particles slows down, and thereby, relatively small particles are formed. (iii) Higher gas pressure results in more nanoparticle collisions and coarser particle sizes. Mean particle diameter is almost proportional to the pressure for a given type of gas. Increased atomic weight of the gas is also favorable for the formation of larger particles. Mn₃O₄ particles ranging from 2 nm to above 100 nm are produced by flowing moist helium over a manganese granule (99.99% pure) boat, with the majority of particles falling in the range below 20 nm with a modal particle size (the size that occurs most frequently in the frequency distribution) of 6 nm. The smaller particles are single crystals, but the larger particles appear to have a dense region around their edges with a less dense center [16].

Composite nanoparticles with different composition distributions are also synthesized by inert gas condensation. Nonstoichiometric CuO_x/CeO₂ composite consists of aggregated CeO₂ nanocrystallites over which amorphous copper clusters (or a thin film of the solid solution) are finely dispersed. In the range of 6–20 at% copper, copper is predominantly located on the surface. Development of core/shell structures occurs in the 30–70 at% copper concentration range and is attributed to a sequential oxidation of cerium followed by copper. The composition of nonstoichiometric CuO_x/CeO₂ nanocomposite particles can be changed over almost the entire composition range (2–98 at% copper) [17]. Again, the

helium gas pressure controls the nanoparticle size and aggregation. Resistive evaporation and laser ablation can be combined in an inert gas condensation system to synthesize core/shell nanoparticles composed of different materials. Resistively evaporated nickel and laser ablated CoO form core/shell particles with improved magnetic properties [18]. The particles have single domain and superparamagnetic behavior at room temperature as a result of their small sizes.

Molecular dynamic simulation is employed to provide a detailed analysis of the coalescence of iron clusters over the course of their growth in an inert gas atmosphere. The changes in atomic structure and morphology show that the duration of the coalescence depends on the state of the colliding clusters. At elevated temperatures an exponential decay of the cluster shape is found. At lower temperatures, clusters exhibit a regular atomic structure. The coalescence process includes the restructuring of the clusters and has three distinct steps under nonadiabatic conditions: neck formation at the contact area of the particles, transformation from the dumbbell shape to an oval shape, and coalescence from the oval shape toward a spherical shape. Each of these steps is related to a different extent of heat exchange with the carrier gas [19].

Inert gas condensation has the advantages of single-step production, involvement of only inorganic and easy-to-obtain precursors, production of high-purity nanoparticles, and potential for large-scale production with a high yield. Due to the high-temperature nature of the synthesis approach, nanoparticles usually have good thermal stability. The main issues are poor particle size distribution control and agglomeration. Also, the species that can be synthesized are also relatively limited.

Physical vapor deposition: In addition to evaporating the source material, a vapor phase can be generated by plasma. This different type of precursor generation process can be generalized as physical vapor deposition as shown in Figure 2.5 and holds much promise for the synthesis of nanoparticles. Different from conventional thermal process, a reduction in the residence time of the particles in the reaction zone and rapid cooling of the formed particles fundamentally change nanoparticle formation mechanisms. The thermal diffusion-controlled mass transport is replaced by the collision with a carrier gas.

Metal and oxide nanoparticles such as gold, copper, TiO_2 , ZnO , $\gamma\text{-Al}_2\text{O}_3$, and Cu_2O are synthesized by physical vapor deposition. The mean particle size and crystallographic orientation are mainly influenced by the sputtering power, the substrate temperature, and the nature, pressure, and flow rate of the sputtering gas. Chromium clusters in the size range of 7.6–13 nm produced by physical vapor deposition are shown in Figure 2.6 [20]. Inert gas flow first favors smaller particle size but then increases the particle size. Particles are mostly spherical. As the argon pressure increases, particle size and size distribution increase [21]. Mg–Cu alloy nanoparticles are prepared by physical vapor deposition in a mixture of argon and hydrogen using micron-sized magnesium and copper as raw materials [22]. A series of intermetallic compounds (Mg_2Cu , MgCu_2) form during the synthesis [23].

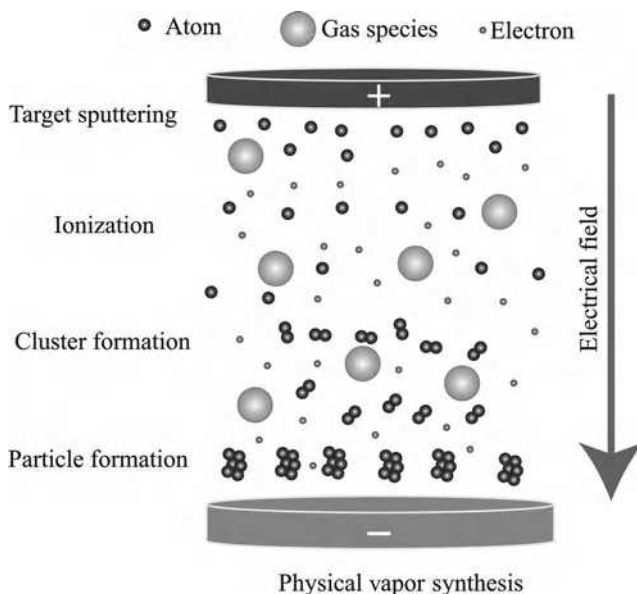


FIGURE 2.5 An illustration of physical vapor deposition process. (For a color version of this figure, see the color plate section.)

Some interesting features that physical vapor deposition has include the abilities to deposit nanoparticles on a substrate and form core/shell nanoparticle structures. The substrate temperature can be controlled to achieve different particle size. Titanium is deposited at 300 K (a fairly low temperature) on reconstructed Au(111) substrate. The elbow sites of the herringbone reconstruction serve as selective nucleation sites for the growth of titanium islands. These tiny islands at the specific sites evolve into titanium nanoparticles in regular arrays (Fig. 2.7). TiO_2 nanoclusters are synthesized by subsequent exposure of the titanium nanoparticles to oxygen at 300 K [24]. Monolayer islands with an apparent height of ~ 0.2 nm are observed in the coverage range from 0.05 to 0.25 ML (monolayer), and both the size and density of the titanium islands increase with increasing titanium coverage. Second, layer features appear when the titanium coverage reaches ~ 0.5 ML, and distinct particles are evident up to the titanium coverage of 1 ML. The oxidation of titanium leads to (i) a more disordered arrangement of the clusters, (ii) an increase in the nanoparticle height (from ~ 0.2 to 0.28–0.38 nm), and (iii) a broader size distribution (from ~ 3 to 1.8–8.5 nm) [24]. SiO_2 -coated iron nanocapsules are synthesized using micron-sized powders as the raw materials. Most of these nanocapsules are spherical with a “core/shell” type structure. The shell is amorphous SiO_2 with around 10–20 nm thickness; and the core is ferromagnetic iron. The iron core has a body-centered cubic structure and may act as a catalyst [25]. The SiO_2 shell may protect iron nanoparticles from corrosion and oxidation.

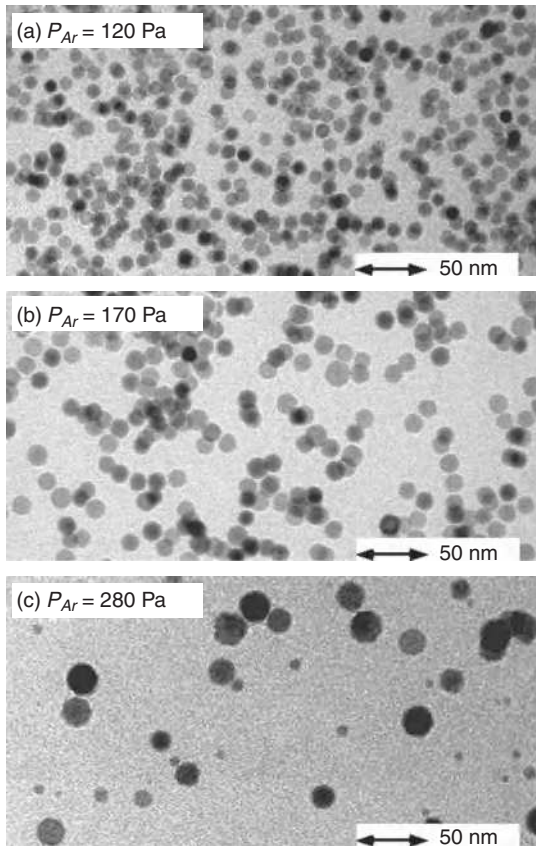


FIGURE 2.6 Transmission electron images of chromium clusters produced by varying argon gas pressure: (a) 120 Pa, (b) 170 Pa, and (c) 280 Pa. The argon gas flow rate is constant at $1.0 \times 10^{-5} \text{ m}^3 \text{ s}^{-1}$ [20]. (Reprinted with permission from Yamamuro S, Sumiyama K, Suzuki K. Monodispersed Cr cluster formation by plasma-gas-condensation. *J App Phys* 1999;85:483–489, Copyright 1999, American Institute of Physics.)

2.3.1.2 Chemical Vapor Synthesis When single component raw material used in physical vapor synthesis is replaced by chemical compounds, or different vapors are introduced to participate in reactions, the process evolves into chemical vapor synthesis. Chemical vapor synthesis has reaction(s) proceeding the nucleation and growth of nanoparticles from the vapor-phase precursors (Fig. 2.8). In chemical vapor synthesis, gas-phase reactions and particle formation take place at high temperatures under nonequilibrium conditions. The process is mainly concerned with vapor-phase chemical reaction, nucleation from supersaturated vapors to form particles, particle growth by vapor condensation and/or heterogeneous chemical reactions, coagulation by particle–particle collisions induced by their Brownian motion, and coalescence or sintering between particles. It is possible to create fine particles with a wide size range, such as 5–200 nm. Just

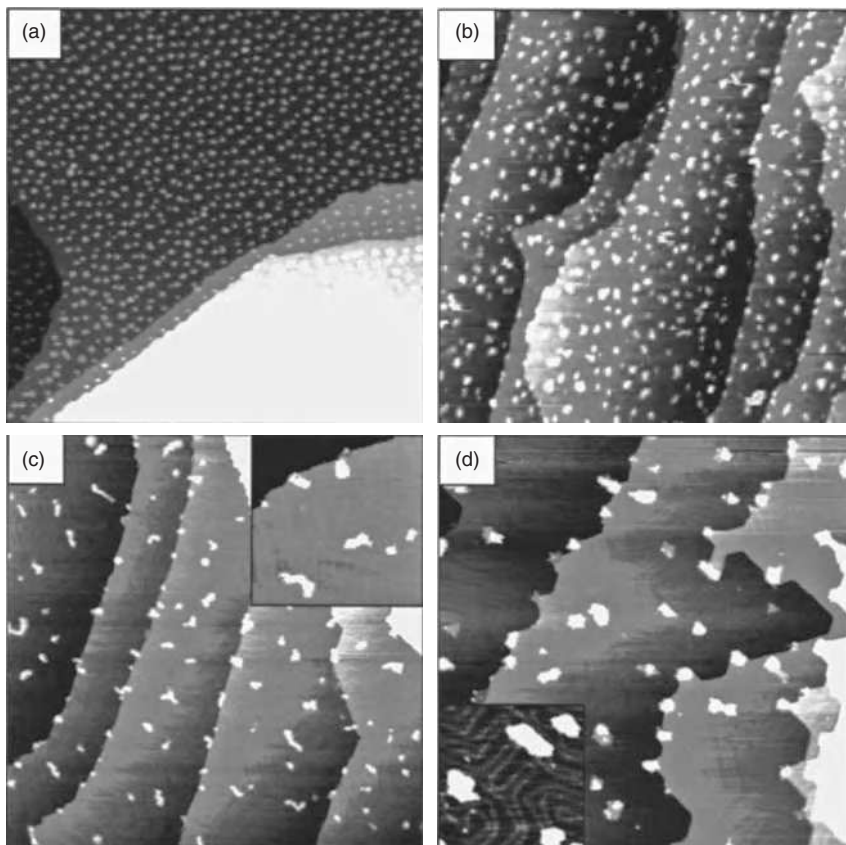


FIGURE 2.7 Scanning tunneling microscopy images illustrating the morphological changes of titanium clusters on Au(111) due to oxidation and subsequent annealing. (a) Well-ordered arrays of titanium clusters after physical vapor deposition of 0.1 ML titanium at 300 K onto reconstructed Au(111) surface. (b) Subsequent oxidation of the titanium clusters by oxygen exposure (5×10^{-5} mbar for 200 s) at 300 K leading to disordering and growth of the particles. Faceted TiO_2 crystallites are observed after annealing to 600 K (c) and 900 K (d), respectively (10 minutes at each temperature). Details of the herringbone reconstruction and the “turns” around the oxide particles are shown in the insets. The images correspond to an area of $200 \times 200 \text{ nm}^2$ (a–c) and $160 \times 160 \text{ nm}^2$ (d). The insets correspond to an area of $40 \times 40 \text{ nm}^2$ [24]. (Reprinted with permission from Biener J, Farfan-Arribas E, Biener M, Friend CM, Madix RJ. Synthesis of TiO_2 nanoparticles on the Au(111) surface. *J Chem Phys* 2005;123:094705, 6pp., Copyright 2005, American Institute of Physics.)

as for physical vapor synthesis, a carrier gas, often argon or nitrogen, transports the evaporated precursors through a heated reaction zone. A tubular furnace with temperatures up to 1500 K may be used as a heat source. Chlorides, carbonyls, and metal organic compounds are often used as precursors. Chemical reactions may leave some traces behind that might be dissolved in the matrix of particles or adsorbed on the particle surfaces, which should be avoided for high-purity

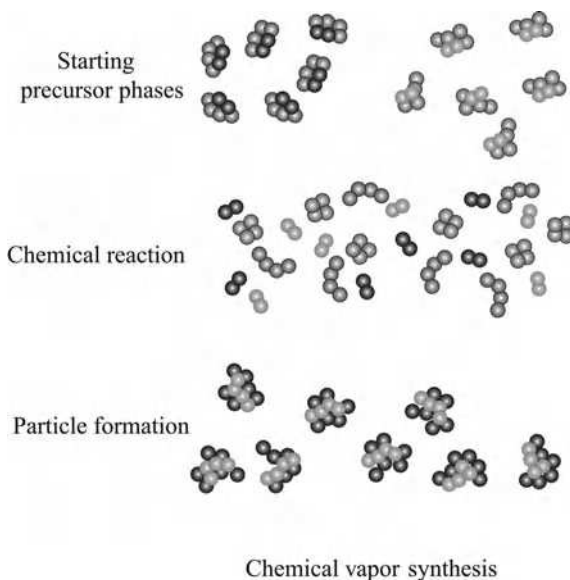


FIGURE 2.8 Illustration of chemical vapor synthesis process. (For a color version of this figure, see the color plate section.)

nanoparticle synthesis. Low synthesis temperatures lead to extremely fine, fluffy, and in most cases, glassy nanoparticles. Nucleation of oxide species is virtually instantaneous due to the very rapid oxidation and high concentration(s) of the precursor vapors, and only the physical coalescence determines the final particle size and morphology. When the particle size is very small, it is generally assumed that whenever two spherical particles collide they form a larger particle; that is, coalescence is instantaneous. This is mainly due to an enhanced surface diffusion coefficient for clusters only a few nanometers in size. However, as the particles grow larger, this assumption fails, since the particle coalescence is no longer “instantaneous.” Thus, beyond a critical size the particles stop growing by instantaneous coalescence and fractal-like aggregates begin to form.

Magnetic cobalt nanoparticles are synthesized by a chemical vapor decomposition method using cobalt carbonyl ($\text{Co}_2(\text{CO})_8$) precursor as the source under a flowing inert gas atmosphere [26]. When the carrier gas is argon, spherical or long-string particles with the coexistence of face-centered cubic and hexagonal close packing structures are obtained. When the carrier gas is helium, cobalt metallic cores distribute in CoO and only face-centered cubic structure forms (oxidation is severe). Iron nanoparticles are synthesized by the pyrolysis of iron pentacarbonyl ($\text{Fe}(\text{CO})_5$) under argon or helium atmosphere. The synthesized nanoparticles consist of core/shell-type structure comprised of metal core and oxide shell with a nearly spherical shape and 6–25 nm mean diameter. Average particle size increases and size distribution becomes wider and more asymmetric with increasing decomposition temperature [27]. This is understandable

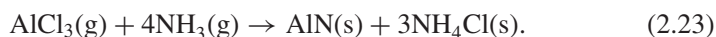
because of the accelerated and overlapping nucleation and particle growth processes. In addition to metal nanoparticles, oxide nanoparticles are also routinely synthesized using chemical vapor synthesis. Volatile organometallic precursor $[\text{CH}_3\text{ZnOCH}(\text{CH}_3)_2]_4$ (subsequently denoted “heterocubane”) decomposition in a microwave plasma combined with a hotwall zone leads to the formation of ZnO particles with controlled morphology, high crystallinity, and high purity [28]. The synthesis setup and reaction temperature have substantial influence not only on the yield but also on the crystallite size and crystallinity of the ZnO nanoparticles. A hot-wall reactor in series with a microwave reactor helps to grow ZnO nuclei into nanoparticles of improved crystallinity [29].

Besides simple metal and oxide nanoparticles, a thin layer of secondary species nanoparticles can be coated on core particles. Coating of 20–40 nm Cr_2O_3 particles on Al_2O_3 particles is achieved by chemical vapor deposition in a fluidized bed, in which a $\text{Cr}(\text{CO})_6$ precursor is decomposed and deposited on the surface of Al_2O_3 particles. Further heat treatment in vacuum in a graphite furnace converts Cr_2O_3 to Cr_3C_2 , and Al_2O_3 – Cr_3C_2 composite particles are obtained [30]. In this case, heterogeneous nucleation and growth of the secondary phase on the surface of existing particles is a must.

Another useful feature of chemical vapor synthesis is doping minor elements into matrix particles, a process that is difficult to achieve through other quasi-equilibrium processes because the synthesis path is thermodynamically unfavorable. The high temperature and nonequilibrium nature of the chemical vapor synthesis process enables doping of nanoparticles with high dopant concentrations. When ZnO is doped with chromium, the chromium dopant atoms are incorporated into the wurtzite host lattice and do not form a second phase [31]. Chromium atoms reside partially on ideal and partially on distorted tetrahedral sites (substitutional zinc sites or tetrahedral interstitial sites, or both). The atomic level mixing during the chemical vapor reaction stage makes this doping feasible in the first place. Aluminum-doped ZnO nanoparticles are synthesized by chemical vapor synthesis, which facilitates the incorporation of a higher percentage of dopant atoms, far above the thermodynamic solubility limit of aluminum [32]. In addition to metal doping of oxides, oxides can also be dopants. For example, Al_2O_3 is doped into ZrO_2 particles by chemical vapor synthesis using a variable, modular gas flow reactor. Three different $\text{ZrO}_2/\text{Al}_2\text{O}_3$ nanoparticles result: single-phase particles formed by doping ZrO_2 with Al_2O_3 , coated particles, and composite consisting of mixed nanoparticles of Al_2O_3 and ZrO_2 [33]. ZrO_2 nanoparticles doped with up to 50 mol% Al_2O_3 are prepared. Doping with Al_2O_3 decreases the fraction of monoclinic ZrO_2 phase and stabilizes tetragonal or cubic ZrO_2 phase, forming different $\text{ZrO}_2/\text{Al}_2\text{O}_3$ solid solutions. Tetragonal ZrO_2 solid solution is obtained in the as-synthesized nanoparticles doped with 3 and 5 mol% Al_2O_3 , whereas cubic ZrO_2 solid solution is formed in the nanoparticles with 15 mol% Al_2O_3 . ZrO_2 nanoparticles with higher Al_2O_3 content (30 and 50 mol% Al_2O_3) are amorphous and crystallize during annealing, forming single-phase tetragonal ZrO_2 at 800°C and a mixture of tetragonal ZrO_2 and γ - η - Al_2O_3 at 850°C, respectively. The formation of metastable solid

solutions is possible because chemical vapor synthesis is a highly nonequilibrium process [34].

In addition to making metal and oxide nanoparticles with flexible doping ability, chemical vapor synthesis also allows the synthesis of intermetallics, carbides, nitrides, and composites such as SiC–BN [35] and α -Al₂O₃–TiN [36]. The capability to produce uniformly mixed particles of different compositions is an added advantage. Particles typically have a high crystallinity and a low defect density. TiAl₃-containing aluminum nanoparticles are prepared by a chemical vapor synthesis process using AlCl₃ and TiCl₃ as precursors and magnesium as the reducing agent. The resulting particles are spherical with the average size in the range of 10–50 nm [37]. Nano-sized WC–Co composite particles, which sometimes contain W₂C or tungsten phase, are produced by reacting vaporized chlorides (WCl₆ and CoCl₂) with methane–hydrogen mixtures. The particle size is <70 nm [38]. Highly crystalline AlN nanoparticles are synthesized at over 900°C by chemical vapor reaction in an AlCl₃–NH₃–N₂–H₂ system. The starting material is gasified AlCl₃, generated using a preheating system. AlCl₃ gas is transported to a tube furnace in the NH₃–N₂–H₂ atmosphere:



NH₄Cl can be washed away with water or anhydrous ethanol. The average size of the spherical AlN particles decreases from 250 to 40 nm with increasing reaction temperature [39]. The particles are porous and have a specific surface area of 80 m² g⁻¹. Crystalline WS₂ nanoparticles are synthesized by decomposing W(CO)₆ over sulfur vapor in an inert gas flow, which leads to a direct reaction between as-formed pure tungsten nanoclusters and sulfur vapor. The produced nanoparticles have a spherical shape with a mean size in the range of 20–70 nm [40].

Chemical vapor synthesis has considerable flexibility in producing a wide composition range of nanoparticles using a wide variety of precursors. The key advantages of the process are the homogeneity of the composition at atomic or molecular level, the ease of doping various elements in one synthesis step, and a well-defined reaction zone in which temperature, pressure, and mass flow are controllable and reproducible.

2.3.1.3 Laser Ablation When a pulsed laser beam is used as a source of energy, the nanoparticle synthesis approach is called laser ablation. The general process is illustrated in Figure 2.9. This process can use both metals and oxides as precursors. During the laser ablation, high-power laser pulses are focused on the surface of the precursor target to evaporate the material at more than 1300 K. A supersonic jet of evaporated materials (plume) is ejected perpendicularly to the target surface and expands into the gas space above the target. Within the plume, there is a supersaturated vapor favoring the formation of particles. Immediately after the laser pulse, the temperature in the plume can be 3800 K or more. During the adiabatic expansion of the plume, the temperature decreases. The formed

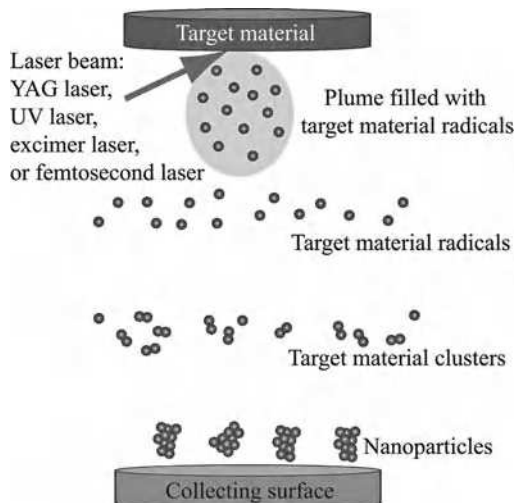


FIGURE 2.9 Illustration of laser ablation process. (For a color version of this figure, see the color plate section.)

particles are transported by a continuous stream of the carrier gas to a powder collector. Due to the rapid evaporation of the precursor(s) in the high-power laser pulse, the stoichiometry of even a complex, mixed target can be preserved in the vapor phase. As the duration of the supersaturated condition is limited by the adiabatic expansion of the plume, the gas pressure in the reaction vessel plays a critical role in particle nucleation and growth. At a low gas pressure, the plume expands very rapidly and the concentration of the reactive species in the plume decreases very rapidly, which effectively limits the particle growth. The higher the supersaturation, the smaller the nucleus size required for condensation. This leads to a large number of nuclei and a small particle size.

During the laser ablation, small clusters and particles are either directly emitted from the target surface or formed as a result of condensation in the decaying plume. Generally, condensation leads to the formation of particles composed of several tens or more (up to several thousands) atoms/molecules. Particles begin to grow after a decrease in temperature during the adiabatic expansion of the plasma plume to supersaturation. Nanoparticles of complex compositions are made possible by the laser ablation. The possibility of synthesizing new (in particular, metastable) materials, which cannot be obtained under equilibrium conditions, is an important advantage of pulsed laser ablation. The shape of the nanoparticles can be controlled by adjusting the wavelength of the laser used.

Usually, the targets used for laser ablation nanoparticle synthesis are bulk sizes, and the lasers are pulsed yttrium aluminum garnets (YAG) lasers, UV laser, excimer lasers, or femtosecond lasers. The quality and sizes of the nanoparticles prepared by this process are controlled by laser parameters and the densities of the evaporation plumes. When a high-power laser density is used, the evaporation process is more intense and the plume expands more quickly all around to lower

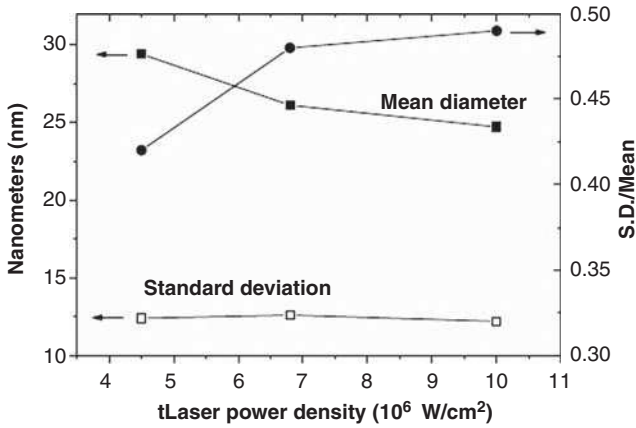


FIGURE 2.10 γ -Fe $_2$ O $_3$ nanoparticle statistics at different laser power densities with a constant mixed gas of 0.18 MPa nitrogen and 0.02 MPa oxygen [44]. (Reprinted with permission from Wang Z, Liu Y, Zeng X. One-step synthesis of γ -Fe $_2$ O $_3$ nanoparticles by laser ablation. Powder Technol 2006; 161:65–68, Copyright 2006, Elsevier.)

the plume density, which is favorable for generating smaller nanoparticles by increasing the average free distance of the nuclei and reducing the collision time of the nuclei particles. Nanoparticle formation using short laser pulses is a well-developed technique. Interesting nanoparticle structures with variable physical and chemical properties can be created [41]. As the carrier gas is concerned, higher pressure reduces the collision time of the nuclei particles and favors small nanoparticles. Similarly, higher oxygen ratio increases not only the evaporation rate and reaction intensity but also the gas flow velocity, which is beneficial for obtaining smaller nanoparticles.

Micron-sized metal particles, including copper, aluminum, and silver, are consolidated before laser irradiation by a cold isostatic press with pressures up to a few hundred MPa. Nanoparticles are synthesized in air by ablation of micron-sized particle compacts using a Nd:YAG laser. The degree of compaction plays a significant role in determining the size of the produced nanoparticles [42]. A Nd:YAG pulsed laser is used to ablate a 0.5 mm diameter iron wire in a mixed gas flux of nitrogen and oxygen to generate α -Fe nanoparticles covered with a shell of γ -Fe $_2$ O $_3$ and pure γ -Fe $_2$ O $_3$ nanoparticles at atmospheric pressure [43]. When irradiated by the pulsed laser beam, the tip of the iron wire is heated to a very high temperature in a very short time, and intense explosive evaporation occurs to generate the plume that contains atoms, ions, and clusters of iron, which react with oxygen of the mixed flowing gas immediately and form many nuclei particles. With the movement of the flowing carrier gas, the nuclei particles collide with each other to grow and then are cooled by colliding with molecules of the carrier gas to form nanoparticles. The mean particle size decreases with the increase in the laser power density, the total gas pressure, and the oxygen species, respectively. Figure 2.10 shows the γ -Fe $_2$ O $_3$ nanoparticle size statistics for a range of laser power densities and a mixed gas composed of 0.18 MPa N $_2$

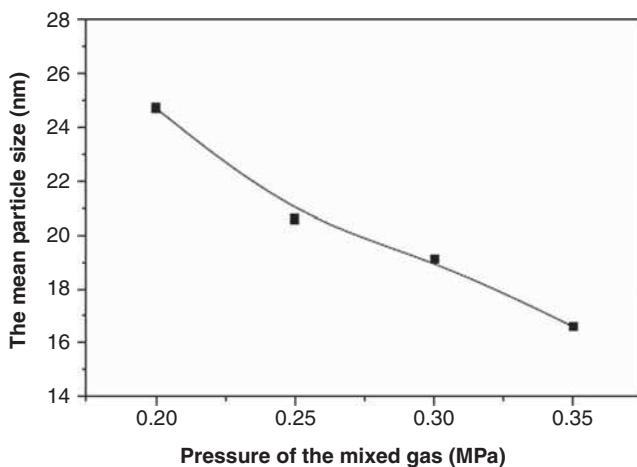


FIGURE 2.11 Relationship of total pressure of the mixed gas with the mean particle size at a laser power density of $1 \times 10^7 \text{ W cm}^{-2}$ and a fixed oxygen pressure of 0.02 MPa [44]. (Reprinted with permission from Wang Z, Liu Y, Zeng X. One-step synthesis of $\gamma\text{-Fe}_2\text{O}_3$ nanoparticles by laser ablation. *Powder Technol* 2006;161:65–68, Copyright 2006, Elsevier.)

and 0.02 MPa O_2 . The mean particle size decreases gradually with increasing laser power density. Except for the laser parameters, the carrier gas pressure is another important factor that controls the mean diameter of the nanoparticles. According to Figures 2.11 and 2.12, the particle size of $\gamma\text{-Fe}_2\text{O}_3$ nanoparticles can be controlled by varying the total ambient pressure or the partial pressure of nitrogen or oxygen. In Figure 2.11, the mean particle size of the prepared $\gamma\text{-Fe}_2\text{O}_3$ nanoparticles decreases with increasing total pressure of the mixed gases when the oxygen pressure is kept at 0.02 MPa. Figure 2.12 displays the effect of oxygen ratio on the mean diameter of $\gamma\text{-Fe}_2\text{O}_3$ nanoparticles at a fixed total mixed gas pressure of 0.25 MPa. The mean particle size decreases rapidly with increasing oxygen pressure. The oxygen in the mixed gas plays an important role in synthesizing $\gamma\text{-Fe}_2\text{O}_3$ nanoparticles; it not only provides the reaction elements for nanoparticle formation but also controls the particle sizes. Comparing the mean particle size plot in Figure 2.10 with Figures 2.11 and 2.12, it can be seen that it is more effective to adjust the particle size in a wide range by varying the carrier gas pressure than by varying laser power density [44].

Nanostructuring of thin metal films by nanosecond UV laser pulses is used for the production of metal nanoparticles supported on a range of different oxide substrates, including indium-doped SnO_2 . This process is performed at low temperatures. After exposure to a laser fluence of $\sim 200 \text{ mJ cm}^{-2}$, a nickel film melts and breaks up into discrete nanometer-scale hemispherical islands. The initial film thickness and the thickness of the oxide layer on the substrate determine the fluence required to achieve this breakup. Higher laser fluences are required to create nanostructures for thinner nickel films. At lower fluences, the films are

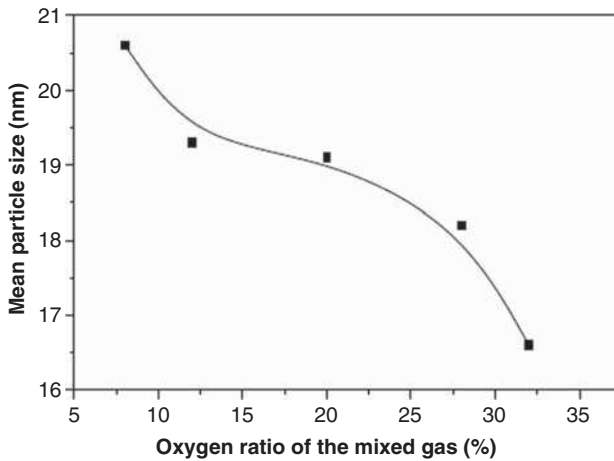


FIGURE 2.12 Effect of the oxygen ratio of the mixed gas on the mean particle size at a laser power density of $1 \times 10^7 \text{ W cm}^{-2}$ and a fixed total pressure of 0.25 MPa [44]. (Reprinted with permission from Wang Z, Liu Y, Zeng X. One-step synthesis of $\gamma\text{-Fe}_2\text{O}_3$ nanoparticles by laser ablation. *Powder Technol* 2006;161:65–68, Copyright 2006, Elsevier.)

observed to perforate, but the breakup into discrete droplets is incomplete. At fluences higher than the threshold for the breakup, no change in the nickel droplet size distribution is observed; the defining parameter that determines the droplet size is the film thickness. The mean particle diameter is observed to increase as the initial film thickness increases [45]. Figure 2.13 shows images of silicon nanoparticles deposited on a SiO_2 wafer by pulsed laser ablation [46]. Silicon nanoparticles of 4–5 nm are synthesized. The particle size distribution is reduced

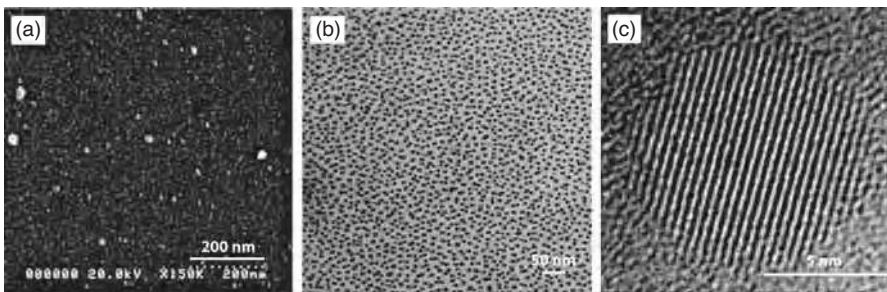


FIGURE 2.13 Images of silicon nanoparticles deposited on a SiO_2 wafer. (a) Scanning electron image of silicon nanoparticles by pulsed laser ablation without a voltage bias. (b) Transmission electron (plain-view) image of silicon nanoparticles by pulsed laser ablation with +300 V bias. (c) High-resolution transmission electron image of a silicon nanoparticle shown in (b) [46]. (Reprinted with permission from Khang Y, Lee J. Synthesis of Si nanoparticles with narrow size distribution by pulsed laser ablation. *J Nanopart Res* 2010;12:1349–1354, Springer Science + Business Media, Fig. 2.)

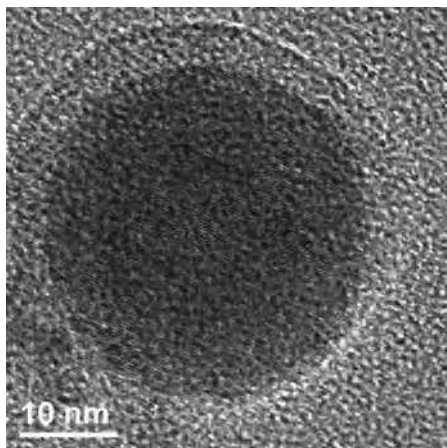


FIGURE 2.14 High-resolution transmission electron micrograph of a CdSe/ZnS core/shell nanoparticle. The darker spherical core and lighter covering shell can be observed [47]. (Reprinted with permission from Gallardo I, Hoffmann K, Keto JW. CdSe & ZnS core/shell nanoparticles generated by laser ablation of microparticles. *Appl Phys A* 2009;94:65–72, Springer Science + Business Media, Fig. 3.)

by a positive voltage bias. The geometrical standard deviation of the nanoparticles is 1.35 and the number density is $1.6 \times 10^{12} \text{ cm}^{-2}$.

When micron-sized particles are continuously ablated by a high-power KrF excimer laser in a flowing aerosol, composite nanoparticles can be created. CdSe/ZnS core/shell nanoparticles are prepared this way. This process can be inverted to produce ZnS/CdSe core/shell nanoparticles. The generated core and shell materials are crystalline. Figure 2.14 shows the crystal fringes and faceted domains. For 10 nm radius cores, shell thickness ranges from 4 to 8 nm. Smaller (~ 2.5 nm), dark clusters have smoother shells, but crystal planes at the interface of the core/shell structure are difficult to resolve [47].

Femtosecond laser is another powerful source that can be utilized for nanoparticle synthesis. Gold and copper are irradiated under a vacuum. Only a few laser pulses are applied to each irradiation site. Under these conditions, the size distribution of nanoparticles does not exhibit a maximum and the particle abundance monotonically decreases with size. Furthermore, two populations of nanoparticles exist within the plume: small clusters that are more abundant in the plume front and larger particles that are located mostly at the back. The ablation efficiency is strongly related to the presence of nanoparticles in the plume [48].

One general problem of the laser ablation process is that a high concentration of evaporated material gathers in the plume. In the case of an insufficiently rapid expansion, this may lead to fractal agglomerate formation. To ensure small nanoparticle sizes, carrier gas pressure and composition need to be considered in order to generate a rapidly expanding plume. Complex phenomena (phase separation, chemical reactions, and interactions with the residual gas) during the

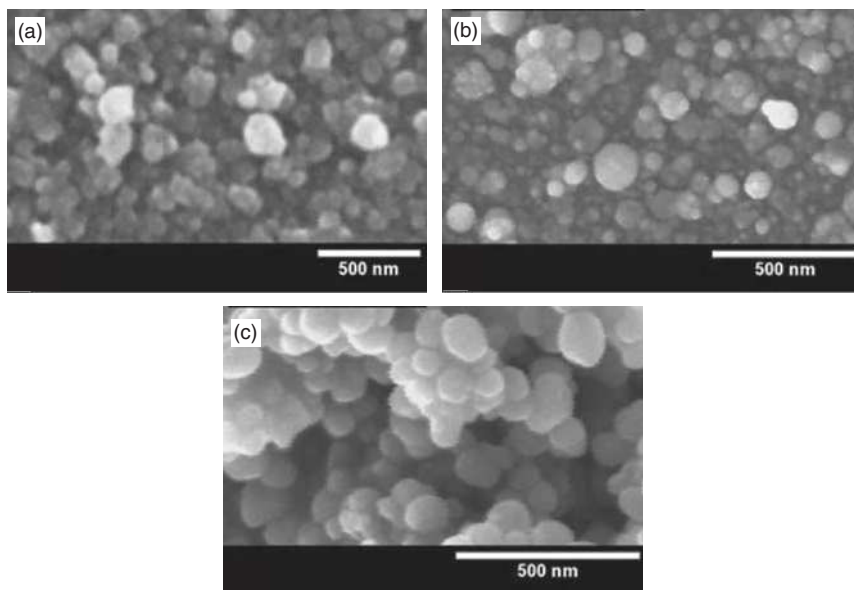


FIGURE 2.15 SEM images of the surfaces of the films grown by femtosecond laser ablation on (a) titanium, (b) silicon, and (c) AlN targets (fluence: 9.6 J cm^{-2} , deposition time: 1 hour) [49]. (Reprinted with permission from Perriere J, Boulmer-Leborgne C, Benzerga R, Tricot S. Nanoparticle formation by femtosecond laser ablation. *J Phys D* 2007;40:7069–7076, IOP Publishing Ltd.)

laser–matter interaction and plasma expansion require further study. Figure 2.15 shows the SEM images of the surfaces of the films grown by femtosecond laser ablation on titanium, silicon, and AlN targets. Nano-sized particles are formed. However, the particle size distribution is different and agglomeration is evident [49].

2.3.2 Gas–Liquid Reaction

When a liquid phase and a gas phase are involved during the nanoparticle formation, we group it as gas–liquid reaction process. The earliest case is spraying aerosols (small liquid droplets) into the reaction chambers, enabling nanoparticle formation upon vaporization, which can be termed flame aerosol synthesis. Carbon black was made in ancient times using this approach. The flame reactor generally consists of a primary flame that is fueled by hydrogen, methane, or air in the burner. In addition to a gaseous or vaporized precursor, it is also possible to directly spray liquid precursors into the primary flame. Liquid-fed flame processes are distinguished for their flexibility in producing nanoparticles of various compositions and morphologies that result in unique product functionalities.

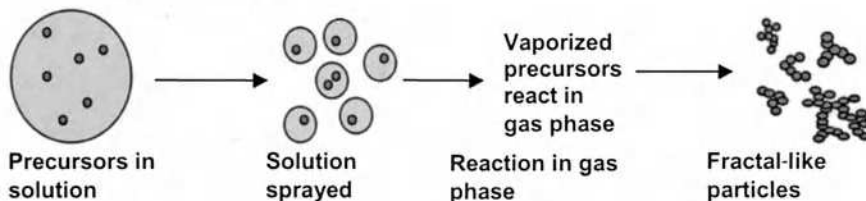
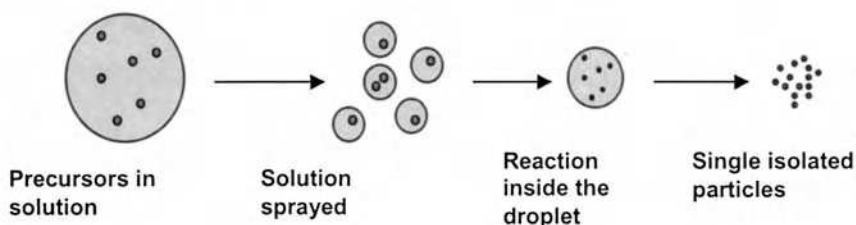
Vapor phase pathwayLiquid phase pathway

FIGURE 2.16 Mechanisms of liquid- and vapor-phase pathways related to flame aerosol process of nanoparticle synthesis [50]. (Reprinted with permission from Limaye AU, Helble JJ. Morphological control of zirconia nanoparticles through combustion aerosol synthesis. *J Am Ceram Soc* 2002;85:1127–1132, John Wiley & Sons.)

During flame aerosol synthesis, liquid feedstock is injected and atomized in a flame where the liquid phase is evaporated. Thermochemical reactions occur to produce fine particles. Flame aerosol synthesis has features in common with spray drying as it combines the pulverization of the sol solution with injection and heating in a flame. The process partially dries the aerosol droplets when they cross the flame. Atomization of the liquid stream, characteristics of the flame, and flame–droplet interactions are important factors to consider. Using the flame aerosol process, high-purity nanoparticles with novel metastable phases are made that are not accessible by conventional liquid phase or solid-state processes. The competing vapor- and liquid-phase pathways are shown schematically in Figure 2.16. In both cases, the first two steps are the same, regardless of whether particles are agglomerated or unagglomerated. In the liquid-phase pathway, the reaction of the precursors occurs in the liquid phase within each precursor droplet [50]. As a result, agglomeration is avoided.

Flame-assisted spray pyrolysis has produced BaTiO_3 nanoparticles with relatively high tetragonality and controlled sizes from 23 to 33 nm in a one-step process. The addition of urea into the precursor is the key factor for the formation of tetragonal BaTiO_3 nanoparticles; lack of urea addition leads to the formation of submicron BaTiO_3 . The formation of BaTiO_3 nanoparticles is believed to result from the disintegration of submicron BaTiO_3 particles with the assistance of the

decomposition of urea present at the contacts. Also, combustion of the decomposed gases of urea produces additional heat, which improves the tetragonality of BaTiO₃ nanoparticles [51].

Flame aerosol synthesis can produce highly pure nanoparticles; however, agglomeration is almost unavoidable when nanoparticles are generated at high concentrations. Efforts to control agglomeration have had only limited success. The aggravation of nanoparticle coalescence by laser beam irradiation can vary the size, morphology, and crystalline phase of high concentration nanoparticles. Figure 2.17 shows the evolution of SiO₂ nanoparticles without CO₂ laser beam irradiation (a1–a4 and b1); the change in the particle sizes depends on laser powers (b1, b2, b3, and b4) [52]. The first value P in the images indicates the laser power used. The second value in the images is the distance from the burner surface. Aggregates composed of small primary particles are seen without laser irradiation (Fig. 2.17a3). The longer distance of the particles from the burner surface leads to more developed particles but with fractal morphologies. Fast coalescence of SiO₂ nanoparticles is observed in Figures 2.17a4 and b1. Aggregates are sintered to become more spherical particles at 19 mm (note that some of the particles in Fig. 2.17b1 still have a nonspherical shape). When a CO₂ laser beam (3.3 mm in beam diameter) irradiates at 14 mm distance where aggregates begin to form, the sizes of the particles captured at the same height of 19 mm decrease monotonically and maintain a spherical shape at all laser power levels (Fig. 2.17b1–b4).

The flame aerosol technique is one of the most scalable techniques for producing nanoparticles, and flame generators can be conveniently configured. The process is much simpler and more effective to generate a well-defined nanoaerosol and to disperse a deagglomerated commercial nanopowder into an airborne suspension. The main drawback is the agglomeration of nanoparticles. The other problem is the broad distribution of particle sizes.

2.3.3 Gas–Solid Reaction

Using gas–solid reaction for nanoparticle synthesis has been rare. This is likely because the reaction cannot be easily controlled to maintain nanoparticle sizes due to the continuous reaction between the solid and the gas and/or the corresponding agglomeration. One successful example, though, is the synthesis of hollow SiC spherical nanoparticles using a vapor–solid reaction between carbon nanoparticles and SiO vapor generated from a mixture of silicon and SiO₂. The hollow spherical nanoparticle sizes are related to the diameters of the pristine carbon nanoparticles. The thickness of the hollow spherical nanoparticles can be controlled by the siliconization degree and carbon nanoparticle multilayer structures. Different characterization techniques show the phase conversion of the amorphous carbon into graphitic carbon and further into SiC nanoparticles [53].

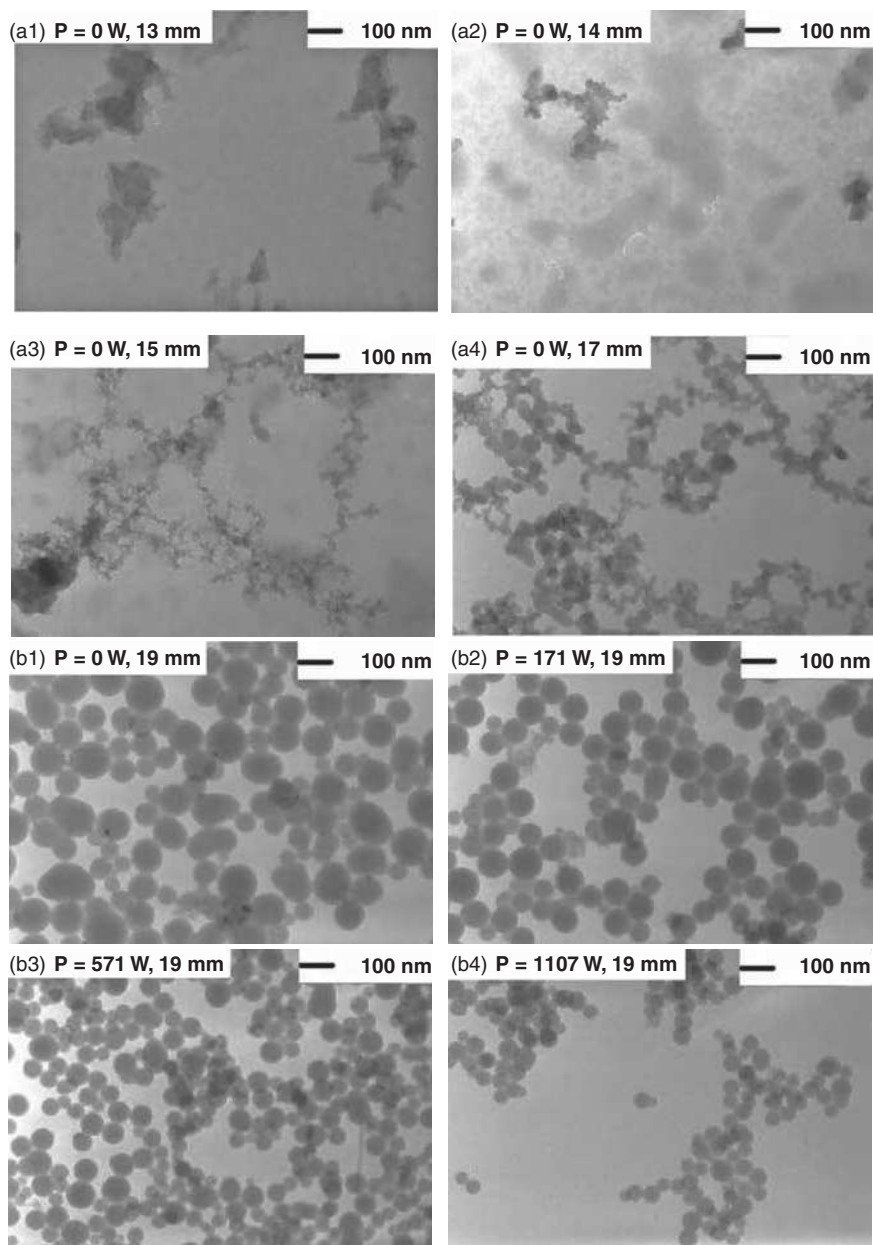


FIGURE 2.17 Transmission electron micrographs showing the evolution of SiO_2 particles with and without CO_2 laser beams; the CO_2 laser irradiation height above the burner surface, h_L , is 14 mm; the height where the local sampling is done above the burner surface, h_p , is 19 mm [52]. (Reprinted with permission from Lee D, Choi M. Coalescence enhanced synthesis of nanoparticles to control size, morphology and crystalline phase at high concentrations. *J Aerosol Sci* 2002;33:1–16, Copyright 2002, Elsevier.)

2.4 LIQUID NANOPARTICLE SYNTHESIS

2.4.1 Fundamental Method

Liquid nanoparticle synthesis is a well-studied area and there have been many variations in the process. The conventional approaches can be divided into precipitation, metal salt reduction, hydrolysis, solvothermal synthesis, and cryochemical synthesis, as shown in Figure 2.18.

2.4.1.1 Precipitation Aqueous precipitation is one of the earliest techniques in nanoparticle synthesis. The technique is simple, inexpensive, and can be used to synthesize single or multicomponent nanoparticles. The process generally starts with a solution of metal salts, such as alkoxides, nitrates, or chlorides. Upon the addition of a proper reagent, precipitate forms:



Under supersaturation, the precipitate nucleates and grows, which can stay as synthesized or be dehydrated to form simple or complex nanoparticles. In a strict sense, precipitation is mainly suited for the synthesis of oxides. A prerequisite for aqueous precipitation is that the formed precipitates must have a very low solubility in water. During precipitation, the kinetics of nucleation and particle growth in a solution should be carefully adjusted to control the particle size. Once the solution reaches a critical supersaturation for the participating species to form particles, only one burst of nuclei should occur. Thus, it is essential to control the precipitation factors such as the pH, temperature, and concentration of the reactants. Organic molecules can be used to control the release of the reactants in the solution during the precipitation process. The nanoparticle growth process follows that discussed earlier.

ZrO₂-SnO₂ composite nanoparticles are prepared by heating the hydrate precursors from the co-precipitation reaction of ZrOCl₂ and SnCl₄ [54]. The reaction

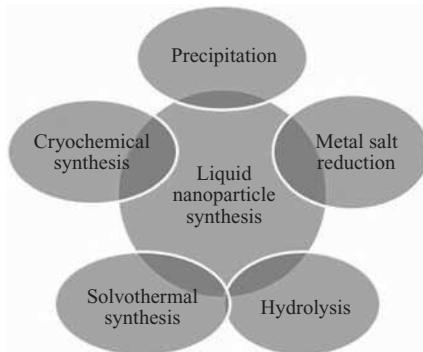


FIGURE 2.18 Fundamental methods of liquid nanoparticle synthesis.

process is simple but difficult to control. SrRuO₃ perovskite is synthesized by co-precipitation of Sr(NO₃)₃ and RuCl₃·xH₂O. The particle size calculated from X-ray diffraction measurements is 42.2 nm [55]. Nanoparticles of single spinel phase Co_{1-x}Zn_xFe₂O_{4+γ} with a mean size of 3–23 nm are synthesized by the co-precipitation method followed by a thermal treatment [56]. Ce_{1-x}Zr_xO₂ nanoparticles ($x = 0-1$) are synthesized by hydroxide co-precipitation of a mixed precursor solution of cerium ammonium nitrate ((NH₄)₂Ce(NO₃)₆) and zirconyl chloride (ZrOCl₂), followed by sonication redispersion in an aqueous medium using nitric acid [57]. The obtained nanoparticles are highly concentrated, stable for weeks, and have a particularly narrow particle size distribution with an average particle size of about 3.5 nm for CeO₂ nanoparticles and 2.5 nm for ZrO₂ nanoparticles. Co–Fe-based complex oxide nanoparticles are also formed using co-precipitation [58]. An average particle size between 10 and 15 nm is obtained. The nanoparticle size is controlled by stirring speeds and no apparent change in the standard deviation is observed. The desired results are attributed to the effective diffusion during the nanoparticle formation and growth under turbulent stirring.

CoFe₂O₄ ferrite nanoparticles of spinel structure are prepared by a modified chemical co-precipitation route (Fig. 2.19). The particles are spherical with diameters ranging from 20 to 30 nm. The Curie temperature (the temperature at which a ferromagnetic or a ferrimagnetic material becomes paramagnetic on heating) of the nanoparticles in the process of increasing temperature is slightly higher than that in the process of decreasing temperature. This can be understood by the fact that heating changes Co²⁺ ion redistribution in tetrahedral and octahedral sites. The coercivity of the synthesized CoFe₂O₄ nanoparticles is lower than the theoretical values, which can be explained by the mono-domain structure and a transformation from ferrimagnetic to superparamagnetic state [59]. Monodispersed FeCo nanoparticles of 20 nm size are synthesized with borohydride as a reducing agent by the co-precipitation method in an aqueous solution. The composition and size of the FeCo nanoparticles are controlled by the molar ratio of the starting material, the reaction time, and the precipitation rate. To obtain crystalline nanoparticles, amorphous FeCo nanoparticles need to be annealed [60].

SiO₂–CaO–P₂O₅ ternary bioactive glass–ceramic nanoparticles are prepared via the combination of sol–gel and co-precipitation processes. Precursors of silicon and calcium are hydrolyzed in an acidic solution and gelled in an alkaline condition along with ammonium dibasic phosphate ((NH₄)₂HPO₄). Gel particles are separated by centrifugation, followed by freeze-drying and calcination. The reaction temperature plays an important role in the crystallinity of the nanoparticles. The glass–ceramic particles synthesized at 55°C include about 15% crystalline phase, while at 25°C and 40°C, entirely amorphous nanoparticles are obtained [61].

For quantum dot (QD) synthesis, the most popular and successful aqueous method is arrested precipitation, which has been used to synthesize a wide range of semiconductor nanoparticles, including CdS, CdSe, CdTe, and HgTe. For

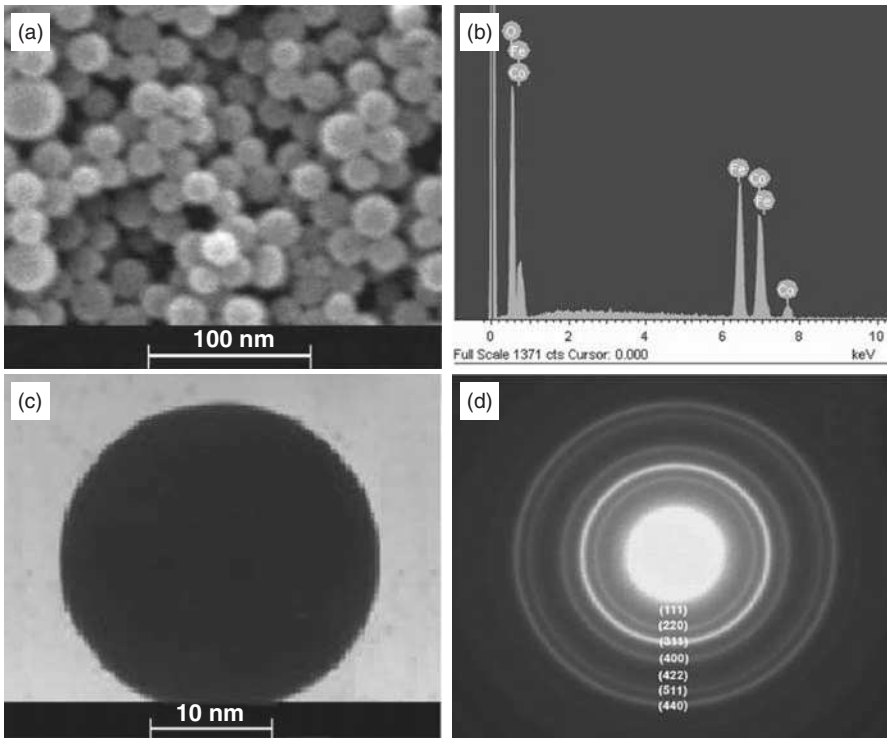


FIGURE 2.19 (a) Scanning electron image of as-prepared CoFe_2O_4 ferrite nanoparticles, (b) energy-dispersive spectroscopy result of the CoFe_2O_4 particles, (c) transmission electron image of one CoFe_2O_4 particle, and (d) selected area electron diffraction pattern of the CoFe_2O_4 particles [59]. (Reprinted with permission from Zi Z, Sun Y, Zhu X, Yang Z, Dai J, Song W. Synthesis and magnetic properties of CoFe_2O_4 ferrite nanoparticles. *J Magn Magn Mater* 2009;321:1251–1255, Copyright 2009, Elsevier.)

example, cadmium perchlorate ($\text{Cd}(\text{ClO}_4)_2 \cdot 6\text{H}_2\text{O}$) is dissolved in water and hydrogen selenide (H_2Se) gas is supplied [62]. Replacement reaction yields CdSe nanoparticles in the solution. Additives such as phosphates, amines, and thiols need to adsorb onto the QD particle surface right away to protect the QDs, enhance their suspension in water, stabilize the reaction, and control QD size growth, resulting in reasonably bright and narrow photoluminescence emission in their use.

For precursors that are unstable in an aqueous solution or synthesis processes that are difficult to control the rate of precipitation, a nonaqueous solvent is often used as the counterpart of an aqueous solvent. Semiconductor nanoparticle synthesis serves as good examples in this regard. Nonaqueous precipitation offers excellent crystallinity, monodispersity, and high-purity nanoparticles. It can also be particularly advantageous when precipitating dissimilar nanoparticles

that cannot be simultaneously precipitated from an aqueous solution due to large variations in the pH values necessary to induce precipitation of the constituting cations. The disadvantages for nonaqueous precipitation include use of expensive and sometimes toxic organics, sensitivity to moisture, and complicated experimental setups. These factors often act as barriers for nanoparticle synthesis of large quantities.

PbSe nanoparticles are prepared by chemical reaction between lead-cyclohexanebutyrate (Pb-cHxBu) and selenium precursors. A stock solution is prepared by dissolving the precursors in a tributylphosphine (TBP, C₁₂H₂₇P) solution at room temperature under standard inert conditions in a glove box. A mother solution of trioctylphosphine oxide (TOPO) surfactant is placed under inert conditions (with argon flow) at 150°C. Then, the stock solution is injected rapidly into the mother solution, followed by an immediate drop of the temperature to 118°C for the reaction to proceed. A reaction time of 10–60 minutes leads to the formation of monodispersed spherical polycrystalline PbSe particles of 50–500 nm in diameter [63]. Figure 2.20 shows images of PbSe at different synthesis time and precursor ratios. The crystallinity is well defined. The nonaqueous solution conditions prevent the QD oxidation. TOPO acts as the capping agent after the QD formation to suspend particles and prevent corrosion. For oxide nanoparticle synthesis, CeO₂, ZrO₂, and ZnO are formed using soluble cerium, zirconium, or zinc salts in decan-1-ol, undecan-1-ol, and ethane-1,2-diol [64]. When the solution becomes supersaturated with the constituting species of the oxides, nucleation and growth of oxide particles occur. Only those metal salts whose dissociation temperature or decomposition temperature is less than or equal to the reflux temperature of the solvent are effective. Ferrite nanoparticles are prepared by nonaqueous precipitation of a homogeneous solution of stearic acid and iron (III) nitrate. The particles have an average size of ~9 nm even though they are agglomerated [65]. Taking advantage of the increased solubility of formed nanoparticles at elevated temperatures, small particles may be redissolved and the particle size distribution may be narrowed. This is the well-known Ostwald ripening process. However, the average particle size increases subsequently.

Bis(2-hydroxy-1-naphthaldehydato) manganese(II) ([Mn(HNA)₂]) complex is used in the presence of oleylamine (C₁₈H₃₇N) as both a surfactant and a solvent to synthesize manganese oxide (Mn₃O₄) nanoparticles [66]. The obtained Mn₃O₄ nanoparticles have a tetragonal structure with an average size of 9–24 nm. The surfactant also plays an important role in lowering the reaction temperature. A diagram illustrating the formation of Mn₃O₄ nanoparticles is given in Figure 2.21. First, Mn(OOCCH₃)₂·4H₂O is dissolved into methanol to form a homogeneous solution. Then, 2-hydroxy-1-naphthaldehyde (HNA) dissolved in methanol is added dropwise into the above solution under magnetic stirring. The solution is refluxed at 60°C for about 2 hours, and then heated up to 160°C for 60 minutes. After this the temperature is increased to 260°C for 60 minutes of aging. The obtained brown precipitate is centrifuged and washed with ethanol several times. The same approach can be used for SnO₂ and ZnO synthesis [67, 68]. For

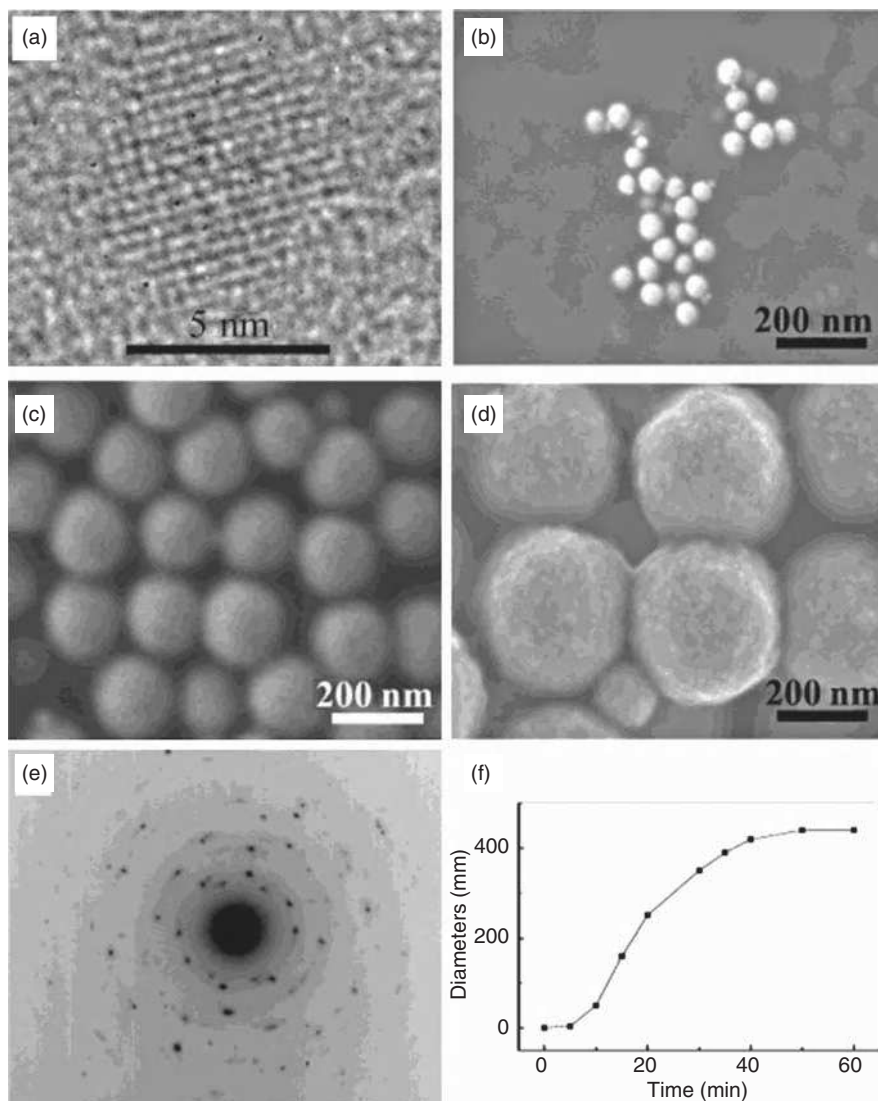


FIGURE 2.20 High-resolution transmission electron image of a cubic-shaped individual PbSe nanoparticle, using 0.25:0.6:50 mass ratio of Se/lead-cyclohexanebutyrate/tributylphosphine precursors at 118°C, with a reaction time of about 5 minutes (a). High-resolution scanning electron images of PbSe nanoparticle assembly prepared with 0.5:1:50 mass ratio of Se/lead-cyclohexanebutyrate/tributylphosphine precursors at 150°C, with a reaction time of (b) 10, (c) 25, and (d) 40 minutes. (e) Representative selected area electron diffraction pattern of spherically shaped nanoparticle assemblies. (f) Plot of the spherical PbSe assembly diameter versus the reaction time (minutes) [63]. (Reprinted with permission from Sashchiuk A, Amirav L, Bashouti M, Krueger M, Sivan U, Lifshitz E. PbSe nanocrystal assemblies: synthesis and structural, optical, and electrical characterization. *Nano Letters* 2004;4(1):159–165, Copyright 2004, American Chemical Society.)

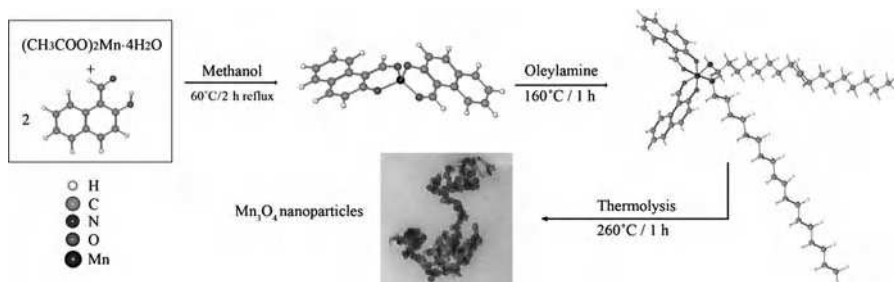


FIGURE 2.21 Schematic diagram illustrating the formation of Mn_3O_4 nanoparticles [66]. (Reprinted with permission from Davar F, Salavati-Niasari M, Mir N, Saberyan K, Monemzadeh M, Ahmadi E. Thermal decomposition route for synthesis of Mn_3O_4 nanoparticles in presence of a novel precursor. *Polyhedron* 2010;29:1747–1753, Copyright 2010, Elsevier.) (For a color version of this figure, see the color plate section.)

SnO_2 , [bis(2-hydroxy-1-naphthaldehydato) tin(II)] precursor is used in the presence of oleylamine ($\text{C}_{18}\text{H}_{37}\text{N}$). This precursor has steric hindrance, and therefore, cosurfactants are not needed for size control. The as-synthesized SnO_2 nanoparticles show tetragonal phase without other impurities and the particle size is 1.5–4 nm. [Bis(acetylacetonato) zinc(II)] has been used as a precursor to prepare ZnO nanoparticles of 12–20 nm. Different combinations of triphenylphosphine ($\text{C}_{18}\text{H}_{15}\text{P}$) and oleylamine ($\text{C}_{18}\text{H}_{37}\text{N}$) are used as surfactants to control the particle size. The synthesized ZnO nanoparticles have a hexagonal zincite structure.

The advantage of the precipitation process is that it is straightforward and a vast variety of nanoparticles can be made. However, there are several disadvantages for the technique. One is different rates of precipitation for different components, which can result in deviation from homogeneous precipitation. Suitable conditions must be obtained so that the precipitation can take place at desired rates. Also, synthesized nanoparticles are usually amorphous if the process occurs at or near room temperature. Hydroxides or carbonates can precipitate from the solution and have to be removed by postsynthesis thermal processes. If the synthesis is a nonaqueous process, expensive or even toxic precursors and stabilizers are often involved. To effectively control nanoparticle sizes, controlled release of the precipitating ions is often necessary.

2.4.1.2 Metal Salt Reduction During nanoparticle synthesis, metal salt reduction can be expressed as



There must be a corresponding oxidation process of some species X, such that



Whether the redox reaction (chemical reactions in which atoms have their oxidation number (oxidation state) changed) takes place or not relies on whether the standard electrode potential of the metals/ions is higher than that of the other redox pair. In order for the electron transfer to occur, the free energy change for Equations (2.24) and (2.25) to occur simultaneously, ΔG , must be favorable. The species present in the solution have an impact on the resulting nanoparticles. Metal precursor choice has a major effect on the resulting nanoparticles and their behaviors.

Faraday was the first to systematically study phosphorous reduction of AuCl_4^- in forming gold particles [62]. The approach is generally called citrate reduction method. Since then, numerous methods of metal salt reduction have been developed. Nanoparticles of gold, platinum, and silver are prepared by reduction in their metal salts with sodium borohydride (NaBH_4) in the presence of poly(amidoamine) dendrimers in water. The dendrimer concentration required for obtaining stable nanoparticles is dependent on the interactions between the metal nanoparticles and the dendrimers. When the ratio of (surface group of dendrimer)/(metal salt) is above unity, nanoparticles of gold and silver are obtained, while stable platinum nanoparticles are only obtained above the ratio of 40/1 [69]. Gold nanoparticles in the 1.5–4.0 nm range are obtained and their size decreases with increasing concentration of the dendrimers and the generation rate of the dendrimers. Similarly, platinum nanoparticles with a diameter of 2.4–3.0 nm are obtained, but their size is insensitive to the concentration or type of the dendrimer. Apparently, the dendrimers have reconfigurable attachment to the gold particles but not to the platinum particles.

For the synthesis of palladium nanoparticles with mean sizes from 1.5 to 15 nm [70], the particle size is controlled by the concentrations of the stabilizing polymer and precursor salt, the reduction temperature, as well as the initial pH of the solution. Understandably, lower temperature and higher pH lead to the formation of smaller particles. Again, the relative nucleation and particle growth rates are the decisive factors in determining the particle size and dispersion. On a different note, competing nucleation(s) should be avoided in order to obtain pure and desired nanoparticles. Gold–silver alloy nanoparticles are synthesized via reduction in HAuCl_4 and AgNO_3 by NaBH_4 in the presence of sodium citrate ($\text{Na}_3\text{C}_6\text{H}_5\text{O}_7$) [71]. The solution concentrations need to be carefully controlled to avoid the precipitation of AgCl during the reaction.

High-temperature reduction in metal salts in the presence of stabilizing agents can be employed to produce transition metal nanoparticles (cobalt, nickel) that do not crystallize well at room temperature. For example, ferromagnetic nanoparticles are obtained by reduction of metal salts with aqueous sodium or potassium borohydride. A good review on this is available and will not be detailed here [72]. Polymer stabilizer can be used to form a monolayer on the surface of nanoparticles to prevent fast nanoparticle growth, Ostwald ripening, or agglomeration. Crystalline iron colloids with particle sizes between 5 and 20 nm are produced by thermolysis of $\text{Fe}(\text{CO})_5$ in a polymer solution [73]. Cobalt nanoparticles of

45 nm are prepared by decomposition of $\text{Co}_2(\text{CO})_8$ at 130–170°C under an inert atmosphere in decalin or ethylene glycol solvent [74]:



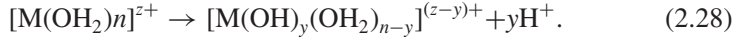
This technique can produce nanoparticles in a high rate. However, not all metals can be synthesized with the metal salt reduction technique. Agglomeration can also occur because of the high reaction rate. Therefore, choosing a proper reducing agent so that the redox reactions take place at a desirable rate is an important step that should be taken in advance.

Metallic alloy nanoparticles can be produced by reducing agents in organic solvents, such as alkali metals in hydrocarbon solvents. FePt nanoparticles of ~4 nm size are made with compositions ranging from $\text{Fe}_{30}\text{Pt}_{70}$ to $\text{Fe}_{80}\text{Pt}_{20}$ [75]. The synthesis process is fairly involved. Under air-free conditions, platinum acetylacetonate ($\text{C}_{15}\text{H}_{21}\text{PtO}_6$), 1,2-hexadecanediol ($\text{C}_{16}\text{H}_{34}\text{O}_2$), and dioctyl ether ($(\text{CH}_3(\text{CH}_2)_7)_2\text{O}$) are mixed and heated to 100°C; oleic acid ($\text{C}_{18}\text{H}_{34}\text{O}_2$), oleylamine ($\text{C}_{18}\text{H}_{37}\text{N}$), and $\text{Fe}(\text{CO})_5$ are added; and the mixture is refluxed at 297°C for 30 minutes. The heat source is then removed and the reaction mixture is cooled to room temperature. The as-synthesized FePt nanoparticles possess disordered face-centered cubic structure and show superparamagnetic behavior. Thermal annealing induces particle structure change and thus magnetic properties. An annealed FePt nanoparticle assembly with a composition around $\text{Fe}_{55}\text{Pt}_{45}$ has highly ordered face-centered tetragonal phase and yields high coercivity. PtNi nanoparticles are synthesized air free by a similar method using acetylacetonate (acac) precursors. After the synthesis, the acac ligands bind tightly with the PtNi particles and cannot be easily removed through washing. After annealing to nucleate the intermetallic phase, these ligands decompose into a carbonaceous coating, rendering the particles inactive toward formic acid (HCOOH) oxidation [76].

Polymers can act as the nucleation sites for nanoparticles. The functionality of the polymers influences the kinetics of the decomposition reactions and thus the nanoparticle size. Nanostructured nickel–chromium (Ni–Cr) and nickel–chromium carbide (NiCr_3C_2) of 10–18 nm are prepared [77]. The process involves reductive decomposition of an organic solution of metal chloride precursors using sodium triethylborohydride ($\text{NaBH}(\text{C}_2\text{H}_5)_3$). After co-precipitation of a nanoscale Ni–Cr mixture, low-temperature annealing is used to form nanostructured Ni–Cr alloy particles. After that, low-temperature gas-phase carburization is used to form nanostructured $\text{Ni–Cr}_3\text{C}_2$ cermet particles.

Metal salt reduction is well suited for metal and metal alloy nanoparticle synthesis. In most cases, the synthesis is carried out at elevated temperatures and under a reducing atmosphere. This facilitates pure, well-controlled nanoparticle formation with desired crystallinity. However, the reaction process can be complicated and the reaction by-products can be toxic.

2.4.1.3 Hydrolysis Hydrolysis is based on promoting the deprotonation of hydrated cations, often times by heating the solution at elevated temperatures. For a metal M with a valence z , the reaction can be written as [78]



After hydrolysis, the precipitates often need to be calcined to obtain the final products. Like many other synthesis processes, the nucleation and growth stages do not lead to desired nanoparticle species. The postsynthesis treatment converts the precipitates into the intended compositions/phases but can also introduce a plethora of morphological and size problems.

Monoclinic ZrO_2 nanoparticles are synthesized via forced hydrolysis of zirconyl salt solutions such as zirconyl chloride ($\text{ZrOCl}_2 \cdot x\text{H}_2\text{O}$) [79]. The nucleation and growth processes of ZrO_2 nanoparticles are monitored *in situ*, and a first-order model is used to understand the kinetic mechanism. The predominant mechanism for particle growth is the aggregation of primary particles. ZnO nanoparticles are synthesized through hydrolysis of organic salt zinc acetate ($(\text{CH}_3\text{COO})_2\text{Zn} \cdot 2\text{H}_2\text{O}$) [80, 81]. The hydroxyl groups are either provided by bubbling a $\text{NH}_3\text{-N}_2$ mixture into the precursor, or using NaOH or LiOH . The surface of the ZnO particles is modified to prevent particle agglomeration. However, greater than 100 nm particles are always present.

Chromia (Cr_2O_3) nanoparticles are prepared by urea-forced hydrolysis in the presence of chromium (III) nitrate using NaCl as a precipitating agent. Polyvinylpyrrolidone (PVP) is used as a surfactant to prevent aggregation. In the presence of PVP, nonaggregated spherical-like nanoparticles (3 ± 1 nm) are formed, whereas in the absence of PVP, spherical-like weakly agglomerated nanoparticles (85 ± 16 nm) comprised of 10 nm nanoparticle subunits are produced. The as-formed, hydrated Cr_2O_3 nanoparticles are amorphous and can be easily converted into crystalline form by heating to 400°C for 1 hour, with minimal particle aggregation and size reduction [82].

Fe_3O_4 nanoparticles are synthesized by hydrolysis in an aqueous solution containing ferrous and ferric salts at various ratios with 1,6-hexanediamine as a base. Ferrous to ferric ratio influences the reaction mechanism for the formation of Fe_3O_4 . When the ratio of ferrous to ferric ions increases, the formation of large hydroxide particles as a precursor to Fe_3O_4 is promoted, which results in an increase in the size of Fe_3O_4 nanoparticles. As a result, the mean diameter of Fe_3O_4 nanoparticles increases from ~ 9 to ~ 37 nm as the molar percentage of ferrous ions with respect to the total iron ions increases from 33% to 100%. Figure 2.22 shows that the particle size depends on the valence of the iron species. Namely, the use of ferrous salt alone as the source material results in the formation of large particles (Figs. 2.22a, c), while the use of both ferrous and ferric salts leads to the formation of fine particles (Figs. 2.22b, d). Additionally, the electron diffraction patterns shown in the insets of Figure 2.22, each of which is attributed to the diffraction from the crystal planes of Fe_3O_4 , also reflect the difference in

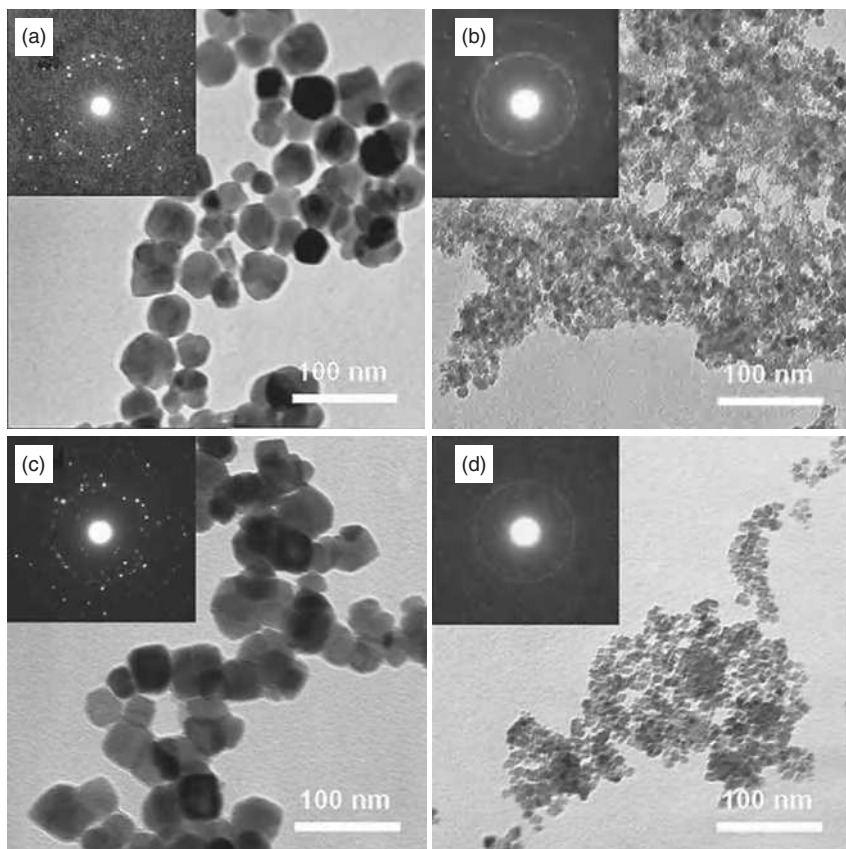


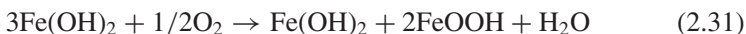
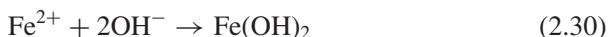
FIGURE 2.22 Transmission electron images and electron diffraction patterns of samples synthesized with ferrous sulfate (a), ferrous and ferric sulfate (b), ferric chloride (c), and ferrous and ferric chloride (d) [83]. (Reprinted with permission from Iida H, Takayanagi K, Nakanishi T, Osaka T. Synthesis of Fe_3O_4 nanoparticles with various sizes and magnetic properties by controlled hydrolysis. *J Colloid Interface Sci* 2007;314:274–280, Copyright 2007, Elsevier.)

the particle size of the samples. Spotty electron diffraction patterns are obtained from the samples consisting of large particles (insets of Figs. 2.22a, c), while broad-ring patterns are obtained from the samples consisting of fine particles (insets of Figs. 2.22b, d) [83].

As to the mechanism for the formation of Fe_3O_4 nanoparticles with ferrous and ferric salts at the ratio of 1 to 2, the co-precipitation reaction represented by Equation (2.29) is generally known, in which stoichiometric amounts of ferrous and ferric ions react to produce Fe_3O_4 :



For the alkalization reaction of ferrous ions in regard to the formation of iron hydroxide and iron oxide, the following is believed to be the mechanism:

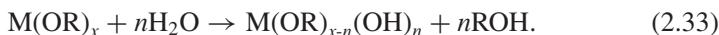


In the synthesis with ferrous ions alone, Fe_3O_4 is formed as a result of the dehydration reaction of ferrous hydroxide and ferric oxyhydroxide represented by Equation (2.32), in which the latter compound is produced by the partial oxidation of ferrous hydroxide by oxygen in dissolved air according to Equation (2.31). In addition, the intermediates formed during the synthesis are suggested to be ferrous and ferric hydroxides. Furthermore, during the formation of ferric hydroxide by the partial oxidation of ferrous hydroxide according to Equation (2.31), the ferrous hydroxide particles produced by the hydrolysis reaction of Equation (2.30) are expected to grow in size via hydroxylation. Consequently, it is likely that large Fe_3O_4 particles with ~ 37 nm in mean diameter are produced as a result of dehydration of ferrous and ferric hydroxides, which grow in size via the hydration process [83].

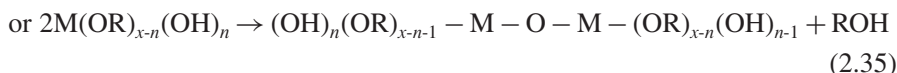
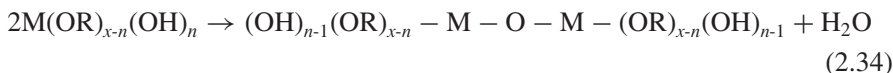
Compared to the hydrolysis of metal alkoxides to be discussed later, hydrolysis of metal salt solution has the advantage of producing a wide range of chemical compositions, including oxides, sulfates, carbonates, phosphates, and sulfides. However, for hydrolysis of inorganic metal salts, experimental conditions need to be carefully controlled in order to obtain the desired particle size. Even though theoretically it is only necessary to raise the temperature for the desired reaction to proceed, in practice, nanoparticle synthesis conditions can be hard to control; the morphology of final particles is difficult to predict. Because of these problems, organic salt hydrolysis is preferred. With the advancement of sol–gel nanoparticle synthesis, simple hydrolysis of metal salt(s) to form nanoparticles is not being actively pursued. Higher crystallinity, purity, and morphology control of other synthesis techniques offer more attractive opportunities in nanoparticle synthesis.

Sol–gel nanoparticle synthesis is a technique based on inorganic network polymerization reactions and requires the hydrolysis of organic salt precursors. A sol and a gel are involved in the process. A sol is an inorganic or polymeric salt solution. A gel is a semirigid state when the inorganic or polymeric species are cross-linked to form a network. The sol–gel process usually consists of four steps: sol formation, polycondensation (polyesterification), gelation, and thermal decomposition. Although both inorganic and organic metal compounds can be used as starting materials, metal alkoxides are more widely used in sol–gel synthesis. Examples of alkoxides include organometallic precursors of SiO_2 ,

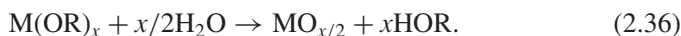
Al_2O_3 , TiO_2 , and ZrO_2 . In the initial step, the hydrolysis of precursors (metal alkoxides) with water or alcohol occurs to form a sol:



Then, condensation takes place to produce a gel:



The overall reaction can be expressed as



After the solution is condensed to a gel, the solvent must be removed. The particle size, morphology, and surface chemistry are dictated by the rate of hydrolysis, the solvent removal process, and the thermal process afterwards.

Sol-gel synthesis has been extensively studied for oxide nanoparticle formation. BaTiO_3 nanoparticles of 6–12 nm size are synthesized using the sol-gel process. Hydrogen peroxide (30% H_2O_2 aqueous solution) and metal alkoxide reaction with fatty acids as ligands in phenol ether results in equimolar stoichiometry [84]. BaSnO_3 with a primary particle size of 40–60 nm is prepared through hydrolysis of a barium tin isopropoxide followed by crystallization [85]. Carbides, nitrides, and other nonoxides can also be synthesized through this process [86–89]. The prerequisite is that the reaction is carried out in aprotic solvents and under an inert atmosphere. As the sol-gel synthesis technique advances, new forms of nanomaterials have also been developed. One is BaTiO_3 nanofibers, which has been created by electrospinning of a sol-gel precursor [90]. Another is SiC–TiC hybrid nanofiber composite [91]. Since nanofiber synthesis is not within the scope of this book, detailed discussion of such techniques is omitted.

Sol-gel processes can be used to make composite nanoparticles based on heterocoagulation. This is carried out by mixing the preformed nanoparticles with a sol containing the species of interest or by direct precipitation of nanoparticles with a sol. The composite nanoparticle size is more dependent on the step before the sol-gel process. Examples of this approach include Au– SiO_2 , Co– SiO_2 , Ni– SiO_2 , Ag– SiO_2 , and Si– SiO_2 [92, 93]. ZrO_2 nuclei of 40 nm are coated with a 15-nm thick SiO_2 glass layer in an ethanol solution using ethyl silicate [94].

Sol-gel processes can provide high purity and controllable size nanoparticles, both single and complex oxides. For multicomponent oxides, atomic level homogeneity can be expected. The precipitation rates of different cations can be controlled to a certain extent by adjusting sol formation conditions, such as water content, alkoxide chain length, or temperature. The challenges are the removal of solvent and organic compositions. As a gel is dried, the microstructure changes.

When a liquid is present during drying, capillary forces induce a stress on the gel that increases the coordination numbers of the particles and leads to the collapse of the network (xerogel). This may induce agglomeration of nanoparticles. Supercritical drying of the solvent from a gel can avoid capillary stresses because of the lack of solvent–vapor interfaces (aerogel). As a result, the dry gel is more porous and open in microstructure. To obtain nanoparticles, especially to achieve the desired crystallinity, after drying the gel needs to be calcined. Nanoparticle growth and agglomeration during calcination is a common problem similar to other nanoparticle synthesis approaches.

2.4.1.4 Solvothermal Synthesis Solvothermal synthesis is a method of producing compound nanoparticles at elevated temperatures. It allows for precise control over particle size, shape, and their distributions while facilitating the crystallinity development of nanoparticles. These characteristics can be altered by changing certain experimental parameters, including reaction temperature, reaction time, solvent type, surfactant type, and precursor type. Based on the solvent type, solvothermal synthesis can be divided as shown in Figure 2.23.

Hydrothermal synthesis is a special case of solvothermal synthesis and is widely used to synthesize nanoparticles. As known, water has its critical point at 374°C and 22.1 MPa, above which it is supercritical. Supercritical water exhibits the characteristics of both liquid water and water vapor. Water–nanoparticle interface has no measurable surface tension while still having high solubilities for the precursors for nanoparticle synthesis, thus offering high supersaturation. Although supercritical state is sometimes used, most hydrothermal processes are just carried out at elevated temperatures and pressures (sub-supercritical conditions) that will enhance the solubility and reactivity of the reactants, which otherwise will be very low at ambient conditions. During hydrothermal synthesis, a solution of the starting materials in water is heated to >100°C. At such conditions, the solubilities of the dissolved species are higher than those at ambient conditions, thus offering a high nucleation rate. During the synthesis of nanoparticles, reaction pressure, temperature, time, and the respective precursor-product systems can be tuned to simultaneously obtain a high nucleation rate and a narrow particle size distribution.

There are different types of hydrothermal synthesis, such as hydrothermal decomposition, hydrothermal precipitation, hydrothermal hydrolysis, and hydrothermal metal oxidation. TiO₂ is one of the most common oxides synthesized via hydrothermal process. Rutile particles of 20 nm size are synthesized by vigorous stirring of titanium isopropoxide (Ti(OC₃H₇)₄) and nitric acid solution [95]. The significant effects of stirring and longtime aging suggest that most of TiO₂ formation occurs during the autoclaving step. The large nanoparticle size distribution and the formation of anatase structure in the absence of stirring are attributed to the inhomogeneity developed in the solution. In a separate study, tetraalkyl ammonium hydroxides ((CH₃)₄NOH, C₁₆H₃₇NO, C₈H₂₁NO) are used as peptizing agents for the hydrothermal synthesis of nanocrystalline TiO₂ [96]. The carbon chain length of tetraalkyl ammonium hydroxides has great influence on particle size, shape, and phase transformation. Anatase phase is obtained in

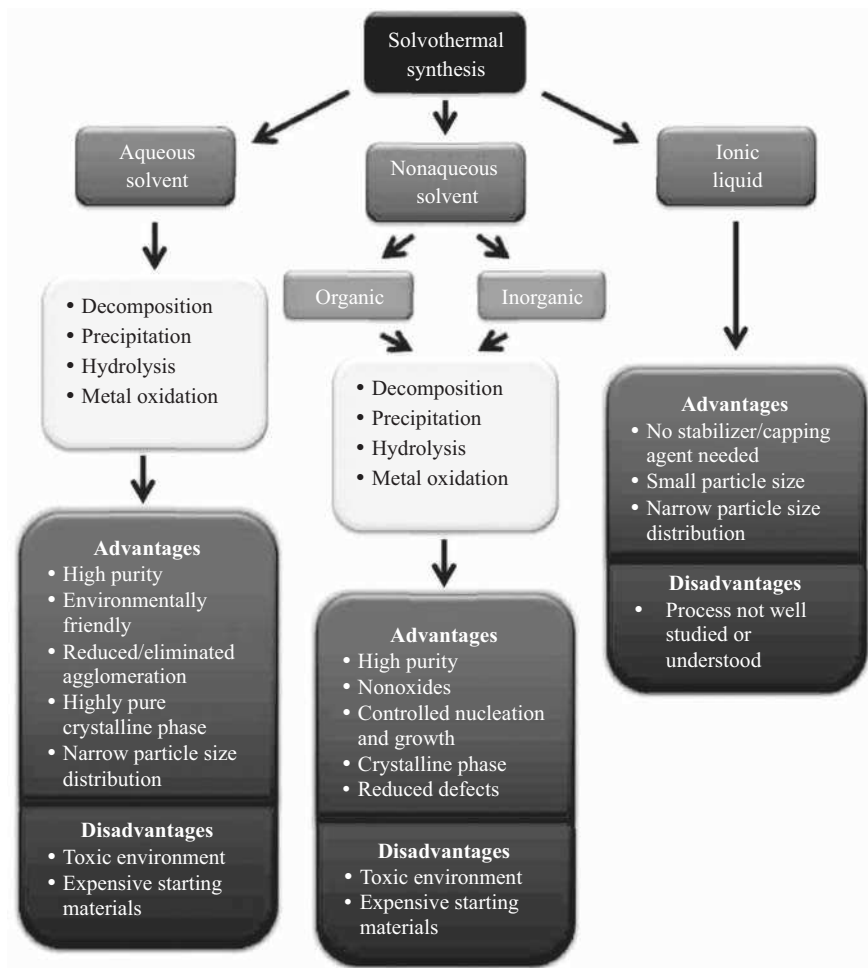
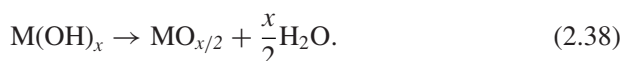
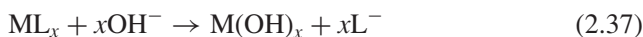


FIGURE 2.23 Solvothermal synthesis approaches and characteristics. (For a color version of this figure, see the color plate section.)

all the samples, regardless of the peptizer used, and the particle size increases as the peptizer cation size decreases.

Fe_2O_3 , Co_3O_4 , NiO , ZnO , and TiO_2 nanoparticles are obtained under conventional hydrothermal conditions. Hydrolysis of the corresponding metal salts happens first, followed by dehydration and metal oxide formation, as shown in the following equations [97]:



The hydrothermal synthesis time varies from 1 second to 2 minutes. To address the scale-up issue, a nozzle reactor may be used to mix an aqueous metal salt stream and a supercritical water stream. A variety of nano-sized metal oxide particles including TiO_2 , CeO_2 , ZrO_2 , ZnO , and CuO are synthesized using this approach [98]. The high reproducibility and reliability show promising potentials for further optimization. Following similar approaches, ZnFe_2O_4 nanoparticles are synthesized using a hydrothermal method with $\text{Fe}(\text{NO}_3)_3$ and $\text{Zn}(\text{NO}_3)_2$ as starting materials [99]. In an unconventional sense, a hydrothermal route is used to produce carbon by decomposition of β -SiC in the presence of water and organic compounds. When SiC decomposes at 200–300 MPa and 600–800°C, SiO_2 and elemental carbon form. The yield of carbon is reduced by the excess water in the system [100].

The advantages of hydrothermal synthesis are that the process is simple and environmentally friendly. Compared to other techniques such as co-precipitation, nanoparticles are directly formed by hydrothermal synthesis; no calcination or milling is required. Hydrothermal synthesis also enables the elimination of mineralizers that can induce impurities into nanoparticles. Highly pure phase and narrow particle size distribution can be obtained. However, hydrothermal synthesis requires the composition be precisely determined and controlled in advance; the materials need to be as fine and pure as possible and form a homogeneous dispersing system.

The presence of water in hydrothermal synthesis can cause problems in synthesizing nonoxide species. Using nonaqueous solvents can circumvent such problems. Pressure vessels and temperatures above the boiling point of the organic solvents are necessary. The number of nuclei formed and the reaction rate increase with increasing temperature, resulting in a decrease in particle size. Even though the synthesis process can use any kind of solvent other than water, there are generally two categories of solvents: inorganic and organic, with organic solvents being more widely used.

For inorganic solvents, liquid ammonia (boiling point: 78°C, critical temperature: 132°C, critical pressure: 11.4 MPa) has been used to synthesize nitrides [101]. By utilizing the reactions of $\text{CuCl}_2 \cdot 2\text{H}_2\text{O}$ and $\text{NiCl}_2 \cdot 6\text{H}_2\text{O}$ with elemental phosphorus in ammonia liquid, nanocrystalline Cu_3P and Ni_2P are obtained under mild solvothermal conditions [102]. For organic solvents, cadmium precursors such as cadmium carbonate (CdCO_3), cadmium nitrate ($\text{Cd}(\text{NO}_3)_2$), and cadmium sulfate (CdSO_4) are dissolved in ethanol, tetrahydrofuran, butane-1,4-diol, or ethylene glycol for QD synthesis [103]. To obtain spherical particles, solvothermal temperatures must stay below 120°C in these solvents. Cobalt-substituted ferrite nanoparticles with diameters between 9 nm and 13 nm are synthesized by the thermodecomposition of metal (iron and cobalt) acetylacetonate in octadecene, in the presence of oleic acid and oleylamine. The use of oleic acid and oleylamine as surfactants enables the formation of nonagglomerated and narrowly dispersed (geometrical deviation $\ln\sigma < 0.25$) nanoparticles. Smaller size particles are obtained with higher nucleation temperature and lower particle growth temperature. High temperature also favors the formation of highly

crystalline cobalt-substituted ferrite with inverse spinel structure [104]. Mn_3O_4 nanoparticles and nanorods with different lengths are synthesized by using manganese nitrate as the precursor material. Other metal oxide nanocrystals such as NiO, ZnO, CeO_2 , CoO, and Co_3O_4 are also prepared by this method. Figure 2.24 shows various metal oxides with unique morphologies. Figures 2.24a and b display the as-obtained NiO nanoflowers and ZnO triangular nanoplates with an average size of 20 and 100 nm, respectively, when nickel nitrate and zinc nitrate are used as the decomposition precursors separately. When cerium nitrate is decomposed with a higher monomer concentration, at a higher temperature, and for a shorter period of time, flower-shaped CeO_2 is synthesized (Fig. 2.24c); if the reaction conditions are changed to that of lower monomer concentration, lower temperature, and longer time, cube-shaped CeO_2 is obtained (Fig. 2.24d). By the decomposition of cobalt nitrate, cobalt oxides with different compositions (CoO and Co_3O_4) and morphologies (polyhedron and cube) are synthesized under different conditions. Figure 2.24e shows the transmission electron image of CoO nanopolyhedrons, and the inset displays the obvious polyhedral structure of the nanocrystals, while Figure 2.24f shows the transmission electron image of Co_3O_4 nanocubes, and the inset displays the self-assembly property of the nanocrystals [105].

In a nonpolar version of the solvothermal synthesis, dodecanethiol ($\text{C}_{12}\text{H}_{25}\text{SH}$) capping ligand, cadmium stearate ($(\text{C}_{17}\text{H}_{35}\text{COO})_2\text{Cd}$), and selenium metal are heated under a pressure in tetralin ($\text{C}_{10}\text{H}_{12}$). Tetralin converts to naphthalene (C_{10}H_8), producing a necessary hydrogen selenide precursor. The resulting CdSe QDs suspend well in toluene and other nonpolar solvents. The nanoparticles are about 3 nm in average diameter even though the size distribution is rather wide. In the meantime, other organometallic routes have been developed to form CdSe QDs and then extended to CdTe; the solvent is generally TOPO. In a typical synthesis process for the steric acid/TOPO/CdO system, CdO is dissolved in TOPO at $>300^\circ\text{C}$, while selenium metal dissolves in TOPO at room temperature. Once the selenium solution is injected into the hot CdO solution, the nanoparticle nucleation and growth typically proceed at $\sim 300^\circ\text{C}$.

Solvothermal synthesis has several advantages over aqueous synthesis. First, nucleation is abruptly shut off and does not continue during the growth stage, which helps to maintain a narrow size distribution. At the higher temperatures allowed by organometallic synthesis, reaction rates are faster and crystallinity is generally higher. There is also more thermal energy to help each add-atom find more energetically favorable bonding positions in the crystal lattice, thus reducing defects. The particle size is mostly monodispersed, and the particle shape is well defined. The challenges for solvothermal synthesis remain in exact control of synthesis atmosphere, toxic species involved, and expensive starting materials.

Ionic liquids, including ambient temperature molten salts, provide an excellent medium for the formation and stabilization of metal nanoparticles, enabling the preparation of nanoparticles without any stabilizing additives or capping molecules. Such favorable environments are in contrast to the nanoparticle preparation in aqueous or conventional organic solvents, which inevitably requires the

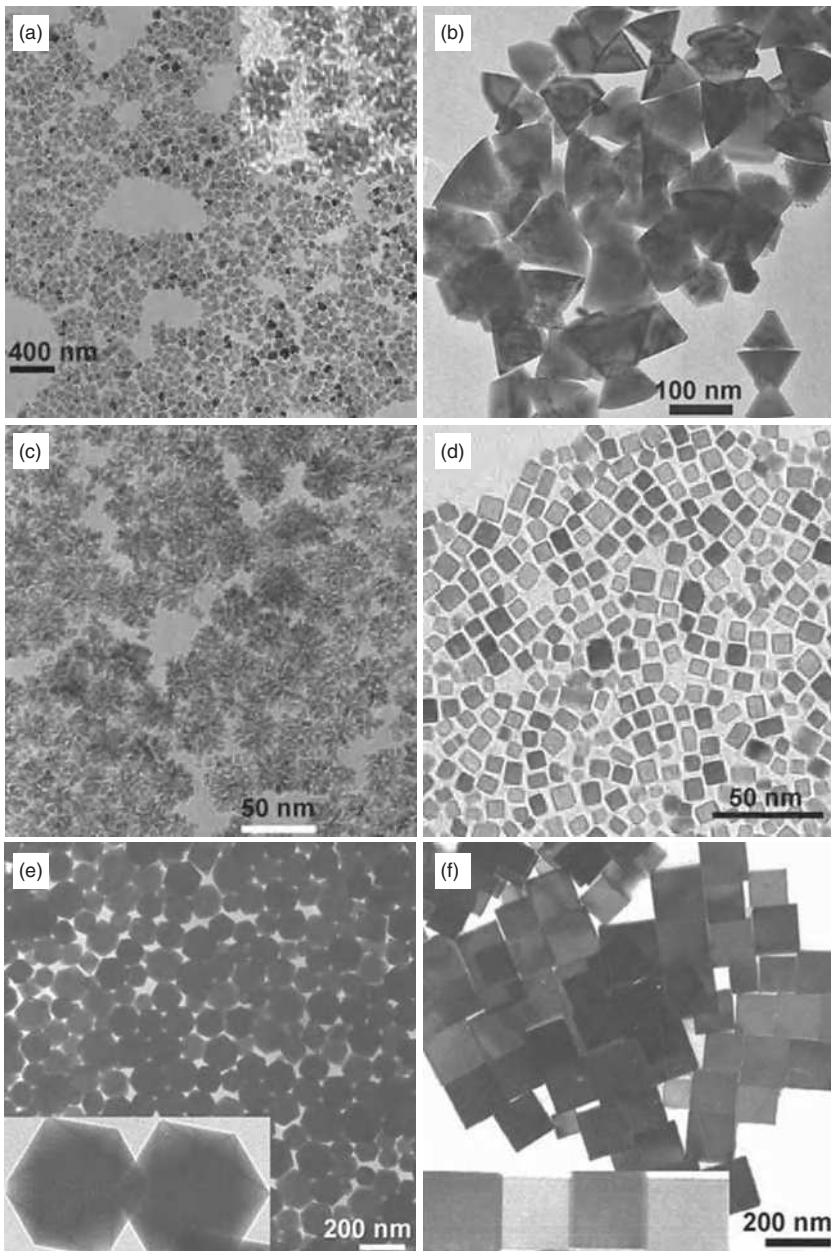


FIGURE 2.24 Transmission electron images of metal oxide nanocrystals: (a) NiO nanoflowers, (b) ZnO triangular nanoplates, (c) CeO₂ nanoflowers, (d) CeO₂ nanocubes, (e) CoO nanopolyhedrons, and (f) Co₃O₄ nanocubes [105]. (Reprinted with permission from Wang D-S, Xie T, Peng Q, Zhang S-Y, Chen J, Li Y-D. Direct thermal decomposition of metal nitrates in octadecylamine to metal oxide nanocrystals. *Chem Eur J* 2008;14:2507–2513, John Wiley & Sons.)

addition of stabilizing agents, such as thiols, amines, or polymers, to prevent the agglomeration and coalescence of particles synthesized. Iridium nanoparticles with 2.0 nm size are prepared from cod 1/41,5-cyclooctadiene [IrCl(cod)]₂ in butylmethylimidazolium hexafluorophosphate (BuMeImPF₆) in hydrogen atmosphere (4 atoms) at 75°C [106]. The same method is applicable to the preparation of rhodium nanoparticles (2.3 nm) from RhCl₃. Reduction in H₂AuCl₄ by CO in 1-butyl-3-methylimidazolium tetrafluoroborate (BuMeImBF₄) produces gold nanoparticles; the size changes from 1.7 to 12.8 nm with the increment of the amount of water. Overall, smaller particle size and narrower particle size distribution are obtained than through other approaches. Since ionic liquids themselves are still being studied, nanoparticle synthesis relying on ionic liquids is not widespread.

2.4.1.5 Cryochemical Synthesis Chemical techniques using low temperature as a key operating parameter are classified as cryochemical synthesis. In most cases, aqueous solutions are used even though organic solvents such as benzene or toluene are also options. Low temperature is mainly used after precursor mixing for solidification of the dispersing system (gelation or simple freezing).

Many of the cryochemical syntheses are based on the fast cooling of solutions and mostly achieved by freezing in liquid nitrogen (freezing rates over 10 K s⁻¹) to prevent separate crystallization of the compositions involved [107]. Controlled cooling of the mixing systems is also used at modest temperatures such as a few degrees below the freezing point of the system. The general process of cryochemical synthesis is shown in Figure 2.25. For nanoparticle synthesis, the first step is formation of a precursor solution containing the compositions of the targeted material in a stoichiometric ratio. This solution can then be sprayed into a low-temperature liquid such as liquid nitrogen by a pneumatic or ultrasonic nozzle. Cryochemical synthesis also involves the elimination of frozen water by physical or chemical means. To maintain the homogeneity of the system, special attention should be paid to the solvent removal step. Under the cryogenic conditions, the liquid is removed and the solid phase is obtained. Because of the low-temperature nature of the process, amorphous and intermediate phases are often the case at the freezing condition and further thermal treatment is needed to convert these intermediates into final crystalline nanoparticles. When the reactant contents are low, the domains tend to have the same size, which leads to a narrow particle size distribution.

Silver nanoparticles stabilized by poly(2-dimethylaminoethyl methacrylate) are synthesized by the cryochemical method [108, 109]. Sols prepared with cryochemically synthesized silver nanoparticles in different dispersion media (water, acetone, and toluene) are sterically stabilized by polymer layers. The thickness of the polymer layer depends on the nature of the solvents. Bimetallic Ag–Pb nanoparticles <5 nm in size are synthesized using the same technique [110].

More often, a cryochemical process is used as a step to remove the solvent while maintaining the homogeneous mixing of a more complex system.

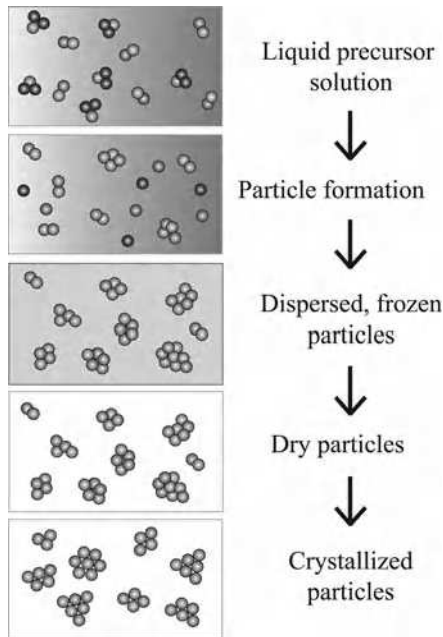


FIGURE 2.25 Illustration of the cryochemical synthesis process. (For a color version of this figure, see the color plate section.)

ZnO nanoparticles are synthesized by rapid freezing of a sprayed $\text{Zn}(\text{NO}_3)_2$ precursor solution, drying under vacuum by sublimation of the solvent, and heating the salt, which decomposes into the oxide [111]. YAGs by hydroxide co-precipitation are realized using the cryochemical process. Complete replacement of yttrium by ytterbium and synthesis of limited solid solutions $(\text{Nd}_x\text{Y}_{1-x})_3\text{Al}_5\text{O}_{12}$ with 19 mol% Nd_2O_3 maximum solubility are possible. The use of these synthetic methods has obvious advantages as they provide considerable decrease in the synthesis temperature (such as from 1800°C to 950°C) and duration and give more homogeneous and finely dispersed compositions [112]. Nano-sized (2–8 nm) amorphous powders of ZrO_2 and HfO_2 solid solution are synthesized through co-precipitation from $+20^\circ\text{C}$ to -6°C , which results in a size decrease in gel agglomerates from 30 to $1\ \mu\text{m}$ and thus also enables the achievement of smaller final nanoparticle size. The crystallite size for the recrystallization at $500\text{--}1200^\circ\text{C}$ does not exceed 25 nm [113]. The shortcoming is the time required to remove the ice from the frozen droplets.

Since freeze-drying is time consuming, cryoextraction has been developed as an alternative for solvent removal. The product formed from cryochemical synthesis is put in an organic solvent at low temperatures. The original solvent dissolves into the organic solvent, but the salt is not changed. The intact salt can be further processed to obtain nanoparticles.

Due to its low-temperature nature, cryochemical synthesis is an ideal technique to synthesize those species that have only a fleeting existence because of their high reactivity and instability at higher temperatures. Nonetheless, cryochemical processes are more often used as an intermediate state of nanoparticle synthesis. It is very rare to directly obtain nano-sized crystalline particles by this method alone.

2.4.2 Confinement Method

2.4.2.1 Spray Pyrolysis As indicated earlier, it is challenging to control the stoichiometry of multicomposition nanoparticles. As an alternative, spray pyrolysis can be used to avoid phase separation and improve the homogeneity at the molecular level. Spray pyrolysis is a droplet-to-particle process, in which a solution of precursors serves as the starting material and is misted into droplets that are carried by gas into a hot zone where they are rapidly heated and decomposed to form nanoparticles (Fig. 2.26). The chemical precursors decompose into solid species and the unwanted waste evaporates away. It is widely assumed that one droplet forms one particle. The average size of the particles can be roughly determined from the droplet size and the concentration of the sprayed solution. Sometimes, liquid-only synthesis cannot produce desired nanoparticle sizes or compositions. Pyrolysis offers control over the reaction process by forming small droplets or enabling removal of organic groups in the precursors.

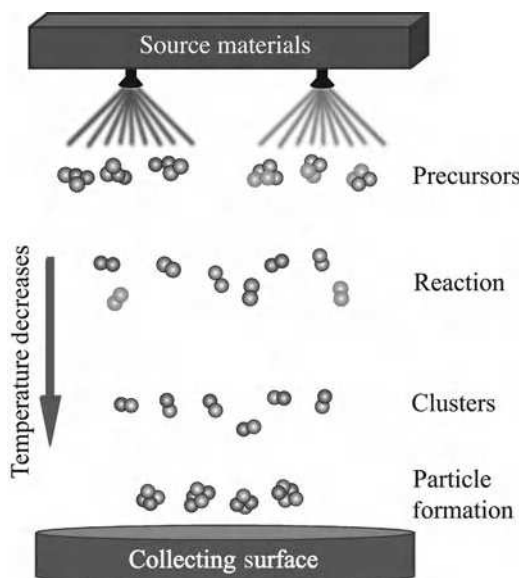


FIGURE 2.26 Illustration of the spray pyrolysis process. (For a color version of this figure, see the color plate section.)

A silver–fatty acid complex is heated at 250°C in a nitrogen atmosphere to make stable, monodispersed silver nanoparticles. The mean particle diameter is 4.7 nm, and the standard deviation is 0.6 nm. The particle surface is coated by the fatty acid, which prevents particle agglomeration even after repeatedly dissolving them in a solvent and evaporating. However, the coating can be easily removed by heating at 210°C in one atmosphere of air [114]. TiO₂ nanoparticles are made by thermal decomposition of titanium tetraisopropoxide using a tubular electric furnace at various synthesis temperatures (700–1300°C) and titanium tetraisopropoxide heating temperatures (80–110°C). An increase in synthesis temperature results in an increase in anatase crystallite size, and the anatase to rutile phase transformation occurs at ~1300°C. In addition, an increase in the titanium tetraisopropoxide heating temperature leads to narrower and higher X-ray diffraction peaks, indicating an increased particle size and improved crystallinity [115].

Magnetic nanocomposites consisting of spherical iron oxide (Fe₂O₃) particles of around 13 nm size dispersed in a mullite (3Al₂O₃·2SiO₂) matrix are obtained by spray pyrolysis at 600°C. The process starts with an aerosol generated from a solution of tetraethyl orthosilicate (TEOS) and iron and aluminum nitrates (Fe(NO₃)₃·9H₂O, Al(NO₃)₃·9H₂O) in methanol. The nanocomposite preserves its magnetic character up to 1400°C. This improvement is believed to come from Fe₂O₃ particles being separated by mullite, thus avoiding sintering and phase transformation [116]. More recently, nickel oxide–silica (NiO–SiO₂) and nickel–silica (Ni–SiO₂) nanocomposites are prepared by spray pyrolysis of aqueous sols of SiO₂ nanoparticles containing nickel nitrate hexahydrate (Ni(NO₃)₂·6H₂O) without and with ethanol, respectively. During spray pyrolysis, SiO₂ nanoparticles are restructured, losing their identities, while the NiO or nickel particles in the composites grow by coalescence and sintering [117]. A Zr-modified polycarbosilane is obtained by reacting a zirconium alkoxide with a polycarbosilane. The new preceramic polymer is nitrated in flowing ammonia at >1300°C to form ZrO₂–Si₃N₄ nanocrystalline composite [118].

Nanoparticle synthesis can be conducted in liquid salt at elevated temperatures. The precursors dissolve, undergo reactions, and produce nanoparticles. The salt solvent remarkably enhances mass transfer. Within an aerosol particle, the dissolution–precipitation cycle can lead to the dissolution of some nanocrystallites and the growth of other crystallites by precipitation. This may break up the three-dimensional network and disintegrate the original nanocrystallites. Meanwhile, the solvent can “wet” the nanocrystallite surfaces, which may aid in the dispersion of the new nanocrystallites in the solvent. Dispersed nanoparticles are thus obtained after removing the solvent [119].

In addition, salt-assisted spray pyrolysis can separate nanoparticles inside a droplet by introducing compounds that distribute on the nanoparticle surfaces to prevent agglomeration. Nanoparticles such as nickel, Ag–Pd, CdS, ZnS, LiCoO₂, and La_{0.8}Sr_{0.2}Ni_{0.5}Co_{0.5}O_{3-x} synthesized by this method require no further thermal processing for crystallinity [119]. Figure 2.27 shows two Y₂O₃–ZrO₂ samples, one synthesized using the conventional aerosol decomposition and the other using the salt-assisted aerosol decomposition [119]. The spherical and dense submicron

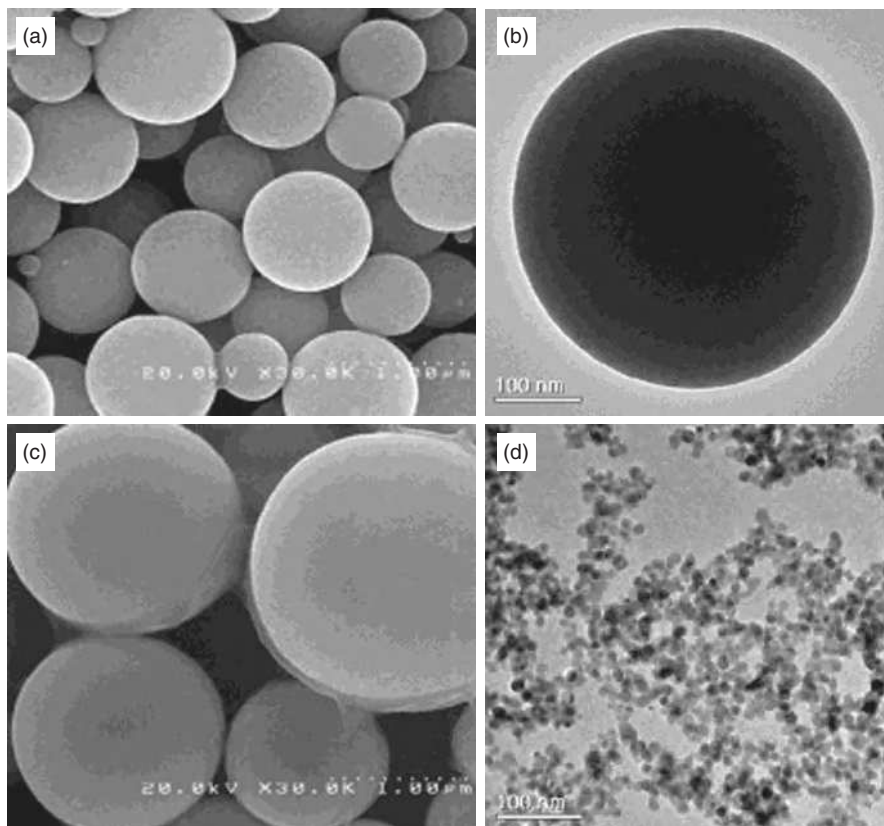


FIGURE 2.27 Y_2O_3 – ZrO_2 samples synthesized by the conventional aerosol decomposition process (a,b) and the salt-assisted decomposition process (c,d). (a,c) Scanning electron images of the samples before washing and (b,d) transmission electron images after washing. Note that the unwashed salt-assisted decomposition particles (c) are larger than the unwashed conventional aerosol decomposition particles (a) due to the presence of salts [119]. (Reprinted with permission from Xia B, Lenggoro IW, Okuyama K. Novel route to nanoparticle synthesis by salt-assisted aerosol decomposition. *Adv Mater* 2001;13:1579–1582, John Wiley & Sons.)

to micron particles created by conventional aerosol decomposition, typical particle morphologies formed in aerosol decomposition processes, remain unchanged after washing. In contrast, the salt-assisted aerosol decomposition sample shows a substantial change after washing, and nanoparticles are obtained. The particle sizes from conventional aerosol decomposition are broadly distributed over a range of 0.11–2.12 μm with a mean size of 0.66 μm and a geometric standard deviation of 1.76, showing a typical polydispersity of 1.3–2.0. Desirably, the salt-assisted aerosol decomposition sample (Fig. 2.27d), formed in the same aerosol process, has a remarkably narrowed size distribution (close to the normal distribution) in the range of 6.3–18.7 nm with a mean size of 12.8 nm and a

geometric standard deviation of 1.19. In other words, the size distribution of the salt-assisted aerosol decomposition particles is independent of that of their parent solution droplets. Addition of the salts causes particle size reduction by a factor of over 50. For nickel, Ag–Pd, CdS, ZnS, LiCoO₂, and La_{0.8}Sr_{0.2}Ni_{0.5}Co_{0.5}O_{3-x} mentioned earlier, adding salts results in particle size reduction by a factor of 30–80, depending on the materials and synthesis conditions [119].

Pyrolysis of metal fatty acid salts is conducted to form semiconducting and magnetic oxide nanoparticles [120, 121]. The size of the semiconducting nanoparticles (InP) is 3.1 nm. Nearly monodispersed Fe₃O₄ nanoparticles over a large size range (3–50 nm) are obtained. The method is further applied to the growth of oxide nanoparticles of other magnetic metals including Cr₂O₃, MnO, Co₃O₄, and NiO. The size and shape control of the nanoparticles is achieved by varying the reactivity and concentration of the precursors. The reactivity is tuned by changing the chain length and concentration of the ligands, the fatty acids. However, sometimes alcohols or primary amines are needed in order to activate the pyrolysis process. Separately, a liquid organosilazane precursor (CH₃SiHNH)_n (*n* = 3, 4) is synthesized by ammonolysis of methyl dichlorosilane (CH₃SiHCl₂). Exposing aerosols of this organosilazane liquid precursor to a laser beam converts them into preceramic polymer particles. The preceramic particles can be further thermally treated to form Si₃N₄/SiC nanoparticles [122, 123].

Before organic precursor pyrolysis proceeds, hydrolysis can be used to produce the precursors for pyrolysis in order to synthesize borides, carbides, and nitrides. For example, binary inorganic/organic gels are prepared by hydrolysis of titanium alkoxide in the presence of soluble, pyrolyzable organic compounds and complexing additives [124]. Upon pyrolysis up to 600–800°C, the gels transform into intimate mixtures of solid carbon and nano-sized anatase TiO₂. The pyrolyzed xerogels serve as precursors to titanium oxycarbide and carbide. The synthesis route to the binary gels can be used to control the elemental composition of the annealed nanoparticles. Inorganic–organic hybrid gels are prepared by simultaneous condensation of a liquid mixture of ethyl silicate ((C₂H₅)₄SiO₄), ethyl borate (B(OC₂H₅)₃), and water-soluble phenol resin. The obtained gels are crushed, dried, and heated in controlled conditions to yield inorganic precursors. Since the tailored inorganic precursors mainly consist of SiO₂ and carbon, SiC can be formed from heat treatment in an argon atmosphere at >1773 K. The nanoparticle sizes are 6–33 nm but the particles are agglomerated [125]. A comprehensive review of the technique can be found elsewhere [72].

Zinc sulfide (ZnS) particles of 20–40 nm size are prepared by spray pyrolysis under an electrical field. First, solutions of ethyl alcohol (C₂H₅OH), zinc nitrate (Zn(NO₃)₂), and thiourea (SC(NH₂)₂) are made. The solutions have electrical conductivities between 10⁻⁴ and 10⁻¹ S m⁻¹. High-voltage DC sources (2–4 kV) are used to electro spray the solutions from steady cone-jets at flow rates from 0.05 to 0.25 ml h⁻¹, with positive and negative polarities. The highly charged drops formed are neutralized by bipolar ions from a radioactive source to increase the overall transmission efficiency through a reactor furnace. Electro spray pyrolysis is hence able to generate nonagglomerated and spherical ZnS nanoparticles [126].

Spray pyrolysis has distinct advantages: multicomponents are homogeneously mixed at the atomic level from the beginning, and the high temperature facilitates the formation of crystalline nanoparticles. Spray pyrolysis also has the advantages of low cost, simplicity, and being effective in controlling the size and shape of the formed particles. Well-controlled morphologies and compositions are produced, giving rise to a series of new nanoparticles and processes that have been dominated by wet chemistry for years [127]. Also, the starting materials used are common, inexpensive, and compatible with nonaqueous media. However, pyrolytic synthesis of multicomponent nanoparticles leads to particles with a wide size distribution extending into the micron size range. The long chains in the precursors always need special care to ensure a reactive environment. To obtain uniform nanoparticles, spray pyrolysis needs to be improved; special reaction conditions are needed such as slowing the reaction rate or decomposing the precursor in an inert solvent. To dry a droplet with an initial diameter of 5 μm to a particle with a diameter of 100 nm, the volume fraction of the involatile solute should not be higher than 0.0008% [126]. Spray pyrolysis is also limited to certain materials due to the thermal stability issue at high pyrolysis temperatures; no pure metal nanoparticles are synthesized using this technique. Another shortcoming is that at high temperatures diffusion bonding is favored, which induces nanoparticle agglomeration and undesired phase transformation. Continuing efforts in spray pyrolysis include synthesis of more sophisticated nanoparticles with new functionalities and mass production of high quality nanoparticles. Advances in synthesis simulation and diagnostics of early particle formation and growth are needed for this development.

2.4.2.2 Solventless Synthesis Solventless synthesis was initially developed for organic material synthesis with CO_2 as a synthesis aid. In recent years, it has been applied to nanoparticle synthesis. Particle encapsulation in supercritical CO_2 helps to overcome the nanoparticle agglomeration problem [128]. Poly(dimethylsiloxane)-graft-polyacrylate (PDMS-g-PA) phase separation and methyl methacrylate (MMA) polymerization on particle surfaces are typical encapsulation processes usable in a batch mode. Both phase separation and polymerization allow for coating of nanoparticles. Use of a surfactant like PDMS-g-PA allows anchoring of MMA monomers and promotes polymerization on the particle surfaces. Surfactant selection is considered a key step for a successful encapsulation process.

Cu_2S is synthesized using copper-thiolate as the precursor [129]. First, an aqueous solution of copper salt and chloroform (CHCl_3) are combined, followed by the addition of sodium octanoate ($\text{CH}_3(\text{CH}_2)_6\cdot\text{COONa}$). Copper ions in the inorganic phase are transferred by sodium octanoate via copper octanoate complex. The aqueous phase is then discarded, after which dodecanethiol ($\text{C}_{12}\text{H}_{25}\text{SH}$) is added to the retained organic phase, resulting in the replacement of octanoate by dodecanethiol. Organic evaporation results in a waxy-like copper-containing precursor, which is then heated and yields nanoparticles. After being redispersed in chloroform and reprecipitated in ethanol to remove impurities, Cu_2S nanorods of

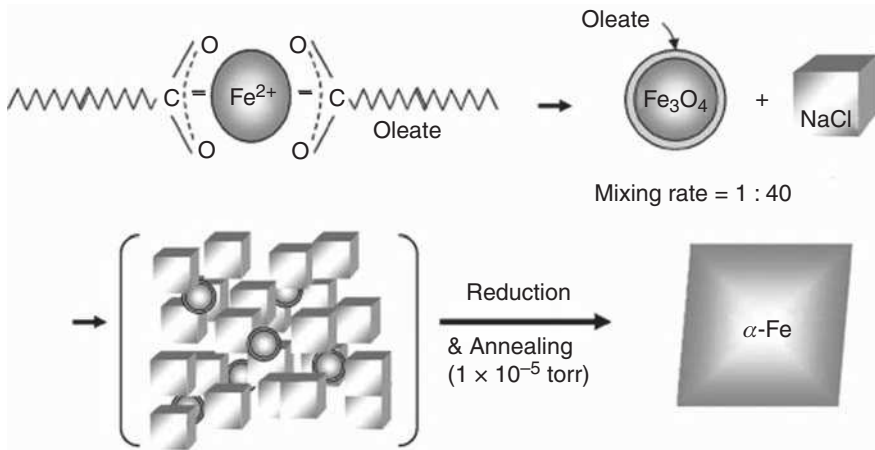


FIGURE 2.28 Overall scheme of a modified thermal decomposition method for α -Fe nanoparticle synthesis [132]. (Reprinted with permission from Han YC, Cha HG, Kim CW, Kim YH, Kang YS. Synthesis of highly magnetized iron nanoparticles by a solventless thermal decomposition method. *J Phys Chem C* 2007;111:6275–6280, Copyright 2007, American Chemistry Society.)

~ 4 nm in diameter and 12 nm in length are formed, with narrow size and shape distribution. Cu_2S nanodisks and nanoplatelets can be formed using the same method [130]. Reaction temperature and time affect the size and shape of the Cu_2S nanoparticles. Copper-thiolate provides organic ligands, which adsorb onto the nanoparticle surfaces for steric stabilization and aggregate growth prevention. This is crucial for monodispersed size and shape. Under appropriate conditions, solventless synthesis can reduce interparticle collisions down to almost zero. NiS nanorods and triangular nanoprisms are synthesized using a similar procedure [131]. The morphology can be self-controlled at the atomic level by the structure of the precursors.

For α -Fe nanoparticle synthesis, the overall synthetic procedure is depicted in Figure 2.28. First, the Fe^{2+} -oleate₂ complex is synthesized using iron (II) chloride tetrahydrate and sodium oleate. Sodium oleate is used as a capping agent because oleate has a C_{18} (oleic) tail with a cis double bond in the middle, forming a kink. Such kinks have been postulated as being necessary for effective stabilization. Fe_3O_4 nanoparticles are obtained by solventless thermal decomposition using a Pyrex tube from the synthesized Fe^{2+} -oleate₂ complexes. The prepared Fe_3O_4 nanoparticles are mixed with NaCl powder by a shaker miller to be as uniform as possible. Through the use of NaCl powder as the separating medium, each Fe_3O_4 nanoparticle is separated during the course of reduction by $\text{Ar} + 4\% \text{H}_2$ mixture gas and annealed under a high vacuum system of 1.8×10^{-5} torr at 700°C to obtain α -Fe nanoparticles [132]. The NaCl powder used instead of a surfactant plays an important role in keeping the size and shape of the nanoparticles.

Platinum particles of 2.0–2.5 nm size are synthesized by decomposing $\text{Pt}_2(\text{dba})_3$ (dba: bis-dibenzylidene acetone) in 1-*n*-butyl-3-methylimidazolium (BMI) hexafluorophosphate ionic liquid at room temperature [133]. Platinum nanoparticles formed are stable and have a narrow particle size distribution. Upon redispersion in an ionic liquid for several times, the catalytic activity of the platinum nanoparticles shows no significant loss.

Solventless synthesis offers narrow particle size distribution and well-controlled particle shapes. Similar to other procedures using organic chemicals, solventless synthesis involves toxic chemicals, which is very undesirable. Caution is required during the experiments because of the high synthesis temperatures.

2.4.3 Composite Nanoparticle Synthesis

2.4.3.1 Core/Shell Structure When producing nanoparticle-based composites, the central challenge is to obtain a perfect distribution of the involved phases. Synthesizing multiple phases separately and blending them after particle formation often do not lead to intended results. Fortunately, the necessary distribution of two phases can be obtained by coating the particles of one phase with a shell of the other phase with an intended thickness. The distribution of the two phases is homogeneous on a nanometer scale. The core particles are arranged at a well-defined distance, therefore, the interaction of the particles can be controlled. The core particles and the shells may have different properties, as shown in Figure 2.29. This allows for a combination of properties, which otherwise would not exist in one particle.

Core/shell composite nanoparticles are very desirable in offering precisely controlled homogeneity in composition and core nanoparticle spacing. However, there are a few basic requirements for the core particles to be coated with a shell: (1) the existing core nanoparticles must withstand the conditions under which

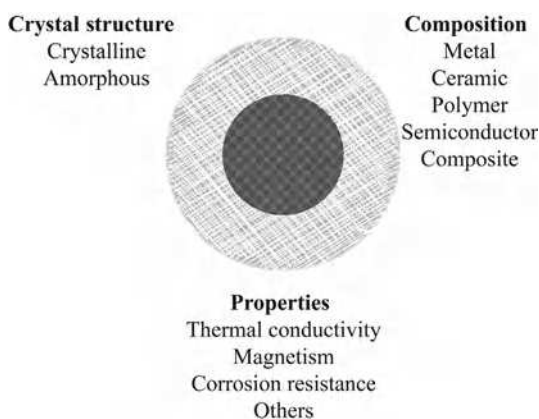


FIGURE 2.29 Illustration of different crystal structure, composition, and properties for core/shell particles. (For a color version of this figure, see the color plate section.)

the second phase is deposited, (2) the surface energies of the two phases must be similar so that the barrier for heterogeneous nucleation of the second phase is lower than that for homogeneous nucleation, and (3) the core nanoparticles and the coating nanoparticles must not readily interdiffuse under the deposition conditions [134]. Several methods have been used to produce a surface shell on nanoparticles, such as solution coating, micelle-assisted coating, and heterocoagulation coating.

For solution coating, typically core nanoparticles are prepared, isolated, size-selected, and then redispersed in a fresh solution of solvent and stabilizer(s). The precursors for the shell are gradually added to allow the species to heterogeneously nucleate on the core nanoparticles, which may be carried out under specific conditions to facilitate heterogeneous nucleation. If the rate of precursor addition does not exceed the rate of deposition on the seeds, the precursor concentration never reaches the threshold for the homogeneous nucleation of the second phase. Core/shell particle structures are obtained. A one-step core/shell structure synthesis of Au/SiO₂, Au/ZrO₂, Ag/TiO₂, and Ag/ZrO₂ is reported. Gold and silver nanoparticles of 30–60 nm covered by an amorphous TiO₂ or ZrO₂ shell with a 3 nm thickness are synthesized using hydrolysis of the metal oxide precursors [135]. Pd–CeO₂ core/shell nanostructures are made by exploiting the self-assembly between functionalized palladium nanoparticles and cerium(IV) alkoxides. The method involves the synthesis of palladium nanoparticles protected by a monolayer of 11-mercaptoundecanoic acid (MUA). The carboxylic groups on the nanoparticle surfaces are used to direct the self-assembly of a cerium(IV) alkoxide around the metal particles, followed by controlled hydrolysis to form CeO₂. The Pd@CeO₂ core/shell nanostructures are effectively dispersible in a range of organic solvents without any sign of agglomeration. The dimensions of the metal core and the thickness of the oxide layer can be tuned and the metal phase is accessible [136]. A schematic representation of the process is shown in Figure 2.30. Individual SiO₂-coated silver nanoparticles are made

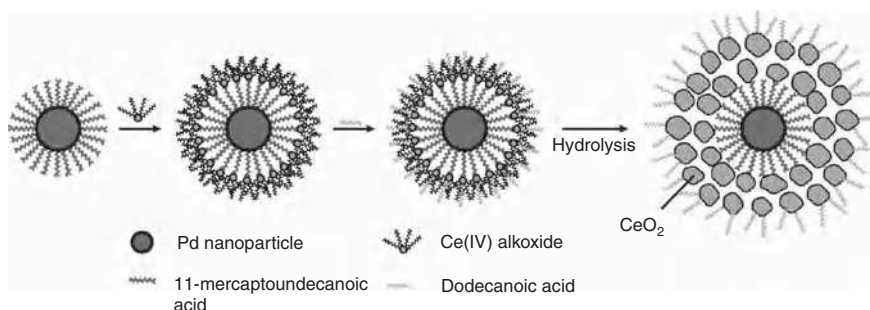


FIGURE 2.30 Schematic representation of the procedure used to obtain dispersible Pd@CeO₂ core–shell nanostructures [136]. (Reprinted with permission from Carnello M, Wieder NL, Montini T, Gorte RJ, Fornasiero P. Synthesis of dispersible Pd@CeO₂ core–shell nanostructures by self-assembly. *J Am Chem Soc* 2010;132:1402–1409, Copyright 2010, American Chemical Society.) (For a color version of this figure, see the color plate section.)

using a reverse micelle method (see Section 2.4.4.1) followed by hydrolysis and condensation of tetraethoxysilane (TEOS). The size of SiO₂-coated silver nanoparticles can be controlled by changing the reaction time and the concentration of TEOS. By maintaining the size of the core silver nanoparticles at around 7 nm, the size of SiO₂-coated silver nanoparticles increases from 13 to 28 nm as the reaction time increases from 1 to 9 hours because of an increase in the SiO₂ thickness. The size of SiO₂-coated silver nanoparticles also increases from 15 to 22 nm as the TEOS concentration increases from 7.8 to 40 mM. The size of SiO₂-coated silver nanoparticles can be accurately predicted using the hydrolysis rate of TEOS.

Bimagnetic core/shell Fe₅₈Pt₄₂/Fe₃O₄ nanoparticles are synthesized from coating of a 4 nm Fe₅₈Pt₄₂ core with an Fe₃O₄ shell. The shell is tunable from 0.5 to 3 nm [137]. Figures 2.31a and b show two typical transmission electron images of core/shell structured Fe₅₈Pt₄₂/Fe₃O₄ nanoparticles, with the darker region in the center being 4 nm Fe₅₈Pt₄₂ and the lighter ring being 0.5 nm (Fig. 2.31a) and 2 nm Fe₃O₄ (Fig. 2.31b). The different contrast between the core and shell regions is due to different electron penetration efficiency on metallic FePt and oxide Fe₃O₄. The detailed structure of a single Fe₅₈Pt₄₂/Fe₃O₄ particle is shown in Figure 2.31c. The lattice fringes of the shell are clearly shown in the image with adjacent fringe spacing at 0.253 nm, corresponding to {311} lattice planes for Fe₃O₄. The structure of the core is chemically disordered face-centered cubic FePt. The images in Figures 2.31a–c confirm that the chemically disordered Fe₅₈Pt₄₂ core is surrounded by a cubic spinel structured Fe₃O₄ shell. Energy-dispersive spectroscopy analyses of the core/shell nanoparticles reveal that the iron content increases with increasing shell thickness. Figure 2.31d shows an energy-dispersive spectroscopy spectrum from an assembled area of Fe₅₈Pt₄₂/Fe₃O₄ nanoparticles with 4 nm core and 1 nm shell. The average composition of these particles is Fe/Pt = 76:24, a ratio larger than 58:42 from the core; this ratio is consistent with the presence of 1 nm coating of Fe₃O₄. Figure 2.32 shows the X-ray diffraction patterns from the assemblies of cubic spinel structured 6 nm Fe₃O₄ nanoparticles (Fig. 2.32a,²⁶ chemically disordered face-centered cubic 4 nm FePt nanoparticles (Fig. 2.32b),²⁵ 4 nm/1 nm core/shell structured Fe₅₈Pt₄₂/Fe₃O₄ nanoparticles (Fig. 2.32c), and 4 nm/3 nm core/shell structured Fe₅₈Pt₄₂/Fe₃O₄ nanoparticles (Fig. 2.32d). Compared with Figures 2.32a and b, Figures 2.24c and d contain two sets of peaks, with one set matching that of the chemically disordered face-centered cubic FePt and the other matching that of the cubic spinel structured Fe₃O₄. The diffraction peak width in Figure 2.24c is broader than that in Figure 2.32d, indicating that the structure-correlated region of Fe₃O₄ in the 1 nm shell is smaller than that in the 3 nm shell. The high intensity from the diffraction peaks of (220) and (440) in Figure 2.32d indicates that the reflections from the (220) and (440) planes in the Fe₃O₄ shell of the core/shell nanoparticle assemblies are stronger than from other planes. Methods for coating semiconductor nanoparticles with a second semiconductor material are also developed. Different kinds of core/shell structures are successfully constructed, including CdSe/ZnS, CdSe/ZnSe, CdSe/CdS, CdTe/CdSe, CdSe/ZnTe, and InP/ZnS core/shell nanoparticles [138–141].

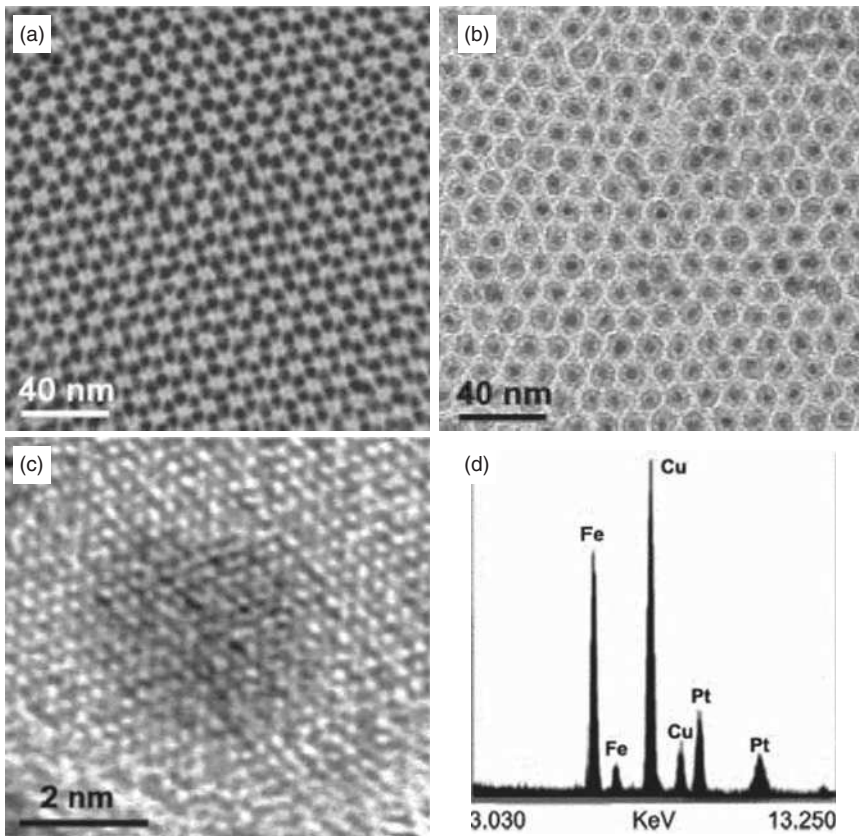


FIGURE 2.31 Transmission electron bright field images of core/shell $\text{Fe}_{58}\text{Pt}_{42}/\text{Fe}_3\text{O}_4$ nanoparticles with core/shell being (a) 4 nm/0.5 nm and (b) 4 nm/2 nm, (c) high-resolution transmission electron micrograph of a single $\text{Fe}_{58}\text{Pt}_{42}/\text{Fe}_3\text{O}_4$ particle with 4 nm core and 2 nm shell, and (d) energy-dispersive spectroscopy spectrum of a group of $\text{Fe}_{58}\text{Pt}_{42}/\text{Fe}_3\text{O}_4$ nanoparticles with 4 nm core and 1 nm shell. The shell thickness is measured statistically with standard deviation at around 11% [137]. (Reprinted with permission from Zeng H, Li J, Wang ZL, Liu JP, Sun SH. Bimagnetic core/shell $\text{FePt}/\text{Fe}_3\text{O}_4$ nanoparticles. *Nano Letters* 2004;4:187–190, Copyright 2004, American Chemical Society.)

Oil drops in water are called micelles; water drops in oil are called reverse micelles. Reverse micelle synthesis (see Section 2.4.4.1) is a powerful technique to prepare core/shell nanoparticles. Generally, a reverse micelle system contains three components: amphiphilic surfactant molecules, water, and a nonpolar solvent [142]. During the preparation, micelles act as microreactors to restrict the nanoparticle nucleation and growth to a nano-sized range. The surfactant molecule is composed of two parts with different affinities for the solvent. One part has affinity for water (polar solvent) and the other for oil (nonpolar solvent).

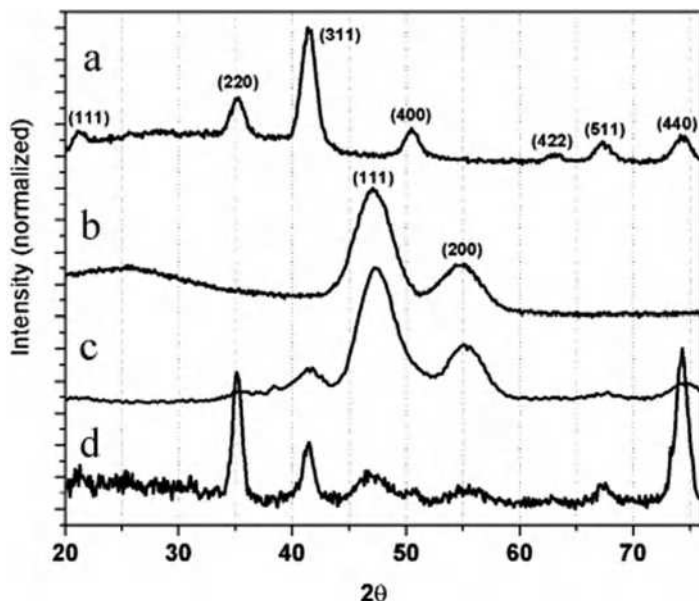


FIGURE 2.32 X-ray diffraction patterns of the assemblies of (a) 6 nm Fe_3O_4 , (b) 4 nm $\text{Fe}_{58}\text{Pt}_{42}$, (c) 4 nm/1 nm $\text{Fe}_{58}\text{Pt}_{42}/\text{Fe}_3\text{O}_4$, and (d) 4 nm/3 nm $\text{Fe}_{58}\text{Pt}_{42}/\text{Fe}_3\text{O}_4$ nanoparticles. The assemblies are prepared by depositing hexane dispersion of the particles on a glass (a, b) or a Si (100) (c, d) substrate and drying at room temperature [137]. (Reprinted with permission from Zeng H, Li J, Wang ZL, Liu JP, Sun SH. Bimagnetic core/shell $\text{FePt}/\text{Fe}_3\text{O}_4$ nanoparticles. *Nano Letters* 2004;4:187–190, Copyright 2004, American Chemical Society.)

For a system containing both water and nonpolar oil, the polar heads of the surfactant molecules direct to the interior of the water-containing sphere, while aliphatic tails point to the nonpolar organic phase. $\text{TiO}_2/\text{MoO}_3$ core/shell nanoparticles are synthesized using a reverse micelle-assisted approach [143]. The $\text{TiO}_2/\text{MoO}_3$ nanoparticle size can be readily adjusted from 4 to 8 nm. A systematic photoabsorption energy red-shift is observed for the core/shell nanoparticles and is attributed to the change in the relative position of the MoO_3 -shell conduction band as it evolves from less than a monolayer to a two-layer shell.

It should be mentioned that these are just a few common approaches for forming core/shell nanoparticles. Based on special needs, there can be variants of the above approaches. For example, different species can be coated layer-by-layer to form onion-type structures. A complex $\text{InAs}/\text{CdSe}/\text{ZnSe}$ core/shell 1/shell 2 structure is created, and the CdSe intermediate layer acts as a buffer layer to reduce the strain between the InAs core and the ZnSe outer shell [144]. A much thicker outer layer can be formed to improve stability. At the same time, fluorescence quantum yield is significantly improved compared to the previous core/shell structure without the intermediate layer.

2.4.3.2 Electroless Deposition Electroless deposition is fundamentally a reduction process. In other words, a coating forms via heterogeneous nucleation and layer-by-layer growth. This technique can produce uniform thin metal layers such as silver, cobalt, and nickel on nanoparticle surfaces. Coating is realized by the autocatalytic reduction in the metal ions in an aqueous solution. An electroless coating bath typically contains the following components: metal salt, reducing agent, complexing agent, and stabilizer. Reaction rate can be controlled and adjusted as needed.

Nickel has been coated onto SiC nanoparticles by electroless coating. Pre-treatment (including oxidation, hydrophilic treatment, and sensitization) plays an important role in the quality and properties of the nickel coating [145]. Carbon nanotube (CNT)-supported nickel-phosphorous nanoparticles are formed using the electroless nickel coating technique [146]. Well-separated nanoparticles with an average size of 40 nm are formed, firmly attaching to CNTs. The synthesized nanoparticles have ~20 at% of phosphorus; the Ni-P loading on CNTs is 14.0 wt%. Nickel has also been coated onto carbon nanofibers [147]. Palladium nanoparticles of 5 nm have been coated onto CNTs [148].

Palladium nanoparticles are obtained directly on aluminum and Al₂O₃ solid surfaces by immersing the specimen in palladium(II) acetate solution and reducing to metallic palladium using sodium hypophosphite. Additionally, the method is combined with electroless nickel plating, which facilitates metallization on the respective surfaces. In these cases, specimens are first immersed in palladium(II) acetate solution followed by immersion in electroless nickel plating solution, where palladium reduced on the specimen surface provides catalytic sites for the subsequent electroless nickel deposition. Using this technique, a 6–8.5 μm thick Ni-P metallic layer is deposited on the specimen surface [149].

With the continuing interest in forming nanoparticles on different surfaces (especially for catalysts) or in forming a conductive layer on nanoparticles, electroless coating can be expected to improve as time progresses. One important issue is to control the nucleation sites (such as substrate surface conditions or dispersed nanoparticles) so that the nanoparticle morphologies are well tuned and the coating layer on the particles is uniform. The second issue is controlling the composition and structure of the coating. The third issue is preventing the oxidation of the metallic coating layer, especially when the metal layer is not very inert.

2.4.3.3 Templating Templating involves synthesis of nanoparticles via structures defined by a predetermined template. Polymers have been proven to be an excellent template that provides uniform size and shape for nanoparticle synthesis and can be easily removed by thermal pyrolysis. Examples are polystyrene or poly(methyl methacrylate) of micron sizes. Surfactants or block copolymers can be used as bicontinuous structures to immobilize nanoparticles and convert nanoparticle-containing precursors into nanostructures. Templates such as long-chain organic monolayers, bimineralized micellar solvents, porous

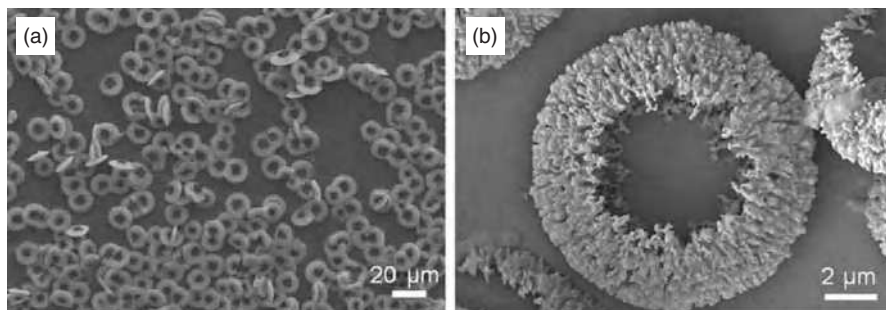


FIGURE 2.33 Typical scanning electron images of CaCO_3 ring structures obtained at a high polymer concentration ($2.0 \text{ g} \cdot \text{L}^{-1}$). (a) Particles obtained after mineralization for 15 days exhibit obvious ring-like shape with uniform size. (b) Magnified image shows that the hollow center is thoroughly developed and the peripheral surface is rough [150]. (Reprinted with permission from Gao Y.X, Yu S-H, Cong H, Jiang J, Xu A-W, Dong WF, Cölfen H. Block-copolymer-controlled growth of CaCO_3 microrings. *J Phys Chem B* 2006;110:6432–6436, Copyright 2006, American Chemical Society.)

aluminum oxide, polymeric matrices, porous silicon, CNTs, and highly oriented graphite have been widely used in the synthesis process.

Solution growth of hollow CaCO_3 structures has been successfully developed based on controlled self-assembly and polymer concentration gradients using a double-hydrophilic block copolymer with a hydrophobic modifier as a directing agent. Figure 2.33 shows the CaCO_3 ring structures. The formation mechanism of such rings is believed to result from the formation of CaCO_3 nanoparticles in unstructured block copolymer assemblies with subsequent aggregation of these primary nanoparticles. This leads to the formation of a polymer concentration gradient from the inside to the outside of the particles. As the polymer contains multiple chelating units, selective dissolution of the centers of the particles and formation of the rings occur [150].

A surface offers much flexibility in templating (either by top-down or self-assembled monolayers) and can be used to seed nanoparticle formation. Lead sulfide (PbS) nanoparticles with an average size of $3.2 \pm 0.4 \text{ nm}$ are synthesized by reacting Pb^{2+} ions on Au(111) substrate in a H_2S atmosphere [151]. The preparation process of the PbS nanoparticles consists of the formation of the self-assembled monolayers of MUA, deprotonation of the self-assembled monolayers, and Pb^{2+} ion adsorption on the outer surface of the self-assembled monolayers, followed by a gas–solid chemical reaction. Cube-shaped cadmium sulfide (CdS) nanoparticles are made using patterned monolayers of alkanethiolates on gold as a template. The average size of the resulting nanoparticles (19–76 nm) can be varied by using different solvents in the synthesis. The structure is mainly utilized as a template to limit the particle nucleation and growth; thus nanoparticles with a specific size and shape are produced. The oriented growth can be rationalized in terms of lattice matching between the template and the nanoparticles grown on

the template surface. However, structures of assembled monolayers and functionalized surfaces of polymers are difficult to manipulate and characterize, which may easily cause a lack of control of the size and shape of the nanoparticles [152].

QDs such as PbS and PbI₂ and magnetic particles such as Fe₂O₃ are formed in the hydrophilic region of a polymer or by incorporating the metal ions into the corresponding monomer before polymerization [153]. CdS is sandwiched between surfactant headgroups [154]. Selenium is incorporated into the pores of a zeolite host [155]. Platinum nanoparticles are deposited onto the exterior walls of CNTs. The size control of the nanoparticles can be achieved by changing the concentration of metal ions, the reaction temperature, the reducing reagent, or the means by which reactive solutions are added [156]. The reduction of metal ions in ethylene glycol by the addition of a salt, such as sodium dodecyl sulfate (SDS), sodium *p*-toluenesulfonate (*p*-CH₃C₆H₄SO₃Na), lithium trifluoromethanesulfonate (LiCF₃SO₃), or lithium perchlorate (LiClO₄), results in good dispersion and a high loading of platinum nanoparticles on CNTs without aggregation. Salt depresses homogeneous nucleation and leads to selective heterogeneous metal nucleation and growth.

One major advantage of the templating approach is the ability to use the size and functionality of the template to fine-tune the nanoparticle size, shape, distribution, and physical and chemical properties. The key challenges are to avoid defect formation and suppress particle growth. Sufficient chemical and interfacial complementarity between the template and the nanoparticles is often necessary. However, the strategy for template-based nanoparticle synthesis is wide-ranging as the structure and composition of the templates as well as the surface chemistry of the nanoparticles can be systematically varied. More activities are expected in this area.

2.4.3.4 Bio-Based Synthesis Biomaterials are becoming one of the most active research areas. Nanoparticle synthesis is no exception in taking advantage of the ingenious design of the bio-world. In the past decade, exploration of novel bioinspired strategies for surface-assembling molecules or colloids to generate nanoparticles with controlled morphologies, structural specialty, complexity, and unique properties has been among the hottest research topics. Biomineralization and bioinspired morphosynthesis have rapidly developed into one of the central objectives of biomimetic chemistry. The biospecific interaction and coupling of biomolecules with inorganic nano-sized building blocks has shown the potential assembly capabilities for generating new organized materials. Surfactant-mediated templating and crystallization techniques have been widely exploited in controlling the shape and size of nanoparticles. A common feature is that ordered nanoparticles are replicated from self-organized soft templates. In addition, supramolecular directed self-assembly of inorganic–organic hybrid nanostructures is also emerging. An example illustration is given in Figure 2.34 using DNAs as a template. Recent advances show remarkable feasibility to mimic natural mineralization systems by a designed artificial organic template, in which

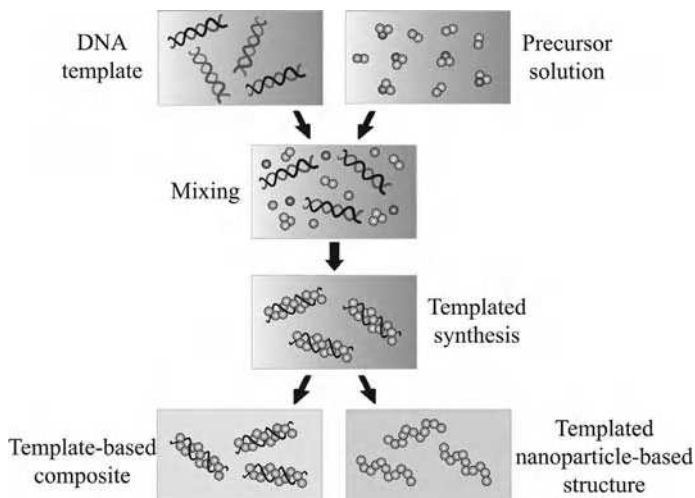


FIGURE 2.34 Illustration of biomimetic synthesis of nanoparticle composite structures or nanoparticle-based assemblies. (For a color version of this figure, see the color plate section.)

a supramolecular functional polymer can be directly employed as a mineralization template for the synthesis of novel inorganic nanoarchitectures such as CdS helices.

Silk fibroin is used as a biomolecular template for the biomimetic synthesis of CdS and ZnS QDs [157]. Even though the exact molecular level interaction is unknown, it is postulated that the coordination nucleation mechanism plays a role in the growth of sulfide semiconductor QDs in the silk fibroin matrix. The functional groups of silk fibroin molecules coordinate with the positive metal ions, enabling uniform spatial distribution of M^{2+} (Cd^{2+} and Zn^{2+}) in the solution. After that, M^{2+} ions further react with the slow-generated S^{2-} ions from the hydrolyzation of thioacetamide, the nuclei formation process. Finally, the growth of the nuclei located on the special sites is well regulated by the biomacromolecules. Sulfide QDs are obtained in the protein matrix because their aggregated growth is inhibited.

Chains of noble metal nanoclusters are synthesized on DNA templates according to a selectively heterogeneous, template-controlled mechanism. A long incubation of double-stranded DNA molecules with Pt(II) complexes is used to obtain a template-directed formation of thin and uniform cluster chains after chemical reduction in the DNA/salt solution. Without this “activation” step, DNA acts as a nonspecific capping agent for the formed clusters and does not hinder the formation of random cluster aggregates. Citrate ions can be used as additional stabilizers for the heterogeneously grown metal clusters, leading to significantly more regular metal cluster chains. Cationic SiO_2 nanoparticles with surface modifications are generated using amino-hexyl-amino-propyltri-methoxysilane [158]. Complete immobilization of DNAs on the nanoparticle surfaces is achieved at

an 80:1 nanoparticle/DNA weight ratio. The surface-modified nanoparticles have an average size of 42 nm with a distribution from 10 to 100 nm. These nanoparticles are tested for their ability to transfer genes *in vivo* in the mouse lung, and a twofold increase in the expression levels is found with SiO₂ particles in comparison to enhanced green fluorescence protein alone. Very low or no cell toxicity is observed, suggesting SiO₂ nanoparticles as a potential alternative for gene transfection.

γ -Fe₂O₃, Mn₃O₄, CoPt, and FePt nanoparticles are grown inside 24-meric ferritin cages. The material properties of these protein-templated nanoparticles are influenced by the processes at different length scales: the chemistry of the material determines the precise arrangement of atoms at very short distances, while the interior volume of the protein cage constrains the maximum nanoparticle size attainable. The domain size of inorganic nanoparticles within protein cages can be tuned. One possibility is to limit the number of nucleation sites within an individual cage [159].

Apo ferritin has a spherical protein shell composed of 24 subunits surrounding an aqueous cavity with a diameter of about 8 nm. Apoferritin-encapsulated copper, cobalt, and nickel nanoparticles are prepared from apoferritin-encapsulated metal ion solutions, which act as precursors for the preparation of apoferritin-encapsulated zero-valent metal nanoparticles, avoiding any precipitation outside the apoferritin protein [160]. As schematically shown in Figure 2.35, encapsulated Cu(II) metal ions are in fact a Cu-oxide/hydroxide apoferritin species in the solution and are completely transformed to a Cu zero-valent metal apoferritin after reduction with NaBH₄. Stained and unstained transmission electron images of the Cu(II)-apoferritin sample appear to have less contrast than those of Cu(0)-apoferritin, although the presence of several small nanoparticles in the interior of apoferritin is evident (see parts (b) and (c) in Fig. 2.36).

An attractive feature of the bio-based approach is that nanoparticle morphology may be tuned based on the ratio of nanoparticle forming species to bio-templates. Upon reduction, the amine moieties of a peptide sequester Pd²⁺ ions in a localized region, which coalesce within the peptidyl framework to grow into three differently shaped structures: spherical nanoparticles, short linear nanoribbons, and nanoparticle networks. The fabrication method is shown to be dependent on the amount of Pd²⁺ ions in the reaction such that below a critical threshold, only spherical palladium nanoparticles exist with ~ 3 nm diameters; however, above this level, linear structures are prepared with ~ 4 nm widths. The synthesis mechanism is probed using various Pd:peptide ratios during the fabrication procedure to understand the effects of Pd²⁺ concentration [161]. The nanoparticles are encapsulated within the peptide framework to maintain their colloidal stability.

It should be pointed out that bio-based nanoparticle synthesis is mostly based on heterogeneous nucleation and growth mechanism. Surface support or volumetric confinement is common features for the synthesized final products. As a result, the resulting materials are mostly composites. Self-standing nanoparticle synthesis through this approach has not been actively pursued.

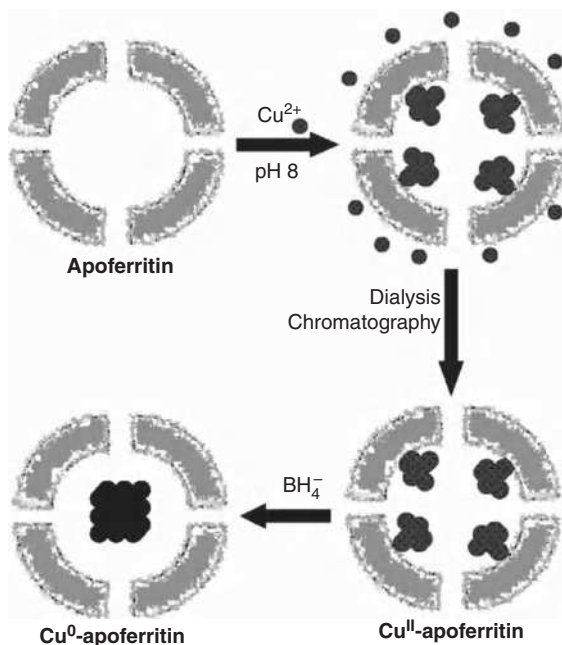


FIGURE 2.35 Structure of apoferritin and schematic representation of the preparation of $\text{Cu}(\text{II})$ - and $\text{Cu}(0)$ -apoferritin nanoparticles [160]. (Reprinted with permission from Ceolín M, Gálvez N, Sánchez P, Fernández B, Domínguez-Vera JM. Structural aspects of the growth mechanism of copper nanoparticles inside apoferritin. *Eur J Inorg Chem* 2008:795–801, John Wiley & Sons.)

2.4.4 Field-Assisted Nanoparticle Synthesis

To control nanoparticle nucleation and growth, an external field can be used. As shown in Figure 2.37, this is an active area for obtaining different nanoparticles with unique attributes.

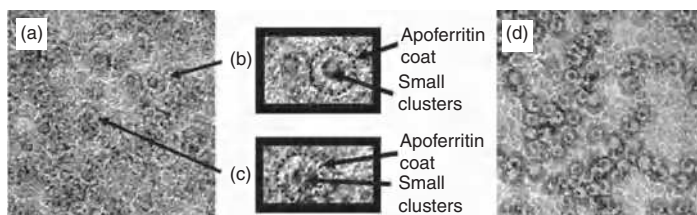


FIGURE 2.36 Transmission electron images negatively stained with uranyl acetate ($\text{UO}_2(\text{CH}_3\text{COO})_2 \cdot 2\text{H}_2\text{O}$): (a) $\text{Cu}(\text{II})$ -apoferritin nanoparticles; (b) and (c) zooms of image (a) where the apoferritin coat and the small clusters are highlighted for clarity; (d) $\text{Cu}(0)$ -apoferritin nanoparticles [160]. (Reprinted with permission from Ceolín M, Gálvez N, Sánchez P, Fernández B, Domínguez-Vera JM. Structural aspects of the growth mechanism of copper nanoparticles inside apoferritin. *Eur J Inorg Chem* 2008:795–801, John Wiley & Sons.)

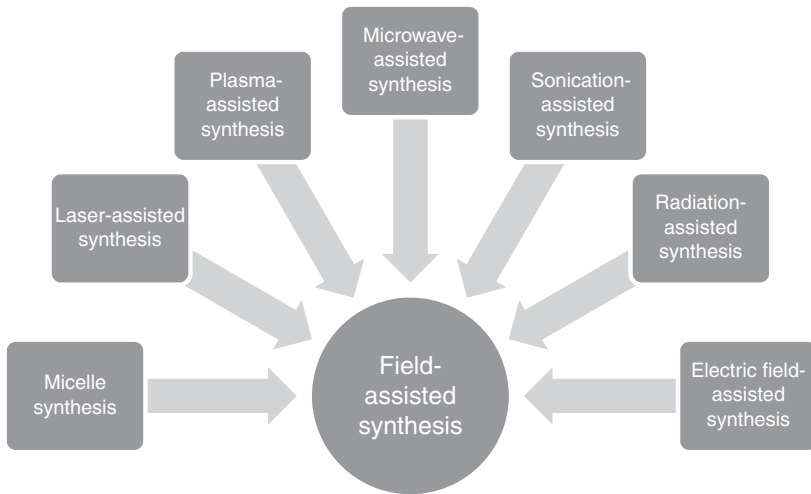


FIGURE 2.37 Different field-assisted nanoparticle synthesis methods.

2.4.4.1 Micelle Synthesis Even though there is no external field to modulate the nucleation and growth process, micelle synthesis of nanoparticles is limited in a restricted space. As explained in 2.4.3.1, oil drops in water are called micelles; water drops in oil are called reverse micelles. Micelle and reverse micelle structures are shown in Figure 2.38. During micelle synthesis, a surfactant with one part being hydrophobic and the other part being hydrophilic is dissolved into a solvent and self-assembles into micelles. Reactants are only available inside the micelles, and nanoparticles stop growing when the reactants are consumed. The preparation of nanoparticles using micelles does not require a special apparatus or extreme temperature and pressure conditions. Because the nanoparticle growth process is self-limiting, it is a well-accepted method for nanoparticle size and morphology control. Water-in-oil emulsions are thermodynamically stable

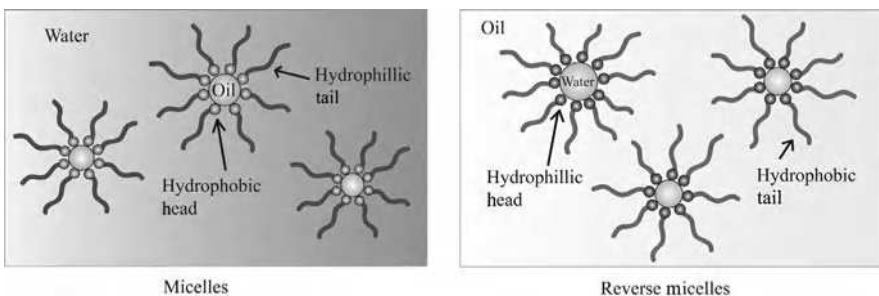


FIGURE 2.38 Micelle and reverse micelle structures. (For a color version of this figure, see the color plate section.)

dispersions of water and surfactant within a continuous oil phase (reverse micelle). In such a system, water droplets are coated with a close-packed surfactant monolayer and nanoparticle synthesis occurs inside the water droplets.

pH-responsive poly(2-(diethylamino)ethyl methacrylate) (PDEA) microgels have been utilized as nano-reactors for the formation of metal nanoparticles, such as platinum by reducing K_2PtCl_6 precursor. Three aspects are involved in the metal nanoparticle synthesis: dispersion of the original microgel in water of an appropriate pH, metal-loaded polymer matrices, and metal nanoparticle-containing microgels after reduction. Platinum nanoparticles are formed with a radius of about 1 nm [162]. Using block copolymer micelles, iron, nickel, and cobalt nanoparticles with precisely controlled size and spacing are made [163]. The obtained particle size varies from 1.9 to 2.3 nm for different metallic nanoparticles. PdRu bimetallic nanoparticles with a narrow particle size distribution are synthesized using reverse micelles in supercritical CO_2 [164]. Perfluorotetradecanoate surfactant and water are used to establish an aqueous microemulsion. The formed water-in- CO_2 micelles are used as nano-reactors where the reduction of metal salts takes place, yielding bimetallic nanoparticles. Particle size analysis shows a monomodal distribution with an average size of 4.0 nm.

TiO_2 of 30–50 nm particle size is synthesized by hydrolyzing titanium alkoxide ($Ti(OC_3H_7)_4$) in a water–oil microemulsion medium [165]. The aqueous phase is dispersed as microdroplets and surrounded by a layer of surfactants. The microdroplets are used as microreactors for the synthesis of nanoparticles. The formed nanoparticles are spherical and have a narrow size distribution. PbSe nanoparticles encapsulated by SiO_2 are also synthesized by a similar approach [166]. Monodispersed SiO_2 particles of 30–70 nm diameter produced by hydrolysis of tetraethoxysilane (TEOS) in a microemulsion show a complex dependence of particle size on water-to-surfactant molar ratio and on the concentration of ammonia. At relatively low ammonia concentration (1.6 wt% NH_3), the particle size decreases monotonically with an increase in the water-to-surfactant molar ratio. However, for higher ammonia concentrations (6.3–29.6 wt% NH_3), a minimum particle size occurs as the water-to-surfactant molar ratio is increased [167]. The growth kinetics of SiO_2 nanoparticles synthesized by reverse microemulsion-mediated alkoxide hydrolysis are investigated with tetraethoxysilane (TEOS) as the SiO_2 precursor and polyoxyethylene (5) nonylphenylether (NP-5)/cyclohexane/ammonium hydroxide as the water-in-oil microemulsion system. The growth rate of SiO_2 particles in the reverse micelle system is controlled by TEOS hydrolysis. At the later stage of the nanoparticle growth, the rate of the surface reaction (condensation), rather than hydrolysis, becomes important for the growth rate [168]. In a different study, reaction of tetramethylorthosilicate (TMOS) inside the water droplets of a water-in-oil microemulsion, under both acidic (pH 1.05) and basic (pH 10.85) conditions, is studied [169]. The addition of TMOS to the microemulsion results in the formation of SiO_2 as TMOS, preferentially located in the oil phase, diffuses into the water droplets. Once in the hydrophilic domain, hydrolysis occurs rapidly as a result of the local high concentration of water. Varying the pH of the water droplets from 1.05 to 10.85,

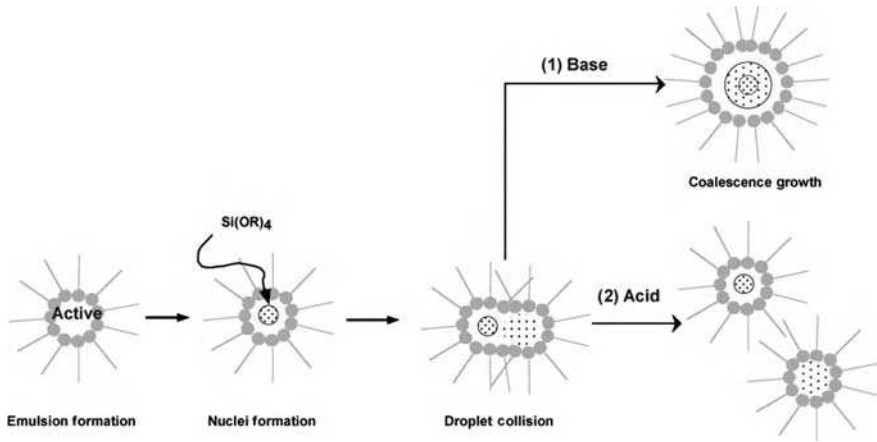


FIGURE 2.39 Mechanism for particle formation under acidic and basic conditions [169]. (Reprinted with permission from Finnie KS, Bartlett JR, Barbé CJA, Kong L. Formation of silica nanoparticles in microemulsions. *Langmuir* 2007;23:3017–3024, Copyright 2007, American Chemical Society.)

however, considerably slows the hydrolysis reaction of TMOS. The formation of a dense SiO_2 network occurs rapidly under basic conditions, and the slower formation of more disordered SiO_2 occurs in acid. Spheres of ~ 11 nm size are formed under basic conditions and stabilized by a water/surfactant layer on the particle surface during the formation. Under acidic conditions, highly uniform ~ 5 nm spheres are formed and retained within the water droplets (~ 6 nm diameter). High surface area ($510 \text{ m}^2 \text{ g}^{-1}$) particles with an average pore size of 1 nm are formed at pH 1.05. In contrast, synthesis at base conditions results in low surface area particles with a negligible internal porosity. The fundamental mechanism for these nanoparticle formation processes is shown in Figure 2.39 [169]. Base catalysis of sol–gel reactions promotes hydrolysis, condensation, and, more importantly, dissolution. At pH 11, the hydrolysis rate is modest and results in a relatively small and heterogeneous nucleation rate (i.e., the nucleation varies from micelle to micelle). This leads to the production of a fairly inhomogeneous and polydispersed system. Rapid condensation results in quick consumption of all the precursors inside the micelles and the formation of a dense SiO_2 structure. Acid catalysis, in contrast, promotes hydrolysis but hinders both condensation and dissolution reactions. Consequently, for the microemulsion synthesis of SiO_2 particles using acid catalysis, many nuclei are generated quickly, but very little growth is observed. This leads to the formation of significantly smaller but more homogeneous particles. No coalescence takes place between the droplets during intermicellar collisions. Particles grow to fill the micelle cores by slowly consuming all of the hydrolyzed precursors present in their pools.

Micelle synthesis mostly uses standard, commercially available, and relatively inexpensive chemicals. The synthesis can reproducibly yield monodispersed nanoparticles. The micelle size has a fundamental impact on the particle size.

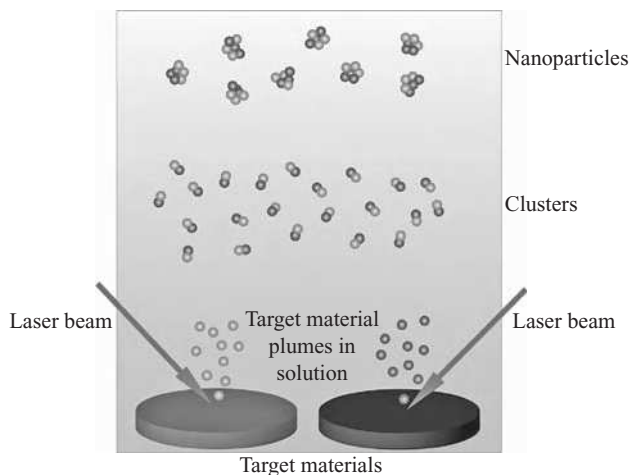


FIGURE 2.40 Illustration of laser-assisted nanoparticle synthesis. (For a color version of this figure, see the color plate section.)

2.4.4.2 Laser-Assisted Synthesis Lasers, especially ultrafast lasers, are increasingly used in nanoparticle synthesis. With a laser, the fundamental timescales of chemical reactions become accessible. Different approaches can be used in the general scheme of laser-assisted nanoparticle synthesis, and both simple and complex compositions can be obtained: laser irradiation of a mixture of two or more colloidal solutions and laser ablation in reactive liquids. The interaction of high-intensity pulsed laser radiation with a solid target in a liquid leads to the formation of a dense plasma cloud with rapidly changing parameters above the target surface (Fig. 2.40). The formed plasma expands with a supersonic speed, being cooled as a result of electron–ion radiative recombination and chemical reactions. The radiative stage of laser-induced plasma is rather short (generally several hundreds of nanoseconds). A hemispherical cavitation bubble, composed of gaseous ablation products and vapor of the surrounding liquid, is formed after the plasma decay. Having formed after the laser pulse, the gas bubble continuously expands, reaches a maximum size for several hundreds of microseconds (depending on the target material and laser pulse energy), and then collapses. Bimetallic nanoparticles (Ag–Cu, Ag–Au), semiconductor nanoparticles (ZnO, CdSe), and doped oxide nanoparticles (ZnO:Ag) are formed as a result of single- and double-pulse laser ablation in different liquids (water, ethanol, acetone, or solutions of polysaccharides).

Lasers have been utilized to irradiate iron and gold nanoparticles in a liquid medium to form Fe/Au nanoparticles with a core/shell structure [170]. A pulsed 532 nm laser beam is absorbed more efficiently by gold than by iron nanoparticles. During this process, gold nanoparticles absorb photons, decompose, and then condense onto iron nanoparticles, forming a shell. The core consists of body-centered cubic iron single domains with an 18 nm diameter and the shell is

composed of face-centered cubic gold nanoparticles with ~ 3 nm thickness. The formed particles are superparamagnetic at room temperature and show good oxidation resistance. Laser photolysis of gold (Au^{III}) salts embedded in the cores of block copolymer micelles derived from polystyrene-poly-4-vinylpyridine is also studied [171]. Gold salt type, loading rate, presence of water, and micelle characteristics all influence the rate of reduction and gold colloid formation. The presence of water in the system containing $\text{HAuCl}_4 \cdot 3\text{H}_2\text{O}$ accelerates Au^{III} reduction, but the gold colloid size is not affected (about 3 nm). The substitution of $\text{HAuCl}_4 \cdot 3\text{H}_2\text{O}$ with AuCl_3 results in much slower accumulation of Au^{I} species and slower nucleation of gold colloids, which results in larger particles with a mean diameter of 6.0 nm. Increasing the amount of the metal compound also leads to an increase in the particle size.

A single-step method is carried out for fast (2–3 minutes), scalable synthesis of inert colloidal metal- SiO_2 nanoparticles in stable colloids based on the laser ablation of a solid target submerged in an aqueous solution of the metal salts, whose reduction gives rise to nanoparticles. At the same time, the evaporated material from the target (Si) produces nanometer-sized SiO_2 nanoparticles that cap metal nanoparticles. The method combines the advantages of chemical synthesis with the versatility of the laser ablation technique. In fact, the high yield and fast processing time are very promising for the scalable production of nanoparticles. In addition, ablation parameters, target materials, and metal salts can be combined and controlled to influence the size, morphology, and composition of nanoparticles. Figure 2.41 shows SiO_2 coated with silver and gold nanoparticles. Silver and gold signals in high-resolution transmission electron chemical mapping images can be measured, as indicated by the arrows in Figure 2.41c, despite the intensity difference due to a smaller content of gold in the alloyed nanoparticles (26.6%). Other than gold and silver signals (Figs. 2.41a, b), a weak signal attributed to the presence of silicon all around the examined area is also measured, being more intense at the positions of the nanoparticles, as shown in Figure 2.41d. An amorphous SiO_2 shell can be observed in some micrographs such as the one indicated by the dotted line in Figure 2.41e and illustrated in Figure 2.41f. The SiO_2 present in the colloid can be due to the fast oxidation of sputtered silicon of the ablated target. A core/shell metal/ SiO_2 nanoparticle is illustrated in Figure 2.41f, where SiO_2 nanoparticles smaller than 2 nm cover the core metal (pure or alloy) nanoparticle [172].

In contrast to chemically synthesized nanoparticles, the nanoparticles formed by laser ablation in liquids do not contain foreign ions or surface-active materials, which is undoubtedly an advantage for a number of applications. Other advantages of laser ablation are universality (it can be used for metals, semiconductors, and insulators of different compositions) and possibility of controlling the characteristics of synthesized particles by changing the irradiation parameters. The laser-assisted techniques also have the advantage of precisely controlling synthesis kinetics and thus particle size and shape. The relatively low cost of the equipment and the high efficiency also make the laser-assisted techniques attractive.

2.4.4.3 Plasma-Assisted Synthesis Plasma is a collection of free moving electrons and ions and is normally in the form of ionized gas. Because of electric charges, plasma responds strongly to electromagnetic fields and can be employed to facilitate nanoparticle synthesis. Hydrogen plasma, nitrogen plasma, and microwave plasma are all possible sources. The plasma-assisted method has the advantage of low cost, ease of use, and ability to produce high-purity nanoparticles.

Synthesis of carbon-doped TiO₂ using TiCl₄ and CO₂ as titanium and carbon sources, respectively, is carried out by thermal plasma at atmospheric pressure. The resulting powders contain mixed anatase and rutile phases with particle sizes

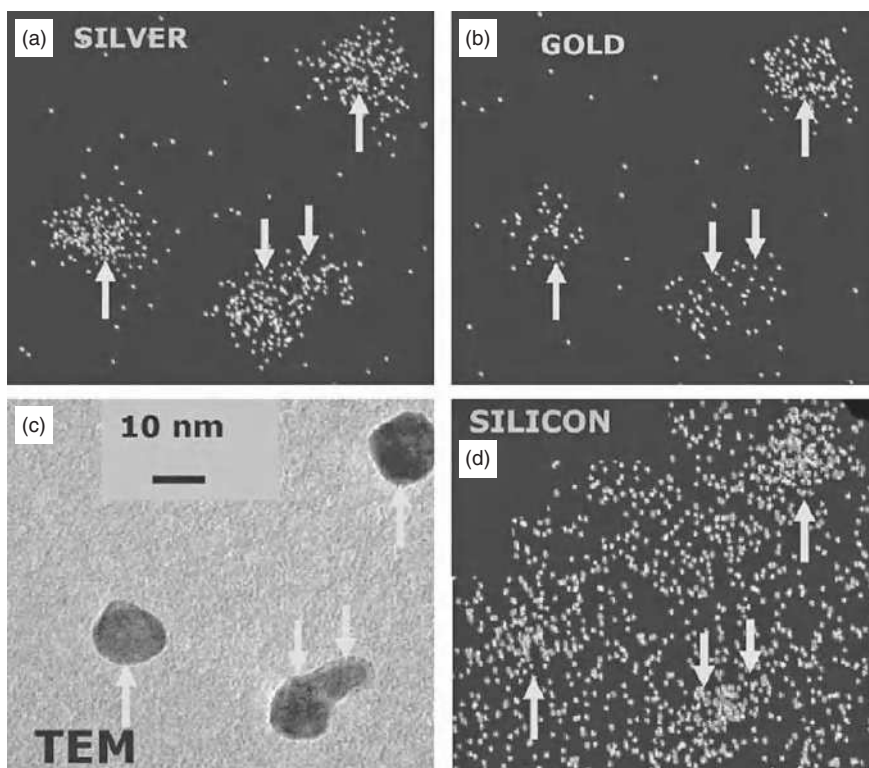


FIGURE 2.41 Energy-dispersive spectroscopy chemical mapping of silver–gold alloy nanoparticles demonstrates the presence of (a) silver and (b) gold in the four nanoparticles marked by arrows and observed in (c) transmission electron image. (d) Other than silver and gold, the energy-dispersive spectroscopy–high-resolution image also reveals the presence of silicon. The limit of the shell is indicated by a dotted line in (e) transmission electron image and illustrated in panel (f) [172]. (Reprinted with permission from Jimenez E, Abderrafi K, Abarques R, Valdes JL, Martinez-Pastor JP. Laser-ablation-induced synthesis of SiO₂-capped noble metal nanoparticles in a single step. *Langmuir* 2010;26:7458–7463, Copyright 2010, American Chemical Society.) (For a color version of this figure, see the color plate section.)

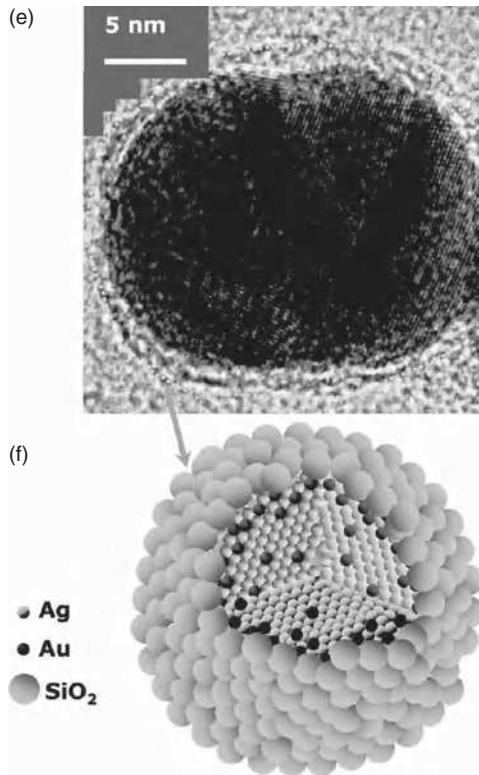


FIGURE 2.41 (Continued)

ranging from 20 to 50 nm [173]. For pure TiO₂ synthesis using Ti(OC₃H₇)₄ and H₂O as precursor solutions, the precursors are vaporized and sent into the plasma reactor via a nitrogen carrier gas. The Ti(OC₃H₇)₄ and H₂O ratio is 11.9:1. The generated particles have a broad size distribution when no plasma is applied; the particle sizes are as large as 1 μm or smaller than 100 nm. On the other hand, when the plasma is present, the particle sizes become smaller and more uniformly distributed. Higher voltage refines particle size distribution and shape. Figures 2.42a–d show the scanning electron images of the particles generated at applied voltages of 0, 6.48, 8.58, and 9.60 kV, respectively [174].

2.4.4.4 Microwave-Assisted Synthesis Microwave heating uses liquids and solids to transform electromagnetic energies into heat. Due to the difference in the dielectric constants of the solvent and the reactant(s), selective dielectric heating can provide significant enhancement in the transfer of energy directly to the reactants, which causes an instantaneous internal temperature rise. Using metal precursors that have large microwave absorption cross sections relative to the solvent, very high effective reaction temperatures can be achieved. This

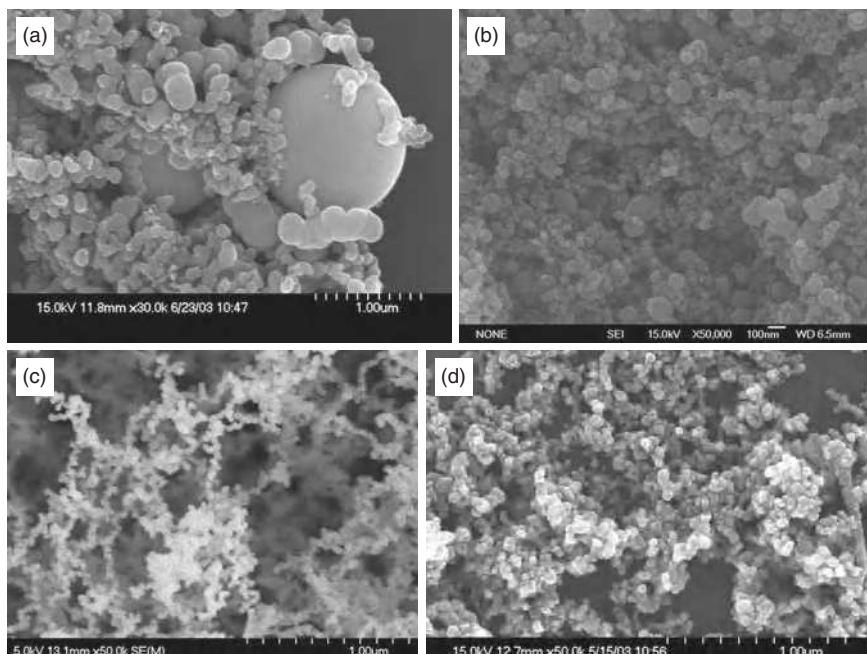


FIGURE 2.42 Scanning electron images of TiO₂ particles collected in the reactor under different applied voltages. (a) No applied voltage, (b) 6.48 kV, (c) 8.58 kV, and (d) 9.60 kV [174]. (Reprinted with permission from Chen C, Bai H, Chein HM, Chen TM. Continuous generation of TiO₂ nanoparticles by an atmospheric pressure plasma-enhanced process. *Aerosol Sci Technol* 2007;41:1018–1028, Copyright 2007, Mount Laurel, NJ.)

allows for rapid decomposition of the precursors, thus creating highly supersaturated solutions where nucleation and growth can take place to produce desired nanoparticles. The main advantage of microwave heating over other conventional heating methods is the rapid and uniform heating of the reaction mixture. Microwaves have the ability to rapidly heat the reactant mixture and remove the heat source when needed to stop the synthesis process. This is much desired since it can lead to small particle size, narrow size distribution, and very short reaction time.

Since microwave heating allows quenching of the reaction very early on (~ 10 seconds), it provides the opportunity to control the size of small nuclei by varying the microwave initiated reaction time and achieve high efficiency with respect to energy consumption. Narrow particle size distributions can be obtained because particle formation in microwave plasma synthesis is, in contrast to conventional gas-phase synthesis, not necessarily a random process; rather, it may be controlled by particle charging. During synthesis, the particles carry electric charges of the same sign. Therefore, particle growth is reduced and agglomeration thwarted by electrostatic repulsion. Furthermore, this process allows for

coating of particles with organic or inorganic phases, reducing the interaction of different particles. This makes it possible to exploit properties and characteristics of isolated particles. Additionally, the coating process allows the combination of different properties such as superparamagnetism and luminescence [175].

Microwaves can decompose organometallic precursors to form transition metal nanoparticles (iron, cobalt, and Co–Mo) with a mean particle size smaller than 10 nm [176]. If the gas carrier is changed from pure argon to 10% H₂/Ar, the mean particle size can be reduced to <2 nm. Carbon-supported PtNi nanoparticles are synthesized by reducing platinum and nickel precursor salts using hydrazine (N₂H₄) under microwave irradiation [177]. The average particle size is 2.9–5.8 nm with a uniform distribution. Nanoparticles formed using this method show good electrocatalytic activity. A one-pot microwave irradiation method is used to prepare different shape gold nanoparticles capped with a mixture of oleylamine and oleic acid [178]. The size, shape, and morphology of the nanoparticles can be tailored by varying the ratio of oleylamine to oleic acid, microwave time, and the concentration of gold ions. Increasing oleic acid makes the particle surfaces faceted and increases the particle size, as shown in Figure 2.43. Hexagons and truncated prisms are more predominant when the oleic acid is more than 60%.

A detailed study of kinetic and thermodynamic aspects in the microwave-assisted synthesis of ZnO nanoparticles from zinc acetate and benzyl alcohol shows that microwave irradiation greatly accelerates nanoparticle formation by (a) facilitating the dissolution of the precursor in the solvent, (b) increasing the rate constant for the esterification reaction by an order of magnitude, resulting in faster production of monomers and, consequently, earlier nucleation, and (c) increasing the rate constant of nanoparticle growth from 3.9 nm³ min⁻¹ (conventional heating) to 15.4 nm³ min⁻¹ (microwave heating) [179]. MoS₂ and WS₂ nanoparticles with layered structures are synthesized by the reaction of hexacarbonyls with H₂S in a microwave plasma. The resulting particles are 5–15 nm in diameter. Additionally, particles exhibiting nested fullerene-like structures and polyhedron-shaped crystals are found [180]. ZrO₂ nanoparticles are prepared using microwave heating with a uniform particle size of about 8 nm. Hafnia (HfO₂) particles are coated with Al₂O₃ using the same technique. Lattice fringes show that the HfO₂ core is crystalline and the Al₂O₃ coating is amorphous [175].

2.4.4.5 Sonication-Assisted Synthesis Recently, ultrasound has been introduced for nanoparticle synthesis. Rapid heating is realized from sonication of a liquid, similar to microwave-induced heating. Ultrasound provides strong mechanical forces that can disperse reactants easily and evenly. During the sonication of a liquid, cavitation forms from the implosive collapse of bubbles, resulting in localized hot spots with effective temperature as high as 5000 K and lifetimes of a few nanoseconds or less [72]. Thus, chemical reactions mostly take place inside the bubbles. However, the extremely rapid cooling rate accompanying the process greatly favors the synthesis of amorphous nanoparticles. The

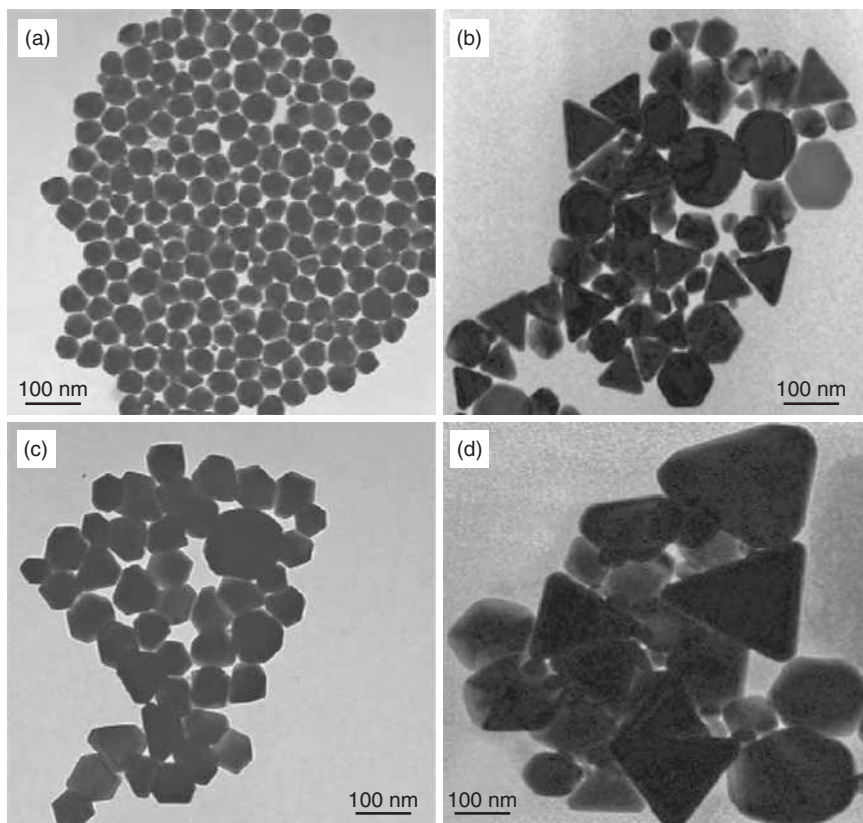


FIGURE 2.43 Transmission electron images of the gold nanoparticles prepared in (i) 60, (ii) 70, (iii) 80, and (iv) 90% oleic acid [178]. (Reprinted with permission from Mohamed MB, AbouZeid KM, Abdelsayed V, Aljarash AA, El-Shall MS. Growth mechanism of anisotropic gold nanocrystals via microwave synthesis: formation of dioleamide of gold nanocatalysis. *ACS Nano* 2010;4:2766–2772, Copyright 2010, American Chemical Society.)

shape and size of the nanoparticles can be controlled by adjusting the power of the ultrasonic irradiation.

Ultrasound is used to facilitate the hydrolysis of zinc and iron acetates, forming zinc ferrite nanoparticles with a uniform size of about 4 nm [181]. Ultrasonic irradiation of an aqueous solution also facilitates the precipitation and synthesis of needle-shaped hydroxyapatite nanoparticles [182]. Hausmannite (Mn_3O_4) nanoparticles are prepared by ultrasound in various media under ambient conditions without any additives. The synthesis is carried out by direct sonication of manganese acetate in water. Nanoparticles with high crystallinity and size <4 nm are obtained after 3 minutes of sonication [183]. CdS/ TiO_2 core/shell nanoparticles are made by microemulsion under ultrasound [184]. TiO_2 and CdS in the resulting particles are anatase and hexagonal, respectively. The TiO_2 coating

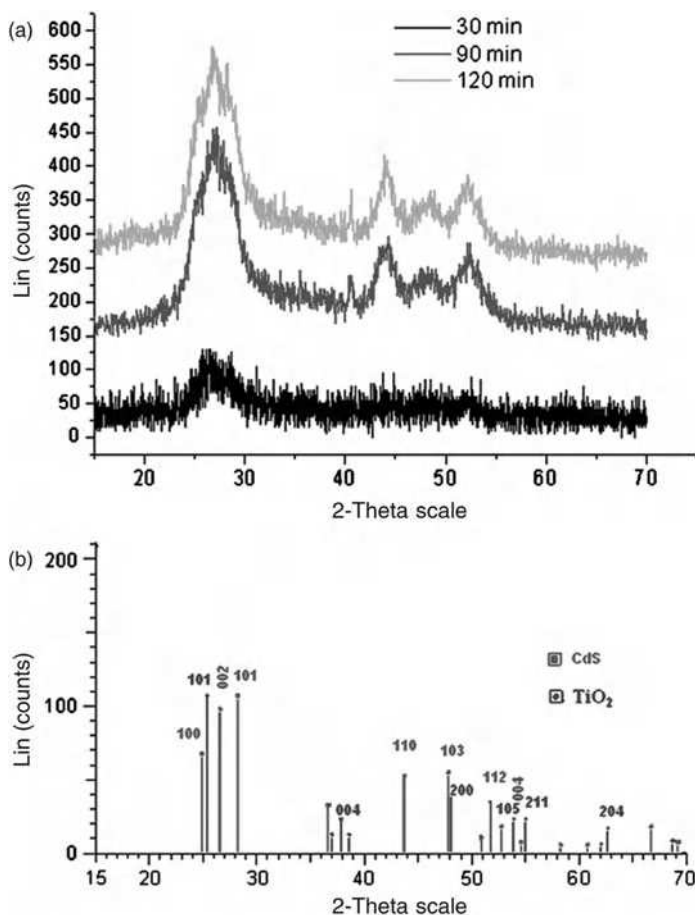


FIGURE 2.44 X-ray diffraction patterns of the prepared CdS/TiO₂ composite at different sonication times (mole ratio = 2.5) [184]. (Reprinted with permission from Ghows N, Entezari MH. Fast and easy synthesis of core-shell nanocrystal (CdS/TiO₂) at low temperature by microemulsion under ultrasound. *Ultrason Sonochem* 2011;18:629–634, Copyright 2011, Elsevier.) (For a color version of this figure, see the color plate section.)

thickness on CdS nanoparticles can be controlled. Figure 2.44 shows the X-ray diffraction patterns of the nanocomposites at three different times of sonication. After 30 minutes of sonication, the particles are mostly amorphous. By increasing the time of sonication to 90 minutes and 120 minutes, the X-ray diffraction peaks become sharper and indicate increased crystallinity. Compared to conventional synthesis, which requires thermal treatment at 673–723 K to induce and improve the crystallinity of the deposited layer, sonochemical synthesis is more effective as it takes advantage of the ultrasonic power for the crystallization of TiO₂ and CdS. Crystalline TiO₂ can be formed in the dispersion and inherently

bind to CdS particles without any post thermal treatment. The average particle size is about 8 nm from the half-width of the X-ray diffraction peak of the (101) plane.

The enhancement of the crystal phase of the composite in the presence of ultrasound can be explained according to the cavitation process. The chemical and physical effects of ultrasound arise from acoustic cavitation. When a bubble is formed in the microemulsion system, there is a possibility for small droplets of oil to accumulate at the interface of the bubble produced by ultrasound. This behavior arises from the higher tendency of the oil droplets to interact with the bubble interface than with the water phase. The implosion of a bubble generates many local hot spots in the solution and promotes the reactions. The formation, growth, and crystallization of composite nuclei are accelerated under these conditions. The high temperature produced during the cavitation facilitates the crystallization of the product. The hot spots produced during the sonication play the same role as the calcination process.

The advantages of the ultrasound-assisted technique include chemical homogeneity and reactivity through mixing at the atomic level, better dispersion even without a surfactant or a dispersant, and high crystallinity of nanoparticles.

2.4.4.6 Radiation-Assisted Synthesis In radiation-assisted nanoparticle synthesis, a source of radiation is employed to produce monodispersed nanoparticles. Absorption of ionizing radiation in aqueous solutions leads to radiolysis of water and creation of reactive radicals and ion-radicals [185]:



The main reducing species are solvated electron e_{aq}^- and $\bullet\text{H}$, whereas $\bullet\text{OH}$ radicals exhibit strong oxidative properties. Therefore, it is necessary to introduce $\bullet\text{OH}$ scavengers into the solution. Formate anion or propan-2-ol serves as convenient $\bullet\text{OH}$ scavengers, forming strong reductive radicals from both $\bullet\text{OH}$ and $\bullet\text{H}$. Presence of dissolved oxygen in water may seriously affect the processes following radiolysis of water by converting reducing species into oxidative (O_2^- , HO_2) and also reacting with already formed particles.

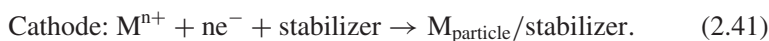
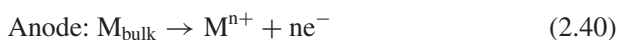
Radiolytic reduction is used widely in metal nanoparticle synthesis. Nickel catalyst is synthesized by adsorbing Ni^{2+} ions onto a CeO_2 support followed by γ -irradiation under a wet condition at room temperature [186]. Highly stable colloidal silver nanoparticles are formed in a suspension using a ^{60}Co γ -ray source. The average silver nanoparticle size is about 12.8 nm. Other examples of radiolytic reduction include the preparation of palladium nanoparticles from PdCl_2 under ^{60}Co radiation with a resulting average particle size of 16–45 nm [187]. Besides metals, radiolysis has been proven to be an adequate technique to produce extremely small and monosized semiconductor nanoparticles. Monodispersed ZnS nanoparticles with 1.5 nm diameter are synthesized by γ -irradiation of an aqueous solution containing Zn^{2+} and thiol ($\text{HOCH}_2\text{CH}_2\text{SH}$). Irradiation

dose has an important effect on the ZnS particle size. Compared to ZnS prepared by chemical methods, the particle size of ZnS formed by irradiation is smaller. Nano-sized spherical copper and octahedral Cu₂O are successfully synthesized by radiation- or photo-induced reduction in Cu²⁺ aqueous solutions containing 10⁻³ mol dm⁻³ copper sulfate or formate, 1.3 mol dm⁻³ propan-2-ol, and polyvinyl alcohol (as a stabilizer). The solutions are irradiated by ⁶⁰Co γ -rays (dose rate 70 Gy h⁻¹) [185]. An increase in the initial copper concentration to 10⁻² mol dm⁻³ results in the formation of a different reaction product—octahedral Cu₂O nanoparticles.

One advantage of radiation-assisted synthesis is that nanoparticles can be made at room temperature so various thermally unstable substances may be used. Other advantages include monodispersed and ultrasmall particle sizes. Particle shape and size can be controlled by varying the applied irradiation dose or dose rate. In a homogeneous radiation field, particles with narrow size distribution may be formed.

2.4.4.7 Electric Field-Assisted Synthesis Less commonly, nanoparticles can be formed by electrochemical reduction at the cathode or oxidation at the anode, which contains the interested species that forms nanoparticles. More often, the anode acts as the sacrificial electrode to provide metal ions. Particle size can be controlled by adjustment of current density.

For pure platinum nanoparticle synthesis, water- and oxygen-free solvents are used under an argon atmosphere [188]. The electrolyte consists of tetraalkylammonium salts, which also serve as stabilizers for the metal clusters. In the overall process, the bulk metal is oxidized at the anode, the metal cations migrate to the cathode, and reduction takes place again with the formation of metal nanoparticles. Undesired agglomeration of metal nanoparticles is prevented by the presence of ammonium stabilizers:



Using the electrochemical method, spherical Cu₂O nanoparticles with an average size of 35 nm are successfully synthesized [189]. The experiment proceeds at a constant current in a NaCl solution with copper slivers as electrodes. Cu₂O nanoparticles are formed on the anode side, while on the cathode side water is reduced to hydrogen. Au–Ag alloy nanoparticles with different atomic ratios are synthesized using electrochemical co-reduction in Au- and Ag-containing chemicals in an aqueous solution with and without the presence of PVP [190]. The average particle size is <20 nm with the presence of PVP. Electrochemical reduction creates nanoparticles with a homogeneous distribution. A proper amount of PVP helps to produce nanoparticles with smaller average size and prevent agglomeration. Cobalt nanoparticles of 2 nm average size are synthesized by adjusting current density [191]. Aggregation and oxidation are avoided

by a surfactant combination of triphenylphosphine and oleic acid. At sufficiently anodic potentials in alkaline media, an iron anode is directly oxidized to FeO_4^{2-} , and thus BaFeO_4 is formed [192]. The underlying reaction is



The process occurs at potentials >0.6 V versus the standard hydrogen electrode followed by precipitation:



In addition to a persistent direct current, cycling potential can be applied on a sacrificial anode to make nanoparticles. For example, copper is used as a raw material in the presence of Na_2S and polyvinylalcohol (PVA). Cu_2S nanoparticles are synthesized by cyclic voltammetry between 0.10 and 1.50 V with polyvinylalcohol as a stabilizer. The results show that electrochemically synthesized Cu_2S nanoparticles are homogeneously dispersed and well separated from one another with a mean diameter of about 12 nm [193].

Overall, electric field-assisted synthesis is a niche process for nanoparticles. The amount of particles produced is generally low.

2.5 SOLID NANOPARTICLE SYNTHESIS

Solid-state nanoparticle synthesis is not as common and can be broadly divided into milling and reaction between solids.

2.5.1 Milling

Milling is a high-energy process that either breaks down large particles to nano size or induces reactions in mixtures by providing high mechanical forces (impact and shear). It is one of the oldest processes of making nanoparticles. Elemental powders or compounds can be used as starting materials. Amorphous, crystalline, and composite nanoparticles can be synthesized. Milling has been a popular method to make nanoparticles because of its simplicity, relatively inexpensive equipment, and applicability to essentially all classes of materials. It produces nanoparticles not by ion/molecule/cluster addition but by structure fragmentation or reaction initiation. The mechanism of milling is fairly complex and does not lend itself easily to rigorous theoretical analysis due to its dynamic nature.

Magnetically hard PrCo_5 nanoparticles are produced by surfactant-assisted high-energy milling of PrCo_5 alloy with steel balls. Heptane is used as the milling medium and oleic acid as the surfactant. The use of the surfactant leads to the dispersion of the crushed particles and prevents them from rewelding during the

milling process. The milled powders consist of nanoparticles with an average size of 8–10 nm [194]. The coercivity increases with milling time increase and particle size decrease with a value of 6.8 kOe after 12 hours of milling, mainly attributed to the use of oleic acid as the surfactant. However, for SmCo_x ($x = 3.5, 4, 5, 6, 8.5, \text{ and } 10$) magnetic nanoparticles prepared by surfactant-assisted ball milling of larger-sized SmCo_x alloy particles, the coercivity decreases with particle size decrease, indicating a complex effect of particle size and composition on magnetic hardening of the nanoparticles [195].

Nanoparticles of iron, cobalt, FeCo , SmCo_5 , and NdFeB with sizes smaller than 30 nm and narrow size distributions are successfully prepared by ball milling of large-sized powders in the presence of surfactants and organic milling media. The iron and FeCo nanoparticles prepared are close to spherical, whereas those of cobalt, SmCo_5 , and Nd-Fe-B show elongated rod shapes. The fracture of large particles along preferred crystalline orientations and nanoparticle growth under local heating from milling are key factors for the creation of different particle shapes. Cobalt, SmCo , and Nd-Fe-B have hexagonal close-packed structures, while iron and FeCo have body-centered cubic structures. This explains the difference in nanoparticle shapes. All these nanoparticles show ferromagnetic behaviors at low temperatures [196]. Figure 2.45 shows iron and SmCo_5 nanoparticles after ball milling for different times. For iron nanoparticles, the particle size decreases with milling time. However, SmCo_5 particles become more elongated as milling time increases.

As can be seen, all the above ball-milling processes use certain surfactants and often organic carrier liquids. These measures can effectively prevent the species from oxidation and agglomeration/rewelding.

In addition to simply breaking down large-sized particles, mechanical alloying was developed in the 1960s by Benjamin and coworkers for producing oxide-strengthened alloys [197]. It is a high-energy ball-milling process and involves repeated deformation, fracturing, and welding of mixed metal powders to produce a homogeneous phase. During the high-energy ball-milling process, metal particles are repeatedly flattened, cold-welded, fractured, and rewelded. Typically, when two grinding balls collide, around 1000 particles with an aggregate weight of ~ 0.2 mg are trapped in-between them during each collision. The force of the impact plastically deforms particles, resulting in work hardening and fracture. However, the new surfaces created may enable the particles to weld together, thereby increasing obtainable particle sizes. Varying the milling time of Ni-Ti powder can produce a lamellar structure, an amorphous alloy, or an intermetallic powder [198]. Equimolar nickel and titanium powder is milled for 10 hours using a Szegvari attritor, and a homogeneous lamellar structure forms. The thickness of these layers is difficult to quantify, since a higher magnification of each rich phase region reveals a nanostructured lamellar within that phase. These regions contain lamellar thicknesses between 10 and 70 nm. Strictly speaking, mechanical alloying cannot produce discrete nanoparticles. It mainly produces nanoscale mixing (alloying) of different species.

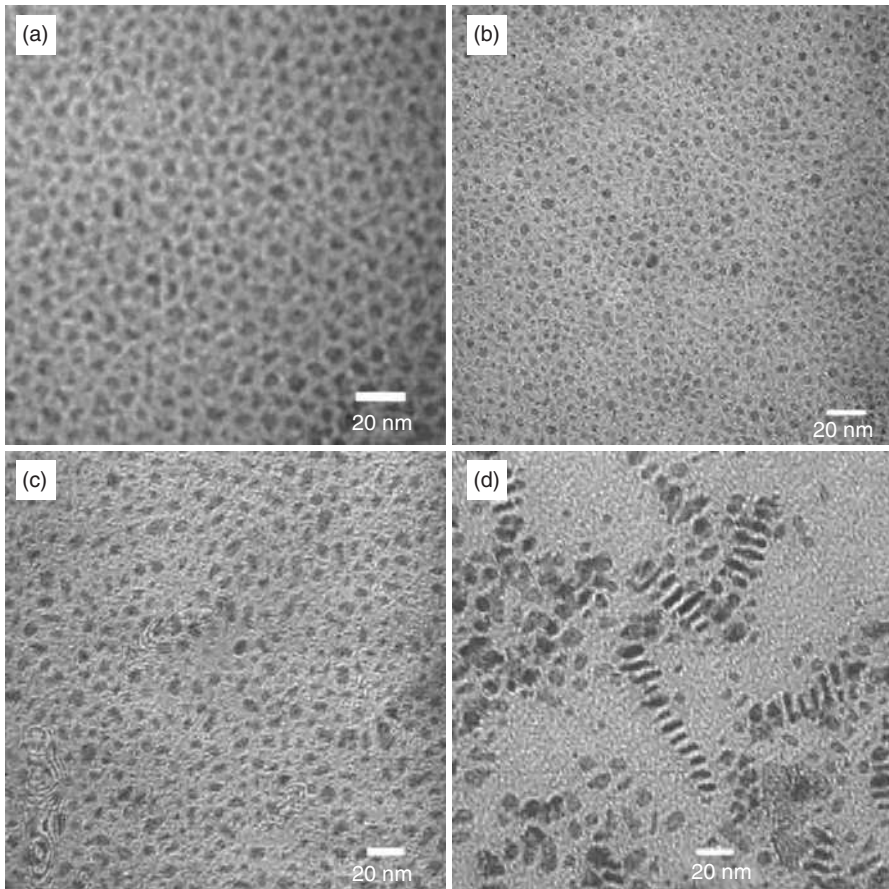


FIGURE 2.45 Transmission electron images of nanoparticles prepared by milling iron powders for (a) 1 hour and (b) 5 hours, and by milling SmCo₅ powders for (c) 5 hours and (d) 25 hours [194]. (Reprinted with permission from Chakka VM, Altuncevahir B, Jin ZQ, Li Y, Liu JP. Magnetic nanoparticles produced by surfactant-assisted ball milling. *J Appl Phys* 2006;99:08E912-1-3, Copyright 2006, American Institute of Physics.)

Chemical reaction(s) may occur and new composition (single or multi-component) nanoparticles may be synthesized during milling. This is termed mechanochemical milling. Silicon nanoparticles are synthesized by ball milling of graphite and SiO₂ powders:



The solid-state reaction leads to the formation of silicon nanoparticles [199]. The process can be easily scaled up. Ti₃Al–SiC is obtained by milling titanium, aluminum, and SiC powders [200]; WC–MgO by milling magnesium, carbon, and

WO₃ powders in argon [201]; TiC–Al₂O₃ by milling titanium, carbon, and Al₂O₃ [202]; and CeO₂ by milling 2CeCl₃ · 6H₂O(s) and 3Na₂CO₃ · 10H₂O(s) followed by calcination [203]. Co₃O₄ nanoparticles are synthesized by thermal treatment of the precursor obtained via mechanochemical reaction of Co(NO₃)₂ · 6H₂O with NH₄HCO₃. Calcination of the precursor at 300°C results in the formation of Co₃O₄ nanoparticles of 13 nm size [204]. CdO nanoparticles of 43 nm size are successfully synthesized by mechanochemical reaction of CdCl₂ and Na₂CO₃ with NaCl as a diluent and subsequent thermal treatment at 700°C for 2 hours [205]. TiO₂ is synthesized by milling titanyl sulfate (TiOSO₄ · xH₂SO₄ · yH₂O) with NaCl as the diluent phase in a planetary ball mill under argon atmosphere at 400 rpm. The TiO₂ nanoparticles synthesized have an equiaxed shape with a mean size in the range of 15–50 nm [206]. PbSe nanoparticles are mechanochemically synthesized by high-energy milling of lead and selenium powders in a planetary ball mill in an argon atmosphere:



The reaction is thermodynamically favorable because of the negative value of enthalpy change ($\Delta H_{298}^{\circ} = 100 \text{ kJ mol}^{-1}$). X-ray diffraction analysis confirms that mechanochemical synthesis is complete after 7 minutes of milling and reveals a crystalline nature of such prepared PbSe nanoparticles. The average size of PbSe nanoparticles is 37 nm [207]. However, agglomeration of PbSe particles is an issue. Cobalt ferrite nanoparticles are prepared by the combination of chemical precipitation, mechanical alloying, and subsequent heat treatment. Sodium chloride (NaCl) is added in order to avoid agglomeration. Cobalt ferrite phase forms directly during the mechanical milling of the precipitated hydroxide/oxidhydroxide precursor. The nanoparticles have a fairly uniform structure and a mean particle size of $\sim 10 \text{ nm}$ [208].

High-energy ball milling of a micron-sized titanium and TiC powder mixture is used to prepare TiC/Ti nanocomposites. The system embodies both ductile metallic (from titanium) behaviors and brittle ceramic (from TiC) behaviors during the milling process. Upon increasing the milling time, titanium experiences a successive structural change from hexagonal close-packed (5 hours) to face-centered cubic (10 hours) and finally to an amorphous state (~ 15 hours). The hydrostatic stresses caused by the excess free volume at the grain boundaries are calculated to be 3.96 and 5.59 GPa for titanium in 5 and 10 hour milled powders, respectively, which is responsible for the hexagonal close-packed to face-centered cubic polymorphic change. The amorphization of the titanium constituent is due to the large defect concentration induced by severe plastic deformation during milling. At the same time, TiC particles are fragmented and comminuted. These fragmented TiC nanoparticles are occluded by the ductile titanium constituent and trapped in the titanium particles. For a milling time above 25 hours, particle characteristics and chemical compositions become stable. The competitive action and the final equilibrium between fracturing and cold welding account for

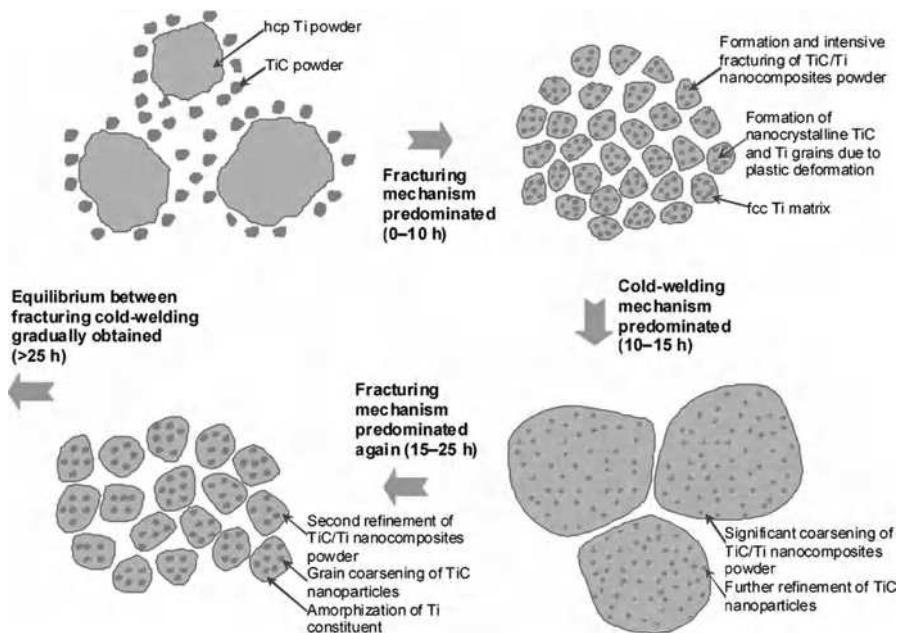


FIGURE 2.46 Schematic diagram of the structural development during milling of TiC/Ti nanocomposite powder [209]. (Reprinted with permission from Gu D, Meiners W, Hagedorn Y-C, Wissenbach K, Poprawe R. Structural evolution and formation mechanisms of TiC/Ti nanocomposites prepared by high-energy mechanical alloying. *J Phys D: Appl Phys* 2010;43:135402-1-1, IOP Publishing, Inc.) (For a color version of this figure, see the color plate section.)

the microstructural evolution. The ball-milled products are composite nanoparticles consisting of a nanocrystalline/amorphous titanium matrix reinforced with uniformly dispersed TiC nanoparticles. An illustration of the milling process is shown in Figure 2.46. Initially, both titanium and TiC break up during the milling process; TiC is encapsulated in the ductile matrix. As the milling continues, TiC continues to fracture, while the titanium particles reweld together under severe plastic deformation. With further milling, titanium fractures again because of work hardening. There can even be some TiC sintering. In the end, a steady state is established between the rate of fracturing and the rate of cold welding of titanium, as well as the rate of fracture and the rate of TiC sintering. The finest sizes for the titanium and TiC constituents are 17.2 nm (after 10 hours of milling) and 13.5 nm (after 20 hours of milling) [209].

Electric discharge-assisted mechanical milling of Co–WC results in a range of products, including micron and submicron fracture products, nanostructural regions of cobalt and WC, and carbon-rich nanorods and nanotubes [210]. Silicon nanoparticles and chemical passivation of the particle surfaces by alkyl/alkenyl

groups covalently linked through strong Si–C bonds are simultaneously achieved by mechanical milling. The ongoing impacts and collisions of the milling media during high-energy ball milling impart a significant amount of mechanical energy to the system, which causes the silicon pieces to fracture, thus reducing particle size and creating a fresh silicon surface. The newly created surface is highly reactive and provides sites for direct reaction between the silicon and the alkene or between the silicon and alkyne through surface radicals and reactive Si = Si bond sites [211].

Milling can also be carried out at cryogenic temperatures with liquid nitrogen flow, which increases fracture events and thus enhances lamellar formation [212]. One major concern for the milling technique is contamination from the wear debris of the milling media and/or the container, which is especially severe in the high-energy ball-milling process.

2.5.2 Reactions between Solids

Solid-state reactions have a very long history in powder synthesis. They are traditionally carried out by mixing two solid reactants and increasing temperature, which allows for reactions to occur. There are four steps in a typical reaction: diffusion, reaction, nucleation, and growth. This approach is convenient, inexpensive, and high yielding. The drawbacks of solid-state reaction are that the process is slow and cannot be easily quantified. The reaction involves only interfacial atoms, and the diffusion may limit the reaction substantially. Ni–B amorphous alloy is prepared by a solid–solid reaction of nickel chloride (NiCl_2) and potassium borohydride (KBH_4) powders at room temperature, and an average diameter of 15–25 nm is obtained. Bismuth (or antimony) metal nanoparticles are prepared by a direct reaction of BiCl_3 (or SbCl_3) and KBH_4 [213]. Oxide nanoparticles (SiO_2 , CeO_2 , SnO_2) are successfully synthesized by solid-state reactions at ambient temperature [214]. Oxides (CuO) and sulfides (CuS , ZnS , CdS , PbS) are prepared at ambient temperatures through rapid (10 seconds to 30 minutes), self-propagating solid-state reactions of hydrated transition metal salts with NaOH and $\text{Na}_2\text{S}\cdot 9\text{H}_2\text{O}$, respectively. Such reactions give spherical products of uniform size and shape (10–80 nm) with over 90% yields [215]. ZnO nanoparticles are synthesized by a one-step solid-state reaction using $\text{ZnSO}_4\cdot 7\text{H}_2\text{O}$ and NaOH as the starting materials. The nanoparticles are hexagonal phase ZnO , mostly in round shapes with a minority of rod shapes and a mean grain size of about 40 nm [216]. By calcining a powder mixture of $\text{Al}(\text{OH})_3$ and MgSO_4 at 800°C and washing with water, single-phase MgAl_2O_4 spinel nanoparticles are prepared. The obtained MgAl_2O_4 spinel nanoparticles have an average particle size of 12 nm, a narrow size distribution, and weak agglomeration. The specific surface area of the MgAl_2O_4 spinel powder is $110\text{ m}^2\text{ g}^{-1}$. The formation of MgAl_2O_4 spinel is attributed to a solid-state reaction between $\gamma\text{-Al}_2\text{O}_3$ and MgSO_4 [217]. MgSO_4 acts as a reactant as well as a diffusion barrier to avoid agglomeration and excessive particle size increase. Figure 2.47 shows MgAl_2O_4 spinel obtained by

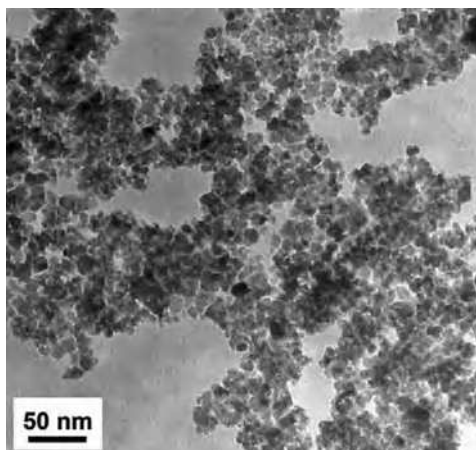


FIGURE 2.47 Transmission electron micrograph of MgAl_2O_4 spinel nanoparticles obtained by calcining $\text{Al}(\text{OH})_3$ and MgSO_4 powder mixture at 800°C for 2 hours [217]. (Reprinted with permission from Su X, Du X, Li S, Li J. Synthesis of MgAl_2O_4 spinel nanoparticles using a mixture of bayerite and magnesium sulfate. *J Nanopart Res* 2010;12:1813–1819, Springer Science + Business Media, Fig. 3.)

calcining the powder mixture of $\text{Al}(\text{OH})_3$ and MgSO_4 at 800°C for 2 hours. The nanoparticles are equiaxed and have a polyhedral morphology. Some nanoparticles are well separated, and some nanoparticles form agglomerates. Uniform β -SiC nanoparticles are synthesized from the reaction of silicon (Si) and carbon black (C). Mixed silicon and carbon black powders are pressed into pellets, and the influence of temperature (1250°C , 1300°C , and 1350°C), heating rate ($20^\circ\text{C min}^{-1}$ and $50^\circ\text{C min}^{-1}$), soaking time (1 hour and 3 hours), and atmosphere (vacuum and argon) are studied. Si–C reaction occurs through gas–solid (SiO–C) and solid–solid (Si–C) reactions that occur simultaneously [218]. Higher temperature, higher heating rate, and longer soaking time in a vacuum system lead to lower free silicon content in the SiC nanoparticles. Temperature has the greatest influence on the silicon content. Because of the simple operation, it is well suited for large-scale production.

To improve the quality of nanoparticles, the fine scale of mixing and size/agglomeration control needed for nanoparticles requires modification of the solid reaction process. This is often achieved by using a gas stream or liquid suspension for mixing and reaction without post processing. The preparation of SiO_2 nanoparticles through solid-fed flame synthesis is investigated experimentally and theoretically. SiO_2 nanoparticles are formed by the nucleation, coagulation, and surface growth of the generated SiO_2 vapors due to solid precursor evaporation [219]. A solid-state synthesis of nanocrystalline silicon is performed by high-temperature reduction in commercial amorphous SiO_2 with

a magnesium powder. The obtained silicon powder contains a crystalline phase with lattice spacings characteristic of diamond cubic structure and an amorphous phase [220]. In order to obtain nano-sized silicon, SiO_2 is first dispersed in an aqueous suspension and then mixed with the magnesium powder before being heated in a nitrogen atmosphere to 520–750°C. AgX (X: Br, Cl) nanoparticles of 3.0–4.5 nm are synthesized by mixing two dry dispersions of AgNO_3 and KX nanoparticles in sodium bis(2-ethylhexyl) sulfosuccinate (AOT)/*n*-heptane solutions. The formation of nano-sized particles takes place after the mixing process and is fast and complete. The AgX nanoparticle formation occurs through redistribution of the AgNO_3 and KX salts among the dry AOT reversed micelles, leading to AOT/*n*-heptane solutions containing AgX nanoparticles at a relatively high concentration. Confinement effects, attributed to surfactant adsorption and the quantum size of the nanoparticles, are detected [221]. Because of the fine-scale mixing and the self-terminating nature of the reaction, this process can achieve much smaller size particles than milling alone. In addition to liquid, an inert salt is used as a dispersant in the solid-state synthesis of CoFe_2O_4 nanoparticles using $\text{CoCl}_2 \cdot 6\text{H}_2\text{O}$, $\text{FeCl}_3 \cdot 6\text{H}_2\text{O}$, and NaOH as precursors [222]. The particle size ranges from 8 to 20 nm. ZnS nanoparticles (a few angstroms) are synthesized by a solid-solid reaction between Na_2S and ZnSO_4 nanoparticles in the confined space of AOT reverse micelles. The reaction is performed by mixing two dry AOT/*n*-heptane solutions, which contain Na_2S and ZnSO_4 nanoparticles, respectively. This synthetic route has the specific advantage of using anhydrous systems with a high nanoparticle concentration. From these systems, interesting AOT/ZnS composites are prepared by simple evaporation of the organic solvent [223].

2.6 SUMMARY

Nanoparticle synthesis has advanced at an astounding pace in the past few decades. Many new nanoparticles have been synthesized. Unique nanoparticle structures and compositions have been reported. In this chapter, gas-phase synthesis is discussed based on gas–gas reaction, gas–liquid reaction, and gas–solid reaction. Gas-phase synthesis generally occurs at high temperatures. Since nanoparticles come in contact during growth, agglomeration can be a serious issue. The capabilities and potential issues for gas-phase synthesis are summarized in Table 2.1. Liquid nanoparticle synthesis is the most preferred and widely used approach for nanoparticle size and shape control. This mainly stems from the much improved ability to control the nucleation and particle growth rates by mediating the atomic diffusion during the synthesis, such as by controlling reactant species and concentration, temperature, and pressure. Liquid nanoparticle synthesis also has the intrinsic advantage of separating the synthesized nanoparticles and avoiding agglomeration. It generally includes fundamental methods, confinement methods, composite nanoparticle synthesis, and field-assisted nanoparticle synthesis. The capabilities and potential issues for gas-phase synthesis are

summarized in Table 2.2. Solid-state synthesis has similar issues as gas-phase synthesis and includes milling and solid-state reaction. The process is simple, low cost, and can be easily scaled up. However, it is not widely practiced because of the difficulty of nanoparticle size and separation control. The capabilities and potential issues for solid-state synthesis are summarized in Table 2.3.

For future nanoparticle synthesis advancement, the challenges lie in large-quantity production. Many nanoparticles have been synthesized in the milligram to gram scale; it remains an extremely challenging task to produce a large quantity of nanoparticles with the same size, shape, crystallinity, and purity. Also, batch-to-batch consistency needs to be adequately addressed for large-scale and sustainable advancement of nanoparticle synthesis. To improve the fundamental understanding and thus obtain better control of the process, predictive models are needed for optimization of nanoparticle synthesis conditions, surface structure and activity, and electronic and transport properties. A more comprehensive understanding of nanoparticle synthesis will help to identify the desired synthesis conditions for a specific set of properties. Furthermore, it will enable better predictive capabilities for nanoparticle applications, such as catalysis, self-assembly, and bulk processing.

TABLE 2.1 Capabilities and Potential Issues for Gas-Phase Synthesis

| Process | Capabilities | Potential issues | References |
|------------|---|--|------------|
| Gas–gas | Single-step production, inorganic and easy-to-obtain precursors, high-purity nanoparticles, potential for large-scale production with a high yield, good thermal stability nanoparticles. | Nucleation and growth stages must be separated. Poor particle size distribution control, aggregation/coalescence of particles. | 9–49 |
| Gas–liquid | Flexibility in producing nanoparticles of various compositions and morphologies, highly pure nanoparticles, scalable techniques, simpler and effective way to generate well-defined nanoaerosols. | Agglomeration is almost unavoidable, broad distribution of particle sizes. | 50–52 |
| Gas–solid | Can make solid as well as hollow particles. | Limited work in the area, reaction cannot be easily controlled to maintain nanoparticle size, agglomeration. | 53 |

TABLE 2.2 Capabilities and Potential Issues for Liquid-Phase Synthesis

| | Process | Capabilities | Potential issues | References |
|--------------------|----------------------|--|---|------------|
| Fundamental method | Precipitation | A vast variety of nanoparticles can be made. For aqueous systems, simple, inexpensive, and can be used to synthesize single or multicomponent nanoparticles. For nonaqueous systems, excellent crystallinity, monodispersity, and high-purity nanoparticles. | Different rates of precipitation for different components can result in deviation from homogeneous precipitation. Nanoparticles are usually amorphous. Hydroxides or carbonates can be precipitated from the solution and have to be removed by post synthesis thermal processes. For aqueous systems, nucleation and growth need to be carefully controlled. For nonaqueous systems, use of expensive and sometimes toxic organics, sensitivity to moisture, and complicated experimental setups, barriers for large quantity synthesis. | 54–68 |
| | Metal salt reduction | Can produce nanoparticles in a high rate. Pure, well-controlled nanoparticle formation with desired crystallinity. | Not all metals can be synthesized with the metal salt reduction technique. Agglomeration can also occur because of the high reaction rate. Reaction process can be complicated and the reaction by-products can be toxic. | 62, 69–77 |
| | Hydrolysis | Can synthesize a wide range of chemical compositions. For sol–gel synthesis, high-purity and controllable size nanoparticles. The nanoparticles can be single or complex oxides. | Experimental conditions need to be carefully controlled in order to obtain desired particle size. The morphology of final particles is hard to predict. Nanoparticle growth and agglomeration during calcination. | 78–94 |

(Continued)

TABLE 2.2 (Continued)

| | Process | Capabilities | Potential issues | References |
|--------------------|------------------------|--|--|------------|
| | Solvothermal synthesis | Precise control over the particle size, shape, and distribution while facilitating the crystallinity development of nanoparticles, no calcination required. Hydrothermal synthesis also enables the elimination of mineralizers that can induce impurities into nanoparticles. Highly pure phase and narrow particle size distribution can be obtained. | Hydrothermal synthesis requires the composition be precisely determined and controlled in advance; the materials need to be as fine and pure as possible and form a homogeneous system. For nonaqueous solvothermal synthesis, toxic species are involved, and starting materials are expensive. | 95–106 |
| | Cryochemical synthesis | Ideal technique to synthesize species that have only a fleeting existence because of their high reactivity and instability at higher temperatures. | More often used as an intermediate state of nanoparticle synthesis. It is very rare to directly obtain nano-sized crystalline particles by this method alone. | 107–113 |
| Confinement method | Spray pyrolysis | Avoid phase separation and improve homogeneity at the molecular level. Multicomponents are homogeneously mixed at the atomic level from the beginning, and the high temperature facilitates the formation of crystalline nanoparticles. Spray pyrolysis also has the advantages of low cost, simplicity, and being effective in controlling the size and shape of the formed particles. Well-controlled morphologies and compositions are produced; starting materials used are common, inexpensive, and compatible with nonaqueous media. | A wide particle size distribution, limited to certain materials due to the thermal stability issue at high pyrolysis temperatures; no pure metal nanoparticles are synthesized using this technique. Diffusion bonding induces nanoparticle agglomeration and undesired phase transformation. | 114–127 |

| | | | | |
|----------------------------------|-----------------------|---|--|---------|
| Composite nanoparticle synthesis | Solventless synthesis | Solventless synthesis offers narrow particle size distribution and well-controlled particle shapes. | Toxic chemicals and high synthesis temperatures are involved. | 128–133 |
| | Core/shell structure | Controlled distribution of the involved phases on a nanometer scale. Core particles and the shells may have different properties, and allows for a combination of properties in one particle. | Small quantity, compatibility between the core and shell species necessary. | 134–144 |
| | Electroless synthesis | Produce uniform metal layers on nanoparticle surfaces. | Nucleation sites should be controlled for desired nanoparticle morphology and uniform coating layer. Composition and structure of the coating should be carefully controlled. Oxidation of the metallic coating layer is possible. | 145–149 |
| | Templating | Nanoparticle size, shape, distribution, and physical and chemical properties can be fine tuned. Strategy for template-based nanoparticle synthesis is wide ranging. | Avoid defect formation and suppress particle growth. Sufficient chemical and interfacial complementarity between the template and the nanoparticles is often necessary. | 150–156 |
| | Bio-based synthesis | Nanoparticle morphology may be tuned based on the ratio of nanoparticle forming species to the bio-templates. | Mostly composites. Self-standing nanoparticle synthesis through this approach has not been pursued. | 157–161 |

(Continued)

TABLE 2.2 (Continued)

| | Process | Capabilities | Potential issues | References |
|---------------------------------------|-----------------------------------|--|---|-------------|
| Field-assisted nanoparticle synthesis | Micelle synthesis | No special apparatus or extreme temperature/pressure conditions. Nanoparticle growth process is self-limiting. Well-accepted method for nanoparticle size and morphology control. Uses standard, commercially available, and relatively inexpensive chemicals. The synthesis can reproducibly yield monodispersed nanoparticles. | Micelle size has a fundamental impact on the particle size. | 162–169 |
| | Laser-assisted synthesis | Both simple and complex compositions can be obtained. Suitable for metals, semiconductors, and insulators. Fast processing time. Relatively low cost of the equipment and high efficiency. | Morphology control, limited quantity. | 170–172 |
| | Plasma-assisted synthesis | Low cost, ease to use, and ability to produce higher purity nanoparticles. | Agglomeration. | 173, 174 |
| | Microwave-assisted synthesis | Rapid and uniform heating of the reaction mixture. Small particle size, narrow size distribution, and very short reaction time. High efficiency with respect to energy consumption | Temperature measurement and control can be difficult. | 175–180 |
| | Sonication-assisted synthesis | Rapid heating, ability to disperse reactants easily and evenly. Chemical homogeneity and reactivity through mixing at the atomic level. | Amorphous particles. Need special effort to crystallize particles. | 73, 181–184 |
| | Radiation-assisted synthesis | Room temperature synthesis, monodispersed and ultra-small particle sizes. Various thermally unstable substances may be used. | Radiation may pose environmental and experimental condition concerns. | 185–187 |
| | Electric field-assisted synthesis | Well-controlled and dispersed nanoparticles. | Special materials, low quantity. | 188–193 |

TABLE 2.3 Capabilities and Potential Issues for Solid-State Synthesis

| Process | Capabilities | Potential issues | References |
|-------------------------|---|---|------------|
| Milling | Amorphous, crystalline, composite nanoparticles can be synthesized. Simplicity. Inexpensive equipment. Applicability to essentially all classes of materials. | Particle oxidation, agglomeration, and rewelding. Contamination from the wear debris of the milling media and/or the container. | 194–212 |
| Reaction between solids | Simple operation. Suited for large-scale production. | Inhomogeneous mixing of reactants. Inefficient reaction process. | 213–223 |

QUESTIONS

1. Compare synthesis of metallic nanoparticles, semiconductor nanoparticles, and oxide nanoparticles, what are the differences in precursors, solvents, temperatures, nucleation process, growth process, polymeric stabilizers, and the resultant particle size distribution and stability? Please give examples to support your discussion. You are encouraged to make a table for comparison.
2. Nanoparticle synthesis can be divided into two stages: nucleation and growth.
 - a. If it is required that uniform size and shape particles be obtained, nucleation should occur in what manner?
 - b. What can be done to achieve such nucleation (give two approaches)?
 - c. Particle growth should occur in what manner?
 - d. What can be done to achieve such growth (give two approaches)?
3. For silver nanoparticle synthesis, if your friend is getting larger than desired average particle size and wide particle size distribution. Please help him/her out by providing suggestions to minimize these issues.
4. How should you control the reactant concentrations during nucleation and growth for narrow particle size distribution? How should you control the viscosity of the liquid system? What else can you do in either nucleation or particle growth process?
5. During nanoparticle growth process, what particle growth mode produces the largest particle size distribution? Surface-controlled mononuclear growth, surface-controlled polynuclear growth, or diffusion-controlled growth? Mathematically explain why?
6. Explain the key differences between physical vapor synthesis and chemical vapor synthesis.
7. What is the mechanism of laser ablation in nanoparticle synthesis?
8. What are the advantages and disadvantages of vapor-phase nanoparticle synthesis?

9. In liquid nanoparticle synthesis, temperature and water contents are two main factors that can be adjusted. Explain how different fundamental methods of liquid nanoparticle synthesis fall into this category?
10. Nanoparticle synthesis conditions can be kinetically controlled in order to tailor nanoparticle sizes. They are exemplified by spray pyrolysis and solventless synthesis. Explain how particle size control is realized in each of these techniques?
11. How can one synthesize core-shell nanoparticles? What are the advantages of such nanoparticle structures?
12. Why can synthesis inside micelles and microemulsion produce small size (nano size) particles?
13. Many field-assisted synthesis techniques are devised in recent years. Based on the special field used, provide examples that rely on additional heat source to facilitate nanoparticle formation and growth and examples that rely on physical separation of species. Explain how each process works in detail.
14. Choose three of your favorite liquid nanoparticle synthesis techniques described in this chapter, explain why you choose them?
15. Solid-state nanoparticle synthesis is not an actively pursued field, why?

REFERENCES

1. Gutzow I, Schmelzer J. *The Vitreous State: Thermodynamics, Structure, Rheology, and Crystallization*. Berlin: Springer; 1995.
2. Burda C, Chen XB, Narayanan R. Chemistry and properties of nanocrystals of different shapes. *Chem Rev* 2005;105:1025–1102.
3. Rahaman MN. *Ceramic Processing*. New York, NY: Taylor & Francis; 2007.
4. Cao G. *Nanostructures & Nanomaterials: Synthesis, Properties & Application*. London: Imperial College Press; 2004.
5. Lifshitz IM, Slyozov VV. The kinetics of precipitation from supersaturated solid solutions. *J Phys Chem Solids* 1961;19:35–50.
6. Wagner C. Theorie der Alterung von Niederschlägen durch Umlösen. *Z Elektrochem* 1961;65:581–594.
7. Steigerwald ML, Alivisatos AP, Gibson JM, Harris TD, Kortan R, Muller AJ, Thayer AM, Duncan TM, Douglass DC, Brus LE. Surface derivatization and isolation of semiconductor cluster molecules. *J Am Chem Soc* 1988;110:3046–3050.
8. Vollath D. *Nanomaterials, An Introduction to Synthesis, Properties and Applications*. Weinheim: Wiley-VCH Verlag GmbH & Co. KGaA; 2008. p 72.
9. Simchi A, Ahmadi R, Seyed Reihani SM, Mahdavi A. Kinetics and mechanisms of nanoparticle formation and growth in vapor phase condensation process. *Mater Des* 2007;28:850–856.
10. Raffi M, Rumaiz AK, Hasan MM, Shah SI. Studies of the growth parameters for silver nanoparticle synthesis by inert gas condensation. *J Mater Res* 2007;22:3378–3384.
11. Birringer R, Gleiter H, Klein HP, Marquardt P. Nanocrystalline materials an approach to a novel solid structure with gas-like disorder? *Phys Lett* 1984;102A:365–369.

12. Wegner K, Walker B, Tsantilis S, Pratsinis SE. Design of metal nanoparticle synthesis by vapor flow condensation. *Chem Eng Sci* 2002;57:1753–1762.
13. Perez-Tijerina E, Gracia Pinilla M, Mejia-Rosales S, Ortiz-Mendez U, Torres A, Jose-Yacamán M. Highly size-controlled synthesis of Au/Pd nanoparticles by inert-gas condensation. *Faraday Discuss*, 2008;138:353–362.
14. Lee K-M, Lee D-J, Ahn H. XRD and TEM studies on tin oxide (II) nanoparticles prepared by inert gas condensation. *Mater Lett* 2004;58:3122–3125.
15. Turker M. Effect of production parameters on the structure and morphology of Ag nanopowders produced by inert gas condensation. *Mater Sci Eng A* 2004;367:74–81.
16. Ward MB, Brydson R, Cochrane RF. Mn nanoparticles produced by inert gas condensation. *J Phys* 2006;26:296–299.
17. Skårman B, Nakayama T, Grandjean D, Benfield RE, Olsson E, Niihara K, Wallenberg LR. Morphology and structure of CuOx/CeO₂ nanocomposite catalysts produced by inert gas condensation: an HREM, EFTEM, XPS, and high-energy diffraction study. *Chem Mater* 2002;14:3686–3699.
18. Ceylan A, Rumaiz AK, Shah SI. Inert gas condensation of evaporated Ni and laser ablated CoO. *J Appl Phys* 2007;101:094302 6pp.
19. Lümmer N, Kraska T. Molecular dynamics investigations of the coalescence of iron clusters embedded in an inert-gas heat bath. *Phys Rev B* 2005;71:205403 10pp.
20. Yamamuro S, Sumiyama K, Suzuki K. Monodispersed Cr cluster formation by plasma-gas-condensation. *J Appl Phys* 1999;85:483–489.
21. Ayyub P, Chandra R, Taneja P, Sharma AK, Pinto R. Synthesis of nanocrystalline material by sputtering and laser ablation at low temperatures. *Appl Phys A* 2001;73:67–73.
22. Lei JP, Huang H, Dong XL, Sun JP, Lua B, Lei MK, Wang Q, Dong C, Cao GZ. Formation and hydrogen storage properties of in situ prepared Mg–Cu alloy nanoparticles by arc discharge. *Int J Hydrogen Energy* 2009;34:8127–8134.
23. Lei J-P, Dong X-L, Zhao F-G, Huang H, Zhang X-F, Lu B, Lei MK. Synthesis and thermodynamic evaluation of intermetallic Mg–Ni/Mg–Cu nanoscale powders. *J Mater Res* 2009;24:2503–2510.
24. Biener J, Farfan-Arribas E, Biener M, Friend CM, Madix RJ. Synthesis of TiO₂ nanoparticles on the Au(111) surface. *J Chem Phys* 2005;123:094705 6pp.
25. Zhang XF, Dong XL, Huang H, Lv B, Zhu XG, Lei JP, Ma S, Liu W, Zhang ZD. Synthesis, structure and magnetic properties of SiO₂-coated Fe nanocapsules. *Mater Sci Eng A* 2007;454–455:211–215.
26. Dong XL, Choi CJ, Kim BK. Chemical synthesis of Co nanoparticles by chemical vapor condensation. *Scr Mater* 2002;47:857–861.
27. Choi CJ, Tolochko O, Kim BK. Preparation of iron nanoparticles by chemical vapor condensation. *Mater Lett* 2002;56:289–294.
28. Polarz S, Roy A, Merz M, Halm S, Schröder D, Schneider L, Bacher G, Krüger FE, Driess M. Chemical vapor synthesis of size-selected zinc oxide nanoparticles. *Small* 2005;1:540–552.
29. Ali M, Friedenberger N, Spasova M, Winterer M. A novel approach for chemical vapor synthesis of ZnO nanocrystals: optimization of yield, crystallinity. *Chem Vap Deposition* 2009;5:192–198.
30. Lin H-T, Huang J-L, Lo W-T, Wei W-C. Investigation on carbonizing behaviors of nanometer-sized Cr₂O₃ particles dispersed on alumina particles by metalorganic chemical vapor deposition in fluidized bed. *J Mater Res* 2005;20:2154.

31. Jin W, Lee I-K, Kompch A, Dörfler U, Winterer M. Chemical vapor synthesis and characterization of chromium doped zinc oxide nanoparticles. *J Eur Ceram Soc* 2007;27:4333–4337.
32. Hartner S, Ali M, Schulz C, Winterer M, Wiggers H. Electrical properties of aluminum-doped zinc oxide (AZO) nanoparticles synthesized by chemical vapor synthesis. *Nanotechnology* 2009;20:445701 8pp.
33. Srdica VV, Winterer M, Miede G, Hahn H. Different zirconia-alumina nanopowders by modifications of chemical vapor synthesis. *Nanostruct Mater* 1999;12:95–100.
34. Srdica VV, Winterer M. Aluminum-doped zirconia nanopowders: chemical vapor synthesis and structural analysis by Rietveld refinement of X-ray diffraction data. *Chem Mater* 2003;15:2668–2674.
35. Hojo J, Oyama N, Nabekura W, Kishi K, Umebayashi S. Multiphase composites of silicon carbide obtained from composite particles. *Key Eng Mater* 1999;2:465–468.
36. Tsugeki K, Kato T, Koyanagi Y, Kusakabe K, Morooka K. Electroconductivity of sintered bodies of α -Al₂O₃-TiN composite prepared by CVD reaction in a fluidized bed. *J Mater Sci* 1993;28:3168–3172.
37. Choi JW, Sohn HY, Choi YJ, Fang ZZ. Chemical vapor synthesis and characterization of aluminum nanopowder. *J Power Sources* 2010;195:1463–1471.
38. Ryu T, Sohn HY, Hwang KS, Fang ZZ. Chemical vapor synthesis and characterization of nanosized WC-Co composite powder and post-treatment. *Ind Eng Chem Res* 2008;47:9384–9388.
39. Pee J-H, Park J-C, Kim Y, Hwang K-T, Kim S. Synthesis of porous nano-sized AlN by chemical vapor synthesis. *Phys Scr* 2010;T139:014049 5pp.
40. Vasilyeva ES, Tolochko OV, Kim BK, Lee DW, Kim DS. Synthesis of tungsten disulphide nanoparticles by the chemical vapor condensation method. *Microelectron J* 2009;40:687–691.
41. Ganeev RA, Elouga Bom LB, Ozaki T. Deposition of nanoparticles during laser ablation of nanoparticle-containing targets. *Appl Phys B* 2009;96:491–498.
42. Jang D, Kim D. Synthesis of nanoparticles by pulsed laser ablation of consolidated metal microparticles. *Appl Phys A* 2004;79:1985–1988.
43. Wang Z, Zeng X, Ji M, Liu Y. The effect of target size on α -Fe nanoparticle preparation by pulsed laser ablation. *Appl Phys A* 2009;97:683–688.
44. Wang Z, Liu Y, Zeng X. One-step synthesis of γ -Fe₂O₃ nanoparticles by laser ablation. *Powder Technol* 2006;161:65–68.
45. Henley SJ, Carey JD, Silva SRP. Metal nanoparticle production by pulsed laser nanostructuring of thin metal films. *Appl Surf Sci* 2007;253:8080–8085.
46. Khang Y, Lee J. Synthesis of Si nanoparticles with narrow size distribution by pulsed laser ablation. *J Nanopart Res* 2010;12:1349–1354.
47. Gallardo I, Hoffmann K, Keto JW. CdSe & ZnS core/shell nanoparticles generated by laser ablation of microparticles. *Appl Phys A* 2009;94:65–72.
48. Noel S, Hermann J, Itina T. Investigation of nanoparticle generation during femtosecond laser ablation of metals. *Appl Surf Sci* 2007;253:6310–6315.
49. Perriere J, Boulmer-Leborgne C, Benzerger R, Tricot S. Nanoparticle formation by femtosecond laser ablation. *J Phys D* 2007;40:7069–7076.
50. Limaye AU, Helble JJ. Morphological control of zirconia nanoparticles through combustion aerosol synthesis. *J Am Ceram Soc* 2002;85:1127–1132.
51. Terashi Y, Purwanto A, Wang W-N, Iskandar F, Okuyama K. Role of urea addition in the preparation of tetragonal BaTiO₃ nanoparticles using flame-assisted spray pyrolysis. *J Eur Ceram Soc* 2008;28:2573–2580.

52. Lee D, Choi M. Coalescence enhanced synthesis of nanoparticles to control size, morphology and crystalline phase at high concentrations. *J Aerosol Sci* 2002;33: 1–16.
53. Liu Z, Ci L, Jin-Phillipp NY, Rühle M. Vapor-solid reaction for silicon carbide hollow spherical nanocrystals. *J Phys Chem C* 2007;111:12517–12521.
54. Yang HM, Zhang XC, Yang WG, Huang CH, Qiu GZ. Chemical synthesis of nanocrystalline ZrO_2 - SnO_2 composite powders. *Rare Met* 2004;23:182–184.
55. Galal A, Darwish SA, Atta NF, Ali SM, Abd El Fatah AA. Synthesis, structure and catalytic activity of nano-structured Sr–Ru–O type perovskite for hydrogen production. *Appl Catal A* 2010;378:151–159.
56. Veverka M, Veverka P, Jirak Z, Kaman O, Knizek K, Marysko M, Pollert E, Zaveta K. Synthesis and magnetic properties of $Co_{1-x}Zn_xFe_2O_{4+y}$ nanoparticles as materials for magnetic fluid hyperthermia. *J Magn Magn Mater* 2010;322:2386–2389.
57. Deshpande AS, Pinna N, Beato P, Antonietti M, Niederberger M. Synthesis and characterization of stable and crystalline $Ce_{1-x}Zr_xO_2$ nanoparticle sols. *Chem Mater* 2004;16:2599–2604.
58. Morais PC, Garg VK, Oliveira AC, Silva LP, Azevedo RB, Silva AML, Lima ECD. Synthesis and characterization of size-controlled cobalt-ferrite-based ionic ferrofluids. *J Magn Magn Mater* 2001;225:37–40.
59. Zi Z, Sun Y, Zhu X, Yang Z, Dai J, Song W. Synthesis and magnetic properties of $CoFe_2O_4$ ferrite nanoparticles. *J Magn Magn Mater* 2009;321:1251–1255.
60. Kim CW, Kim YH, Cha HG, Lee DK, Kang YS. Synthesis and characterization of crystalline FeCo nanoparticles. *J Nanosci Nanotechnol* 2006;6:3417–3421.
61. Hong Z, Liu A, Chen L, Chen X, Jing X. Preparation of bioactive glass ceramic nanoparticles by combination of sol–gel and coprecipitation method. *J Non-Cryst Solids* 2009;355:368–372.
62. Masala O, Seshadri R. Synthesis routes for large volumes of nanoparticles. *Annu Rev Mater Res* 2004;34:41–81.
63. Sashchiuk A, Amirav L, Bashouti M, Krueger M, Sivan U, Lifshitz E. Synthesis and structural, optical, and electrical characterization. *Nano Lett* 2004;4:159–165.
64. Collins IR, Taylor SE. Nonaqueous thermal-decomposition route to colloidal inorganic oxides. *J Mater Chem* 1992;2:1277–1281.
65. Deb P, Biswas T, Sen D. Characteristics of Fe_2O_3 nanoparticles prepared by heat treatment of a nonaqueous powder precipitate. *J Nanopart Res* 2002;4:91–97.
66. Davar F, Salavati-Niasari M, Mir N, Saberyan K, Monemzadeh M, Ahmadi E. Thermal decomposition route for synthesis of Mn_3O_4 nanoparticles in presence of a novel precursor. *Polyhedron* 2010;29:1747–1753.
67. Salavati-Niasari M, Mir N, Davar F. Synthesis, characterization and optical properties of tin oxide nanoclusters prepared from a novel precursor via thermal decomposition route. *Inorg Chim Acta* 2010;363:1719–1726.
68. Salavati-Niasari M, Davar F, Mazaheri M. Preparation of ZnO nanoparticles from [bis(acetylacetonato)zinc(II)]–oleylamine complex by thermal decomposition. *Mater Lett* 2008;62:1890–1892.
69. Esumi K, Suzuki A, Yamahira A, Torigoe K. Role of poly(amidoamine) dendrimers for preparing nanoparticles of gold, platinum, and silver. *Langmuir* 2000;16:2604–2608.
70. Choo HP, Liew KY, Liu HF. Factors affecting the size of polymer stabilized Pd nanoparticles. *J Mater Chem* 2002;12:934–937.
71. Mallin MP, Murphy CJ. Solution-phase synthesis of sub-10 nm Au–Ag alloy nanoparticles. *Nano Lett* 2002;2:1235–1237.

72. Cushing BL, Kolesnichenko VL, O'Connor CJ. Recent advances in the liquid-phase syntheses of inorganic nanoparticles. *Chem Rev* 2004;104:3893–3946.
73. Smith TW, Wychick D. Colloidal iron dispersions prepared via the polymer-catalyzed decomposition of iron pentacarbonyl. *J Phys Chem* 1980;84:1621–1629.
74. Kato Y, Sugimoto S, Shinohara K, Tezuka N, Kagotani T, Inomata K. Magnetic properties and microwave absorption properties of polymer-protected cobalt nanoparticles. *Mater Trans* 2002;43:406–409.
75. Sun SH, Murray CB, Weller D, Folks L, Moser A. Monodisperse FePt nanoparticles and ferromagnetic FePt nanocrystal superlattices. *Science* 2000;287:1989–1992.
76. Leonard BM, Zhou Q, Wu D, DiSalvo FJ. Facile synthesis of PtNi intermetallic nanoparticles: influence of reducing agent and precursors on electrocatalytic activity. *Chem Mater* 2011;23:1136–1146.
77. Xiao TD, Torban S, Strutt PR, Kear BH. Synthesis of nanostructured Ni/Cr and Ni-Cr₃C₂ powders by an organic solution reaction method. *Nanostruct Mater* 1996;7:857–871.
78. Rahaman MN. *Ceramic Processing and Sintering*. New York, NY: Marcel Dekker, Inc.; 2003, pp. 88–92.
79. Hu MZC, Harris MT, Byers CH. Nucleation and growth for synthesis of nanometric zirconia particles by forced hydrolysis. *J Colloid Interface Sci* 1998;198:87–99.
80. Khrenov V, Klapper M, Koch M, Mullen K. Surface functionalized ZnO particles designed for the use in transparent nanocomposites. *Macromol Chem Phys* 2005;206:95–101.
81. Sakohara S, Honda S, Yanai Y, Anderson MA. Preparation and optical properties of nano-sized ZnO colloidal particles using NH₃ gas as volatile catalyst. *J Chem Eng Jpn* 2001;34:15–21.
82. Gulley-Stahl HJ, Schmidt WL, Bullen HA. Characterization and reactivity of chromia nanoparticles prepared by urea forced hydrolysis. *J Mater Sci* 2008;43:7066–7072.
83. Iida H, Takayanagi K, Nakanishi T, Osaka T. Synthesis of Fe₃O₄ nanoparticles with various sizes and magnetic properties by controlled hydrolysis. *J Colloid Interface Sci* 2007;314:274–280.
84. O'Brien S, Brus L, Murray CB. Synthesis of monodisperse nanoparticles of barium titanate: toward a generalized strategy of oxide nanoparticle synthesis. *J Am Chem Soc* 2001;123:12085–12086.
85. Lu W, Schmidt H. Synthesis of nanosized BaSnO₃ powders from metal isopropoxides. *J Sol-Gel Sci Technol* 2007;42:55–64.
86. Garnweitner G, Niederberger M. Nonaqueous and surfactant-free synthesis routes to metal oxide nanoparticles. *J Am Chem Soc* 2006;89:1801–1808.
87. Ismail AA. Synthesis and characterization of Y₂O₃/Fe₂O₃/TiO₂ nanoparticles by sol-gel method. *Appl Catal B* 2005;85:115–121.
88. Zhang YF, Zhang JX, Lu QM, Zhang QY. Synthesis and characterization of Ca₃Co₄O₉ nanoparticles by citrate sol-gel method. *Mater Lett* 2006;60:2443–2446.
89. Xiu ZL, Lu MK, Liu SW, Zhou GJ, Su BY, Zhang HP. Barium hydroxyapatite nanoparticles synthesized by citric acid sol-gel combustion method. *Mater Res Bull* 2005;40:1617–1622.
90. Yuh J, Nino JC, Sigmund WA. Synthesis of barium titanate (BaTiO₃) nanofibers via electrospinning. *Mater Lett* 2005;59:3645–3647.
91. Hasegawa I, Nakamura T, Kajiwara M. Synthesis of continuous silicon carbide-titanium carbide hybrid fibers through sol-gel processing. *Mater Res Bull* 1996;31:869–875.

92. Ming M, Chen Y, Katz A. Synthesis and characterization of gold-silica nanoparticles incorporating a mercaptosilane core-shell interface. *Langmuir* 2002;18:8566–8572.
93. Lu Y, Yin YD, Li ZY, Xia YA. Synthesis and self-assembly of Au@SiO₂ core-shell colloids. *Nano Lett* 2002;2:785–788.
94. Ruys AJ, Mai Y-W. The nanoparticle-coating process: a potential sol-gel route to homogeneous nanocomposites. *Mater Sci Eng A* 1999;265:202–207.
95. Aruna ST, Tirosh S, Zaban A. Nanosize rutile titania particle synthesis via a hydrothermal method without mineralizers. *J Mater Chem* 2000;10:2388–2391.
96. Yang J, Mei S, Ferreira JMF. Hydrothermal synthesis of nanosized titania powders: influence of tetraalkyl ammonium hydroxides on particle characteristics. *J Am Ceram Soc* 2001;84:1696–1702.
97. Adschiri T, Kanazawa K, Arai K. Rapid and continuous hydrothermal crystallization of metal-oxide particles in supercritical water. *J Am Ceram Soc* 1992;75:1019–1022.
98. Lester E, Blood P, Denyer J, Giddings D, Azzopardi B, Poliakov M. Reaction engineering: the supercritical water hydrothermal synthesis of nano-particles. *J Supercrit Fluids* 2006;37:209–214.
99. Chu XF, Jiang DL, Zheng CM. The gas-sensing properties of thick film sensors based on nano-ZnFe₂O₄ prepared by hydrothermal method. *Mater Sci Eng B* 2006;129:150–153.
100. Basavalingu B, Byrappa K, Yoshimura M, Madhusudan P, Dayananda AS. Hydrothermal synthesis and characterization of micro to nano sized carbon particles. *J Mater Sci* 2006;41:1465–1469.
101. Wang BG, Callahan MJ. Ammonothermal synthesis of III-nitride crystals. *Cryst Growth Des* 2006;6:1227–1246.
102. Su HL, Xie Y, Li B, Liu XM, Qian YT. A simple, convenient, mild solvothermal route to nanocrystalline Cu₃P and Ni₂P. *Solid State Ionics* 1999;122:157–160.
103. Dickerson B. Organometallic synthesis kinetics of CdSe quantum dots, Ph.D [Dissertation]. Blacksburg (VA): Virginia Polytechnic Institute and State University; 2005;24–57.
104. Calero-DdelC VL, Gonzalez AM, Rinaldi C. A statistical analysis to control the growth of cobalt ferrite nanoparticles synthesized by the thermodecomposition method. *J Manuf Sci Eng* 2010;132:030914 7pp.
105. Wang D-S, Xie T, Peng Q, Zhang S-Y, Chen J, Li Y-D. Direct thermal decomposition of metal nitrates in octadecylamine to metal oxide nanocrystals. *Chem Eur J* 2008;14:2507–2513.
106. Torimoto T, Tsuda T, Okazaki K, Kuwabata S. New frontiers in materials science opened by ionic liquids. *Adv Mater* 2010;22:1196–1221.
107. Tretyakov YD, Shlyakhtin OA. Recent progress in cryochemical synthesis of oxide materials. *J Mater Chem* 1999;9:19–24.
108. Sergeev BM, Kasaikin VA, Litmanovich EA, Sergeev GB, Prusov AN. Cryochemical synthesis and properties of silver nanoparticle dispersions stabilised by poly(2-dimethylaminoethyl methacrylate). *Mendeleev Commun* 1999;4:130–132.
109. Sergeev BM, Sergeev GB, Kasaikin VA, Litmanovich EA, Prusov AN. Low-temperature synthesis and properties of silver nanoparticles stabilized. *Mol Cryst Liq Cryst* 2001;356:121–129.
110. Sergeev BM, Sergeev GB, Prusov AN. Cryochemical synthesis of bimetallic nanoparticles in the silver-lead methyl acrylate system. *Mendeleev Commun* 1998;1:1–2.

111. Marinkovic ZV, Miloshević O, Nikoli MV, Kakazey MG, Karpec MV, Tomila TV, Ristić MM. Evolution of the microstructure of disperse ZnO powders obtained by the freeze-drying method. *Mater Sci Eng A* 2004;375–377:620–624.
112. Zimina GV, Novoselov AV, Smirnova IN, Spiridonov FM, Pushkina GYa, Komissarova LN. Synthesis and study of yttrium aluminum garnets doped with neodymium and ytterbium. *Russian J Inorg Chem* 2010;55:1833–1836.
113. Panova TI, Glushkova VB, Lapshin AE. Synthesis of nanocrystalline solid solutions based on zirconia and hafnia. *Glass Phys Chem* 2008;34:206–212.
114. Nagasawa H, Maruyama M, Komatsu T, Isoda S, Kobayashi T. Physical characteristics of stabilized silver nanoparticles formed using a new thermal-decomposition method. *Phys Status Solidi A* 2002;191:67–76.
115. Chin S, Park E, Kim M, Jurng J. Photocatalytic degradation of methylene blue with TiO₂ nanoparticles prepared by a thermal decomposition process. *Powder Technol* 2010;201:171–176.
116. Morales MP, Gonzalez-Carreno T, Ocana M, Alonso-Sanudo M, Serna CJ. Magnetic iron oxide/mullite nanocomposite stable up to 1400°C. *J Solid State Chem* 2000;155:458–462.
117. Kim HS, Kim CS, Kim SG. Preparation of nickel oxide- and nickel-silica nanocomposites by spray pyrolysis. *J Non-Cryst Solids* 2006;352:2204–2212.
118. Soraru GD, Ravagni A, Dal Maschio R, Carturan G, Babonneau E. Polymer-derived Si₃N₄-ZrO₂ nanocomposite powders. *J Mater Res* 1992;7:1266–1270.
119. Xia B, Lenggoro IW, Okuyama K. Novel route to nanoparticle synthesis by salt-assisted aerosol decomposition. *Adv Mater* 2001;13:1579–1582.
120. Battaglia D, Peng XG. Formation of high quality InP and InAs nanocrystals in a noncoordinating solvent. *Nano Lett* 2002;2:1027–1030.
121. Jana NR, Chen YF, Peng XG. Size- and shape-controlled magnetic (Cr, Mn, Fe, Co, Ni) oxide nanocrystals via a simple and general approach. *Chem Mater* 2004;16:3931–3935.
122. Seyferth D, Wiseman GH. High-yield synthesis of Si₃N₄/SiC ceramic materials by pyrolysis of a novel polyorganosilazane. *Commun Am Ceram Soc* 1984;67:C-132–C-133.
123. Gonsalves KE, Strutt PR, Xiao TD. Synthesis of ceramic nanoparticles by the ultrasonic injection of an organosilazane precursor. *Adv Mater* 1991;3:202–204.
124. Preiss H, Berger LM, Schultze D. Studies on the carbothermal preparation of titanium carbide from different gel precursors. *J Eur Ceram Soc* 1999;19:195–206.
125. Narisawa M, Okabe Y, Iguchi M, Okamura K. Synthesis of ultrafine SiC powders from carbon-silica hybridized precursors with carbothermic reduction. *J Sol-Gel Sci Technol* 1998;12:143–152.
126. Lenggoro IW, Okuyama K, De La Mora JF, Tohge N. Preparation of ZnS nanoparticles. *J Aerosol Sci* 2000;31:121–136.
127. Stark WJ, Pratsinis SE. Aerosol flame reactors for manufacture of nanoparticles. *Powder Technol* 2002;126:103–108.
128. Audrey H, Stéphane S, Christian G, Anne J. Synthesis and encapsulation of yttria stabilized zirconia particles in supercritical carbon dioxide. *J Eur Ceram Soc* 2006;26:1195–1203.
129. Larsen TH, Sigman M, Ghezelbash A, Doty RC, Korgel BA. Solventless synthesis of copper sulfide nanorods by thermolysis of a single source thiolate-derived precursor. *J Am Chem Soc* 2003;125:5638–5639.
130. Sigman MB, Ghezelbash A, Hanrath T, Saunders AE, Lee F, Korgel BA. Solventless synthesis of monodisperse Cu₂S nanorods, nanodisks, and nanoplatelets. *J Am Chem Soc* 2003;125:16050–16057.

131. Ghezelbash A, Sigman MB, Korgel BA. Solventless synthesis of nickel sulfide nanorods and triangular nanoprisms. *Nano Lett* 2004;4:537–542.
132. Han YC, Cha HG, Kim CW, Kim YH, Kang YS. Synthesis of highly magnetized iron nanoparticles by a solventless thermal decomposition method. *J Phys Chem C* 2007;111:6275–6280.
133. Scheeren CW, Machado G, Dupont J, Fichtner PFP, Texeira SR. Nanoscale Pt(0) particles prepared in imidazolium room temperature ionic liquids: synthesis from an organometallic precursor, characterization, and catalytic properties in hydrogenation reactions. *Inorg Chem* 2003;42:4738–4742.
134. Murray CB, Kagan CR, Bawendi MG. Synthesis and characterization of monodisperse nanocrystals and close-packed nanocrystal assemblies. *Annu Rev Mater Sci* 2000;30:545–610.
135. Tom RT, Nair AS, Singh N, Aslam M, Nagendra CL, Philip R, Vijayamohan K, Pradeep T. Freely dispersible Au@TiO₂, Au@ZrO₂, Ag@TiO₂, and Ag@ZrO₂ core-shell nanoparticles: one-step synthesis, characterization, spectroscopy, and optical limiting properties. *Langmuir* 2003;19:3439–3445.
136. Cargnello M, Wieder NL, Montini T, Gorte RJ, Fornasiero P. Synthesis of dispersible Pd@CeO₂ core-shell nanostructures by self-assembly. *J Am Chem Soc* 2010;132:1402–1409.
137. Zeng H, Li J, Wang ZL, Liu JP, Sun SH. Bimagnetic core/shell FePt/Fe₃O₄ nanoparticles. *Nano Lett* 2004;4:187–190.
138. Bhattacharjee B, Hsu CH, Lu CH, Chang WH. Colloidal CdSe-ZnS core-shell nanoparticles: dependence of physical properties on initial Cd to Se concentration. *Phys E* 2006;33:388–393.
139. Pan DC, Wang Q, Jiang SC, Ji XL, An LJ. Synthesis of extremely small CdSe and highly luminescent CdSe/CdS core-shell nanocrystals via a novel two-phase thermal approach. *Adv Mater* 2005;17:176–179.
140. Haubold S, Haase M, Kornowski A, Weller H. Strongly luminescent InP/ZnS core-shell nanoparticles. *Chem Phys Chem* 2001;2:331–334.
141. Chen CY, Cheng CT, Yu JK, Pu SC, Cheng YM, Chou PT, Chou YH, Chiu HT. Spectroscopy and femtosecond dynamics of type-II CdSe/ZnTe core-shell semiconductor synthesized via the CdO precursor. *J Phys Chem B* 2004;108:10687–10691.
142. Marhuenda-Egea FC, Piera-Velazquez S, Cadenas C, Cadenas E. Reverse micelles in organic solvents: a medium for the biotechnological use of extreme halophilic enzymes at low salt concentration. *Archaea* 2002;1:105–111.
143. Elder SH, Cot FM, Su Y, Heald SM, Tyryshkin AM, Bowman MK, Gao Y, Joly AG, Balmer ML, Kolwaite AC, Magrini KA, Blake DM. The discovery and study of nanocrystalline TiO₂-(MoO₃) core-shell materials. *J Am Chem Soc* 2000;122:5138–5146.
144. Aharoni A, Mokari T, Popov I, Banin U. Synthesis of InAs/CdSe/ZnSe core/shell1/shell2 structures with bright and stable near-infrared fluorescence. *J Am Chem Soc* 2006;128:257–264.
145. Chen YJ, Cao MS, Xu Q, Zhu J. Electroless nickel plating on silicon carbide nanoparticles. *Surf Coat Technol* 2003;172:90–94.
146. Wang F, Arai S, Park KC, Takeuchi K, Kim YJ, Endo M. Synthesis of carbon nanotube-supported nickel-phosphorus nanoparticles by an electroless process. *Carbon* 2006;44:1307–1310.
147. Arai S, Endo M, Hashizume S, Shimojima Y. Nickel-coated carbon nanofibers prepared by electroless deposition. *Electrochem Commun* 2004;6:1029–1031.

148. Ang LM, Hor TSA, Xu GQ, Tung CH, Zhao SP, Wang JLS. Electroless plating of metals onto carbon nanotubes activated by a single-step activation method. *Chem Mater* 1999;11:2115–2118.
149. Jha H, Kikuchi T, Sakairi M, Takahashi H. Palladium nanoparticle seeded electroless metallization of Al/Al₂O₃ surfaces. *Mater Lett* 2009;63:1451–1454.
150. Gao Y-X, Yu S-H, Cong H, Jiang J, Xu A-W, Dong WF, Cölfen H. Block-copolymer-controlled growth of CaCO₃ microrings. *J Phys Chem B* 2006;110:6432–6436.
151. Jiang P, Liu ZF, Cai SM. Growing monodispersed PbS nanoparticles on self-assembled monolayers of 11-mercaptoundecanoic acid on Au(111) substrate. *Langmuir* 2002;18:4495.
152. Chen C-C, Lin JJ. Controlled growth of cubic cadmium sulfide nanoparticles using patterned self-assembled monolayers as a template. *Adv Mater* 2001;13:136.
153. Ziolo RF, Giannelis EP, Weinstein BA, Ohoro MP, Ganguly BN, Mehrotra V, Russell MW, Huffman DR. Matrix-mediated synthesis of nanocrystalline gamma-Fe₂O₃ - a new optically transparent magnetic material. *Science* 1992;257:219–223.
154. Xu SQ, Zhao XK, Fendler JH. Ultrasmall semiconductor particles sandwiched between surfactant headgroups in langmuir-blodgett films. *Adv Mater* 1990;2:183–185.
155. Terasaki O, Yamazaki K, Thomas JM, Ohsuna T, Watanabe D, Sanders JV, Barry JC. Isolating individual chains of selenium by incorporation into the channels of a zeolite. *Nature* 1987;330:58–60.
156. Wang Y, Xu X, Tian ZQ, Zong Y, Cheng HM, Lin CJ. Selective heterogeneous nucleation and growth of size-controlled metal nanoparticles on carbon nanotubes in solution. *Chem Eur J* 2006;12:2542–2549.
157. An XQ, Cao CB, Zhu HS. Optical and photocatalytic properties of sulfide semiconductor quantum dots (QDs) synthesized by silk fibroin template. *Mater Lett* 2008;62:2754–2757.
158. Kumar MNVR, Sameti M, Mohapatra SS, Kong X, Lockey RF, Bakowsky U, Lindenblatt G, Schmidt H, Lehr CM. Cationic silica nanoparticles as gene carriers: synthesis, characterization and transfection efficiency in vitro and in vivo. *J Nanosci Nanotechnol* 2004;4:876–881.
159. Jolley CC, Uchida M, Reichhardt C, Harrington R, Kang S, Klem MT, Parise JB, Douglas T. Size and crystallinity in protein-templated inorganic nanoparticles. *Chem Mater* 2010;22:4612–4618.
160. Ceolín M, Gálvez N, Sánchez P, Fernández B, Domínguez-Vera JM. Structural aspects of the growth mechanism of copper nanoparticles inside apoferritin. *Eur J Inorg Chem* 2008;2008:795–801.
161. Jakhmola A, Bhandari R, Pacardo DB, Knecht MR. Peptide template effects for the synthesis and catalytic application of Pd nanoparticle networks. *J Mater Chem* 2010;20:1522–1531.
162. Pavlopoulou E, Portale G, Christodoulakis KE, Vamvakaki M, Bras W, Anastasiadis SH. Following the synthesis of metal nanoparticles within pH-responsive microgel particles by SAXS. *Macromolecules* 2010;43:9828–9836.
163. Lu J, Yi SS, Kopley T, Qian C, Liu J, Gulari E. Fabrication of ordered catalytically active nanoparticles derived from block copolymer micelle templates for controllable synthesis of single-walled carbon nanotubes. *J Phys Chem B* 2006;110:6655–6660.
164. Yu KMK, Meric P, Tsang SC. Micelle-hosted bimetallic Pd-Ru nanoparticle for in situ catalytic hydrogenation in supercritical CO₂. *Catal Today* 2006;114:428–433.
165. Zhang RB, Gao L. Preparation of nanosized titania by hydrolysis of alkoxide titanium in micelles. *Mater Res Bull* 2002;37:1659–1666.

166. Darbandi M, Lu WG, Fang JY, Nann T. Silica encapsulation of hydrophobically ligated PbSe nanocrystals. *Langmuir* 2006;22:4371–4375.
167. Arriagada FJ, Osseo-Asare K. Synthesis of nanosize silica in a nonionic water-in-oil microemulsion: effects of the water/surfactant molar ratio and ammonia concentration. *J Colloid Interface Sci* 1999;211:210–220.
168. Osseo-Asare K, Arriagada FJ. Growth kinetics of nanosize silica in a nonionic water-in-oil microemulsion: a reverse micellar pseudophase reaction model. *J Colloid Interface Sci* 1999;218:68–76.
169. Finnie KS, Bartlett JR, Barbé CJA, Kong L. Formation of silica nanoparticles in microemulsions. *Langmuir* 2007;23:3017–3024.
170. Zhang J, Post M, Veres T, Jakubek ZJ, Guan JW, Wang DS, Normandin F, Deslandes Y, Simard B. Laser-assisted synthesis of superparamagnetic Fe@Au core-shell nanoparticles. *J Phys Chem B* 2006;110:7122–7128.
171. Bronstein L, Chernyshov D, Valetsky P, Tkachenko N, Lemmetyinen H, Hartmann J, Forster S. Laser photolysis formation of gold colloids in block copolymer micelles. *Langmuir* 1999;15:83–91.
172. Jimenez E, Abderrafi K, Abargues R, Valdes JL, Martinez-Pastor JP. Laser-ablation-induced synthesis of SiO₂-capped noble metal nanoparticles in a single step. *Langmuir* 2010;26:7458–7463.
173. Park J-W, Kim D-W, Seon H-S, Kim K-S, Park D-W. Synthesis of carbon-doped TiO₂ nanoparticles using CO₂ decomposition by thermal plasma. *Thin Solid Films* 2010;518:4113–4116.
174. Chen C, Bai H, Chein HM, Chen TM. Continuous generation of TiO₂ nanoparticles by an atmospheric pressure plasma-enhanced process. *Aerosol Sci Technol* 2007;41:1018–1028.
175. Vollath D, Szabo DV. The microwave plasma process—a versatile process to synthesise nanoparticulate materials. *J Nanopart Res* 2006;8:417–428.
176. Brenner JR, Harkness JBL, Knickerbein MB, Krumdick GK, Marshall CL. Microwave plasma synthesis of carbon-supported ultrafine metal particles. *Nanostruct Mater* 1997;8:1–17.
177. Deivaraj TC, Chen WX, Lee JY. Preparation of PtNi nanoparticles for the electrocatalytic oxidation of methanol. *J Mater Chem* 2003;13:2555–2560.
178. Mohamed MB, AbouZeid KM, Abdelsayed V, Aljarash AA, El-Shall MS. Growth mechanism of anisotropic gold nanocrystals via microwave synthesis: formation of dioleamide by gold nanocatalysis. *ACS Nano* 2010;4:2766–2772.
179. Bilecka I, Elser P, Niederberger M. Kinetic and thermodynamic aspects in the microwave-assisted synthesis of ZnO nanoparticles in benzyl alcohol. *ACS Nano* 2009;3:467–477.
180. Vollath D, Szabo DV. Synthesis of nanocrystalline MoS₂ and WS₂ in a microwave plasma. *Mater Lett* 1998;35:236–244.
181. Sivakumar M, Towata A, Yasui K, Tuziuti T, Iida Y. A new ultrasonic cavitation approach for the synthesis of zinc ferrite nanocrystals. *Curr Appl Phys* 2006;6:591–593.
182. Cao LY, Zhang CB, Huang HF. Synthesis of hydroxyapatite nanoparticles in ultrasonic precipitation. *Ceram Int* 2005;31:1041–1044.
183. Bastami TR, Entezari MH. Sono-synthesis of Mn₃O₄ nanoparticles in different media without additives. *Chem Eng J* 2010;164:261–266.
184. Ghows N, Entezari MH. Fast and easy synthesis of core-shell nanocrystal (CdS/TiO₂) at low temperature by micro-emulsion under ultrasound. *Ultrason Sonochem* 2011;18:629–634.

185. Barta J, Pospisil M, Cuba V. Photo- and radiation-induced preparation of nanocrystalline copper and cuprous oxide catalysts. *J Radioanal Nucl Chem* 2010;286:611–618.
186. Chettibi S, Wojcieszak R, Boudjennad EH, Belloni J, Bettahar MM, Keghouche N. Ni-Ce intermetallic phases in CeO₂-supported nickel catalysts synthesized by gamma-radiolysis. *Catal Today* 2006;113:157–165.
187. Sarkany A, Papp Z, Sajo I, Schay Z. Unsupported Pd nanoparticles prepared by gamma-radiolysis of PdCl₂. *Solid State Ionics* 2005;176:209–215.
188. Reetz MT, Helbig W. Size-selective synthesis of nanostructured transition-metal clusters. *J Am Chem Soc* 1994;116:1401–1402.
189. Yang HM, Ouyang J, Tang AD, Xiao Y, Li XW, Dong XD, Yu YM. Electrochemical synthesis and photocatalytic property of cuprous oxide nanoparticles. *Mater Res Bull* 2006;41:1310–1318.
190. Zhou M, Chen SH, Zhao SY, Ma HY. One-step synthesis of Au-Ag alloy nanoparticles by a convenient electrochemical method. *Phys E* 2006;33:28–34.
191. Ledo-Suarez A, Rodriguez-Sanchez L, Blanco MC, Lopez-Quintela MA. Electrochemical synthesis and stabilization of cobalt nanoparticles. *Phys Status Solidi A* 2006;203:1234–1240.
192. Licht S, Tel-Vered R, Halperin L. Toward efficient electrochemical synthesis of Fe(VI) ferrate and super-iron battery compounds. *J Electrochem Soc* 2004;151:A31–A39.
193. Fotouhi L, Rezaei M. Electrochemical synthesis of copper sulfide nanoparticles. *Microchim Acta* 2009;167:247–251.
194. Akdogan NG, Hadjipanayis GC, Sellmyer DJ. Anisotropic PrCo₅ nanoparticles by surfactant-assisted ball milling. *IEEE Trans Magn* 2009;45:4417–4419.
195. Poudyal N, Rong C-B, Liu JP. Effects of particle size and composition on coercivity of Sm-Co nanoparticles prepared by surfactant-assisted ball milling. *J Appl Phys* 2010;107:09A703 3 pp.
196. Chakka VM, Altuncevahir B, Jin ZQ, Li Y, Liu JP. Magnetic nanoparticles produced by surfactant-assisted ball milling. *J Appl Phys* 2006;99:08E912 3pp.
197. Benjamin JS. Mechanical alloying. *Sci Am* 1976;234:40–48.
198. Murty BS, Rao MM, Ranganathan S. Milling maps and amorphization during mechanical alloying. *Acta Metall Mater* 1995;43:2443–2450.
199. Lam C, Zhang YF, Tang YH, Lee CS, Bello I, Lee ST. Large-scale synthesis of ultrafine Si nanoparticles by ball milling. *J Cryst Growth* 2000;220:466–470.
200. Zhang DL, Liang J, Wu J. Processing Ti₃Al-SiC nanocomposites using high energy mechanical milling. *Mater Sci Eng A* 2004;375–77:911–916.
201. El-Eskandarany MS, Omori M, Konno TJ, Sumiyama K, Harai T, Suzuki K. Synthesizing of nanocomposite WC/MgO powders by mechanical solid-state reduction and subsequent plasma-activated sintering. *Metall Mater Trans* 2001;32:157–164.
202. Li J, Li F, Hu K, Zhou Y. TiB₂/TiC nanocomposite powder fabricated via high energy ball milling. *J Eur Ceram Soc* 2001;21:2829–2833.
203. Lia YX, Chena WF, Zhoua XZ, Gua ZY, Chen CM. Synthesis of CeO₂ nanoparticles by mechanochemical processing and the inhibiting action of NaCl on particle agglomeration. *Mater Lett* 2005;59:48–52.
204. Yang H, Hu Y, Zhang X, Qiu G. Mechanochemical synthesis of cobalt oxide nanoparticles. *Mater Lett* 2004;58:387–389.
205. Yang H, Qiu G, Zhang X, Tang A, Yang W. Preparation of CdO nanoparticles by mechanochemical reaction. *J Nanopart Res* 2004;6:539–542.
206. Salari M, Mousavi khoie SM, Marashi P, Rezaee M. Synthesis of TiO₂ nanoparticles via a novel mechanochemical method. *J Alloys Compd* 2009;469:386–390.

207. Achimovičová M, Daneu N, Rečnik A, Ďurišin J, Baláž P, Fabián M, Kováč J, Šatka A. Characterization of mechanochemically synthesized lead selenide. *Chem Pap* 2009;63:562–567.
208. Shi Y, Ding J, Yin H. CoFe₂O₄ nanoparticles prepared by the mechanochemical method. *J Alloys Compd* 2000;308:290–295.
209. Gu D, Meiners W, Hagedorn Y-C, Wissenbach K, Poprawe R. Structural evolution and formation mechanisms of TiC/Ti nanocomposites prepared by high-energy mechanical alloying. *J Phys D* 2010;43:135402 11pp.
210. Calka A, Wexler D, Mosbah AY. Synthesis of nanopowders under high frequency electric discharge assisted mechanical milling. *J Alloys Compd* 2007;434–435:463–466.
211. Heintz AS, Fink MJ, Mitchell BS. Mechanochemical synthesis of blue luminescent alkyl/alkenyl-passivated silicon nanoparticles. *Adv Mater* 2007;19:3984–3988.
212. Suryanarayana C. Mechanical alloying and milling. *Prog Mater Sci* 2001;46:1–184.
213. Zhonga GQ, Zhou HL, Jia YQ. Preparation of amorphous Ni–B alloys nanoparticles by room temperature solid–solid reaction. *J Alloys Compd* 2008;465:L1–L3.
214. Li F, Yu X, Pan H, Wang M, Xin X. Syntheses of MO₂ (M=Si, Ce, Sn) nanoparticles by solid-state reactions at ambient temperature. *Solid State Sci* 2000;2:767–772.
215. Ye XR, Jia DZ, Yu JQ, Xin XQ, Xue Z. One-step solid-state reactions at ambient temperatures—a novel approach to nanocrystal synthesis. *Adv Mater* 1999;11:941–942.
216. Zhu Y, Zhou Y. Preparation of pure ZnO nanoparticles by a simple solid-state reaction method. *Appl Phys A* 2008;92:275–278.
217. Su X, Du X, Li S, Li J. Synthesis of MgAl₂O₄ spinel nanoparticles using a mixture of bayerite and magnesium sulfate. *J Nanopart Res* 2010;12:1813–1819.
218. Larpiattaworn S, Ngerchuklin P, Khongwong W, Pankurdee N, Wada S. The influence of reaction parameters on the free Si and C contents in the synthesis of nano-sized SiC. *Ceram Int* 2006;32:899–904.
219. Widiyastuti W, Purwanto A, Wang W-N, Iskandar F, Setyawan H, Okuyama K. Nanoparticle formation through solid-fed flame synthesis: experiment and modeling. *AIChE J* 2009;55:885–895.
220. Kravitz K, Kamyshny A, Gedanken A, Magdassi S. Solid state synthesis of water-dispersible silicon nanoparticles from silica nanoparticles. *J Solid State Chem* 2010;183:1442–1447.
221. Calandra P, Longo A, Marciano V, Turco Liveri V. Physicochemical investigation of lightfast AgCl and AgBr nanoparticles synthesized by a novel solid-solid reaction. *J Phys Chem B* 2003;107:6724–6729.
222. Qin R, Li F, Jiang W, Liu L. Salt-assisted low temperature solid state synthesis of high surface area CoFe₂O₄ nanoparticles. *J Mater Sci Technol* 2009;25:69–72.
223. Calandra P, Longo A, Turco Liveri V. Synthesis of ultra-small ZnS nanoparticles by solid-solid reaction in the confined space of AOT reversed micelles. *J Phys Chem B* 2003;107:25–30.

CHAPTER 3

NANOPARTICLE CHARACTERIZATION

3.1 INTRODUCTION

The development potentials and performance to be achieved for nanoparticle-based materials depend on a variety of state-of-the-art instruments and facilities for characterization of these materials. After nanoparticles are successfully synthesized, the first necessary step before any further processing or application is characterization. For nanoparticle superstructure construction, shaping, and sintering, the understanding of nanoparticle characterization is equally important. This chapter serves the role of addressing the characterization issues for all these processes, either the nanoparticles under examination are in discrete, dispersed, or connected format. Because of the small size of nanoparticles (<100 nm), some conventional particle characterization techniques are no longer applicable. Judicious selection of characterization techniques is required for obtaining meaningful evaluation of nanoparticles on hand. When inappropriate techniques are chosen or suitable techniques are used incorrectly, the results will not represent the true characteristics of the nanoparticles and can thus lead to failures in the subsequent processing or applications. Additionally, even though nanoparticle-based superstructures and bulk materials are yet to be covered in the following chapters, the characterization techniques discussed in this chapter are meant to be inclusive. They can easily be applied to nanoclusters, as well as shaped and sintered nanoparticle-based materials. Characterization of nanoparticles and nanoparticle-based materials generally includes the following six aspects: size and morphology, energetics and global thermodynamics, surface area, porosity

and pore size, structure, and composition. Each aspect can be characterized by multiple techniques, as summarized in Table 3.1. Even though this full battery of characterization techniques is not always necessary, a good understanding of these aspects will greatly facilitate the achievement of the processing and performance goals. In most cases, at least three of the above aspects are needed to characterize a specific type of nanoparticles or nanoparticle-based materials.

TABLE 3.1 Nanoparticle Characterization Techniques

| Characteristics | Techniques |
|--------------------------------------|--|
| Size, shape, and morphology | <i>Microscopy</i> Scanning electron microscopy Transmission electron microscopy Scanning probe microscopy (scanning tunneling microscopy and atomic force microscopy) <i>Dynamic laser light scattering</i> <i>X-ray diffraction line broadening</i> <i>Small-angle scattering</i> Neutron scattering X-ray scattering <i>Optical spectroscopy</i> |
| Energetics and global thermodynamics | <i>Oxide melt solution</i> <i>Calorimetry</i> <i>Solution calorimetry</i> <i>Water adsorption calorimetry</i> |
| Surface area | <i>BET gas adsorption</i> |
| Porosity and pore size | <i>Transmission electron microscopy</i> <i>Gas adsorption</i> |
| Crystal structure | <i>Surface structure</i> Low-energy electron diffraction Atomic force microscopy Scanning tunneling microscopy <i>Bulk structure</i> X-ray diffraction Transmission electron microscopy |
| Composition | <i>Surface composition</i> Auger electron spectroscopy X-ray photoelectron spectroscopy Secondary ion mass spectroscopy <i>Bulk composition</i> Optical atomic spectroscopy X-ray fluorescence spectroscopy Energy dispersive X-ray spectroscopy Electron energy-loss spectroscopy Fourier transform infrared spectroscopy UV-vis spectroscopy Raman spectroscopy |

When determining whether a technique is suitable to characterize the nanoparticles or nanoparticle-based materials of interest, a key point is to understand the extensibility and limits of different existing characterization approaches. A good understanding of the fundamental principles and approximations for a specific technique can easily explain some of the potential deviations. Even though some of the techniques were specifically developed for nanoparticles and nanoparticle-based materials, some of the other tools presented here are extended applications of the characterization capabilities for conventional materials. Also, some widely used techniques in analytical chemistry are being increasingly used in the characterization of nanoparticles and nanoparticle-based materials.

3.2 SIZE, SHAPE, AND MORPHOLOGY

Particle-beam interaction reveals important characteristics of particles such as size, shape, and morphology. When particles are at the nanoscale, more stringent requirements on beam wavelength and focus are needed in order to improve the resolution of the characterization techniques or evaluate more challenging samples. Four commonly used beam sources are electron, laser, X-ray, and neutron. Based on these sources, there are three characterization approaches: microscopy, dynamic laser light scattering, and small-angle (X-ray and neutron) scattering.

3.2.1 Microscopy

Microscopy is a technique that offers simultaneous measurements of particle size, shape, morphology, and arrangement of nanoparticles by providing two-dimensional images of three-dimensional objects. When performed on cross-sectioned samples, it can image buried features, layers, interfaces, and crystalline structures at high magnifications. There are three dominant microscopic techniques: scanning electron microscopy (SEM), transmission electron microscopy (TEM), and scanning probe microscopy (SPM). Even though microscopy is the most straightforward technique in nanoparticle characterization, it is limited to only offering two-dimensional projections of three-dimensional objects.

3.2.1.1 Scanning Electron Microscopy SEM is the most mature and widely used imaging technique for characterizing nanoparticle size, shape, arrangement, and degree of agglomeration. In SEM, an electron beam (5–30 keV acceleration) is focused on the sample, and the reflected electrons (back scattered) or ejected electrons from the sample are collected for imaging. Based on the modes of electron beam generation, there are thermionic emission and field emission SEMs. Field emission SEM is preferred because of its fine resolution (down to 1–2 nm range) and good contrast. Nowadays, most SEMs have a field emission mode. For SEM analysis, nanoparticles or a drop of nanoparticle suspension can be directly spread onto conductive tapes and imaged. SEM can provide information about nanoparticle size, shape, and agglomeration extent if

the particles under examination represent the true state of the sample. If assembled superstructures or bulk nanoparticle-based materials are directly examined, nanoparticle size, shape, and packing morphology can also be obtained. However, dispersed particles in a liquid may “pile up” or agglomerate after drying; dry nanoparticle agglomeration is a ubiquitous problem and often hinders quantitative nanoparticle size or shape analysis. Figure 3.1 shows the SEM images and

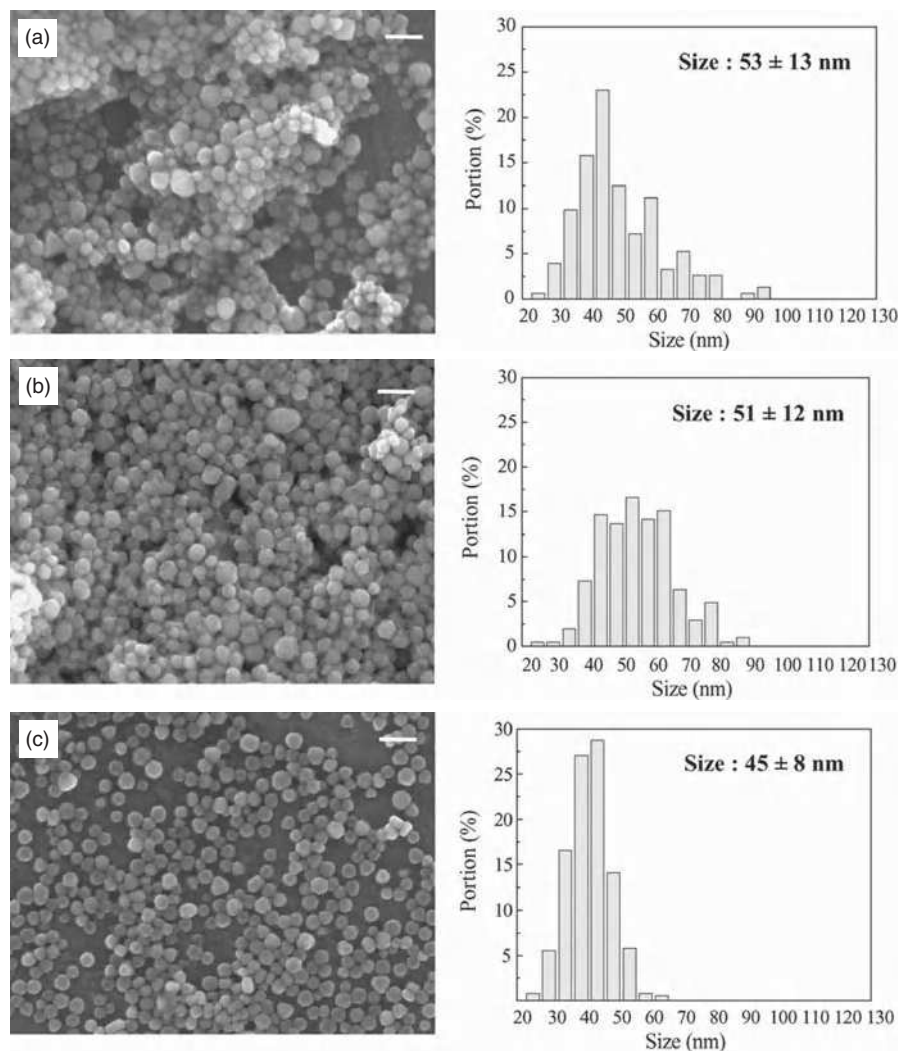


FIGURE 3.1 SEM images and particle size distributions of synthesized copper particles as a function of reaction temperature: (a) 200°C, (b) 170°C, and (c) 140°C. Scale bar = 100 nm [1]. (Reprinted with permission from Park BK, Jeong S, Kim D, Moon J, Lim S, Kim JS. Synthesis and size control of monodisperse copper nanoparticles by polyol method. *J Colloid Interface Sci* 2007;311:417–424, Copyright 2007, Elsevier.)

of copper particles synthesized in the presence of poly(vinylpyrrolidone), employed as a protecting agent, in ambient atmosphere at different temperatures. With decreasing reaction temperature, the size of the resulting particles becomes smaller and the size distribution also narrows. At 200°C, the obtained particle size is 53 ± 13 nm (Fig. 3.1a), whereas that at the synthesis temperature of 140°C is 45 ± 8 nm (Fig. 3.1c) [1]. The particle shapes are fairly round. Quantitative particle size distribution histograms are also presented. This quantification can largely be attributed to the consistent size and equiaxed shape of copper particles. For other less than ideal nanoparticles, quantification can be difficult.

Overall, SEM serves as a quick and convenient technique for nanoparticle size, shape, and arrangement analysis because of its widespread availability and ease of sample preparation. However, SEM can only be regarded as a quick but qualitative tool. Quantitative or statistical evaluation of nanoparticles is generally not accurate.

3.2.1.2 Transmission Electron Microscopy TEM uses transmitting electrons to obtain high magnification images of nanoparticles and measure particle size, shape, and morphology. Since electrons are accelerated at a much higher voltage (200–300 keV) than in an SEM, the electron beam can be focused on a very small region to obtain high-resolution images of nanoparticles. For TEM analysis, nanoparticles can be first dispersed in a liquid and form a very dilute suspension. A drop of the suspension is placed on a metal grid with carbon coating, and the liquid is then evaporated, leaving nanoparticles deposited on the carbon coating of the metal grid. Since the nanoparticles are well dispersed, images of individual nanoparticles can be obtained. By taking advantage of the contrast between the images of the nanoparticles and the carbon coating of the metal grid, nanoparticles can be quantified in size, size distribution, and shape (still two-dimensional projection). The biggest advantage of TEM analysis is the high resolution (as low as sub-angstrom level for high-resolution TEM) and the ability to examine individual nanoparticles. Statistical analysis of particle size and shape also becomes possible and can be carried out quickly with designated software. In addition, the sample preparation for nanoparticle analysis is the easiest among all the TEM sample preparation methods. Because of these desirable features, TEM analysis of nanoparticles is commonly used. Figure 3.2 shows a TEM image of gold nanoparticles transferred from the original gold hydrosol into toluene.

Both SEM and TEM utilize nanoparticle projections onto a two-dimensional surface for size, shape, and morphology characterization. Because of this limitation, these techniques cannot effectively capture the three-dimensional features of nanoparticles. Also, SEM and TEM techniques cannot distinguish composite nanoparticles if the image contrast from different compositions is small or if one composition fully coats the core particles of another composition. In addition, both techniques are dry methods. If special properties need to be characterized in a wet state, such as nanoparticle interaction or hydrodynamic size in a colloidal suspension, these techniques are not feasible.

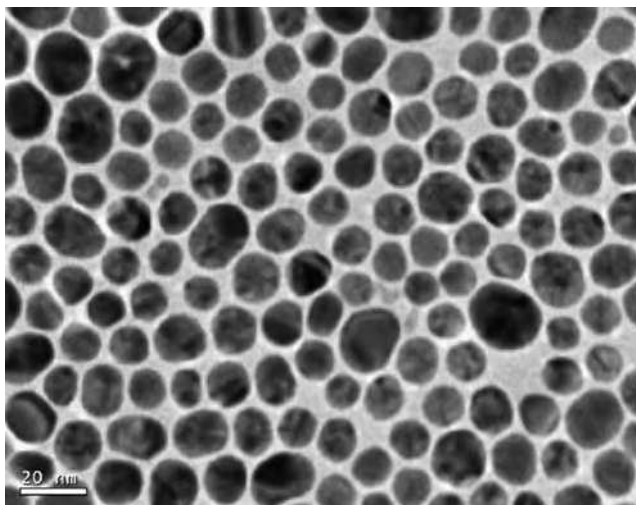


FIGURE 3.2 TEM image of gold nanoparticles transferred from the original gold hydrosol into toluene [2]. (Reprinted with permission from Yang J, Lee JY, Too H-P. Size sorting of Au and Pt nanoparticles from arbitrary particle size distributions. *Analytica Chimica Acta* 2005;546:133–138, Copyright 2005, Elsevier.)

3.2.1.3 Scanning Probe Microscopy Scanning probe microscope (SPM) was invented as scanning tunneling microscope in 1981 [3]. Since then, a vast family of scanning probe microscopes have been developed. Both scanning tunneling microscopy (STM) and atomic force microscopy (AFM) belong to this family. Each type of SPM is characterized by the nature of the local probe and its interaction with the sample surface. Despite the large number of modes in which an SPM can be operated and an image contrast obtained, the underlying operation principle is the same. The three main classes of interaction between the probe and the substrate are contact mode, tapping mode, and noncontact mode. Different forces or interactions can be detected in different modes. SPM is a complementary tool for nanoparticle size, shape, and morphology measurements. It can be used for either single composition nanoparticles or mixed nanoparticle composites. Also, SPM can be operated in air and liquid environments, which is very desirable for nanoparticle suspensions. SPM can generally achieve a spatial resolution of 4 nm and has the advantage of easy sample preparation and fast data acquisition. It also provides better particle morphology information in the z direction than SEM and TEM.

Instead of using an electron beam as in an electron microscope such as SEM and TEM, STM uses an ultrathin conductive tip to interact with the sample. When the tip is brought within $\sim 10 \text{ \AA}$ of the sample, there is an electron tunneling current between the tip and the specific nanoparticle. The resulting voltage difference generates a current (tunneling current), which exponentially decreases with the distance that the electrons travel. Surface images and z dimensions of particles

can thus be obtained. Even when there are other factors modifying the tunneling current, it is this current exponential dependence on the separation between the probe and the sample that allows the atomic resolution. The quantitative relationship between the tunneling current I_t and the tip-sample distance d can be described as

$$I_t \sim e^{-d/g}, \quad (3.1)$$

where g is a constant in the unit of length. This high-resolution technique allows atomic information to be gathered not from an average over many nanoparticles, but from particle to particle. By monitoring the current over each point of the sample, the topography of the particles on a substrate is recorded. When the tip-to-sample separation is kept constant, the current is recorded over each point. This operation is called constant height mode. Alternatively, when the current is kept constant during the scan, the scanning probe moves up and down during the measurement and the nanoparticle topography is recorded. The operation mode is called constant current mode. Each mode has its own advantages. The constant current mode is more common and reproduces the “topography” of the surface. For both modes, the resulting image is a gray-scale map of the surface where bright spots correspond to high current values or high locations and dark spots correspond to low current values or low locations.

AFM was invented in 1986 [4]. In the contact mode, AFM utilizes a sharp probe moving over the surface of a sample in a raster scan. The probe is a tip on the end of a cantilever that bends in response to the force between the tip and the sample. Since the cantilever obeys Hooke’s law for a small displacement, the interaction force between the tip and the sample can be obtained. The movement of the tip or the sample is performed by an extremely precise positioning device made from piezoelectric ceramics. The scanner is capable of sub-angstrom resolution in the x , y , and z directions. In noncontact mode, the distance between the tip and the sample surface is $>10 \text{ \AA}$, and van der Waals, electrostatic, magnetic, or capillary forces produce images of the sample topography. In the contact mode, ionic repulsion forces are dominant. Tapping mode is the second most common mode next to the contact mode used in AFM. When operated in air or other gases, the cantilever oscillates at its resonant frequency (often hundreds of kilohertz) so that it only taps the surface for a very small fraction of its oscillation period.

AFM can provide three-dimensional imaging/visualization of the nanoparticles distributed on a flat surface, which can render qualitative and/or quantitative information about physical properties of nanoparticles including size, morphology, surface texture, and roughness. However, the influence of the AFM tip size and shape on the acquired images must be properly accounted and corrected for. A collection of images can be used to extract information about particle size distributions and volumes. AFM can be conducted in vacuum, under ambient conditions, in liquids, or in other environments. Figure 3.3 shows an AFM image of Cu_2O nanodots formed on a flat SrTiO_3 substrate [5]. The particles are roundish with the bottom fully attached to the substrate. The particle thickness is $<50 \text{ nm}$ while the lateral size is submicron.

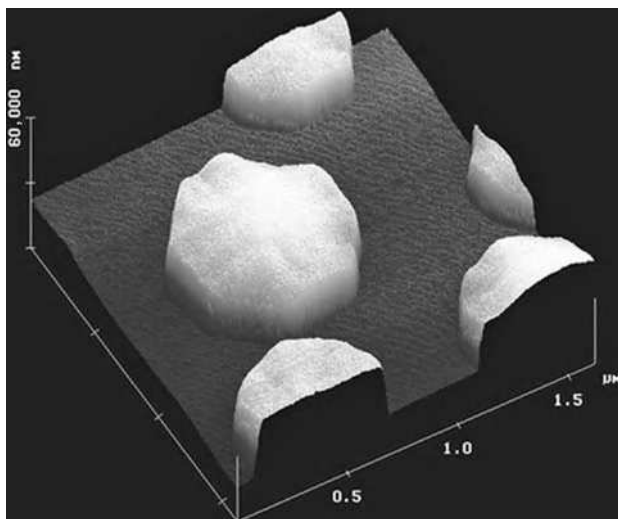


FIGURE 3.3 Atomic force microscopy image of Cu₂O nanodots formed on a SrTiO₃ substrate [5]. (Reprinted with permission from Baer DR, Gaspar DJ, Nachimuthu P, Techane SD, Castner DG. Application of surface chemical analysis tools for characterization of nanoparticles. *Anal Bioanal Chem* 2010;396:983–1002, Springer Science + Business Media, Fig. 6.) (For a color version of this figure, see the color plate section.)

The images obtained from STM and AFM are similar to those from TEM except for the height information in the z direction. The difference between STM and AFM is that STM uses a conductive tip and can only characterize conductive samples while AFM uses a cantilever and can measure all types of samples (conductive, semiconducting, and insulating). Also, single atom contact happens in STM, while several atoms may contact with the cantilever in AFM. Besides measuring nanoparticle size, shape, and morphology, both STM and AFM can be applied to the characterization of nanoparticles on a substrate that cannot be removed.

In addition to the well-developed techniques discussed above, *in situ* microscopy can be used to study mechanical stress, magnetic-field-induced phase transformation, and structural and chemical evolution of nanoparticles. Essentially, the technique involves microscopic observation of nanoparticles under an applied field. Interested readers are encouraged to read more detailed descriptions elsewhere [6]. It should also be pointed out that even though SPM can provide information about particle depth, a true nanoscale three-dimensional imaging technique has yet to be developed, especially when particles have a diminishing contour from the top to the bottom.

3.2.2 Dynamic Light Scattering

In dynamic light scattering (DLS), also known as photo correlation spectroscopy (PCS), particle size measurement is carried out by measuring the intensity of the scattered light. DLS is a well-established method for particle size and size

distribution analysis and is mostly only suited for nanoparticle size measurement. The fundamental mechanism can be understood by considering nanoparticle motion in a suspension. There are three types of forces acting on a particle: Brownian forces arising from collisions with thermally agitated liquid molecules, direct interaction between particles (e.g., a shielded Coulombic force between charged particles), and “excluded-volume” or “hard-sphere” forces between uncharged particles. Particle motion increases with the decrease in particle size. Brownian motion leads to scattering of the incident light and to fluctuations in the average intensity. Since particles with different sizes scatter the incident light with different angles and frequencies, the scattered light intensity and frequency can be measured at different scattering angles (forward scattering and 90° scattering). The results can be used to determine the particle size based on the Stokes–Einstein equation [7]:

$$r = \frac{kT}{3\pi\eta D_{\text{diff}}}, \quad (3.2)$$

where r is the particle radius (assumed spherical shape), k is Boltzmann’s constant, T is the absolute temperature, η is the viscosity of the liquid, and D_{diff} is the diffusion coefficient.

Since nanoparticles are always dispersed in a liquid for DLS measurement, surface hydrolyzation, charge attraction, and adsorbed species can alter particle sizes. The measured value is often the hydrodynamic size of nanoparticles in a specific liquid. DLS can be used to measure particle sizes in the 2–2000 nm range. The light source is commonly a He–Ne laser with 630 nm wavelength. Important factors to consider are the concentration and dispersion of the nanoparticles. If the nanoparticles are not properly dispersed, the measurement will vary drastically and not provide useful data. The suspension should be dilute (normally <1 vol% of solid nanoparticles) and optically clear.

In recent years, DLS has become the most readily available technique for nanoparticle size distribution measurement because of the availability of intense, monochromatic laser sources, and reduced cost of computers for data analysis. However, this technique is not as widely used as it should be. Most of the studies report nanoparticle size and size distribution based on electron imaging results. The quality of the nanoparticle suspension, for example, the flocculates, can easily bias measurement results. When a nanoparticle suspension is properly prepared, the measurement can be done accurately and rapidly, providing a number percent of nanoparticles within a certain size range. With the simplification of nanoparticle shapes such as spheres, particle weight/volume distribution versus particle size curves can be easily obtained. For example, particle size distribution of Al₂O₃ nanoparticles with 45 m²·g⁻¹ specific surface area and 37.5 nm average size are measured by the DLS technique. From the number-based particle size distribution, the population of large particles (>100 nm) is negligible. However, the large particles have a greater weight than the small particles; a clear large particle peak can be observed on the weight-based analysis curve. For ZnO nanoparticles, a size distribution of 15–100 nm is seen when 21,000 (◀), 31,000

(▼), and 51,000 (▲) molecular weight copolymers are adsorbed on the nanoparticle surfaces, as shown in Figure 3.4a. Only in the case of particles prepared from copolymers with a molecular weight of 160,000 (●) and 323,000 (■) is a bimodal curve obtained, and aggregates up to 1 μm are observed. A comparison with the TEM imaging results is shown in Figure 3.4b. The TEM measurement shows more large particles even though the distribution shows similar shape curves [8].

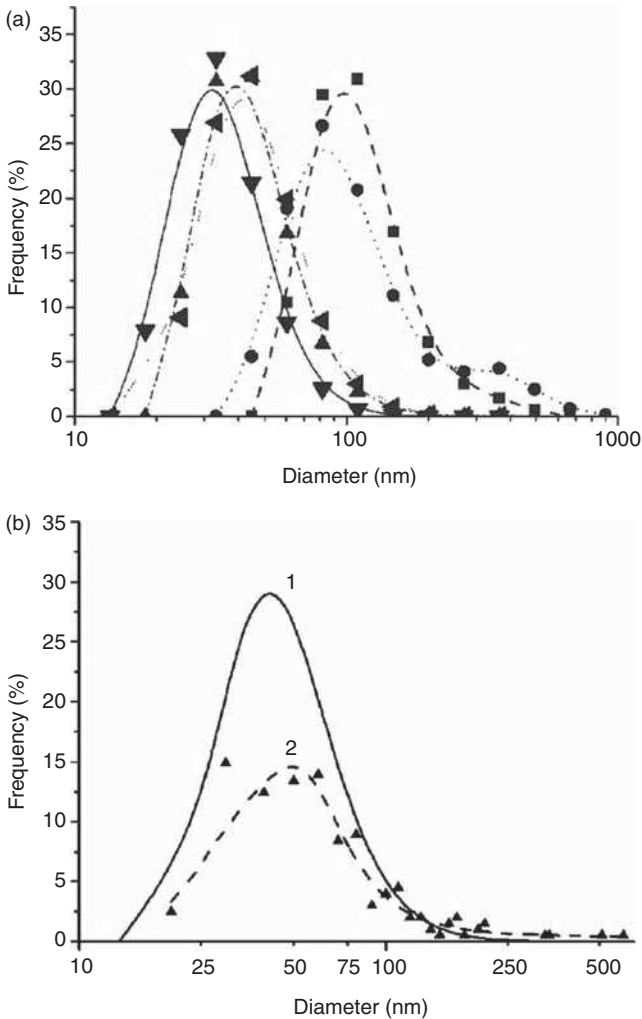


FIGURE 3.4 (a) Size distributions of redispersed and functionalized particles. (◄) ZnO/21,000; (▼) ZnO/31,000; (▲) ZnO/51,000; (●) ZnO/160,000; (■) ZnO/323,000. (b) Size distributions of redispersed ZnO/21,000 particles. Curve 1-DLS measured, curve 2-evaluation of TEM images [8]. (Reprinted with permission from Khrenov V, Klapper M, Koch M, Müllen K. Surface functionalized ZnO particles designed for the use in transparent nanocomposites. *Macromolecular Chemistry and Physics* 2005;206:95–101, John Wiley & Sons.)

3.2.3 X-ray Diffraction Line Broadening

X-ray diffraction (XRD) line broadening is essentially more of a nanocrystallite size measurement technique than a nanoparticle size measurement technique. The particles may be any size as long as the nanocrystallites inside the particles are at the nanoscale. The technique can measure nanocrystallite size down to as small as 10 Å. The fundamental mechanism for nanocrystallite size measurement can be explained as follows. Diffraction only occurs when the distance between the adjacent lattice planes satisfies Bragg's law for the X-ray to be diffracted from the first atomic plane. If the angle θ of the incidence light is close but not exactly at Bragg angle, the distance can be equal to $1.001\lambda_X$ instead of $1\lambda_X$ (λ_X is the wavelength of the X-ray beam). As a result, the scattering from the first plane will be cancelled by the scattering from the plane 500 layers deep within the crystal, with a phase shift of $500.5\lambda_X$. Similarly, if the distance for the X-ray diffracted from the first plane is $1.00001\lambda_X$, the scattering will be cancelled by a plane 50,000 layers deep in the crystal. Bragg diffraction should occur only exactly at the Bragg diffraction angle, producing a sharp peak. However, if a particle is only 1 nm in size, then the planes needed to cancel the scattering from the initial plane (such as (hkl) plane with a diffracted distance of $1.0001\lambda_X$, it will be the 5000th plane and on) are not present. The diffraction peak will show intensity at a lower θ and end at a higher θ than the Bragg angle. The nanocrystallite size causes diffraction peak broadening. Conversely, the crystallite size D_{hkl} can be estimated from the line broadening of the diffraction peak:

$$D_{hkl} = \frac{S_{Sch}\lambda_X}{B \cos \theta}, \quad (3.3)$$

where B is the full width at half maximum intensity, θ is the diffraction angle (in radians) of the considered diffraction peak, and S_{Sch} is Scherrer constant (~ 0.9). Equation (3.3) is called the Scherrer equation.

For $(1-x)\alpha\text{-Fe}_2\text{O}_3\text{-}x\text{SnO}_2$ nanoparticle composites, the peaks broaden with SnO_2 content increase, but there are no new peaks. The particle size versus SnO_2 content x can be calculated based on the peak broadening, which shows an exponential decay based on the diffraction peak widths, from 70 to 10 nm when the SiO_2 content increases from 0 to 1 [9]. For surface modification of tungsten by implanting nitrogen, the crystallite size increases with the substrate temperature, within a range between 40 and 77 nm [10]. This is understandable since higher temperature is more conducive for particle growth. NbC produced from niobium oxide (Nb_2O_5) precursor is examined using *in situ* XRD. The typical diameter of the crystallites obtained from XRD broadening is in the range of 16–24 nm [11]. The XRD patterns of the Co_3O_4 nanoparticles after calcination at different temperatures are shown in Figure 3.5. The intensity and definition of the diffraction peaks associated with Co_3O_4 increase with increasing heat treatment temperature. Figure 3.6 shows the variation of XRD crystal size (D_{hkl}) of Co_3O_4 nanoparticles prepared by the thermal treatment of the precursor at

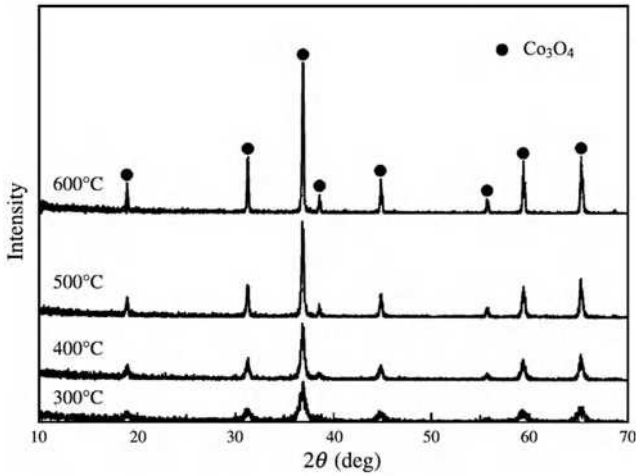


FIGURE 3.5 XRD patterns of the Co_3O_4 nanoparticles synthesized by reaction between $\text{Co}(\text{NO}_3)_2 \cdot 6\text{H}_2\text{O}$ and NH_4HCO_3 at different calcination temperatures [12]. (Reprinted with permission from Yang H, Hu Y, Zhang X, Qiu G. Mechanochemical synthesis of cobalt oxide nanoparticles. *Mater Lett* 2004;58:387–389, Copyright 2004, Elsevier.)

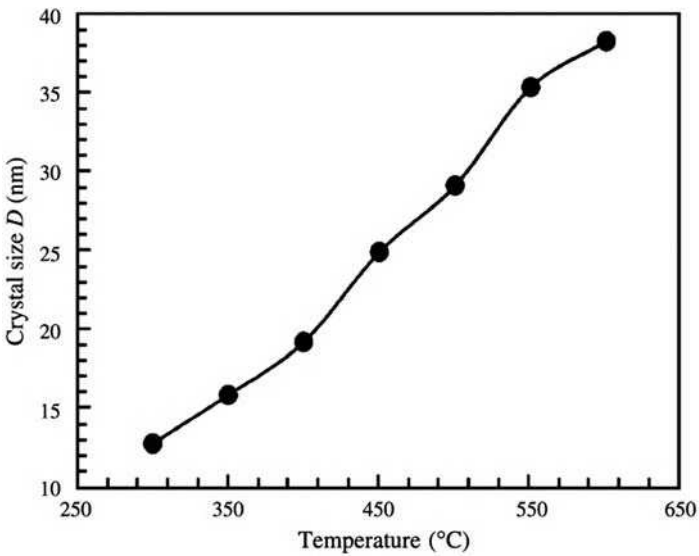


FIGURE 3.6 Variation of XRD crystal size with heat treatment temperature for synthesized Co_3O_4 nanoparticles [12]. (Reprinted with permission from Yang H, Hu Y, Zhang X, Qiu G. Mechanochemical synthesis of cobalt oxide nanoparticles. *Mater Lett* 2004;58:387–389, Copyright 2004, Elsevier.)

different temperatures. The crystal size rapidly increases from approximately 13 nm at 300°C to ~38 nm at 600°C [12].

However, care should be taken with the use of XRD patterns in extracting data regarding nanocrystallite sizes. Background noise can compromise the results, in particular since the intensity is different for different samples and must be subtracted in data analysis. Discrepancies between volume-averaged sizes obtained by XRD and two-dimensional projection-averaged sizes by TEM have been observed. There are several sources of uncertainty in sizes calculated by XRD. First, background subtraction in the presence of broad, weak reflections is difficult, and this introduces a refined statistical uncertainty of at least ± 1 nm. Second, the Scherrer equation provides only an approximate value for nanocrystallite sizes. Third, since the XRD data represent a volume average over the entire assembly of particles, this method is more sensitive than TEM to the presence of a relatively small fraction of larger particles. Fourth, XRD measures nanocrystallite size while TEM measures nanoparticle size. An additional uncertainty is that more than half of the atoms in a 2–4 nm size cluster experience a low coordination environment. Although the structural consequences of this are unclear at present, it is not surprising that the XRD results appear to reflect a larger size, with the smaller particles providing a weaker contribution to the XRD line broadening. Thus, while it is not possible to directly measure the size distribution of particles from the XRD results, the discrepancy between the smaller size particles can be biased by the presence of a small fraction of large particles. The values derived from XRD are related to volume averages; care should be taken when applying the results to applications in which surface average properties are important [13].

3.2.4 Small-Angle Scattering

In SAS, a sample is irradiated by an applied beam, generating scattering patterns, which provide information on the size of particles and the interactions between them. Depending on the type of beam used, it includes two different techniques: small-angle X-ray scattering (SAXS) and small-angle neutron scattering (SANS). SAXS detects the difference in electron density, while SANS detects the variation of the so-called scattering length density. The underlying principles, however, are the same for the two techniques.

For SAXS, X-ray with a typical wavelength of ~ 0.15 nm is used. During the measurement, a low-divergence X-ray beam is focused onto the sample. The electron density inhomogeneities in the sample cause a scattering pattern. By analyzing the inverse relationship between the particle size and the scattering angle, size, and shape, information about the nanoparticles can be obtained. Nanoparticle sizes as small as single nanometers can be measured within a narrow range of angular scattering. The upper size limit that can be measured is about 150 nm. SAXS provides information about the external form of nanoparticles. Scattering happens only when the average density of the nanoparticles is different from that of the medium. The technique can be used for structural investigation of dry nanoparticles or suspended nanoparticles.

SAXS has been applied to iron nanoparticle assemblies for characterizing the degree of structural order, for determining the average interparticle spacing, and for identifying possible lattice structures that otherwise would be difficult to obtain [14]. The rapidly quenched sample shows no defined peaks on the SAXS pattern. For the face-centered cubic iron nanoparticles, the size is 15 nm with several well-defined crystalline peaks. For TiO₂ nanoparticles made by a sol-gel method, SAXS shows that the nanoparticle size distribution is 4–12 nm [15]. Also, SAXS is used to investigate silver nanocrystal phase transitions [16]. Surface sensitive SAXS technique (grazing incidence SAXS) is carried out for the morphology study of Pt–Al₂O₃ thin films [17]. The measurements show that the ellipsoidal platinum nanoparticles distributed in the amorphous Al₂O₃ matrix elongate slightly in the z direction. The average separation of particles along z direction is more than that in the in-plane direction. SAXS curves for gold nanoparticle in suspensions and on glass (gold particle sizes of 11.6 nm and 39.2 nm) are shown in Figure 3.7. The solid lines are the simulated results based on a spherical form factor of the particles. Compared to the scattering from the suspension, the data from the particles on the glass surface shows a strongly decreased scattering at low scattering vectors. The scattering intensity approaches the form factor calculation at a value below the first oscillation minimum at 0.075 Å⁻¹ [18].

Since SAXS is sensitive to inhomogeneities in electron density distribution, the size and shape of individual nanoparticles can be measured regardless of the local structure of the medium in which the nanoparticles might be embedded. SAXS can probe not only the structure of individually dispersed nanoparticles but also the superstructures of condensed nanoparticle arrays, as well as fluid–solid and solid–solid phase transitions.

SANS uses neutrons that have up to 2 nm wavelength and detects the variation of scattering length density. Nanoparticle size up to 1000 nm can be easily measured. SANS is a powerful tool to extract unique information about nanoparticle size. Unlike X-ray scattering, in which the wavelength of X-ray increases linearly with atomic number, neutron-scattering wavelength changes irregularly with atomic number [19]. In a typical experiment, neutrons are scattered from a source (e.g., a spallation source). Scattering takes place in a radially symmetric manner and is measured by a two-dimensional detector. The scattered neutron intensities measured by the detector are then radially averaged and normalized. The advantages of using neutrons include the sensitivity to isotopic composition, the ability to probe bulk properties of thick samples because of the weak interaction of neutrons with nuclei and consequent deep penetration into the material, and the capability of acting as a magnetic probe of the sample because of the magnetic moment that neutrons possess. The scattering vector \vec{Q} can be analyzed and expressed as [19]

$$Q = |\vec{Q}| = (4\pi/\lambda_N) \sin \omega_s, \quad (3.4)$$

where ω_s is the scattering angle and λ_N is the wavelength of the incident neutron beam. Inhomogeneities larger than atomic distances (1–100 nm) produce scattering patterns with Q ranging between $1/L_N$ and $10/L_N$, where L_N is the dimension

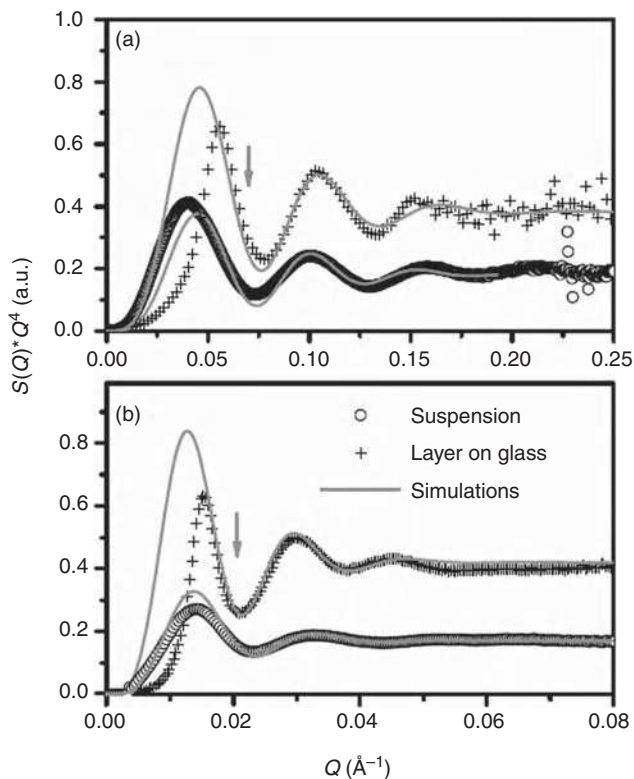


FIGURE 3.7 Small-angle X-ray scattering data from a gold particle suspension (circles) and the corresponding layer (crosses) on a glass surface together with a calculation of the sphere form factor (full lines). The x -axis is the scattering vector and the y -axis is the scattering intensity. In (a), the curves for the smaller particles (11.6 nm) are shown, while in (b), the SAXS from larger particles (39.2 nm) is depicted. The arrows mark the position of a structure factor maximum, when a close packing of particles is assumed. In both cases, the observed maximum is shifted to smaller scattering vectors [18]. (Reprinted with permission from Ciesca F, Plech A. Gold nanoparticle membranes as large-area surface monolayers. *J Colloid Interface Sci* 2010;346:1–7, Copyright 2010, Elsevier.) (For a color version of this figure, see the color plate section.)

of inhomogeneities. The scattering angle ω corresponds to the upper limit of Q . For $L = 10$ nm, ω is about 9.1° for neutrons of 1 nm wavelength.

Because SANS is sensitive to magnetic moment orientations on a very short time scale ($\sim 10^{-11}$ second) and to the length scale of magnetic ordering, it offers a unique tool to address the spin structures within interacting nanoparticle assemblies. Iron nanoparticles that consist of either disordered arrays or ordered, face-centered cubic crystals are investigated using SANS [14]. As shown in Figure 3.8, the SANS signal for the crystal sample shows peaks that are consistent with the

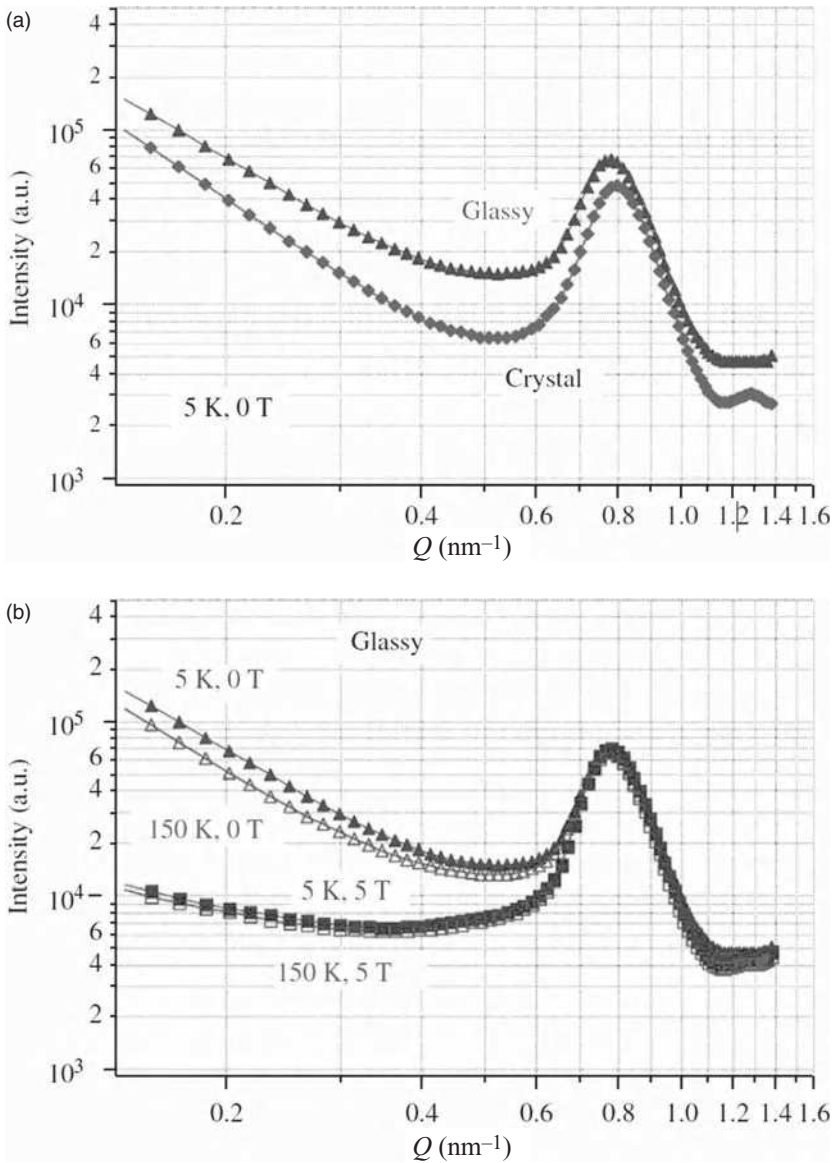


FIGURE 3.8 (a) SANS intensity versus scattering vector \vec{Q} for an iron nanoparticle crystal and a glassy assembly of iron nanoparticles. (b) SANS intensity versus scattering vector \vec{Q} for the glassy assembly (a) at different temperatures and applied fields. All data are angle averaged [14] (Reprinted with permission from Farrell MDF, Ijiri Y, Kelly CV, Borchers JA, Rhyne JJ, Ding Y, Majetich SA. Small-angle neutron scattering study of disordered and crystalline iron nanoparticle assemblies. *J Magn Magn Mater* 2006;303:318–322, Copyright 2006, Elsevier.)

face-centered cubic structure. For the glassy sample, the SANS signal shows increased intensity at the lower Q region (Fig. 3.8a). When a large magnetic field is applied, the intensity reduces quickly (Fig. 3.8b). SANS provides a measurement of the magnetic length scale that may be associated with long-range interparticle interactions. SANS is also used to study the phase behavior of a SiO_2 nanoparticle suspension containing organic and inorganic cations. It shows that the nanoparticles have a core/shell structure in the monomer/oligomer/nanoparticle region [20].

SANS can analyze opaque materials. In addition, it is the only technique that can identify magnetic and temperature fluctuation effects on structures in liquid systems. Nanoparticle size, size distribution, and volume fraction can all be obtained as macroscopic averages. However, SANS only works when the average scattering density of nanoparticles is different from that of the medium.

SANS and SAXS have been used jointly for three-dimensional structural characterization of FePt and $(\text{FePt})_{95}\text{Au}_5$ nanoparticles with an average size of about 4 nm [21]. SANS measures the in-plane coherence length parameter, and SAXS measures the perpendicular coherence length parameter. With the measured parameters, a hexagonal close-packed superstructure for both FePt and FePtAu nanoparticle arrays is constructed.

3.2.5 Optical Spectroscopy

A less commonly used technique in measuring nanoparticle size is optical spectroscopy. The technique studies the electromagnetic radiation that the system interacts with or produces. More specifically, optical spectroscopy measures the intensities and wavelengths of the visible part of the electromagnetic spectrum. The optical properties of nanoparticles reflect size-induced changes in electronic structures. Optical spectroscopy detects the energy difference between electronic states and the lifetime of excited states. When the photons in light interact with the electrons in matter, the light is either created or destroyed. Each line is characteristic of the element that emits light. For a single InAs/GaAs quantum dot in high magnetic fields, optical spectroscopy indicates that the observed multiline emission is due to different charge states of a single dot [22]. For InGaN/GaN quantum dots examined at different temperatures, the quantum dot height change is correlated to photoluminescence [23]. The competitive influence of radioactive and nonradioactive recombinations is observed. However, optical spectroscopy is mainly applicable to photoluminescence materials at or close to room temperature.

3.3 ENERGETICS AND GLOBAL THERMODYNAMICS

Nanoparticles have too few atoms to be considered as bulk materials. They have some properties, unlike either atoms/molecules or the bulk, and represent a transition between these states [24]. In one aspect, as the particle size becomes

smaller, the energetics and global thermodynamics of nanoparticles need to be addressed.

Instead of any single, well-defined characterization technique, the understanding and characterization of energetics and global thermodynamics of nanoparticles are more a fresh look of some existing characteristics when it comes to nanoparticles. The first of these is stable phases at a given condition. The other is related to the activity/reactivity of the nanospecies.

Nanoparticles precipitated from aqueous solutions often crystallize in structures different from those of coarsely crystalline materials: γ -alumina instead of corundum, anatase and brookite instead of rutile, maghemite instead of hematite, and a host of complex hydrous iron oxyhydroxides [25]. This is generally attributed to surface energy difference, which stabilizes polymorphs for nanoparticles that are metastable in the bulk. One of the techniques that can be used to characterize such phase differences and transitions is oxide melt solution calorimetry, which measures the enthalpies of phase transformation and surface enthalpies of different oxide polymorphs [26]. In addition, solution calorimetry can be used to determine surface enthalpy and heat capacity for nanoparticles, and water adsorption calorimetry can be used to measure the surface energy [27]. Energy crossover between polymorphs at the nanoscale is believed to be the cause for the phase differences. For example, γ - Al_2O_3 is energetically stable when the specific surface area exceeds $\sim 125 \text{ m}^2 \text{ g}^{-1}$. Due to the presence of tetrahedral and octahedral sites in its spinel-type structure, and the fairly random distribution of Al^{3+} and vacancies over these sites, γ - Al_2O_3 has a greater entropy than α - Al_2O_3 . The entropy change of α - Al_2O_3 to γ - Al_2O_3 transition is about $15.7 \text{ J K}^{-1} \text{ mol}^{-1}$. Therefore, at room temperature, γ - Al_2O_3 is thermodynamically stable with respect to α - Al_2O_3 at specific surface areas $> 100 \text{ m}^2 \text{ g}^{-1}$. At 800 K (a temperature typical of oxyhydroxide decomposition), γ - Al_2O_3 might become thermodynamically stable at specific surface areas greater than only $75 \text{ m}^2 \text{ g}^{-1}$. For ZrO_2 , oxide melt solution calorimetry shows that the surface energy decreases in the order of monoclinic, tetragonal, and amorphous. These crossovers correspond well to observation that monoclinic ZrO_2 , the stable bulk polymorph, is readily synthesized with particle size $> 50 \text{ nm}$, tetragonal ZrO_2 is synthesized with intermediate particle size, and amorphous ZrO_2 exists for particles smaller than about 4–8 nm.

Small gold particles present structural fluctuations at $\sim 2 \text{ nm}$ size, changing between cubo-octahedral, icosahedral, and single-twined structures [28]. In order to explain the structural fluctuations, two main models have been proposed. The first one involves the complete melting of the particles followed by a recrystallization to a new structure [29, 30]. The energy for the melting is provided by the inelastic scattering of the incoming electrons on the particle. The second model assumes that different particle configurations have similar energies and low-energy barrier without melting [31, 32]. This phenomenon has been termed quasimelting and refers to the fluid-like behavior observed in nanoparticles.

It should be pointed out that many polymorphs are only 5–10 kJ mol^{-1} higher in enthalpy than the stable, well-crystallized forms, opening the door to

crossovers in stability. The large internal surface area of zeolite requires a small surface energy to make the system energetically accessible. The surface energy is considerably larger for oxides, which do not form framework structures with a low density. The existence of a large number of polymorphs with microporous structures requires them to be similar in energy and not too much higher than dense frameworks. If the energy of internal and external surfaces is similar, this implies little dependence of energy on particle size for microporous materials. Because of the small surface energy, crossovers in stability of microporous materials as a function of particle size are unlikely, in contrast to the behavior of dense polymorphs. Also, the thermodynamic driving force for particle coarsening of microporous materials is very small [25].

The energetics of nanoparticles affects the reactivity/activity of the nanoparticles in discussion. For example, anatase TiO_2 particle size and shape are quantitatively correlated through density functional theory with the photocatalytic activity of the oxygen evolution reaction. The equilibrium shape of TiO_2 nanoparticles is sensitive to its size from 1 to 30 nm, and sharp crystals possess much higher activity than flat crystals in oxygen evolution reaction, which in combination leads to the morphology dependence of photocatalytic activity [33].

Another approach to understand the energetics of nanoparticles is modeling. The dependence of the oxidation enthalpy of aluminum nanoparticles on particle size is modeled. The model includes the size dependence of the cohesive energy of the reactant particles, the size dependence of the nanoparticle lattice energy, the extent of nanoparticle agglomeration, and surface capping effects. The strongest effects on aluminum nanoparticle energy release occur for particle diameters <10 nm [34].

3.4 SURFACE AREA

As particle size decreases to nanoscale, the specific surface area (usually in $\text{m}^2 \text{g}^{-1}$) increases drastically. The specific surface area of nanoparticles with an average size <10 nm can rise to several hundred $\text{m}^2 \text{g}^{-1}$. That is, 2–3 g of nanoparticles, which fit into a small volume of a few cubic centimeters, can have the same surface area as an entire football field. In many applications, specific surface area can be the single most important factor to consider, such as for catalysis or sensing.

The Brunauer–Emmett–Teller (BET) gas adsorption method is widely used to measure the specific surface area of nanoparticles and remains the most accepted approach. The BET technique starts with Langmuir monolayer adsorption of gas molecules on the particle surfaces. By considering multilayer adsorption of the condensing gas molecules, an adsorption equation for specific surface area measurement can be derived:

$$\frac{1}{V(p_0/p_A - 1)} = \frac{1}{V_{\text{gm}c}} + \frac{c - 1}{V_{\text{gm}c}} \left(\frac{p_A}{p_S} \right), \quad (3.5)$$

where V is the volume of gas adsorbed per unit mass of nanoparticles ($\text{cm}^3 \text{g}^{-1}$) at relative pressure $\frac{p_A}{p_S}$, p_A is the gas pressure applied during the gas adsorption measurement, p_S is the saturation pressure of the adsorbed gas at the testing temperature, V_{gm} is the volume of gas required to form a monolayer per unit mass of nanoparticles ($\text{cm}^3 \text{g}^{-1}$), and c is a constant. In order to obtain specific surface area, the amount of gas adsorbed onto a fixed mass of nanoparticles at a certain temperature is measured at different gas pressure p_A . In most cases, nitrogen is used as an adsorbate with a molecular cross-sectional area of $16.2 \times 10^{-20} \text{ m}^2$ (16.2 \AA^2). Plotting the left-hand side of Equation (3.5) versus $\frac{p_A}{p_S}$ yields a straight line, with $\frac{p_A}{p_S}$ normally varying in a range between 0.05 and 0.30. Combining the obtained slope and intercept gives V_{gm} . The specific surface area can be further calculated with the following equation:

$$S_w = \frac{N_A \sigma_A V_{\text{gm}}}{V_0}, \quad (3.6)$$

where S_w is specific surface area ($\text{m}^2 \text{g}^{-1}$), N_A is the Avogadro's number ($6.023 \times 10^{23} \text{ mol}^{-1}$), σ_A is the cross-sectional area of the adsorbate molecule, and V_0 is the molar volume of the gas at standard temperature and pressure (22.4 L mol^{-1}). With the assumption that nanoparticles are spherical and dense, particle size D_p can be estimated based on

$$S_w = \frac{S_T}{W_S}, \quad (3.7)$$

where S_T is the total surface area and W_S is the weight of the measured sample. For spherical particles,

$$D_p = \frac{6}{S_w \rho_t}, \quad (3.8)$$

where ρ_t is nanoparticle theoretical density.

During the specific surface area measurement, multiple points can be obtained on the $\frac{1}{V(p_0/p - 1)} \sim (\frac{p}{p_0})$ curve to extract V_{gm} . For quick analysis or quality control purposes, single point BET can be used for specific surface area measurement. In single point BET analysis, it is assumed that the intercept mentioned above is zero and only one gas adsorption point is needed. Because of these assumptions, single point BET measurement is only an approximation.

CdSe aerogel shows a mesoporous interconnected network of nanoparticles and the surface area measured by the BET method is $224 \text{ m}^2 \text{g}^{-1}$ [35]. For Ni–Al nanoparticles synthesized via hydrogen plasma-metal reaction, the specific surface area is in the range of $16.5\text{--}100 \text{ m}^2 \text{g}^{-1}$, and the mean particle diameter estimated from the specific surface area is $14\text{--}62 \text{ nm}$ [36]. The BET results on the particle size are in good agreement with the TEM results. When BET is used to calculate the particle size from specific surface area for hydrothermally

synthesized TiO₂ nanoparticles, the particle size is 32–100 nm and consistent with the SEM measurement [37]. For CeO₂ nanoparticles synthesized by thermal decomposition, single point BET results demonstrate that CeO₂ synthesized at different precipitation rates have different specific surface areas, with 45 m² g⁻¹ for slow precipitation and 17 m² g⁻¹ for rapid precipitation [38].

The advantage of the BET gas adsorption technique is that it can measure a large number of nanoparticles. Also, the technique is relatively quick, inexpensive, and simple. Nanoparticle sizes can be inferred by assuming regular particle shapes. However, the BET technique cannot distinguish loosely packed nanoparticles, agglomerated nanoparticles, or mesoporous three-dimensional nanoparticle network. The results only reflect the surface area of the nanoparticle collections regardless of the nanoscale details. This should be kept in mind when nanoparticle size extrapolation is exercised.

3.5 POROSITY AND PORE SIZE

First, it should be mentioned that, dimension-wise, pore size has a very different definition compared to particle size. Pores with size <2 nm are called micropores, with size >2 nm but <50 nm are called mesopores, and with size >50 nm are called macropores. There are four aspects in describing pores: pore size, pore size distribution, pore volume (porosity), and pore shape. However, just as for particle shape, pore shape measurement is rare and most descriptions on pore shape are qualitative. In light of this, most pores are assumed to have simple shapes, such as spherical or cylindrical. Because of the small size of nanoparticles, pores inside individual nanoparticles are mostly ignored. Pores measured are most likely interparticle pores rather than intraparticle pores. Most pore size and porosity characterization efforts are focused on pores generated by a collection of nanoparticles or nanoparticle-based bulk samples instead of the internal pores of individual nanoparticles. Since pore size scales with particle size and nanoparticles do not pack as densely as micron-sized particles, porosity is generally very high and pore sizes are mostly in the nanometer range. If nanoparticles are agglomerated, the agglomerates can generate micron-sized pores. Different techniques can be used to measure pores, but the most important ones are electron imaging and BET gas adsorption. For micropores <2 nm, it is difficult to quantitatively determine pore size distribution; and direct imaging observation provides some qualitative description. For mesopores between 2 and 50 nm, gas condensation by BET is more suitable. For macropores >50 nm, conventional techniques such as liquid intrusion by mercury porosimetry become applicable and will not be discussed here.

3.5.1 Electron Imaging

As a direct observation technique, pore size and shape characterization within or between individual nanoparticles can be carried out by TEM. Nanoparticles

can be imbedded in a matrix, cross-sectioned, and observed in a TEM. This approach provides direct evaluation of pores. However, TEM sample preparation is challenging, especially when the original nanoparticle arrangement needs to be preserved or the samples are porous. Artificial defects such as filling and smearing of pores can be easily created. Also, the evaluation is mostly qualitative in very local areas in order to obtain a high resolution. For pores in the single nanometer range, imperfect pore wall structures such as roughness in the subnanometer scale cannot be neglected. Several new techniques are proposed for nanopore characterization, such as small-angle neutron scattering, superwide pressure range adsorption, and X-ray absorption spectroscopy [39]. However, the reliability and maturity of these techniques are yet to be tested. Readers are encouraged to study these different techniques for details. So far, TEM has not been widely used to analyze interior nanoparticle pores. We expect this technique to be put into practice more often as nanoparticle research progresses, especially with more widespread availability of high-resolution TEM.

As for the pores in a nanoparticle-based bulk sample, the two-dimensional nature of the imaging aspect and the extensive effort required to prepare the samples make it a less appealing technique. SEM imaging of the fracture surface (if the resolution is high enough) and gas adsorption (assuming pores are open pores) are often more useful and statistically more significant.

3.5.2 Gas Adsorption

In gas adsorption, the adsorbed gas condenses into a liquid in the nanopores when the gas pressure is high. The amount of condensed gas versus the gas pressure can be used to analyze the pore size and pore size distribution based on the Kelvin equation:

$$\ln \frac{p}{p_{s,L}} = \frac{-2\gamma_{LV}V_L \cos \varphi}{RT_b r_m}, \quad (3.9)$$

where p is the gas pressure over a meniscus with radius r_m , $p_{s,L}$ is the saturation pressure of the liquid on a plane surface, γ_{LV} is the surface tension of the liquid–solid interface, V_L is the molar volume of the liquid, φ is the contact angle between the liquid and the pore wall, R is gas constant, and T_b is the boiling point of the gas used. Nitrogen condenses at 77 K and is the most common adsorbate. The total pore volume V_P can be obtained from the amount of gas adsorbed when the relative pressure $\frac{p}{p_{s,L}}$ is close to unity, assuming that the pores are filled with condensed liquid adsorbate [40]:

$$V_P = \frac{P_a V_{ads} V_{Lads}}{RT}, \quad (3.10)$$

where P_a is ambient pressure, V_{Lads} is the molar volume of liquid adsorbate, and V_{ads} is the volume of adsorbed gas. Pore size can then be calculated from the above pore volume, assuming cylindrical pore geometry:

$$r_p = \frac{2V_p}{S_w}, \quad (3.11)$$

where r_p is the average pore radius.

For BaO- and MgO-modified ZrO₂ nanoparticles synthesized using coprecipitation, pore volume and average pore size are obtained from the desorption data of nitrogen adsorption/desorption versus $p/p_{s,L}$ (up to 1.0) isotherm [41]. The isotherms show a type-V adsorption pattern (for different type of gas adsorption isotherms, refer to some excellent books [7, 42], which is typical of mesoporous structure adsorption with pore sizes between 2 and 50 nm. The actual pore size is in the range of 8.4–19.1 nm. Nitrogen adsorption is used to measure the micropore sizes and the pore size distribution of colloidal SiO₂ nanoparticles synthesized by a sol–gel method [43]. The measurement yields a mean micropore size of ~1 nm, consistent with the dimensions of nearly close-packed particles determined by AFM technique. For the pore size and distribution of TiO₂ nanoparticles prepared by hydrolysis, nitrogen adsorption shows that the pore size is about 10 nm and the distribution is unimodal [44].

While other techniques such as TEM require very small sample size and often times removal of the sample of interest from a substrate, BET can measure the packing characteristics of nanoparticles/nanograins on a substrate. For colloidal SiO₂ nanoparticles layer-by-layer coated onto organic pigment particles, the pore size distribution is broad, from 40 to 80 nm when only one layer of SiO₂ is coated [45]. This means the measurement is from the voids/missing particles of the coating layer. When the second layer of SiO₂ is coated, a narrow peak with an average pore size of 5 nm is observed. This indicates that the measurement is from the interstitial pores among three SiO₂ particles.

Gas adsorption is almost the only technique available to measure micro- and mesopores and has been extremely useful for the evaluation of nanoparticle collections. The assumption, however, is that the pores are cylindrical. When the pore diameter becomes comparable to the pore wall roughness, substantial errors can occur. Since the adsorbate gas has to access and condense inside the pores, only open pores are measured.

3.6 STRUCTURE

There are two aspects in nanoparticle structure characterization: surface structure and bulk structure. As the particle size approaches nanoscale, the volume fraction of the outermost layer increases dramatically. Nanoparticle surface structures play critical roles in processing and applications. Also, the surface structure can be very different from that of the micron or submicron counterparts in defects and

adsorbed species; it may also be significantly different from that of bulk materials. However, the differences can be difficult to measure, let alone to understand. For the nanoparticle-based bulk structure characterization, the resolution of the corresponding techniques often needs to be improved and specific care is needed in sample preparation. The most widely used techniques in surface structure analysis include low-energy electron diffraction (LEED) and SPM (including AFM and STM). For bulk structure analysis, important techniques include XRD and TEM.

3.6.1 Surface Structure

3.6.1.1 Low-Energy Electron Diffraction LEED is the principal technique for quantitative determination of surface structures in atomic resolution (~ 0.01 nm). It uses an electron beam with well-defined low-energy (typically in the range of 20–200 eV) incident normally on the sample. The incident electron energy should be low enough to ensure that most of the electrons (incident at right-angles to the surface) do not penetrate too deep beyond the outer atomic layer of the solid, thus enabling surface analysis. The sample itself must be a single crystal with a well-ordered surface structure in order to generate a back-scattered electron diffraction pattern. For two-dimensional surface structures, there are only five types of atomic arrangements: square, rectangular, centered rectangular, hexagonal, and oblique. Since nanoparticles are small, they generally contain a single crystallite and meet such a requirement. By the principles of wave-particle duality, the electron beam may be equally regarded as a succession of electron waves hitting the sample. These waves will be scattered by regions of highly localized electron density (i.e., the surface atoms), which can therefore be considered to act as point scatterers. The wavelength of electrons λ_e is given by the de Broglie relation:

$$\lambda_e = \frac{h}{(2m \cdot e \cdot E_a)^{1/2}}, \quad (3.12)$$

where m is electron mass (9.11×10^{-31} kg), e is electron charge (1.6×10^{-19} C), E_a is acceleration voltage (energy in eV), and h is the Planck constant (6.626×10^{-34} J s). Only elastically scattered electrons (changing direction without energy loss) contribute to the diffraction pattern; the lower energy (including secondary) electrons are removed by energy-filtering grids placed in front of the fluorescent screen that is employed to display the pattern.

LEED may be used qualitatively or quantitatively. For qualitative analysis, a diffraction pattern is recorded and analysis of the spot positions yields information on size, symmetry, and rotational alignment of a nanoparticle unit cell. For quantitative analysis, the intensities of various diffracted beams are recorded as a function of the incident electron beam energy to generate current–voltage curves that, by comparison with theoretical curves, may provide accurate information on positions and identities of all atoms in a unit cell.

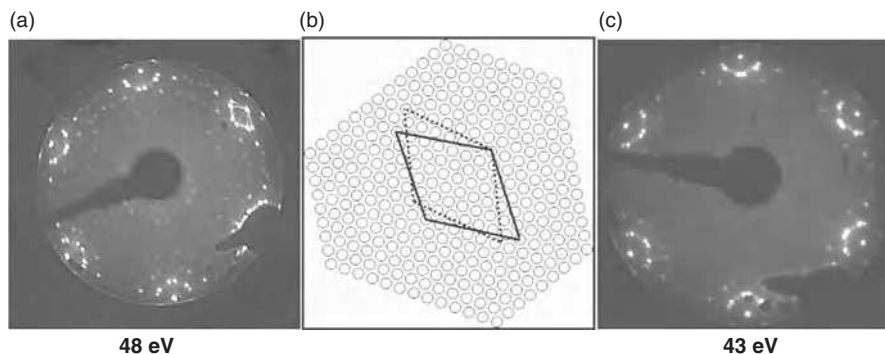


FIGURE 3.9 LEED images of $\text{TiO}_x/\text{Pt}(111)$ after a deposition time of 4 minutes (a) and 28 minutes (c). The two domains of the coincidence lattice with $18.2 \text{ \AA} \times 18.2 \text{ \AA}$ unit cell on the $\text{Pt}(111)$ substrate (circles) are shown in the real space representation (b) [46]. (Reproduced with permission from Sedona F, Eusebio M, Rizzi GA, Granozzi G, Ostermann D, Schierbaum K. Epitaxial TiO_2 nanoparticles on $\text{Pt}(111)$: A structural study by photoelectron diffraction and scanning tunneling microscopy. *Phys Chem Chem Phys* 2005;7(4):697–702. PCCP Owner Societies.)

For the growth mode of TiO_x nanoparticles on $\text{Pt}(111)$ surface, LEED shows a difference when TiO_x is first deposited (Fig. 3.9) [46]. The diffused background intensity increases with each deposition step (e.g., from 4 to 28 minutes). The diffraction pattern indicates superstructure formation with a unit cell size of $18.2 \times 18.2 \text{ \AA}$. LEED also provides long-range order information. The as-deposited $\text{Pd}/\text{TiO}_2(110)$ surface shows a hexagonal pattern and the size of the unit cells can be deduced from LEED with known palladium and TiO_2 lattice constants [47].

LEED can determine structural parameters very precisely. Atomic positions can be given within a tenth of an angstrom or better. However, the analysis requires a correct structural model, which can be refined in a trial-and-error iterative analysis. This can be a major problem for surfaces where reconstructions of large surface unit cells are needed. Many structural parameters have to be obtained correctly for reliable structural determination. Also, any unintentional adsorption of foreign species can lead to incorrect structural determination if the adsorbate is ordered, or to fruitless conclusions if the adsorbate has no order at all. The other issue is the challenge in studying insulating surfaces. The surface has to be knowingly made conductive by creating defects or by placing it on a conductive substrate while avoiding or removing the impact on the actual structure.

3.6.1.2 Atomic Force Microscopy In addition to nanoparticle size and shape measurement, the phase imaging mode of AFM can be used to detect variations in composition and other properties of nanoparticles or nanoparticle mixtures. Even though this approach cannot identify the exact nature of unknown phases, it can distinguish differences in crystallographic structures. Phase

imaging measures the phase difference between the oscillations of the cantilever and the detected oscillations. Properties such as stiffness and viscoelasticity are derived from image contrast. For example, AFM in phase imaging mode can distinguish different particles in a mixture. When AFM is used to characterize the surface morphology of $\text{Y}_2\text{O}_3/\text{Fe}_2\text{O}_3/\text{TiO}_2$ nanoparticle mixtures, differences in roughness and ordering of the studied surfaces are observed [48].

AFM can also provide a topographical map of a sample surface with a resolution down to a few nanometers and distinguish different nanoparticle species if these species have different morphologies. When MoO_3 nanocrystals slide on single crystal MoS_2 surfaces, highly anisotropic friction is observed when MoO_3 nanocrystals move along certain directions in the MoS_2 lattice, for example, in the channels defined by the sulfur atom rows of the MoO_2 surface [49]. Motion along the other two MoO_2 equivalent directions requires interfacial atoms to directly pass over each other. As a result, highly anisotropic friction is observed. Pure TiO_2 shows some degree of ordering with high roughness, indicating large nanoparticle size. TiO_2 doped with Fe^{3+} using an acid catalyst shows a random distribution of roughness. TiO_2 doped with Fe^{3+} using an ammonia catalyst shows lower surface roughness, implying that the grain growth of TiO_2 is inhibited [48].

One advantage of AFM over STM (to be discussed next) in composition analysis is that no current is required in the operation of AFM. Insulating surfaces and fragile surfaces that will be damaged by the tunneling current used in STM can be studied. The advantage of AFM over SEM is that it can provide nanoscale morphological results on a surface with a resolution of <0.1 nm, compared to ~ 5 nm resolution for SEM. Additionally, z direction measurement is available. For AFM itself, tapping mode is usually a better choice than contact mode when imaging poorly immobilized or soft samples.

3.6.1.3 Scanning Tunneling Microscopy Scanning tunneling microscopy is based on the concept of quantum tunneling. When a conducting tip is brought very near to a conductive surface, a bias (voltage difference) applied between the two allows electrons to tunnel through the vacuum or some other insulating media between them. The resulting tunneling current is a function of tip position, applied voltage, and the local density of states of the sample. Information about the surface is acquired by monitoring the current as the tip scans across the surface, and is usually displayed in an image form. STM can be a challenging technique as it requires extremely clean and stable surfaces, sharp tips, excellent vibration control, and sophisticated electronics. Binnig and Rohrer (at IBM Zürich) won the Nobel Prize in Physics in 1986 for inventing this technique [50]. STM has been widely used in characterizing nanostructures since its invention [51].

Figure 3.10 shows a sequence of STM images ((a)–(d)) during which atoms are extracted from Ge (111) surface [52]. In (a) and (b), atom 1 is labeled. In (b), atom 2 is labeled. In (c), atoms 1 and 2 are extracted while atoms 3 and 4 are labeled. In (d), atoms 3 and 4 are extracted. A line profile XX' through (b) (lower left corner) shows the missing atom 1, which correlates well with the

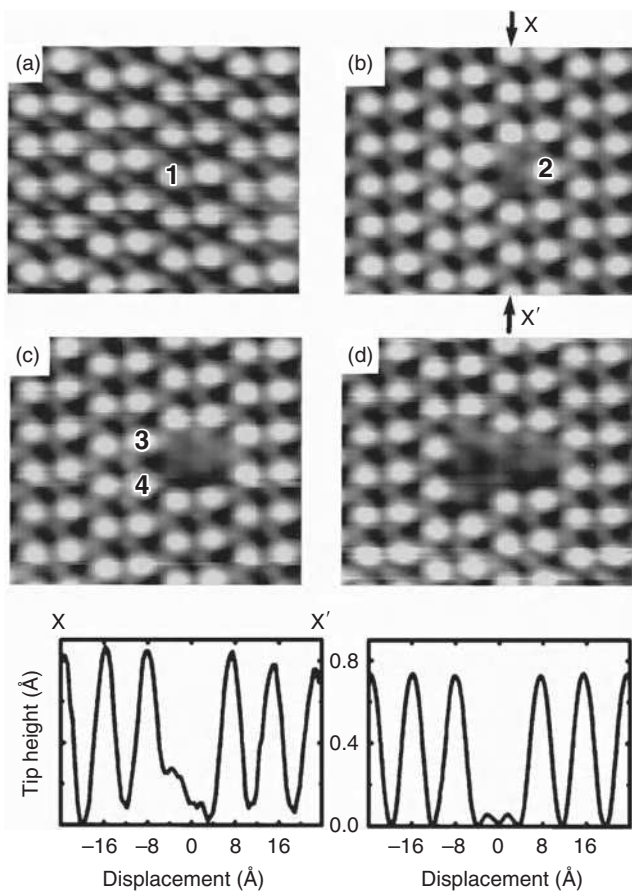


FIGURE 3.10 A sequence of STM images [(a)–(d)] during which atoms are extracted (area $53 \times 47 \text{ \AA}$, sample bias 1 V, tunnel current 1 nA). The selected atoms are indicated by numbers 1–4. A line profile XX' through (b) is shown at the lower left and a corresponding calculated line profile, for $I = 1 \text{ nA}$ at the bottom of the conduction band, at the lower right [52]. (Reprinted with permission from Dujardin G, Mayne A, Robert O, Rose F, Joachim C, Tang H. Vertical manipulation of individual atoms by a direct STM tip-surface contact on Ge(111). *Phys Rev Lett* 1998;80:3085–3088. Copyright 1998, American Physical Society.)

calculated line profile (lower right corner). Atomic-level resolution STM images of various TiO_2 particles formed after annealing at 700 K are obtained [53]. Some particles have a surface structure with a unit cell of $0.46 \text{ nm} \times 0.30 \text{ nm}$, which is consistent with TiO_2 rutile (100) structure. Some TiO_2 nanoparticle structures have short-range periodic arrangements not consistent with any TiO_2 structure. However, there are regions of the surfaces showing two lattice constants, 0.37 and 0.30 nm, which are typical for anatase (0.37 nm) and rutile (0.30 nm) TiO_2 , respectively. These images show an intermediate state of the transformation

from anatase to rutile phase. Such fine level and transition state crystal structure information can only be revealed by STM. Growth of iron nanoparticle assemblies on Au(111) herringbone surface is systematically studied by STM through the variation of (1) deposition coverage, (2) substrate temperature, (3) xenon buffer layer, and (4) nucleation seed effect. Iron deposited at 230–250 K results in regular nanoparticle arrays, which can serve as templates with well-ordered nucleation sites [54].

The subnanometer resolution of STM is very desirable. However, STM requires that the surface studied is conductive or is made conductive. Also, the surface structure is strictly obtained from direct measurement, not from diffraction pattern calculations. This can be a disadvantage if the surface structure is poorly defined or is a mixture of multiple phases.

3.6.2 Bulk Structure

3.6.2.1 X-ray Diffraction XRD was discovered by von Laue in 1912 and thereafter has been widely used for structural and chemical composition analyses of crystalline materials. When X-ray photons collide with the electrons orbiting around an atom, some photons from the incident beam will be deflected away from the direction where they were originally traveling, much like billiard balls bouncing off one another. If the wavelength of these scattered X-rays does not change (meaning that the X-ray photons do not lose any energy), the process is called elastic scattering, and the momentum is only transferred in the scattering process. These are the X-rays measured in diffraction experiments. The fundamental basis is that the XRD pattern is unique for each crystalline material because of its own unique combination of unit cell structures/dimensions. By determining the interplanar spacing of a crystal structure, unknown materials can be identified. Changes in peak positions can be attributed to composition variations or structure differences. This technique is capable of providing qualitative and quantitative information about the crystalline phase(s) of nanoparticles and nanoparticle-based materials and can be used to analyze both single crystals and polycrystals. The compositions of the crystalline phases can be determined by comparing the intensities of the diffraction peaks with standards.

After synthesis, nanoparticles can exist as an amorphous phase, a crystalline phase, or mixed crystalline phases. XRD of hydrothermally synthesized Fe_2O_3 – SnO_2 nanoparticles shows drastic phase changes in relation to tin concentration x [9]. Peak broadening is observed at different tin concentrations. At $x = 0.0$, the XRD pattern corresponds to pure α - Fe_2O_3 phase. Small changes in the line positions and broadening are observed at $x = 0.08$. At $x = 0.21$, the characteristic lines of SnO_2 appear. As the tin content in the samples increases, the amount of α - Fe_2O_3 phase diminishes. At $x = 0.86$, only the large peaks corresponding to SnO_2 structure are observed. At $x = 1.0$, the XRD pattern corresponds to pure tetragonal SnO_2 phase.

For 1.5–15 nm palladium nanoparticles synthesized by reduction of PdCl_2 , XRD results indicate the existence of face-centered cubic structure [55]. The

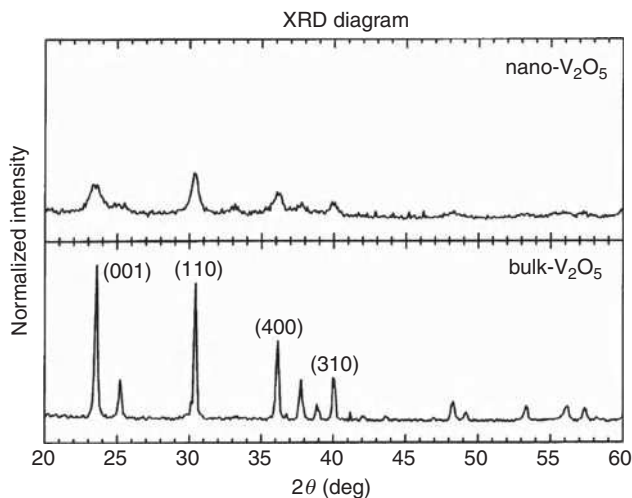


FIGURE 3.11 XRD patterns of bulk and nanostructured V₂O₅ [57] (Reprinted with permission from Guimarães JL, Abbate M, Betim SB, Alves MCM. Preparation and characterization of TiO₂ and V₂O₅ nanoparticles produced by ball-milling. *J Alloys Compd* 2003;352:16–20, Copyright 2003, Elsevier.)

XRD patterns for Cu₃P and Ni₂P nanoparticles synthesized via a solvothermal method show hexagonal phases for both materials [56]. The mean crystalline sizes are 26 nm and 16 nm for Cu₃P and Ni₂P, respectively, based on the Scherrer equation explained previously.

Figure 3.11 shows the XRD patterns of both bulk and nanostructured V₂O₅. All the diffraction peaks in the XRD pattern of bulk V₂O₅ can be indexed (for simplicity, only the most intense diffraction peaks are labeled in Fig. 3.11). The structure is orthorhombic with $a = 11.510 \text{ \AA}$, $b = 3.559 \text{ \AA}$, and $c = 4.371 \text{ \AA}$. This shows that the bulk V₂O₅ is single phase and free from impurities [57]. For V₂O₅ nanoparticles, the peaks are wider (line broadening effect) and the peak intensity is lower (less diffraction from the limited nanoparticle population). However, the peak positions remain the same.

XRD has the significance of characterizing structures with long-range order, although it is not as valid for disordered, amorphous structures. Each crystalline phase has a unique XRD pattern, which can be used as the “fingerprint.” Other advantages of XRD include the nondestructive nature, the capability to quickly identify materials, the large library source of crystalline structures, and the ability to analyze crystalline mixtures. The XRD technique has a detection limit of 0.1~1 wt%.

3.6.2.2 Electron Diffraction TEM can provide not only images of nanoparticles but also diffraction patterns for structural characterization. The fundamental principle is the same as that of XRD except that the incident beam is electrons

instead of X-rays. Since high-resolution TEM can resolve up to sub-angstrom, characterization of crystallographic structures at atomic scale is also possible. When a local structure cannot be examined by XRD, high-resolution TEM is the best alternative. It can focus on single nanometer-sized areas and acquire different electron diffraction patterns. Because of the limited number of crystals (sometimes only one) in the view, only segmented diffraction rings or spots can be obtained.

One example is shown in Figure 3.12 [58]. Crystalline Ni_3B with a fused nanoparticle porous network is synthesized using a modified polyol method (synthesis of metal-containing compounds in poly(ethylene glycol)s). Ethylene glycol acts as both the solvent and the reducing agent. KBH_4 serves both as a reducing agent for Ni^{2+} and as a boron source, while tetraethylene glycol serves as a solvent capable of achieving reaction temperatures that can crystallize Ni_3B . The TEM image of the particles obtained immediately after reduction shows an aggregated network made up of 50–90 nm particles that are amorphous based on the diffuse ring pattern observed by electron diffraction (Fig. 3.12a). This stage corresponds to the nucleation burst and aggregation that occur quickly due to the introduction of a large excess of borohydride. Many small nuclei are produced, which quickly aggregate into larger spherical particle networks to minimize their exposed surface area. The aliquot (a portion of a larger whole, especially a sample taken for chemical analysis) taken at 120°C shows similar fused nanoparticle morphology and remains amorphous by selected area electron diffraction (Fig. 3.12b). At this stage, intraparticle ripening begins, leading to a slight smoothing of the hierarchical nanoparticle surface. The smoother surface minimizes the surface energy of the network, further stabilizing the nanoparticles. Further heating (Fig. 3.12c) results in the crystallization of the Ni_3B phase, evidenced by the appearance of crystalline diffraction spots in the selected area electron diffraction. Here, the primary particles making up the aggregates in Figures 3.12a and b are no longer evident, having coalesced into a dense, fused, nanowire-like aggregate. Sintering of the smaller aggregated spheres into the larger crystalline spheres (e.g., the progression from Figs. 3.12b and c) possibly helps to facilitate the entrapment of the boron in the final product since boron usually has a very low solubility in nickel and would otherwise be prone to phase separation. Finally, the sample annealed at 450°C under argon is face-centered cubic nickel, consisting of a similar network-like fused nanoparticle morphology (Fig. 3.12d).

TEM can determine the positions of defects and the types of defects present if the orientation of the sample is carefully selected. When a sample is oriented such that one particular plane is only slightly tilted away from the strongest diffracting Bragg angle, any distortion of the crystal plane that locally tilts the plane to the Bragg angle will generate strong variations in contrast. However, defects only produce displacement of atoms that do not tilt the crystal to the Bragg angle and do not generate strong contrast. This difference allows for distinction between crystal distortion and defect presence. In TEM, images are generated from the contrast due to the difference in the phase of electron waves. As a result, image

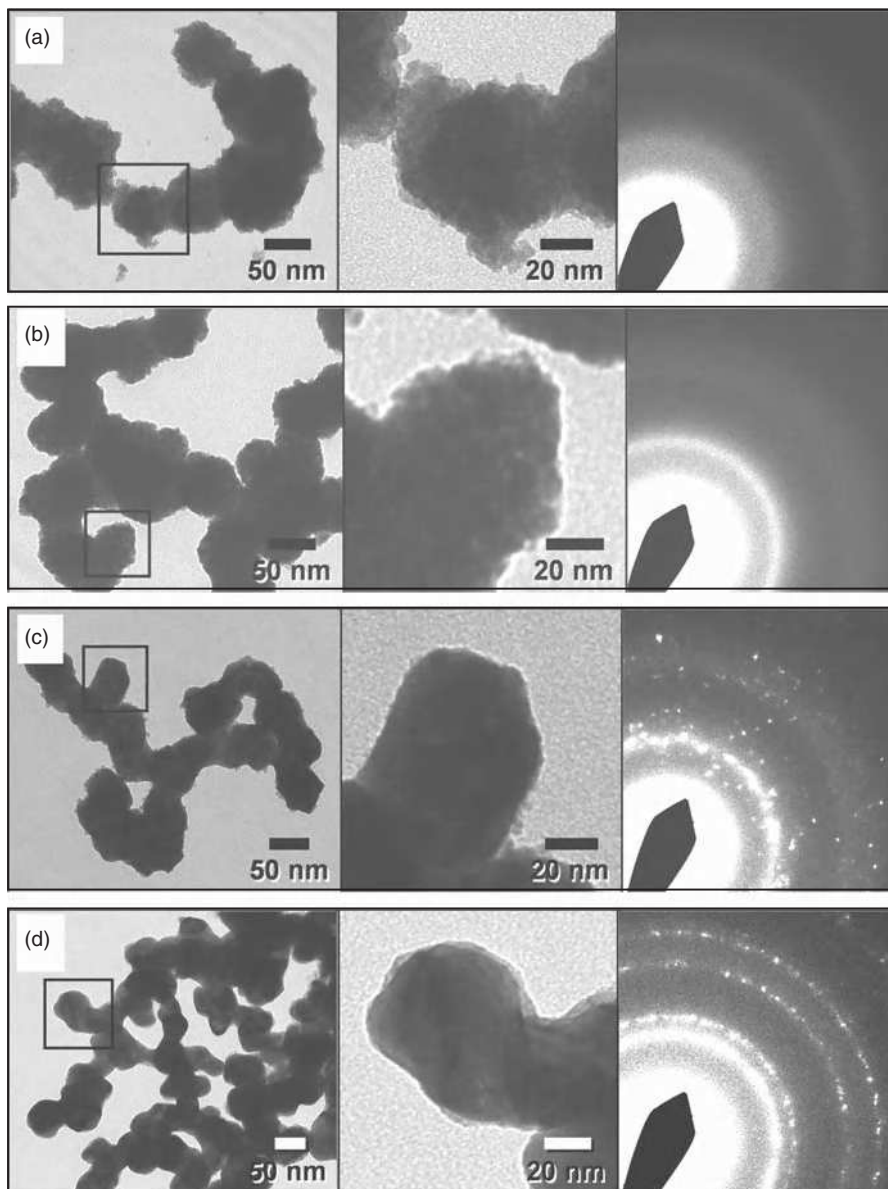


FIGURE 3.12 TEM images (left and middle in two magnifications) and electron diffraction patterns (right) for (a) amorphous Ni–B alloy at 100°C in tetraethylene glycol, (b) amorphous Ni–B alloy at 120°C in tetraethylene glycol, (c) crystalline Ni₃B at 280°C in tetraethylene glycol, and (d) boron-containing face-centered cubic nickel prepared by heating isolated Ni₃B powder in argon at 450°C [58]. (Reprinted with permission from Schaefer ZL, Ke X, Schiffer P, Schaak RE. Direct solution synthesis, reaction pathway studies, and structural characterization of crystalline Ni₃B nanoparticles. *J Phys Chem C* 2008;112:19846–19851, Copyright 2008, American Chemical Society.)

contrast difference can also provide phase information, similar to an atomic force microscope in the phase imaging mode.

Palladium nanoparticles are made by reducing H_2PdCl_4 with different alcohols and stabilizing with polyvinylpyrrolidone (PVP). High-resolution TEM analysis shows different geometric shapes including triangular, rhombohedral, square, pentagonal, and hexagonal shapes [55]. For monodispersed BaTiO_3 nanoparticles, lattice images are recorded and a perovskite cubic structure is indicated by the TEM results (Fig. 3.13) [59]. A bimetallic alkoxide molecular precursor is used to ensure the correct stoichiometry of the product during the sol-gel synthesis. The reactant precursor is highly sensitive to moisture, and there is no need for acid/base catalyzed hydrolysis in this case. Figure 3.13a shows the lattice image of a BaTiO_3 particle viewed along the [110] projection. A single

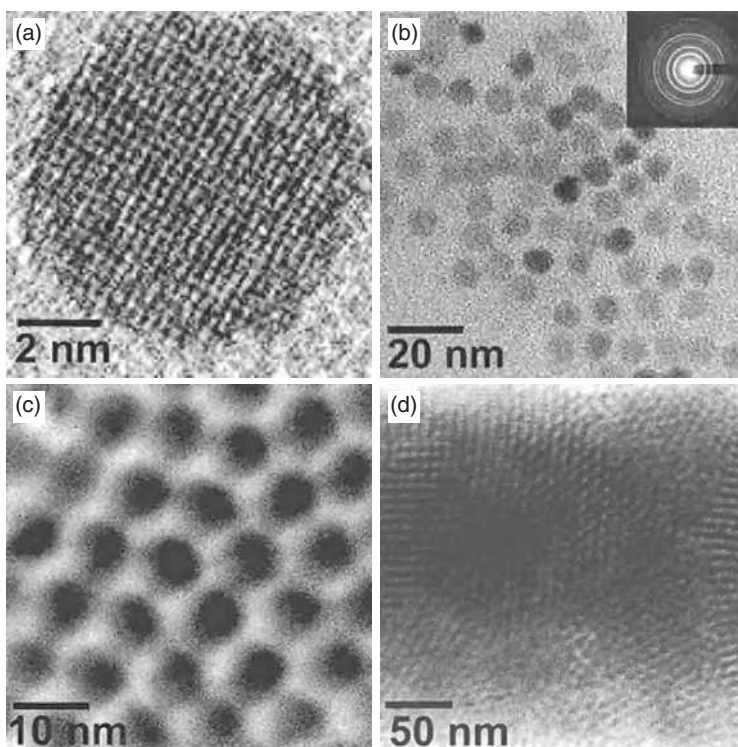


FIGURE 3.13 Transmission electron micrographs of (a) a high-resolution lattice image of an individual, 8 nm diameter BaTiO_3 nanoparticle and (b) an ensemble of discrete, 8 nm BaTiO_3 nanoparticles. Inset: selected area electron diffraction pattern. (c) Self-organization of BaTiO_3 nanoparticles. (d) Superlattice of 8 nm diameter BaTiO_3 nanoparticles [59]. (Reprinted with permission from O'Brien S, Brus L, Murray CB. Synthesis of monodisperse nanoparticles of barium titanate: toward a generalized strategy of oxide nanoparticle synthesis. *J Am Chem Soc* 2001;123:12085–12086, Copyright 2001, American Chemical Society.)

crystal domain can be seen. The selected area electron diffraction pattern (Fig. 3.13b, inset) can be indexed to cubic symmetry, indicating that BaTiO₃ is in the perovskite cubic phase. Ionic displacement in BaTiO₃ that gives rise to ferroelectricity results in distortions to the noncentrosymmetric tetragonal phase. Changes in lattice constants are typically $\geq 1\%$ ($c = 4.036 \text{ \AA}$; $a = 3.992 \text{ \AA}$). Figure 3.13c shows the self-organization of BaTiO₃ nanoparticles, and Figure 3.13d shows the superlattice of 8 nm diameter BaTiO₃ nanoparticles.

Because of its ability to determine the crystal structure of a species adsorbed/coated/imbedded in a different matrix and to identify impurities at specific atomic locations, high-resolution transmission electron diffraction has become an indispensable tool for nanoparticle and nanoparticle-based material characterization. However, it should be emphasized that transmission electron diffraction only examines very localized areas. The results should be carefully examined when used to represent nanostructures across a larger scale.

3.6.2.3 Neutron Diffraction Neutron diffraction for crystal structure analysis is similar in principle to XRD and electron diffraction except that the beam source is neutrons, which interact directly with the nucleus of an atom. Consequently, the contribution to the diffracted intensity is different for each isotope; for example, hydrogen and deuterium contribute differently during the neutron diffraction analysis. It is also often the case that light (low atomic number) atoms contribute strongly to the diffracted intensity even in the presence of high atomic number atoms. The scattering length varies from isotope to isotope rather than linearly with the atomic number. Nonmagnetic neutron diffraction is sensitive to the positions of the nuclei of the atoms and can give very precise values for the atomic positions in the structure. Although neutrons are uncharged, they carry a spin, and therefore interact with magnetic moments, including those arising from the electron cloud around an atom. Neutron diffraction can therefore reveal the microscopic magnetic structure of a material.

During characterization, a sample is placed in a neutron beam; the beam is diffracted by the periodic lattice of the crystalline material according to Bragg's law. The temperature evolution of CuO nanoparticles in the temperature range of 1.5–250 K has been investigated by neutron diffraction. The CuO particles are obtained by Cu(NO₃)₂·3H₂O decomposition directly in the pores of a porous glass. The average particle size is 15 nm and is almost temperature-independent. Neutron diffraction of ZrO₂ nanoparticles at several temperatures allows one to monitor the reconstructive tetragonal to monoclinic phase transition as a function of nanoparticle size [60]. During the experiments, the diffraction patterns at each temperature are collected, just as what is done in XRD. These diffraction patterns also simultaneously reflect the change of the tetragonal and monoclinic volume fractions in the sample. Rietveld refinements on diffraction patterns allow one to measure accurately the intrinsic integral breadths of Bragg peaks of nanocrystals. The evolution of the peak breadths versus the Bragg angles gives an estimation

of nanoparticle sizes at each temperature. The structure of the tetragonal phase observed in the nanocrystals is identical to that observed in micron-sized ZrO_2 above 1400 K. A uniaxial strain dependency on grain size is observed. The phase transition occurs above a threshold crystal size. These results can be understood as a mechanism of size-dependent phase transition where the primary order parameter is altered by the nanoparticle size.

3.7 COMPOSITION

Similar to crystal structure characterization, composition analysis can be divided into surface and bulk composition analyses. Surface composition plays an important role in nanoparticle processing and properties, especially for nanoparticles that have at least 10% constituting species residing on the surface [61]. There are three techniques currently used in nanoparticle surface composition analysis: Auger electron spectroscopy (electron emission, AES), X-ray photoelectron spectroscopy (photoelectron emission, XPS), and secondary ion mass spectroscopy (ion emission, SIMS). All these surface analytical techniques can provide both qualitative and quantitative surface composition data but need to be carried out in an ultrahigh vacuum. Even though they are primarily used for surface composition analysis (≤ 2 nm), these surface analytical techniques can obtain information from much deeper layers by sequential surface removal (also called depth profiling). Nanoparticle or nanostructured bulk material composition can be quantitatively analyzed by several techniques: optical atomic spectroscopy, X-ray fluorescence spectroscopy (XFS), energy dispersive X-ray spectroscopy (EDS), electron energy-loss spectroscopy (EELS), Fourier transform infrared spectroscopy (FT-IR), ultraviolet-visible absorption spectroscopy (UV-vis spectroscopy), and Raman spectroscopy. Even though XRD can provide compositional information for crystalline nanoparticles, the accuracy of the technique is often lower than desired and will not be discussed here.

3.7.1 Surface Composition

3.7.1.1 Auger Electron Spectroscopy When an incident electron beam of 3–20 keV hits nanoparticles, electrons in the nanoparticle surface layers will emit from the inner electron orbitals upon collision with incident electrons. When the resultant vacant sites are filled by the electrons from the outer orbitals of the atom, the released energy can be transferred to other electrons and cause them to eject from the atom. These ejected electrons are called Auger electrons, which can be detected by an electron spectrometer when they escape from the sample surface. This is called Auger electron spectroscopy (AES) (Fig. 3.14). AES involves the detection of electrons emitted from the samples with kinetic energies typically below 2000 eV and has a high surface sensitivity that arises

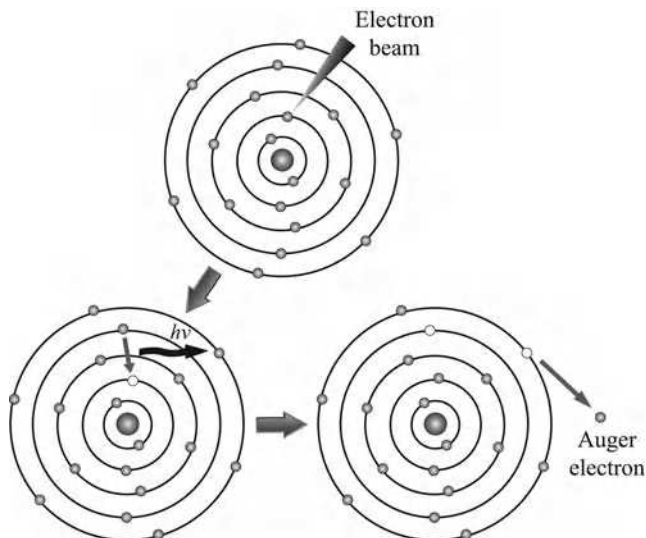


FIGURE 3.14 Auger electron generation process. (For a color version of this figure, see the color plate section.)

from the short distances that electrons travel at these energies without undergoing inelastic scattering and energy loss. The low energies of these electrons also mean that the electrons detected in Auger peaks are from the outer few nanometers of a sample. The released energy associated with the electron emission from the atom is characteristic of the specific element. Therefore, the identity of the elements and the determination of the surface compositions can be realized by comparing the experimental and standard Auger spectra for individual elements. Because an electron beam can be focused to <5 nm in size, it is possible to analyze the compositions of individual nanoparticles with AES. At the same time, AES is very sensitive to surface composition variations. It can desirably measure particle coatings, contamination, and oxidation states.

AES is used to study GaP and silicon semiconductors in order to understand the surface chemical change as a function of exposure to the atmosphere, electron irradiation, and Ar^+ ion etching [62]. By comparison with the corresponding atomically clean surfaces obtained by ultrahigh vacuum cleavage, the quantitative results show that exposure to air produces the build-up of an oxidation/contamination layer. GaP develops a P_xO_y -rich layer in the more external regions (~ 0.4 nm), whereas the chemistry of the inner regions (2–3 nm) is comparatively less affected. Electron irradiation affects the surface chemistry of atomically clean GaP to a much greater extent than that of silicon. Indeed, short (3 hours) irradiation is already sufficient to “deposit” sizable amounts of oxidic and carbonaceous species, which spread coherently over the entire GaP surface. Conversely, no appreciable chemical change is observed in the AES spectra of

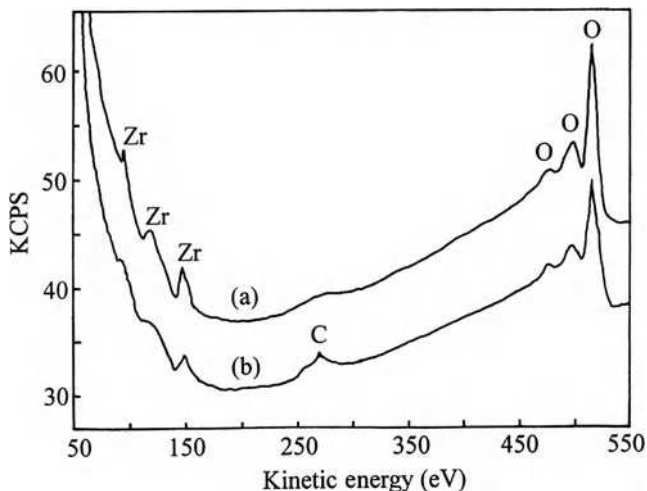


FIGURE 3.15 AES spectra of: (a) ZrO₂ particles, (b) PEI adsorbed ZrO₂ particles [63]. (Reprinted with permission from Wang J, Gao L. Surface properties of polymer adsorbed zirconia nanoparticles. *Nanostruct Mater* 1999;11:451–457, Copyright 1999, Elsevier.)

silicon for durations ≤ 24 hours. The silicon surface is covered with a SiO₂-like film, which can be removed for the most part by Ar⁺ etching. The surface left after this treatment is meaningfully less carbon- and oxygen-rich than that obtained by exposing the cleaved material to the atmosphere for a few seconds.

For ZrO₂ nanoparticle (3 mol% yttria doped) aqueous suspensions dispersed with polyethylenimine (PEI), the surface bond structure of PEI adsorbed on ZrO₂ is investigated by AES analysis [63]. The PEI coatings influence the surface structure of core ZrO₂ particles as shown in Figure 3.15. The AES spectra of uncoated ZrO₂ nanoparticles show distinctive peaks of zirconium at 94, 120, and 150 eV in curve (a). After PEI adsorption, however, the low kinetic energy peaks of zirconium at 94 and 120 eV are almost annihilated. Simultaneously, a broad carbon peak appears at about 285 eV, the characteristic position for the carbon 1s electrons. The apparent intensity decreases of low-energy zirconium peaks suggest that PEI adsorption is a surface chemisorption process. The formation of O–H–N hydrogen bonds between ZrO₂ and PEI molecular chains on the solid/liquid interfaces affects the AES spectra of ZrO₂ at the low-energy terminal, which reflects the surface atomic structure within a limited depth. The chemisorption of PEI onto ZrO₂ nanoparticles affects the interfacial features of ZrO₂ aqueous suspensions. Electrochemically prepared silicon nanoparticles without and with titanium or nickel are characterized using AES [64]. Metal deposition on the nanoparticle surface decreases the oxygen and carbon contents but increases the size of silicon nanoparticles.

AES is a popular technique for determining the composition of the top few atomic layers of nanoparticles or nanoparticle-based materials. The analysis

depth is normally between 10 and 100 Å. Except for hydrogen and helium, AES is sensitive to all the other elements in the periodic table, and it is especially sensitive to the low atomic number elements, in which electrons are more tightly bound to a nucleus. The advantages of AES are that the characterization process is fairly rapid and provides high reproducibility of the results. The disadvantages are that it is largely used for elemental analysis and not reliable for nonconductive nanoparticles because of electrostatic charging. Even though oxidation states should be detected by a chemical shift for Auger transitions, such shifts cannot always be easily correlated to a shift of a particular level. A fine structure of Auger peaks is needed, but sometimes the peaks are convoluted, which hinders oxidation state analysis. The size of nanoparticles (and interactions with the substrate) can impact the binding energy and peak width of photoelectrons, change the valence band peak shapes, and alter the Auger parameters. As explained before, surface species can be removed layer-by-layer for consecutive analysis and three-dimensional data acquisition (depth profiling), mostly by ion bombardment.

3.7.1.2 X-ray Photoelectron Spectroscopy In XPS, the sample surface is irradiated by a low-energy X-ray photon source and photoelectrons are ejected from the sample surface (Fig. 3.16):

$$E_{\text{binding}} = h\nu - E_{\text{kinetic}} - W, \quad (3.13)$$

where E_{binding} is the binding energy of photoelectrons, h is the Planck constant, ν_X is the frequency of the X-ray photons used, E_{kinetic} is the kinetic energy of the ejected photoelectrons, and W is the work function of the spectrometer. E_{binding} is characteristic of the analyzed elements and the orbit from which the electrons are emitted. According to Equation (3.13), the binding energy can be determined by measuring the kinetic energy with known W . A typical XPS spectrum is a plot of the number of photoelectrons ejected versus a set of binding energies of these electrons being detected. Elements on the sample surface can thus be identified

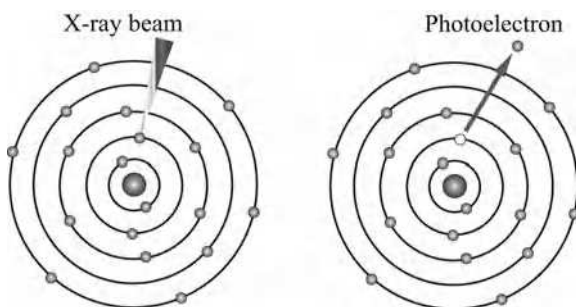


FIGURE 3.16 X-ray photoelectron generation process. (For a color version of this figure, see the color plate section.)

using XPS peaks rising at their characteristic binding energies. The peak areas can be used to calculate the amounts of the elements, from which the atomic ratio of the surface elements can be obtained after normalization.

Although a wider range of energies is available when synchrotron X-ray sources are used for XPS, most of the X-ray photoelectron spectrometers use laboratory-based X-ray sources, which have much lower energies than the synchrotron X-ray source. XPS does not have the spatial resolution to analyze individual nanoparticles (with the possible exception of a few special synchrotron-based systems with a highly focused and bright source of X-rays). However, it is often possible to analyze collections of particles (in a single layer or, effectively, in a powder form). For nanoparticles and nanoparticle-based materials, XPS has become one of the most highly used and important tools for surface composition analysis. Even though sometimes it is not considered a “nanoscale analysis method,” XPS can provide a great deal of information about elemental distributions, layer or coating structures and thicknesses, surface functionality, and even particle sizes on the 1–20 nm scale for sample types that may not be readily analyzed by other methods. This information is important for both nanoparticles and a variety of nanostructured bulk materials. Nonetheless, surface contamination, oxidation, and adsorption should be carefully controlled to avoid unintentional errors in XPS analysis.

XPS is employed to monitor the chemical states during the synthesis of TiO_2 nanoparticles [53]. Titanium oxidation state change is observed when the temperature is increased. The influence of organic materials on the reactivity of iron metal-core/oxide-shell nanoparticles in deionized water serves as an example of both the formation of coatings and their impact. The XPS measurements (Fig. 3.17) show that the iron near the surface starts as Fe^{3+} , but an Fe^{2+} component forms after the exposure to the solution. The XPS results also show that the nature of the surface carbon and oxygen is altered by both water exposure and the presence of organic materials [5].

XPS is a unique technique that can provide not only qualitative and quantitative information of the elemental composition of the surface but also information about chemical bonding (oxidation state) of surface atoms. Also, XPS can detect elements with atomic number from 3 to 103. Similar to AES, XPS is not suitable for hydrogen and helium detection and can only penetrate 1–10 nm depth into the sample surface because of the low energy of the X-ray source. XPS generally has a lateral resolution of 1 μm and depth resolution <3 nm. The detection limit is 100–1000 parts per million. Surface contamination should be strictly avoided, and high vacuum is needed during XPS characterization. As with AES, XPS can characterize sample depth compositions with layer-by-layer ion bombardment (depth profiling).

3.7.1.3 Secondary Ion Mass Spectroscopy In SIMS, secondary ions are detected and analyzed by a mass spectrometer when the surface of nanoparticles or nanoparticle-based materials is bombarded by an energetic primary

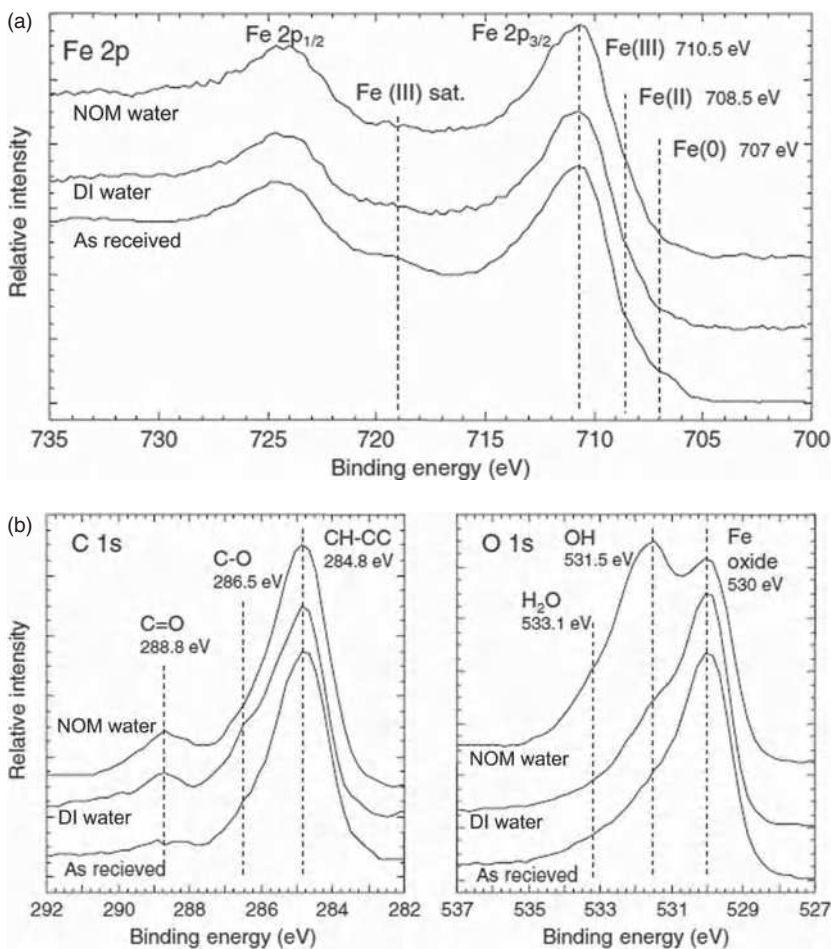


FIGURE 3.17 XPS data from iron metal-core/oxide-shell nanoparticles as received, after 24 hours of exposure to deionized water, and after 24 hours of exposure to deionized water containing 20 mg L⁻¹ natural organic material. The iron 2p photoelectron peaks are consistent with an initial oxide shell of mostly Fe³⁺. After the solution exposure, the decrease in the ~719 eV satellite and some peak broadening suggest the appearance of an Fe²⁺ component. More apparent is an increase of C = O bonds at ~289 eV in the carbon 1s photoelectron peaks for water and natural organic material exposure samples and the significant increase in the ~531.5 eV peak feature for oxygen 1s due to OH⁻ and other oxygen in the natural organic material [5]. (Reprinted with permission from Baer DR, Gaspar DJ, Nachimuthu P, Techane SD, Castner DG. Application of surface chemical analysis tools for characterization of nanoparticles. *Anal Bioanal Chem* 2010;396:983–1002, Springer Science + Business Media, Fig. 3.)

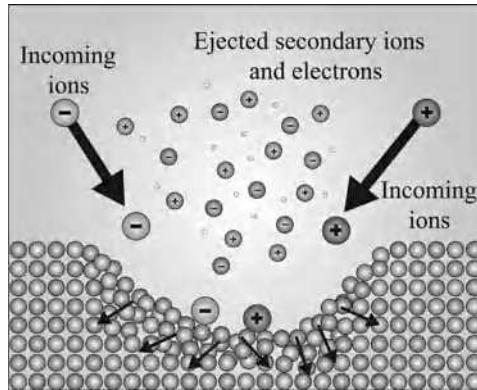


FIGURE 3.18 Ion bombardment process during secondary ion mass spectroscopy. (For a color version of this figure, see the color plate section.)

beam (Fig. 3.18). The primary beam can be electrons, ions, neutral particles, or photons. The primary source is capable of generating a beam of ions or atoms with energy in a range of 0.5–50 keV. The emitted ions are analyzed directly by a mass spectrometer to provide the chemical compositions of the surface. Positively and negatively charged species are collected and analyzed in separate spectra. Information on the chemical bonding of the atoms can also be extracted.

Ion beams can be used in a variety of ways to obtain information about the nature of nanoparticles and nanoparticle-based materials. SIMS is capable of one part per million to one part per billion sensitivity. The lateral resolution is 1 μm and the depth detection limit is ~ 0.1 nm. Depending on the rate of the surface ionization process, there are two modes of SIMS: static and dynamic. In static SIMS, a very low primary ion flux is directed at the nanoparticle surface so that the surface is ionized and removed slowly. Generally, the beam diameter is between 50 nm and 200 μm with the beam current in a range of 10^{-10} – 10^{-8} A, depending on the area analyzed. Dynamic SIMS employs a high flux of primary ions to obtain a high yield of secondary ions. The surface is ionized and removed rapidly, thus probing the bulk material down below the surface to obtain a depth profile. Beam current densities up to several $\text{A}\cdot\text{cm}^{-2}$ and beam energies > 5 keV are used in dynamic SIMS.

At a finer scale, time-of-flight mass spectrometry utilizes the fact that ions with the same energy but different masses travel with different velocities for composition analysis. Ions formed by a short ionization event are accelerated by an electrostatic field to a common energy and travel over a drift path to the detector. The lighter ions arrive before the heavier ones and a mass spectrum is recorded. Measuring the flight time for each ion allows for the determination of its mass. This cycle is repeated with a repetition rate that depends on the flight time of the highest mass to be recorded. Time-of-flight SIMS is useful for obtaining molecular information about surface layers, functional groups added

to the surface, and contamination. The advantages include the ability to detect all elements (including hydrogen) and high mass molecular species, high sensitivity (ppt per billion), and high surface specificity. One of the primary uses of time-of-flight SIMS is to extract molecular information about the functional groups and, possibly, the molecular orientation of coatings on particle surfaces. During time-of-flight SIMS measurements, primary ion beams of Ga^+ , Ar^+ , O^{2+} , Cs^+ , C_{60}^+ , Au^+ , Bi^+ , or other atomic, molecular, and cluster ions with energies between 3 and 20 keV strike the sample surface and result in the ejection of secondary ions. To extract surface molecular information, time-of-flight SIMS is used in a “static” mode that involves a low density and a low dose of ions such that the surface damage and alteration are minimized. Both atomic and molecular secondary ions are used to extract the surface information.

SIMS is used to study the nanostructural modification of the surface of tungsten samples made by nitrogen ion implantation [10]. The density of implanted nitrogen ions and the depth profile of nitrogen ions in tungsten as a function of temperature are measured. Both the N^+ density and the penetration depth of N^+ in tungsten samples show a minimum at a certain temperature, consistent with XRD results. For silver nanoparticle dispersion in SiO_2 -based sol-gel films, SIMS is carried out in ultrahigh vacuum conditions to measure the concentration profiles along the depth [65]. Silver concentration decreases with the treatment temperature. Silver diffusion toward the substrate is related to ion exchange with Na^+ ions from the soda-lime glass substrate. TiO_2 nanoparticle surfaces are modified by depositing a poly(acrylic acid) thin film through plasma polymerization [66]. Time-of-flight SIMS is employed to characterize the chemistry of the coated nanoparticles. It shows that plasma polymerization is an effective method to coat TiO_2 nanoparticles.

The advantages of SIMS are high spatial resolution, high sensitivity for quantitative elemental analysis, and the ability to provide a detailed analysis of the chemical composition of surfaces. Since only ions in the uppermost atomic layers of the bombarded surface are excited, SIMS has a high surface sensitivity. A unique feature of SIMS is its ability to analyze H^+ , which cannot be detected using other techniques. However, SIMS can be very sensitive to contamination during the sample preparation and measurement. To effectively use the technique, a pristine surface and a high vacuum are required. Also, SIMS causes damage to the surface during the analysis.

3.7.2 Bulk Composition

3.7.2.1 Optical Atomic Spectroscopy Optical atomic spectroscopy involves atomic absorption (AA) and atomic emission (AE). This method is based on transitions of electrons between the outer energy levels in atoms. Since each element has its own characteristic energy levels, elemental composition can be identified from the wavelength of absorbed or emitted radiation during the transition of electrons. The intensity of the radiation can be used to determine the relative amounts of the compositions. A high precision and a low detection limit

make the technique very valuable for the determination of major, minor, and trace elements.

In AA analysis, nanoparticles are dissolved in a liquid to form a solution. The liquid is then broken into fine droplets and vaporized into individual atoms by heating. Vaporization is mostly achieved by introducing droplets into a flame (flame atomic absorption spectrometry or flame AA). The advantage of flame AA is that it is rapid even though it often times analyzes compositions in a sequential manner. The main problems with flame AA are incomplete dissociation of refractory elements in the flame and difficulty in determining elements that have resonance lines in the far UV region. Therefore, elements such as boron, vanadium, tantalum, tungsten, phosphorous, sulfur, and halogens cannot be precisely determined by flame AA. Vaporization in a graphite furnace (furnace AA) provides better detection limits than flame AA. Optical absorption spectra are obtained to demonstrate the properties of CdSe nanoparticles synthesized by standard airless arrested precipitation from $\text{Cd}(\text{ClO}_4)_2 \cdot 6\text{H}_2\text{O}$ and bis(trimethylsilyl) selenium [67]. It shows that the absorption threshold shifts red with increasing average yield, as expected with increasing particle size. The stability of an Ag-containing organic dispersion is studied using optical absorption spectroscopy [68]. The insignificant change of the spectra indicates that the sol is highly stable under the examination conditions.

When a plasma is used for vaporizing a solution (inductively coupled plasma (ICP)), the incomplete elemental dissociation in flame AA can be eliminated because of higher decomposition temperatures. ICP also allows simultaneous analysis of several elements. However, ICP analysis of trace elements is slow and should only be used when the other two techniques cannot provide adequate information. $\text{TiO}_2/(\text{MoO}_3)_x$ core/shell nanoparticles are dissolved in concentrated sulfuric acid (H_2SO_4). The solution is then diluted and analyzed using ICP [69]. The results show different values of x from 0.18 to 1.8. For Fe/Au core/shell nanoparticles made from laser-assisted synthesis, ICP is used to characterize the composition, and the iron mass fraction measured by ICP is 23.5% [70]. For Ti-Fe nanoparticles synthesized using a hydrogen plasma-assisted technique, ICP is used to analyze the composition of different samples. Different titanium contents from 0 to 100 at% are detected [71].

In AE spectroscopy, a sample is put in a radiation environment to produce free atoms and excited states where transitions with high emission efficiency start [72]. As mentioned earlier, a radiation source is necessary in AE spectroscopy although different sources may be used. The most common source is a flame, which provides low temperature but satisfactory spatial and temporal stability. Arcs and sparks find their applications when analyzing solid samples and when many elements need to be analyzed. Plasma is an important source in the AE technique and is suitable for multielement detection and analysis of liquid samples. Electrically generated discharge can overcome the shortcoming of the low temperatures associated with flames while maintaining desirable radiation stability. At atmospheric pressure, the lowest temperature that the discharges can achieve is 5000 K, which is much higher than what a flame source can produce

(2000–3000 K). AE is capable of both qualitative and quantitative analysis. The unique spectral line of each element provides elemental identification. Nowadays, with the large database of reference spectra, line identification has become easy and without ambiguity. The intensity of an elemental line in the spectrum is used to quantitatively determine the content of the element interested. Since all elements in the sample emit light simultaneously in the radiation source, the AE technique has the advantage of multielement analysis. It can also carry out the analysis in sequence. Sequential spectroscopy is flexible since any elemental line and background wavelength within the spectral range (normally from 200 to 600 nm) can be measured. However, the technique is time consuming when many elements need to be analyzed.

It should be mentioned that optical atomic spectroscopy has long been in existence and is widely used for conventional materials. It generally requires gram-level samples for analysis. For nanoparticle materials, this is not always practical and the use of such a technique is not widespread.

3.7.2.2 X-ray Fluorescence Spectroscopy XRF is a technique for qualitatively and quantitatively determining elemental compositions by measuring the wavelengths and intensities of electron transitions from the outer to the inner energy levels of an atom. The energy associated with these transitions (0.6–60 keV) is significantly greater than that associated with those in optical atomic spectroscopy (a few eV). A beam of energetic X-rays is used in this method. The absorption of an X-ray leads to excited atoms due to the transition of electrons to higher energy levels. When excited atoms readjust to their ground states, there are two possible processes. One involves the rearrangement of the electrons, which leads to the ejection of electrons from higher energy levels—Auger electrons, which are the basis for AES discussed earlier. The other process leads to the emission of X-rays when the electrons transit from the outer levels to fill the vacant electron sites in the inner energy levels. This secondary X-ray beam emitted from the specimen is the basis for XRF (Fig. 3.19). The emitted radiation from a

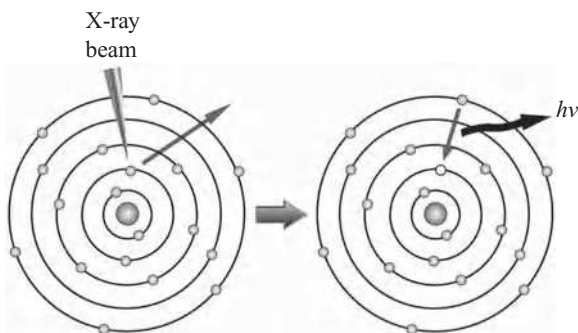


FIGURE 3.19 X-ray fluorescence spectroscopy working mechanism. (For a color version of this figure, see the color plate section.)

specimen can be diffracted through a single crystal to isolate narrow wavelength bands or analyzed with a proportional detector to isolate narrow energy bands. The relationship between wavelength and atomic number is then used to determine the specific element. The intensity of the spectral line is used to determine the concentration of the element.

By photolytic decomposition from ammine complex, palladium nanoparticles with sizes ranging from 1 to 5 nm are synthesized [73]. XRF is employed as a sensitive tool to detect the impurities and shows that PdO is not detected, which confirms that the product is palladium metal nanoparticles. For WO₃ nanoparticles of 18–25 nm size, XRF is used to determine the chemical composition of the particles and the relative deposition rate under different conditions [74]. However, the measurement only provides the relative amount of elemental tungsten in the deposits.

The difference between optical atomic spectroscopy and XRF is that the former works well for solutions and requires complete dissolution of the particles while the latter is ideal for solid samples. The XRF technique has been used for the measurement of major, minor, and trace elemental concentrations. The disadvantages are that the sensitivity of XRF decreases dramatically with decreasing atomic number and cannot be used for elements with atomic number smaller than 9.

3.7.2.3 Energy Dispersive X-ray Analysis The EDS technique detects X-rays emitted from the sample during the bombardment by an electron beam to characterize the elemental composition of the analyzed volume. When the sample is bombarded by an electron beam, electrons are ejected from the atoms comprising the sample (surface). The resulting electron vacancies are filled by electrons from a higher state, and an X-ray is emitted to balance the energy difference between the two electron states (Fig. 3.20). The X-ray energy is characteristic of the element from which it is emitted. The EDS X-ray detector measures the relative abundance of emitted X-rays versus their energies. The detector is typically

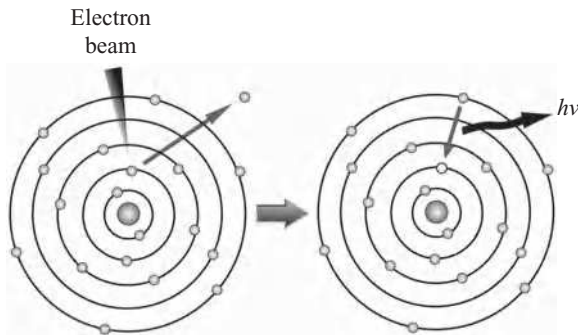


FIGURE 3.20 Energy dispersive spectroscopy working mechanism. (For a color version of this figure, see the color plate section.)

a lithium-drifted silicon solid-state device. When an incident X-ray strikes the detector, it creates a charge pulse that is proportional to the energy of the X-ray. The charge pulse is converted to a voltage pulse (which remains proportional to the X-ray energy) by a charge-sensitive preamplifier. The signal is then sent to a multichannel analyzer, where the pulses are sorted by voltage. The energy for each incident X-ray, as determined from the voltage measurement, is sent to a computer for display and further data evaluation. The spectrum of X-ray energy versus counts is evaluated to determine the elemental composition of the sampled volume. EDS analysis is available on TEM, SEM, and STEM (scanning transmission electron microscope) instruments to identify unknown species or to obtain information on the spatial distribution of certain species of interest. Specimen drift correction is usually required in order to obtain statistically meaningful X-ray signals when very small particles/samples are analyzed. Nevertheless, EDS can detect the presence of just a few atoms if the analyzed volume is small enough. Depending on the electron beam focusing capability, material properties, and sample size, features or phases as small as 1 nm can be analyzed. For EDS analysis from an SEM, the lateral and depth resolutions are $\sim 1 \mu\text{m}$ and the detection limit is 1000 parts per million. For EDS analysis from a TEM, the lateral and depth resolutions are $< 2 \text{ nm}$ and the detection limit is 1000 parts per million. Composition–location plots can provide the compositional profiles of individual nanoparticles or clusters, and reveal whether the compositions of individual nanoparticles vary with their sizes or their relative locations.

For qualitative EDS analysis, X-ray energy values from the EDS spectrum are compared with known characteristic X-ray energy values to determine the presence of an element in the sample. Elements with atomic numbers ranging from that of beryllium to uranium can be detected. Quantitative results can be obtained from the relative X-ray counts at the characteristic energy levels for the sample constituents. Semiquantitative results are readily available without standards by using mathematical corrections based on the analysis parameters and the sample composition. The accuracy of standardless analysis depends on the sample composition. Greater accuracy is obtained using known standards with similar structure and composition to that of the unknown sample. For elemental mapping, characteristic X-ray intensity is measured relative to lateral position on the sample. Variations in the X-ray intensity at a characteristic energy value indicate concentration changes of the examined element across the surface. Maps of multiple elements can be recorded simultaneously. In the line scan mode, an electron beam is scanned along a preselected line across the sample while X-rays are detected for discrete positions along the line. Analysis of the X-ray energy spectrum at each position provides plots of the elemental concentration of each element versus position along the line.

A composition–nanoparticle size plot obtained from a 2wt%Pd/1wt%Cu/ γ - Al_2O_3 bimetallic catalyst [75] shows that the composition of the individual Pd–Cu nanoparticles does not vary much with the size of the particles, but changes significantly with the examination location in individual particles. In a different

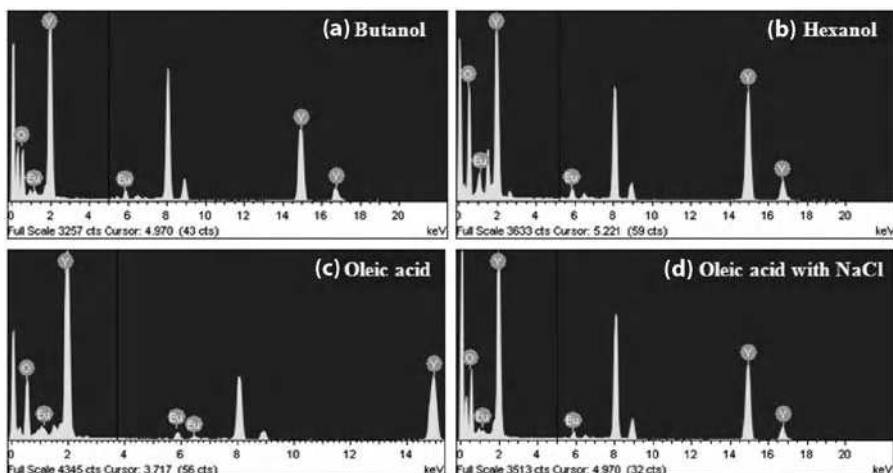


FIGURE 3.21 EDS spectra of annealed $\text{Y}_2\text{O}_3:\text{Eu}^{3+}$ nanoparticles prepared with (a) butanol, (b) hexanol, (c) oleic acid, and (d) oleic acid as surfactants [77]. (Reprinted with permission from Jadhav AP, Kim CW, Cha HG, Pawar AU, Jadhav NA, Pal U, Kang YS. Effect of different surfactants on the size control and optical properties of $\text{Y}_2\text{O}_3:\text{Eu}^{3+}$ nanoparticles prepared by coprecipitation method. *J Phys Chem C* 2009;113:13600–13604, Copyright 2009, American Chemical Society.) (For a color version of this figure, see the color plate section.)

example, the composition–size plot shows that the composition of the individual Pd–Ni particles for a 5wt%Pd/1wt%Ni/TiO₂ bimetallic catalyst changes significantly with the sizes of the individual nanoparticles and also varies with their relative locations. Smaller particles contain more palladium and larger particles contain more nickel. For SiO₂ on PbSe core/shell nanoparticles, EDS spectra indicate the presence of platinum and selenium in the cores, and silicon and oxygen in the shell [76]. EDS is also used to analyze the surface chemistry of nanoparticle mixtures, such as tungsten and MoO₃, and SiO₂ and TiO₂ [79]. However, it cannot provide information down to the nanoscale since the interaction volume of the electron beam with the sample is in the micron range. Nanoparticles of europium-doped yttrium oxide ($\text{Y}_2\text{O}_3:\text{Eu}^{3+}$) are synthesized by a coprecipitation method using different surfactants such as butanol, hexanol, and oleic acid. The as-prepared $\text{Y}_2\text{O}_3:\text{Eu}^{3+}$ samples are annealed at 800°C [77]. Figure 3.21 shows the EDS spectra of $\text{Y}_2\text{O}_3:\text{Eu}^{3+}$ nanoparticles synthesized. The existence of europium in the samples is clear in their corresponding EDS spectra. No other emissions appear apart from yttrium, europium, oxygen, copper, and carbon in the EDS spectra of the samples. The yttrium to europium atomic ratio is 95:5, which is close to their nominal compositions ($\text{Y}_{2(0.095)}\text{Eu}_{2(0.005)}\text{O}_3$). Given the fact that the existence of carbon and copper is from the copper grid used in the characterization, it is easy to see the effective incorporation of Eu^{3+} into the matrix.

The availability of fast computers for automation and online data analysis makes it possible to analyze extremely complex nanomaterial systems and to quickly diagnose their basic compositions. Small electron probes can achieve high spatial resolutions because the X-ray signal originates from a much smaller volume. In the meantime, a weaker signal is collected and longer acquisition time is usually needed to obtain statistically meaningful data points. EDS is easy to use, sensitive to heavy elements, excellent at identifying atomic compositions, and readily available on most electron microscopes (TEM, SEM, electron probe, and STEM). Since EDS requires standards, it is better to be used together with other, more accurate characterization techniques in order to quantitatively interpret data.

3.7.2.4 Electron Energy Loss Spectroscopy When an electron beam hits and traverses nanoparticles, it loses some energy. In EELS, inelastically scattered electrons are collected and spectroscopically analyzed to provide the energy spectra of the electrons after their interaction with the sample, from which quantifiable elemental information can be obtained. The spectra can be collected in series or in parallel. Serial collection has low efficiency—only one channel can be investigated at one time but is easy to operate. Parallel collection gathers the entire energy spectrum simultaneously and is two to three times more efficient than serial collection. When a spectrum from EELS is filtered and the filtered electrons are combined, images can be generated, which is known as electron spectroscopy (Fig. 3.22).

For GaP and silicon semiconductors, surface chemical changes are examined as a function of atmosphere, electron irradiation, and Ar⁺ etching [62]. The electron irradiation from EELS does not affect the surface chemistry. EELS can qualitatively detect chemical shifts as high as ~6 eV due to different chemical states while quantitatively analyzing certain elements such as Si⁰ and Si⁴⁺. For niobium carbonitride nanoparticles in ferrite, chemical composition analysis

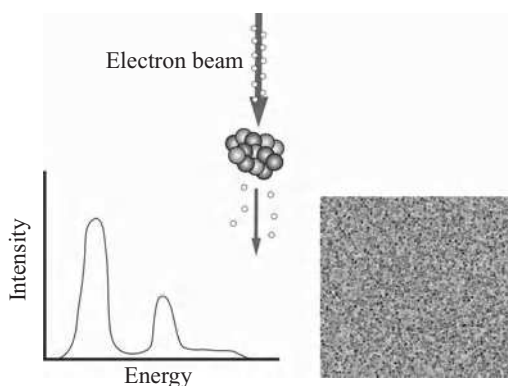


FIGURE 3.22 Electron energy loss spectroscopy illustration. (For a color version of this figure, see the color plate section.)

of the particles down to 6 nm is investigated by EELS [78]. The addition of a considerable amount of nitrogen into the alloy Fe-(Nb, C, N) results in a complex precipitation sequence with the coexistence of two kinds of particles: pure nitrides and homogeneous carbonitrides. EELS imaging is able to achieve both angle selection and energy selection of elastically and inelastically scattered electrons [79]. By assigning an “energy window” in an energy loss spectrum region, EELS is able to image certain elements in a sample while a global image can be recorded simultaneously under zero energy loss conditions. A comparison between the global image and the elemental image provides the distribution of different species. EELS demonstrates its unique advantage in energy filtering. By providing a high-resolution elemental map, EELS can fully characterize nanoparticle mixtures of TiO_2 and SiO_2 [79].

The morphological and structural features of core/shell iron/iron oxide nanoparticles with respect to particle size, shell thickness, and crystallographic orientation between the iron core and the oxide shell have been reported. EELS spectra for a specific atomic species are influenced by both the coordination chemistry and the valence state of the atomic species being measured. A side-by-side comparison of the EELS spectra (around 530 eV) obtained on the core/shell structured iron nanoparticles and the fully oxidized nanoparticles is carried out [80]. As is evident from Figure 3.23, significant differences can be seen in the intensity of the prepeak *a* for standard Fe_3O_4 , the core/shell structured

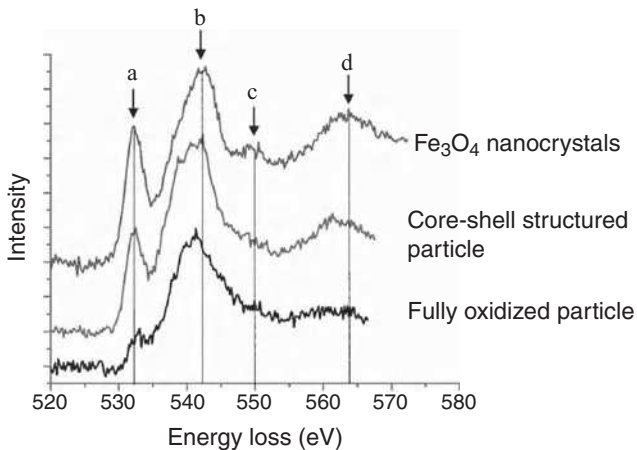


FIGURE 3.23 Comparison of EELS spectra (around 530 eV) collected on standard Fe_3O_4 nanoparticles, core/shell structured iron nanoparticles, and fully oxidized nanoparticles (no iron core at the center). To exclude the uncertainty for the absolute energy-loss scale, the prepeak is aligned at 532 eV, and, for clarity, each spectrum is vertically shifted [80]. (Reprinted with permission from Wang C, Baer DR, Amonette JE, Engelhard MH, Antony J, Qiang Y. Morphology and electronic structure of the oxide shell on the surface of iron nanoparticles. *J Am Chem Soc* 2009;131:8824–8832, Copyright 2009, American Chemical Society.) (For a color version of this figure, see the color plate section.)

nanoparticles, and the fully oxidized nanoparticles. The prepeak *a* is located at ~ 532 eV, which can be interpreted as a transition from the oxygen 1s core state to the unoccupied state of oxygen 2p hybridized with the iron 3d state. Therefore, the intensity of the prepeak *a* reflects the unoccupied 3d state in the iron atoms available for mixing with the oxygen 2p state, as well as the bond length of Fe–O. This explains why the intensity of the prepeak *a* relative to that of peak *b* increases in the sequence of FeO to Fe₃O₄. The iron in FeO has a valence of +2 and a correspondingly longer Fe–O bond length (six Fe–O bonds at 2.15 Å) than the iron in Fe₃O₄ (one Fe–O bond at 1.89 Å and three Fe–O bonds at 2.06 Å). Furthermore, it is known that FeO is normally defective with a large fraction of iron vacancies.

EELS can provide detailed information on the composition, chemistry, and electronic structure of nanoparticles with atomic resolution and sensitivity. It can also attain spatial resolution down to ~ 0.1 nm with modern aberration-corrected probe-forming systems. In addition, the technique measures atomic composition, chemical bonding, valence and conduction band electronic properties, and examines low atomic number elements that other techniques cannot do. However, EELS is a low-energy technique and can be difficult to use. If transmitted electrons need to be collected, then the nanoparticles or nanoparticle-based materials need to be thin enough to be electron transparent.

3.7.2.5 Fourier Transform Infrared Spectroscopy FT-IR is often used in the analysis of functional group structural changes and new species present on nanoparticles or nanoparticle-based material surfaces. It detects the vibration characteristics of chemical functional groups in a sample. When IR light interacts with a sample, chemical functional groups absorb IR radiation in a certain wave number range due to the stretching, contracting, and bending of chemical bonds, no matter what the molecular structure is. FT-IR measures the absorption of various IR light wavelengths by the sample of interest and gives the percentage of transmission versus wavelength (Fig. 3.24).

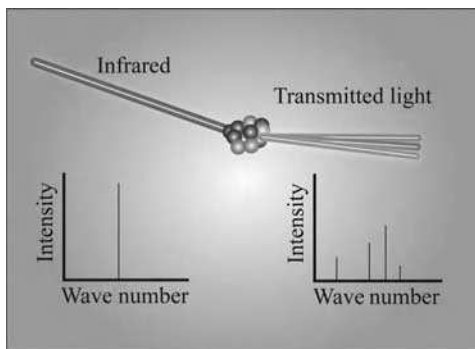


FIGURE 3.24 FT-IR characterization process. (For a color version of this figure, see the color plate section.)

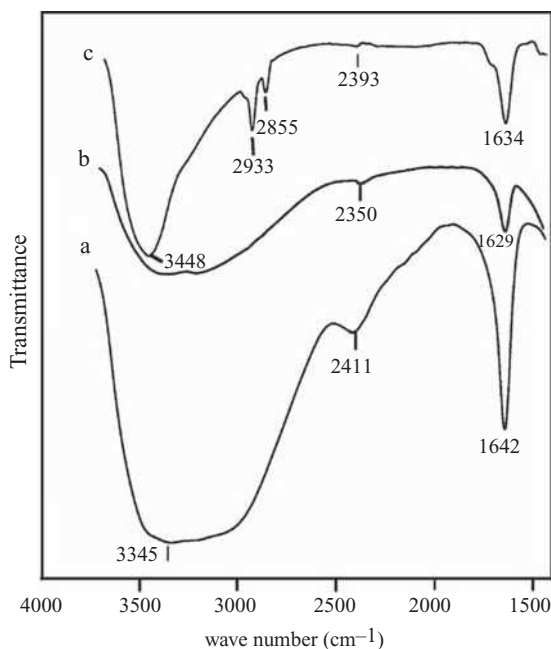


FIGURE 3.25 FT-IR spectra of (a) fresh titanyl sulfate, (b) titanyl sulfate dried at 350°C for 1 hour, and (c) as-milled powder [82]. (Reprinted with permission from Salari M, Mousavikhoie SM, Marashi P, Rezaee M. Synthesis of TiO₂ nanoparticles via a novel mechanochemical method. *J Alloys Compd* 2009;469:386–390, Copyright 2009, Elsevier.)

FT-IR is used to characterize dispersed Fe₃O₄ nanoparticles in aqueous suspensions [81]. Combined with XPS, FT-IR shows that the Fe₃O₄ nanoparticle surface is covered with hydroxide (OH⁻) groups incorporated with (CH₃)₄N⁺ through electrostatic interactions. A broad and intense band in the region of 3200–3600 cm⁻¹ indicates O–H stretching vibrations, while the band at 1634 cm⁻¹ represents C–N stretching vibrations. Compared to the vibration peak of pure N(CH₃)₄OH, the C–N band indicates the adsorption of N(CH₃)₄OH on Fe₃O₄ nanoparticles. Figure 3.25 shows the FT-IR spectra of untreated titanyl sulfate (a), dried titanyl sulfate at 350°C (b), and as-milled powder (c). The broad IR absorption peak in the range of 3200–3500 cm⁻¹ with a maximum at 3345 cm⁻¹ arises from the superposition of the interacting hydroxyl groups (i.e., involved in hydrogen bonds) and symmetric and asymmetric molecular water coordinated to Ti⁴⁺ cations. The band at 1624 cm⁻¹ is assigned to the bending mode of molecular water. The effect of heat treatment on the spectrum of the untreated titanyl sulfate is shown by a significant drop in the broad absorption in the range of 3200–3500 cm⁻¹ and in the band at 1624 cm⁻¹, indicating the removal of a large part of weakly bonded and adsorbed water (curves (a) and (b) in Fig. 3.25). The band observed at 2411 cm⁻¹ is assigned to S–O vibrations. The

treatment of the dried titanyl sulfate causes a large decrease in the 2411 cm^{-1} band and a shift toward lower frequencies, indicating the weakening of the band strength. From the spectrum, it can be concluded that the sample largely consists of weakly adsorbed water, which is produced during mechanochemical reduction. The bands observed at 2855 cm^{-1} and 2933 cm^{-1} are assigned to S–O vibrations, which are produced during mechanochemical reduction and removed by annealing [82].

Qualitatively, FT-IR can identify specific molecular components and structures by obtaining the IR absorption bands of the sample of interest and comparing them with the standard spectra in a computer database. The process is quick and has high signal to noise ratio. Since the concentration is reflected by the strength of the absorption peak, FT-IR can also quantitatively determine the concentration of a compound from the area under the absorption peak in the characteristic region of the spectra. Sample preparation for FT-IR is simple and only a small amount of sample is needed. However, FT-IR does not measure spectra. It measures interferograms, which are difficult to interpret without first performing a Fourier transformation to produce a spectrum. With the aid of fast computers, this is becoming less of an issue. For highly sensitive and long duration measurements, changes in IR absorbing gas concentration can severely affect the results.

3.7.2.6 Ultraviolet-Visible Absorption Spectroscopy UV-vis spectroscopy is another technique for composition analysis based on absorption. Hydrogen or deuterium is normally the light source for UV wavelength measurement. Tungsten is the light source for visible wavelength measurement. Although falling in different regions of the electromagnetic spectrum, the UV and visible regions of the electromagnetic spectrum are linked in UV-vis spectroscopy because of the similarities between the two regions, allowing UV and visible absorption spectroscopies to be used at the same time. When UV or visible light strikes atoms or molecules, it can either be bounced off or cause the electrons in the atoms or molecules to jump from a lower energy level to a higher energy level by absorbing energy. Different species absorb radiation at different wave numbers. The atom or molecule types existing in the sample can thus be identified (Fig. 3.26). According to Beer's law, absorbance is directly proportional to the concentration of absorbing species:

$$A' = \varepsilon bc_a, \quad (3.14)$$

where A' is the absorbance, ε is the absorptivity, b is the path length, and c_a is the concentration of absorbing species. Therefore, the species concentration can be measured precisely.

UV-vis spectra of solutions containing gold nanoparticles are measured before and after the reduction of metal ions [83]. Before the reduction, a strong

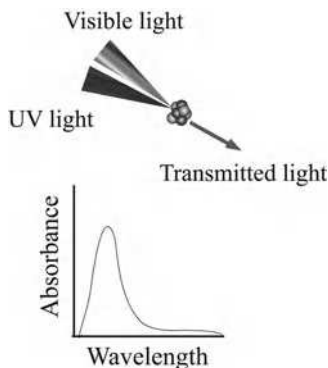


FIGURE 3.26 UV-vis spectroscopy illustration. (For a color version of this figure, see the color plate section.)

absorption band at 200 nm is observed, indicating the existence of HAuCl_4 . After the reduction, this band vanishes, indicating that AuCl_4^- is completely reduced to gold, the absorption bands of which appear at 280 nm and 520 nm in the UV spectra. When UV-vis spectroscopy is applied to Au–Ag alloy nanoparticles, a comparison shows that an alloy formed from the reduction is different from a mixture [84]. For gold nanoparticles formed via laser photolysis of Au(III) salts, UV-vis spectroscopy is used to investigate the influence of the gold salt type, presence of water, and laser irradiation on the rate of reduction reaction and gold nanoparticle formation [85]. The reduction of Au(III) to metal nanoparticles is observed stepwise. The existence of water in the system containing $\text{HAuCl}_4 \cdot 3\text{H}_2\text{O}$ accelerates the reduction while the gold particle size is not affected. Figure 3.27a shows the UV-vis spectra of thioglycolic acid-capped gold nanoparticles with different volume ratios of water/acetone. Compared with the UV-vis spectra of as-prepared thioglycolic acid-capped gold nanoparticles in Figure 3.27b with decreasing water/acetone ratios, an additional peak gradually appears above 600 nm besides the absorbance band located at 520 nm, which is attributed to the longitudinally coupled plasmon band along the linear chains of gold nanoparticles. From the appearance of this peak, it can be inferred that the gold nanoparticles assemble into chains in the solution. These mixtures are further dropped on the surface of a silicon wafer. After they are naturally dried at room temperature, the self-assembly behaviors of the nanoparticles on the silicon wafer are studied by SEM. Four different self-assembly structures of gold nanoparticles are observed in the center of the solution as shown in Figures 3.25b–e. However, no chain-like morphologies are found in these images, which indicate that the self-assembly behaviors of gold nanoparticles on the silicon wafer are different from that in the solution. In Figure 3.27b, the volume ratio of water/acetone is 1:1, the gold nanoparticles assemble into 1 μm size structures with an irregular shape. The

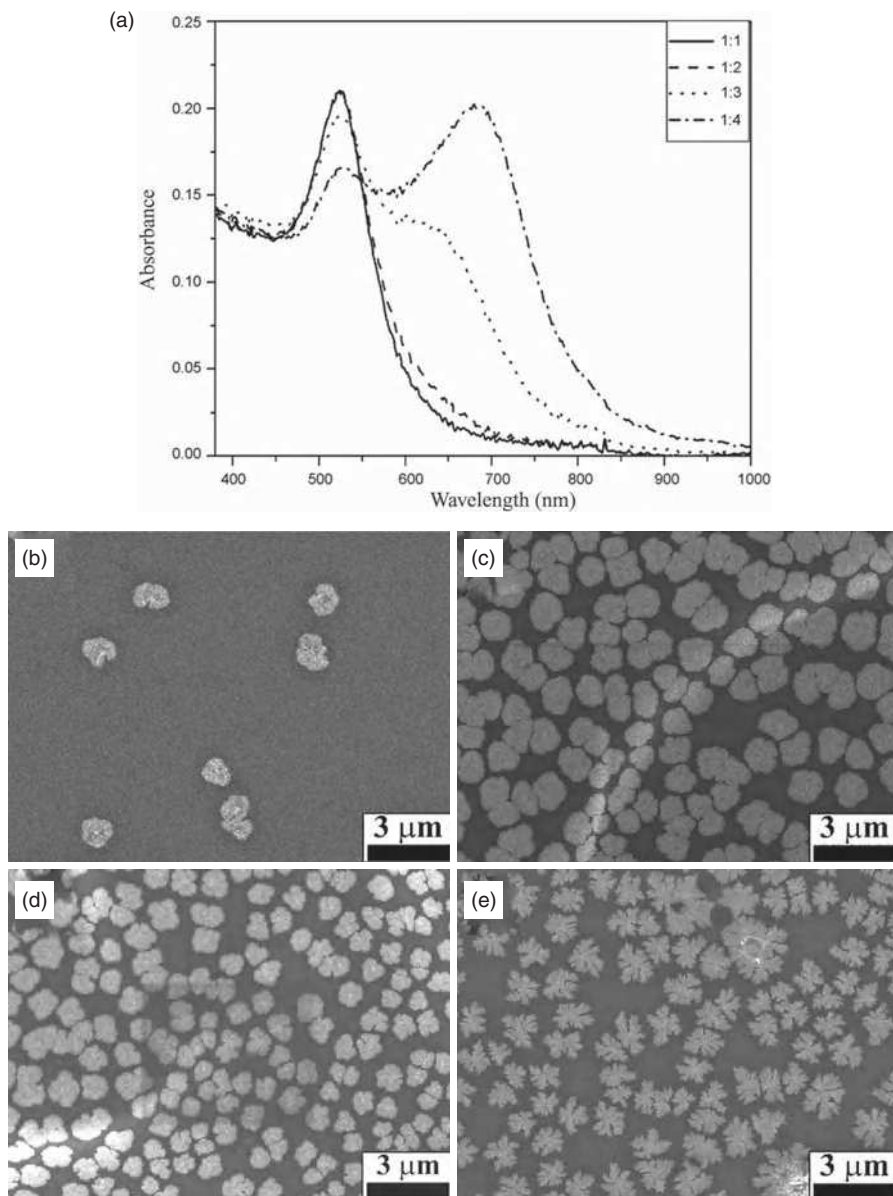


FIGURE 3.27 (a) UV-vis spectra of solutions of thioglycolic acid-capped gold nanoparticles with different water/acetone ratios: 1:1 (solid), 1:2 (dash), 1:3 (dot), and 1:4 (dash dot); (b)–(e) SEM images of thioglycolic acid-capped gold nanoparticles with different water/acetone ratios: (b) 1:1, (c) 1:2, (d) 1:3, and (e) 1:4 [86]. (Reprinted with permission from Wu J, Zhang H, Zhang J, Yao T, Sun H, Yang B. Control of the self-assembly behaviors of charged gold nanoparticles. *Colloids Surf A* 2009;348:240–247, Copyright 2009, Elsevier.)

edge of these structures is smooth and few branches are seen. However, with decreasing volume ratios of water/acetone, from Figures 3.25b–e, the edge of the self-assembled structures becomes rougher and rougher, and more and more branches are observed in these structures. This change is most obvious in Figure 3.27e; the self-assembled structures have dendritic morphologies, looking like maple leaves [86].

UV-vis spectroscopy is useful for two main reasons. First, it can identify certain functional groups, which means the electronic structure of certain species can be detected. Second, it can quantify the composition of nanoparticles. However, the species to be examined must absorb radiation from 200 to 800 nm wavelength and be free from the interference of other species.

3.7.2.7 Raman Spectroscopy Raman spectroscopy collects inelastic scattering (Raman effect) of photons by molecules. A monochromatic light or a laser in the visible, near IR, or near UV range is usually used as the source. The Raman effect occurs when light impinges upon a molecule and interacts with the electron cloud of the bonds of that molecule. Vibrational, rotational, and other low-frequency modes in a system are studied (Fig. 3.28). The energy of a vibrational mode depends on the molecular structure and the environment. Since the chemical bonds in different molecules have their specific vibrational modes, different molecules can be identified. Changes in chemical bonding can also be detected using Raman spectroscopy. When used for the characterization of nanoparticles, the polarization of the species scatters light with respect to the crystal and can be used to identify the crystallographic orientation.

For $\text{Ce}_{1-x}\text{Zr}_x\text{O}_2$ crystalline nanoparticles, Raman spectroscopy is carried out to examine the solid solution formed with increasing zirconium content [87]. The spectra indicate disordered structure although only weak reflection is observed in XRD. One explanation is that XRD provides information on the periodicity of a material while Raman spectroscopy reveals the vibrational behavior of the chemical bonds. Raman spectra are also collected on pressed powders to examine

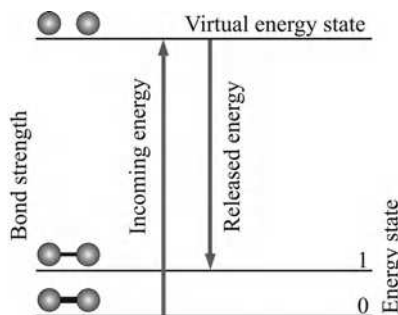


FIGURE 3.28 Different energy states during Raman spectroscopy. (For a color version of this figure, see the color plate section.)

the core/shell arrangement of $\text{TiO}_2/(\text{MoO}_3)_x$ materials since the measurement is quite sensitive to species connectivity [69]. There is a band broadening with the existence of MoO_3 that can be explained by the decrease in TiO_2 nanoparticle size as MoO_3 coverage increases. The broad peak at 820 cm^{-1} in the Raman spectra of MoO_3 -containing samples is attributed to Mo-O-Mo stretching. Another peak at 1000 cm^{-1} matches symmetric Mo=O stretching.

Raman spectra of silicon nanoparticles at room temperature are measured using a micro-Raman system with a resolution of 1 cm^{-1} and a reproducibility of 0.4 cm^{-1} . The excitation source is a 514.5 nm Ar^+ laser with a power of 2 mW . Peak shifting, broadening, and asymmetry of the Raman bands relative to bulk silicon are observed for silicon nanoparticles [88]. Raman spectra of two samples with milling time of 240 hours and 168 hours, respectively, are recorded (Fig. 3.29). The Raman peak of silicon wafer at 520 cm^{-1} is symmetrical with a full-width at half-maximum (FWHM) of 6 cm^{-1} (curve (d)). Raman scattering from the sample milled for 240 hours shows a peak that is slightly broadened (FWHM: 13 cm^{-1}) (curve (c)). Curve (b) in Figure 3.29 is the Raman spectrum of the sample milled for 168 hours. The Raman peak is asymmetric with a FWHM of 21 cm^{-1} and has an extended tail at low frequencies. The Raman spectrum of the starting materials (graphite powder mixed with silicon dioxide powder in 1:1 molar ratio) is also shown as curve (a) for comparison. No characteristic silicon peak is found. Only two peaks of graphite nanopowders are shown at 1350

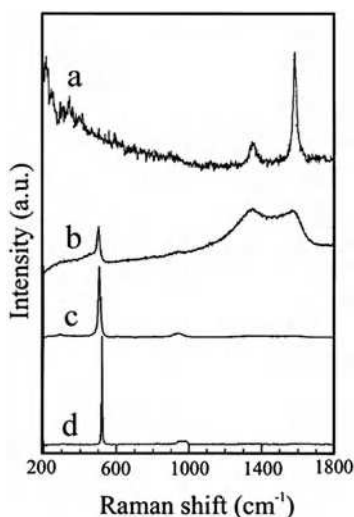


FIGURE 3.29 Raman spectra of (a) reference starting material, (b) the powders milled for 168 h, (c) the powders milled for 240 hours, and (d) reference crystalline silicon wafer [88]. (Reprinted with permission from Lam C, Zhang YF, Tang YH, Lee CS, Bello I, Lee ST. Large-scale synthesis of ultrafine Si nanoparticles by ball milling. *J Cryst Growth* 2000;220:466–470, Copyright 2000, Elsevier.)

and 1580 cm^{-1} . The wide broad tail at low wave numbers comes from the SiO_2 powders. Curve (a) from starting materials rules out the possibility of silicon particles contained in the original powders.

Raman spectroscopy is a powerful tool for investigating the structure of nanoparticles and nanoparticle-based materials. The advantage of Raman spectroscopy is that no sample pretreatment is necessary. The laser and the sample are not in contact, and the samples are not destroyed. If a fiber optics is in place, remote analysis of nanoparticles by Raman spectroscopy can be carried out. Raman spectroscopy exhibits high specificity and the analysis can be as quick as a few seconds. Also, the Raman spectrum of water is weak and unobtrusive, allowing good spectra for species in aqueous solutions to be acquired. Raman spectra are also easier to analyze than IR spectra. The disadvantage of Raman spectroscopy is that it is not very sensitive (need $\sim 10^6$ incident photons to generate 1 Raman scattered photon), the detection limit is only part(s) per thousand, and fluorescence interference can bias the results.

3.8 NEEDS IN NANOSCALE CHARACTERIZATION

For nanoscale characterization, some techniques offer only the average or distribution of properties, not the specific properties at individual sites. Only a couple of techniques can characterize individual nanoparticles or individual sites on nanoparticle-based material surfaces. The lack of instrumentation with sufficient temporal and spatial resolution impacts the validation and qualification of nanomaterials with less than 100 atoms and subpicosecond dynamics. A high-resolution means of quantifying the nanoparticle surface is needed other than SEM or TEM, which might modify the nanoparticles during the examination. Techniques involving probe-sample interaction during nanoparticle characterization can create artifacts and provide false data. A variety of studies have shown that nanoparticles can be unstable with respect to the environment. The inherently lower level of stability for many types of nanostructured materials significantly increases the attention that needs to be paid to the impacts that an analysis probe, environmental conditions, and time can have on material analyses. For example, the adsorption of water onto the surface of ZnS nanoparticles changes the particle structure. The energies associated with many of the probes used for particle analysis equal to or exceed those needed to transform the particles in a variety of ways. To accurately characterize nanoparticles at single nanometer level, an atomically precise tip with subnanometer precision is needed.

Also, characterization techniques need to be developed for three-dimensional nanoparticle size, shape, chemical, and elemental evaluation. Most of the microscopy techniques can only offer two-dimensional projection data. Another necessary area is indirect, but affordable and fast in-line analysis ability during nanoparticle synthesis. Overall, tools that can measure properties, compositions, structures, and interactions at surfaces and interfaces near atomic resolution will

be critical, as will be the development of the probes that couple electron microscopy to characterization of properties at the nanometer scale. The lack of *in situ* instrumentation limits the development of computational models to analyze the manufacturing process and predict the outcome in large-scale systems. Also, most of the nanoparticle characterization techniques in existence today are dry-particle-based approaches. Since nanoparticles have a strong tendency to agglomerate, many applications of nanoparticles are liquid-based or require thorough dispersion of nanoparticles in a solid matrix. Because of this, statistical evaluation of nanoparticles in dispersion is much desired. The analysis needed includes not only the dispersion of nanoparticles but also the chemical and physical behaviors of nanoparticles in the specific dispersing medium.

Nanoparticles have huge specific surface areas and a natural tendency to be coated with a thin coating. Coatings can be organic dispersants or surfactants, or thin inorganic coatings. For composite nanoparticles with a core/shell structure, coatings are purposely designed onto the core nanoparticle surfaces. This requires a well-defined approach to determine the coating coverage, thickness, structure, and uniformity on nanoparticles. Determining the coverage and perfection of nanometer-thick surface coatings on nanoparticles presents a significant challenge. There are also challenges in measuring particle size distribution when the particles are anisotropic in shape. Multiple parameters are desired to describe such complex systems rather than averaged parameters. As in other areas of nanotechnology, research and development of standards and reference materials are essential in order to sustain the progress in nanoparticle-based materials. It should ultimately link key, easily controlled process parameters to nanoscale methodologies or features that define a material's performance. Platforms for simultaneously characterizing multiple properties on a single sample are also needed. Techniques that can span multiple length scales simultaneously are needed. When deviation is detected, further high-resolution, time-consuming, and expensive characterization techniques can be warranted. At this scale, where background noise is a significant issue, environmental impacts such as vibrations and small changes in temperature and humidity can cause significant changes in a measurement.

3.9 SUMMARY

Characterization of nanoparticles and nanoparticle-based materials includes size, shape, morphology, energetics, global thermodynamics, surface area, porosity, pore size, structure, purity, composition, surface chemistry, surface charge, and surface activity. The nanoparticle characterization techniques covered in this chapter have greatly facilitated and benefited from the advancement of nanoscience and nanotechnology as a whole. In summary, the measured properties, working principles, and detection ranges of different characterization techniques are given in Table 3.2.

TABLE 3.2 Properties Measured, Working Principles, and Detection Limits of Various Nanoscale Characterization Techniques

| Techniques | Properties measured | Working mechanism | Detection limit |
|--|--|--|---|
| Scanning electron microscopy (SEM) | Sample morphology, elemental information when EDS or WDS is coupled. | A focused electron beam raster scans the surface, the backscattered and secondary electrons are used to produce an image, the generated X-rays are analyzed for elemental composition. | Lateral resolution: 3 nm; Depth resolution: 500 nm (for SEM mode only) |
| Transmission electron microscopy (TEM) | Sample morphology, interface microstructure, crystallographic structure, and elemental information when EDS or EELS is coupled. | A monochromatic electron beam is highly focused on a very thin sample, the interaction between the transmitting electron beam and the sample is analyzed. | Lateral resolution: 0.05–2 nm; Depth resolution: ~200 nm |
| Small-angle scattering (SAS) | Structural arrangement of atoms. | A sample is placed in an X-ray or neutron beam and the very low-angle scattered electrons are analyzed. | 1–300 nm |
| Scanning probe microscopy (SPM) | Depending on the mode of operation, three-dimensional surface topology and morphology, elasticity, friction, magnetic and electrical properties can be detected. Shape, texture, and roughness of individual particles and their distribution in an assembly of particles can be measured. When particle structure is known, can provide information about crystallographic orientation. | A probe tip slowly raster scans across a sample surface. The interaction between the tip and the sample is recorded. | Spatial resolution: 0.5–1 nm; Depth resolution: 0.1 nm |

(Continued)

TABLE 3.2 (Continued)

| Techniques | Properties measured | Working mechanism | Detection limit |
|--|--|---|---|
| Scanning tunneling microscopy (STM) | Depending on the mode of operation, three-dimensional surface topology and morphology, current–voltage spectroscopy, electrical characteristics of individual nanoparticles, nanoparticle formation and/or size distribution of particles deposited or grown on a surface are characterized. | A conductive tip is brought very close to a conductive sample surface to induce a tunneling current when a voltage is applied. The tip slowly raster scans across the surface. | Spatial resolution: 0.5–1 nm |
| Diffraction | Crystallographic information. | A sample is placed in an X-ray, electron, or neutron beam; the beam is diffracted by the periodic lattice of the crystalline material according to Bragg's law. | TEM electron diffraction: ~ 1 nm; XRD: Lateral resolution: 50 μm ; Depth resolution: 2 μm |
| Auger electron spectroscopy (AES) | Surface composition, bulk composition if three-dimensional profiling is available. Surface composition of individual large nanoparticles or a distribution of smaller nanoparticles (depending on spatial resolution of the specific instrument), enrichment or depletion of elements on surface, presence and/or thickness of coatings and/or contaminants. | Electrons impinge on sample surface, resulting in the ejection of secondary electrons. The emitting electrons are detected by an electron spectrometer according to their respective kinetic energies. | Lateral resolution: 10 nm; Depth resolution: 0.3–3 nm |
| Secondary ion mass spectroscopy (SIMS) | Surface composition, bulk composition if three-dimensional profiling is available, impurity and dopant information, a collection of particles or larger individual particles deposited on a supporting substrate, presence of surface coatings or contaminants on a collection of nanoparticles, functional groups on a surface. | An ion beam bombards the surface, resulting in the sputtering of ions from the sample (secondary ions). The secondary ions from the sample are analyzed in a mass spectrometer according to their energies and mass ratios. | Lateral resolution: ~ 1 μm ; Depth resolution: ~ 1 nm, 2 μm with depth profiling |

| | | | |
|--|--|--|---|
| X-ray photoelectron spectroscopy (XPS) | Surface composition and valence state, bulk composition and valence state if three-dimensional profiling is available, presence and nature of functional groups on the surface, enrichment or depletion of elements on a surface, presence and/or thickness of coatings or contaminants. | X-rays impinge on sample surface, resulting in the ejection of electrons with varying energies. The emitting electrons are detected by an electron spectrometer according to their respective kinetic energies. | Lateral resolution: ~10 μm ; Depth resolution: 0.5–10 nm |
| Energy dispersive spectroscopy (EDS)/ wavelength dispersive spectroscopy (WDS) | Elemental composition. | An energetic electron beam interacts with a sample, the resulting X-ray spectrum is analyzed for composition analysis. | For EDS mode: Lateral resolution: >200 nm; Depth resolution: >1 μm . For TEM mode: Lateral resolution: 1 nm; Depth resolution: 100–200 nm |
| Electron energy loss spectroscopy (EELS) | Chemical composition, electronic structure and bonding in nanoparticles and at interfaces. | When electrons pass through a sample (often in TEM), some lose energy along the way. The amount of energy lost is unique to the atomic species that the electron beam interacts with. A spectrum can be obtained and analyzed to determine the chemical composition of the sample. | Lateral resolution: 1–100 nm |
| Fourier transform infrared spectroscopy (FT-IR) | Structural and chemical compositions. | A sample is placed in an IR beam sent through an interferometer. Frequencies that match the natural vibration frequencies of the molecules present are absorbed by the sample. The collected interferogram is converted into a spectrum using the Fourier transform. | Lateral resolution: 20 μm |

(Continued)

TABLE 3.2 (Continued)

| Techniques | Properties measured | Working mechanism | Detection limit |
|---------------------|---------------------------------------|---|--------------------------------|
| UV-vis spectroscopy | Functional groups, compositions. | When UV or visible light strikes atoms or molecules, electrons in the atoms or molecules can jump from a lower energy level to a higher energy level by absorbing energy. Different species absorb radiation at different wave numbers. The atom or molecule types existing in the sample can thus be identified. | Lateral resolution: microns |
| Raman spectroscopy | Structural and chemical compositions. | A sample is placed in a laser path and the inelastically scattered photons having a different wavelength from the incident radiation are collected for chemical bond and composition identification. | Spatial resolution: microns |

QUESTIONS

1. Nanoparticle size and size distribution measurements are basic aspects in characterization. Explain how they can be accomplished properly.
2. Based on the BET equation, derive the expression for specific surface area.
3. List two main differences between scanning tunneling microscopy and atomic force microscopy.
4. In scanning tunneling microscopy, the tunneling current has such a relationship:

$$I = I_0 \exp(-2ks),$$

where s is the distance between the tip atom and the surface atom. I_A , I_B are the tunneling current due to tunneling between atom A-surface atom and atom B-surface atom. (B is one level higher than A). Calculate I_B/I_A . Assume $k = 5 \times 10^9 \text{ m}^{-1}$, the diameter of the atoms is 0.5 nm, and $s = 2 \text{ nm}$.

5. For nanoparticle and nanoparticle-based material surface structure characterization, what three techniques are generally used? What is the basic principle for each technique?
6. For nanoparticle and nanoparticle-based material crystal structure analysis, diffraction is necessary. What sources can be used for diffraction? What is the fundamental beam-atom interaction process?
7. In an X-ray photoelectron spectrum, would you expect the C 1s peak to be at a higher or lower binding energy compared to that for the O 1s peak? Explain your answer.
8. Compare the three surface composition analysis techniques: Auger electron spectroscopy, X-ray photoelectron spectroscopy, and secondary ion mass spectroscopy. What are the advantages and disadvantages for each technique?
9. For nanoparticle and nanoparticle-based material bulk composition analysis, energy dispersive spectroscopy, electron energy loss spectroscopy, Fourier transform infrared spectroscopy, UV-vis spectroscopy, and Raman spectroscopy provide different information and are suited to different materials. Explain what each technique is best suited for and how it works during the characterization process.

REFERENCES

1. Park BK, Jeong S, Kim D, Moon J, Lim S, Kim JS. Synthesis and size control of monodisperse copper nanoparticles by polyol method. *J Colloid Interface Sci* 2007;311: 417–424.
2. Yang J, Lee JY, Too H-P. Size sorting of Au and Pt nanoparticles from arbitrary particle size distributions. *Anal Chim Acta* 2005;546:133–138.
3. Binnig G, Rohrer H, Gerber C, Weibel E. Tunneling through a controllable vacuum gap. *Appl Phys Lett* 1982;40:178–180.

4. Binnig G, Quate CF, Gerber C. Atomic force microscope. *Phys Rev Lett* 1986;56: 930–933.
5. Baer DR, Gaspar DJ, Nachimuthu P, Techane SD, Castner DG. Application of surface chemical analysis tools for characterization of nanoparticles. *Anal Bioanal Chem* 2010;396:983–1002.
6. Wang ZL. *Characterization of Nanoparticle Materials*. Weinheim, Germany: Wiley-VCH; 2000. pp. 54–60.
7. Rahaman MN. *Ceramic Processing and Sintering*. New York, NY: Marcel Dekker, Inc.; 2003. pp. 143–145.
8. Khrenov V, Klapper M, Koch M, Müllen K. Surface functionalized ZnO particles designed for the use in transparent nanocomposites. *Macromol Chem Phys* 2005;206:95–101.
9. Sorescu M, Diamandescu L, Tarabasanu-Mihaila D, Teodorescu VS, Howard BH. Hydrothermal synthesis and structural characterization of $(1-x)\alpha\text{-Fe}_2\text{O}_3\text{-xSnO}_2$ nanoparticles. *J Phys Chem Solids* 2004;65:1021–1029.
10. Savaloni H, Modiri F, Hajhosseini H, Shokouhy A. Characteristics of surface nanostructural modifications in nitrogen ion implanted W as a function of temperature. *Appl Surf Sci* 2006;252:5419–5423.
11. Witkowski S, Ruzsak M, Sayag C, Pielaszek J, Djega-Mariadassou G. Nanocrystalline NbC formation from mesostructured niobium oxide studied by HRTEM, SAED and in situ XRD. *Appl Catal A* 2006;307:205–211.
12. Yang H, Hu Y, Zhang X, Qiu G. Mechanochemical synthesis of cobalt oxide nanoparticles. *Mater Lett* 2004;58:387–389.
13. Bayati M, Abad JM, Bridges CA, Rosseinsky MJ, Schiffrin DJ. Size control and electrocatalytic properties of chemically synthesized platinum nanoparticles grown on functionalized HOPG. *J Electroanal Chem* 2008;623:19–28.
14. Farrell DF, Ijiri Y, Kelly CV, Borchers JA, Rhyne JJ, Ding Y, Majetich SA. Small-angle neutron scattering study of disordered and crystalline iron nanoparticle assemblies. *J Magn Magn Mater* 2006;303:318–322.
15. Turkovic A, Ivanda M, Popovic S, Tonejc A, Gotic M, Dubcek P, Music S. Comparative Raman, XRD, HREM, and SAXS studies of grain sizes in nanophase in TiO_2 . *J Mol Struct* 1997;410:271–273.
16. Korgel BA, Fitzmaurice D. Small-angle X-ray-scattering study of silver-nanocrystal disorder-order phase transitions. *Phys Rev B* 1999;59:14191–14201.
17. Hazra S, Gibaud A, Desert A, Sella C, Naudon A. Morphology of nanocermet thin films: X-ray scattering study. *Phys B* 2000;283:97–102.
18. Ciesa F, Plech A. Gold nanoparticle membranes as large-area surface monolayers. *J Colloid Interface Sci* 2010;346:1–7.
19. Lifshin E. *X-ray Characterization of Materials*. Weinheim, Germany: Wiley-VCH; 1999. pp. 213–254.
20. Fedeyko JM, Vlachos DG, Lobo RF. Formation and structure of self-assembled silica nanoparticles in basic solutions of organic and inorganic cations. *Langmuir* 2005;21:5197–5206.
21. Kang SS, Jia Z, Zoto I, Reed D, Nikles DE, Harrell JW, Thompson G, Mankey G, Krishnamurthy VV, Porcar L. Sintering behavior of spin-coated FePt and FePtAu nanoparticles. *J Appl Phys* 2006;99:08N704-1–08N704-3.
22. Babinski A, Potemski M, Raymond S, Korkusinski M, Sheng W, Hawrylak P, Wasilewski Z. Optical spectroscopy of a single InAs/GaAs quantum dot in high magnetic fields. *Phys E* 2006;34:288–291.

23. Taliercio T, Lefebvre P, Morel A, Gallart M, Allegre J, Gil B, Mathieu H, Grandjean N, Massies J. Optical properties of self-assembled InGaN/GaN quantum dots. *Mater Sci Eng B* 2001;82:151–155.
24. Yacamán MJ, Ascencio JA, Liu HB, Gardea-Torresdey J. Structure shape and stability of nanometric sized particles. *J Vac Sci Technol B* 2001;19:1091–1103.
25. Navrotsky A. Energetics of nanoparticle oxides: interplay between surface energy and polymorphism. *Geochem Trans* 2003;4:34–37.
26. Xu F, Zhou W, Navrotsky A. Cadmium selenide: surface and nanoparticle energetics. *J Mater Res* 2011;26:720–725.
27. Wang L, Vu K, Navrotsky A, Stevens R, Woodfield BF, Boerio-Goates J. Calorimetric study: surface energetics and the magnetic transition in nanocrystalline CoO. *Chem Mater* 2004;16:5394–5400.
28. Iijima S, Ichihashi T. Structural instability of ultrafine particles of metals. *Phys Rev Lett* 1986;56:616–619.
29. Bovin J, Wallenberg R, Smith DJ. Imaging of atomic clouds outside the surfaces of gold crystals by electroscopy. *Nature* 1985;317:47–49.
30. Howie A. Electron microscopy: Coulomb explosions in metals. *Nature* 1986;320:684.
31. Marks LD. Experimental studies of small particle structures. *Rep Prog Phys* 1994;57:603–649.
32. Dundurs J, Marks LD, Ajayan PM. Structural fluctuations in small particles. *Philos Mag* 1988;57:605–620.
33. Li Y-F, Liu Z-P. Particle size, shape and activity for photocatalysis on titania anatase nanoparticles in aqueous surroundings. *J Am Chem Soc* 2011;133:15743–15752.
34. Chung SW, Gulians EA, Bunker CE, Jelliss PA, Buckner SW. Size-dependent nanoparticle reaction enthalpy: oxidation of aluminum nanoparticles. *J Phys Chem Solids* 2011;72:719–724.
35. Arachchige IU, Brock SL. Sol–gel assembly of CdSe nanoparticles to form porous aerogel networks. *J Am Chem Soc* 2006;128:7964–7971.
36. Wang Z, Fan AL, Tian WH, Wang YT, Li XG. Synthesis and structural features of Ni–Al nanoparticles by hydrogen plasma-metal reaction. *Mater Lett* 2006;60:2227–2231.
37. Yang J, Mei S, Ferreira JMF. Hydrothermal synthesis of nanosized titania powders: influence of tetraalkyl ammonium hydroxides on particle characteristics. *J Am Chem Soc* 2001;84:1696–1072.
38. Collins IR, Taylor SE. Nonaqueous thermal-decomposition route to colloidal inorganic oxides. *J Mater Chem* 1992;2:1277–1281.
39. Kaneko K, Ohba T, Hattori Y, Sunaga M, Tanaka S, Kanoh H. Role of gas adsorption in nanopore characterization. *Stud Surf Sci Catal* 2002;144:11–18.
40. Lowell S, Shields JE, Thomas MA, Thommes M. *Characterization of Porous Solids and Powders: Surface Area, Pore Size, and Density*. Boston, MA: Kluwer Academic Publishers; 2004. pp. 15–57, 101–156.
41. Liu AG, Nyavor K, Ankumah R. Structural and adsorptive properties of Ba or Mg oxide modified zirconia. *J Colloid Interface Sci* 2005;284:66–70.
42. Shaw DJ. *Introduction to Colloid and Surface Chemistry*. Oxford, England: Butterworth Heinemann; 1989.
43. Meixner DL, Gilicinski AG, Dyer PN. “Figure/ground” study of colloidal silica nanoparticles and corresponding microporous xerogels. *Langmuir* 1998;14:3202–3209.
44. Zhang RB, Gao L. Preparation of nanosized titania by hydrolysis of alkoxide titanium in micelles. *Mater Res Bull* 2002;37:1659–1666.

45. Yuan JJ, Zhou SX, You B, Wu LM. Organic pigment particles coated with colloidal nano-silica particles via layer-by-layer assembly. *Chem Mater* 2005;17:3587–3594.
46. Sedona F, Eusebio M, Rizzi GA, Granozzi G, Ostermann D, Schierbaum K. Epitaxial TiO₂ nanoparticles on Pt(111): a structural study by photoelectron diffraction and scanning tunneling microscopy. *Phys Chem Chem Phys* 2005;7:697–702.
47. Bennett RA, Pang CL, Perkins N, Smith RD, Morrall P, Kvon RI, Bowker M. Surface structures in the SMISI state; Pd on (1 × 2) reconstructed TiO₂(110). *J Phys Chem B* 2002;106:4688–4696.
48. Ismail AA. Synthesis and characterization of Y₂O₃/Fe₂O₃/TiO₂ nanoparticles by sol–gel method. *Appl Catal B* 2005;85:115–121.
49. Sheehan PE, Lieber CM. Nanotribology and nanofabrication of MoO₃ structures by atomic force microscopy. *Science* 1996;272:1158–1161.
50. Binnig G, Rohrer H. Scanning tunneling microscopy. *IBM J Res Dev* 1986;30:355.
51. Friedbacher G, Hansma PK, Ramli E, Stucky GD. Imaging powders with the atomic force microscope from biomaterials to commercial materials. *Science* 1991;253:1261–1263.
52. Dujardin G, Mayne A, Robert O, Rose F, Joachim C, Tang H. Vertical manipulation of individual atoms by a direct STM tip-surface contact on Ge(111). *Phys Rev Lett* 1998;80:3085–3088.
53. Song D, Hrbek J, Osgood R. Formation of TiO₂ nanoparticles by reactive-layer-assisted deposition and characterization of XPS and STM. *Nano Lett* 2005;5:1327–1332.
54. Lin W-C, Chang H-Y, Hu Y-T, Kuo C-C. Fabrication of Fe nanoparticle assemblies on Au(111) with Xe buffer layer and low temperature growth. *Jpn J Appl Phys* 2009;48:08JB07 5pp.
55. Choo HP, Liew KY, Liu HF. Factors affecting the size of polymer stabilized Pd nanoparticles. *J Mater Chem* 2002;12:934–937.
56. Su HL, Xie Y, Li B, Liu XM, Qian YT. Mild solvothermal route to nanocrystalline Cu₃P and Ni₂P. *Solid State Ionics* 1999;122:157–160.
57. Guimarães JL, Abbate M, Betim SB, Alves MCM. Preparation and characterization of TiO₂ and V₂O₅ nanoparticles produced by ball-milling. *J Alloys Compd* 2003;352:16–20.
58. Schaefer ZL, Ke X, Schiffer P, Schaak RE. Direct solution synthesis, reaction pathway studies, and structural characterization of crystalline Ni₃B nanoparticles. *J Phys Chem C* 2008;112:19846–19851.
59. O'Brien S, Brus L, Murray CB. Synthesis of monodisperse nanoparticles of barium titanate: toward a generalized strategy of oxide nanoparticle synthesis. *J Am Chem Soc* 2001;123:12085–12086.
60. Baldinozzi G, Simeone D, Gosset D, Dutheil M. Neutron diffraction study of the size induced tetragonal to monoclinic phase transition. *Phys Rev Lett* 2003;90:216103 4pp.
61. Lu K. In: Tseng TY, Nalwa HS, editors. *Shaping of 3D Nanoceramics and Their Composites: Handbook of Nanoceramics and Their Based Devices*. Stevenson Ranch, CA: American Scientific Publishers; 2009. Vol 2, pp. 151–177.
62. Paparazzo E, Moretto L, Brolatti M. Auger electron spectroscopy (AES) and electron energy loss spectroscopy (EELS) studies of GaP and Si surfaces. *Vacuum* 2002;65:193–206.
63. Wang J, Gao L. Surface properties of polymer adsorbed zirconia nanoparticles. *Nanostruct Mater* 1999;11:451–457.
64. Vdovenkova T, Strikha V, Tsyganova A. Silicon nanoparticles characterization by Auger electron spectroscopy. *Surf Sci* 2000;454–456:952–956.
65. Villegas MA, García MA, Paje SE, Llopis J. Parameters controlling silver nanoparticle growth in sol-gel silica coatings. *Mater Res Bull* 2005;40:1210–1222.

66. Zhu F, Kong ES, Zhang J, Zhang YF. Surface modification of TiO₂ nanoparticles through plasma polymerization of acrylic acid. *Chem Phys Lett* 2006;423:270–275.
67. Steigerwald ML, Alivisatos AP, Gibson JM, Harris TD, Kortan R, Muller AJ, Thayer AM, Duncan TM, Douglass DC, Brus LE. Surface derivatization and isolation of semiconductor cluster molecules. *J Am Chem Soc* 1988;110:3046–3050.
68. Sergeev BM, Kasaikin VA, Litmanovich EA, Sergeev GB, Prusov AN. Cyrochemical synthesis and properties of silver nanoparticle dispersions stabilized by poly(2-dimethylaminoethyl methacrylate). *Mendeleev Commun* 1999;4:130–132.
69. Elder SH, Cot FM, Su Y, Heald SM, Tyryshkin AM, Bowman MK, Gao Y, Joly AG, Balmer ML, Kolwaite AC, Magrini KA, Blake DM. The discovery and study of nanocrystalline TiO₂-(MoO₃) core-shell materials. *J Am Chem Soc* 2000;122:5138–5146.
70. Zhang J, Post M, Veres T, Jakubek ZJ, Guan JW, Wang DS, Normandin F, Deslandes Y, Simard B. Laser-assisted synthesis of superparamagnetic Fe@Au core-shell nanoparticles. *J Phys Chem B* 2006;110:7122–7128.
71. Li XG, Liu T, Sato M, Takahashi S. Synthesis and characterization of Fe-Ti nanoparticles by nitrogen plasma metal reaction. *Powder Technol* 2006;163:183–187.
72. Broekaert JAC. *Analytical Atomic Spectrometry with Flames and Plasmas*. Weinheim, Germany: Wiley-VCH; 2002.
73. Narayan A, Landström L, Boman M. Laser-assisted synthesis of ultra small metal nanoparticles. *Appl Surf Sci* 2003;208–209:137–141.
74. Alm O, Landström L, Boman M, Granqvist CG, Heszler P. Tungsten oxide nanoparticles synthesized by laser assisted homogeneous gas-phase nucleation. *Appl Surf Sci* 2005;247:262–267.
75. Liu JY. Scanning transmission electron microscopy and its application to the study of nanoparticles and nanoparticle systems. *J Electron Microsc* 2005;54:251–278.
76. Darbandi M, Lu WG, Fang JY, Nann T. Silica encapsulation of hydrophobically ligated PbSe nanocrystals. *Langmuir* 2006;22:4371–4375.
77. Jadhav AP, Kim CW, Cha HG, Pawar AU, Jadhav NA, Pal U, Kang YS. Effect of different surfactants on the size control and optical properties of Y₂O₃:Eu³⁺ nanoparticles prepared by coprecipitation method. *J Phys Chem C* 2009;113:13600–13604.
78. Courtois E, Epicier T, Scott C. EELS study of niobium carbo-nitride nano-precipitates in ferrite. *Micron* 2006;37:492–502.
79. Wei DG, Dave R, Pfeffer R. Mixing and characterization of nanosized powders: an assessment of different techniques. *J Nanopart Res* 2002;4:21–41.
80. Wang C, Baer DR, Amonette JE, Engelhard MH, Antony J, Qiang Y. Morphology and electronic structure of the oxide shell on the surface of iron nanoparticles. *J Am Chem Soc* 2009;131:8824–8832.
81. Cheng FY, Su CH, Yang YS, Yeh CS, Tsai CY, Wu CL, Wu MT, Shieh DB. Characterization of aqueous dispersions of Fe₃O₄ nanoparticles and their biomedical applications. *Biomater* 2005;26:729–738.
82. Salari M, Mousavikhoie SM, Marashi P, Rezaee M. Synthesis of TiO₂ nanoparticles via a novel mechanochemical method. *J Alloys Compd* 2009;469:386–390.
83. Esumi K, Suzuki A, Yamahira A, Torigoe K. Role of poly(amidoamine) dendrimers for preparing nanoparticles of gold, platinum, and silver. *Langmuir* 2000;16:2604–2608.
84. Mallin MP, Murphy CJ. Solution-phase synthesis of sub-10 nm Au–Ag alloy nanoparticles. *Nano Lett* 2002;2:1235–1237.
85. Bronstein L, Chernyshov D, Valetsky P, Tkachenko N, Lemmetyinen H, Hartmann J, Forster S. Laser photolysis formation of gold colloids in block copolymer micelles. *Langmuir* 1999;15:83–91.

86. Wu J, Zhang H, Zhang J, Yao T, Sun H, Yang B. Control of the self-assembly behaviors of charged gold nanoparticles. *Colloids Surf A* 2009;348:240–247.
87. Deshpande AS, Pinna N, Beato P, Antonietti M, Niederberger M. Synthesis and characterization of stable and crystalline $Ce_{1-x}Zr_xO_2$ nanoparticle sols. *Chem Mater* 2004;16:2599–2604.
88. Lam C, Zhang YF, Tang YH, Lee CS, Bello I, Lee ST. Large-scale synthesis of ultra fine Si nanoparticles by ball milling. *J Cryst Growth* 2000;220:466–470.

CHAPTER 4

NANOPARTICLE-BASED SUPERSTRUCTURES

4.1 INTRODUCTION

In recent years, a new class of nanoparticle-based materials has emerged thanks to the advancement in nanoparticle interaction understanding as well as the availability of new nanoparticle characterization and manipulation tools. This group of materials can be identified as nanoparticle-based superstructures or synthetic structures. Based on the approaches used to create them, five different processes can be identified: (1) top-down, such as by different lithographic techniques; (2) bottom-up, whereby superstructures are constructed from nanoscale via self-assembly, directed assembly, or manipulation of nanoparticles; (3) the hybrids of the top-down and bottom-up approaches; (4) templating, in which unique structures act as the skeletons for the creation of nanoparticle-based superstructures; and (5) three-dimensional assembly, where nanoparticles are arranged into three-dimensional structures based on some fundamental interparticle interactions. This group of superstructure materials bridges the scale between discrete nanoparticles and nanoparticle-based bulk materials. One example of the advancements is the progressive ability to fabricate smaller and smaller structures, and another is the continuous improvement in the precision with which such structures are made.

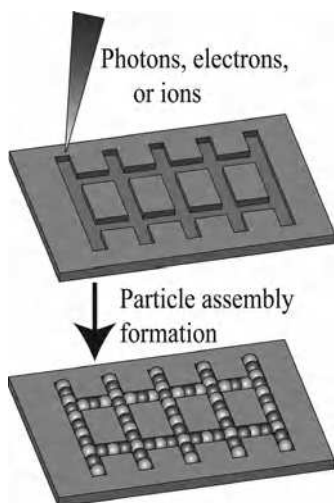


FIGURE 4.1 Top-down process of creating superstructures. (For a color version of this figure, see the color plate section.)

4.2 TOP-DOWN PROCESSES

The top-down process of creating nanoparticle-based superstructures means starting with bulk materials and producing the intended structures or sizes at <100 nm by breaking down the bulk materials into nanoscale entities. It is also described as a “subtractive” nanostructure creation process (Fig. 4.1). Different from the milling process addressed in Chapter 2, the top-down process for nanoparticle-based synthetic structure creation organizes nanoparticles in a controlled rather than a random manner. The beam sources used include photons, electrons, and ions. Also, the amount of nanoparticles involved is much smaller. The arrangement of nanoparticles is carefully controlled and often exhibits periodicity. Usually a substrate is required to support the carefully constructed superstructures.

Among the techniques reported, nanoparticle-based structures are often generated on a surface via projection patterning methods. During this process, a mask may be imaged via photons; or electrons, ions, or atoms may directly bombard a sensitive substrate. As a result of these external stimulants, nanoparticle superstructures (often in a specific arrangement) are created for novel functions and performance. The patterning rate generally decreases from photons, to ions, to electrons because of the operation mode difference (parallel for photons while mostly serial for electrons and ions) and the bombardment energy difference (ions have much higher energy than electrons). The minimum superstructure sizes are determined by the diffraction limits during the exposure with photons, electrons, or ions.

4.2.1 Photolithography

Photolithography is a process used to selectively remove parts of a thin film or the surface of a substrate. It uses light to transfer a geometric pattern from a photomask to a light-sensitive chemical photoresist, or simply “resist,” on a substrate. An illustration of the general photolithography process is shown in Figure 4.2a. Depending on whether the mask is in contact with the substrate or not, it can be further divided into contact, proximity, and projection modes. The process has good control over the shape and size of the features up to submicron. The minimum structure size that can be obtained in photolithographic methods scales with the wavelength of light λ_L and is given by the Rayleigh criterion, which can be understood as follows. Far away from the aperture, the angle θ_{\min} at which the first minimum occurs, measured from the direction of incoming light, is given by the approximate formula:

$$\sin \theta_{\min} \approx 1.22 \frac{\lambda_L}{d_A} \quad (4.1)$$

or, for small angles, simply

$$\theta_{\min} \approx 1.22 \frac{\lambda_L}{d_A}, \quad (4.2)$$

where θ_{\min} is in radians, λ_L is the wavelength of the light, and d_A is the diameter of the aperture. The Rayleigh criterion for barely resolving two objects that are point sources of light is that the center of the Airy disk (the diffraction pattern resulting from a uniformly illuminated circular aperture has a bright region in the center, known as the Airy disk) for the first object occurs at the first minimum of the Airy disk of the second. This is also the point when the angular separation of the two objects is $2\theta_{\min}$. For a spatial resolution below 100 nm, shorter light wavelengths (e.g., $\lambda_L = 157$ nm from an F2 excimer laser) or phase shifting photolithography has to be used (Fig. 4.2b). The latter case uses photomasks that take advantage of the interference generated by phase differences to improve image resolution in photolithography. When the thickness is suitably chosen, the interference of the phase-shifted light with the light coming from the unmodified regions of the mask is minimized and has the effect of improving the contrast at adjacent boundaries, which may ultimately increase the resolution of the designed features. The ideal case is a phase shift of 180° , which results in the boundary light intensity at zero.

Photolithography can create patterns over an entire surface simultaneously. It is well suited for scaling-up. The main disadvantages are that it requires a flat substrate to start with, it is not very effective in creating shapes that are not flat, and it requires extremely clean operating conditions. Photolithography is one of the most mature techniques in the top-down nanostructure creation process. Depending on the nature of nanoparticles, nanoparticle superstructure construction relying on photolithography can be divided based on the type of species: metals, ceramics, or semiconductors. For metal species, the formation of nanoparticle

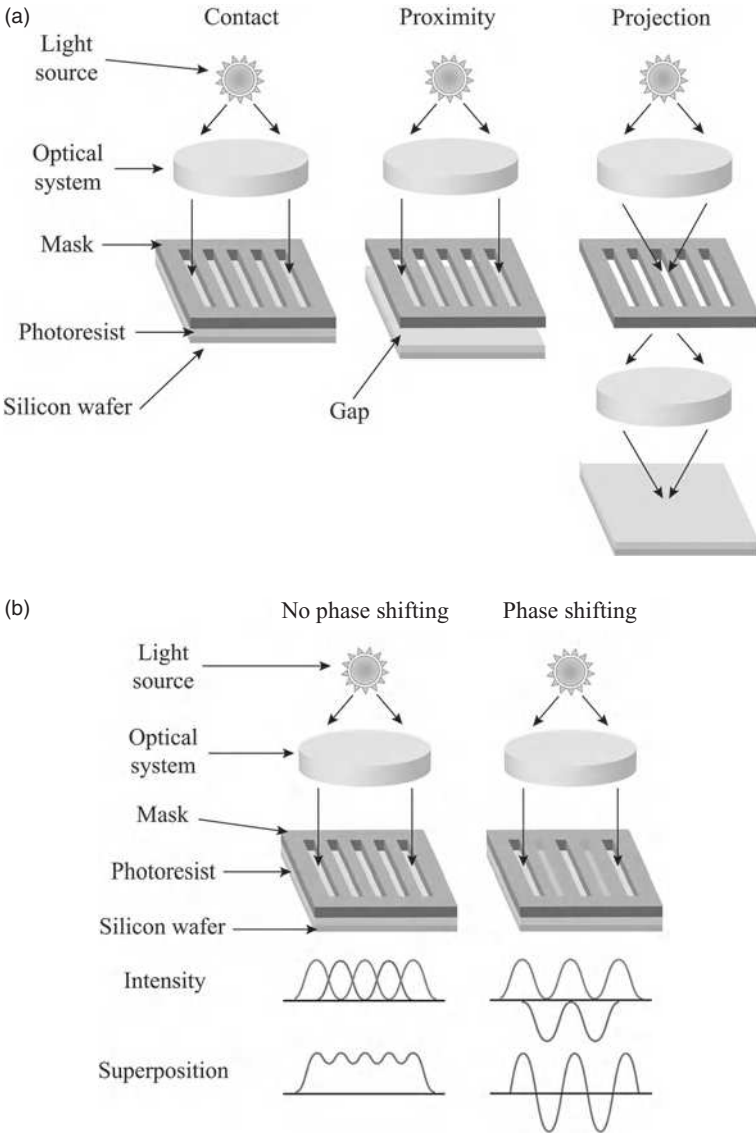


FIGURE 4.2 Photolithography process: (a) contact, proximity, and projection methods, (b) phase shifting photolithography. (For a color version of this figure, see the color plate section.)

superstructures mostly involves metal ion reduction to elemental metal. For ceramic species, both chemical reactions and direct nanoparticle assembly may be involved. For semiconductor species, chemical reaction is necessary in light of the instability of the involved species, such as quantum dots.

Pattern metallization of diamond film surfaces is studied by photolithography. First, hydrogen-terminated diamond film surfaces are activated through bonding with allylamine ($C_3H_5NH_2$) molecules under 254 nm ultraviolet (UV) light irradiation. Then, amino prepatterns on the diamond surfaces are constructed by a photolithographic process. Subsequently, gold nanoparticle patterns are obtained through the immobilization of 15 ± 3 nm gold nanoparticles on the amino prepatterns, and the remnant photoresist is removed by rinsing with acetone. Finally, the gold nanoparticle patterns are enhanced through silver deposition and intact silver-gold micropatterns are constructed on diamond surfaces [1] (Fig. 4.3).

Periodic arrays of silver nanoparticles are fabricated on various solid substrates by block copolymer photolithography. Spin-coated block copolymer thin films with well-ordered and vertically oriented cylindrical nanodomains are utilized as the templates. Ag^+ is selectively doped in the cylindrical nanodomain by just placing a few drops of $AgNO_3$ aqueous solution on the film. Both photochemical reduction of Ag^+ to metallic silver and concomitant photo-etching of the block copolymer template are achieved under UV light irradiation in a vacuum, resulting in a direct transcription of the periodic pattern of block copolymer template to the metallic silver nanoparticle array with consistent periodicity [2]. Nanoparticles

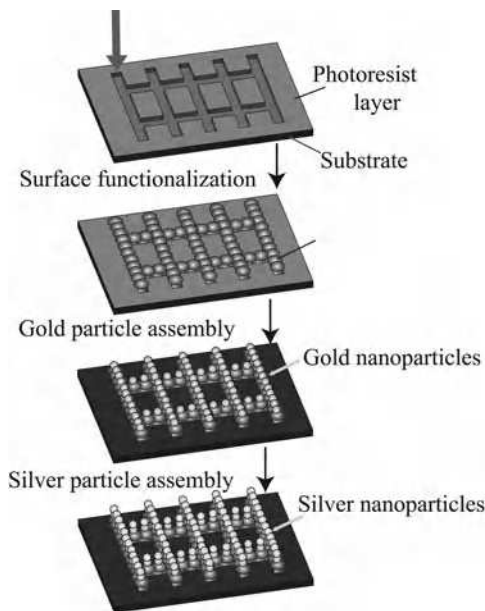


FIGURE 4.3 Silver-gold micropatterns via photolithography. (For a color version of this figure, see the color plate section.)

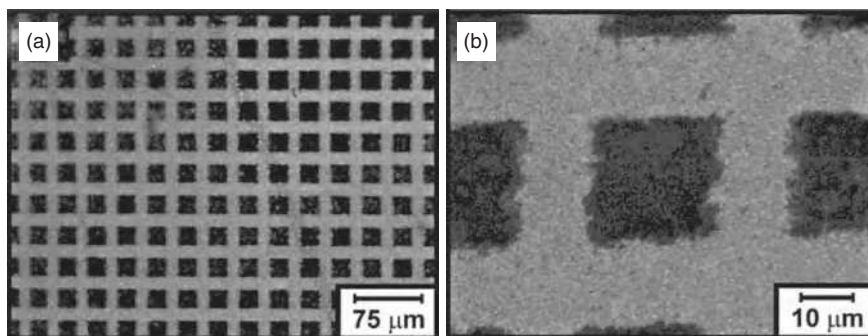


FIGURE 4.4 Scanning electron micrographs of photopatterned deposition of palladium on a Ge(100) surface. The square regions are dodecyl terminated; the grid lines remain hydride terminated. The organic monolayers act as an effective ultrathin resist, and immersion in 2 mM aqueous PdCl_4^{2-} for 30 seconds results in selective deposition within the hydride-terminated grid lines [3]. (Reprinted with permission from Porter LA Jr., Choi HC, Schmeltzer JM, Ribbe AE, Elliott LCC, Buriak JM. Electroless nanoparticle film deposition compatible with photolithography, microcontact printing, and dip-pen nanolithography patterning technologies, *Nano Lett* 2002;2:1369–1372, Copyright 2002, American Chemical Society.)

of gold, palladium, and platinum can also spontaneously form thin, morphologically complex metallic films on various semiconducting or metal substrates such as Ge(100), copper, zinc, and tin, via galvanic displacement from aqueous metal salt solutions. Patterning of these metal films into ordered structures utilizing photolithography is demonstrated on flat Ge(100) [3]. Thin, well-adhering nanoparticle films are prepared via immersion of Ge(100) and metal substrates into dilute, aqueous solutions of AuCl_4^- , PdCl_4^{2-} , or PtCl_4^{2-} salts. Deposition proceeds via galvanic displacement in the absence of fluoride, pH buffers, complexing agents, or external reducing agents. Figure 4.4 shows the images of photopatterned deposition of palladium on a Ge(100) surface. 1-Dodecene ($\text{CH}_3(\text{CH}_2)_9\text{CH}=\text{CH}_2$) forms bonds with the Ge(100) surface via $\text{Ge}(100)\text{-H}_x$ bonds, mediated by UV light in the unmasked areas, which results in dodecyl termination in the square regions; the grid lines remain hydride terminated. The organic monolayers act as an effective ultrathin resist, and immersion in 2 mM aqueous PdCl_4^{2-} for 30 seconds results in selective deposition of palladium within the hydride-terminated grid lines.

Photolithography techniques are also used to pattern nanoparticles on glass surfaces. SiO_2 nanoparticles are assembled in a monolayer fashion through the use of halogenated silanes. The concentration of the SiO_2 nanoparticles in the solution controls the surface coverage of the nanoparticles on the glass surface. Different patterned SiO_2 arrays are made with controlled surface coverage. The nanoparticle-covered surface is successfully tested for surface-enhanced enzymatic reactivity for the detection of a neurotransmitter, glutamate [4].

Metal nanoparticle-based microelectrode arrays are made by combining photolithography and photocatalytic deposition (Fig. 4.5) [5]. Photolithographically

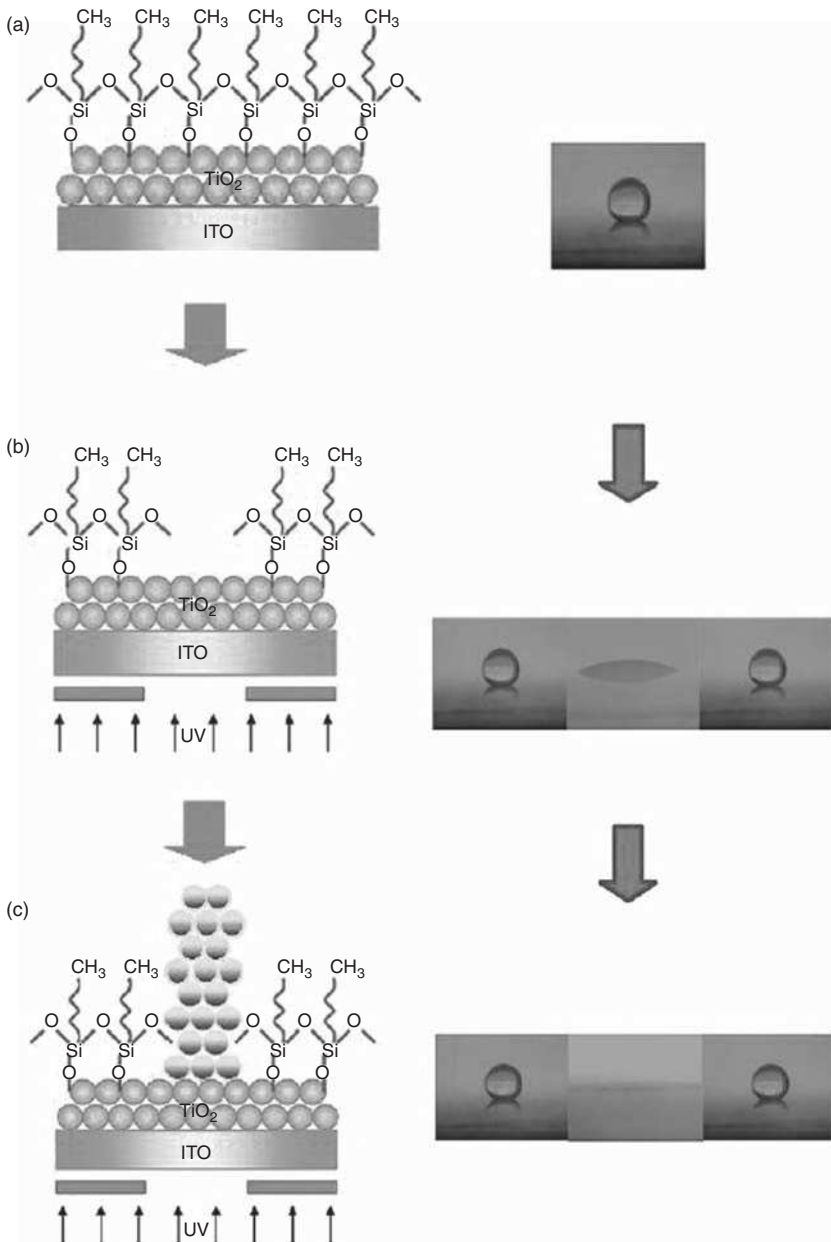


FIGURE 4.5 Fabrication procedure of microelectrode arrays: (a) superhydrophobic ODS-modified TiO_2 film, (b) TiO_2 nanoparticle-based microelectrode arrays after photolithography with a photomask, and (c) metal nanoparticle-based microelectrode arrays after site-selective photocatalytic deposition of metal nanoparticles [5]. (Reprinted with permission from Li X, Tian Y, Xia P, Luo Y, Rui Q. Fabrication of TiO_2 and metal nanoparticle-microelectrode arrays by photolithography and site-selective photocatalytic deposition. *Anal Chem* 2009;81:8249–8255, Copyright 2009, American Chemical Society.) (For a color version of this figure, see the color plate section.)

selective decomposition of superhydrophobic *n*-octadecyltriethoxysilane (ODS) is used to create superhydrophobic TiO₂ patterns. As schematically shown in Figure 4.5, TiO₂ nanoparticles are first deposited layer-by-layer on a glass surface. Then, superhydrophobic ODS is attached to the TiO₂ surface. After that, ODS is selectively removed by photolithography from the backside of the glass substrate. Finally, metal nanoparticles are selectively deposited on the patterned areas by site-selective photocatalytic deposition. As a result, metal nanoparticle-based microelectrode arrays are produced.

As a specific example, Figure 4.6 shows the fluorescence micrographs of TiO₂ patterns with 6 μm radius disks (Fig. 4.6a) and 10 μm bandwidths (Fig. 4.6b), indicating that the patterned TiO₂ films retain the dimensions of the photomasks without noticeable spreading. Figures 4.6c and d are at higher magnifications and show the details of the nanoparticles. The diameter of the TiO₂ nanoparticles dispersed onto the indium-doped tin oxide substrate is in the range of 20–50 nm, and

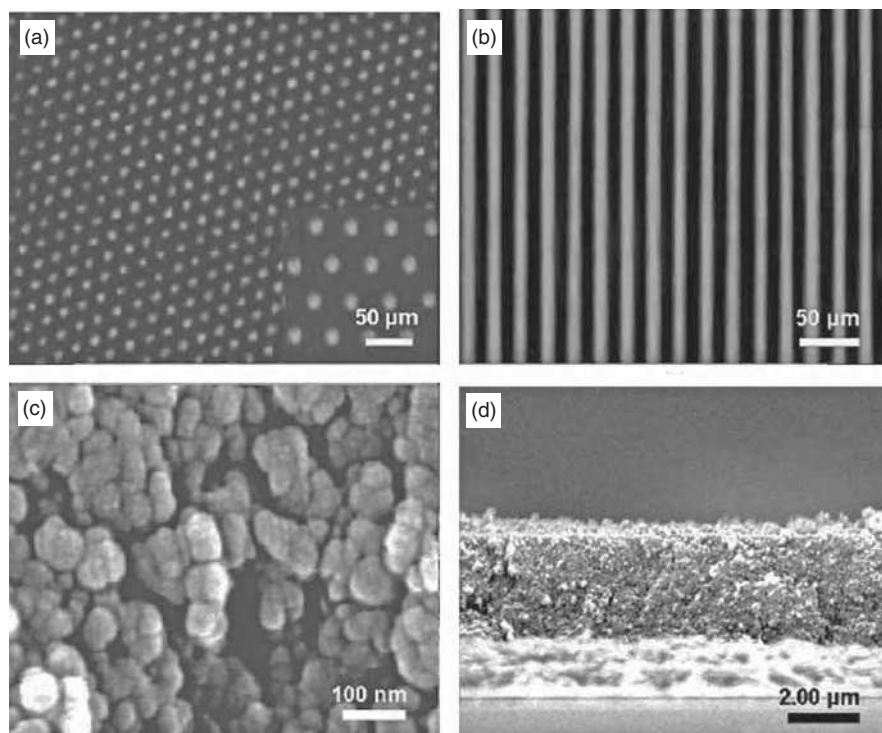


FIGURE 4.6 (a, b) Fluorescence micrographs of TiO₂ nanoparticle-based microelectrode arrays (a) with a disk radius of 6 μm and (b) with a bandwidth of 10 μm. (c, d) SEM images of TiO₂ film (Panel d shows a cross-sectional image.) [5]. (Reprinted with permission from Li X, Tian Y, Xia P, Luo Y, Rui Q. Fabrication of TiO₂ and metal nanoparticle-microelectrode arrays by photolithography and site-selective photocatalytic deposition. *Anal Chem* 2009;81:8249–8255, Copyright 2009, American Chemical Society.)

the thickness of the TiO_2 film is $\sim 3 \mu\text{m}$. The superhydrophobic/superhydrophilic TiO_2 surface, which functions as a template, can be employed to selectively fill superhydrophilic regions with water-soluble materials. For gold nanoparticle-based patterns, a solution of 0.1 M HAuCl_4 is introduced drop-wise on the superhydrophobic/superhydrophilic surface. UV light goes through the photomask and irradiates onto the back of the indium-doped tin oxide substrate to reduce the metal ions in solution to metal nanoparticles. Because TiO_2 has well-studied photocatalytic properties, it is an excellent choice for reducing metal ions from the solution by UV illumination. Figures 4.7a and b present gold nanoparticle patterns produced from the $10 \mu\text{m}$ bandwidth of superhydrophobic/superhydrophilic TiO_2 templates. From microscopic (Fig. 4.7a) and atomic force microscope (AFM) (Fig. 4.7b) images, elevated patterns of gold nanoparticles with $10 \mu\text{m}$ width and $\sim 750 \text{ nm}$ height bands are observed. Meanwhile, the patterns of gold nanoparticles with $6 \mu\text{m}$ radius disks are also shown in Figures 4.7c and d. The sizes of these patterns are in good agreement with the respective TiO_2 nanoparticle-based patterns, suggesting that TiO_2 patterns have been successfully employed as templates for the production of metal nanoparticle-based patterns. For the patterned surface, large wettability and electrochemical activity contrasts are found, which can be used to further applications in microelectrode arrays.

Coupling with photolithography, a promising approach for nanoparticle-based superstructure construction is colloidal epitaxy, that is, the deposition of colloidal particles onto lithographically fabricated substrates. Use of prepatterned substrates enables fabrication of two-dimensional and three-dimensional surface structures via substrate-guided self-assembly of nanoparticles. In one instance, photolithography is used to create a matrix for the selective deposition of nanoparticles by immersion in a colloidal suspension. Commercial SiO_2 nanoparticles are directly dispersed; TiO_2 nanoparticles are deposited after being prepared by hydrolysis of titanium isopropoxide and thermal treatment. During the deposition, the substrates are immersed into the corresponding nanoparticle suspensions and vertically drawn at a controlled rate. Structures of SiO_2 particles on the TiO_2 surface and TiO_2 particles on the SiO_2 surface are formed by deposition of SiO_2 or TiO_2 nanoparticles on prepatterned substrates. Although two-dimensional colloidal patches of TiO_2 nanoparticles are obtained on the SiO_2 surfaces, SiO_2 nanoparticles form three-dimensional, U-shaped channels on the TiO_2 surfaces. The isoelectric points of the particles, the prepatterned matrix, and the photoresist are key parameters and may be manipulated to achieve various microstructures. The two-dimensional nanoparticle arrays of TiO_2 on the SiO_2 surfaces and the three-dimensional channels of SiO_2 nanoparticles on the TiO_2 surfaces are of potential interest in lab-on-a-chip applications [6].

Instead of immersion, dewetting can be used to guide the assembly of colloidal nanoparticles. First, a surface is photolithographically patterned. Then, it is immersed in an aqueous dispersion of colloidal particles. During dewetting, the colloidal particles are trapped by the recessed regions and assembled into aggregates, whose shapes and sizes are determined by the geometric confinement provided by the template.

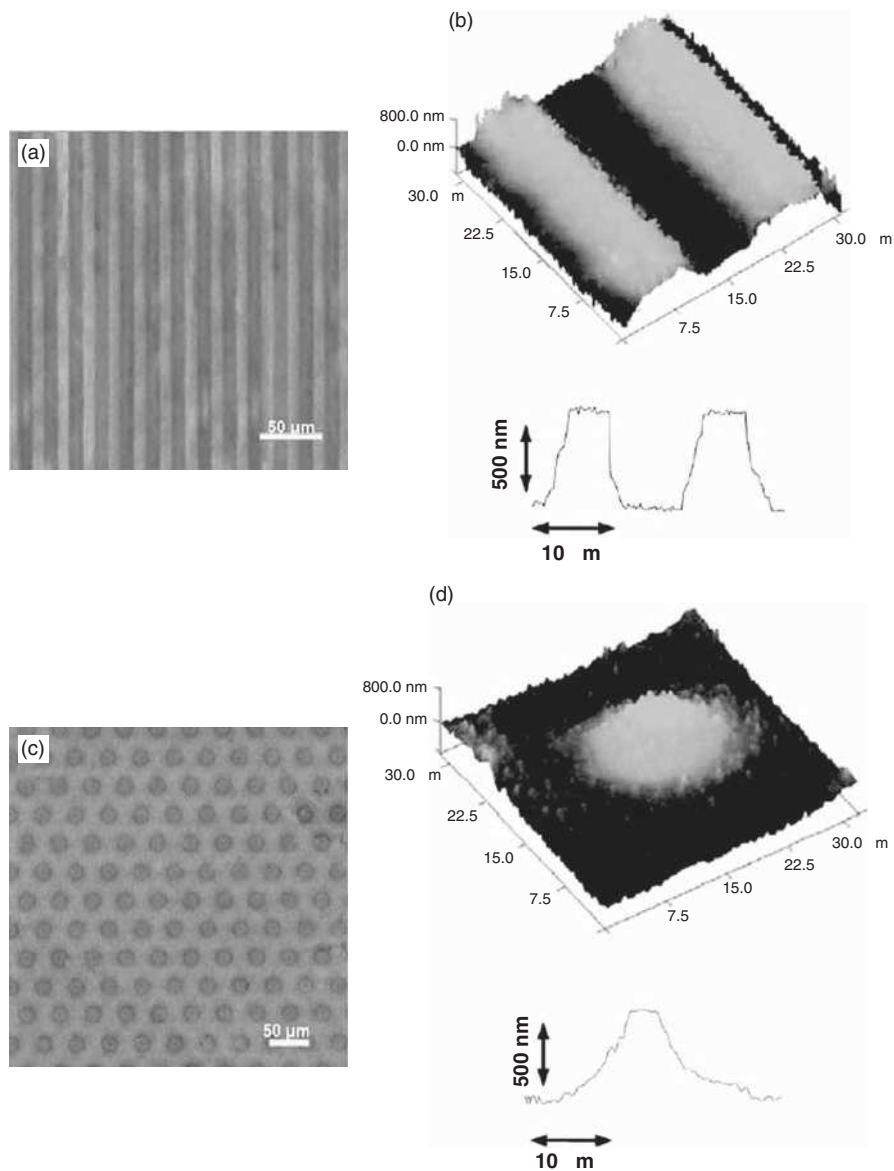


FIGURE 4.7 (a, c) Microscopic images and (b, d) AFM images of elevated gold nanoparticle-based microarray electrodes (a, b) with 10 μm bandwidth and (c, d) with 6 μm disk radius [5]. (Reprinted with permission from Li X, Tian Y, Xia P, Luo Y, Rui Q. Fabrication of TiO₂ and metal nanoparticle-microelectrode arrays by photolithography and site-selective photocatalytic deposition. *Anal Chem* 2009;81:8249–8255, Copyright 2009, American Chemical Society.) (For a color version of this figure, see the color plate section.)

Nanosphere lithography is yet another process that relies on photons to immobilize nanoparticles. It begins with self-assembly of a nanosphere mask onto a substrate followed by line-of-sight deposition of nanoparticles through the mask. This is a parallel, rather than serial, nanoparticle fabrication method. In general, the substrate to be patterned is positioned normal to the direction of nanoparticle deposition. The shape and interparticle spacing of the resultant nanoparticle clusters are determined by the projection of the nanosphere mask interstices onto the substrate. A monolayer mask produces nanoparticles with a triangular shape and hexagonal symmetry. An array of $\text{La}_{0.67}\text{Sr}_{0.33}\text{MnO}_3$ nanoparticle superstructures is made via nanosphere lithography. During the process, a monolayer of hexagonally arranged SiO_2 microspheres is employed as a mask for pulsed laser deposition. Nanoparticle superstructures around 100 nm are obtained with a KrF laser of $\lambda_L = 248$ nm. This approach opens the possibility of fabricating nanopatterned multicomponent oxides, which include magnetoresistive manganites, superconducting cuprates, and other perovskite oxides [7].

Angle-resolved nanosphere lithography is a variant of nanosphere lithography that yields vastly different and increasingly flexible nanostructures by fine-tuning the size, shape, and spacing of nanoparticle superstructures. Patterning is accomplished by controlling the angle between the surface normal of the substrate and the propagation vector of the photon beam. One limitation of the angle-resolved nanosphere lithography technique is the inability to pattern an entire substrate with a single superstructure geometry without control of the mask domain orientation [8]. Although the presence of multiple superstructure shapes in any given mask complicates the fabrication of large-area, homogeneous nanoparticle arrays, this quality is, in fact, useful in laboratory scale experiments requiring a diverse set of nanostructure features on a single sample. The precise tuning of nanoparticle-based superstructure size, shape, and spacing in a parallel fashion using angle-resolved nanosphere lithography can improve surface-enhanced spectroscopy, near-field optical microscopy, nanoscopic object manipulation, and chemical/biological sensing. Figure 4.8 depicts four examples of angle-resolved nanosphere lithography-generated nanoparticle arrays. The simulated nanoparticle superstructure shape is overlaid on the actual nanoparticle positions in the panels on the right. The substrate is Si(111) and the deposited nanoparticles are chromium. θ is the angle between the surface normal of the substrate and the propagation vector of the photon beam. Φ is the azimuthal angle of the mask (the angle between the line connecting the origin and the point of interest and the reference line projected perpendicularly on the substrate).

CdS quantum dots are fabricated photolithographically on substrates and in the bulk of SiO_2 hydrogels. When substrates are used, superstructures are patterned by illuminating a precursor solution spin coated on the substrates. For the SiO_2 hydrogels, the process starts with a base-catalyzed route, and the solvent is exchanged with an aqueous solution of $\text{Cd}(\text{NO}_3)_2$, NH_4OH , thiourea, and a capping agent, for example, 2-mercaptoethanol. The samples are then exposed to a focused infrared beam produced by a continuous-wave Nd:YAG laser. The precursors react upon heating, and CdS nanoparticles form in the illuminated

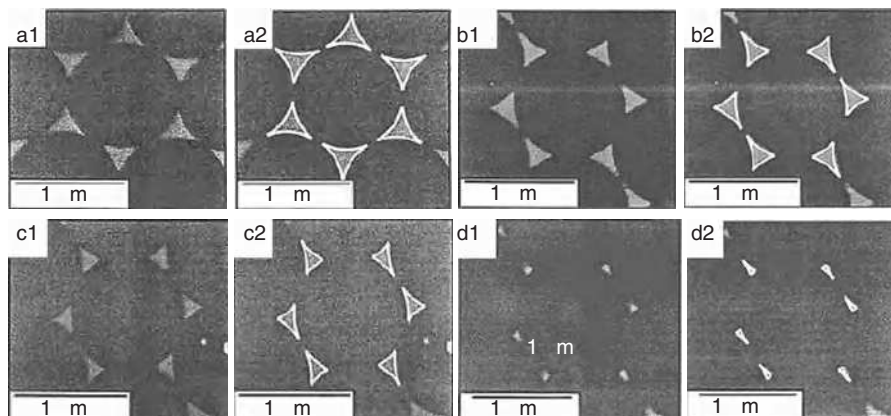


FIGURE 4.8 Field-emission scanning electron micrographs of angle-resolved nanosphere lithography-fabricated nanoparticle arrays and images with simulated geometry superimposed, respectively. (a1, a2) $\theta = 10^\circ$, $\varphi = 28^\circ$, (b1, b2) $\theta = 20^\circ$, $\varphi = 2^\circ$, (c1, c2) $\theta = 26^\circ$, $\varphi = 16^\circ$, and (d1, d2) $\theta = 40^\circ$, $\varphi = 2^\circ$. All samples are chromium deposited onto Si (111) substrates [8]. (Reprinted with permission from Haynes CL, McFarland AD, Smith MT, Hulteen JC, Van Duyn RP. Angle-resolved nanosphere lithography: manipulation of nanoparticle size, shape, and interparticle spacing. *J Phys Chem B* 2002;106:1898–1902, Copyright 2002, American Chemical Society.)

regions. The average size of the CdS nanoparticles can be varied between 1.5 and 4.5 nm by varying the type and the concentration of the capping agents [9]. However, the process needs to be carefully controlled to avoid quantum dot defect formation. CdS nanoparticles are also created based on the photo dissociation of thiols and cadmium–thiolate complexes [10]. Again, SiO₂ hydrogels are prepared by following a conventional base-catalyzed route. The hydrogels are then washed and bathed in a solution of CdSO₄ and 2-mercaptoethanol (HOCH₂CH₂SH) for about 2 hours. The best results are obtained by using a thiol concentration at least 10 times higher than the metal ion concentration and adding NH₄OH to reach a pH of at least 7.5, for example, [CdSO₄] = 0.1 mol l⁻¹, [HOCH₂CH₂SH] = 1 mol l⁻¹, and [NH₄OH] = 4 mol l⁻¹. The hydrogel samples are placed in a glass cuvette filled with the bathing solution for index matching and are exposed to UV light. The laser power on the sample is on the order of 50 mW, and the illuminated spots have a diameter between 3 and 100 μm. CdS nanoparticles form in the illuminated spots and have a diameter below about 2 nm. However, UV beam irradiation can create various undesirable intermediate compounds and CdS aggregates and should be carefully controlled.

4.2.2 Electron Beam Lithography

Electron beam lithography is one of the best tools for patterning nanostructures on a substrate, which can be subsequently used for nanoparticle-based superstructure

construction. In electron beam lithography, nanostructures are “written” in an electron resist (usually a polymer such as poly(methyl methacrylate), PMMA). “Writing” in terms of electron irradiation means that the structure of the resist is changed at the irradiation such that in a subsequent process, the irradiation area can be dissolved in a chemical reagent, and a nanoscale template can be obtained.

Compared to photolithography, electron beam lithography mainly involves metal nanoparticle superstructure creation. This is because the leading step for nanoparticle superstructure creation involves deposition of nanoparticles into very small size features. Metal species can be easily made into small, uniform sizes and then modified, resulting in well-controlled sizes and relatively stable states. Deposition of ceramic or semiconducting nanoparticles is theoretically possible in creating patterns. However, the small size of the electron beam patterned features means that the nanoparticles must be very small in size (typically a few nanometers), have a narrow size distribution, and be stable during the patterning process, which are difficult to achieve.

SiO₂ surfaces are patterned with colloidal gold nanoparticles. The patterns are created by electron beam lithography and treated with aminopropyltriethoxysilane (APTES). APTES covalently attaches to the surface and displays positively charged amine groups. These groups in turn attract the negatively charged citrate-stabilized colloidal gold nanoparticles. Nanoparticles can be placed in continuous and straight lines just one nanoparticle wide and many nanoparticles long (Fig. 4.9a) [11]. By controlling the width of the SiO₂ trenches, the nanoparticles may also be deposited in two-particle wide lines or even in zigzag patterns (Fig. 4.9b). In the final electron beam lithography step, two or more metal contacts can be placed across the nanoparticle chain (Fig. 4.9c). This makes pairs of electrodes separated by gaps of tens of nanometers. Many of these electrode pairs are bridged by just one nanoparticle.

Thiol-capped gold and silver nanoparticles of 2–10 nm size are directly bombarded by an electron beam. The beam spot size is ~70 nm. Three wafers are exposed with subsequent layers in (1) silver–silver–silver, (2) silver–gold–silver, and (3) gold–gold–gold configurations to test the superstructure construction. Multiple layers and multiple materials with line width resolutions of 80–100 nm are built [12]. In a different study, gold and platinum nanoparticles of 2–15 nm are made by pulsed laser ablation in helium gas and negatively charged after the size selection. Anionic nanoparticles are deposited onto silicon substrates (phosphorous (P)-doped *n*-type, 3–5 Ω cm resistivity) with features designed by electron beam lithography. Extra nanoparticles deposited on the photoresist are removed by dissolving the resist, resulting in designable patterns of gold and platinum nanoparticle arrays [13]. Figure 4.10 shows the scanning electron images of gold nanoparticles (average diameter 13.8 nm) deposited onto the silicon substrate patterned by electron beam lithography. Two patterns of circular dots of 500 nm in diameter (Fig. 4.10a and c) and two one-dimensional channels of 100 nm width (Fig. 4.10b and d) are demonstrated. Nanoparticles are uniformly deposited on the photoresist and on the bare silicon patterns (see Fig. 4.10a and b). By removing the photoresist, the gold nanoparticles on the photoresist are also

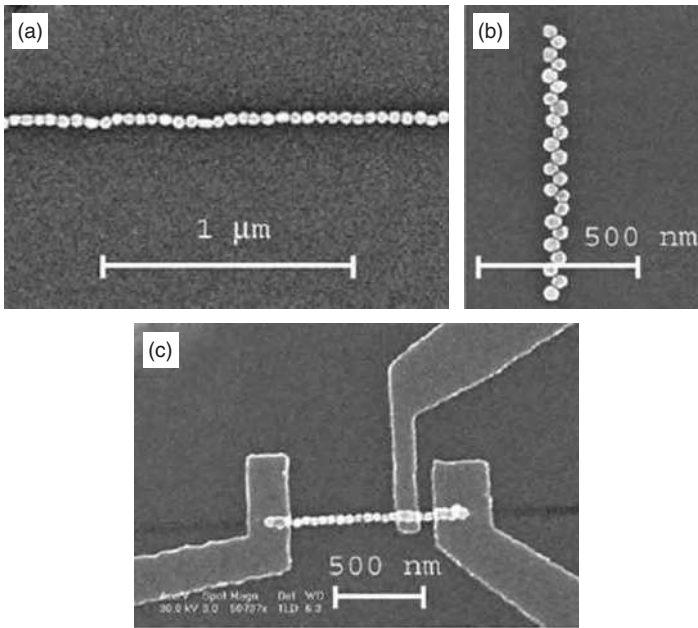


FIGURE 4.9 (a) Gold nanoparticles are selectively deposited on a SiO_2 surface along a patterned line. (b) By controlling the width of the line, more complex structures are achieved. (c) Contacts to the particles are made by electron beam lithography [11]. (Reprinted with permission from Coskun UC, Mebrahtu H, Huang P B, Huang J, Sebba D, Biasco A, Makarovski A, Lazarides A, LaBean TH, Finkelstein G. Single-electron transistors made by chemical patterning of silicon dioxide substrates and selective deposition of gold nanoparticles. *Appl Phys Lett* 2008;93:123101 3pp, Copyright 2008, American Institute of Physics.)

removed, while the gold nanoparticles on the silicon surface stay as they are. Since the silicon surface is covered with an oxide layer, the bonding between gold and SiO_2 is strong enough to remain even during the chemical procedures used to dissolve the photoresist layer. Similar to the gold nanoparticles, an assembly of platinum nanoparticles is formed when platinum nanoparticles are used instead of gold nanoparticles in the foregoing procedures. When more gold nanoparticles are deposited, an assembly of granular nanoparticle islands forms. Figures 4.11a and b show the scanning electron images of gold nanoparticles deposited for 60 minutes in which the silicon substrate used is patterned by circular dots of 500 nm in diameter. The AFM image in Figure 4.11(c) shows that each island exhibits a hemispherical shape, rather than a pillar one, yet nanoparticles still retain their shape. More specifically, these features are granular gold nanoparticle islands.

Direct electron beam writing in a layer of nanoparticles is a technique that allows the patterning of nanoparticle assemblies through a three-step process: coating, writing, and rinsing. Electron beam lithography is used to fabricate

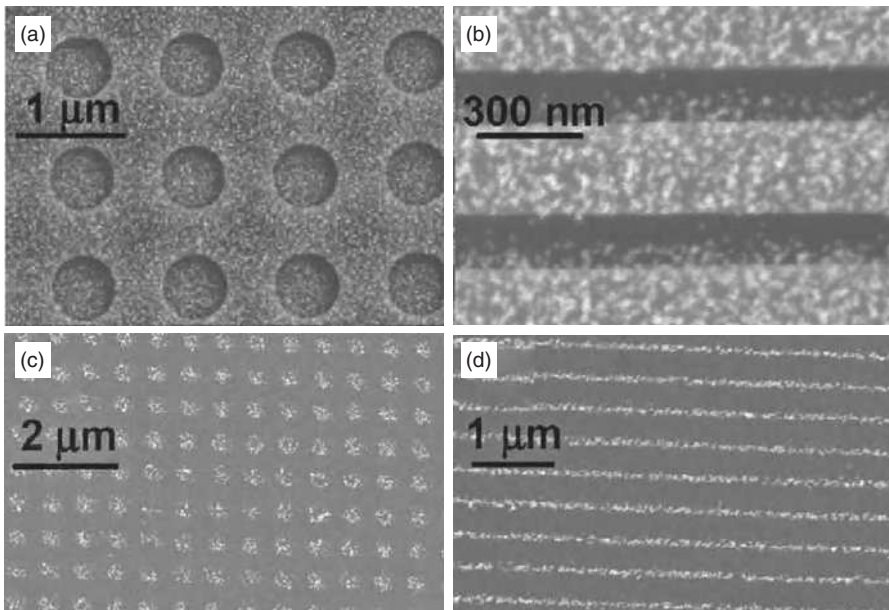


FIGURE 4.10 Scanning electron images of gold nanoparticles (average diameter 13.8 nm) deposited for 3 minutes onto a silicon substrate designed by electron beam lithography; images (a) and (b) are taken before and (c) and (d) are taken after the removal of the photoresist. The patterns in (a) and (c) are circular dots with 500 nm diameter, while those in (b) and (d) are one-dimensional channels of 100 nm width. The gold nanoparticles deposited on the silicon substrates are unaffected by the removal of the photoresist layer [13]. (Reprinted with permission from Kawabata S, Naono Y, Taguchi Y, Huh SH, Nakajima A. Designable formation of metal nanoparticle array with the deposition of negatively charged nanoparticles. *Appl Surf Sci* 2007;253:6690–6696, Copyright 2007, Elsevier.)

platinum nanoparticle (28 nm size) arrays on 15 nm thick SiO_2 and Al_2O_3 layers deposited onto silicon wafers by spin casting. A combination of characterization techniques (scanning electron microscopy (SEM), AFM, X-ray photoelectron spectroscopy, and Auger electron spectroscopy) is used to determine the size, spatial arrangement, and purity of these fabricated arrays. In addition, these platinum arrays demonstrate the ability to resist poisoning by CO, and a correlation is established between the number of oxide–Pt interface sites and the CO-poisoned turnover frequency [14]. Direct electron beam writing in nanoparticle films is also employed to create nanoscale wires between prepatterned gold electrodes on SiO_2/Si wafers. The matrix consists of a distribution of metal cores in a carbon network. The nanoparticle network is created through cross-linking of the ligands of adjacent particles [15]. Figure 4.12a shows a high-angle annular dark field scanning transmission electron image of the nanowires. The line width increases with the electron beam dose. A high-resolution scanning transmission electron image, Figure 4.12b, of a nanowire written with an electron dose of

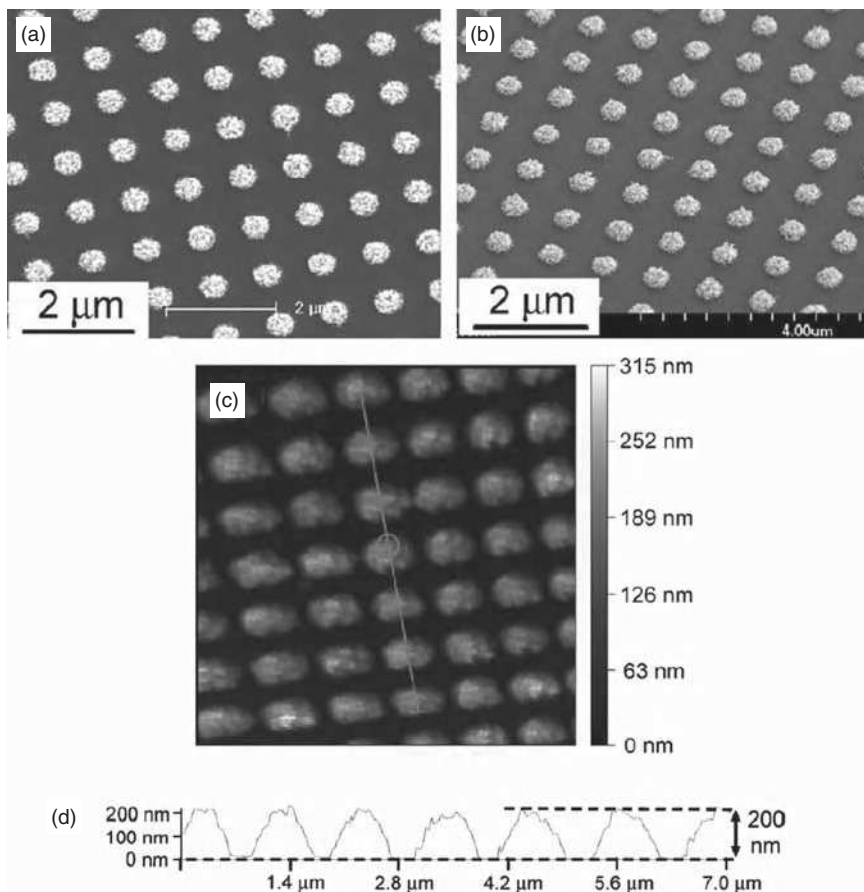


FIGURE 4.11 Scanning electron images of gold nanoparticles (average diameter 13.8 nm) deposited for 60 minutes onto a silicon substrate patterned with circular dots of 500 nm in diameter: (a) top view, (b) 45° tilted view, (c) atomic force microscope image, and (d) height analysis of the image of (c) [13]. (Reprinted with permission from Kawabata S, Naono Y, Taguchi Y, Huh SH, Nakajima A. Designable formation of metal nanoparticle array with the deposition of negatively charged nanoparticles. *Appl Surf Sci* 2007;253:6690–6696, Copyright 2007, Elsevier.) (For a color version of this figure, see the color plate section.)

$4 \times 10^5 \mu\text{C cm}^{-2}$ at 7 keV beam energy reveals close-packed nanoparticle islands, without apparent sintering of the metal particles. By exposing the arrays to intense electron beam doses, pattern transfer into the underlying silicon wafer is improved because of the cross-linking of the surfactant [16].

For patterned nanoparticles, a good application example is related to plasmonics from near-field interactions between noble metal nanoparticles. The two most important consequences of such near-field coupling are pronounced shifts of the plasmon resonance wavelengths compared to the single particle case, leading to a color change, and a significant increase in local electromagnetic fields at

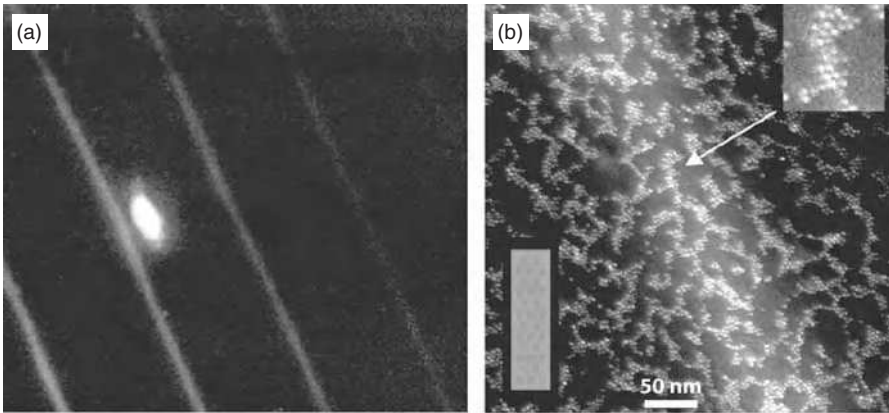


FIGURE 4.12 Scanning transmission electron images of (a) nanowires created by direct electron-beam writing in a submonolayer nanoparticle film (beam energy of 7 keV) and (b) a nanowire at high resolution together with a scheme depicting the network of discrete nanoparticles interconnected by a carbon matrix [15]. (Reprinted with permission from Plaza JL, Chen Y, Jacke S, Palmer RE. Nanoparticle arrays patterned by electron-beam writing: structure, composition, and electrical properties. *Langmuir* 2005;21:1556–1559, Copyright 2005, American Chemical Society.) (For a color version of this figure, see the color plate section.)

interstitial sites between the particles. Dipolar plasmon modes of nanoparticle trimers formed by three silver particles of 100 nm located on the vertices of an equilateral triangle are investigated. Samples are fabricated by electron beam lithography as shown in Figure 4.13 [17]. Similar to nanoparticle dimers, the trimer system exhibits two hybridized dipole resonances to the red and to the blue of the single particle resonance.

Because of the low energy of electrons, electron beam lithography is a slow patterning process. To enhance the patterning rate, a low-dose electron beam is used to generate a “latent” charge pattern, and then a real pattern is created by attaching positively charged particles by electro spray. For example, positively charged silver nanoparticles are generated this way in which a nanoparticle solution mixed with hexane is sprayed through a 15 μm diameter capillary tip with an applied potential of 4.5 kV. Silver nanoparticles are deposited in the charge-patterned sites by electrostatic attraction with a resolution of 0.7 μm . This electrostatic lithography patterning approach represents a rate increase of ~ 20 times over standard electron beam resists and has the potential for faster patterning of nanoparticle building blocks without additional etching or other processing steps. Arbitrarily nested 0.7 μm wires are fabricated by electrostatic lithography. As seen in Figure 4.14, a large overall area can be uniformly covered by electro spray within seconds. The dose used (50 nC cm^{-2}) for patterning is several orders of magnitude lower than typical electron beam resist doses ($1 \mu\text{C cm}^{-2}$) [18].

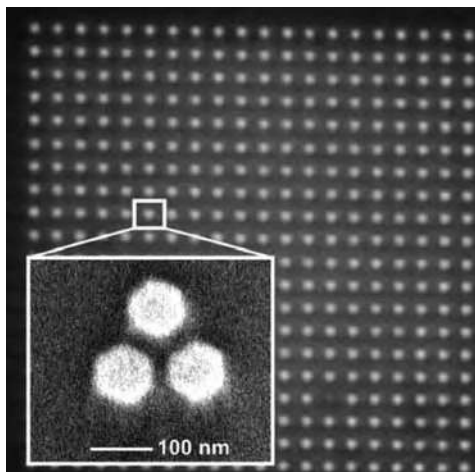


FIGURE 4.13 An array of silver nanoparticle trimers on glass in immersion oil. Each dot corresponds to one individual trimer composed of silver particles with 100 nm diameter and 25 nm height. The nanoparticles have an edge-to-edge distance of 20 nm, while the lattice constant of the array is 1 μm . The inset shows a scanning electron image of one representative silver nanoparticle trimer [17]. (Reprinted with permission from Alegret J, Rindzevicius T, Pakizeh T, Alaverdyan Y, Gunnarsson L, Kall M. Plasmonic properties of silver trimers with trigonal symmetry fabricated by electron-beam lithography. *J Phys Chem C* 2008;112:14313–14317, Copyright 2008, American Chemical Society.) (For a color version of this figure, see the color plate section.)

4.2.3 Ion Beam Lithography

Ion beam lithography is a powerful technique for directly writing patterns on many substrates. The most common ion sources are Ga^+ and Ar^+ . It is a maskless and resistless technique that allows a very wide range of materials (metals, ceramics, semiconductors, and polymers) to be patterned, providing a resolution down to 10 nm. The substrate used most often is silicon wafer. The technique is more aptly termed as focused ion beam lithography (FIB), which has been widely used for high-resolution nanofabrication. FIB finds its use in various modes such as ion implantation, exposure of resist, ion milling, gas-assisted etching, and ion-assisted deposition of materials. This versatility makes it possible to apply this technique to a wide range of applications that other techniques are not capable of or are too difficult and complex to use.

Cobalt nanoparticles of controlled size are deposited on Si(111) using pulsed electrodeposition. When deposited on FIB patterned substrates, well-organized nanoparticles with adjustable magnetic anisotropy are obtained [19]. Random particle nucleation on preexisting defects can be avoided. This induces the growth of organized cobalt nanoparticles in well-defined arrays. Self-aligned gold nanoparticles on a silicon substrate, covering a large area, are also created with FIB

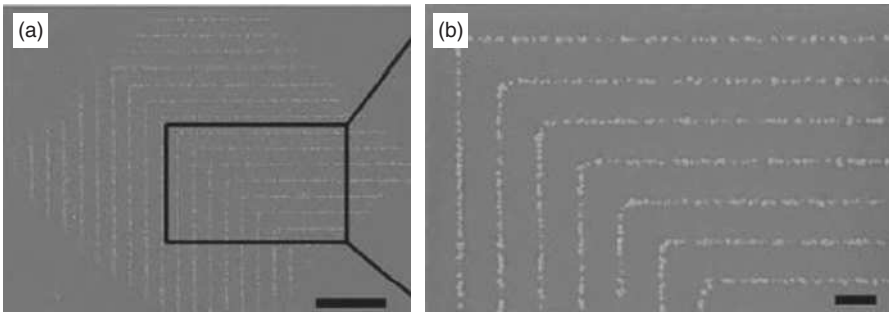


FIGURE 4.14 Scanning electron images after positively charged silver nanoparticles are sprayed onto the negatively charged electron beam pattern. $0.7\ \mu\text{m}$ thick lines are generated over a large area with doses as low as $50\ \text{nC cm}^{-2}$. (a) Scale bar = $50\ \mu\text{m}$. (b) Scale bar = $10\ \mu\text{m}$ [18]. (Reprinted with permission from Joo J, Moon S, Jacobson JM. Ultrafast patterning of nanoparticles by electrostatic lithography. *J Vac Sci Technol B* 2006;24:3205–3208, Copyright 2006, American Vacuum Society.)

assistance. The process involves three consecutive steps: first, the substrate is laser-irradiated to produce a periodic nanorippled structure; second, a thin film of gold is grown using ion beam sputter deposition; and third, a thermal treatment is conducted to induce the formation and self-alignment of gold nanoparticles. Nanoparticles form along strips parallel to the nanoripple lines. The strip spacing equals the nanoripple spacing and the strip width depends on the angle of the deposition and the divergence of the ion beam. The nanoparticle diameter is a function of the annealing temperature and time. Deposition of the film at a very shallow grazing angle ($\sim 0^\circ$) induces, upon thermal annealing in air at 800°C , the formation of single nanoparticle rows aligned along the ripple ridges [20]. An example sample has $16\ \text{nm}$ high and $\sim 80\ \text{nm}$ wide ripples, with a line spacing of $288\ \text{nm}$. The deposition is conducted at a grazing angle of 5° for 5 minutes, and subsequent annealing in air at 800°C for 3 hours promotes the clustering. Figure 4.15a shows the gold particle distribution at a grazing value of 3° . Gold nanoparticles of $30\text{--}40\ \text{nm}$ diameter, together with smaller ones, are seen aligned along the ripples in two to three particle-wide rows. At this angle, the ripple structure casts a shadow over the entire surface, with the exception of a narrow band adjacent to the ridges. Figure 4.15a also shows that parallel to the ripple lines, two rows of smaller particles, $10\text{--}15\ \text{nm}$ in diameter, are seen close to the larger ones, apparently only to the right side. The origin of these satellite lines can be attributed to beam divergence, as parts of the beam arrive at actual grazing angles larger than 3° . The effect of beam divergence can be seen in Figure 4.15b, where the gold beam arrives at a grazing angle set at 0° . The nanoparticle strip has a similar width to that seen in Figure 4.15a for the larger angle, demonstrating that the beam divergence is large enough to compensate for the shallower grazing angle. Higher annealing temperatures produce larger nanoparticles, as can be seen by comparing Figures 4.15a and b.

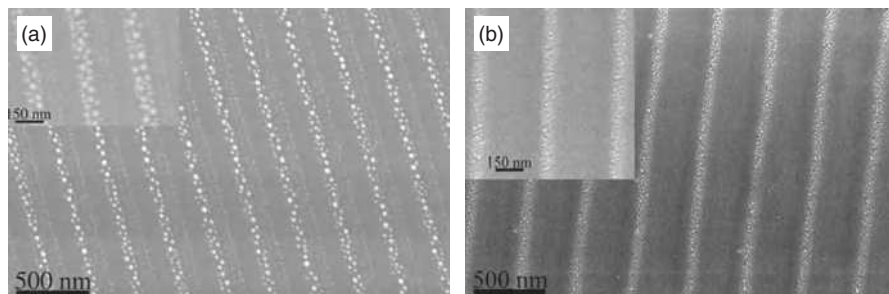


FIGURE 4.15 Scanning electron images of nanorippled surface showing the distribution of gold nanoparticles after 5 minutes of film deposition. (a) Grazing angle of 3° , and subsequent annealing at 800°C for 3 hours. (b) Grazing angle of 0° , and subsequent annealing at 700°C for 2 hours [20]. (Reprinted with permission from Guan YF, Pedraza AJ. Synthesis of aligned nanoparticles on laser-generated templates. *Nanotechnology*. 2005;16:1612–1618, IOP Publishing Ltd.)

Charged nanoparticles are also directly deposited in specific patterns created by FIB. The deposition method relies on the implantation of positive Ga^+ ions on an insulated surface, which creates the basis for attracting nanoparticles to the substrate. An aqueous suspension of gold nanoparticles is used in the method. The diameters of the particles used are 200 nm and 30 nm, and the standard deviation of the size distribution is $<10\%$ of the average. The deposition process is carried out ~ 7 months after generating the charge pattern. The gold nanoparticles can still be patterned. This shows the high stability and long lifetime of the implanted Ga^+ ions and, thus, their applicability for reliable and long-term usage in tunable devices such as modulators and sensors. The main advantages of this technology are high speed and precise deposition [21].

FIB milling is used to fabricate micron and submicron scale patterns in sintered SiO_2 nanoparticle layers. Rectangular cavities with both solid and porous boundaries, channels, and isolations of a small number of packed particles are patterned. The ion beam can pattern areas covering up to $40\ \mu\text{m}^2$ in <15 minutes. The amount of redeposited material on the surface of a milled cavity determines whether the surface will be porous or solid [22]. Figure 4.16 shows a staircase-shaped cavity created by milling to three different depths. In a different study, silicon substrates are coated with CH_3 -terminated silane self-assembled into monolayer resists. A fine beam of Ga^+ ions with different doses removes these self-assembled monolayers to correspondingly form a pattern containing sets of lines. The FIB patterned monolayers are refilled with an SH-terminated silane self-assembled monolayer. An organometallic chemical vapor deposition process is carried out to grow gold nanoparticles onto the SH-groups in the lines. The average spacing between the gold nanoparticles can be controlled by varying the FIB dose and decreases exponentially with an increasing dose [23].

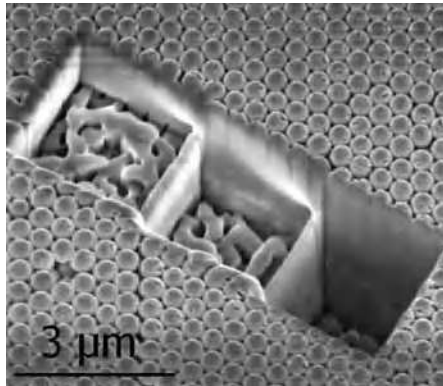


FIGURE 4.16 A staircase-shaped cavity created by milling to three different depths. From left to right, the three cavities have depths of 2, 4, and 6 μm , respectively. The porous cavity bottoms result from the combined effects of partially milled spheres and redeposited material [22]. (Reprinted with permission from Moran JL, Wheat PM, Posner JD. Submicron scale patterning in sintered silica colloidal crystal films using a focused ion beam. *Langmuir* 2008;24:10532–10536, Copyright 2008, American Chemical Society.)

4.2.4 Other Top-Down Processes

In addition to the direct “writing” capabilities of photons, electrons, and ions, other patterning techniques may also be used for nanoparticle superstructure construction. Arrays of silver nanoparticles are fabricated on predefined positions by a combination of electrochemical deposition and nanoimprint lithography. The silver nanoparticle arrangement, especially the density, can be tuned by varying the pattern designs and the preparation conditions. By this approach, various arrays of silver nanoparticles with feature sizes down to submicrons are fabricated over several square centimeters on a substrate. The silver nanoparticle arrays can be readily extended to other conductive substrates, which have potential applications in detection and sensing fields, such as surface-enhanced Raman scattering [24]. Figure 4.17 schematically illustrates the procedure for fabricating arrays of silver nanoparticles. First, a resist polymer is spin-coated onto an indium-doped tin oxide substrate. Second, nanoimprint lithography is used to create patterns. Third, reactive-ion etching removes the patterned areas. Fourth, silver nanoparticles are electrochemically deposited into the etched regions. Finally, the retained resist layer is lifted off, and only silver nanoparticle patterns remain. Figure 4.18 shows SEM images of silver nanoparticle arrays with different feature arrangements and spacing. Dot arrays and square arrays with different spacings are made.

Various processing techniques have been applied to superstructure nanofabrication using scanning tunneling microscopy (STM). The inhomogeneous, high electric field in the tip-sample gap and the narrow beam of low energy electrons, in combination with chemical effects, allow for many methods of nanopattern formation, and are applicable to metals, semiconductors, and organic materials.

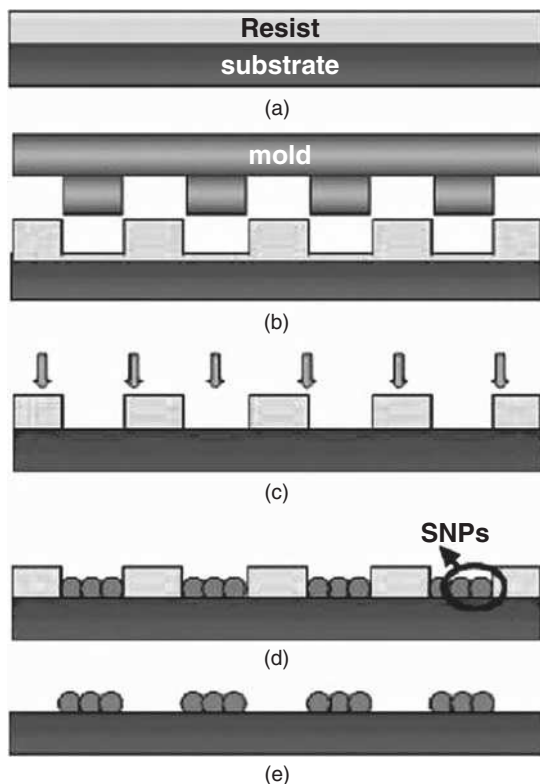


FIGURE 4.17 Schematic illustration of the procedure for fabricating arrays of silver nanoparticles (SNPs). (a) Spin-coating resists polymer onto an indium-doped SnO_2 substrate, (b) imprinting, (c) reactive-ion etching process, (d) electrochemical deposition of silver nanoparticles, and (e) “lift-off” of the resist layer [24]. (Reprinted with permission from Yang B, Lu N, Huang C, Qi D, Shi G, Xu H, Chen X, Dong B, Song W, Zhao B, Chi L. Electrochemical deposition of silver nanoparticle arrays with tunable density. *Langmuir* 2009;25:55–58, Copyright 2009, American Chemical Society.) (For a color version of this figure, see the color plate section.)

In particular, STM-induced nanolithography of silicon has been studied. H-atoms can locally be desorbed from hydrogenated silicon and repassivated with oxygen or other atoms. Individual silicon atoms can be removed from clean silicon single crystals. Silicon nanoparticle films can be processed for nanotexturing by the extraction of atoms or by the fusion of nanoparticles [25]. However, bulge formation during the indentation process is a serious obstacle to trapping nanoparticles in dent holes or trenches. Treating a polymer surface (such as PMMA) with a deionized water and isopropanol mixture in an electric field can avoid bulges and enable the placement of 40 nm gold particles at precise locations using capillary interactions [26].

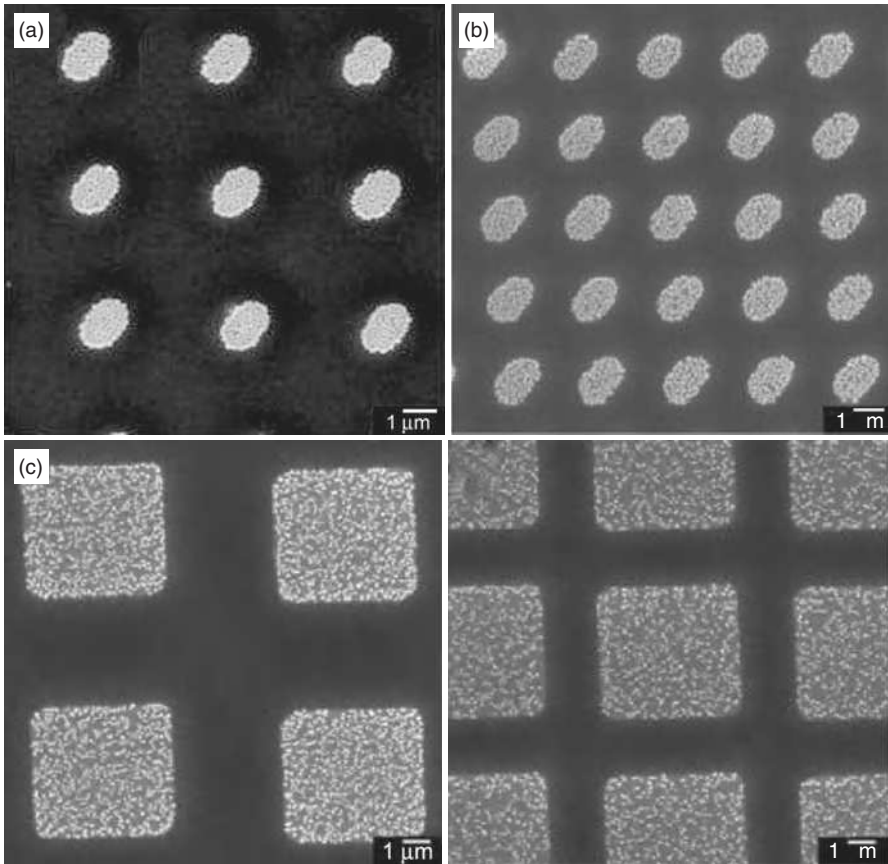


FIGURE 4.18 SEM images of silver nanoparticle arrays. (a) $1.3 \times 1.5 \mu\text{m}$ dots with a spacing of $3.8 \mu\text{m}$, (b) $1.3 \times 1.5 \mu\text{m}$ dots with a spacing of $1.9 \mu\text{m}$, (c) $4.8 \mu\text{m}$ squares with a spacing of $3.8 \mu\text{m}$, and (d) $4.8 \mu\text{m}$ squares with a spacing of $1.9 \mu\text{m}$. Scale bar: $1 \mu\text{m}$ [24]. (Reprinted with permission from Yang B, Lu N, Huang C, Qi D, Shi G, Xu H, Chen X, Dong B, Song W, Zhao B, Chi L. Electrochemical deposition of silver nanoparticle arrays with tunable density. *Langmuir*. 2009;25:55–58, Copyright 2009, American Chemical Society.)

4.3 BOTTOM-UP PROCESSES

Monodispersed nanoparticles can act as “artificial atoms” and “bottom-up” assemble into nanoparticle-based superstructures. When nanoparticles are used as building blocks to produce nanoparticle-based superstructures, the process is called bottom-up approach and “additive” in nature. The process mainly uses nonspecific interactions, such as van der Waals (vdW) forces, electrostatic interactions, dipole moments, electrostatic–magnetic interactions, and capillary forces, to connect nanoparticles of various shapes and sizes into highly ordered

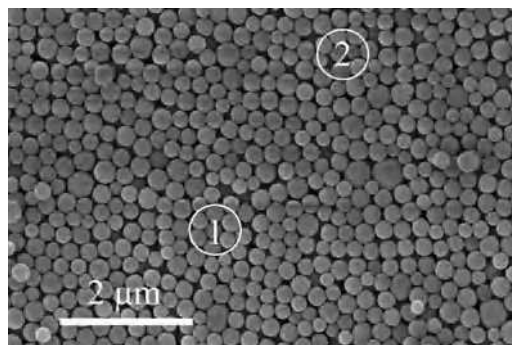
TABLE 4.1 Interaction Forces for Bottom-Up Nanoparticle Assembly

| Directionality | Interaction force | Attribute |
|----------------|---|------------------------------------|
| Nondirectional | van der Waals Dipole moment Electrostatic | Size-imposed saturation limit |
| Directional | Magnetic Capillary Covalent bonding Hydrogen bonding | Direction-imposed saturation limit |

superstructures. Directional interactions, such as covalent bonding and hydrogen bonding, are also pursued (Table 4.1). In comparison to the top-down processes, bottom-up superstructure construction includes a much wider range of interactions and systems.

The monodispersity of nanoparticles is very important for effective, accurate self-assembly of nanostructures with minimal defects. Polydispersity is one of the main sources of errors in nanoparticle superstructure construction because of the intrinsic disruption in nanoparticle packing. Figure 4.19 shows different SiO₂ particle assemblies. When particles are close in size, they assemble into hexagonal arrangement as shown in circle 1. When particles have a wider size distribution, the arrangement becomes random as shown in circle 2.

The ability to assemble nanoparticles into large structures and arrangements depends crucially on the ability to understand in quantitative detail, and subsequently “engineer” the interparticle interactions. The prevalent approach has been to use the theories and equations previously derived for colloids, changing only the dimensions of the interacting particles. Before examining the specific types of interactions useful for nanoparticle assembly, it is instructive to address some general questions regarding the “generic” characteristics of interaction potentials. For example, the ability of a given interaction potential to induce nanoparticle

**FIGURE 4.19** SiO₂ particle assembly variation dictated by particle sizes.

self-assembly depends on both its magnitude and its length scale. The particle interactions to induce self-assembly from a solution need to be quantified and predicted. The interaction length scale in the assembly process should be evaluated. The range of the interaction relative to the sizes of interacting particles can determine whether or not these particles will assemble into an ordered structure or into an amorphous phase.

For simplicity, the widely used Lennard–Jones potential $u_{L,J}(r)$ can be considered to approximate the interaction between spherical particles and account for both attractive vdW forces and repulsive interactions due to the overlap of electron orbitals:

$$u_{L,J}(r) = 4 \cdot \varepsilon_{pw} \left[\left(\frac{\sigma_{L,J}}{r_{a-a}} \right)^{12} - \left(\frac{\sigma_{L,J}}{r_{a-a}} \right)^6 \right]. \quad (4.3)$$

Here, r_{a-a} is the distance between atom centers, ε_{pw} is the depth of the potential well, and $\sigma_{L,J}$ is the finite distance at which the interparticle potential is zero ($u_{L,J}(r) = 0$). For nanoparticles comprised of many atoms, one may derive an analogous interparticle potential by summing the Lennard–Jones potentials across all atom–atom pairs within two given particles. This procedure can be carried out analytically for two spherical particles of radii a_1 and a_2 , and the resulting potential for small separations is approximated as

$$u_{L,J}(r) = \left(\frac{2\pi a_1 a_2}{a_1 + a_2} \right) \left[\frac{\pi \varepsilon_{pw} (\sigma_{L,J}^6 - 210L^6)}{630L^7} \right] \quad \text{for } L \ll \frac{a_1 a_2}{a_1 + a_2}, \quad (4.4)$$

where $L = r - (a_1 + a_2)$ is the distance between particle surfaces [27]. The magnitude of the interaction scales linearly with the size of the particles (for similarly sized particles), while the length scale of the interaction is independent of particle sizes. Consequently, the interaction potential decreases with the inverse of particle size. This scaling can have profound effects on the ability (or inability) to form self-assembled structures from increasingly large particles.

Self-assembly is typically associated with thermodynamic equilibrium; the organized structures are characterized by a minimum in the system's free energy. Using nanoparticle interactions for the manipulation of nanoparticles has been recognized from the very beginning of nanoscience. Yet, it is only recently that the intricacies of not only vdW forces but also other nanoparticle interactions have emerged in an unexpectedly large number of research areas; they govern the stability of superstructures, which are essential for the design of nanodevices and nanoarchitectures. Creation of superstructures of controlled size, shape, and chemical functionality requires an understanding of the phase behavior, structure, and assembly of nanoparticle motifs. A fundamental understanding of the behaviors of superstructures would provide the guidelines for creating building blocks that self-assemble into desired equilibrium (crystalline)

and nonequilibrium (gel or glassy) phases, while avoiding undesired (such as jammed) states.

Factors governing the creation of nanoparticle assemblies stem from the desire to precisely manipulate and drastically improve nanostructured properties (such as optical, microelectronic, magnetic, catalytic, and chemical/biological). This desire is highlighted by attributes of engineered metallic or semiconductor nanoparticles as building blocks in terms of size monodispersity, core/shell processability, solubility, stability, self-assembly capability, and interfacial reactivities. Two important questions are how the unique nanoscale properties of building blocks are retained in the assembly and how the nanostructured assembly can be engineered to display the targeted properties. In comparison to individual nanoparticles, the challenge in the exploration of an ensemble of nanoparticles is understanding the interparticle interactions of the nanoscale building blocks in either dispersed state (e.g., in solutions) or solid state (e.g., in superstructures).

4.3.1 Nondirectional Interactions

4.3.1.1 van der Waals Forces vdW forces originate from the electromagnetic fluctuations due to the incessant movements of positive and negative charges within atoms, molecules, nanoparticles, and bulk materials. They are therefore present between any two material bodies, usually acting in an attractive fashion to bring the bodies together. The magnitude of these attractive interactions can be considerable, from few to hundreds of times of kT even between nanoparticles. Because of this, vdW forces are often considered an untoward effect, causing undesired flocculation and sedimentation of nanoparticles from suspensions. Through the use of stabilizing dispersants or appropriate solvents, however, vdW interactions can be controlled to provide a useful tool with which to guide nanoparticle assembly and to build, for example, two-dimensional and three-dimensional superstructures composed of nanoparticles.

Bare, that is, uncoated, nanoparticles of metals, oxides, and semiconductors have strong vdW forces and tend to aggregate when in inert, nonpolar liquids, such as hydrocarbons. In most systems of practical importance, long-range vdW forces must be balanced by Coulombic, steric, or other repulsive interactions to provide control over phase behavior, structure, and assembly. Below a critical internanoparticle repulsion, the system becomes unstable, yielding an amorphous sediment [28].

Air–water interface can be used to produce ordered nanoparticle monolayers, enabled by either vertical deposition (Langmuir–Blodgett (LB) technique [29]) or horizontal deposition (Langmuir–Schaefer (LS) technique [30]) on a substrate. For hydrophobic substrates, the LS technique is an excellent tool for controlled multilayer production. For hydrophilic substrates, dewetting induces a cellular superstructure. The LS technique has been used to make multilayer quantum dot arrays using CdSe quantum dots as a model system [31]. A combination of

different nanoparticle sizes (CdSe and Fe₃O₄) allows for the formation of two-dimensional binary superstructures. The LS and LB techniques provide important advantages over other solution processing techniques such as drying-mediated assembly [32] and spin-coating [33], as they allow deposition of closely packed nanoparticle layers of large areas, even on nonflat substrates [34].

Understanding the kinetic and thermodynamic factors governing the assembly of nanoparticles is important for the design and control of superstructures. The ordering of nanoparticles via vdW interactions depends on size monodispersity. Gold nanoparticle cores (~5 nm) encapsulated with tetraoctylammonium bromide ((CH₃(CH₂)₇)₄NBr) shells are studied as a model system [35]. A thioether-based multidentate ligand (e.g., MeSi(CH₂SMe)₃) functions as a mediator, whereas tetraoctylammonium bromide capping molecules function as templating agents. The templating agent directed assembly of gold nanoparticles is an enthalpy-driven process. The enthalpy change (−1.3 kcal mol^{−1}) is close to the magnitude of the vdW interaction energy for alkyl chains and the condensation energy for hydrocarbons. Figure 4.20 shows transmission electron images of silver nanoparticle arrays viewed along the [110]_s direction [36]. The hexagonal arrangement of the nanoparticles with multiple domains can be observed. Figure 4.21 shows the self-assembled patterns of gold nanoparticles with cubic and hexagonal shapes [37]. Cubic nanoparticles form either hexagonal or square networks, whereas nanoparticles with hexagonal shapes only show two-dimensional hexagonal close packing. Figure 4.21a shows that cubic nanoparticles form hexagonal networks in two different ways. In one kind, cubic nanoparticles form chains

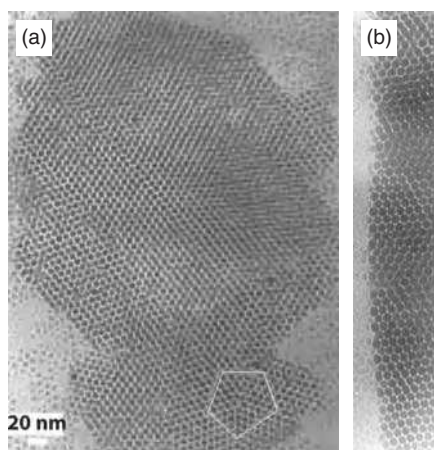


FIGURE 4.20 Transmission electron images of silver nanoparticle arrays viewed along [110]_s, showing (a) an entire thin crystal (with a twinned region marked at lower right) and (b) the facet edge of an extended array [36]. (Reprinted with permission from Harfenist SA, Wang ZL, Alvarez MM, Vezmar I, Whetten RL. Highly oriented molecular Ag nanocrystal arrays. *J Phys Chem* 1996;100:13904–13910, Copyright 1996, American Chemical Society.)

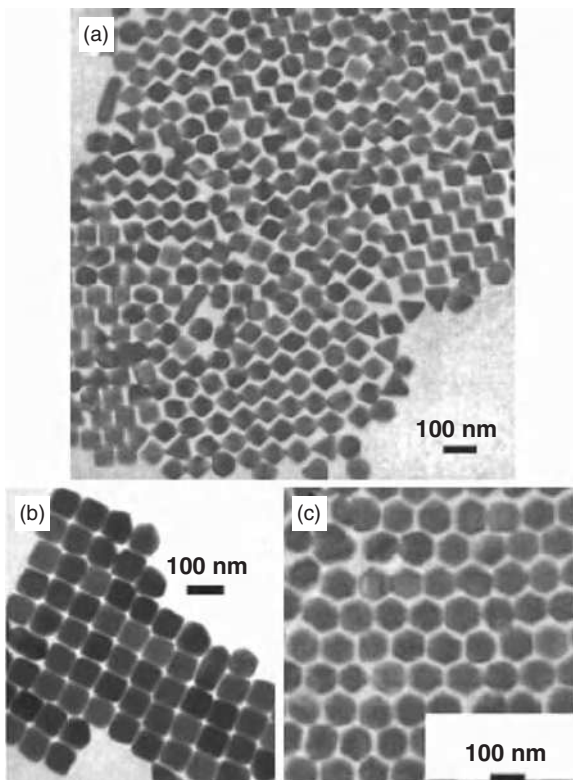


FIGURE 4.21 Self-assembled patterns formed by gold nanoparticles with cubic shapes (a, hexagonal assembly; b, square assembly) and hexagonal shapes (c, hexagonal assembly) [37]. (Reprinted with permission from Sau TK, Murphy CJ. Self-assembly patterns formed upon solvent evaporation of aqueous cetyltrimethylammonium bromide-coated gold nanoparticles of various shapes. *Langmuir*. 2005;21:2923–2929, Copyright 2005, American Chemical Society.)

by sharing only two diagonally opposite corners; in the other kind, all four corners of a cubic nanoparticle are shared with four other nanocubes. In the square arrangement, cube-shaped nanoparticles share maximal surface area with each other (Fig. 4.21b). The cubic nanocrystal faces are bounded by $\{100\}$ planes and the corners by $\{111\}$ planes. This suggests that different crystal faces, with their attendant surface-bound molecules, are available for assembly.

4.3.1.2 Dipole Moments Electric dipole moments are prevalent in semiconductor and metal nanoparticles due to their anisotropic crystal lattices and possible surface defects. However, strong electrostatic or steric repulsion from surface stabilizers normally screens the electric dipole attraction between nanoparticles, which makes the formation of nanoparticle assemblies difficult. Studies have been

conducted to decrease the mutual repulsion and thus expose the dipole attraction through partial removal of the surface stabilizers using antisolvents. By partially removing thioglycolic acid stabilizers, one-dimensional CdTe nanoparticle assemblies are prepared [38, 39]. Recently, two-dimensional assemblies of CdTe nanoparticles are prepared without any template, but by spontaneous assembly using charge dipole interactions [40]. An AC voltage is applied to a single-walled carbon nanotube immersed in a colloidal suspension of gold nanoparticles. The AC voltage generates an AC electric field perpendicular to the walls of the carbon nanotube and induces a (AC) dipole moment in the gold nanoparticles. Because of the cylindrical geometry of the nanotube, the dipole moment is directed toward the surface of the nanotube. The induced dipole moment in the nanoparticles is attracted to the high-intensity field regions at the surface of the nanotube, thus causing a gold particle nanowire to grow on the surface of the nanotube. Interestingly, gold nanowires grow even on nanotubes that are not electrically in contact with but in close proximity to the electrode. The gold nanowire so formed from gold nanoparticles remains after drying and after the voltage is turned off [41]. Based on similar mechanisms, highly uniform nanoparticles with isotropic interactions can form three-dimensional nanoparticle arrays in suspensions. However, demonstration of such assembly feasibility and applicability of the process to a wide array of materials still needs to be proven.

4.3.1.3 Electrostatic Interactions Electrostatic interactions can be attractive (between oppositely charged particles), repulsive (between like-charged particles), and even directional (even though less common), as in the case of particles with asymmetric surface charge distributions or permanent electric polarization. Furthermore, the magnitude and length scale of electrostatic interactions can be tuned through the choice of solvent (e.g., dielectric constant) as well as the concentration and chemical nature (e.g., size and valence) of the surrounding counterions. Due to these unique attributes, electrostatic interactions are useful both for stabilizing particles in suspensions and for guiding their assembly into superstructures. In this section, only nondirectional electrostatic interactions are considered.

Through the usage of high magnetic fields arranged in parallel, it is possible to create three-dimensional superstructures. A typical result of three-dimensional deposition is shown in Figures 4.22a–c. With a magnetic field strength of 0.7 T, only two-dimensional ordering is obtained (Fig. 4.22a). With a magnetic field strength of 1.5 T, a double layer is observed (Fig. 4.22b). The particles become more closely packed and begin assembling in the third dimension with increasing magnetic field strength; the minimum interparticle distance is limited by the stabilizing organic layer. The final three-dimensional structure, consisting of a triple layer, is created with a magnetic field strength of ~ 6 T (Fig. 4.22c). To aid the interpretation of the three-dimensional superstructures in Figure 4.22c, schematic representations of the top view and the side view are also given in Figure 4.22c [42].

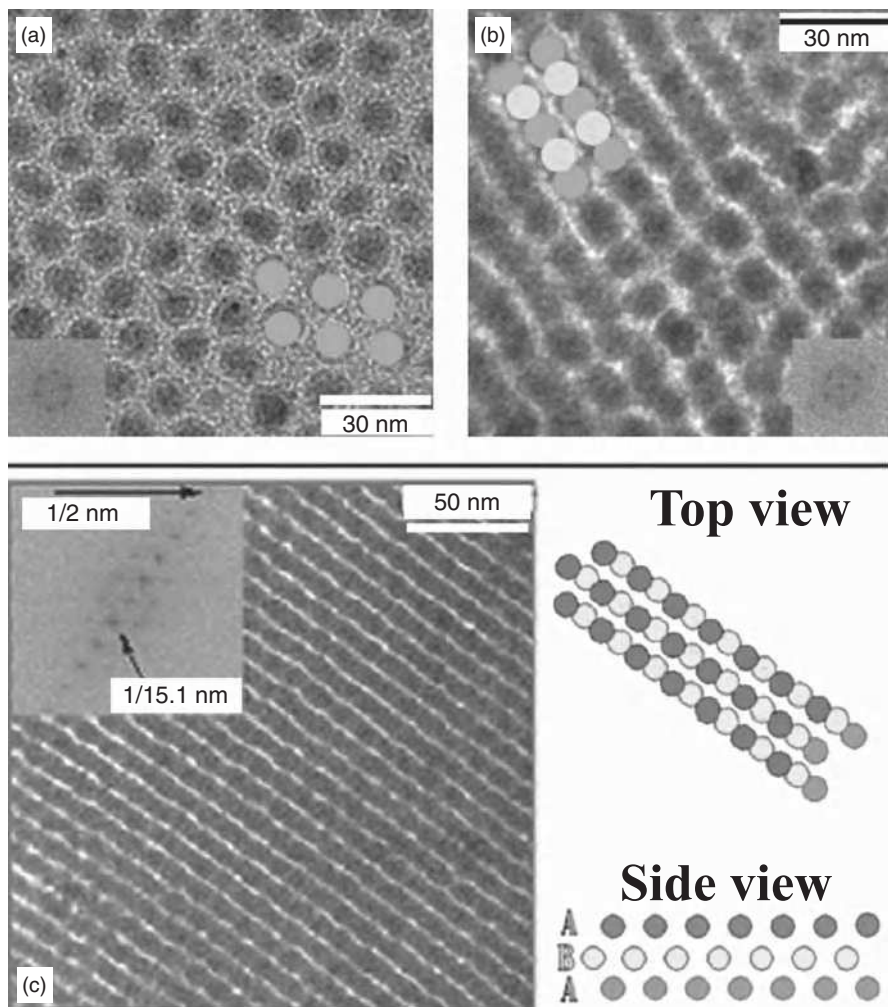


FIGURE 4.22 Transmission electron images of ordered cobalt particles with external applied magnetic fields of (a) 0.8 T, (b) 1.5 T, and (c) 6 T. The schematic diagrams are a guide to understanding the structure of the presented superstructure images [42] (Reproduced with permission from Hilgendorff M, Tesche B, Giersig M. *Aust J Chem* 2001;54(8): 497–510, Copyright CSRIO 2001. Published by CSRIO PUBLISHING, Collingwood, Victoria, Australia – <http://www.publish.csiro.au/nid/51/paper/CH01119.htm>). (For a color version of this figure, see the color plate section.)

4.3.2 Directional Interactions

Although vdW forces, dipole moments, and electrostatic interactions are common interparticle forces responsible for the formation of ordered arrays of nanoparticles, particles held together by such nonspecific forces are, however, not fully controllable, or chemically or mechanically stable on a macroscopic scale. In contrast, chemically specific binding (e.g., covalent or hydrogen bonding) can overcome these weaknesses, though observations of large domains of highly ordered superstructures are limited.

When magnetic nanoparticles self-assemble, they tend to align their magnetic moments in the direction of the local magnetic field due to neighboring particles or applied fields. This gives rise to a specific directionality of interactions, enabling magnetic nanoparticles to form micron-sized, one-dimensional chains/wires or rings. Owing to the magnetic or electrical dipole moments of their unique axes, anisotropic crystal lattices, and nonuniformly stabilized distribution, nanoparticles have the ability to spontaneously assemble without any templates. Cd–Te nanoparticles are assembled into one-dimensional chains [43–45]. The linear chain subsequently recrystallizes into crystalline nanowires, whose diameters are determined by the size of the nanoparticles. The self-assembled nanowires show high aspect ratios and uniformity. In this chapter, the discussion on directional interactions will focus on covalent bonding and hydrogen bonding only. Directed nanoparticle assembly widens the nanoparticle superstructure possibilities and is a burgeoning field.

4.3.2.1 Covalent Bonding Superstructure construction using covalent bonding involves sharing pairs of electrons between atoms. The balance of attractive and repulsive forces between atoms ascertains that the assembled superstructures are fairly stable. Covalency is greatest between atoms of similar electronegativities. Thus, covalent bonding does not necessarily require the two atoms to be the same elements, only that they are of comparable electronegativity. Although covalent bonding entails sharing of electrons, it is not necessarily delocalized. Furthermore, in contrast to electrostatic interactions (“ionic bonds”), the strength of a covalent bond depends on the angular relationship between atoms in polyatomic molecules.

Self-assembled monolayers of cobalt nanoparticles formed on a hydroxyl-terminated silicon surface exhibit two-dimensional island networks with locally ordered arrays via covalent linkage between nanoparticles and the surface [46]. A monolayer of Br-terminated cobalt nanoparticles on functionalized silicon surfaces is assembled using chemical covalent bonding. This approach involves attaching different functional groups to the cobalt nanoparticles and to the silicon substrate, and then linking the two functional groups covalently. The nature of the resulting nanoparticle assembly is dependent on the properties of the functional group attached to the silicon surface. The number density of the nanoparticles can be controlled by changing the immersion time of the silicon surface in the

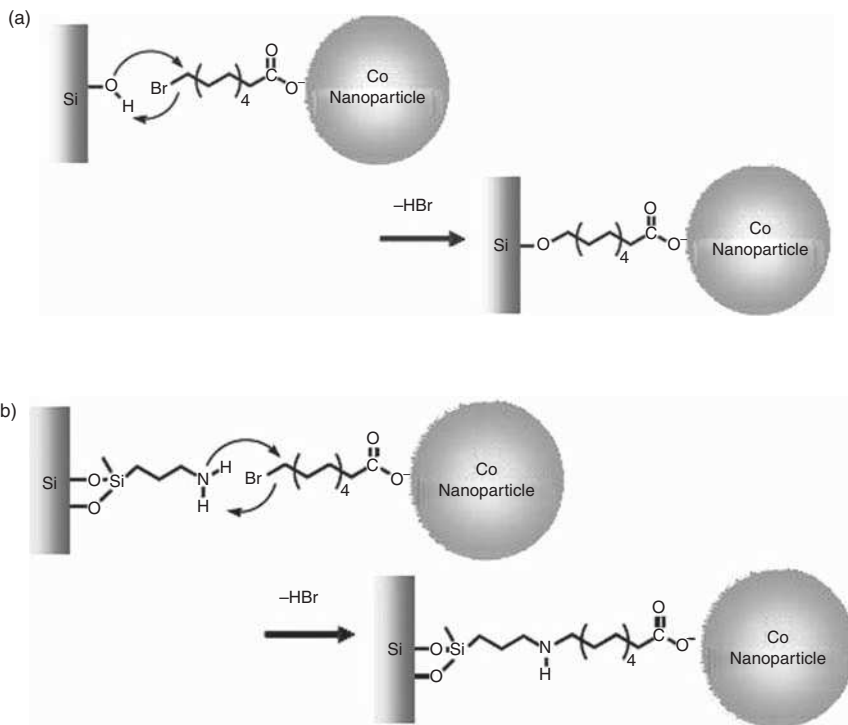


FIGURE 4.23 Direct nucleophilic substitution reaction between the terminal bromine group of the cobalt nanoparticle and the functional group on the silicon surface: the formation of chemical covalent bonding by nucleophilic attack of (a) the $-OH$ group, and (b) the $-NH_2$ of the aminopropyl group [46]. (Reprinted with permission from Bae SS, Kim DK, Park JI, Cheon J, Jeon IC, Kim S. Monolayer assembly and striped architecture of Co nanoparticles on organic functionalized Si surfaces. *Appl Phys A* 2005;80:1305–1310, Springer Science + Business Media, Fig. 2.)

nanoparticle suspension. Hence, the covalent bonding after the immersion enables the selective fabrication of nanoparticle assemblies on surfaces, the control of the distribution of nanoparticles on surfaces, and the enhancement of the thermal stability and adhesion of the adsorbed nanoparticles. Figure 4.23 illustrates direct nucleophilic substitution reaction (forming a chemical bond with the silicon surface by donating both bonding electrons) between the terminal bromine group of the cobalt nanoparticle and the functional group on the silicon surface. Figure 4.24 shows a transmission electron image of 10 nm cobalt nanoparticles capped with 11-bromoundecanoic acid ($C_{11}H_{21}BrO_2$), the assembly of cobalt nanoparticles on an OH-terminated silicon surface, an aminopropyl-terminated ($NH_2CH_2CH_2CH_2-$) silicon surface after immersion for 9 hours, and the number density of cobalt nanoparticles adsorbed on the two different functionalized silicon surfaces as a function of immersion time.

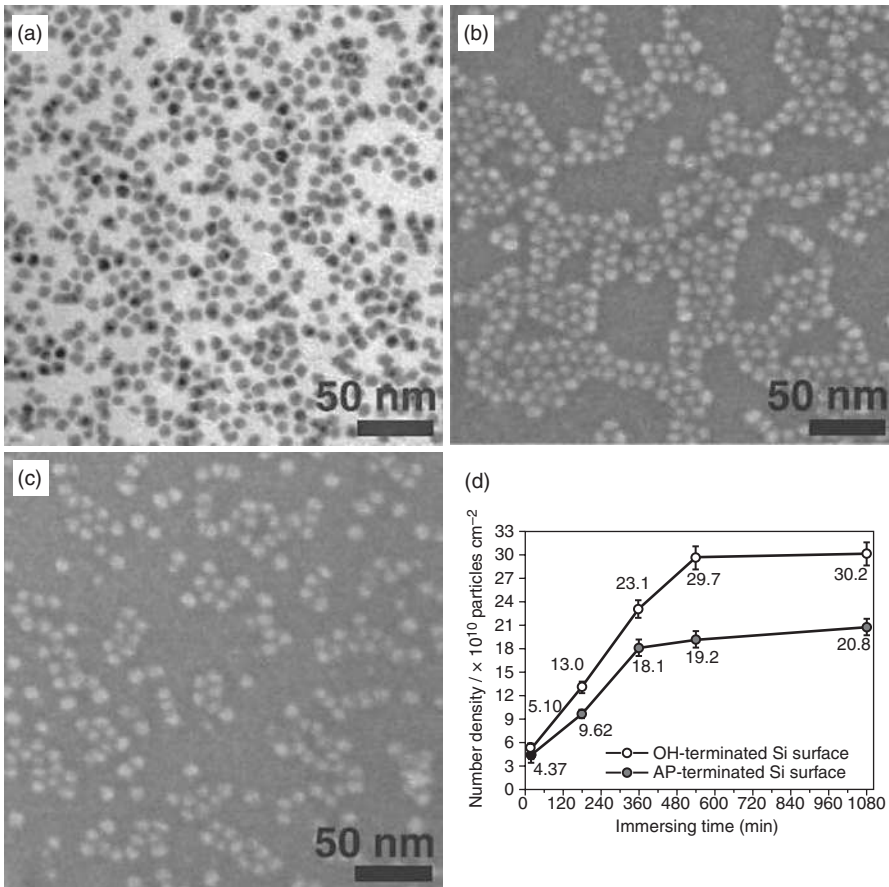


FIGURE 4.24 (a) Transmission electron image of 10 nm cobalt nanoparticles capped with 11-bromoundecanoic acid. Scanning electron images showing an assembly of cobalt nanoparticles on (b) an OH-terminated silicon surface, and (c) an aminopropyl-terminated silicon surface after immersion for 9 hours, respectively. (d) The number density of cobalt nanoparticles adsorbed on the two functionalized silicon surfaces as a function of immersion time [46]. (Reprinted with permission from Bae SS, Kim DK, Park JI, Cheon J, Jeon IC, Kim S. Monolayer assembly and striped architecture of Co nanoparticles on organic functionalized Si surfaces. *Appl Phys A* 2005;80:1305–1310, Springer Science + Business Media, Fig. 2.)

4.3.2.2 Hydrogen Bonding A hydrogen bond is the attractive interaction of a hydrogen atom with an electronegative atom, such as nitrogen, oxygen, or fluorine, which comes from another molecule or chemical group. The hydrogen must be covalently bonded to the other electronegative atom to create the bond. In comparison to covalent, electrostatic, or vdW interactions, hydrogen bonding has an intermediate binding strength and binding reversibility, which offers a flexible and controllable pathway for superstructure construction, especially

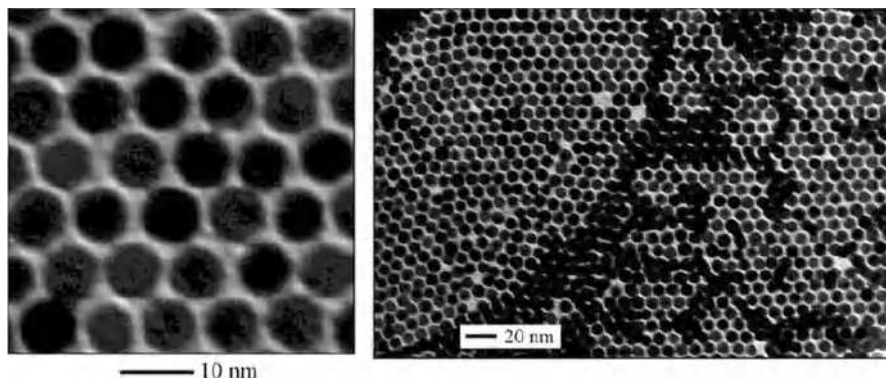


FIGURE 4.25 Transmission electron micrographs of 16-mercaptohexadecanoic acid ($C_{16}H_{32}O_2$)-linked 6 nm gold nanoparticle assembly in a hexane solution. The gold nanoparticle concentration is $0.24 \mu\text{M}$ and the 16-mercaptohexadecanoic acid concentration is $0.39 \mu\text{M}$. The assembly time is 15 minutes [47]. (Reprinted with permission from Han L, Luo J, Kariuki NN, Maye MM, Jones VW, Zhong CJ. Novel interparticle spatial properties of hydrogen-bonding mediated nanoparticle assembly. *Chem Mater* 2003;15:29–37, Copyright 2003, American Chemical Society.)

for nanoparticle assemblies. The intermolecular hydrogen bonding mediation of gold nanoparticle assembly by carboxylic acid groups and the hydrophobic interaction of alkanethiolate constitutes are explored. A very small fraction of the hydrogen bonding agents is sufficient for mediating the assembly toward chemically stable and ordered array morphologies [47]. Interparticle ordering has been observed when using a different chain length mediator structure, that is, 16-mercaptohexadecanoic acid, to assemble 6 nm gold particles (Fig. 4.25). The assembly displays large domains of ordered arrays with hexagonal packing. For the mixed $-\text{CO}_2\text{H}$ and $-\text{CH}_3$ shell, the relatively limited sites of hydrogen bonding mediate the interparticle linking, and the interpenetration of decanethiol thiolate components maximizes the interdigitative cohesive interaction. The combination of these two forces leads to a “squeezed” interparticle spatial property (Fig. 4.26), which is neither purely vdW interdigitation nor purely interdigitated hydrogen bonding.

Hydrogen bonding through nanoparticle shell molecules can provide tunable molecular interactions for enhanced selectivity [48]. Nonaqueous dispersions of CdSe nanoparticles and layer-by-layer assembly of hybrid poly(vinylpyridine) (PVP)/CdSe multilayer thin films are created based on hydrogen bonding. The resulting films have a high degree of flatness and smoothness as indicated by small-angle X-ray diffraction. Hydrogen bonds, the driving force for the formation of PVP/CdSe multilayer thin films, between the pyridine group of PVP and the carboxylic acid group on CdSe are verified by Fourier transform infrared spectroscopy [49]. Polymer/Au nanoparticle multilayer assemblies are fabricated layer-by-layer via hydrogen bonding between carboxylic acid terminal

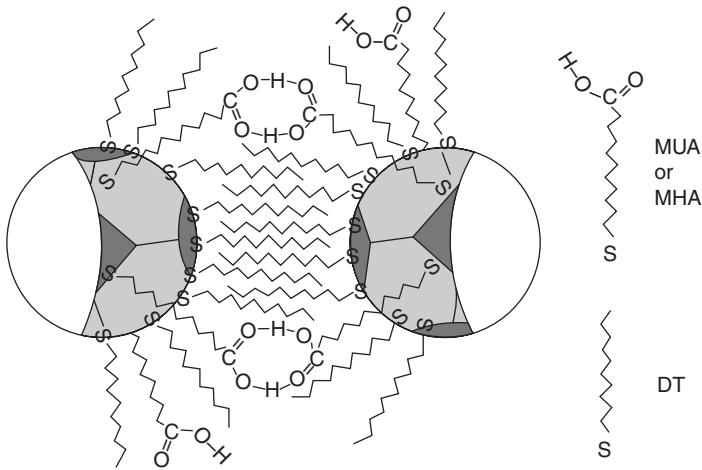


FIGURE 4.26 “Squeezed” packing model involving hydrogen bonding through carboxylic acid groups and cohesive interaction through interdigitation of the alkyl chains. DT represents decanethiol, 11-MUA represents mercaptoundecanoic acid, and MHA represents 16-mercaptohexadecanoic acid [47]. (Reprinted with permission from Han L, Luo J, Kariuki NN, Maye MM, Jones VW, Zhong CJ. Novel interparticle spatial properties of hydrogen-bonding mediated nanoparticle assembly. *Chem Mater* 2003;15:29–37, Copyright 2003, American Chemical Society.)

groups on gold nanoparticles. Gold nanoparticles surface-modified with pyridine groups of poly(4-vinylpyridine) (PVP) are prepared in dimethylformamide. Poly(3-thiophene acetic acid) (PTAA) and poly(acrylic acid) (PAA) are utilized to form hydrogen bonds with PVP, respectively. Gold particles act as physical cross-link points in the multilayers. Due to the additional interaction caused by the gold nanoparticles except for the hydrogen bonding interaction between PTAA (or PAA) and PVP, the stability of the Au-containing multilayer film is ensured even though changes in the pH values may result in the breaking of the hydrogen bonds [50].

4.3.3 Field-Assisted Assembly

External fields have emerged as key methods to direct the assembly of nanoparticles. Electric or magnetic fields are obvious candidates for field-directed assembly, but assembly in fluid flow and even electromagnetic fields have also been demonstrated to be promising. The induced field surrounding a polarized particle takes the form of a dipole and leads to strong, anisotropic dipole–dipole interaction between particles. When the interaction is sufficiently strong to overcome Brownian motion, particles will initially form dipolar chains, then, over a longer time, coarsen as chains laterally coalesce. Ideally, the coarsening proceeds *ad infinitum* to form the lowest energy structure, which may be a body-centered

tetragonal, hexagonal close-packed, or face-centered cubic lattice, depending on the particle concentration and the strength of the field.

Citrate- and alkanethiol-stabilized gold nanoparticles are electrophoretically assembled onto carbon-coated copper grids. The nanoparticles form ordered monolayers, and the core-to-core interparticle spacing is determined by the size of the alkane chains on the stabilizers used in the preparation of the suspensions. In the case of longer alkane chains, some interpenetration of the chains occurs when the gold particles form monolayers. When the gold suspensions are stabilized by sodium 3-thiopropionate [51], the monolayer is built up of a large number of smaller crystalline domains, each containing 50–200 particles in the form of hexagonal close-packed gold particles. Close examination shows that “grain boundaries” form at particles that are either aspherical or too large to fit into the superstructure. The size of the monolayers is limited by the tendency of the monolayers to tear as they are removed from the solution after the deposition. Monolayers several micrometers long and containing several hundred thousand particles may be prepared. Gold nanoparticles of 141 Å size crystallize into a hexagonal close-packed structure with an average core-to-core separation of 151 Å. The thickness of the stabilizing layer between the particles is 10 Å. Furthermore, the second- and third-order reflexes are evident, which confirms the strong degree of ordering in the superstructure. The absence of higher ordering at lattice constants of about 5 Å shows that the individual gold particles are randomly oriented within the hexagonal lattice superstructure. High-resolution images, in which the lattice planes of neighboring particles can be discerned, also show little evidence of individual gold nanoparticle alignment.

Most studies of directed assembly in electric and magnetic fields use spherical particles. However, recent work has shown that particle shape can have a surprising and potentially powerful influence on the spatial organization of nanoparticles in external fields. Fields can be used to control both the translational and orientational order of anisotropic particles and lead to structures that are otherwise unattainable using spherical particles. For instance, “peanut” hematite nanoparticles with permanent transverse dipole moments self-assemble into kinked chains in two-dimensions and, at higher concentrations, hematite nanoparticles form superstructures with an oblique geometry [52].

4.3.4 Capillary Forces

Capillary forces are interactions between particles mediated by fluid interfaces. Recent advances in this field have been achieved by experimentations on and development of theories about lateral capillary forces, which arise due to the overlap of menisci formed around separate particles attached to an interface. Nanoparticles have been assembled on substrates by immersing the substrates in a nanoparticle suspension and then relying on the capillary forces to arrange the nanoparticles [53–56]. Attractive capillary forces arise from the Laplace pressure within the curved menisci formed by condensation of liquid or vapor

bridges around two adhering particles. Interparticle capillary forces at the drying front of the meniscus and the substrate lead to the close packing of particles. The meniscus method [57] is popular because of its ease of application and the close packing of the resulting nanoparticle arrays. Such forces have been used to obtain ordered two-dimensional and three-dimensional nanoparticle packings on substrates. To apply this principle to large-area substrates, the meniscus can be moved mechanically using a withdrawing motor [57] or by evaporation of the solvent [58]. The number of layers of particles is controlled in part by the meniscus translation rate. For gold nanorods, capillary forces can align them parallel to each other; and depending on the nanoparticle and surfactant concentrations, solvent evaporation rate, ionic strength, and other solution conditions, they assemble into well-defined one-, two-, or three-dimensional superstructures [59].

Solvent drying is another approach to synthesize two-dimensional nanoparticle superstructures [60]. A silicon substrate, modified with an APTES monolayer, is exposed to a gold nanoparticle suspension to deposit randomly scattered gold nanoparticles. This is followed by a treatment with an alkanethiol solution and the organization of nanoparticles into small patches of two-dimensional nanoparticle clusters. Finally, an alcohol solvent is used to drive these small patches of gold nanoparticle clusters to self-organize together and form continuous ordered arrays of gold nanoparticles on the silicon surface. The two-dimensional ordered arrays of gold nanoparticles are formed over a very large area with hexagonal closed-packed structures. Such procedures hold promise to construct ordered mesoscopic superstructures. Figure 4.27 illustrates the solvent drying process on a flat silicon surface, inducing the formation of a close-packed array of gold nanoparticles. Figure 4.28 shows scanning electron images of a 13 nm gold nanoparticle array on a silicon substrate at different magnifications.

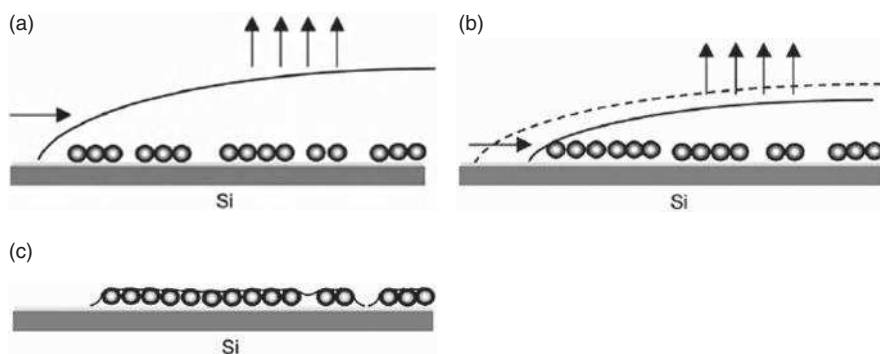


FIGURE 4.27 Schematic illustration of solvent drying on a flat silicon surface, inducing the formation of a close-packed array of gold nanoparticles [60]. (Reprinted with permission from Liu S, Zhu T, Hu R, Liu Z. Evaporation-induced self-assembly of gold nanoparticles into a highly organized two-dimensional array. *Phys Chem Chem Phys* 2002;4:6059–6062, the PCCP Owner Societies.)

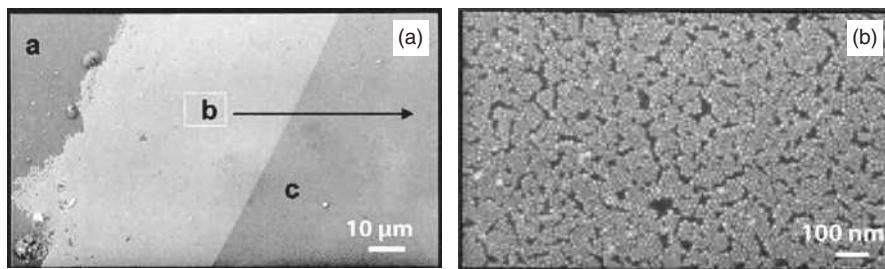
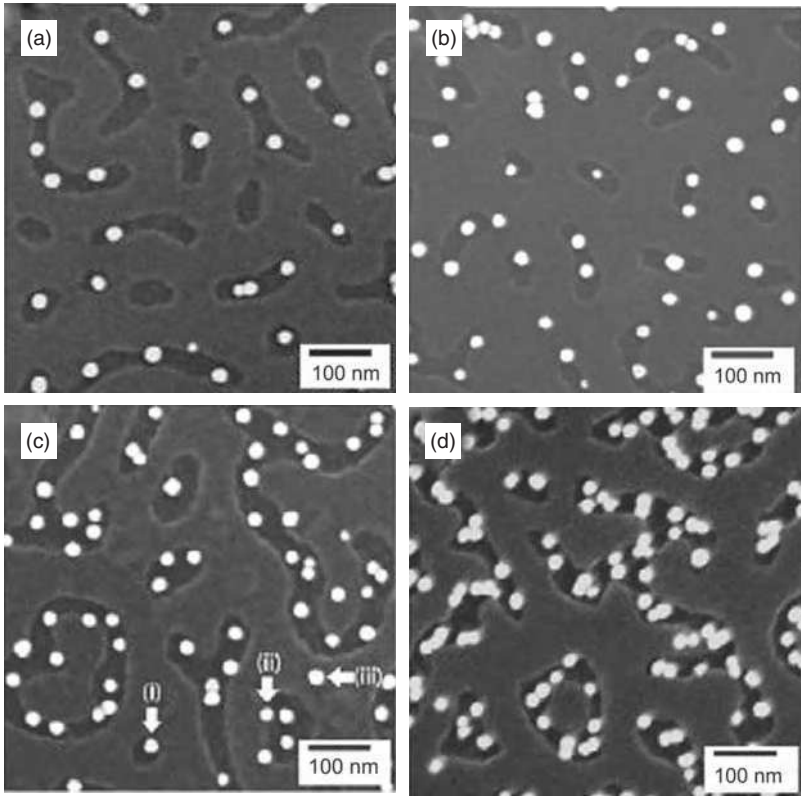


FIGURE 4.28 (a) SEM images of a 13 nm gold nanoparticle array on a silicon substrate induced by alcohol methanol solvent evaporation. (b) High-magnification image of the gold nanoparticles shown in (a) [60]. (Reprinted with permission from Liu S, Zhu T, Hu R, Liu Z. Evaporation-induced self-assembly of gold nanoparticles into a highly organized two-dimensional array. *Phys Chem Chem Phys* 2002;4:6059–6062, the PCCP Owner Societies.)

In addition to substrate surface functionalization, nanoparticles can also be functionalized before assembly. Colloidal gold nanoparticles functionalized with thioctic acid are immobilized in amine-functionalized PMMA domains on polystyrene-block-poly(methyl methacrylate) template. Nanoparticles form into clusters of single particles, dimers, and linear chains as directed by the PMMA domain size and shape. Capillary forces influence the spacing between gold nanoparticles in the PMMA domains. Interparticle spacings below 3 nm are achieved, and these assemblies of closely spaced nanoparticle clusters are expected to exhibit strong localized electromagnetic fields. A larger population of multiparticle clusters such as dimers, trimers, and linear chains results with increased coverage but does not result in uncontrolled aggregation in the PMMA domains. Figure 4.29 shows scanning electron images of thioctic acid functionalized–Au nanoparticles on the chemically modified polystyrene-block-poly(methyl methacrylate) templates after incubation with gold nanoparticles having various thioctic acid–Au nanoparticle concentration: (a) $\approx 4.65 \times 10^{11} \text{ ml}^{-1}$, (b) $\approx 9.3 \times 10^{11} \text{ ml}^{-1}$, (c) $\approx 13.9 \times 10^{11} \text{ ml}^{-1}$, and (d) $\approx 18.6 \times 10^{11} \text{ ml}^{-1}$. The nanoparticles labeled with (i), (ii), and (iii) in (c) show specific nanoparticles

FIGURE 4.29 Scanning electron images of thioctic acid functionalized–Au nanoparticles on chemically modified polystyrene-block-poly(methyl methacrylate) templates after incubation with gold nanoparticles having various thioctic acid–Au nanoparticle concentrations: (a) $\approx 4.65 \times 10^{11} \text{ ml}^{-1}$, (b) $\approx 9.3 \times 10^{11} \text{ ml}^{-1}$, (c) $\approx 13.9 \times 10^{11} \text{ ml}^{-1}$, and (d) $\approx 18.6 \times 10^{11} \text{ ml}^{-1}$. The nanoparticles labeled with (i), (ii), and (iii) show individual nanoparticles attached to poly(methyl methacrylate), poly(methyl methacrylate)–polystyrene domain boundary, and polystyrene, respectively. (e) The normalized number of particles per square micron on poly(methyl methacrylate) domains (diagonal hatching), polystyrene–poly(methyl methacrylate) domain boundaries (solid black), and polystyrene domains (crosshatching) as a function of thioctic acid–Au nanoparticle concentration [61]. (Reprinted with permission from Choi JH, Adams SM, Ragan R. Design of a versatile chemical assembly method for patterning colloidal nanoparticles. *Nanotechnology*. 2009;20:065301 6pp, IOP Publishing Ltd.)



- (e)
- (i) # of particles on PMMA
 - (ii) # of particles on PS
 - (iii) # of particles on boundary

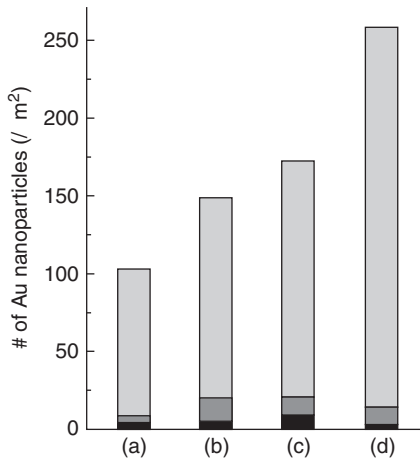


FIGURE 4.29

attached to PMMA, PMMA-polystyrene (PS) domain boundary, and PS, respectively. Figure 4.29e shows gold nanoparticles bound to domain boundaries, to PS, and to PMMA [61]. As the gold nanoparticle coverage increases, there is a sharp increase in the number of nanoparticles attached to the PMMA domains.

By utilizing the strong capillary attraction between interfacial nanoparticles, large-scale one-dimensional gold nanochain networks are fabricated at the *n*-butanol–water interface and can be conveniently transferred onto hydrophilic substrates. Furthermore, the length of the nanochains can be adjusted simply by controlling the density of gold nanoparticles at the *n*-butanol–water interface. The resultant gold nanochains can further transform into smooth nanowires by increasing the aging time, forming a nanowire network. The formation of gold nanochains stems from a stochastic assembly of interfacial gold nanoparticles due to strong capillary attractions, and the evolution of nanochains to nanowires follows an Ostwald ripening mechanism rather than an oriented attachment. This method can be utilized to fabricate large-area nanochain or nanowire networks more uniformly on solid substrates than evaporating a solution of nanochains since it eliminates the three-dimensional aggregation behavior [62].

Recent advances in colloidal synthesis and self-assembly enable the creation of multicomponent superlattices in which two or three types of nanoparticles are cocrystallized into ordered structures. In particular, binary nanoparticle superlattices consisting of two nanoparticle components distinct in size and/or composition have attracted rapidly growing interest, due to their intriguing diverse superlattice structures as well as wide applications in electronic and magnetic devices. Liquid–air interfacial assembly approach allows routine formation of large-scale, transferable binary superlattice films [63, 64]. One example is shown in Figure 4.30 [65]. The structures are realized by drying a dilute binary nanoparticle dispersion in hexane on the surface of diethylene glycol under ambient conditions (drying-mediated self-assembly process). Figure 4.30a shows a photograph of a SiO₂/Si wafer (~8 mm × 8 mm) coated with a typical binary superlattice monolayer consisting of 16.5 nm Fe₃O₄ and 6.4 nm gold nanoparticles, demonstrating the nearly complete coverage of the wafer by the binary nanoparticle superlattice membrane (Fig. 4.30a, upper left inset). Transmission electron image (Fig. 4.30a and b), selected area electron diffraction (Fig. 4.30a, upper right inset), and high-resolution SEM (Fig. 4.30c and d) confirm the membrane is a monolayer with an AB-type superlattice structure, in which the large Fe₃O₄ nanoparticles are arranged to form a square sublattice, with the small gold nanoparticles sitting in the interstices. The structural models depicting the top and side views of the AB-type binary superlattice monolayer are displayed in panels (e) and (f) of Figure 4.30, respectively. Low-magnification transmission electron images reveal that the monolayers are consisting of AB-type superlattice domains growing in different directions, with the average domain size approaching several micrometers in lateral dimensions. In addition to the Fe₃O₄–Au nanoparticle combination, AB-type binary superlattice monolayers are also obtained by the cocrystallization of 16.5 nm Fe₃O₄ and 5.5 nm FePt nanoparticles (Fig. 4.30g) as well as of

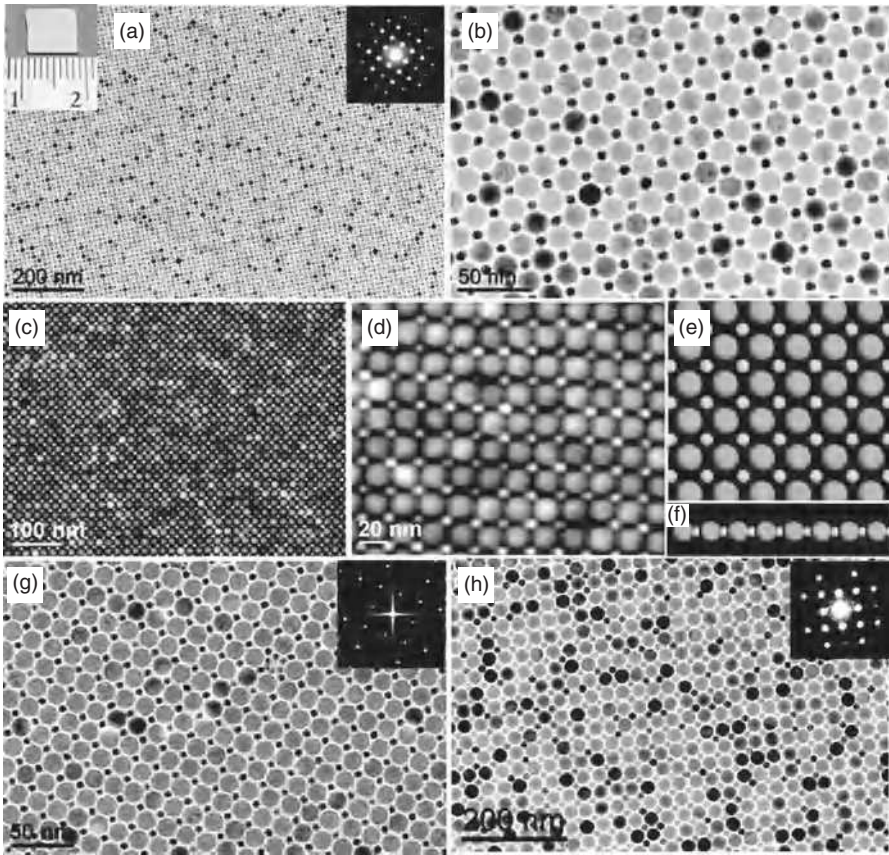


FIGURE 4.30 (a) Transmission electron image and selected area electron diffraction pattern (upper right inset) of an AB-type binary superlattice monolayer self-assembled from 16.5 nm Fe_3O_4 and 6.4 nm Au nanoparticles. The upper left inset shows a photograph of a SiO_2/Si wafer coated with a typical AB-type binary superlattice monolayer membrane. (b) High-magnification transmission electron image of the AB-type binary superlattice monolayer. (c) High-resolution scanning electron images of an AB-type binary superlattice monolayer at low (c) and high (d) magnifications, respectively. Structural models of the AB-type binary superlattice monolayer from top (e) and side (f) views, respectively. (g) Transmission electron image and Fourier transform (inset) of an AB-type binary superlattice monolayer self-assembled from 16.5 nm Fe_3O_4 and 5.5 nm FePt nanoparticles. (h) Transmission electron image and selected area electron diffraction pattern (inset) of an AB-type binary superlattice monolayer consisting of 28.9 nm $\text{NaFY}_4:\text{Yb/Er}$ and 13.4 nm Fe_3O_4 nanoparticles [65]. (Reprinted with permission from Dong A, Ye X, Chen J, Murray CB. Two-dimensional binary and ternary nanocrystal superlattices: the case of monolayers and bilayers. *Nano Lett* 2011;11:1804–1809, Copyright 2011, American Chemical Society.) (For a color version of this figure, see the color plate section.)

28.9 nm NaYF₄:Yb/Er and 13.4 nm Fe₃O₄ nanoparticles (Fig. 4.30h), demonstrating the generality of the liquid–air interfacial assembly in the growth of binary superlattice monolayers.

4.3.5 Other Approaches

Different from the discussion so far that focuses on systems synthesizing and assembling nanoparticles in separate steps, nanoparticles can be assembled immediately following the synthesis step if the arrangement of the nanoparticles can be properly controlled. In a two-phase reaction system, dodecanethiol (or its toluene solution) acts as the upper oil phase, which plays the roles of sulfur source, ligand, and reducer. The lower aqueous phase contains copper ions and other added anions (Ac⁻ or Cl⁻, used for adjusting the growth of Cu₂S). The synthesis is performed in an autoclave at 200°C. The Cu₂S nanoparticles form at the interface of water and dodecanethiol and are capped by dodecanethiol molecules. The spherical nanoparticles close-packed into a layer, and the second-layer nanoparticles fit into the voids between the first-layer nanoparticles. Two types of packing symmetry can be adopted by the third-layer nanoparticles to build face-centered cubic (Fig. 4.31a) or hexagonal close packing (Fig. 4.31b) superstructures. The inset Fourier transform patterns show a high stacking order with a sixfold axis. The ordering is up to hundreds of nanometers [66].

4.4 HYBRID

Top-down nanofabrication techniques have advanced to a point where process integration with bottom-up self-assembly is possible. This includes photolithography, microcontact printing, and nanoimprint lithography. Because most lithographic techniques are constrained to two-dimensional planes, investigation of integrated nanoparticle superstructure construction also usually focuses on two-dimensional organization.

During the hybrid nanostructure construction process, topographical or chemical heterogeneities at the nanoscale are used to confine and regulate nanoparticles. Top-down methods are used to make patterns of various sizes to serve as the templates to direct the deposition and assembly of various nanoparticles in a confined space or position. External fields such as electrical, magnetic, shear, or pressure may be used to further improve the precision, speed, or efficiency of the nanoparticle superstructure building processes.

4.4.1 Functionalized Interactions

Microelectrode arrays based on either TiO₂ or metal nanoparticles are made by combining photolithography and photocatalytic deposition as discussed in Section 4.2.1. The procedure involves photolithographically selective decomposition of superhydrophobic *n*-octadecyltriethoxysilane (C₁₈H₃₇Cl₃Si)

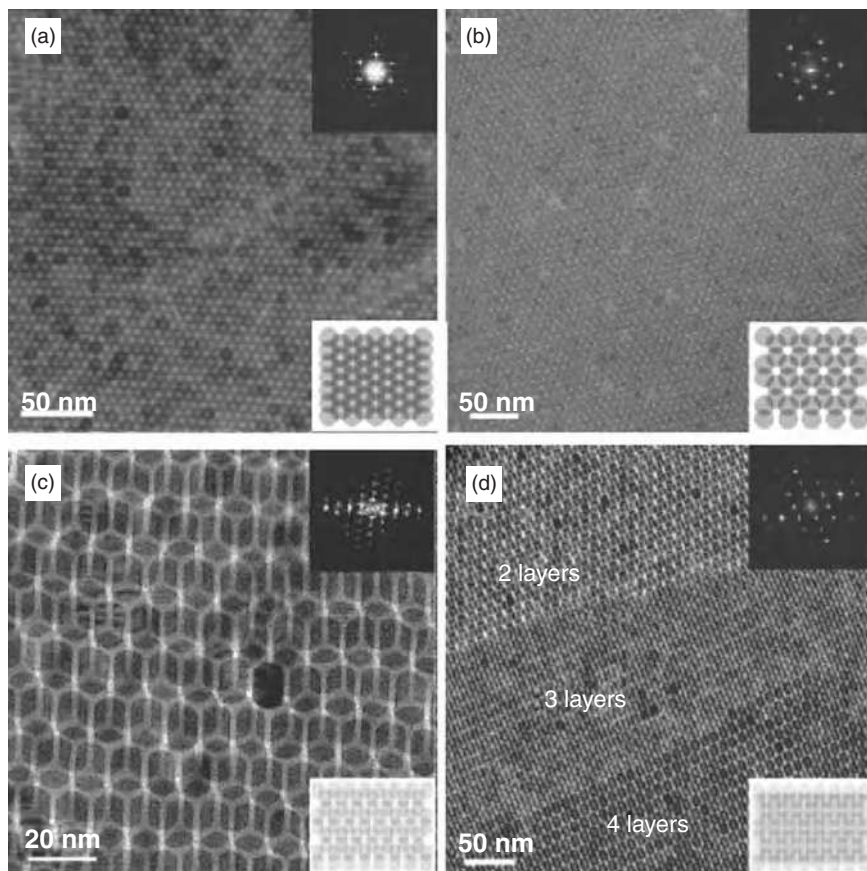


FIGURE 4.31 Transmission electron images of Cu_2S nanoparticle assemblies: (a) face-centered cubic-packed spherical nanoparticles, (b) hexagonal close-packed spherical nanoparticles, (c) two layers of close-packed elongated nanoparticles, and (d) multilayers of elongated nanoparticles. The top insets are the corresponding Fourier transform patterns, and the bottom insets are the schemes of the stacking of nanoparticles [66]. (Reprinted with permission from Zhuang Z, Peng Q, Zhang B, Li Y. Controllable synthesis of Cu_2S nanocrystals and their assembly into a superlattice. *J Am Chem Soc* 2008;130:10482–10483, Copyright 2008, American Chemical Society.) (For a color version of this figure, see the color plate section.)

to create superhydrophobic/superhydrophilic TiO_2 patterns. The generated TiO_2 patterns then function as the new templates to produce metal nanoparticle-based microelectrode arrays by photocatalytic deposition. The metal nanoparticles grow site-selectively inside the TiO_2 templates. This hybrid approach can be used to create microelectrode arrays composed of TiO_2 nanoparticles and various metal nanoparticles, such as gold, silver, and platinum, with different patterns [67].

Self-assembled polymer monolayers fabricated by microcontact printing can be used as the guiding templates for nanoparticle superstructure construction. Superstructures of gold nanoparticles are obtained on a solid substrate with precise position and density control by the self-assembled monolayers terminated with different functional groups. Two examples are $-\text{CH}_3/-\text{NH}_2$ and $-\text{CH}_3/-\text{SH}$, which offer different affinities to gold nanoparticles. Gold nanoparticles assemble selectively on $-\text{NH}_2$ or $-\text{SH}$ terminated locations; and the $-\text{NH}_2$ functional group binds electrostatically to the nanoparticles whereas the $-\text{SH}$ groups bind chemically. The coverage of $-\text{CH}_3$ terminated self-assembled monolayers is controlled by changing the concentration of the polymer “ink” solution for the stamp. After immersing the printed and self-assembled monolayer into $-\text{SH}$ or $-\text{NH}_2$ thiol solutions for 2 hours, a predetermined coverage of $-\text{SH}$ or $-\text{NH}_2$ with the $-\text{CH}_3$ terminated and self-assembled monolayer is formed in the contact regions, and a pure $-\text{SH}$ or $-\text{NH}_2$ self-assembled monolayer is formed in the intervening area. The position and density of gold nanoparticles on the surface are determined by the distribution of the underlying functional groups [68].

Nanoimprint lithography, which allows control of lateral dimensions down to 6 nm [69], in combination with self-assembly of silanes on SiO_2 in the micron to submicron range is used to direct nanoparticle assembly. A thin polymer layer is patterned on a substrate with a hard stamp at a temperature above the glass transition temperature of the polymer [70]. After a residual layer removal step, the substrate consists of a polymer relief pattern with exposed substrate regions in-between. These substrates can be converted to chemically patterned substrates by removing the polymer template and covering the bare SiO_2 areas with self-assembled monolayers of a different functionality. Both types of substrates are used to attach functionalized nanoparticles by drop-casting or immersion. Although drop-casting of functionalized nanoparticle suspensions on the substrates results in a high selectivity, the coverage is not homogeneous on the entire surface, and only short-range order is observed because of a lack of control over the solvent evaporation process.

A multistep process based on nanoimprinting and chemically directed nanoparticle assembly by vertical deposition is studied, employing the moving meniscus principle to allow versatile patterning of nanoparticles on different types of substrates [70]. In this manner, hexagonal close packing is achieved on micron-sized features. By topographical confinement, a resolution of 60 nm is achieved for particle lines attached to aminoalkyl self-assembled monolayers, while resolutions of 300 nm are achieved on chemically confined substrates.

Functionalized nanoparticle assembly can also be carried out by using a combination of three methods: nanoimprint lithography to control the lateral size, gas-phase self-assembly of silanes for anchoring the functionalized nanoparticles, and meniscus method to control their ordering. Two types of substrates are studied: substrates patterned topographically and chemically and flat substrates patterned only chemically [70]. Figure 4.32 shows a schematic representation of the process to fabricate patterns of nanoparticles using chemical templates in combination with (Fig. 4.32a) or without physical barriers

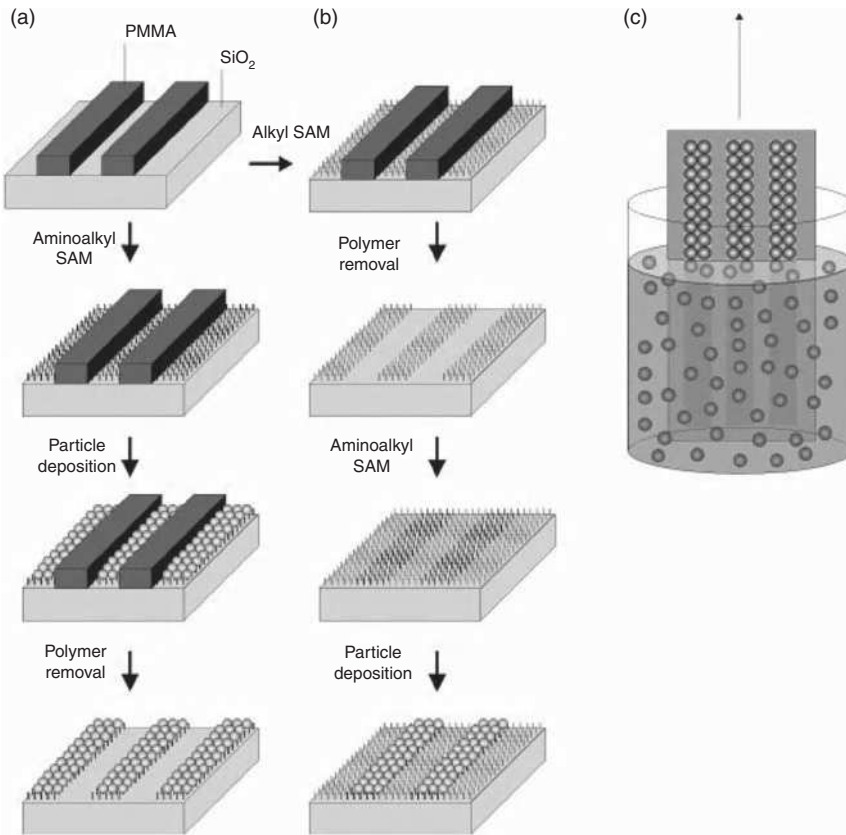


FIGURE 4.32 (a–c) Schematic representation of the process to fabricate patterns of nanoparticles using chemical templates in combination with (a) or without physical barriers (b). The polymer templates are prepared by nanoimprint lithography, self-assembled monolayers are formed by gas-phase deposition, and nanoparticles are attached using a vertical deposition setup (c), in which the samples are withdrawn vertically from the nanoparticle suspensions at a constant speed [70]. (Reprinted with permission from Maury P, Escalante M, Reinhoudt DN, Huskens J. Directed assembly of nanoparticles onto polymer-imprinted or chemically patterned templates fabricated by nanoimprint lithography. *Adv Mater* 2005;17:2718–2723, John Wiley & Sons.)

(Fig. 4.32b). Self-assembled monolayers are formed by gas-phase deposition, and nanoparticles are attached using a vertical deposition setup (Fig. 4.32c), in which the samples are withdrawn vertically from the nanoparticle suspensions at a constant speed.

Sub-300 nm features are made using patterns produced by nanoimprint lithography. Figures 4.33a and b show images of 55 nm SiO₂ particles confined in 100 nm and 60 nm wide imprinted lines, leading to zigzag arrays and single

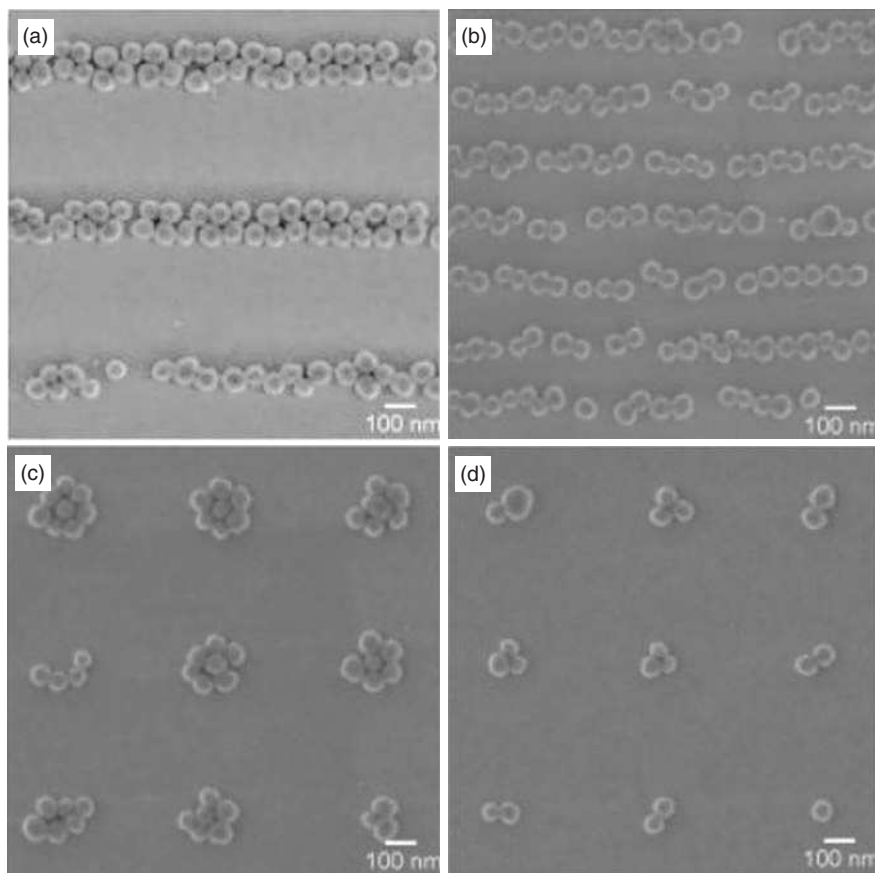


FIGURE 4.33 Scanning electron images of 55 nm carboxylate-functionalized SiO_2 nanoparticles assembled on poly(methyl methacrylate) imprinted sub-300 nm patterns with aminoalkyl self-assembled monolayers. The effect of confinement on the particle assembly is achieved by using lines with line widths of (a) 100 nm and (b) 60 nm, and holes with diameters of (c) 180 nm and (d) 100 nm [70]. (Reprinted with permission from Maury P, Escalante M, Reinhoudt DN, Huskens J. Directed assembly of nanoparticles onto polymer-imprinted or chemically patterned templates fabricated by nanoimprint lithography. *Adv. Mater.* 2005;17:2718–2723, John Wiley & Sons.)

particle lines, respectively. The initial polymer height is 100 nm, and the residual layer is removed by exposure to oxygen plasma for 10 seconds. The withdrawal speed is $1 \mu\text{m s}^{-1}$. After particle adsorption, the polymer template is removed by sonication in acetone for 1 minute. For Figures 4.33c and d, imprinted holes of 180 nm and 100 nm sizes are used, respectively. In all cases, the aminoalkyl (amino derivative of an alkyl radical) self-assembled monolayer acts as an anchor

when using a topographical template as the substrate, which allows easy removal of the polymer.

4.4.2 Nonfunctionalized Interactions

Topographical templates can confine nonfunctionalized particles within the patterns. Pattern confinement can be used to obtain special nanoparticle arrangements, to control superstructure symmetry, and to pattern multilayers of nanoparticles on both large and small scales.

Periodic arrays of silver nanoparticles are fabricated on various solid substrates by block copolymer photolithography. By employing a block copolymer to spatially organize silver nanoparticles, laser light can be concentrated via plasmon resonance to locally expose a photoresist. By subsequent development, this plasmonic lithography can provide deep subwavelength scale features [71]. A spin-coated diblock copolymer thin film with well-ordered and vertically oriented cylindrical nanodomains is utilized as the template. Ag^+ is selectively doped in the cylindrical nanodomain by placing a few drops of AgNO_3 aqueous solution on the film. Both photochemical reduction of Ag^+ to metallic silver and concomitant photo-etching of the diblock copolymer template are realized under UV light irradiation in a vacuum, resulting in a direct transcription of the periodic pattern of the diblock copolymer template to the metallic silver nanoparticle array with consistent periodicity [72]. A periodic hexagonal close-packed nanoparticle two-dimensional array photomask can transfer a nanopattern into a photoresist. This method can be made to precisely control the spacing between nanoparticles by using different temperatures. High-density nanoparticle thin film is accomplished by self-assembly through the LS technique on a water surface and then transferring the particle monolayer to a temperature-sensitive polymer membrane. The observed transmission strongly depends on the wavelength and the period of the hexagonal close-packed two-dimensional nanoparticle array. A 30 nm hexagonal close-packed two-dimensional silver nanoparticle array with a 50 nm period is successfully transferred into S1813 photoresist by this method (Fig. 4.34). The resultant feature sizes are 34 nm with a period of 46 nm [73].

SiO_2 nanoparticle superstructures on a TiO_2 surface and TiO_2 nanoparticle superstructures on a SiO_2 surface are formed by deposition of SiO_2 or TiO_2 nanoparticles on prepatterned substrates as discussed in Section 4.2.1. Photolithography creates a matrix for selective deposition of nanoparticles by immersing the substrates in a colloidal suspension. Although two-dimensional colloidal patches of TiO_2 nanoparticles are obtained on SiO_2 surfaces, SiO_2 nanoparticles form three-dimensional, U-shaped channels on TiO_2 surfaces. The influence of electrostatic forces on the assembled structure is vital. The isoelectric points of the particles, the prepatterned matrix, and the photo-resist are key parameters that may be manipulated to achieve various microstructures. The two-dimensional nanoparticle arrays of TiO_2 on SiO_2 and three-dimensional channels of SiO_2 on flat TiO_2 surfaces are of potential interest in lab-on-a-chip applications [6]. For CdSe quantum

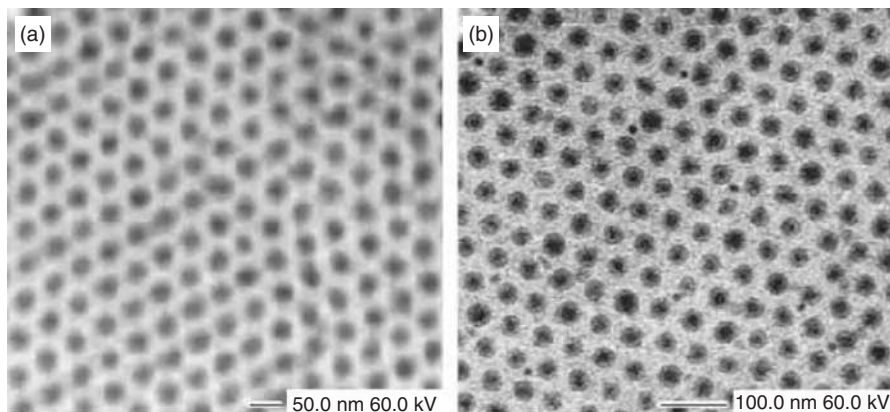


FIGURE 4.34 (a) Silver nanoparticle hexagonal close-packed two-dimensional array achieved by self-assembly, (b) developed S1813 photoresist exposed at 365 nm wavelength [72]. (Reprinted with permission from Lewis S, Wheeler-Jones R, Haynes V, Perks RM. High density self assembled nanoparticle film with temperature-controllable interparticle spacing for deep subwavelength nanolithography using localized surface plasmon modes on planar silver nanoparticle tunable grating. *Microelectron Eng* 2008;85:486–491, Copyright 2008, Elsevier.)

dots, a combination of nanoparticle patterning with photolithography leads to micropatterned multilayers [31]. Separately, SiO_2 nanoparticles are synthesized and assembled in a monolayer manner through halogenated silanes. Photolithography techniques are used to pattern the glass surface prior to nanoparticle attachment. The concentration of the SiO_2 nanoparticles in the solution controls the surface coverage of the nanoparticles on the glass surface. Different SiO_2 arrays can be patterned with controlled surface coverage. The nanoparticle-covered surface has enhanced enzymatic reactivity in biosensor development [74].

4.5 TEMPLATING

Template-assisted assembly, where a prefabricated “template” orients and directs the nanoparticles and controls the morphology and pattern of the resulting assemblies, provides a straightforward and effective route to fabricate novel structures that would be otherwise unfavorable in the absence of the template. A broad range of objects have been used as templates for nanoparticle superstructure construction, which can be classified into soft and hard categories. Although soft templates (such as small molecules, block copolymers, and DNAs) possess distinct chemical structures and provide multiple well-defined binding sites for the attachment of nanoparticles, such assembly strategies are typically applicable to a limited subset of particles that meet specific surface chemistry requirements. Alternatively, hard templates, such as relief structures patterned on the surfaces of solid substrates, provide greater toughness and structural characteristics for

assembling nanoparticles. Compared to template-free methods, template-based nanoparticle superstructure construction through nonspecific interactions has the advantage of universality, feasibility, and controllable and tunable functionality. Based on the origin of the template, template-based methods can be divided into natural and synthetic. In general, synthetic templates have more varieties and better control of feature characteristics.

4.5.1 Natural Template

Nature offers a rich source of nanostructured templates. Biospecific interactions are used to assemble low-dimensional hybrid objects. Biomolecules, such as lipids, carbohydrates, DNAs, proteins, and viruses, have advantages over non-biological species as templates owing to their uniform size, shape stability, and robust specific biorecognition interactions. DNA-based self-assembly offers precise structural control and responsive functionality. Two-dimensional crystalline protein surface layer from bacterium *Sporosarcina ureae* can be utilized to arrange the orientation and spatial distribution of nanoparticles [75]. Direct synthesis and organization of platinum, rhodium, palladium, iron, cobalt, and nickel nanoparticles on a viral capsid are achieved by incubating T4 virions in a solution of the corresponding metal salt and treating with a reductant. Different chemical groups inherent in the capsid protein are used as ligands to electrostatically bind metal ions. Centrifugation is carried out to decrease the unbound metal ions around the virions in order to ensure that the reduction and nucleation of metal ions occur on the binding sites. The growth of metal particles *in situ* yields a highly dispersed configuration and a small size distribution, which contribute to high electrocatalytic activities of the obtained noble metal particles. Also, the coverage density of nanoparticles can be tuned simply by changing the incubation time or cycles of the virions [76]. In addition, proteins are used as a template to assemble gold nanoparticles in a rod-like fashion [77]. An antibody, C225 (epidermal growth factor receptor), is used as a template during the synthesis of gold nanoparticles. Association of the protein with the gold salt, tetrachloroauric acid (HAuCl_4), before the reduction is essential for this antibody-mediated self-assembly. Figure 4.35 shows a transmission electron image of gold nanoparticles formed in the presence of C225 as a template. Figure 4.35a shows a transmission electron image of the Au–C225 conjugate before cooling. Spherical/elongated gold nanoparticles about 5 nm in diameter are observed. Figure 4.35b shows the transmission electron image of Au–C225 after cooling to -20°C . The unique organization of gold nanoparticles in a rod-like fashion is observed (Fig. 4.35b). A higher magnification image of the same rod shows the compact organization of discrete gold nanoparticles (Fig. 4.35c). These natural templates enable the design of robust self-assembly systems with desired morphologies.

Epitaxial templates can be matched with the dimensional and stereochemical needs of the crystalline planes of nanoparticles. The patterned templates do not require prior knowledge of the guest crystal structure but necessitate that nanoparticles discriminate among heterogeneous surface structures. A surface

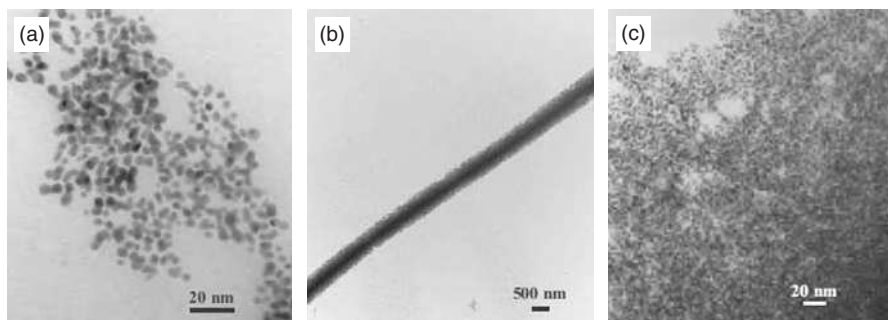


FIGURE 4.35 Transmission electron images of (a) Au-C225 conjugates, where C225 is present during the reduction in the gold salt by sodium borohydride ($\text{Au/C225} = 10:1$). (b) Transmission electron image of the same conjugate cooled to -20°C followed by thawing at room temperature. (c) A higher magnification image at the edge of the rod shown in (b) [76]. (Reprinted with permission from Bhattacharya R, Patra CR, Wang S, Lu L, Yaszemski MJ, Mukhopadhyay D, Mukherjee P. Assembly of gold nanoparticles in a rod-like fashion using proteins as templates. *Adv Funct Mater* 2006;16:395–400, John Wiley & Sons.)

pattern with periodically active sites separated by inactive barriers can serve as a site-specific template for the synthesis of nanoparticle arrays. Chemically modified Au55 nanoclusters (a cuboctahedral structure consisting of one central atom, an inner shell of 12 atoms, and an outer one of 42 atoms) are incorporated into highly oriented molecular templates by substitution of individual molecules of the template. The required molecular templates form spontaneously at the solid–liquid interface of highly oriented pyrolytic graphite and can be directly investigated by STM at the solid–solution interface. Strands of linearly arranged superstructures with a periodicity down to a few nanometers of gold clusters are arranged along the template direction [78].

Using self-assembled monolayer patterns, two approaches can be taken to make nanoparticle arrays: one relying on the self-assembled monolayer pattern to selectively attract nanoparticles from their suspensions by surface-particle interactions and the other by nucleating and regulating nanoparticle growth directly on the self-assembled monolayer pattern. The self-assembled monolayers provide diverse surface functionalities such as $-\text{OH}$, $-\text{COOH}$, or $-\text{SH}$, which can be used to attract functionalized nanoparticles. Layers of nanoparticles have been adsorbed on self-assembled monolayers [46, 68, 79–83]. The specific affinity between the exposed tail groups on self-assembled monolayers and the surface properties of nanoparticles is critical for the selective deposition. The types of interactions used include electrostatic attraction between self-assembled monolayers and nanoparticles [83], the metal–thiol bond between nanoparticles and thiols [80], and other chemical bonds between the tail group and the capping agent. Efforts have also been made to control the immobilized nanoparticle density [82].

Templating of nanoparticles into three-dimensional superstructures by a pre-determined template opens the route to creation of chemical, optical, magnetic, and electronic devices with endless possibilities and outstanding properties. Example applications include supports for organic synthesis, separation processes, bioreactors, and photonic band gap materials.

4.5.2 Synthetic Template

Polymers are excellent synthetic templates that provide uniform size and shape and can be easily removed by thermal pyrolysis. Close packing of nanoparticles into macroscopically ordered polymer templates can be induced by solvent evaporation, filtration, sedimentation, or centrifugation. Long-range ordering of colloidal particles is often promoted by attractive forces between the template and the nanoparticles in the suspension. The polymer is often PS or PMMA with micron sizes. The simplest approach involves controlled adsorption and/or reactions (e.g., heterocoagulation and sol-gel condensation) on the surface of the templates. Templating of nanoparticles involves three steps: immersion of the synthetic template (often an organic species) into the nanoparticle precursor solution (e.g., metal alkoxide, metal salts, and monomers), filtration of the inorganic particles into the interstitial sites of the organic template, and removal of the organic template by calcination, chemical etching, or dissolution. This procedure can integrate a large variety of colloidal particles into a porous organic solid with a periodic three-dimensional structure.

Crystalline assemblies of organic species such as PS spheres offer a host matrix to produce highly hierarchical nanostructured organic-inorganic materials. The template can be subsequently removed chemically or thermally, leaving behind a porous material that is an inverse replica of the template microstructure. The superstructure and form of the resulting porous sample depend directly on the characteristics of the starting template. Polymeric colloidal particle films are an ideal starting template. These materials are three-dimensionally ordered and close-packed arrays of spherical polymer particles. The templates can be prepared using a variety of methods, including gravity sedimentation, filtration, and convective assembly, and can be highly ordered over centimeter length scales, uniform in thickness, and strongly diffractive at visible wavelengths. When defect-free, the templates may contain only 24% free space. Precursors of metal, ceramic, or semiconductor nanoparticles can be infiltrated into the free space and subsequently condensed to their solid forms. This strategy has been used to prepare a wide variety of macro- and mesoporous materials.

One example of the synthetic template approach is shown in Figure 4.36 [84]. Core/shell structures are exploited as combined building blocks and sacrificial templates for the construction of hierarchical nanostructures. Porous ceramic nanoparticle superstructures such as TiO_2 , ZrO_2 , SiO_2 , and Al_2O_3 from the corresponding metal alkoxides are made using PS spheres as templates [85–87]. In a fast, single-step reaction, the monomeric alkoxide precursors permeate the array of PS sphere packing and condense. Oxide nanoparticle close packing

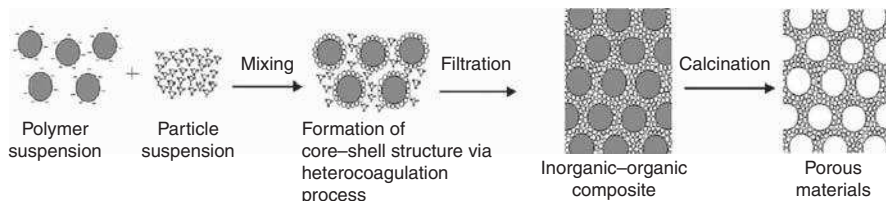


FIGURE 4.36 Schematic procedure for fabrication of macroporous materials via polymer/nanoparticle core/shell flocculation [84]. (Reprinted with permission from Tang F-Q, Fudouzi H, Uchikoshi T, Sakka Y. Preparation of porous materials with controlled pore size and porosity. *J Eur Ceram Soc* 2004;24:341–344, Copyright 2004, Elsevier.)

with periodic three-dimensional arrays and 320–360 nm diameter macropores is obtained after calcination of the organic component at 575°C. In one example, SiO₂ nanolayers of 15–40 nm are coated onto PS via tetraethyl orthosilicate (TEOS) hydrolysis [88]. The SiO₂ layer growth rate and the maximum layer thickness are strongly dependent on the reaction time and pH. The structures consist of uniform hexagonal close-packed spherical pores interconnected with each other. The pore size and the thickness of the nanoparticle walls in the final superstructures can be varied independently by choosing different templates and reaction conditions. Infiltration of a TiO₂ sol-gel precursor into the PS template is also possible [89]. The pores are highly ordered in a hexagonal array, the channel size is 180 ± 20 nm, and the wall thickness is 100 ± 20 nm, depending on the TiO₂-PS compositions. The coated PS array can be dried and dissolved, leaving a regularly packed TiO₂ porous structure. The PS array can also be sonicated to obtain TiO₂ hollow spheres with a nanoscale wall thickness.

Another approach for nanoparticle superstructure construction using synthetic templates is particle surface charge modification. The critical step is to obtain well-dispersed suspensions of polymer and ceramic particles such as Al₂O₃, TiO₂, or ZrO₂ with opposite charges at the same pH condition. Upon mixing of the two suspensions, polymer core/nanoparticle shell structures are formed via electrostatic attraction. The flocculated core/shell particles are subsequently closely packed by vacuum filtration, slip casting, or other means. The polymers are finally removed by calcination, resulting in porous structures. Ordered arrays of monodispersed SiO₂ nanoparticles are produced [90, 91]. Colloidal codispersion of SiO₂-coated gold particles and PS particles has generated regular composite nanostructures without complex chemical reactions (Fig. 4.37) [92].

The structure of nanoparticle-based macroporous superstructures produced by synthetic templates is highly dependent on the properties of the starting materials and the suspension conditions, such as zeta potential, particle size, and volume ratio of nanoparticles to polymer spheres. In order to fabricate core/shell composites with uniform structures, a key point is to prepare well-dispersed suspensions with both the template particles and the nanoparticles in the same pH range; otherwise, uniform core/shell structures can be difficult to obtain due to the agglomeration of one or both of the suspensions.

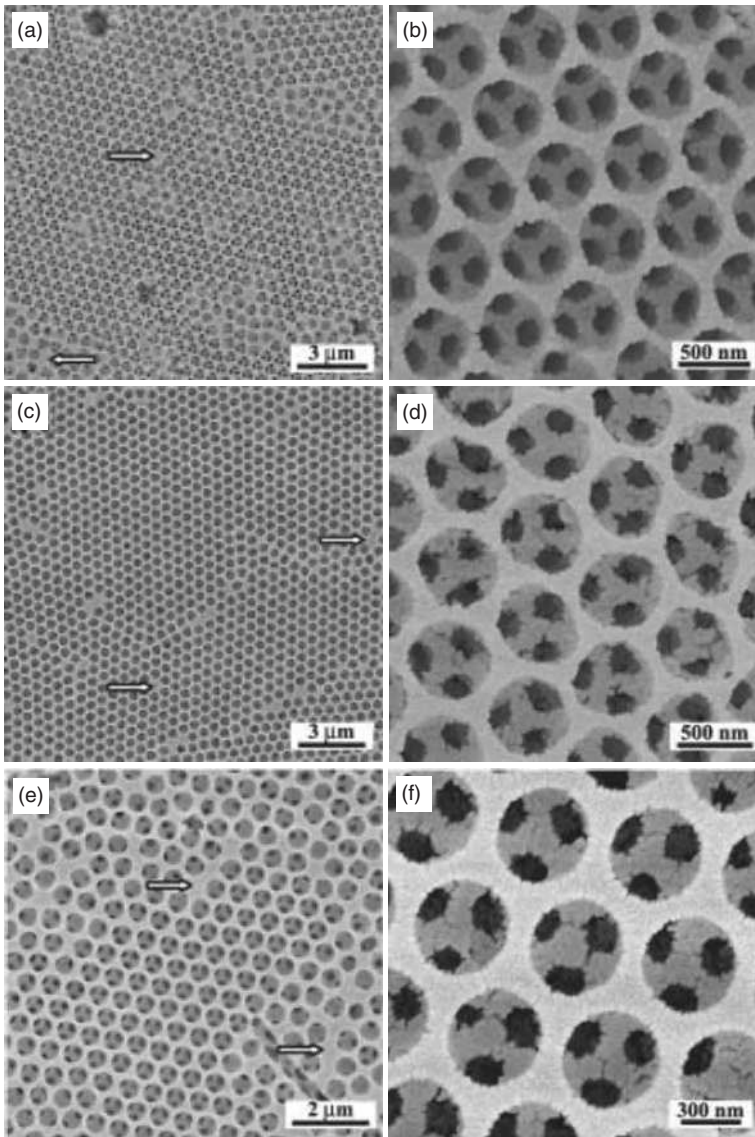


FIGURE 4.37 Lower (left) and higher (right) magnification scanning electron images of gold/SiO₂ core/shell nanoparticle superstructures formed by templating 640 nm polystyrene particles with SiO₂-coated gold nanoparticles. (a) and (b) are for 70 nm SiO₂-coated gold nanoparticles; (c) and (d) are for 50 nm SiO₂-coated gold nanoparticles; (e) and (f) are for 30 nm SiO₂-coated gold nanoparticles [92]. (Reprinted with permission from Wang DY, Salgueirino-Maceira V, Liz-Marzan LW, Caruso F. Gold-silica inverse opals by colloidal crystal templating. *Adv Mater* 2002;14:908–912, Wiley-VCH.)

Although the general area of templating has been very active over the last decade, the application of templating methods to the synthesis of macroporous metal nanoparticle-based materials is in its early stages. Macroporous metals can be created from colloidal crystal templates, may have over 70% porosity, resulting in a net surface area of several square meters for a thin layer only 1 cm across, and are sturdy enough to withstand routine handling. The pores of these samples are highly ordered over large length scales and are interconnected by small windows that give solvents and gases ready access to the entire internal surface of the metal. Moreover, since the porous structure is ordered and the surface is relatively flat, the materials possess striking optical features reminiscent of highly blazed gratings. The unique combination of both micro- and nanostructures, as well as the thin layer format, suggests that these samples may be useful in a wide variety of applications ranging from sensing to catalysis [93]. Figure 4.38a shows the top view of a macroporous copper film with 325 ± 15 nm diameter voids. The bottom left inset shows the Fourier transform pattern of a low-magnification image of a $40 \times 40 \mu\text{m}^2$ region.

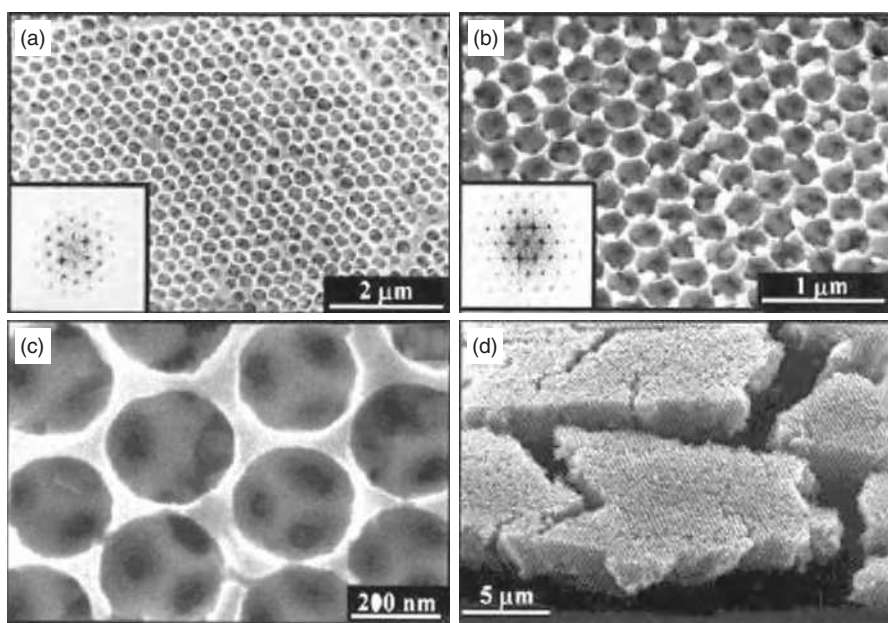


FIGURE 4.38 Typical scanning electron images of macroporous metal films. (a) Top view of a macroporous copper film with 325 ± 15 nm diameter pores. The bottom left inset shows the Fourier transform pattern of a low-magnification image of a $40 \times 40 \mu\text{m}^2$ region. (b) Top view and Fourier transform pattern of a silver film with 353 ± 17 nm diameter voids. (c) A high-magnification image of a macroporous nickel film showing the smaller pores (60 ± 10 nm) that interconnect the larger pores. (d) Top and cross-sectional view of the macroporous copper film from (a) at lower magnification [93]. (Reprinted with permission from Kulinowski KM, Jiang P, Vaswani H, Colvin VL. Porous metals from colloidal templates. *Adv Mater* 2000;12:833–838, John Wiley & Sons.)

image of a $40 \times 40 \mu\text{m}^2$ region. Figure 4.38b shows the top view and Fourier transform pattern of a silver film with 353 ± 17 nm diameter pores. Figure 4.38c shows a high-magnification image of a macroporous nickel film showing the smaller pores (60 ± 10 nm) that interconnect the air cavities. Figure 4.38d shows the top and cross-sectional view of the macroporous copper film from (a) at lower magnification. The sample is scraped using a sharp razor blade to expose the cross section and tilted at $30\text{--}40^\circ$, which reveals the porous morphology throughout the film [93].

Filtration can be used both to create the PS particle crystals (with PS diameters from 200–1000 nm) and to draw a solution of gold nanoparticles (15–25 nm) into the interstices of the crystal. Nanoparticles can penetrate into the colloidal multilayer easily because of the small size. The PS/gold nanoparticle superstructure can be detached from the filter and dried in air. Removal of the PS spheres is accomplished either by calcination, yielding macroporous gold-based superstructures, or by chemical means, such as oxidation by concentrated sulfuric acid and/or dissolution in trichloromethane (CHCl_3), yielding meso/macroporous samples. Pore size can be controlled by varying either the size of the gold nanoparticles (smaller particles yield thicker walls and smaller pores) or the chosen method of template removal (oxidation produces thicker walls than dissolution).

Synthetic templates provide control over pore dimensions and the physical or chemical properties of the resulting porous superstructures. This approach also offers the possibility of creating multiscale porosities by dual templating [94, 95]. The key challenges involve avoiding defect formation and suppressing grain growth. Due to the intricate and regular nanostructures, any defects from the templating process cannot be repaired and will remain in the three-dimensional structures. Also, it is impossible to consolidate the template nanostructures by applying external pressures since that will inevitably destroy them. Tremendous challenges exist to strengthen the formed superstructure without invoking nanoparticle grain growth or defect formation while achieving the ruggedness needed. The ordered porous structure can be affected considerably by mechanical compression at pressures as low as 86 MPa and essentially destroyed at 224 MPa. Care must be taken to ensure that the porous superstructure in use has not been altered.

PMMA colloidal crystal monoliths with sphere diameters of 416 ± 11 nm are used as templates for the generation of three-dimensional and ordered mesoporous materials through confinement of a concentrated triconstituent precursor solution (a soluble phenol-formaldehyde prepolymer, TEOS, and a nonionic triblock copolymer) by infiltration. The external morphology of the mesostructured products can be controlled. The hierarchical (ordered macropores from PMMA spheres and large mesopores from the copolymer) superstructures are shown in Figure 4.39 [96].

Bicontinuous polymeric gels have also been used as templates to form porous nanoparticle-based superstructures. The pores are often irregular and of large size. Examples include *in situ* mineralization of magnetite (Fe_3O_4) and TiO_2 . This type of polymer templates generally uses molecular precursors that infiltrate and

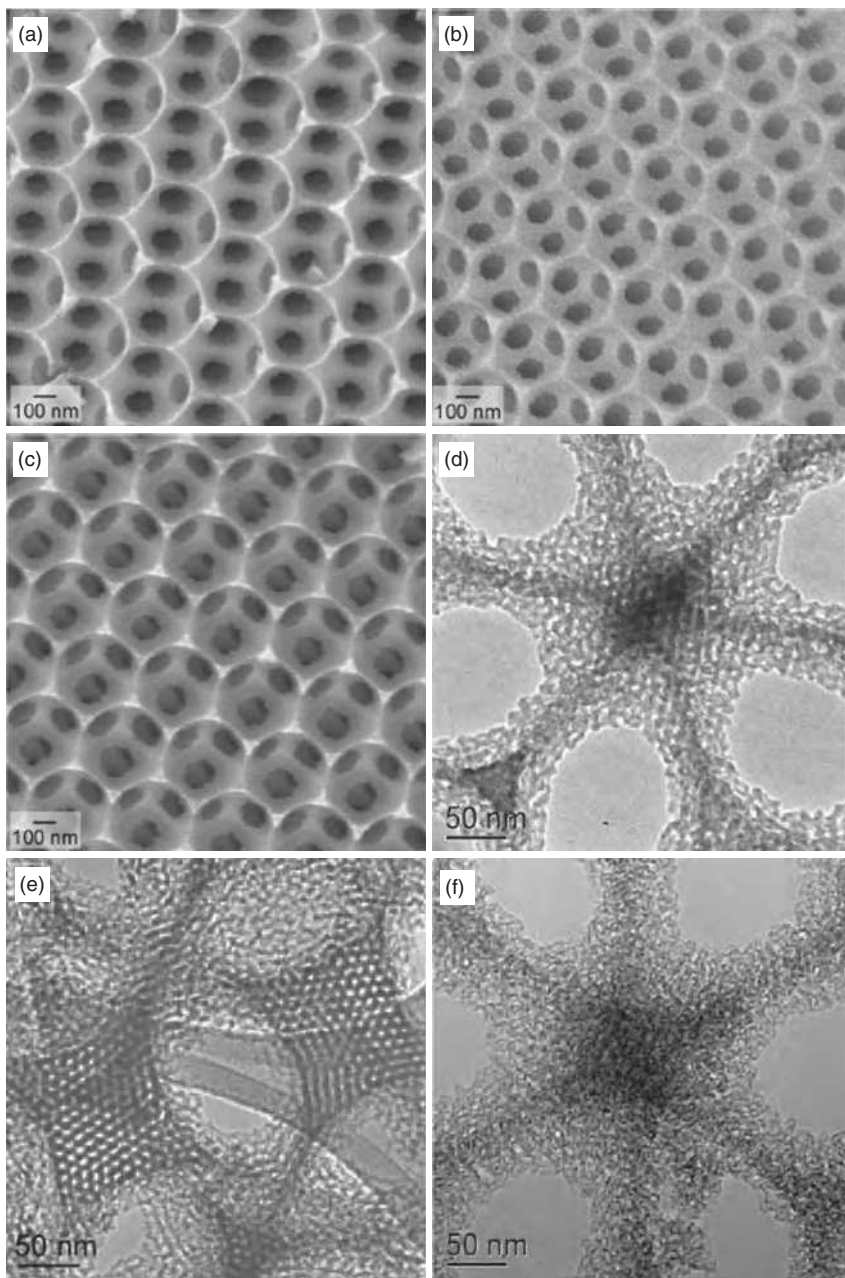


FIGURE 4.39 Scanning electron images (a, b, and c) and transmission electron images (d, e, and f) of three-dimensional-ordered macro-/mesoporous carbon-SiO₂ (a and d), three-dimensional-ordered macro-/mesoporous SiO₂ (b and e), and three-dimensional-ordered macro-/mesoporous carbon (c and f) monoliths after carbonization in nitrogen at 900°C for 2 hours [96]. (Reprinted with permission from Wang Z, Stein A. Morphology control of carbon, silica, and carbon/silica nanocomposites: from 3D ordered macro-/mesoporous monoliths to shaped mesoporous particles. *Chem Mater* 2008;20:1029–1040, Copyright 2008, American Chemical Society.)

react within confined but structured spaces. Acrylic acid-based copolymers with different proportions of carboxylic acid and hydroxyl functional groups are infiltrated with colloidal suspensions of Fe_3O_4 or TiO_2 to prepare three-dimensional inorganic monoliths with a sponge-like texture [97]. The copolymer- Fe_3O_4 composite shows almost no detectable coercivity, while the calcined replicas show coercivity. Macroporous PMMA/ SiO_2 nanocomposite monoliths are synthesized in supercritical CO_2 [98]. Dispersed SiO_2 particles are pretreated with functional 3-(trimethoxysilyl)-propyl methacrylate. This results in SiO_2 -PMMA nanocomposites forming interconnected structures with micron-sized pores and grafted polymer layers on the SiO_2 surface.

Gold nanoparticles are evenly deposited on polyaniline nanofibers by simply introducing an acid (typically thioglycolic acid) that shows strong affinity for gold nanoparticles. Redox reaction occurs between polyaniline and noble metal salts; and the acid affects reaction kinetics, size, and uniformity of polyaniline/noble metal assemblies. Gold nanoparticles can be tuned from 2 to 10 nm in a controlled manner in the case of thioglycolic acid-doped polyaniline nanofibers. This method is also applicable to synthesizing uniform polyaniline nanofiber composites with other noble metal nanoparticles, such as platinum. From an application point of view, polyaniline nanofiber/gold nanoparticle composites can be used as catalysts for the reduction in 4-nitrophenol (4NP) in the presence of NaBH_4 [99]. Figure 4.40 shows the gold nanoparticles synthesized using polyaniline nanofibers as templates.

For nano- and mesoscale structures, the polymeric gel templating approach generally works well, provided that there is sufficient chemical and interfacial

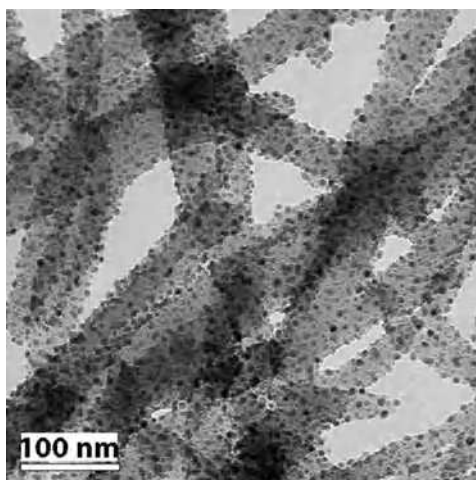


FIGURE 4.40 Transmission electron image of gold nanoparticles synthesized using polyaniline nanofibers as templates [99]. (Reprinted with permission from Han J, Li L, Guo R. Novel approach to controllable synthesis of gold nanoparticles supported on polyaniline nanofibers. *Macromolecules* 2010;43:10636–10644, Copyright 2010, American Chemical Society.)

complementarity between the organic and inorganic components. The hybrid structures can be subsequently transformed into inorganic monoliths with macroporous structures. This strategy is wide-ranging because the structure and composition of the polymer gel phase and the surface chemistry and nature of the inorganic nanoparticles can be systematically varied. The potential drawback is the irregularity of the pores formed.

4.6 THREE-DIMENSIONAL ASSEMBLY

Several approaches have been developed to precisely position nanoparticles into three-dimensional arrays either by directed assembly [100] or by layer-by-layer assembly [101, 102]. Even though the three-dimensional array can be fairly small in size [103, 104], the technique itself bears no limitation on dimensions if extended shaping time is given.

One possibility is based on the principle of depositing oppositely charged nanoparticles by electrostatic self-assembly onto an existing colloidal polymer template. The first step involves the deposition of a charged polymer layer onto colloidal particles. The charged polymer layer, which exhibits the opposite charge versus the particle surface, is added to the colloidal suspension and allowed to adsorb through electrostatic interactions. Subsequent exposure of the polymer-coated particles to oppositely charged nanoparticles results in the deposition of a new nanoparticle layer. Additional layers can be deposited by repeated deposition cycles, making use of the surface charge reversal that occurs upon adsorption of each nanoparticle layer, thereby producing colloidal core and multilayer shell assemblies. Calcination (a thermal treatment process applied to the assembled structures to bring about a thermal decomposition and removal of the volatile fraction) of the coated particles removes both the colloidal core and the bridging polymer, thereby producing hollow inorganic spheres. This is generalized as colloidal templating and self-assembly hybrid approach [105]. Colloidal templates of different composition and size (submicron or micron) can be employed. The multilayer shell structure produced can be only a couple of nanometers thin. An increase in the thickness of the multilayer shell on the colloidal nanoparticles creates single particle light scattering intensity shifts. Complete, unbroken SiO_2 hollow spheres, which preserve the original shape of the template, are obtained when the wall thickness consists of two or more SiO_2 layers, whereas both broken and unbroken hollow spheres are produced when the wall comprises a single SiO_2 layer. Even oxide-organic composite hollow spheres can be obtained by using a solvent that decomposes the templated core but leaves the polymer bridging the nanoparticles in the shell.

Controllable self-assembly of star-shaped PbS nanocrystals into both close-packed arrays and patterned arrays is demonstrated by evaporation-induced assembly routes [106]. First, large-area three-dimensional and two-dimensional hexagonal close-packed assemblies of PbS nanostars are obtained on a clean silicon substrate by drop coating and vertical deposition, respectively. Interestingly,

by using monolayer colloidal crystals and inverted monolayer colloidal crystals as the template, various nonclose-packed arrays of PbS nanostars with controllable patterns are fabricated through the vertical deposition method. Figure 4.41a shows PbS nanostars. Figure 4.41b shows that PbS nanostars self-assembled into films with a significant number of cracks after solvent evaporation. Figure 4.41c shows an enlarged scanning electron image of the obtained PbS assemblies, which suggests that the close-packed arrays exhibit hexagonal geometry in a large area, as indicated by the Fourier transform. As shown in Figure 4.41d, PbS nanostars self-assemble into hexagonal close-packed arrays with an average distance at ~ 60 nm. Considering the peculiar morphology of the six-horn stars, PbS nanoparticles tend to deposit with three horns standing on the lower layer of the substrate, and the horns of neighboring nanostars interdigitated to form assemblies with close packing. The oblique view in Figure 4.41e confirms the multilayer three-dimensional array of PbS nanostars. As expected from the hexagonal arrangement, each PbS monolayer is shifted by half of the inter-PbS distance with respect to the adjacent layers (Fig. 4.41f). With the 130 nm monolayer colloidal crystal template, a nonclose-packed array of PbS nanostars with three horns standing on the template is prepared, leading to the formation of novel star–sphere binary colloidal crystals with a stoichiometric star/sphere ratio of 1. A proper concentration of initial PbS dispersions and the peculiar shape of six-horn stars are crucial for the exclusive formation of the nonclose-packed array of PbS nanostars. With the 130 nm inverted monolayer colloidal crystal template, a nonclose-packed array of [001]-oriented PbS nanostars with a single horn stretched vertically upward is prepared. The circular gap size on the surface plane of the inverted monolayer colloidal crystal template (i.e., the proper SiO₂ filling height) is essential besides the peculiar six-horn star shape of PbS nanoparticles.

The patterns of the PbS nanostar arrays can be readily adjusted by using monolayer colloidal crystals with different sphere diameters as the template under otherwise identical conditions. For example, two monolayer colloidal crystal templates consisting of 340 nm PMMA spheres and 500 nm PS spheres are employed for the vertical deposition of PbS nanostars. Figure 4.42a shows the nonclose-packed array of PbS stars assembled in a lower PbS dispersion concentration (~ 0.75 mM) by using 340 nm spheres in the monolayer colloidal crystal template. Since the sphere diameter is larger than the critical diameter (~ 150 nm), one PbS nanostar occupies one interstitial site in the ordered monolayer colloidal crystal template layer, leading to a star-to-sphere number ratio of ~ 2 . However, it is noteworthy that the size matching between the triangle-shaped interstices of the monolayer colloidal crystals and the star-shaped particles decreases with increasing diameters for the polymer spheres, resulting in a significant deviation from the perfect binary star–sphere colloidal crystals with a star/sphere ratio of 2. If the PbS dispersion concentration is increased to ~ 1.5 mM, nanonet-like PbS nanostar arrays with a pore size of ~ 260 nm are assembled on the monolayer colloidal crystal template (Fig. 4.42b). In this case, PbS nanostars fill the gaps among the template layer with local ordered structure, leading to nanonet-like arrays with ordered, hexagonally packed circular pores that are inherited from the

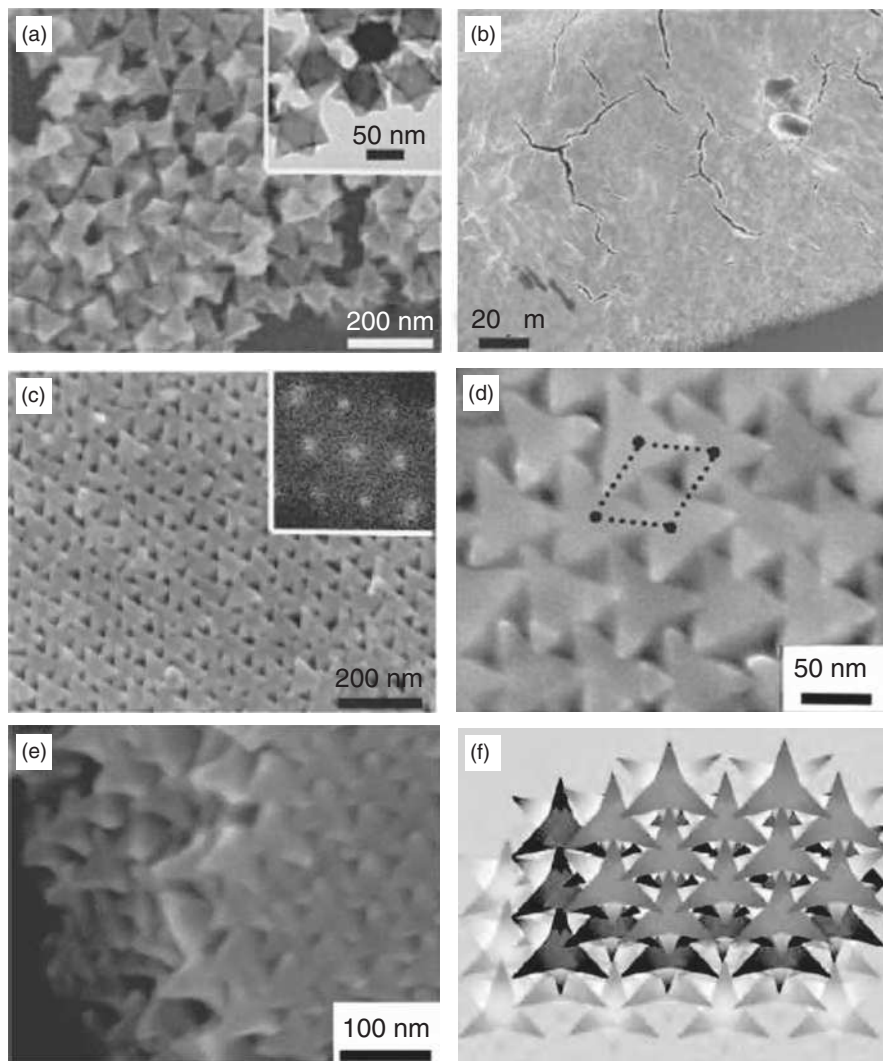


FIGURE 4.41 Scanning electron images of (a) PbS nanostars and (b–e) their three-dimensional hexagonal close-packed assemblies obtained by drop coating. (f) Schematic illustration of the three-dimensional hexagonal close-packed structures of six-horn stars. Inset in (a) is a transmission electron image of PbS nanostars, and the inset in (c) is the corresponding Fourier transform [106]. (Reprinted with permission from Huang T, Zhao Q, Xiao J, Qi L. Controllable self-assembly of PbS nanostars into ordered structures: close-packed arrays and patterned arrays. *ACS Nano* 2010;4:4707–4716, Copyright 2010, American Chemical Society.) (For a color version of this figure, see the color plate section.)

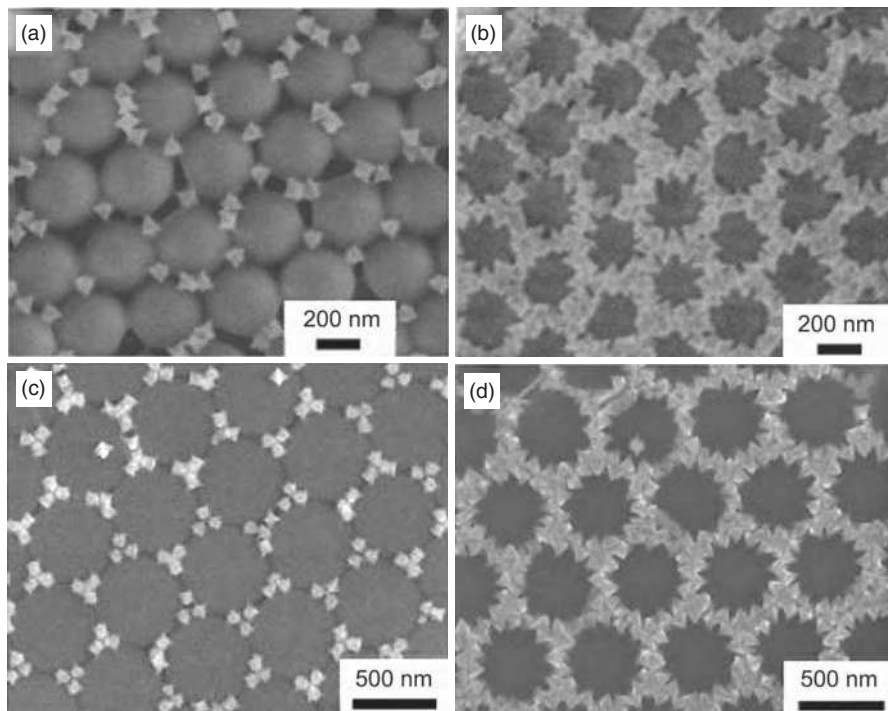


FIGURE 4.42 Scanning electron images of patterned arrays of PbS nanostars assembled on the 340 nm (a, b) and 500 nm (c, d) monolayer colloidal crystal templates with lower (a, c) and higher (b, d) packing densities by vertical deposition [106]. (Reprinted with permission from Huang T, Zhao Q, Xiao J, Qi L. Controllable self-assembly of PbS nanostars into ordered structures: close-packed arrays and patterned arrays. *ACS Nano*. 2010;4:4707–4716, Copyright 2010, American Chemical Society.)

original monolayer colloidal crystal templates. For the 500 nm monolayer colloidal crystal template, each interstitial site of the template can trap three to five PbS nanostars in an ordered arrangement under a lower PbS dispersion concentration (~ 1 mM), resulting in another novel pattern for the nonclose-packed PbS nanostar array, as demonstrated in Figure 4.42(c). Similarly, if the PbS dispersion concentration is increased to ~ 2 mM, nanonet-like PbS nanostar arrays with a pore size of ~ 390 nm are assembled on the monolayer colloidal crystal template (Fig. 4.42d). For the template-assisted assembly of PbS nanostars, almost all of the PbS nonclose-packed arrays inherit the long-range hexagonal order from the initial monolayer colloidal crystal template. The obtained PbS close-packed and patterned arrays may exhibit novel physical properties by virtue of the peculiar six-horn star shape of PbS nanocrystals as well as their well-defined locations and orientations. Potential applications include photoelectronic and photonic nanodevices. The assembly strategy described here shows a new route for the

controlled assembly of anisotropic nanoparticles into large-scale ordered arrays with desirable patterns.

Three-dimensional assembly is certainly an active field in nanoparticle materials research. It presents the ultimate opportunity to manipulate particle arrangement one layer at a time. Different species can arrange in a well-controlled manner and create unique structures and functions. The main drawback is the need for precise control of the species in the suspension and the time-consuming process required to build large dimension structures.

4.7 SUMMARY

Nanoparticle superstructures are essential for constructing ultrasensitive sensors, molecular electronics, high-density storage devices, high-throughput screening instruments, and drug delivery devices. The available templates have now expanded from the epitaxy type of solid substrates to self-assembled monolayers, nanolithographical patterns, mesoporous media, and various biological organisms. Rather than the strict dimensional match, these templates offer more flexibility through built-in molecular recognition or new confinement mechanisms. They can be very effective in inducing the desired morphology for nanoparticle assembly and superstructure construction.

In this chapter, the discussion is divided into three categories: top-down, bottom-up, and hybrid superstructure assemblies. The top-down processes include photolithography, electron beam lithography, and ion beam lithography. The bottom-up approaches rely on the fundamental interaction forces between nanoparticles, which can originate from nondirectional and directional interactions. For the former, this includes vdW forces, dipole moments, and electrostatic forces. For the latter, it includes covalent bonding and hydrogen bonding. In addition to the innate interactions between nanoparticles, special fields (such as an electric field) can be used to assemble nanoparticles into superstructures. In addition, capillary forces are effective in assembling nanoparticles at liquid–air boundaries. When the top-down and bottom-up processes are combined to assemble nanoparticles, the interaction can be from functionalized or nonfunctionalized surfaces. The biological world also provides a host array of templates for superstructure construction. They can be grouped into natural templates and synthetic templates. In addition, the template-directed assembly can expand into three dimensions.

QUESTIONS

1. Conventional photolithography technique cannot produce nanosize features. What approaches can be used to extend photolithography technique to nanosize feature creation? Give two approaches and explain how they work.
2. List three lithography techniques that you know; what are the differences in the lithographic sources?

3. What are the fundamental requirements on nanoparticle size for superstructure assembly?
4. What are the advantages and disadvantages relying on nondirectional particle interactions to assemble superstructures?
5. Can directional bonding produce densely packed superstructures? If so, why?
6. Give two examples of template-assisted superstructure construction process and explain what the applications are for the superstructures.

REFERENCES

1. Tian R, Zhi J. Gold-nanoparticles-induced pattern metallization on high-roughness diamond film surfaces. *Appl Phys Lett* 2006;88:203102 3pp.
2. Li J, Kamata K, Iyoda T. Tailored Ag nanoparticle array fabricated by block copolymer photolithography. *Thin Solid Films* 2008;516:2577–2581.
3. Porter LA Jr, Choi HC, Schmeltzer JM, Ribbe AE, Elliott LCC, Buriak JM. Electroless nanoparticle film deposition compatible with photolithography, microcontact printing, and dip-pen nanolithography patterning technologies. *Nano Lett* 2002;2:1369–1372.
4. Qhobosheane M, Zhang P, Tan W. Assembly of silica nanoparticles for two-dimensional nanomaterials. *J Nanosci Nanotechnol* 2004;4:635–640.
5. Li X, Tian Y, Xia P, Luo Y, Rui Q. Fabrication of TiO₂ and metal nanoparticle-microelectrode arrays by photolithography and site-selective photocatalytic deposition. *Anal Chem* 2009;81:8249–8255.
6. Kanta A, Sedev R, Ralston J. Fabrication of silica-on-titania and titania-on-silica nanoparticle assemblies. *Colloids Surf A* 2007;292:1–7.
7. Liu HJ, Sow CH, Ong CK. Fabrication of quasi-one-dimensional oxide nanoconstriction array via nanosphere lithography: A simple approach to nanopatterns of multicomponent oxides. *J Appl Phys* 2006;100:014306 3pp.
8. Haynes CL, McFarland AD, Smith MT, Hulteen JC, Van Duyne RP. Angle-resolved nanosphere lithography: manipulation of nanoparticle size, shape, and interparticle spacing. *J Phys Chem B* 2002;106:1898–1902.
9. Gadipalli RR, Martin LA, Heckman B, Story JG, Bertino MF, Fraundorf P, Guha S, Leventis N. Infrared quantum dot photolithography. *J Sol-Gel Sci Technol* 2006;40:101–107.
10. Bertino MF, Gadipalli RR, Martin LA, Story JG, Heckman B, Guha S, Leventis N. Patterning porous matrices and planar substrates with quantum dots. *J Sol-Gel Sci Technol* 2006;39:299–306.
11. Coskun UC, Mebrahtu H, Huang PB, Huang J, Sebba D, Biasco A, Makarovski A, Lazarides A, LaBean TH, Finkelstein G. Single-electron transistors made by chemical patterning of silicon dioxide substrates and selective deposition of gold nanoparticles. *Appl Phys Lett* 2008;93:123101 3pp.
12. Griffith S, Mondol M, Kong DS, Jacobson JM. Nanostructure fabrication by direct electron-beam writing of nanoparticles. *J Vac Sci Technol B* 2002;20:2768–2772.
13. Kawabata S, Naono Y, Taguchi Y, Huh SH, Nakajima A. Designable formation of metal nanoparticle array with the deposition of negatively charged nanoparticles. *Appl Surf Sci* 2007;253:6690–6696.
14. Contreras AM, Grunesa J, Yan X-M, Liddle A, Somorjai GA. Fabrication of 2-dimensional platinum nanocatalyst arrays by electron beam lithography: ethylene hydrogenation and CO-poisoning reaction studies. *Top Catal* 2006;39:123–129.

15. Plaza JL, Chen Y, Jacke S, Palmer RE. Nanoparticle arrays patterned by electron-beam writing: structure, composition, and electrical properties. *Langmuir* 2005;21:1556–1559.
16. Hogg CR, Majetich SA, Bain JA. Investigating pattern transfer in the small-gap regime using electron-beam stabilized nanoparticle array etch masks. *IEEE Trans Magn* 2010;46:2307–2310.
17. Alegret J, Rindzevicius T, Pakizeh T, Alaverdyan Y, Gunnarsson L, Kall M. Plasmonic properties of silver trimers with trigonal symmetry fabricated by electron-beam lithography. *J Phys Chem C* 2008;112:14313–14317.
18. Joo J, Moon S, Jacobson JM. Ultrafast patterning of nanoparticles by electrostatic lithography. *J Vac Sci Technol B* 2006;24:3205–3208.
19. Rastei MV, Colis S, Meckenstock R, Ersen O, Bucher JP. Pulsed electrodeposition and magnetism of two-dimensional assembly of controlled-size Co particles on Si substrates. *Surf Sci* 2006;600:2178–2183.
20. Guan YF, Pedraza AJ. Synthesis of aligned nanoparticles on laser-generated templates. *Nanotechnology* 2005;16:1612–1618.
21. Shahmoon A, Limon O, Girshevitz O, Fleger Y, Demir HV, Zalevsky Z. Tunable nano devices fabricated by controlled deposition of gold nanoparticles via focused ion beam. *Microelectron Eng* 2010;87:1363–1366.
22. Moran JL, Wheat PM, Posner JD. Submicron scale patterning in sintered silica colloidal crystal films using a focused ion beam. *Langmuir* 2008;24:10532–10536.
23. Rezaee A, Kathrena A, Aliganga A, Pavelkab LC, Mittler S. Control of the average spacing between aligned gold nanoparticles by varying the FIB dose. *Phys Chem Chem Phys* 2010;12:4104–4111.
24. Yang B, Lu N, Huang C, Qi D, Shi G, Xu H, Chen X, Dong B, Song W, Zhao B, Chi L. Electrochemical deposition of silver nanoparticle arrays with tunable density. *Langmuir* 2009;25:55–58.
25. Sattler K. Nanolithography using the scanning tunneling microscope. *Jpn J Appl Phys* 2003;42:4825–4829.
26. Shin C, Jeon I, Jeon S, Khim ZG. Single nanoparticle alignment by atomic force microscopy indentation. *Appl Phys Lett* 2009;94:163107 3pp.
27. Bishop KJM, Wilmer CE, Soh S, Grzybowski BA. Nanoscale forces and their uses in self-assembly. *Small* 2009;5:1600–1630.
28. Martinez CJ, Liu J, Rhodes SK, Luijten E, Weeks ER, Lewis JA. Interparticle interactions and direct imaging of colloidal phases assembled from microsphere-nanoparticle mixtures. *Langmuir* 2005;21:9978–9989.
29. Kotov NA, Meldrum FC, Wu C, Fendler JH. Monoparticulate layer and Langmuir-Blodgett-type multiparticulate layers of size-quantized cadmium sulfide clusters: a colloid-chemical approach to superlattice construction. *J Phys Chem* 1994;98:2735–2738.
30. Santhanam V, Andres RP. Microcontact printing of uniform nanoparticle arrays. *Nano Lett* 2004;4:41–44.
31. Lambert K, Capek RK, Bodnarchuk MI, Kovalenko MV, Van Thourhout D, Heiss W, Hens Z. Langmuir-Schaefer deposition of quantum dot multilayers. *Langmuir* 2010;26:7732–7736.
32. Lin XM, Jaeger HM, Sorensen CM, Klabunde KJ. Formation of long-range-ordered nanocrystal superlattices on silicon nitride substrates. *J Phys Chem B* 2001;105:3353–3357.
33. Coe S, Woo W, Bawendi M, Bulovic V. Electroluminescence from single monolayers of nanocrystals in molecular organic devices. *Nature* 2002;420:800–803.

34. Lambert K, Moreels I, Van Thourhout D, Hens Z. Quantum dot micropatterning on Si. *Langmuir* 2008;24:5961–5966.
35. Lim I-IS, Maye MM, Luo J, Zhong C-J. Kinetic and thermodynamic assessments of the mediator-template assembly of nanoparticles. *J Phys Chem B* 2005;109:2578–2583.
36. Harfenist SA, Wang ZL, Alvarez MM, Vezmar I, Whetten RL. Highly oriented molecular Ag nanocrystal arrays. *J Phys Chem* 1996;100:13904–13910.
37. Sau TK, Murphy CJ. Self-assembly patterns formed upon solvent evaporation of aqueous cetyltrimethylammonium bromide-coated gold nanoparticles of various shapes. *Langmuir* 2005;21:2923–2929.
38. Tang Z, Ozturk B, Wang Y, Kotov NA. Simple preparation strategy and one-dimensional energy transfer in CdTe nanoparticle chains. *J Phys Chem B* 2004;108:6927–6931.
39. Li J, Hong X, Li D, Zhao K, Wang L, Wang H, Du Z, Li J, Bai Y, Li T. Mixed ligand system of cysteine and thioglycolic acid assisting in the synthesis of highly luminescent water-soluble CdTe nanorods. *Chem Commun* 2004;1740–1741.
40. Tang ZY, Zhang ZL, Wang Y, Glotzer SC, Kotov NA. Self-assembly of CdTe nanocrystals into free-floating sheets. *Science* 2006;314:274–278.
41. Zheng L, Li S, Burke PJ. Self-assembled gold nanowires from nanoparticles: an electronic route towards DNA nanosensors. *Proc SPIE* 2004;5515:117–123.
42. Hilgendorff M, Tesche B, Giersig M. Creation of 3-D crystals from single cobalt nanoparticles in external magnetic fields. *Aust J Chem* 2001;54:497–501.
43. Tang Z, Kotov NA, Giersig M. Spontaneous organization of single CdTe nanoparticles into luminescent nanowires. *Science* 2002;297:237–240.
44. Tang Z, Ozturk B, Wang Y, Kotov NA. Simple preparation strategy and one-dimensional energy transfer in CdTe nanoparticle chains. *J Phys Chem B* 2004;108:6927–6931.
45. Tang Z, Wang Y, Sun K, Kotov NA. Spontaneous transformation of stabilizer-depleted binary semiconductor nanoparticles into selenium and tellurium nanowires. *Adv Mater* 2005;17:358–363.
46. Bae SS, Kim DK, Park JI, Cheon J, Jeon IC, Kim S. Monolayer assembly and striped architecture of Co nanoparticles on organic functionalized Si surfaces. *Appl Phys A* 2005;80:1305–1310.
47. Han L, Luo J, Kariuki NN, Maye MM, Jones VW, Zhong CJ. Novel interparticle spatial properties of hydrogen-bonding mediated nanoparticle assembly. *Chem Mater* 2003;15:29–37.
48. Wang L, Luo J, Schadt MJ, Zhong C-J. Thin film assemblies of molecularly-linked metal nanoparticles and multifunctional properties. *Langmuir* 2010;26:618–632.
49. Hao E, Lian T. Layer-by-layer assembly of CdSe nanoparticles based on hydrogen bonding. *Langmuir* 2000;16:7879–7881.
50. Jiang Y, Shen Y, Wu P. Self-assembly of multilayer films containing gold nanoparticles via hydrogen bonding. *J Colloid Interface Sci* 2008;319:398–405.
51. Giersig M, Mulvaney P. Preparation of ordered colloid monolayers by electrophoretic deposition. *Langmuir* 1993;9:3408–3412.
52. Lee SH, Liddell CM. Anisotropic magnetic colloids: a strategy to form complex structures using nonspherical building blocks. *Small* 2009;5:1957–1962.
53. Aizenberg J, Braun PV, Wiltzius P. Patterned colloidal deposition controlled by electrostatic and capillary forces. *Phys Rev Lett* 2000;84:2997–3000.
54. Chen KM, Jiang X, Kimerling LC, Hammond PT. Selective self-organization of colloids on patterned polyelectrolyte templates. *Langmuir* 2000;16:7825–7834.
55. Xia Y, Yin Y, Lu Y, McLellan J. Template-assisted self-assembly of spherical colloids into complex and controllable structures. *Adv Funct Mater* 2003;13:907–918.

56. Quin D, Xia Y, Xu B, Zhu YC, Whitesides GM. Fabrication of ordered two-dimensional arrays of micro- and nanoparticles using patterned self-assembled monolayers as templates. *Adv Mater* 1999;11:1433–1437.
57. Gu Z, Fujishima A, Sato O. Fabrication of high-quality opal films with controllable thickness. *Chem Mater* 2002;14:760–765.
58. Ye Y-H, Badilescu S, Truong V-V, Rochon P, Natasohn A. Self-assembly of colloidal spheres on patterned substrates. *Appl Phys Lett* 2001;79:872–873.
59. Nikoobakht B, Wang ZL, El-Sayed MA. Self-assembly of gold nanorods. *J Phys Chem B* 2000;104:8635–8640.
60. Liu S, Zhu T, Hu R, Liu Z. Evaporation-induced self-assembly of gold nanoparticles into a highly organized two-dimensional array. *Phys Chem Chem Phys* 2002;4:6059–6062.
61. Choi JH, Adams SM, Ragan R. Design of a versatile chemical assembly method for patterning colloidal nanoparticles. *Nanotechnol* 2009;20:065301 6pp.
62. Wang M-H, Li Y-J, Xie Z-X, Liu C, Yeung ES. Fabrication of large-scale one-dimensional Au nanochain and nanowire networks by interfacial self-assembly. *Mater Chem Phys* 2010;119:153–157.
63. Ye X, Chen J, Murray CB. Polymorphism in self-assembled AB₆ binary nanocrystal superlattices. *J Am Chem Soc* 2011;133:2613–2620.
64. Claridge SA, Castleman AW, Khanna SN, Murray CB, Sen A, Weiss PS. Cluster-assembled materials. *ACS Nano* 2009;3:244–255.
65. Dong A, Ye X, Chen J, Murray CB. Two-dimensional binary and ternary nanocrystal superlattices: the case of monolayers and bilayers. *Nano Lett* 2011;11:1804–1809.
66. Zhuang Z, Peng Q, Zhang B, Li Y. Controllable synthesis of Cu₂S nanocrystals and their assembly into a superlattice. *J Am Chem Soc* 2008;130:10482–10483.
67. Li X, Tian Y, Xia P, Luo Y, Rui Q. Fabrication of TiO₂ and metal nanoparticle-microelectrode arrays by photolithography and site-selective photocatalytic deposition. *Anal Chem* 2009;81:8249–8255.
68. He HX, Zhang H, Li QG, Zhu T, Li SFY, Liu ZF. Fabrication of designed architectures of Au nanoparticles on solid substrate with printed self-assembled monolayers as templates. *Langmuir* 2000;16:3846–3851.
69. Chou SY, Krauss PR, Renstrom PJ. Imprint lithography with 25-nanometer resolution. *Science* 1996;272:85–87.
70. Maury P, Escalante M, Reinhoudt DN, Huskens J. Directed assembly of nanoparticles onto polymer-imprinted or chemically patterned templates fabricated by nanoimprint lithography. *Adv Mater* 2005;17:2718–2723.
71. Kim WS, Jia L, Thomas EL. Hierarchically ordered topographic patterns via plasmonic mask photolithography. *Adv Mater* 2009;21:1921–1926.
72. Li JZ, Kamata K, Iyoda T. Tailored Ag nanoparticle array fabricated by block copolymer photolithography. *Thin Solid Films* 2008;516:2577–2581.
73. Lewis S, Wheeler-Jones R, Haynes V, Perks RM. High density self assembled nanoparticle film with temperature-controllable interparticle spacing for deep sub-wavelength nanolithography using localized surface plasmon modes on planar silver nanoparticle tunable grating. *Microelectron Eng* 2008;85:486–491.
74. Qhobosheane M, Zhang P, Tan WH. Assembly of silica nanoparticles for two-dimensional nanomaterials. *J Nanosci Nanotechnol* 2004;4:635–640.
75. Wahl R, Engelhardt H, Pompe W, Mertig M. Multivariate statistical analysis of two-dimensional metal cluster arrays grown in vitro on a bacterial surface layer. *Chem Mater* 2005;17:1887–1894.

76. Hou L, Gao F, Li N. T4 virus-based toolkit for the direct synthesis and 3D organization of metal quantum particles. *Chem Eur J* 2010;16:14397–14403.
77. Bhattacharya R, Patra CR, Wang S, Lu L, Yaszemski MJ, Mukhopadhyay D, Mukherjee P. Assembly of gold nanoparticles in a rod-like fashion using proteins as templates. *Adv Funct Mater* 2006;16:395–400.
78. Hoepfener S, Chi L, Fuchs H. Formation of Au₅₅ strands on a molecular template at the solid–liquid interface. *Nano Lett* 2, 459–463, 2002.
79. Hata K, Yoshida S, Fujita M, Yasuda S, Makimura T, Murakami K, Shigekawa H. Self-assembled monolayer as a template to deposit silicon nanoparticles fabricated by laser ablation. *J Phys Chem B* 2001;105:10842–10846.
80. Nakanishi T, Ohtani B, Uosaki K. Fabrication and characterization of CdS-nanoparticle mono- and multilayers on a self-assembled monolayer of alkanedithiols on gold. *J Phys Chem B* 1998;102:1571–1577.
81. Chan EWL, Yu L. Chemoselective immobilization of gold nanoparticles onto self-assembled monolayers. *Langmuir* 2002;18:311–313.
82. Peng Z, Qu X, Dong S. Immobilization of the nanoparticle monolayer onto self-assembled monolayers by combined sterically enhanced hydrophobic and electrophoretic forces. *Langmuir* 2004;20:5–10.
83. Gole A, Orendorff CJ, Murphy CJ. Immobilization of gold nanorods onto acid-terminated self-assembled monolayers via electrostatic interactions. *Langmuir* 2004;20:7117–7122.
84. Tang F-Q, Fudouzi H, Uchikoshi T, Sakka Y. Preparation of porous materials with controlled pore size and porosity. *J Eur Ceram Soc* 2004;24:341–344.
85. Holland BT, Blanford CF, Stein A. Synthesis of macroporous minerals with highly ordered three-dimensional arrays of spheroidal void. *Science* 1998;281:538–540.
86. Bamnolker H, Nitzan B, Gura S, Margel S. New solid and hollow, magnetic and non magnetic, organic-inorganic monodispersed hybrid microspheres: synthesis and characterization. *J Mater Sci Lett* 1997;16:1412–1415.
87. Jia Y, Duran C, Hotta Y, Sato K, Watari K. Macroporous ZrO₂ ceramics prepared from colloiddally stable nanoparticles building blocks and organic templates. *J Colloid Interface Sci* 2005;291:292–295.
88. Hotta Y, Alberius PCA, Bergstrom L. Coated polystyrene particles as templates for ordered macroporous silica structures with controlled wall thickness. *J Mater Chem* 2003;13:496–501.
89. Zhong ZY, Yin YD, Gates B, Xia YN. Preparation of mesoscale hollow spheres of TiO₂ and SnO₂ by templating against crystalline arrays of polystyrene beads. *Adv Mater* 2000;12:206–209.
90. Bourgeat-Lami E. Organic-inorganic nanostructured colloids. *J Nanosci Nanotechnol* 2002;2:1–24.
91. Hammond PT. Form and function in multilayer assembly: new applications at the nanoscale. *Adv Mater* 2004;16:1271–1293.
92. Wang DY, Salgueirino-Maceira V, Liz-Marzan LW, Caruso F. Gold-silica inverse opals by colloidal crystal templating. *Adv Mater* 2002;14:908–912.
93. Kulinowski KM, Jiang P, Vaswani H, Colvin VL. Porous metals from colloidal templates. *Adv Mater* 2000;12:833–838.
94. Yang PD, Deng T, Zhao DY, Feng PY, Pine D, Chemlka BF, Whitesides GM, Stucky GD. Hierarchically ordered oxides. *Science* 1998;282:2244–2246.
95. Lebeau B, Fowle CE, Mann S, Farcet C, Charleux B, Sanchez C. Synthesis of hierarchically ordered dye-functionalised mesoporous silica with macroporous architecture by dual templating. *J Mater Chem* 2000;10:2105–2108.

96. Wang Z, Stein A. Morphology control of carbon, silica, and carbon/silica nanocomposites: from 3D ordered macro-/mesoporous monoliths to shaped mesoporous particles. *Chem Mater* 2008;20:1029–1040.
97. Breulmann M, Davis SA, Mann S, Hentze H-P, Antonietti M. Polymer-gel templating of porous inorganic macro-structures using nanoparticle building blocks. *Adv Mater* 2000;12:502–507.
98. Yue BH, Yang J, Huang C-Y, Dave R, Pfeffer R. Synthesis of macroporous PMMA/silica nanocomposite monoliths in supercritical carbon dioxide. *Macromol Rapid Commun* 2005;26:1406–1411.
99. Han J, Li L, Guo R. Novel approach to controllable synthesis of gold nanoparticles supported on polyaniline nanofibers. *Macromolecules* 2010;43:10636–10644.
100. Chung H-J, Ohno K, Fukuda T, Composto RJ. Self-regulated structures in nanocomposites. *Nano Lett* 2005;5:1878–1882.
101. Tsuruoka T, Akamatsu K, Nawafune H. Synthesis, surface modification, and multilayer construction of mixed-monolayer-protected CdS nanoparticles. *Langmuir* 2004;20:11169–11174.
102. Hua F, Shi J, Lvov Y, Cui T. Patterning of layer-by-layer self-assembled multiple types of nanoparticle thin films by lithographic technique. *Nano Lett* 2002;2:1219–1222.
103. Hammond PT. Form and function in multilayer assembly: new applications at the nanoscale. *Adv Mater* 2004;16:1271–1293.
104. Davis SA, Breulmann M, Rhodes KH, Zhang BJ, Mann S. Template-directed assembly using nanoparticle building blocks: a nanotectonic approach to organized materials. *Chem Mater* 2001;13:3218–3226.
105. Caruso F. Hollow capsule processing through colloidal templating and self-assembly. *Chem Eur J* 2000;6:413–419.
106. Huang T, Zhao Q, Xiao J, Qi L. Controllable self-assembly of PbS nanostars into ordered structures: close-packed arrays and patterned arrays. *ACS Nano* 2010;4:4707–4716.

CHAPTER 5

NANOPARTICLE-BASED MATERIAL SHAPING

5.1 INTRODUCTION

With a thorough analysis of nanoparticle characteristics such as particle size, shape, and chemistry on hand, nanoparticles can be formed into a specific bulk shape for structural or functional uses. The nanoparticle shaping processes to be discussed in this chapter deal with particle collections in large quantities and often in random arrangements. As a matter of fact, this field has been well studied and practiced for micron and submicron particles. Extension of these processes into nanoparticle-based materials is a natural step. Some techniques require little processing change, while others require extensive retooling of the technique involved. Naturally, some techniques are newly developed and only suited for nanoparticle-based materials.

There are diverse requirements for the shaping/forming of nanoparticle-based materials. Some applications, such as structural components and electronic devices, require fully dense components, while other applications, such as sensors and catalysts, require porous nanostructures and large response areas. As a general guide, dense nanoparticle-based materials are used more often in the structural areas that require high strength or high hardness, or in functional areas that require a high dielectric constant, conductivity, or magnetism. On this front, dense nanoparticle-based materials have not progressed as fast as what was envisioned more than a decade ago [1]; many to-be-discussed techniques derived from conventional forming processes fall into this category, such as superhigh pressure compaction and tape casting. The hurdles mainly originate from the limitation

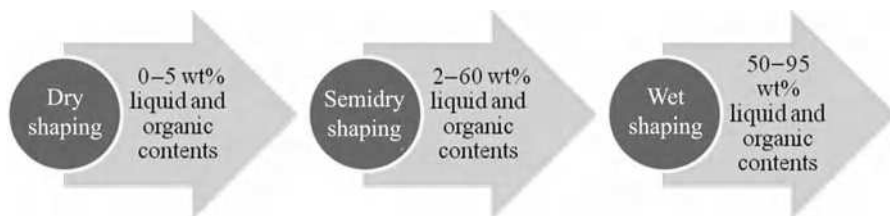


FIGURE 5.1 Different shaping techniques based on liquid and organic contents.

of the conventional techniques themselves. On the other front, active research in porous nanoparticle-based materials has produced an amazing array of new techniques. These approaches are often driven by functional needs such as catalysts, sensors, optics, separation technologies, or bio-related applications. These materials can be randomly porous or periodically porous nanoparticle-based materials.

In selecting a forming process, there are many factors to consider, such as the use of the material, the size of the component, and the fabrication cost. To obtain the desired density while maintaining nanostructures for the final components, nanoparticle packing at the shaping state must be well controlled. Among the well-developed shaping techniques are dry forming processes such as dynamic compaction, semidry processes such as molding and extrusion, and wet processes such as casting and electrophoretic deposition (Fig. 5.1). There is also a group of new techniques including digital processing and bio-derived processing. Since nanoparticles have very large specific surface areas, the most active research has been in the wet processing regime, starting with colloidal suspensions of various nanoparticles. In this section, we will examine various methods of forming nanoparticles into green shapes based on water content: dry, semidry, and wet. We will then discuss the extremely active areas of digital processing and bio-derived processing. For the well-developed forming processes such as dry forming and semidry forming, only the most recent developments will be highlighted. Interested readers are strongly encouraged to read some of the excellent books for more information [2–4]. Our intent here is to emphasize the forming processes that have extended into nanoparticle-based materials or have been developed solely for nanoparticle-based materials.

5.2 DRY FORMING TECHNIQUES

5.2.1 Uniaxial Compaction

Uniaxial compaction, also called dry compaction, is one of the simplest methods of forming nanoparticles into green compacts. Usually the water content of the nanoparticle system is low (<2 wt%). For simple geometries, a die is filled with nanoparticles and a pressure is applied, pushing the nanoparticles closer together

into a monolithic shape. Lubricants and binders may be added to facilitate particle packing and enhance green compact strength. As a general technique, the practice of uniaxial compaction can be traced back centuries ago. In modern days, the process has been advanced with automatic control and sensor feedback. This technique is most often used for ceramic nanoparticles and some metal nanoparticles. For polymer or semiconductor materials, the process is rarely used, mainly because other approaches are more economical or the applications never warrant a compaction step. For ceramic nanoparticles, the pressure applied onto the nanoparticles is generally not enough for particle deformation and densification is mostly achieved by particle rearrangement. For metal nanoparticles, this remains mostly true, which is different from the behavior of micron-sized metal particles. Although the externally applied pressure can be very high, it is mainly consumed to overcome the frictional forces among the particles and between the die and the particles. Even though fundamental nanoparticle interactions are not different from their micron or submicron counterparts (electrostatic force, van der Waals force, surface adsorption, or mechanical hindrance), the specific surface area and the particle–particle contact points of a nanoparticle collection can be orders of magnitude greater than those of the corresponding micron-sized particles. These characteristics present tremendous challenges for dry compaction. For example, TiO_2 powders of 5 μm and 20 nm can be used as a comparison based on idealized spherical shape. Particle–particle contact points are calculated based on 40% relative density using an empirical particle coordination number equation [5]:

$$N = 14 - 10.4(1 - \rho_{\text{rel}})^{2/5}, \quad (5.1)$$

where N is coordination number and ρ_{rel} is relative density. For 20 nm particles, there are 3.51×10^{17} contact points in 1 cm^3 . For 5 μm particles, there are 2.25×10^{10} contact points in 1 cm^3 . There are seven orders of magnitude of more particle–particle contact points for the 20 nm TiO_2 particles than for the 5 μm TiO_2 particles in each cubic centimeter. The increase in frictional force among nanoparticles is obvious.

When nanoparticle shapes are less regular than spherical and nanoparticle surfaces have various defects such as kinks, steps, adatoms, and broken bonds, the interparticle friction will drastically increase, hinder particle rearrangement during uniaxial compaction, and thus result in low compact density and inhomogeneous microstructures. One example is the dry compaction of 40 nm SnO_2 particles [6]. Only 55% green density is achieved at 500 MPa pressure. For species with higher hardness, the green density under the conventional uniaxial compaction pressure is even lower. For Al_2O_3 particles of 30 nm size, only about 53% green density is achieved at 200 MPa compaction pressure [7]. For B_4C particles of 100 nm size, only 46.5% density is achieved under 530 MPa compaction pressure. To make the situation worse, nanoparticles have a natural tendency of forming agglomerates, again because of the large specific surface area and the defective particle surfaces. These agglomerates, in turn, result in

poor compaction behaviors and various defects. Visible light translucency can be used as a gauge for pore size and microstructure homogeneity evaluation. When the sample is translucent, it means that large pores (micron level) have been removed and homogenous packing has been achieved.

To mitigate one of the key barriers of nanoparticle uniaxial compaction, interparticle frictional forces, one approach is to coat the core nanoparticles with a thin layer of a more compliant species. This method is very similar to the conventional use of lubricant(s) in uniaxial pressing; but the coating is much thinner, has better particle surface coverage, and can be a metallic element. Even though uniformly coating nanoparticles is not a trivial task, the potential benefit of using the low cost and fast uniaxial pressing process still makes the coating approach very enticing. This coating approach has been reported to improve the nano- Al_2O_3 consolidation process [8]. Also, graphite encapsulated metal nanoparticles have a very special core/shell spherical structure (5–100 nm in diameter). The shell consists of several to over 10 layers of graphitic sheets. A simple packing method using a magnetic field can achieve >90% density for the graphite encapsulated metal bulk composite without any mechanical load [9]. However, the coating layer thickness and uniformity must be carefully selected so that the compliant phase does not hinder sintering densification or targeted performance. One such undesirable example is SiO_2 – ZrO_2 composite. SiO_2 is coated onto ZrO_2 by heterogeneous growth, but the toughness of the composite is severely compromised due to the brittle nature of SiO_2 [10]. Another more common approach is to make ceramic or metal nanoparticle–polymer matrix or ceramic nanoparticle–metal matrix composites. The uniaxial compaction process can be effectively used to compact the nanoparticle reinforced polymer/metal matrix into high, if not full, density.

To date, uniaxial nanoparticle compaction has encountered almost insurmountable hurdles as discussed above. An additional issue that has not been mentioned is die filling. Dry nanoparticles have very poor packing behaviors, commonly labeled as “being fluffy.” Normally, loose nanoparticles have only about 5% packing density. To make a 50% dense compact, a die cavity space that is 10 times of the component size is needed for the to-be-formed component. This problem gets especially worse for large samples, and explains why the component size for nanoparticle uniaxial compaction is limited to the centimeter level. Nevertheless, nanoparticle material forming by uniaxial compaction has been and will continue to be experimented with in many research labs due to its simplicity and low cost. Also, uniaxial compaction of nanoparticles seems to retain some competitive edge when it comes to small size samples and simple shapes. This is because a higher compaction pressure is more achievable and the die filling problem can be correspondingly subdued.

5.2.2 Cold Isostatic Pressing

In cold isostatic pressing, a deformable and leakproof mold is filled with nanoparticles, lightly compacted, and then immersed in a hydraulic fluid and pressurized.

The approach involving total immersion of the sample in a fluid is called wet bag pressing. Alternatively, a rigid plug may be inserted into a suspended bag to yield a hollow shape. Since the bag is not totally immersed, the process is called dry bag pressing. In comparison to uniaxial compaction, which relies on direct pressure transfer between the rigid punch and the nanoparticles, the hydraulic fluid in cold isostatic pressing applies pressure uniformly on all the nanoparticle compact surfaces. Because of this enveloping pressure, higher packing density and more uniform microstructure are generally believed to be the advantages of the process. However, these expectations are based on the knowledge for micron or submicron particles and remain to be tested for nanoparticles. Up to now, they have not materialized. Recent work shows that cold isostatic pressing of ZrO_2 nanoparticles forms an exterior “skin” of higher but variable surface density at a compaction pressure as low as 276 MPa [11]. Four ZrO_2 nanopowders stabilized by 3 mol% Y_2O_3 are prepared by cold isostatic pressing at a pressure of 300–1000 MPa. The size of the pores in the green bodies and their evolution during sintering correlate with the characteristics of individual nanopowders. The powder with uniform particles of 10 nm size yields green bodies of required microstructures. Only homogeneous green bodies with pores of <10 nm can be sintered into dense bodies (>99% theoretical density) at a sufficiently low temperature to keep the grain sizes in the <100 nm range (Fig. 5.2) [12]. Although not always the case, typical cold isostatic pressing is limited to a pressure of ~550 MPa, and this low pressure seriously limits the ultimate density that can be achieved [13]. For example, cold isostatic pressing of $\text{ZrO}_2\text{-Fe}_2\text{O}_3$ nanocomposites results in a lower green density (49%) than dry compaction (60%) due to the lower pressure available (400 MPa vs. 1 GPa) [14]. Other researchers report similar findings for $\text{ZrO}_2\text{-Al}_2\text{O}_3$ nanocomposites [15]. It seems that cold isostatic pressing may serve as an intermediate refining step but not a self-sufficient

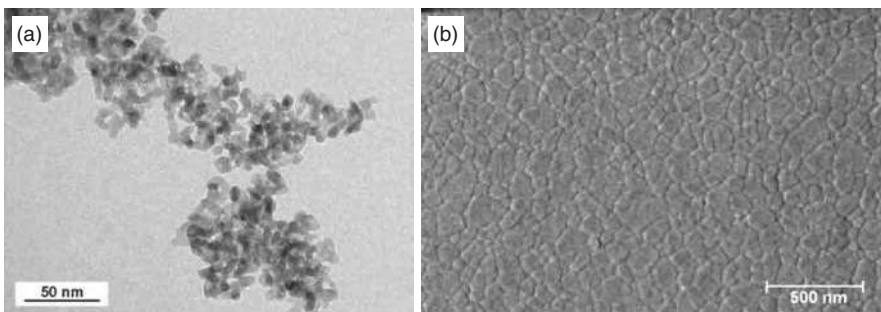


FIGURE 5.2 (a) Transmission electron micrograph of ZrO_2 powder synthesized by a sol-gel process. (b) Scanning electron micrograph showing the microstructure of ZrO_2 sample sintered at 1100°C for 4 hours. The forming process is carried out by cold isostatic pressing [12]. (Reprinted with permission from Trunc M, Maca K. Compaction and pressureless sintering of zirconia nanoparticles. *J Am Ceram Soc* 2007;90:2735–2740, John Wiley & Sons.)

step in improving nanoparticle packing. Inherently, cold isostatic pressing also requires more complex equipment than uniaxial pressing. To provide higher compaction pressure and thus achieve higher green density, researchers have moved away from uniaxial pressing and cold isostatic pressing into other more effective approaches such as superhigh pressure compaction.

5.2.3 Superhigh Pressure Compaction

Understandably, to overcome the extremely large surface frictional forces among nanoparticles, break the ever-present agglomerates, and achieve high green densities, a natural approach is to increase the compaction pressure and rate so that the highest compaction energy and momentum can be imparted to nanoparticles. These kinds of efforts can be categorized as superhigh pressure compaction, which was actively pursued at the beginning of nanoparticle-based bulk material research. Although the pressing equipment is often sophisticated and various safeguards need to be put in place, several different superhigh pressure forming techniques have emerged. Among these are conventional high-pressure compaction, shock wave compaction, dynamic compaction (drop weight, magnetic-impulse), explosive compaction, and combustion-driven compaction [16–23]. Most of these techniques can increase green densities to 60–75% range, which is a very desirable level for nanoparticles and comparable to the density of micron-sized particle-based materials that are achieved by conventional uniaxial pressing.

For the conventional high-pressure compaction, an isostatic pressure of ~ 3 GPa is used to form 3 mol% $\text{Y}_2\text{O}_3\text{-ZrO}_2$ nanoparticle compact. The formed compact has a relative density of $\sim 60\%$, which is 12% higher than that achieved by a typical cold isostatic compaction process with 450 MPa pressure [17]. At least 1 GPa pressure is needed for the ZrO_2 nanoparticles of 12 nm size to achieve $>55\%$ relative density. Similar efforts are also carried out for SnO_2 nanoparticles of 40 nm size at 4.5 GPa compaction pressure; 78% relative density has been achieved [6]. A diamond anvil cell is used to compact $\gamma\text{-Al}_2\text{O}_3$ nanoparticles of 20 nm size into a transparent component at 3 GPa [16, 24]. The green density of the $\gamma\text{-Al}_2\text{O}_3$ compact plays a critical role during sintering. For a compaction pressure <3 GPa, microstructures containing a significant amount of porosity develop at all temperatures studied due to the development of a highly porous or vermicular structure during the $\gamma \rightarrow \alpha$ phase transformation, occurring at temperatures between 1000°C and 1150°C . At >3 GPa compaction pressure, the development of a porous, vermicular structure during the $\gamma \rightarrow \alpha$ phase transformation can be entirely avoided, and a dense $\alpha\text{-Al}_2\text{O}_3$ sintered microstructure is achieved [16, 25]. Compacts of 15 nm SiO_2 and 13 nm Al_2O_3 are produced under nearly hydrostatic pressure up to 5.6 GPa in a toroidal-type apparatus. Over 90% densities are achieved for the $\gamma\text{-Al}_2\text{O}_3$ samples and over 80% densities are obtained for the SiO_2 samples, and the samples are crack free [26, 27]. For nanocrystalline $\text{Al}_{88}\text{Mm}_5\text{Ni}_5\text{Fe}_2$ alloy powder (where Mm denotes Mischmetal, which is a mixture of different lanthanides), compaction at even 7.7 GPa fails

to make an intact sample [28]. High-velocity compaction has been applied to titanium nanoparticles to form high-density metallic parts, whose densification is realized through the strong impact wave generated by the liquid pressure from a heavy hammer. This technology is believed to have a good balance between properties and cost, and can produce components with high and homogeneous green densities, low springback, and high precision. The maximum green density for the titanium ring-shape sample is 4.0 g cm^{-3} and the relative density is 88.9% at an impact energy of 3.804 kJ. However, for cylindrical samples, the maximum green density is 4.38 g cm^{-3} and the relative density is 97.4% at an impact energy of 1.217 kJ. For both kinds of samples, the green density increases with increasing impact energy but decreases with increasing filling weight. Impact energy per unit weight is helpful to characterize the green density obtained at different dimensions, impact energies, and filling weights [29].

Superhigh pressure compaction presents a promising outlook for overcoming the tremendous nanoparticle frictional forces and paving the path for nanoparticle forming by dry processes. The advantages of superhigh pressure compaction lie in high manufacturing efficiency and the potential for mainstream applications. However, superhigh pressure compaction cannot address the green sample inhomogeneity problem that is intrinsic to the dry forming process. Another potential problem with superhigh pressure compaction is cracking. When the compaction pressure is so high that it elastically deforms the nanoparticles, the nanoparticle compact will recover some of the strain instantaneously when the pressure is released, referred to as “springback.” Although the elastic contribution to the overall deformation may be small, springback forces can cause serious defects in the green samples. Also, most of these experiments are conducted using specialized equipment such as a high-pressure chamber or a diamond anvil press. These techniques are only suitable for making small, sometimes tiny samples. Samples with more than 1 cm diameter or height cannot be easily processed. By simply pushing the limit of existing die compaction presses, it is very difficult to achieve $>1 \text{ GPa}$ compaction pressure, making it unlikely that conventional high-pressure compaction will fulfill the needs of nanoparticle-based component dry state shaping. Because of these limitations, superhigh pressure compaction is not being as actively studied as before.

In shock wave compaction, high-velocity compressive waves are used to compact and sinter nanoparticles simultaneously [30]. As the shock waves travel through the particles, they compact and heat the nanoparticles simultaneously to overcome the interparticle friction; the pressure exerted by the shock waves may be as high as 11 GPa. Since the temperature and pressure are high, rapid densification takes place by plastic flow and frictional self-heating, which causes pressing and sinter bonding. Dense ceramic parts such as TiSi_2 and TiSi_5 with nanoparticles in the size range of 30–40 nm have been prepared by this process [31]. The kinetics of shock wave compaction is complex, and the parameters are not well defined. These often mean compaction variations and trial-and-error efforts must be undertaken for an unfamiliar material. Also, the heating is highly localized.

One advantage of shock wave compaction is that the process is effective in maintaining small grains and uniform microstructures; it is also extremely fast and offers high-density components. The disadvantages of shock wave compaction are that the tooling is very specialized and expensive. Although shock wave compaction seems to be able to maintain nanostructures during the consolidation process, it is very difficult to control the shock waves effectively. The process often creates microcracks in the produced samples [32].

5.2.4 Dynamic Compaction

A review is available on dynamic compaction [33]. For the process to be effective, the compaction process should move beyond the quasi-static state. This dictates that dynamic compaction is more efficient at higher green sample densities because shock wave propagation is proportional to sample density. High density leads to better wave propagation, causing the particles to move more closely and densify. For nanoparticle-based materials, however, this presents a challenge since the corresponding green density is generally low, poor packing of smaller particles causing high attenuation of the compressive stress waves. Most of the energy input in this case is used to overcome interparticle friction. In this case, thermal softening and interparticle melting may not occur. The effect of plastic deformation of the compact at high strain rates and the efficiency of high speed processing are compromised compared to micron-sized counterparts. Nonetheless, the high pressure benefits are still favored for the same nano-sized powder in achieving higher compact densities.

Compared to superhigh pressure compaction, the key difference for dynamic compaction is that the high pressure is applied to the nanoparticles in a dynamic, instead of quasi-static, fashion. There are two different types of dynamic compaction: explosive compaction and combustion-driven compaction.

Explosive compaction starts with nanoparticles enclosed in a thin-walled metal tube [22]. The tube is surrounded by an explosive. When the explosive is ignited, pressures >3 GPa can be generated. For TiN particles of 25 nm size, 80% density is achieved by explosive compaction. SnO₂ of 40 nm size is compacted under 4.5 GPa pressure to 79% relative density by a similar process [6]. Magnetic pulse compaction is applied to 3 mol% Y₂O₃ stabilized ZrO₂ (8 nm) and α -Fe₂O₃ (20–60 nm) composite with a peak pressure of 1 GPa and 60% green density is achieved [14]. The densities of the formed components are a strong function of the material properties. The harder the material is, the lower the density is. α -Al₂O₃ nanoparticle (100 nm) reinforced copper alloy is made by explosive compaction. Three levels of explosion pressure—2 GPa, 4 GPa, and 6 GPa—are used, and the results show that the density and hardness of the samples increase with an increase in the explosion pressure. The most suitable explosion pressure for Cu/ α -Al₂O₃ mixed powder is 4 GPa. Under this pressure, the sample relative density reaches 98.6% and hardness reaches 112 HV [34] (Fig. 5.3).

The shock-compaction responses of magnetic Fe₃O₄ nanopowders of ~ 12 nm and ~ 6 nm size and their bimodal mixture (~ 12 nm and ~ 6 nm powders in a

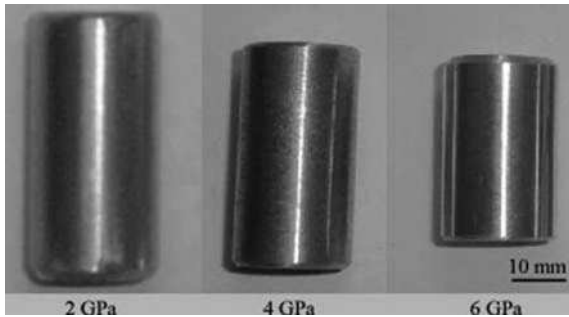


FIGURE 5.3 Cu/ α -Al₂O₃ bulk sample under three levels of explosion pressure [34]. (Reprinted with permission from Zhao Z, Li X-J, Tao G. Manufacturing nano-alumina particle-reinforced copper alloy by explosive compaction. *J Alloys Compd* 2009;478:237–239, Copyright 2009, Elsevier.) (For a color version of this figure, see the color plate section.)

4:1 ratio) are investigated to determine the densification behavior of nanoparticles at impact velocities of $\sim 800 \text{ m s}^{-1}$ and $\sim 1100 \text{ m s}^{-1}$. The maximal densification is $\sim 80\%$ for $\sim 12 \text{ nm}$ particles, $\sim 70\%$ for $\sim 6 \text{ nm}$ particles, and $\sim 75\%$ for the bimodal mixture particles. The compacts show the presence of a laminar structure with interlayer voids and microscopic gaps between nanoparticle agglomerates, which are responsible for the incomplete consolidation. Powder compaction occurs by the rapid deposition of the shock energy at interparticle regions. Heterogeneous plastic deformation of particles and the resultant localized heating and partial melting lead to interparticle fusion or even solid-state bonding. The rapid dissipation of heat from the surface to the interior of particles during shock compaction limits the growth of grains and inhibits the decomposition of metastable phases. It is much more difficult for nonmetallic or ceramic nanoparticles to achieve high density owing to their lower ductility and plasticity compared to metallic nanoparticles. Shock consolidation of ceramic nanoparticles is limited, and only partial densification is observed. In the above example, the Fe₃O₄ particle sizes grow from 6–12 nm to 10–25 nm, roughly twice that of the original sizes [35].

Different from explosive compaction, another dynamic compaction technique is combustion-driven compaction. Combustion-driven compaction employs a high compaction pressure generated from a combustion gas. The setup is simple and requires no specific field. Combustion gas (such as CH₄) is stored in a gas cylinder. During the process, the combustion gas is released into the gas chamber and mixed with air. The mixed gases are ignited and high-velocity compressive waves induce high pressures to form solid components. There are three stages for combustion-driven compaction: preload stage, compaction stage, and pressure release stage. During the preload stage, the combustion gas and air create a preload, pushing the upper ram down, precompacting the particles, and removing the entrapped air among the particles. During the compaction stage, an ignition stimulus is applied, causing combustion in the gas chamber and generating a high pressure

(1–3 GPa) within a fraction of a second; the increased pressure further compacts the particles to a high green state. During the pressure release stage, some spring-back gradually occurs to release compact internal stresses while avoiding cracks. The end result is a highly compacted component created in a couple of minutes. For B_4C nanoparticles of ~ 100 nm size, 60% density is achieved by combustion-driven compaction. Sm-Co and Fe mixture nanostructured magnets are prepared using combustion-driven compaction, which significantly reduces loss in coercivity. It is also possible to retain some degree of crystallographic alignment with this compaction process [36]. For combustion-driven compaction, the equipment has a small footprint and simple layout like a conventional compaction press. The whole system has only one moving part during the compaction process (the upper ram). The combustion pressure and stored elastic energy can be controlled and released slowly to avoid cracking. Similar to other superhigh pressure compaction techniques, one problem with combustion-driven compaction is die filling. The low packing density of nanoparticles requires a large die volume and presents challenges for thick samples.

In addition to the complications with nanoparticle compaction, hardness also increases for metal nanoparticles. Although the plasticity of metals can be beneficial during the compaction process, it can quickly disappear in the nanoparticle forming process due to strain hardening. Another issue is that the dry compaction process is mostly aimed at achieving fully dense end products after sintering. If the objective is to obtain porous nanoparticle-based materials, compaction, even in all its variations, often has very limited control over pore size, pore size distribution, and porosity. In light of these limitations, there is a predicament for simply applying high compaction pressure to nanoparticle-based materials. The requirements of uniform green microstructure and controlled porosity/pore size often make higher liquid content forming processes more effective.

5.3 SEMIDRY FORMING TECHNIQUES

Because of the excessive pressure demanded for nanoparticle-based material shaping by dry processes, the inhomogeneity that is intrinsic to dry nanoparticles, and the defects (voids, cracks) that can be easily created, semidry techniques are often preferred for certain nanoparticle-based material forming. The expectation is that the organic additives will alleviate the internanoparticle frictional force and produce more homogeneous microstructures. As an additional advantage, semidry processes can produce much more complicated shapes because of the added ability to change the mold geometries. Techniques used in the semidry shaping category include molding and extrusion. These processes are also called plastic forming methods because the deformation of a semirigid system containing nanoparticles, solvent, and organic binders is involved. The plastic phase content in the system is generally 40–60 vol% and mostly polymeric, especially when the nanoparticles involved have limited or no plasticity. Water may or may not be present depending on the system. Two requirements must be satisfied for

plastic forming to be successful: the mixture must flow plastically for the formation of the desired shape, and the shaped article must be strong enough to resist deformation under gravity or under stresses associated with handling.

5.3.1 Molding

Two types of processes can be discussed for nanoparticle-based molding: powder injection molding and micromolding.

5.3.1.1 Powder Injection Molding The most obvious trait of powder injection molding is its ability to produce parts of complex shapes with high precision and surface finish at relatively high production rates [37]. First, nanoparticles are mixed with a binder system (usually a mixture of polymers) to create a viscous feedstock. Then, parts are formed by injecting the powder/binder mixture into an impermeable mold, where the binder is solidified, usually by a temperature gradient. Comprehensive powder injection molding books have been published [2, 38]. Binders can be selected so that the mixture fills complex mold geometries without difficulty. A binder system normally consists of the following components: a major binder, a minor binder, a processing aid, a surfactant, and a lubricant. The major binder controls the rheology of the feeding material and provides strength to the green body. The minor binder facilitates the filling of the mold and, upon being removed, creates a network of pores through which the decomposition product of the major binder is removed more easily. The processing aid reduces the glass transition temperature of the thermoplastic binders. The surfactant improves the wetting between the particle surfaces and the polymer melt. The lubricant reduces the interparticle and mold-wall friction. When the binder freezes, the molded part is formed and ejected, and the injection molding process is complete.

ZrO₂ nanoparticle (12 nm and 35 nm sizes) toughened Al₂O₃ (180 nm size) is injection molded [39]. Proper selection of the molding parameters not only makes the injection molding feasible but also can refine the microstructure and lower the sintering temperature by 100–150 K. The samples can be sintered to full density by pressureless sintering; the Al₂O₃ grain size is decreased by a factor of 2–3.

Powder injection molding is an excellent forming technique for small and complex objects. The hydrostatic pressure associated with the process can minimize inhomogeneities in the molded parts. Even though the process is easily scalable to mass production, the high organic content makes this process less desirable for nanoparticle systems. In addition, particle packing is not enhanced during forming since powder injection molding introduces no further particle–particle approach within the organic matrix. Proper binder systems have to be designed to enable efficient packing of nanoparticles to start with. Binder removal must proceed at a slow rate (taking up to several days) to avoid problems with slumping and crack formation. Since binder removal time increases drastically with the size of the green body, it is difficult, if not impossible, to produce

parts with thick cross sections. Several factors can affect product quality for the nanoparticle injection molding process. The small size of nanoparticles is helpful for shape retention during binder removal because of more particle interlocking, but the viscosity of the mixture can be much higher. In addition, the interparticle spacing scales with particle size, so binder removal can be much slower for nanoparticles. A wide particle size distribution yields higher packing density and higher green strength. However, particle segregation is possible, which may result in nonuniform microstructures. The solid content of the feedstocks should be optimized within very narrow margins. Excessive binder can lead to problems during compounding. Too little binder can result in inhomogeneous and difficult to granulate feedstock and the formation of voids; it would also require very high pressure and temperature during the injection molding process.

Due to the stringent requirements in feedstocks, as well as the high technological needs to optimize injection molding parameters and mold design, injection molding is a sophisticated forming technique for nanoparticle-based materials. Currently, nanoparticle injection molding is not widely practiced, possibly because of the difficulty in obtaining high solids loading nanoparticle-binder mixture in the first place. In recent years, micromolding has greatly advanced. For small, complex, and detailed components, the use of nanoparticles becomes a must [40,41].

5.3.1.2 Micromolding Compared to powder injection molding, scaling down to microlevel opens a new arena for cost-effective production of microcomponents. One example application is the manufacture of cutting tools with sharp edges for machining. However, scaling down to such a level creates challenges in starting material preparation and molding. The requirements are far more stringent and necessitate additional precautions. Deagglomeration, optimization of solids loading versus flowability, molding profile, demolding, and debinding all need to be considered. Different from powder injection molding, micromolding uses spontaneous capillary-driven infiltration of liquid into channels of a flexible mold to make nanoparticle-based components. It is fundamentally related to soft lithographic molding discussed in Chapter 4 and has the potential for mass production.

Nearly dense (>98% of theoretical density) tensile bars and 3 mm microgears are produced using Y_2O_3 stabilized tetragonal ZrO_2 of 50 nm size. The sintered gear teeth are well defined and visually defect free. The microgear also yields the same Vickers hardness as the tensile bar [42]. Figure 5.4a shows the green and sintered tensile bars with the size relative to a paper clip. Figure 5.4b shows the microgear attached to a plastic base. For micromolding, however, even with good feedstock flow and complete mold filling, defects can be generated during demolding. The adhesive force between the feedstock and the microcavities can exceed the material strength, resulting in incomplete demolding. A proper mold should be used to ensure complete filling of the microfeatures and high green strength from molding. Aqueous and ethanol-based suspensions of TiO_2 nanoparticles are micromolded into polydimethylsiloxane (PDMS) molds. The

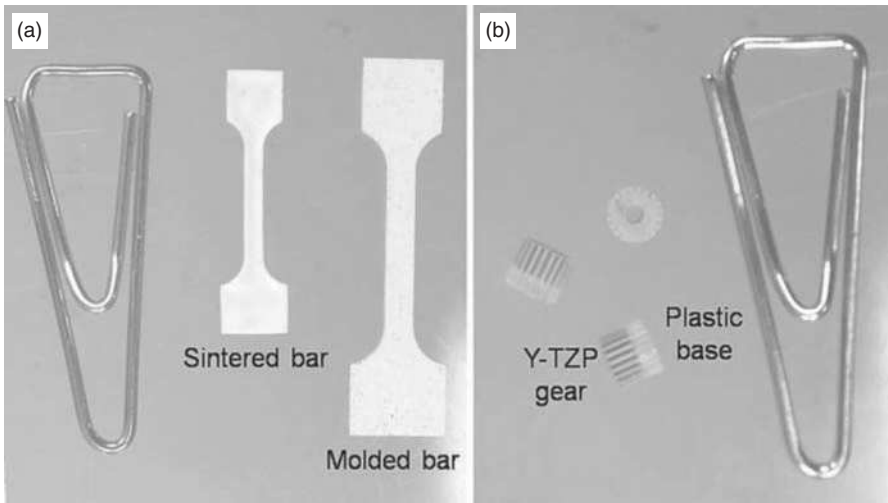


FIGURE 5.4 Photographs showing (a) green and sintered tensile bars and (b) green micro-gear with attached plastic gear base for ease of ejection. Specimen size is visually compared to a paper clip [42]. (Reprinted with permission from Yu PC, Li QF, Fuh JYH, Li T, Ho PW. Micro injection molding of micro gear using nano-sized zirconia powder. *Microsyst Technol* 2009;15:2009:401–406, Springer Science + Business Media, Fig. 5.)

particle size is about 20 nm and the solids loading is only 2 vol%. The mold channels have 23 μm width and 5.3 μm depth. To make uniform, thick films from low solids loading suspensions, the suspensions must spontaneously concentrate in the mold as a result of inflow of the suspensions from the entrance along with solvent evaporation from the exit of the mold. Therefore, suspension preparation is important. By comparing the uniformity of the fabricated samples and the particle distributions of the suspensions, it shows that the condition required for uniform patterning over a wide area is well-dispersed nanoparticles without any agglomerate formation [43].

A direct micromolding method for patterning gold nanoparticle structures using a PDMS stamp is reported. The method involves *in situ* synthesis of Au(I) dodecanethiolate, decomposition of Au(I) dodecanethiolate leads to gold nanoparticles in the microchannels of the stamp, and self-ordering of gold nanoparticles leads to the formation of patterned nanostructure stripes in conformity with the stamp geometry. Dodecanethiolate is made by reacting $\text{Au}(\text{PPh}_3)\text{Cl}$ and dodecanethiol *in situ* inside the microchannels by injecting first the former solution into toluene at room temperature followed by the thiol solution at 120°C. Annealing the reaction mixture at 250°C results in the formation of gold nanoparticles (with a mean diameter of 7.5 nm) and hexagonal ordering. When an external pressure is used during molding, parallel stripes with sub-100 nm widths are obtained (Fig. 5.5). The injection temperature and the concentrations of the thiol

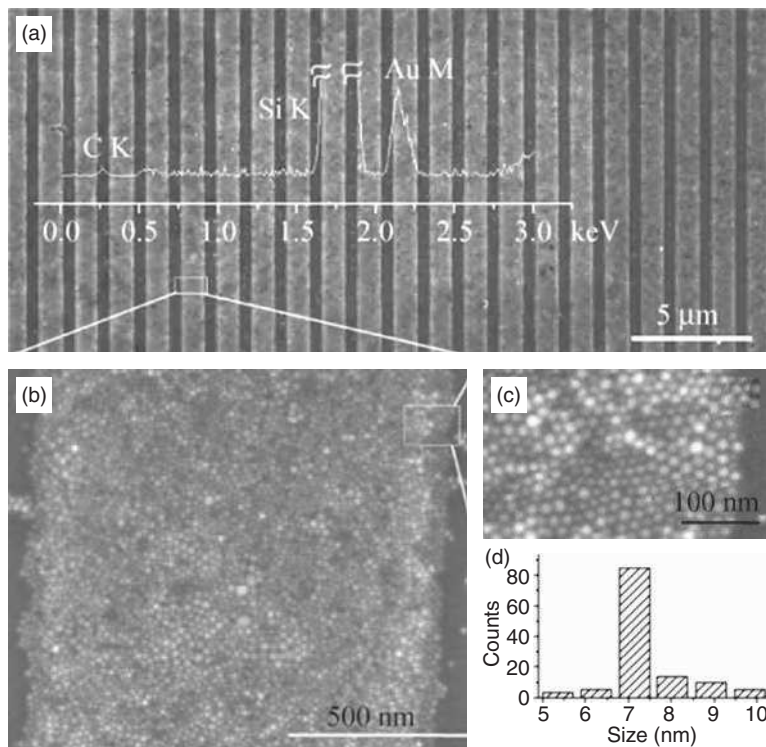


FIGURE 5.5 (a) Scanning electron image showing patterned gold nanoparticles formed by thermolysis at 250°C for 30 minutes with the energy dispersive spectroscopy data from the patterned region overlaid. Magnified views are shown in (b) and (c), and (d) shows a histogram the size of the gold nanoparticles from (c) [44]. (Reprinted with permission from Radha B, Kulkarni GU. Micro- and nanostripes of self-assembled Au nanocrystal superlattices by direct micromolding. *Nano Res* 2010;3:537–544, Springer Science + Business Media, Fig. 3.)

solution are important if an ordered structure is to be obtained. In addition, these parameters can be varied as a means to control the nanoparticle size [44].

Gold and platinum nanoparticles (> 100 nm size) and a molding process are used to fabricate two- and three-dimensional patternable structures with a height-to-width ratio up to 10:1. By means of this process, a neural stimulation circuit, including electrode, connection trace, and contact pad, is fused into one continuous, integrated structure where different sections have different heights, widths, and shapes. The approach involved is suitable for mass production, and the fabricated electrode is robust and flexible [45]. The molded structures exhibit excellent flexibility, robustness, and durability, and their conductivities are close to what is found in bulk materials. The molded structures can be released onto a thin, flexible, and biocompatible substrate. The molded gold and platinum electrodes outperform their sputtered thin-film counterparts in all aspects of electrochemical

properties: lower electrode impedance, higher charge storage capacity, and lower voltage excursion.

Since micromolding involves introducing an “ink” into defined microchannels and evaporating the solvent, it is considered more efficient and therefore has been widely employed in patterning a variety of materials. However, using micromolding methods to produce nanoparticle patterns is a challenging task. If one starts with a premade sol, the particle–particle and particle–mold surface interactions dictate the nanoparticle organization, which is usually discontinuous over larger areas. Cracks and defects are also problems that need to be addressed.

5.3.2 Extrusion

5.3.2.1 Microextrusion Extrusion is a desirable technique to produce components with complex and two-dimensional shapes but consistent cross sections. Example applications are catalyst supports, capacitor tubes, and microelectronic substrates. The feeding material is similar to that used in powder injection molding. The green body must have high particle loading and sufficient strength. The binder is generally selected from medium or high viscosity grade polymers, which can deform under a shear force at ambient temperatures. During extrusion, a nanoparticle–organic mixture is shaped by being forced through a nozzle in a piston extruder or a screw-fed extruder. The piston extruder consists of a barrel, a piston, and a die. A flow in which the velocity is independent of the radius of the tube is desirable, although a differential flow with a central plug is often encountered. In a screw-fed extruder, the screw mixes the nanoparticles and other additives into a homogeneous mass and pushes the mixture into the die. The screw must provide appropriate pressures for every section of the extruder. The flow pattern of the feeding material through the extruder affects the quality of the formed article.

Even though extrusion is best used for complex but consistent cross-sectional objects, the advancement of nanoparticle processing has enabled the realization of some very unconventional shapes. High strength (1270 MPa) and toughness ($>9 \text{ MPa m}^{1/2}$) Al_2O_3 ceramics (toughened by ZrO_2) with a helical spring shape are produced from sol-derived pastes comprising a mixture of 40 nm boehmite ($\gamma\text{-AlOOH}$) and 30 nm ZrO_2 particles [46]. Generally, components with a helical spring shape are considered to be the most difficult to produce because of the brittle nature of particle-based systems. The sol-derived $\gamma\text{-AlOOH}$ and ZrO_2 nanoparticles, however, are truly plastic in nature. The springs have no cracks after drying or even sintering at 1450°C for 4 hours. Other complicated shapes include ceramic tubes (a wall thickness of 2 mm and an external diameter of 8.0 mm) with tightly controlled bends from 50 nm $\gamma\text{-AlOOH}$ particles (Fig. 5.6) [47]. Extrusion is also used for the consolidation of metallic nanoparticles at room temperature. A load is applied to a particle-filled can in the inlet channel and the billet is deformed (consolidated) as it passes through the shear zone and is extruded from the horizontal channel. The process works at lower temperatures than hot isostatic pressing (see Chapter 6). A tensile strength as high as 800 MPa

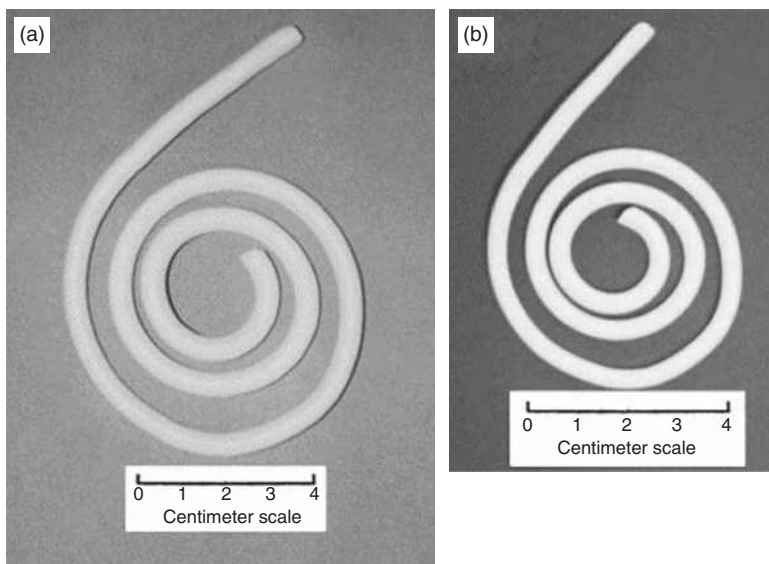


FIGURE 5.6 Photo images of boehmite (γ -AlOOH) tubes with a helical shape (γ -AlOOH has 50 nm particle size): (a) green structure after air drying for 1 day and (b) sintered microstructure after sintering at 1500°C for 2 hours [47]. (Reprinted with permission from Kaya C, Blackburn S. Extrusion of ceramic tubes with complex structures of nonuniform curvatures made from nano-powders. *J Eur Ceram Soc* 2004;243:3663–3670, Copyright 2004, Elsevier.)

and a tensile ductility as high as 7% are achieved for 100 nm size copper particle consolidates, which are >1.5 cm in diameter and 10 cm in length. Extrusion is also used to consolidate 316L stainless steel nanoparticles, resulting in bulk samples with 1180 MPa tensile strength and 4% ductility [48].

With improved control in the extrusion process, fine and textured microstructures can be produced by repeated coextrusion. The requirements for a successful coextrusion are rheological property match of the feeding materials and precise control of extrusion parameters. Kaya and Bulter reported the coextrusion of a two-phase 40 nm Al₂O₃/30 nm ZrO₂ material, which is then reextruded multiple times to reduce the widths of the phases and thus obtain an aligned biphasic structure down to 62.5 μ m [49]. First, the Al₂O₃ and ZrO₂ plastic mixture is coextruded in parallel. Then, the coextrudates are layed-up in close-packed linear array to form a heterogeneous macro-plug for subsequent extrusion. The first-stage reextrusion produces a filament of 1 mm size; the second-stage reextrusion produces a filament of 250 μ m size; and the third-stage reextrusion produces a filament of 62.5 μ m size.

Similar to the molding processes, high nanoparticle solids loading and a suitable combination of different binders are the prerequisites for successful extrusion. If the nanoparticle solids loading is low, the extruded component can be weak. The disadvantages of extrusion are possible separation of the liquid and

the solid phases of the mixture, poor knitting of the plastic mixture, and tearing around the component edge. Modifying the mold or increasing the plasticity of the mixture can improve the situation. Microscopic defects include pores caused by trapped air. The high binder content necessary for the process is expensive and sometimes difficult to be removed. Even though extrusion can be adapted to produce niche nanoparticle-based materials, the challenge is also tremendous for making a quantum leap in the nanoparticle material area. Overall, extrusion has not been a widely used technique for nanoparticle-based materials.

5.3.2.2 Electrospinning A variation in extrusion is to use an electric field to spin polymeric solutions out of an orifice and form nanoparticle-based or nanoparticle-containing wires, fibers, and filaments. This process is well known in the polymer community as electrospinning. An illustration of a general electrospinning setup is shown in Figure 5.7 [50]. In this technique, fibers are extruded from a polymer solution using electrostatic forces; the fibers are often collected as mats. Via carefully selected solvents, polymer(s) and metal precursors can form a homogeneous mixture solution, which can be electrospun to form composite nanofibers. The use of nanoparticle-based materials is a recent development. The fiber diameter is mostly in the range of hundreds of nanometers to microns, even though diameters down to tens of nanometers and lengths up to several centimeters have been demonstrated. Although electrospinning has been used mainly for the fabrication of polymeric nanofibers, nanofibers incorporated with metal nanoparticles and oxide nanoparticles have also received considerable interest because of their potential applications in areas including photovoltaic devices,

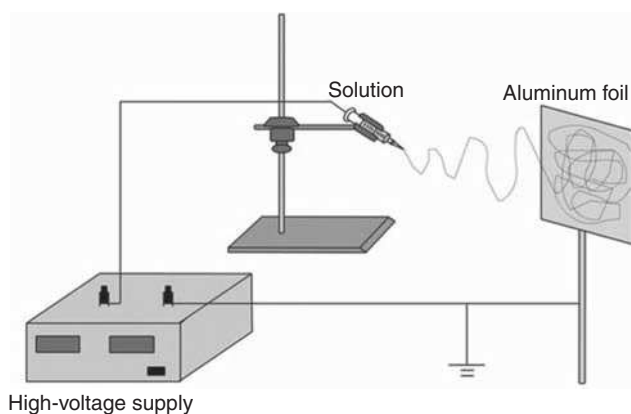


FIGURE 5.7 Illustration of the basic setup for electrospinning [50]. (Reprinted with permission from Fan H-T, Xu X-J, Ma X-K, Zhang T. Preparation of LaFeO_3 nanofibers by electrospinning for gas sensors with fast response and recovery. *Nanotechnology* 2011;22:115502, 7pp, 2011, IOP Publishing Ltd.)

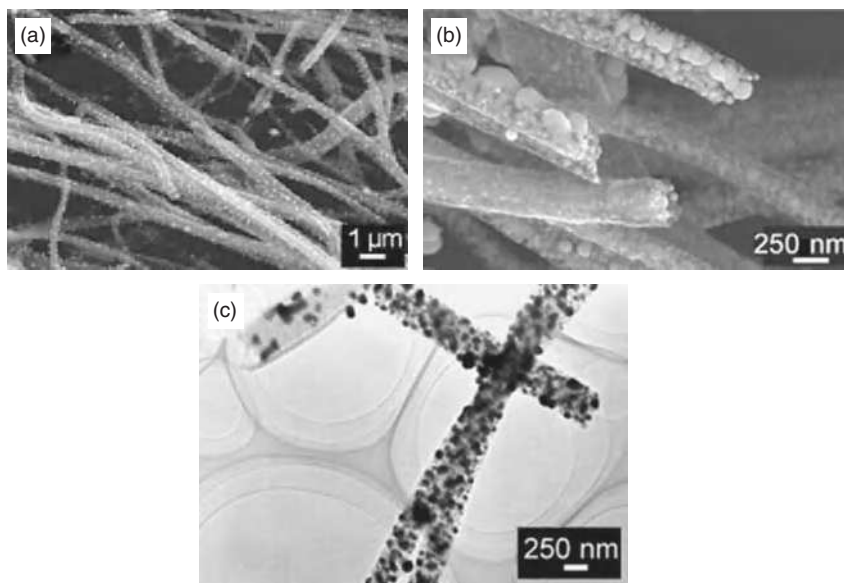


FIGURE 5.8 (a) Scanning electron image of Pd/carbon nanofiber nanocomposites, (b) high-magnification scanning electron image of Pd/carbon nanofiber nanocomposites, and (c) transmission electron image of Pd/carbon nanofiber nanocomposites [51]. (Reprinted with permission from Huang J, Wang D, Hou H, You T. Electrospun palladium nanoparticle-loaded carbon nanofibers and their electrocatalytic activities towards hydrogen peroxide and NADH. *Adv Funct Mater* 2008;18:441–448, John Wiley & Sons.)

piezoelectric materials, gas sensors, and solar cells. Metal precursors in the electrospun composite nanofibers can also convert to metal nanoparticles by UV irradiation or hydrolysis treatment.

Palladium nanoparticle-loaded carbon nanofibers are synthesized by electrospinning and thermal treatment [51]. Spherical palladium nanoparticles are well dispersed on the surfaces of carbon nanofibers or embedded in carbon nanofibers. A cubic palladium phase forms during the reduction and carbonization processes, and the presence of palladium nanoparticles promotes the graphitization of carbon nanofibers. Figure 5.8a shows that the as-prepared carbon nanofibers have a diameter ranging from 200 to 500 nm with tens of micrometers in length. Figure 5.8b shows the presence of palladium on the surface and inside of the carbon nanofibers. Figure 5.8c shows that spherical palladium nanoparticles with a mean diameter of about 73 nm are well-dispersed in the carbon nanofibers.

Metal oxide nanofibers are prepared by electrospinning a metal salt precursor solution in the presence of a proper polymer, followed by calcination to decompose the polymer completely and turn the metal salt into metal oxide. Anatase TiO_2 nanofibers are fabricated directly by electrospinning and sol-gel techniques. The polymeric nature of the sol enables the electrospinning process

[52]. ZnO nanofibers and nanoparticles are made through electrospinning of zinc acetate/cellulose acetate precursor solution in N,N-dimethylformamide/acetone mixed solvent. Depending on the calcination of the precursor zinc acetate/cellulose acetate composite nanofibers, the mean diameters of the ZnO nanofibers and nanoparticles are ~ 78 and 30 nm, respectively [53]. LaFeO₃ nanofibers are also successfully prepared by the electrospinning method. The fibers have a cubic crystal structure. After calcination at 600°C for 3 hours, the diameters of the nanofibers are about 80–90 nm and their surfaces are smooth. The response–recovery properties of the LaFeO₃ nanofiber sensor to ethanol are better than those of the LaFeO₃ nanobelt or nanoparticle sensor [50]. Figure 5.9 shows electron images of the LaFeO₃ nanobelts and LaFeO₃ nanoparticles. As shown in Figure 5.9a, there is no obvious difference in the overall morphologies of the La(NO₃)₃/Fe(NO₃)₃/PVP composite nanobelts. The surfaces are smooth with a width of 1–3 μm and a uniform thickness of 200 nm. Figure 5.9b shows that the widths of the nanobelts become smaller after calcination, ranging from 500 nm to 1 μm . Figure 5.9c shows that the sizes of the LaFeO₃ nanoparticles prepared by the sol–gel method are about 30 nm; agglomeration is also observed in the sample.

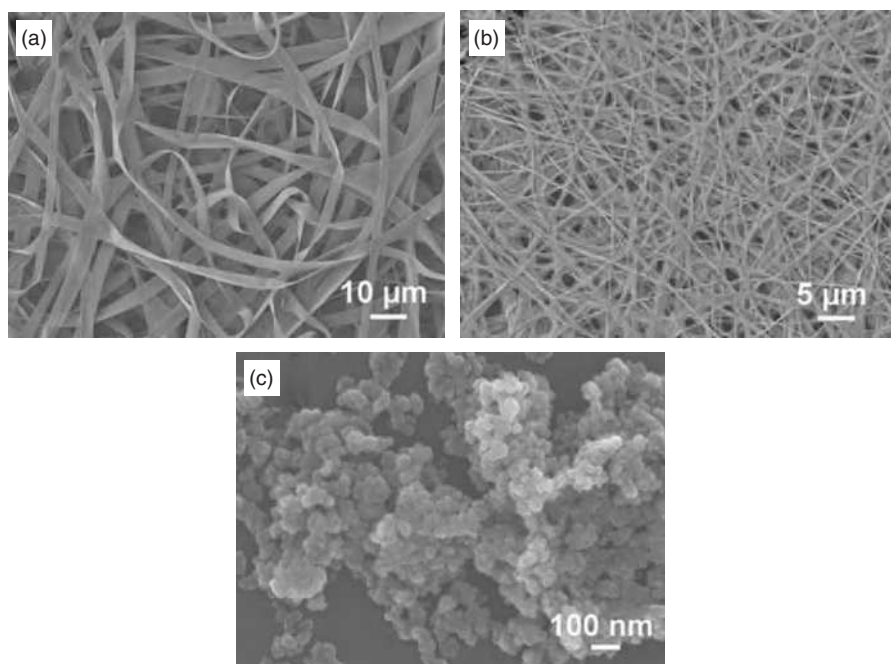


FIGURE 5.9 (a) Scanning electron image of La(NO₃)₃/Fe(NO₃)₃/PVP composite nanobelts, (b) scanning electron image of LaFeO₃ nanobelts calcined at 600°C, and (c) scanning electron image of LaFeO₃ nanoparticles [50]. (Reprinted with permission from Fan H-T, Xu X-J, Ma X-K, Zhang T. Preparation of LaFeO₃ nanofibers by electrospinning for gas sensors with fast response and recovery. *Nanotechnology* 2011;22: 115502, 7pp, IOP Publishing Ltd.)

A hybrid method that integrates the processing capabilities of the twin-screw extrusion process (conveying solids, melting, mixing, pressurization, temperature profiling, devolatilization) with electrospinning is developed. The hybrid process is especially suited to the dispersion of nanoparticles into polymeric binders and the generation of nanoparticle-incorporated nanofibers. This is demonstrated by the dispersion of β -tricalcium phosphate ($\text{Ca}_3(\text{PO}_4)_2$) nanoparticles into poly(ϵ -caprolactone ($\text{C}_6\text{H}_{10}\text{O}_2$)) to generate biodegradable nonwoven meshes that can act as scaffolds for tissue engineering applications [54]. Carboxymethylcellulose, water, and Al_2O_3 nanoparticle gels are extruded; the twin-screw extrusion process generates more homogeneous mixtures of nanoparticles than intensive batch mixing technique, and the use of surfactants further improves the homogeneity. With increasing homogeneity, the suspension exhibits lower elasticity and shear viscosity [55].

5.4 WET FORMING TECHNIQUES

As discussed in the dry forming section, the excessive surface area intrinsic to nanoparticles serves as one of the most striking advantages and disadvantages for nanoparticle-based bulk material forming. Because of the natural tendency of nanoparticles to form agglomerates and poor packing behaviors at dry state, wet forming has become the most active research area. For almost all the nanoparticle-based wet forming processes, the first step is to produce a stable suspension, known as a colloid. Colloidal stabilization of nanoparticle-based systems is generally achieved through three mechanisms: electrostatic stabilization, steric stabilization, and electrosteric stabilization. Also, most of the systems involve inert materials such as oxide nanoparticles; metal and semiconductor nanoparticles are less commonly used. With a stable nanoparticle suspension, a spectrum of wet forming processes can be utilized to produce uniform nanostructures. The shaping techniques include pressure casting, tape casting, freeze casting, gel casting, and electrophoretic deposition.

5.4.1 Colloidal Suspension

Since most of the colloidal processing of nanoparticles is for oxides, the Derjaguin–Landau–Verwey–Overbeek theory (DLVO theory) continues to provide the fundamental basis for understanding nanoparticle interactions and comparing the relative effect of interparticle attraction and repulsion. Most nanoparticles exhibit a net electrodynamic attraction to one another due to oscillating dipoles when dispersed in a polar solvent such as water, commonly referred to as van der Waals forces. A net surface charge thus results. With a change in the pH or electrolyte of the suspension, the nanoparticle surface charge can change sign. For example, Al_2O_3 has positive net surface charge at low pH and negative surface charge at high pH with the isoelectric point at 8.7 in pure H_2O [56, 57]. When the pH of the suspension is adjusted with the aim of

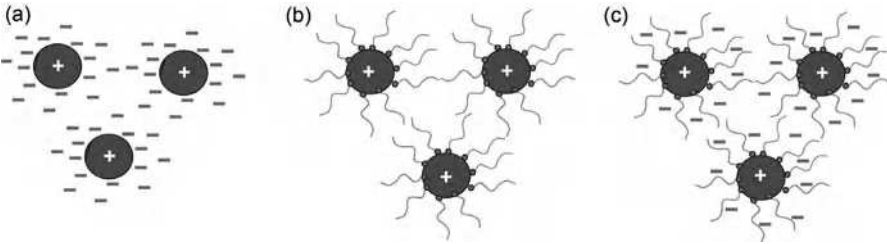


FIGURE 5.10 Different mechanisms of nanoparticle interaction and stabilization: (a) electrostatic stabilization, (b) steric stabilization, and (c) electrosteric stabilization. (For a color version of this figure, see the color plate section.)

modifying the nanoparticle surface charge and thus the interparticle interactions, the stabilization mechanism is called electrostatic stabilization (Fig. 5.10a). Also, polyelectrolytes (polymeric species with functional groups) can be introduced into colloidal systems. If the suspension is properly tailored, one end of the polymer species adsorbs onto the particles and the other end of the polymer species extends into the liquid, causing the particles to physically repel one another; this interaction can stabilize the nanoparticle suspension by steric stabilization (Fig. 5.10b). If the adsorbed polymer is ionic, it generates strong electrostatic forces while polymer chains repel one another [58]; this method of colloidal stabilization is called electrosteric stabilization (Fig. 5.10c) [59].

For most inorganic nanoparticles (metal, ceramic, and semiconductor), a stern and a Helmholtz double-layer configuration forms around a particle surface when dispersed in a polar solvent (mostly water) because of surface hydrolyzation. This attribute lays the foundation for colloidal particle stabilization in suspensions by electrostatic repulsion in order to counter the van der Waals attraction that is always present. The DLVO theory, which involves van der Waals attractive forces and electrostatic interactions from the electrical double layer, is one of the basic tools to evaluate the potential barrier between particles in aqueous media. The DLVO interaction potential between particles, $U_{DLVO}(r)$, can be expressed as [60]

$$U_{DLVO}(r_{a-a}) = \frac{Z_1^* Z_2^* e^2}{\epsilon_m} \left(\frac{e^{ka_1}}{1 + ka_1} \right) \left(\frac{e^{ka_2}}{1 + ka_2} \right) \frac{e^{-kT}}{r_{a-a}}, \quad (5.2)$$

where Z_1^* and Z_2^* are the charges on two particles of radius a_1 and a_2 , e is the electronic charge, ϵ is the static dielectric constant of the medium, and r_{a-a} is the interparticle separation distance. The Debye length, $1/\kappa$, is given by

$$\frac{1}{\kappa} = \sqrt{\frac{4\pi e^2}{\epsilon_m kT} (n_p Z^* + n_i)}, \quad (5.3)$$

where k is Boltzmann's constant, n_p is the particle number density, and n_i is the ionic concentration. The force between particles, neglecting all but nearest neighbor interactions, from the derivative of the DLVO potential with respect to interparticle distance r_{a-a} is

$$F(r_{a-a}) = \frac{-Z_1^*e \cdot Z_2^*e}{\epsilon_m} \left(\frac{e^{ka_1}}{1 + ka_1} \right) \left(\frac{e^{ka_2}}{1 + ka_2} \right) \left(\frac{1 + kr_{a-a}}{r_{a-a}^2} \right) e^{-kr_{a-a}}. \quad (5.4)$$

Based on Equation (5.4), the attractive force can be modulated by adjusting the particle size, particle number density in the suspension, ion concentration, and dispersion medium dielectric constant.

Nanoparticle interactions can be modified by increasing the magnitude of the repulsion between nanoparticles through lowering the ionic strength of the suspension. In the case of submicron sized particles, this is relatively easy to do by adjusting the electrical double layer, which can be tuned by the surface potential of particles and the counter ion concentration. However, in the case of nanoparticles, this is difficult to achieve only by the DLVO interactions because of the small potential barriers between nanoparticles. This can be understood by examining a hypothetical particle suspension with 1.0 mM counter ion concentration. Based on theoretical calculation, when the particle size and the surface potential are 100 and 88.5 mV, respectively, a large normalized potential barrier (total potential normalized by kT) of $U_{DLVO}(r_{a-a})/kT > 30$ is calculated. This $U_{DLVO}(r_{a-a})/kT$ value is large enough to prevent the particles from flocculating. On the contrary, when the particle size is reduced to 30 nm with the same surface potential value, the normalized potential barrier reduces to $U_{DLVO}(r_{a-a})/kT < 10$. In this condition, the particles will flocculate. In order to obtain a large potential barrier, such as $U_{DLVO}(r_{a-a})/kT > 30$, for 30 nm nanoparticles, it is necessary to increase the surface potential up to 177 mV [61].

From a different perspective, the adsorption of polymers onto nanoparticle surfaces is a strong function of particle surface charge and polymer chain length [56, 58, 62, 63]. As particle size decreases to nanoscale, polymer chain length needs to be substantially decreased. Long chains take up volumes that are needed for nanoparticle dispersion and cause undesirable chain entanglement. This can even lead to the need for smaller-sized organic molecules instead of polymers.

The way a polymer adsorbs onto a particle surface depends on the chemical nature of the polymer chain, the nature of the particle surface, and the dispersing medium. Polymers typically adsorb at random points along their backbones, rarely do they collapse onto the particle surface by sacrificing entropy in the transition from three to two dimensions. Instead, the adsorbed chain consists of a collection of trains, loops, and tails. The interaction between particles and polymer chains has been described considering both electrostatic and steric effects. Besides the van der Waals and electrostatic interactions between the particles, steric stabilization should still be present. Both mixing and steric repulsion energies can be involved. If the adsorbed layer thickness is L_A , there is no steric

interaction between the two particles when the particle center-to-center distance h is $> 2L_A$. For the interactions between the adsorbed organics in the region $L_A < h < 2L_A$, the mixing interaction energy $E_{\text{mix}}(h)$ is [64, 65]

$$E_{\text{mix}}(h) = \frac{32\pi kTa}{5\nu} \frac{V_f^2}{L_A^4} \left(\frac{1}{2} - \chi\right) \left(L_A - \frac{h}{2}\right)^6, \quad (5.5)$$

where V_f is the average volume fraction of polymeric molecules in the adsorbed layer, ν_m is the molecular volume of the dispersing medium, and χ is the Flory–Huggins parameter. At small particle–particle separation ($h < L_A$), polymer segment density can be assumed to be uniform, and the contributions from the elastic and mixing interactions are given by

$$E_{\text{mix}}(h) = \frac{4\pi akTL_A^2}{\nu} V_f^2 \left(\frac{1}{2} - \chi\right) \left(\frac{h}{2L_A} - \frac{1}{4} - \ln \frac{h}{L_A}\right) \quad (5.6)$$

$$E_{\text{elastic}}(h) = \frac{2\pi akTL_A^2 \rho}{M_w} V_f^2 \left\{ \frac{h}{L_A} \ln \left[\frac{h}{L_A} \left(\frac{3 - h/L_A}{2}\right)^2 \right] - 6 \ln \left(\frac{3 - h/L_A}{2}\right) + 3(1 - h/L_A) \right\}, \quad (5.7)$$

where $E_{\text{elastic}}(h)$ is the elastic interaction energy, ρ is the density of the polymer, and M_w is the molecular weight of the polymer species [65]. The only factor that substantially affects the steric interaction energy is the adsorbed polymer layer thickness L_A , which is directly determined by the size of the adsorbed polymer species.

Even though it is desirable to use only the electrostatic stabilization mechanism to create stable nanoparticle suspensions, this is not always feasible. When polyelectrolytes are used to stabilize suspensions, a delicate balance must be maintained in the relative amount of the nanoparticles and the dispersant in the system. The adsorbed polymer must have a thick enough layer on the nanoparticle surface to prevent particle–particle close contacts and counteract the van der Waals attractive forces between particles. This means that there must be enough polymer present to provide good coverage of the nanoparticles. Insufficient coverage will cause polymer chains to “bridge” the gap between particles, resulting in bridging flocculation [66]. However, as the adsorption of the polymer dispersant increases, the attraction between the free polymer chains and the nanoparticles also decreases. This results in a barrier for further dispersant adsorption. A suitable amount of excessive dispersant is needed to attain

saturation adsorption. If the dispersant amount is increased further, the non-adsorbed free polymer will flocculate the suspension; this is known as depletion flocculation [67]. The amount of the adsorbed polymer needed to attain nanoparticle surface saturation and stable dispersion is dependent on the particle size, the polymer dispersant, the nanoparticle solids loading, and the pH of the system. For example, the saturation level of sodium poly(methacrylic acid) in submicron Al_2O_3 suspension decreases by a factor of 2 when pH is increased from 8.2 to 9.8 [58].

The high excluded volume around nanoparticles originating from the electric double layer or polymer layer adsorbed onto the surface to prevent agglomeration often results in very high viscosity suspensions for solid loading levels even lower than 15 vol% [68]. Another reason for the high viscosity of nanoparticle suspensions is the increase in electrolyte concentration associated with the high surface area of nanoparticles. A polymer dispersant may be necessary for a well-dispersed suspension to be created. However, the polymer necessarily occupies space, which decreases the maximum solids loading of the suspension and thus the highest green density of nanoparticle samples. Too short a polymer chain yields a thin adsorption layer, resulting in flocculation due to van der Waals attraction, while too long a chain results in a dramatically decreased maximum solids loading. The exact achievable solids loading is dependent on the nanoparticle size, shape, and size distribution as well as the length and morphology of the polymer chains. The polymer dispersant type is also of critical importance for effective dispersion and the maximum solids loading. The pH of the suspension must be controlled to prevent imparting an attractive force between particles since the dispersant efficiency is dependent on the steric mechanism as well as the electrostatic mechanism. Use of ammonium poly(methacrylic acid) (PMAA- NH_4) as a dispersant shifts the isoelectric point of the Al_2O_3 system from 9.14 to 5.65 [69]. The positive surface charge of the Al_2O_3 particles attracts negative ions from the polymer. The net charge of the system is reversed due to the adsorption of the negatively charged polymer. Since the negative surface charge of PMAA- NH_4 polymer dominates the electrical charge of the suspension, the pH needs to be purposely adjusted to alkaline conditions for a well-dispersed suspension.

Rheology is a valuable tool for probing the van der Waals, electrostatic, and steric forces at the nanoscale [70, 71]. With regard to rheological properties, viscosity measures the flowability of a suspension and provides guidance on how easily two nanoparticles pass each other in a suspension. The Krieger–Dougherty equation has been used to provide good estimates between the solids loading and the suspension viscosity [72]:

$$\eta_r = \frac{\eta}{\eta_0} = \left(1 - \frac{\phi_{\text{eff}}}{\phi_{\text{max}}}\right)^{-n\phi_{\text{max}}}, \quad (5.8)$$

where η_r is the relative viscosity, η is the suspension viscosity, η_0 is the viscosity of the suspension medium (in most cases, water), ϕ_{eff} is the effective solids loading,

ϕ_{\max} is the maximum solids loading (~ 0.64), and n is a constant representing the intrinsic viscosity of the suspension. When a polymer dispersant is adsorbed onto nanoparticle surfaces, the effective solids loading can be substantially increased while the nanoparticle content remains the same:

$$\phi_{\text{eff}} = \phi \left(1 + \frac{\delta}{a_p} \right)^3, \quad (5.9)$$

where ϕ is particle solids loading, δ is polymer adsorption layer thickness, and a_p is nanoparticle size. This effective solids loading increase is due to the adsorbed polymers on particle surfaces and will undesirably lead to suspensions of high viscosities. For high solids loading suspensions, the polymer concentrations must be controlled with much more care for nanoparticle suspensions than for submicron-sized particle suspensions [73]. Due to the decrease in size for many components and features demanded by miniaturization, the suspension must flow into smaller molds and fill in the complex details or cavities of the molds easily. Intuitively, a higher solids loading means a more viscous suspension and increased difficulty in flow. However, high solids loading is necessary to obtain a high green density part. A balance must be achieved to address these opposite demands.

Based on particle packing principles, if nanoparticles are perfectly round, uniformly sized, and there are no interparticle sliding and packing hindrances such as friction, the random dense packing model yields a density of 64% [74]. However, nanoparticles may have irregular shapes and often large specific surface areas that adsorb a large amount of dispersant, which can quickly reduce the particle packing efficiency based on Equation (5.9). When an excessive amount of dispersant is used, some polymer chains stay free in the suspension, which further decreases the achievable maximum solids loading. Liu showed that most of the equations describing particle packing-viscosity behavior at a high strain rate ($\sim 100 \text{ s}^{-1}$) follow the simple form of

$$1 - \eta_r^{-\frac{1}{n}} = a' \cdot \phi + b', \quad (5.10)$$

where a' and b' are constants. Assuming nanoparticle suspensions follow Equation (5.10), the viscosity of the suspensions under different solids loading levels can be used to extrapolate the theoretical maximum solids loading at the point where viscosity is infinite [75]. For example, the maximum solids loading at pH 9.5 and 2.0 wt% of Al_2O_3 nanoparticle (average size of 27.5 nm) PAA concentration suspension can be predicted based on the viscosity at lower solids loading levels and is found to be 54.4 vol%.

Nanoparticle colloidal processing has the potential to ultimately eliminate the problematic particle–particle attraction issues arising from the excessive surface area of nanoparticles and the resulting agglomeration. This is an area that great progress can be made as a precursor for nanoparticle wet forming. A suspension

can be tailored to codisperse multicomposition nanoparticles and drastically different shapes (such as equiaxed nanoparticles and large aspect ratio nanotubes). The necessary effort is to tailor the particle–particle interaction energy to achieve high solids loading suspensions. If the nanoparticle solids loading can be achieved at ≥ 30 vol%, the resultant green samples should have high enough integrity for further processing.

5.4.2 Pressure Casting

5.4.2.1 Slip Casting Slip casting is one of the oldest wet forming processes that relies on capillary pressure to remove the dispersing medium, which is often times water. Applying this well-developed technique to nanoparticle systems is a natural outgrowth of particulate processing. In slip casting, a stabilized nanoparticle suspension is poured into a porous plaster of Paris mold to achieve a predetermined shape [76]. Water in the suspension is absorbed into the porous mold by capillary pressure, leaving a nanoparticle cast in the mold. When the mold and the cast are left to dry, the cast shrinks and separates from the mold. Slip casting is capable of producing complex shapes, even undercuts. Because of the relatively rapid formation of the cast layer, slip casting is well suited to making parts with large cavities. Large solid components can also be made by slip casting, although the drying process can be very long and challenging. For nanoparticle-based bulk materials, the pores in the cast can be very small. This can lead to an extremely long time for thick wall formation, which can impose a lower degree of freedom in component size and wall thickness; sometimes, particle size segregation occurs during the cast forming process.

The stability of the colloidal suspension strongly affects the microstructure of the cast. If the suspension is flocculated, the cast will be highly porous. If the suspension is well dispersed, the cast will be relatively dense. The number of species and the dispersibility of different nanoparticles also affect the uniformity and dimensional fidelity of the slip cast sample. If one species settles faster than the other, a composition gradient may be created. As the cast forms, a pressure gradient is developed through the wall of the mold and the cast; therefore, an optimal cast thickness exists, after which additional consolidation will take a long time. The pressure generated is dependent on the particle size. As particle size decreases, pore size decreases, and capillary pressure increases. However, the permeability of water into the mold also decreases. There is an optimum particle/pore size for each system. When the particle size is too small, it will take a long time to form a desired thickness. In this regard, nanoparticle suspension slip casting is not very suitable for thick objects.

Suspension characteristics are important for slip casting. Several Al_2O_3 suspensions with the same viscosity (but different solids loading and different particle size (11, 44, 190, and 600 nm)) are prepared and shaped into solid bodies. The green and sintered densities range between 30–67% and 63–99% of the theoretical values, respectively. These values, together with the microstructures, show that the solids loading of the suspensions and the characteristics of the

nanoparticles have a direct impact on the solid sample properties. Based on both processability (rheological behavior) and microstructure (density and grain size), particles of 100–300 nm are desired for preparing concentrated suspensions with low viscosity and sintered bodies with density close to the theoretical value [68]. A well-dispersed suspension is also very important for successful slip casting [77]. This is demonstrated by the slip casting of 3 mol% Y_2O_3 stabilized ZrO_2 particles of 9–18 nm size. Well-dispersed ZrO_2 nanoparticles can be slip cast to ~51% green density, while agglomerated ZrO_2 nanoparticles can only be slip cast to 46% density. Interestingly, the undesirable segregation behavior of a wide particle size distribution can be used to its advantage. Utilizing the segregation tendency of an unstable suspension under gravity, Al_2O_3 particle suspensions are slip cast and layers of continuously varying particle sizes from 50 to 250 nm are deposited to make functionally gradient Al_2O_3 bioceramics [78].

5.4.2.2 Uniaxial Pressure Casting To overcome the slow cast forming issue in slip casting, uniaxial pressure casting is widely practiced. Uniaxial pressure casting is a modified version of slip casting, more accurately a hybrid of slip casting and uniaxial pressing (Fig. 5.11). During uniaxial pressure casting, a pressure is applied in the liquid permeation direction to accelerate the casting rate and dispersing liquid removal. For this technique, the plaster of Paris molds have to be changed to plastic or metal molds to endure the high pressure. A filter paper or a membrane is placed at the bottom of a perforated die, and a pressure is applied to the suspension by a piston. A cast layer is formed on the filter, which must be permeable for water to be removed. Kaya and Butler used 30 nm $\alpha\text{-Al}_2\text{O}_3$ obtained from $\gamma\text{-AlOOH}$ sols seeded with 30 nm TiO_2 particles for uniaxial pressure casting [79]. The process resulted in 68.5% green density, which is very impressive for nanoparticle systems. The advantages of uniaxial pressure casting over slip casting are a faster casting rate and smaller floor space for the setup. The disadvantages are springback, possible cracking upon pressure release, sucking back of the dispersing liquid, and expensive dies.

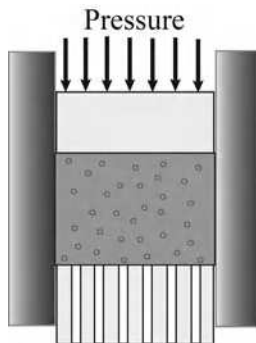


FIGURE 5.11 Uniaxial pressure casting setup illustration. (For a color version of this figure, see the color plate section.)

5.4.2.3 Spin Casting Spin casting is another version of pressure casting that uses the centrifugal force from a rotor to accelerate the deposition of the particles in the radial direction. This forming method combines the advantages of wet forming with a centrifugal force to produce near-net-shape parts. There are two advantages in using spin casting: (1) acceleration of the casting process by applying a centrifugal force and (2) creation of layers of particles with different sizes and thus a graded porous structure or a compositionally graded structure by deposition of mixed composition suspensions. For the first case, 3.0 mol% Y_2O_3 stabilized ZrO_2 ceramic parts are produced. Good particle packing with narrow pore size distributions is achieved. Green densities up to 57% of theoretical density are obtained [80]. For the second case, spin casting tends to apply more to a particle size population that includes submicron or even micron-sized particles. The spread in particle sizes may be three orders of magnitude: more than 1 μm in the lower layers and several nanometers in the upper layers to produce the intended results [81]. Particle sizes become increasingly smaller as the cast layer thickness increases. Compositionally graded Al_2O_3 - ZrO_2 composites are produced with nearly linear variation in compositions. The composition profile can be varied by using ZrO_2 particles of different size ranges or varying contents.

An external field can be utilized to change the nanoparticle arrangement during spin casting. Colloidal suspensions of cobalt nanoparticles of 11 nm size are deposited by spin casting in parallel, perpendicular, and gradient magnetic fields. A uniform layer of cobalt nanoparticles forms, but no long-range order is observed. However, when the suspension is dried in a magnetic field, large and three-dimensional cobalt aggregates are formed. When the suspension is deposited in a perpendicular magnetic field varying along the silicon substrate surface, a stripe structure is observed. Different cluster formations are found within and outside of the stripes. Within the stripes, clusters of uniform size and random distribution, consisting of several hundreds of cobalt nanoparticles, are observed. When a gradient magnetic field is applied, long-range movement of the magnetic particles on the substrate surface occurs [82]. Figure 5.12 shows scanning electron images of cobalt nanoparticles deposited by casting in an external magnetic field, $H = 0.4$ T, applied parallel and perpendicular to the substrate surface (Fig. 5.12a and b), and in a gradient magnetic field perpendicular to the substrate surface (Fig. 5.12c). For a concentrated solution dried in a parallel magnetic field, elongated clusters of various sizes are formed (Fig. 5.12a). For the deposit in perpendicular magnetic fields, a dense array of regular rods of ~ 1 μm diameter and 6 μm length oriented almost perpendicularly to the substrate surface is observed for concentrated solutions (Fig. 5.12b). For diluted solutions, the rods are smaller with various orientations to the substrate surface. The clusters and/or rods observed are agglomerates of hundreds of such cobalt nanoparticles. When a perpendicular magnetic field with in-plane gradient is used to deposit cobalt nanoparticles, formation of stripes with a width depending on the suspension concentration is observed (Fig. 5.12c). In a gradient magnetic field, the magnetic particles move on the substrate surface along the field gradient until the solution dries; in this way, the stripes are formed.

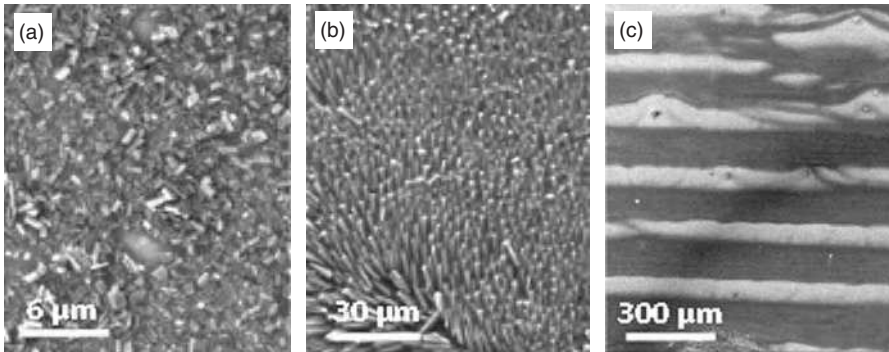


FIGURE 5.12 Scanning electron images of cobalt nanoparticles deposited onto a (100) silicon substrate in an external magnetic field: (a) $H = 0.4$ T, parallel to the substrate surface; (b) $H = 0.4$ T, perpendicular to the substrate; and (c) varying magnetic field perpendicular to the substrate (max 0.5 T) [82]. (Reprinted with permission from Leo G, Chushkin Y, Luby S, Majkova E, Kostic I, Ulmeanu M, Luches A, Giersig M, Hilgendorff M. Ordering of free-standing Co nanoparticles. *Mater Sci Eng C* 2003;23:949–952, Copyright 2003, Elsevier.)

The strength of pressure casting lies in the ability to produce complex shapes and the less stringent requirements on suspension solids loadings. Microstructural defects in the green bodies may include large voids caused by air bubbles in the suspension and segregation caused by different particle sizes. Low viscosity decreases cast formation time and is usually indicative of a well-dispersed system. Agglomeration in the cast can lead to rapid pressure drops and decrease the density of the cast. Increasing the solids loading of the suspension tends to decrease cast formation time. However, the permeation of a dispersing liquid through a very dense cast layer can be poor. A balance is needed between microstructure and processing time, which can possibly be achieved by leaving the suspension partially flocculated.

5.4.3 Tape Casting

Unlike pressure casting, which forms solid samples from nanoparticle suspensions by separating the dispersing medium out, tape casting (also called doctor blade casting) retains suspension solid contents (nanoparticles and binder(s)) during shaping by evaporating the dispersing media. A detailed description of the traditional tape casting process has been described [83]. To make tapes with a desired density, a suspension with a reasonably high solids loading and a low viscosity is essential. High amounts (as much as 10%) of binders and plasticizers may be necessary in addition to the dispersant to impart the necessary compliance for the tape sheet. Tape casting is realized by spreading the nanoparticle suspension over a surface. A doctor blade is used to level the suspension to a constant thickness to form a sheet. The solvent is then evaporated, leaving a tape consisting

of particles and binders. Usually the solvent is a volatile organic compound such as trichloroethane. This solvent removal process actually serves as an effective means of improving the relative density of the dried tape by inducing shrinkage. Solvents with relatively slower evaporation rates must be used for thicker tapes to avoid excessive stress and cracking. The dried tape thickness is about one half of the original thickness, which is equal to the height of the doctor blade. Tapes can be produced in the range of 5–1000 μm in thickness. Tape casting is a low-cost process for manufacturing large areas of nanoparticle-based sheets of controlled thicknesses. These sheets are the basic materials for the production of substrates or multilayer devices, for example, capacitors, inductors, highly integrated circuits, actuators, gas sensors, and solid oxide fuel cells.

Depending on the liquid vehicle used to dissolve the binder, tape casting may involve water- or solvent-based systems. A solvent-based suspension system generally shows a faster drying rate, lower cracking sensitivity, higher green strength and density, and smoother tape morphology. For a β -SiC particle (52 nm) dispersion in a toluene/ethanol mixture system, 40 wt% binder is needed in order to achieve a tape with desirable properties due to the high specific surface area of the nano-sized β -SiC particles, while 15 wt% binder is adequate for the α -SiC suspension with a lower surface area [84]. To acquire stable and low viscosity TiO_2 suspensions, azeotropic mixtures (ethanol/methyl ethyl ketone) and polyester/polyamine copolymer are used as solvent and dispersant, respectively, and a solids loading of 34 vol% is achieved. The TiO_2 films have good homogeneity and surface quality, and are absent of bubbles and cracks [85]. Dispersion of BaTiO_3 nanoparticles of 30 nm average particle size in different solvent systems (toluene–ethanol, methyl ethyl ketone–ethanol, and xylene–ethanol) along with Triton X-100 or phosphate ester as a dispersant shows the influence of solvents and dispersant type and concentration. Xylene–ethanol with phosphate ester is the best solvent and dispersant system for BaTiO_3 tape casting. Defect-free, dense, and smooth green tapes are formed with this system [86].

An aqueous tape casting process is systematically developed and investigated for 10 mol% Gd_2O_3 -doped CeO_2 nanoparticles. High solids loading (55 vol%) and stable suspensions are achieved using poly(acrylic acid) (PAA) as a dispersant, poly(vinyl alcohol) (PVA) as a binder, poly(ethylene glycol) (PEG) as a plasticizer, octanol as a defoamer, and 2,4,7,9-tetramethyl-5-decyne-4,7-diol ethoxylate as a surfactant. The pH values of the suspensions are maintained in the range of 9.0–10.0. Homogeneous, defect-free green tapes (thickness 150–200 μm) with a smooth surface and a high green density (51.5 vol%) are obtained [87]. Tape casting of ~ 75 nm $\text{Pb}(\text{Zr}_x\text{Ti}_{1-x})\text{O}_3$ particle suspensions is studied using xylene–ethanol and phosphate ester as dispersants. Defect-free, dense, and smooth green tapes are also formed [88]. Carbon nanotube– Al_2O_3 composites with carbon nanotube content up to 12 wt% are fabricated by tape casting. The distribution of carbon nanotubes in the Al_2O_3 matrix is significantly improved, resulting in enhanced wear resistance compared to dry processing [89]. Tape casting of α - Al_2O_3 suspensions with 60 nm particle size results in flat, crack-free sintered substrates with >95% density, a submicron microstructure, and a

translucent appearance. A decrease in the sintering temperature, an improvement in the mechanical strength, and a lower surface roughness are achieved for the nanoparticle suspension compared with micron-sized particle suspensions [90].

As an advancement, tape casting is applied as a tool for large area self-assembly of colloidal nanoparticles into thin superlattice films with face-centered cubic and hexagonal close-packed structures. The lateral ordering of the superlattices extends over micron-sized islands, while the vertical arrangement of the layers suggests a top-down growth mechanism at the air–solvent interface. Monodispersed magnetic heterostructured nanoparticles (nano crystallines, NCs), each consisting of a wüstite (Fe_xO) core and a cobalt ferrite (CoFe_2O_4) shell, are made first. Tape casting is performed on freshly hydrophobized silicon substrates and on silicon substrates covered with a 100 nm thick platinum layer (Fig. 5.13). The homogeneous deposition of the nanoparticle suspension is shown to result in a top-down growth of ordered nanoparticle assemblies. The ordering emerges during the drying of the solvent at the liquid–air interface and depends on parameters such as nanoparticle size, choice of solvent, excess of stabilizer, wetting property of the substrate, and nanoparticle shape [91].

The biggest advantage of tape casting is the ability to make very thin sheets (also known as thick films), virtually impossible to accomplish by other methods. However, tape casting also has a prevalent disadvantage that is not mentioned by any of the above studies, which is the preferential orientation of the particles. Even though preferential orientation may not be a serious issue for equiaxed nanoparticles, inclusion of nanotubes/nanofibers or layer-like particles in the suspension will lead to preferential alignment. Tape casting defects include air bubbles, particle segregation, and binder segregation.

5.4.4 Freeze Casting

Freeze casting can be viewed as a special case of gel casting that enables a nanoparticle-based sample to be fabricated into complex shapes. It starts with a well-dispersed nanoparticle suspension (Fig. 5.14). The mold used is generally nonporous, such as a polymer. After the suspension is poured into the mold, it is frozen, dried under vacuum (sublimation), and then demolded. Very desirably, freeze casting induces solid formation by percolating the network of dispersing medium and forms near-net-shape complex geometry parts with low cost, low pressure, and potentially environmentally-benign advantages [92, 93]. The key requirements for the suspension are that it must be stable and un-flocculated [94]. The dispersing medium can be water, camphene, dioxane, cyclohexanol, cyclohexane, or tertiary butanol. Among these, water and camphene are the most commonly used. When the freeze casting conditions are properly controlled, the dispersing medium separates from the solid phases through sublimation and little capillary force exists to cause crack formation or shape distortion [95, 96]. This is very desirable in offering high integrity samples with homogeneous microstructures. Compared to tape casting, freeze casting has the potential to avoid high fugitive organic contents that have to be removed before sintering.

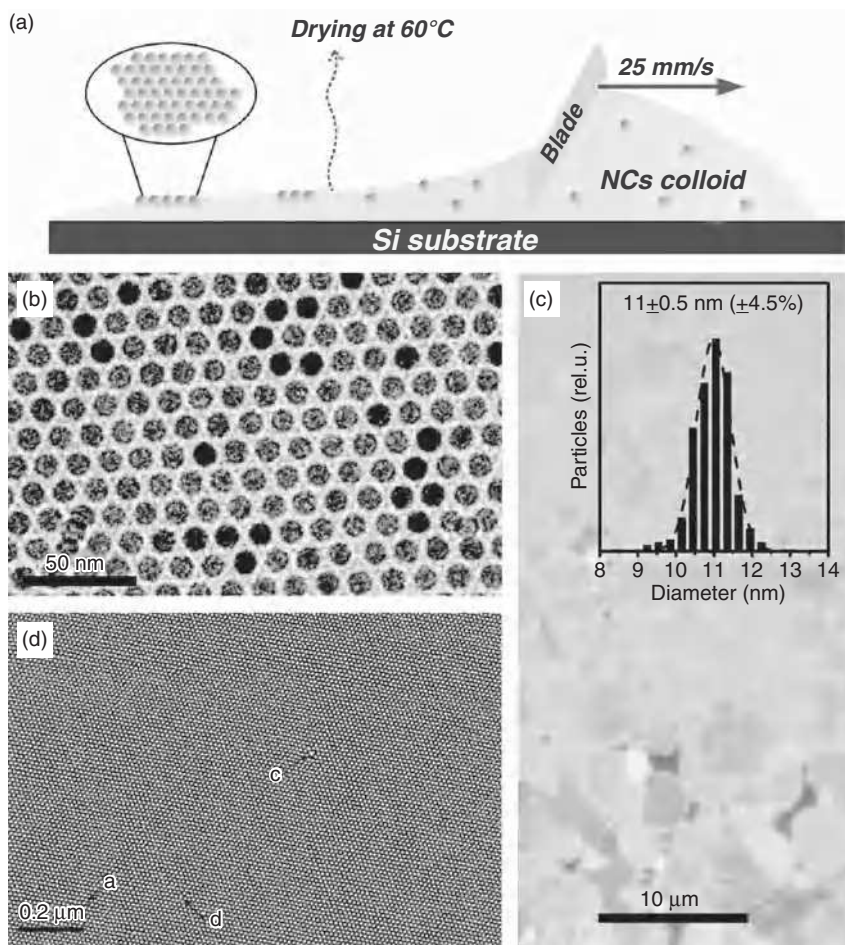


FIGURE 5.13 (a) Sketch of the tape casting process in which nanoparticles assemble at the liquid–air interface. (b) Transmission electron image of $\text{Fe}_x\text{O}/\text{CoFe}_2\text{O}_4$ nanoparticles of 11 nm size. (c) Optical microscope image of the nanoparticle film exhibiting separate islands only at the border of the substrate. The inset shows the size distribution of the 11 nm $\text{Fe}_x\text{O}/\text{CoFe}_2\text{O}_4$ nanoparticles used. (d) Background flattened scanning electron image of the 11 nm $\text{Fe}_x\text{O}/\text{CoFe}_2\text{O}_4$ nanoparticles deposited by doctor blade casting on a Pt-covered silicon substrate. The labeled arrows indicate point defects in the nanoparticle superlattice [91]. (Reprinted with permission from Bodnarchuk M, Kovalenko MV, Pichler S, Fritz-Popovski G, Hesser G, Heiss W. Large-area ordered superlattices from magnetic wustite/cobalt ferrite core/shell nanocrystals by doctor blade casting. *ACS Nano* 2010;4:423–431, Copyright 2010, American Chemical Society.) (For a color version of this figure, see the color plate section.)

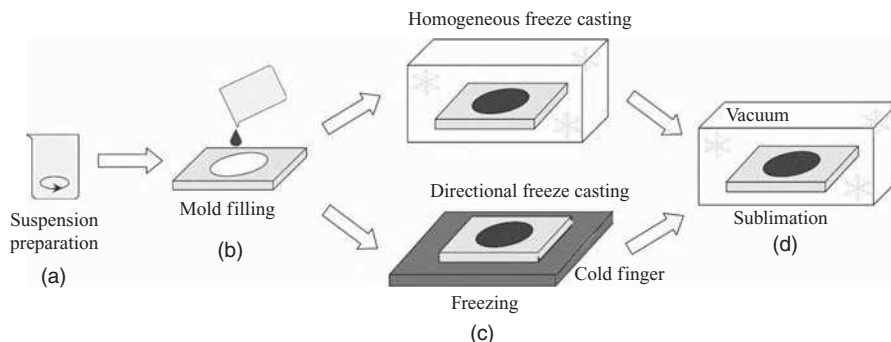


FIGURE 5.14 Illustration of the freeze casting process [99]. (Reprinted with permission from Li W, Lu K, Walz JY. Freeze casting of porous materials—a review of critical factors in microstructure evolution. *Int Mater Rev* 2012;57:37–60, www.maney.co.uk/journals/imr, Maney Publishing.) (For a color version of this figure, see the color plate section.)

Compared to either tape casting or pressure casting, freeze casting can avoid the preferential orientation of nonspherical constituents, such as fibers and nanotubes. Compared to tape casting, slip casting, or gel casting, freeze casting can avoid problematic drying issues due to the presence of capillary forces. Also, if the suspension is not stable during pressure casting and tape casting, segregation can occur because of differences in particle size or density [97,98]. For freeze casting, this issue can be effectively mitigated since the suspension state is preserved during shaping.

Freeze casting has been practiced for some time. However, most studies are either focused on micron-sized particles or metal–organic salt sol–gel systems [100–105]. Recently, some attempts have been made to modify the dispersing media to avoid large defects [106, 107]. However, more expensive organic dispersing media have to be used. Freeze casting is applied to a SiC particle suspension, but the effort only produces millimeter-sized pores [108]. For SiO₂ nanoparticles, materials produced by freeze casting have pores on the order of several microns. An Al₂O₃ nanoparticle suspension of 40 vol% solid loading is freeze cast. The freeze casting molds are developed using poly(dimethylsiloxane) epoxy [62, 109]. After the suspension is frozen, the mold is removed and the sample is exposed to a vacuum ($<10 \times 10^3$ Pa) to allow the ice to sublime. Defect-free samples are obtained with good green strength. SiO₂ nanoparticles and micron-sized kaolinite particles are dispersed to make multicomposition suspensions. The SiO₂ nanoparticles are able to experience a gel formation process when a proper electrolyte, such as NaCl, is added. The gelled SiO₂ nanoparticles are effective in hindering the rejection by the ice growth front; the resulting microstructure contains numerous small pores as seen in Figure 5.15a. The introduction of kaolinite particles is effective in controlling the pore morphology of the kaolinite–SiO₂ composites. Kaolinite particles act as the framework for the sample while SiO₂

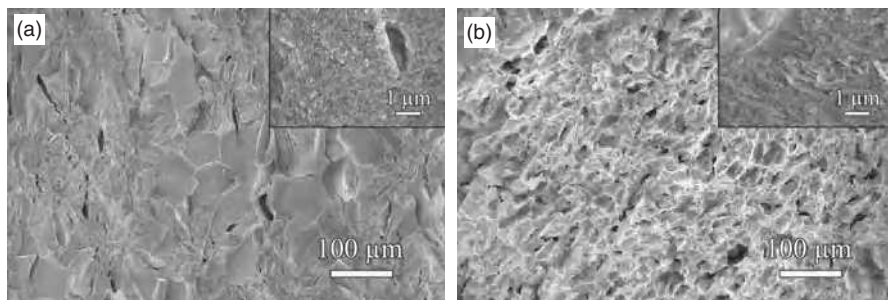


FIGURE 5.15 Freeze cast microstructures of (a) SiO_2 and (b) SiO_2 -kaolinite composite.

nanoparticles forming the bridges to bond the kaolinite particles together, resulting in a network structure. When frozen, the plate-like kaolinite particles and the gelled suspension can effectively block the anisotropic growth of ice crystals and lead to the formation of homogeneous microstructures. Compared with pure SiO_2 samples, the pore sizes of kaolinite- SiO_2 composites increase gradually with the addition of large-sized kaolinite particles as seen in Figure 5.15b.

Unidirectional freezing uses ice crystals as a template to produce honeycomb or lamellar structures, but the robustness of the structures needs to be further studied [110, 111]. Freeze casting is used to develop sophisticated porous and layered hybrid materials, including artificial bones, ceramic-metal composites, and porous scaffolds for osseous tissue regeneration. Although it is promising to see that the structures achieved by freeze casting have strengths up to five times of those of materials currently used for implantation [112], much more work is needed to achieve the desired structure repeatedly and to produce large objects. Even if the microstructural inhomogeneity is not an issue, freeze casting of a thick nanoparticle sample can take days to complete.

Directional freeze casting can be used to produce materials with complex, anisotropic, and porous microstructures, such as lamellar, dendritic, parallel, columnar, or aligned porous scaffolds. By controlling additives, freezing conditions, suspension solids loading, and particle size, directional porous microstructures can be obtained [113–131]. Ice has 15 known crystalline phases, among which hexagonal ice is the most common structure. According to the crystal structure and crystal growth kinetics of ice, the facets parallel to the c axis have a higher chemical potential than the ones parallel to the a axis (perpendicular to the c axis); the ice growth rate along the a axis is 100–1000 times faster than that along the c axis. Thus, the growth of ice crystals with the temperature gradient perpendicular to the c axis is kinetically favorable. When the temperature gradient and particle hindrance are properly controlled, the final structures have lamellar pores with large dimensions along the preferred growth directions and small dimensions along the limited growth directions of ice crystals. Particle size affects pore morphology. Specifically, nanoparticles are more likely to be rejected by the solidification front, and elongated ice crystals are more likely to form during

directional freeze casting. Particle size also influences the solidification behavior of ice crystals [130]. When heterogeneous nucleation is dominant, the nucleation sites are provided by the liquid–solid interface, specifically the particle surfaces. Apparently, nanoparticles provide a larger surface area and increased nucleation sites, which lead to numerous small pores, while large particles produce a smaller number of large pores.

Freeze casting has not been extensively applied to nanoparticle suspensions, partly because of the drastic increase in capillary pressure with a decrease in particle size and the challenges in achieving high solids loading suspensions. For directional porous structures, the small size of nanoparticles also limits their ability to break away from the drag force of the moving liquid front. As a result, directional pore channels might be difficult to form.

5.4.5 Gel Casting

There are two gel casting processes: the first is particulate gel casting—the sol consisting of colloidal nanoparticles, and the other is polymeric gel casting—the sol consisting of polymer precursors for nanoparticles. When the particle size is in the nanometer range, the distinction between a particulate gel and a polymeric gel may not be clear. For particulate gel casting, the interest of this book, the general processing steps are shown in Figure 5.16. First, different species such as nanoparticles, monomers, binders, and solvents are thoroughly mixed. In order to avoid flaw, void, and crack formation, the mixed suspension is deaired under a partial vacuum. After that, a catalyst (polymerization initiator) is added to start the gel forming chemical reaction. Before too much gelation occurs, the suspension is poured into molds made of metal, glass, plastic, or wax to cast it into desired shapes. The chemistry for gel casting can be quite complex. A chain former, a cross-linking agent, and an initiator are incorporated for polymerization. Methacrylamide is a common chain former, and methylene bisacrylamide is a common cross-linker. As the initiator is added, the polymer forms a network. The stiffness of the gel and the rate of polymerization are directly related to the chain former and cross-linker selected. If the gel forming chemical reaction is exothermic and generates enough heat, the solidification process may be automatic. Otherwise, heating is needed for the gelation to occur, which can be realized in a heating oven (such as 80°C). After gelation, the part can be demolded from the mold and dried, which removes most of the solvent, preferably at a high relative humidity (90%) to minimize warping and cracking. The dried material has very high strength. At this stage of the process, the green body can be machined to refine its shape (green machining).

Gel casting has a high potential to achieve homogeneous microstructures and complex geometries. However, there are also problems concerning surface finish, warping, and material handling. Gel casting has been applied to nanoparticles such as Al_2O_3 , Si_3N_4 , and calcium hydroxyapatite [132–135]. SiC nanoparticles are coated with a hydrolyzed aluminum species to produce an Al_2O_3 –SiC codispersion of 55 vol% solids loading. Even though submicron Al_2O_3 particles

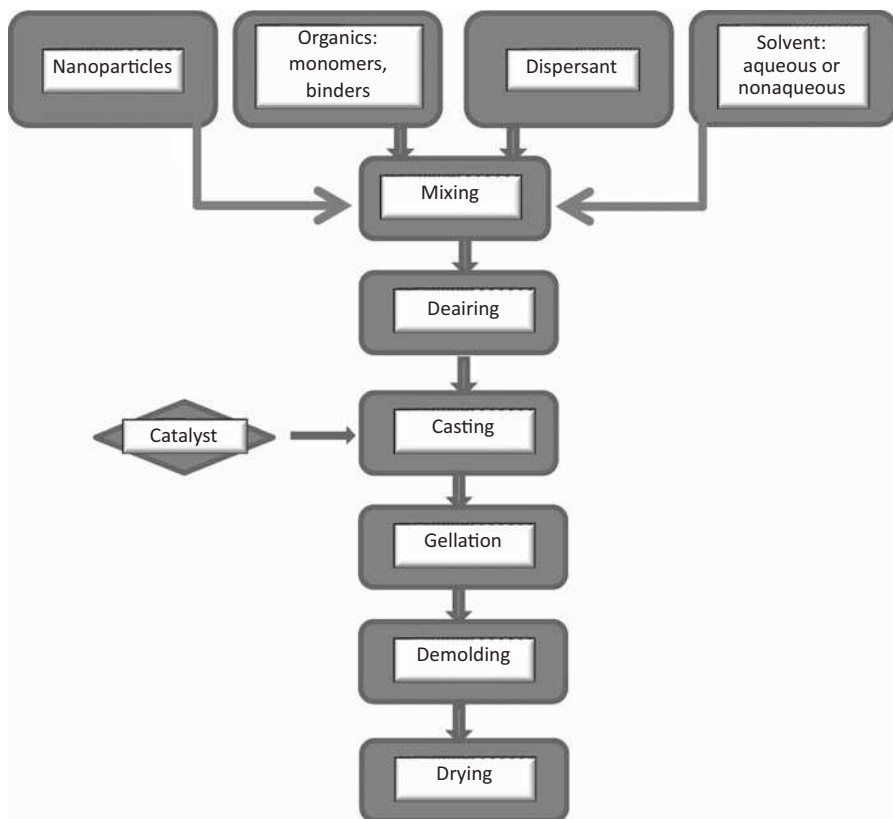


FIGURE 5.16 A schematic representation of the gel casting process: a nanoparticle-containing suspension is first created, followed by polymerization, casting, and drying.

are used and the cast samples have to be dried in an environmental chamber for >40 hours to avoid cracking, composite fabrication from this system by gel casting has been demonstrated [135]. As an advanced use of gel casting, a β -tricalcium phosphate matrix with hydroxyl apatite reinforcing nanofibers is made into a nanocomposite porous scaffold for load-bearing bone tissue engineering [133]. Even though the mechanical properties of the sintered scaffold are improved, the distribution and function of the nanofibers need to be further corroborated. Hierarchically porous zeolite structures are obtained from colloidal zeolite nanoparticle suspensions by gel casting, and zoned zeolite structures with designed shapes are generated by adding a secondary growth step to the gel casting process [136]. Although the results are encouraging, the density and integrity of the zeolite material deserve further study. The collapse of a weak SiO_2 nanoparticle network has been induced to form a denser material without high temperature strengthening [137]. Organic ligands are incorporated to prevent crack formation, and TiO_2 nanoparticles are used to reduce the volume shrinkage

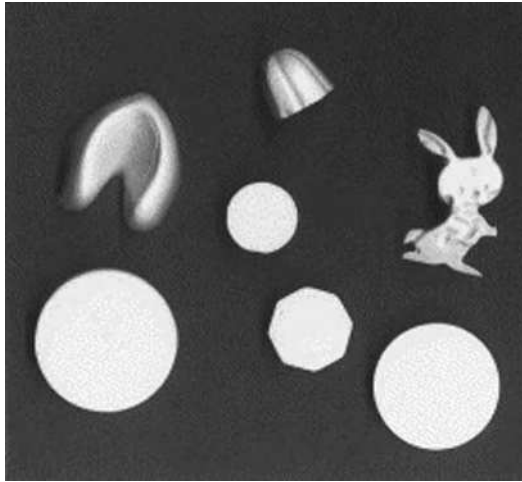


FIGURE 5.17 Al_2O_3 green bodies obtained by gel casting using 58 vol% suspension prepared by adding a four-member copolymer containing acrylic acid, acrylate ester, sulfonic acid, and phosphonic acid groups in the molecule [134]. (Reprinted with permission from Liu YQ, Gao LA. Dispersion of aqueous alumina suspensions using copolymers with synergistic functional groups. *Mater Chem Phys* 2003;82:362–369, Copyright 2003, Elsevier.)

of the gels and enhance the mechanical strength of the components. Complex-shaped parts such as turbines, accelerator magnets, and artificial bones are made (Fig. 5.17). Because of the homogeneous microstructures, gel-cast samples shrink uniformly. Thus, the mold can be designed to compensate for the shrinkage so that the desired shape and size can be produced.

Commercial BaTiO_3 nanoparticles are formed into green bodies using gel casting involving polysaccharides that gel upon cooling, that is, agar. Relatively large gel cast samples are made with a similar density and microstructure and in a shorter time compared to those obtained by slip casting [138].

As a very desirable feature, the polymerized monolithic component can be removed from the mold while still being wet and dried to release the liquid. The formation of a gel also prevents the segregation of different size or density particles; both thick and thin parts can be formed because of the strength that the gel provides. Near-net-shape forming, high green densities, low levels of organic additives, and machinability at green state are clear advantages of the gel casting process. Gel casting also provides an excellent alternative to manufacturing large, complex-shaped components such as turbine rotors, valves, and cam followers for gasoline and diesel engines. The high degree of homogeneity required to produce excellent parts can be retained. Although polymerization is a critical processing step, the polymer content of the green sample (2–4 wt%) is not higher than that in components produced by other wet processes. One disadvantage is that the heat given off by the polymerization reaction may cause cracking. Too

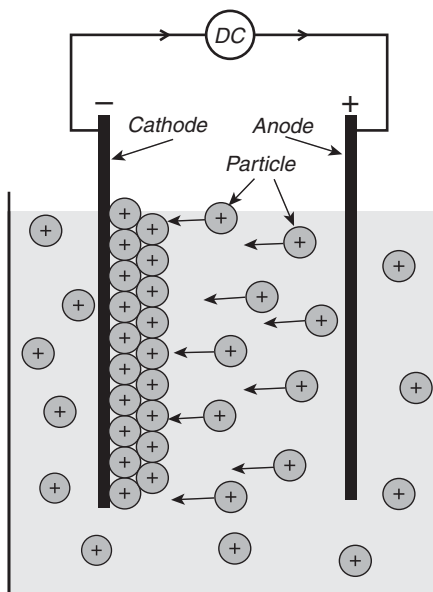


FIGURE 5.18 Schematic drawing of an electrophoretic deposition cell showing the process [139]. (Reprinted with permission from Sarkar P, Nicholson PSJ. *Electrophoretic deposition (EPD): mechanisms, kinetics, and applications to ceramics*. J Am Ceram Soc 1996;79:1987–2002, John Wiley & Sons.)

much or too little polymer will result in poor mechanical properties. Drying after gel casting can become the most daunting task for the process in order to avoid cracking.

5.4.6 Electrophoretic Deposition

Since most nanoparticles develop a net surface charge when immersed in a polar solvent, the particles will move in the presence of an electrical field (electrophoresis). Electrophoretic deposition (EPD) is a shaping method in which a particle suspension is created and a direct current electric field is applied, resulting in the charged particles in the suspension depositing onto the oppositely charged electrode (Fig. 5.18) [139]. The theory behind electrophoretic deposition was proposed by Sarkar and Nicholson [139–141]. It mainly involves three steps: electrophoresis, coagulation, and deposition. Since most nonpolymeric nanoparticles are surrounded by a cloud of ions known as the double layer in an electrolyte, in an electric field the leading edge of the double layer is compressed; there may also be some overlap of the double layers between the particles, allowing the particles to approach one another. When the particles are close enough, the van der Waals forces cause the particles to compact. Although the DLVO theory describes the formation of surface charges in aqueous suspensions quite well, the mechanism of coagulation and deposition during the electrophoretic deposition

is not completely understood. It is believed that the distortion of the lysosphere around individual particles by the electrical field plays a significant role. Since high surface charge allows rapid particle migration and deposition, a high absolute value of zeta potential for the dispersed particles is desirable, which is consistent for stabilizing a suspension and avoiding agglomeration.

The suspensions for EPD are generally dilute (<10 vol% solids) and have a low viscosity. There are two types of electrophoretic deposition: constant voltage and constant current. For the constant voltage electrophoretic deposition, the applied potential is held constant. For the constant current electrophoretic deposition, the applied current is held constant. In the constant voltage electrophoretic deposition, the electrical field driving the particles weakens and the deposition rate slows as the thickness of the deposited layer increases. In the constant current electrophoretic deposition, the voltage is increased to counteract the effects of increased resistance due to the deposited nanoparticles, and the microstructure is thus more homogeneous.

SiO₂ particles of 10–100 nm size are electrophoretically deposited. The pore size distribution of the electrophoretically deposited SiO₂ green bodies is correlated to the solids loading of the suspension [142]. Smaller pore size is achieved by using high solids loading suspensions. However, a general correlation between the two parameters is not available. When mixtures of nano-sized and micron-sized ZrO₂ particles are electrophoretically deposited, no size separation is observed, which is very desirable [143]. In another study, a γ -AlOOH sol of 40 nm size seeded with δ -Al₂O₃ nanoparticles of 13 nm size is used to penetrate and deposit into the voids within/between Ni-coated carbon fiber tows [144]. Full deposition of the sol material throughout the voids is realized. Composites of 67% density are produced using a 15 V electric field and a deposition time of 400 seconds. The effect of voltage on jamming is studied with a poly(styrene-co-methacrylic acid) microsphere crystal template for 180 nm ZnO colloidal nanoparticles (including –25 V, –10 V, –5V, and –2.5 V). When a larger voltage (–25 V) is employed, a large ZnO nanoparticle flux is induced near the template surface. This causes jamming of the mouth of the interstitial space with ZnO nanoparticles near the template surface. After jamming, ZnO nanoparticles agglomerate rapidly on the surface and form a continuous layer. This causes a quick increase in the electrophoretic current values. The entire process exhibits deposition characteristics similar to films deposited on a planar surface by electrophoresis. Figure 5.19a shows a scanning electron image of the top surface of a well-ordered ZnO replica formed by deposition of ZnO nanoparticles into the template. It is similar to the original structure of the colloidal crystal in that each spherical void is surrounded by six spherical cavities. The topmost plane of the cells in the replica exhibits a close-packed pattern. Figure 5.19b shows that each void formed after removing the colloidal particles has three dark spots corresponding to the contact points of the three particles in the layer below. Hence, ZnO inverse opal layers are reproduced accurately through the deposition of ZnO into a colloidal crystal template via a template-mediated electrophoresis process. This material has a well-ordered macroporous structure [145].

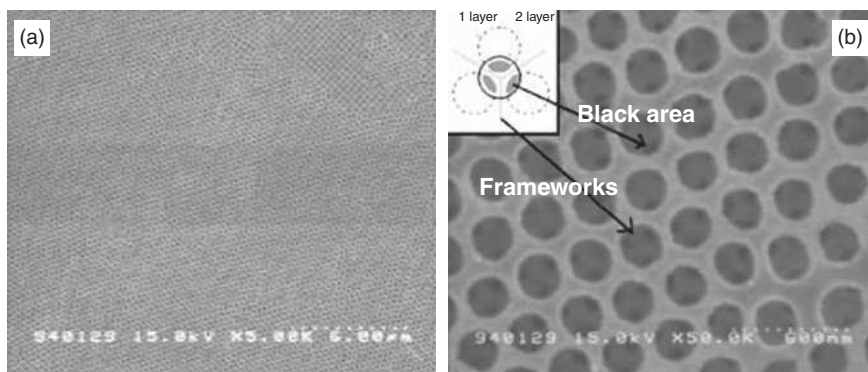


FIGURE 5.19 Scanning electron images showing ZnO macroporous structure fabricated via a template-mediated electrophoresis process at (a) low magnification and (b) high magnification [145]. (Reprinted with permission from Chung Y-W, Leu I-C, Lee J-H. Filling behavior of ZnO nanoparticles into opal template via electrophoretic deposition and the fabrication of inverse opal. *Electrochimica Acta* 2009;54:3677–3682, Copyright 2009, Elsevier.)

TiO₂ nanoparticles are electrophoretically deposited on stainless steel using isopropanol and triethanolamine as a solvent and a dispersant, respectively. The effects of deposition voltage (5–20 V) and deposition time (5–60 seconds) on the microstructure, surface topography, and packing density are investigated. The substrate surface is fully covered with increasing deposition voltage and deposition time, but the surface roughness also increases [146]. The packing density of the deposited films reaches its highest value at 20 V and 60 seconds. A Ba_{0.6}Sr_{0.4}TiO₃ film with 33 μm thickness is prepared by the electrophoretic deposition method on a Pt/Ti/SiO₂/Si substrate using Ba_{0.6}Sr_{0.4}TiO₃ nanoparticles [147]. The deposition rate for tetragonally stabilized, polycrystalline ZrO₂ is independent of particle size. Bimodal starting particles can be used to optimize the green density of the compact in order to minimize the shrinkage during sintering [148].

Tetragonal ZrO₂ partially stabilized with Y₂O₃ (Y-TZP) and Al₂O₃ functionally graded composites of a tubular shape incorporating a tough ZrO₂-containing central layer and a hard outer layer of pure Al₂O₃ are produced from nano-sized sols using electrophoretic deposition. A stainless steel rod with 0.3 mm diameter is used as the deposition electrode (+), while a tubular stainless steel electrode with 40 mm diameter is used as the negative electrode (cathode). The first stage of the electrophoretic deposition is performed with the Al₂O₃–ZrO₂ sol under a constant voltage of 10 V using a deposition time of 2.5 minutes. Under the applied electric field, the boehmite and ZrO₂ particles (possessing a net negative surface charge at pH 9.2) migrate toward the positive electrode (Fig. 5.20). The particles are deposited until a matrix thickness of 1.4 mm is achieved. After the first stage of the electrophoretic deposition, the deposition electrode

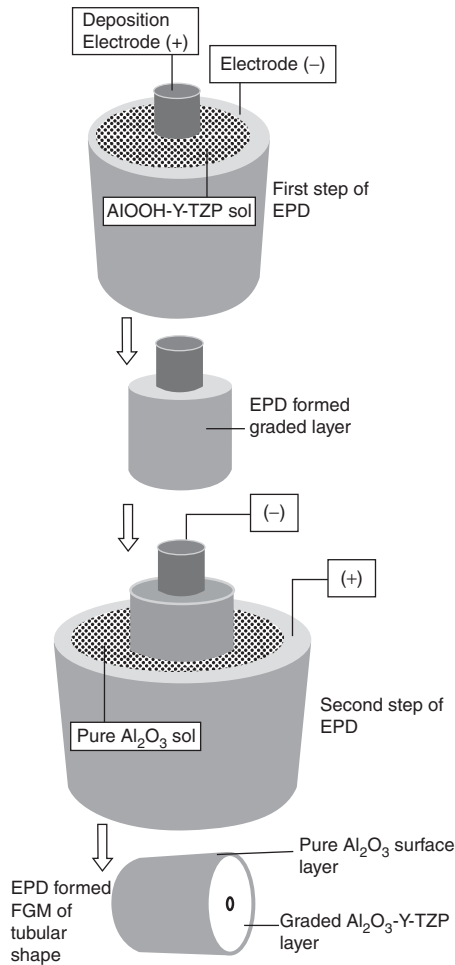


FIGURE 5.20 Processing of Al₂O₃-ZrO₂/Al₂O₃ functionally graded (FGM) tubular shape using two-step electrophoretic deposition (EPD) [149]. (Reprinted with permission from Kaya C. Al₂O₃-Y-TZP/Al₂O₃ functionally graded composites of tubular shape from nano-sols using double-step electrophoretic deposition. *J Eur Ceram Soc* 2003;23:1655–1660, Copyright 2003, Elsevier.)

surrounded by the boehmite plus ZrO₂ deposit layer is put in a pure Al₂O₃ suspension. The central deposition electrode is connected to the negative terminal of a power supply, as Al₂O₃ particles have positive surface charge at the working pH value of 4. The second stage of the electrophoretic deposition is performed using the same voltage of 10 V for a deposition time of 1.5 minutes in order to obtain a thin Al₂O₃ layer around the first formed thicker boehmite plus ZrO₂ layer. The final tubular green body containing an inner layer of boehmite plus ZrO₂ surrounded by a thin layer of pure Al₂O₃ is obtained [149].

One of the most distinct advantages of electrophoretic deposition is that the green density is not affected by the suspension solids loading since the deposition process itself moves and packs particles. As a result, electrophoretic deposition is very attractive for nanoparticle shaping, which is difficult to obtain high solids loading suspensions in the first place [143]. Another advantage of electrophoretic deposition is better control of the process because the rate and extent of the deposition is controlled electrically. Since there is no stress involved during the nanoparticle deposition, the shaping mold can be fabricated from soft or easily formed materials such as polymers or graphite backed by a metallic electrode. Complex shapes become achievable with these kinds of inexpensive molds, and the electric field defines particle deposition areas. One limitation is the difficulty of forming components in large dimensions. Although an aqueous suspension is almost always preferred, the formation of gas bubbles due to water decomposition at the electrodes has to be addressed. Gas bubbles can produce large pores within the formed parts. One alternative is to use an organic solvent [150, 151]. However, an organic solvent brings a plethora of problems such as cost, environmental, and surface charge issues. Using a membrane in an aqueous suspension to separate gas bubbles from the deposition surface seems to be a viable solution [142]. Also, nanoparticle solids loading in a suspension changes with deposition time, which can lead to gradient microstructures. This can be alleviated by circulating the suspension and controlling its solids content. Compared to other methods, the advantages of electrophoretic deposition process are simplicity, material non-specificity, and high reproducibility. The main challenge is to avoid electrolysis of water and gas bubble formation.

5.5 DIGITAL PROCESSING TECHNIQUES

With the vast advancement of computer-aided design (CAD) in the past decade, a number of digital processing techniques have been developed to make complex shapes, such as direct writing, stereolithography, and ink-jet printing [152–157]. The processes often start with a nanoparticle-based paste or suspension, then convert a CAD drawing from a computer into two-dimensional thin layers, and deposit the nanoparticle-based paste or suspension line-by-line to form a three-dimensional part. The advantages of such techniques lie in producing complex three-dimensional structures.

5.5.1 Direct Writing

5.5.1.1 Robocasting The earliest direct writing technique is termed as robocasting. The nanoparticle-based system is more ink- or paste-like. During the process, the rheological changes of the ink after being extruded out of a nozzle are used as the method to change state and to form shapes [158–160]. As the ink is extruded through a narrow orifice and exits the nozzle, it forms a continuous rod-like filament with a rigid core/fluid shell architecture that simultaneously

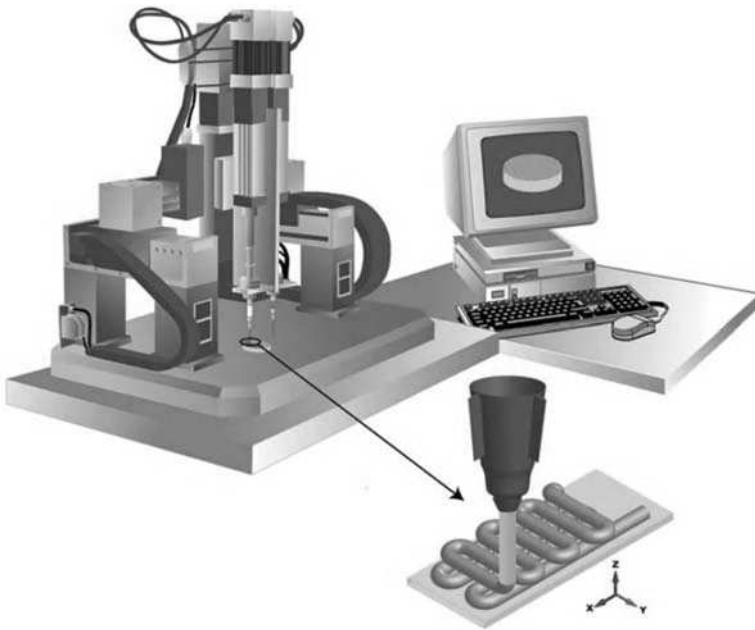


FIGURE 5.21 A schematic representation of the robocasting process. A suspension is extruded through a thin nozzle to build a part layer-by-layer following a computer design [161]. (Reprinted with permission from Munch E, Franco J, Deville S, Hunger P, Saiz E, Tomsia AP. Porous ceramic scaffolds with complex architectures. *JOM* 2008;60:54–58, Springer Science + Business Media, Fig. 1.) (For a color version of this figure, see the color plate section.)

promotes shape retention while allowing the rods to fuse together at the contact points. A second layer is formed after the previously formed layer is dried. Robocasting requires a pseudoplastic suspension with a yield stress high enough to prevent shape changes of the printed structure under its own weight. Therefore, well-dispersed high solids loading suspensions are not suitable for robocasting. Their rheology must be altered to form partially flocculated suspensions where a loosely bound particle network forms [161]. A schematic representation of a robocasting setup is shown in Figure 5.21. The gel-based ink is deposited onto a moving x - y stage, yielding a two-dimensional pattern. After a given layer is generated, the stage is incremented in the z -direction and another layer is deposited. This process is repeated to yield complex three-dimensional structures. Robocasting allows the fabrication of nanoparticle-based scaffolds without the need for a sacrificial support material or mold. Inks are capable of fully supporting their own weight during assembly, thanks to their carefully tailored composition and viscoelastic properties.

The smallest nozzle diameter reported for robocasting is 100 μm [162]. Some of the complex shapes produced using BaTiO_3 nanoparticles and their corresponding microstructures are shown in Figure 5.22. The smoothness of the cast

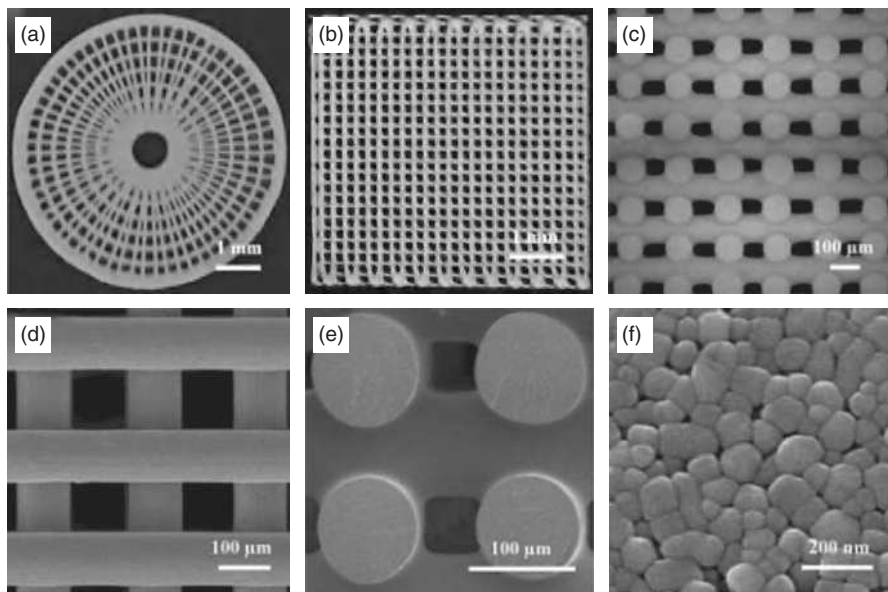


FIGURE 5.22 Top view of (a) three-dimensional radial array, (b) and (d) three-dimensional periodic lattice assembled from BaTiO_3 nanoparticle inks deposited through $100\ \mu\text{m}$ nozzle, (c) and (e) cross-sectional view of three-dimensional periodic lattice shown in (b) and (d), and (f) BaTiO_3 nanoparticle network that comprises the structures after drying [162]. (Reprinted with permission from Li Q, Lewis JA. Nanoparticle inks for directed assembly of three-dimensional periodic structures. *Adv Mater* 2003;15:1639–1643, John Wiley & Sons.)

features can be seen in Figures 5.22d and e, which cannot be achieved if micron-sized particles are used.

Robocasting has the advantage of forming parts with a much higher green density that require little or no machining after fabrication. However, the ink must satisfy two important criteria. First, it must exhibit a well-controlled viscoelastic response, which means it must flow through the deposition nozzle and then “set” immediately to facilitate shape retention of the deposited features, even as it spans gaps in the underlying layer(s). Second, the ink must contain a high nanoparticle solids loading to minimize drying-induced shrinkage after the three-dimensional structure is constructed. These requirements mean careful control of interparticle forces to generate a highly concentrated, stable dispersion to start with. Often times a system change (pH, ionic strength, or solvent) has to be induced as an additional step to promote the fluid-to-gel transition. The highlight of robocasting is that the process is moldless and binderless. It has great promise for the rapid manufacturing of complex, multiphase devices, such as piezoelectric ceramic–polymer composites, photonic band gap lattices, advanced engines and gas turbines [163], and biocomposites [164], Robocasting is also amenable to multimaterial fabrication.

5.5.1.2 Omnidirectional Printing A more advanced version of direct writing is called omnidirectional printing [165]. Arrays of device-level structures spanning three dimensions can be printed with a fine resolution in high aspect ratio layouts. This technique can overcome the limitation of only producing low aspect ratio features that must be supported by an underlying substrate or device and pattern spanning elements in- or out-of-plane. In this filamentary printing approach, a concentrated ink is extruded through a tapered cylindrical nozzle (1–30 μm) that is translated using a three-axis, motion-controlled stage with nanoscale precision. Omnidirectional printing has been used to produce flexible, stretchable, and spanning microelectrodes using concentrated silver nanoparticle ($\sim 20 \pm 5$ nm) inks. Planar microelectrode arrays are made on a silicon wafer by depositing silver nanoparticle ink (71 wt% solids) through 1, 5, and 10 μm cylindrical nozzles (Fig. 5.23a). Printed features with aspect ratios (height to width ratio) of ~ 0.7 are obtained in a single pass, and a minimum width of ~ 2 μm is achieved with the use of a 1 μm nozzle. In addition, high aspect ratio features are patterned in a layer-wise manner, and their width and height are defined solely by the nozzle diameter and number of printed layers, respectively (Fig. 5.23b and c). The microstructural evolution of the printed silver microelectrodes as a function of annealing temperature is shown in Figure 5.23d. As the temperature increases from 150°C to 550°C, the microelectrodes undergo simultaneous loss of organics, grain growth, and densification. Concomitantly, their electrical resistivity decreases sharply over this temperature range (Fig. 5.21e).

Direct writing is superior in the construction of arbitrarily designed three-dimensional structures. A series of organic inks doped with nanoparticles are made to fabricate three-dimensional meshes of interpenetrating rods. The effects of nanoparticle addition on the rheological properties of organic inks reveal a close relationship between the ink's formability and rheological properties. To meet the requirement of arbitrary structure design for various applications, inks used in this technique must satisfy several criteria. First, the ink must be extruded fluently through the deposition nozzle without clogging or fracture. Second, the ink should change from fluid-like to solid-like right after its extrusion out of the nozzle to facilitate the shape retention of the deposited features. Third, the formed structure must maintain its shape and strength during the process and afterward. Organic vaseline inks doped with TiO_2 nanoparticles are written into three-dimensional structures (Fig. 5.24). These structures show superior performance to retain their shapes after repeated bending and stretching as a flexible substrate due to the elastic property contributed by the nanoparticles. The assembled scaffolds and rods exhibit potential capabilities to build complex three-dimensional structures [166].

5.5.2 Stereolithography

Stereolithography is more specifically a multilayer photopolymerization technique and is based on the layered construction of a polymer (in this case, a

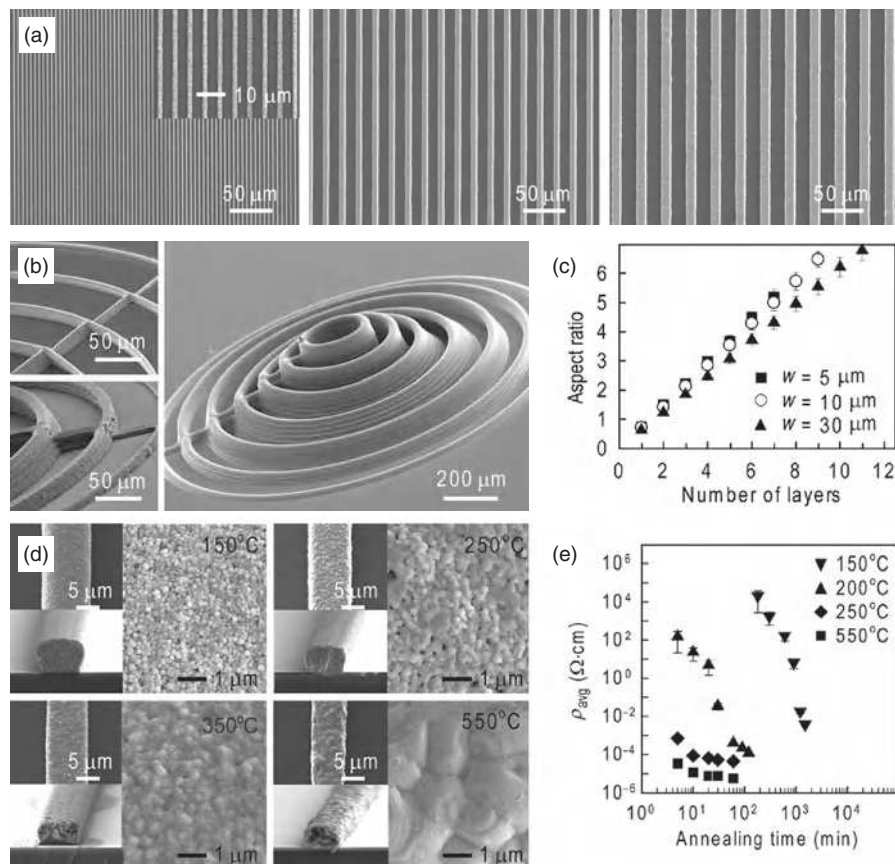


FIGURE 5.23 (a) Scanning electron images of planar arrays of silver microelectrodes patterned with 1- (left), 5- (center), and 10- μm (right) nozzles. (b) Scanning electron images of multilayer silver microelectrodes patterned with 5- (top left), 10- (bottom left), and 30- μm (right) nozzles. (c) Aspect ratio as a function of number of printed layers for the silver microelectrodes shown in (b). (d) Scanning electron images of silver microelectrodes patterned with a 15- μm nozzle as a function of annealing temperature. (e) Electrical resistivity of silver microelectrodes as a function of annealing temperature and time. Error bars indicate the standard deviation measured from three electrodes [165]. (Reprinted with permission from Ahn BY, Duoss EB, Motala MJ, Guo X, Park SI, Xiong Y, Yoon J, Nuzzo RG, Rogers JA, Lewis JA. Omnidirectional printing of flexible, stretchable, and spanning silver microelectrodes. *Science* 2009;323:1590–1593, AAAS.)

nanoparticle-filled polymer) in a tank of photocurable monomer or oligomer (Fig. 5.25). In stereolithography, a laser beam is scanned on the surface of a highly concentrated suspension of nanoparticles in a monomer solution. The monomer is cured to form a layer where the particles are bound by the polymer. Then, the platform is lowered, and the suspension flows over the polymerized

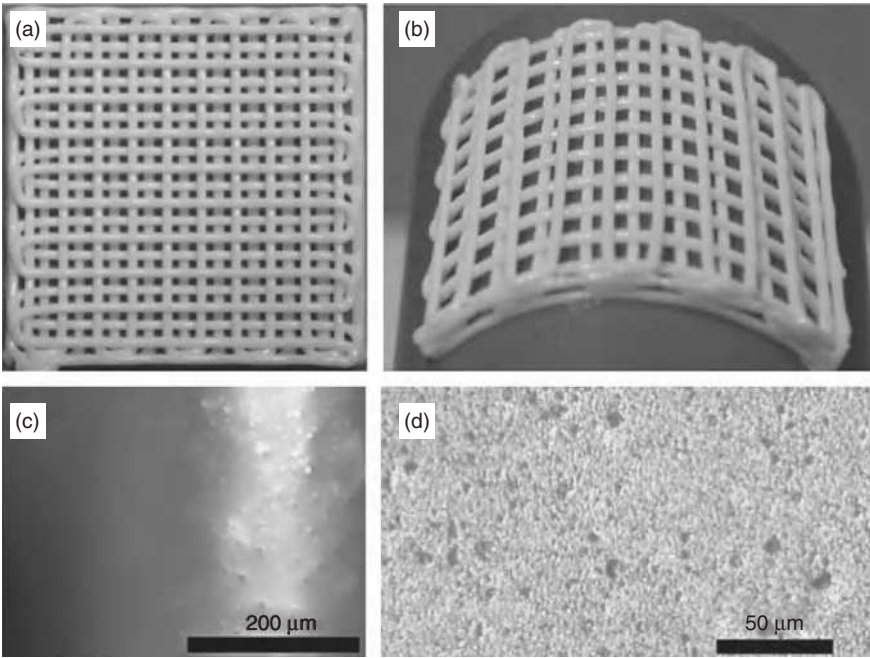


FIGURE 5.24 Images of assembled structures on different scales: (a) a four-layer scaffold piled by perpendicular rods with 500 μm diameter and 2 mm interrod distance in a 20 mm \times 20 mm square, (b) bending of the formed structure, (c) agglomeration of nanoparticles at the rod's surface, and (d) magnified image of the nanoparticle-doped ink [166]. (Reprinted with permission from Cai K, Sun J, Li Q, Wang R, Li B, Zhou J. Direct-writing construction of layered meshes from nanoparticle-vaseline composite inks: rheological properties and structures. *Appl Phys A* 2011;102:501–507, Fig. 6.) (For a color version of this figure, see the color plate section.)

layer. The following layers are repeated the same way as the previous layer until the three-dimensional structure is formed as designed.

Photocurable resins generally contain 2–5% photoinitiator that generates free radicals in the presence of UV light. The monomer or oligomer is polymerized when attacked by free radicals, but the reaction stops in the absence of light because the free radicals react with oxygen. The cured depth is given by [167]

$$C_d = D_{\text{penetration}} \ln \left(\frac{E_{\text{max}}}{E_c} \right), \quad (5.11)$$

where $D_{\text{penetration}}$ is the penetration depth of the resin from the Beer–Lambert law, E_{max} is the peak value of exposure (J m^{-2}) of a laser beam with Gaussian

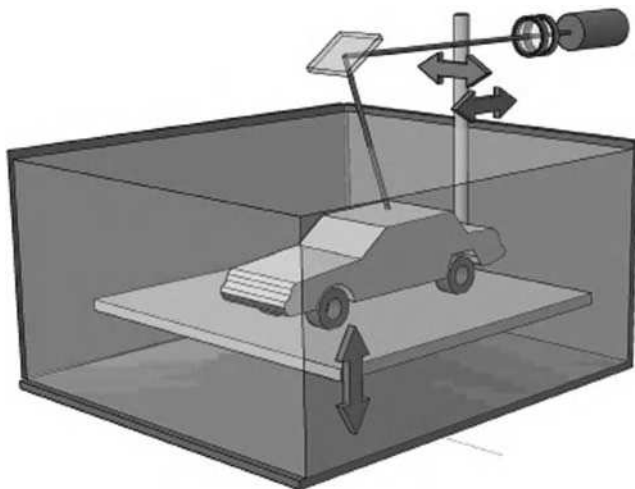


FIGURE 5.25 Schematic representation of the stereolithography process. (For a color version of this figure, see the color plate section.)

distribution of energy, and E_c is the critical energy density below which polymerization will not proceed. The cured line width is given by

$$L_W = \sqrt{2}W_0 \left(\ln \left(\frac{E_{\max}}{E_c} \right) \right)^{1/2}, \quad (5.12)$$

where W_0 is the Gaussian half width of the laser beam.

In this technique, the suspension must have a high solids loading (preferably >50 vol%) and low viscosity. One problem for stereolithography is lack of fine resolution. The dimensional resolution is $200 \mu\text{m}$ [155]. Even though theoretically it is possible to use nano-sized particles, the smallest particles used are generally larger, such as 300 nm [168]. To improve the resolution of the stereolithography technique, both the light source and the particle size need to be refined. This is termed microstereolithography. In microstereolithography, finer resolution can be obtained by adding a UV absorber to reduce the scattering effect of nanoparticles. However, only a few polymers such as acrylates or epoxies can be used. Nano-/microscale composite scaffold materials containing hydroxyapatite (HA) nanoparticles are made [169].

The line structures fabricated with femtosecond laser pulses demonstrate that a feature size down to 400 nm can be achieved and that the resulting structures have a homogeneous shape. Such two-dimensional structures are produced in a TiO_2 resist layer of about $1 \mu\text{m}$ thickness, giving an aspect ratio of ~ 2.5 . More challenging, however, is the photofabrication of three-dimensional structures. For this purpose, TiO_2 resist with a layer thickness of about $10 \mu\text{m}$ is spin-coated

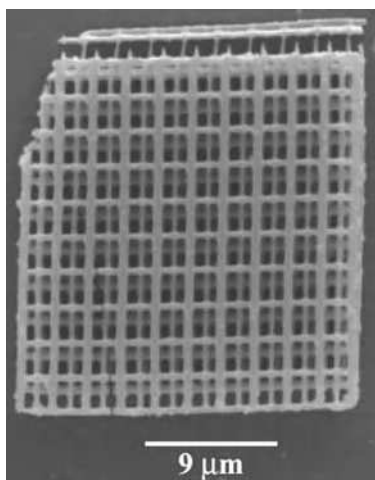


FIGURE 5.26 Scanning electron image of three-dimensional structures fabricated with the spin-coated TiO_2 resist. The periodicity of the structure is $3.5 \mu\text{m}$ with the distance between single layers being $1.2 \mu\text{m}$. The crack in the patterned structure originated from drying and shrinkage of very thick resist on the substrate. The scale bar is $9 \mu\text{m}$ [170]. (Reprinted with permission from Passinger S, Saifullah MSM, Reinhardt C, Subramanian KRV, Chichkov BN, Welland ME. Direct 3D patterning of TiO_2 using femtosecond laser pulses. *Adv Mater* 2007;19: 1218–1221, John Wiley & Sons.)

on a glass substrate. The three-dimensional structures with smooth feature surface are fabricated by scanning a femtosecond laser beam with a speed of $2000 \mu\text{m s}^{-1}$ over the sample. Between each layer, an illumination break of 10 seconds allows the volatile components, possibly lower molecular weight molecules formed during the bond breaking, to leave the structure; it also improves structure quality by reducing distortion. One example structure has a periodicity of $3.5 \mu\text{m}$ with a $1.2 \mu\text{m}$ distance between single layers (Fig. 5.26). By illuminating TiO_2 resist with slightly higher-energy laser pulses, it is possible to produce bulk three-dimensional TiO_2 structures. The periodicity is $1 \mu\text{m}$, and the laser energy is varied between 5 and 18 mW. The distance between the single layers is 350nm [170].

Shrinkage is still a challenging issue for direct patterning of inorganic materials, which occurs during the pyrolysis of polymeric ceramic precursors. This problem is considered to be an obstacle for the practical use of this process. Direct patterning of TiO_2 is reported for the fabrication of photonic crystals. In this case, 50% volume shrinkage is observed during thermal treatment. The barriers for further advancement of this technique have not been thoroughly addressed. The requirement of a high solids loading suspension, the special polymers required, the resolution limitation imposed by the light source, and the time-consuming process all contribute to the slow progress.

5.5.3 Ink-Jet Printing

Ink-jet printing is an important process in light of its potential for low-cost production of large-scale electronic devices. More studies are focused on metal nanoparticle suspensions than on ceramic nanoparticle suspensions because metals (such as gold, silver, and copper) are conductive and more suited for electronic applications. A good review on ink-jet printing has been provided [171]. In ink-jet printing, the ink contains nanoparticles with a relatively high solids loading (30 vol%) and needs to be free from agglomeration; the particles need to have a narrow size distribution. Also, the ratio of the radius of the nozzle aperture and the d_{90} of the particles (the size that 90% of the particles are smaller than) should be at least 50 to avoid blockage of the nozzle [172]. Additives in the ink have important effects on the colloidal and rheological properties of the suspensions [152]. Copper nanoparticles of 35–60 nm in size are ink-jet printed. Figure 5.27 shows complex conductive patterns printed on flexible polyimide substrates using copper nanoparticles prepared with polyvinylpyrrolidone of 40,000 g mol⁻¹ molecular weight. Solvent evaporation from the printed single ink droplet produces a spherical dot pattern with ~ 120 μm diameter. Line patterns are generated by reducing the dot-to-dot distance. Separated dots merge together at a distance of 80 μm , and printing at an interdot distance of 60 μm results in a continuous line with a ~ 130 μm linewidth and relatively smooth edge definition [173]. Another interesting note is that inductive coils, electrostatic-drive motors, and

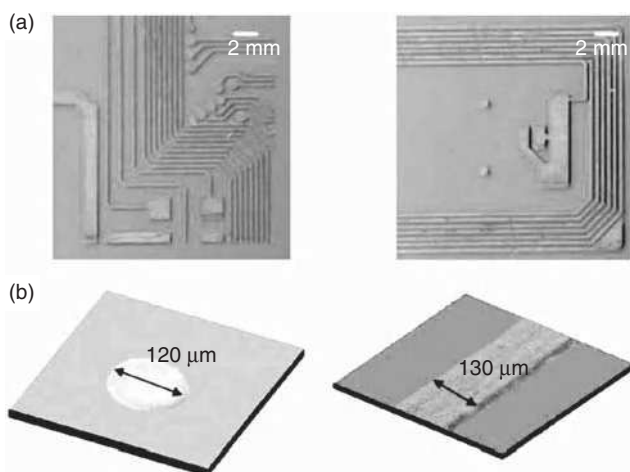


FIGURE 5.27 (a) Conductive patterns ink-jet printed on polyimide substrates using copper nanoparticles and (b) confocal images of a single ink droplet after drying and a single printed line [173]. (Reprinted with permission from Jeong S, Woo K, Kim D, Lim S, Kim JS, Shin H, Xia Y, Moon J. Controlling the thickness of the surface oxide layer on Cu nanoparticles for the fabrication of conductive structures by ink-jet printing. *Adv Funct Mater* 2008;18:679–686, John Wiley & Sons.) (For a color version of this figure, see the color plate section.)

electrothermal actuators with $<100\ \mu\text{m}$ feature size and as many as 400 layers are made from silver and gold nanoparticles with a high conductivity [174]. Cobalt nanoparticles are patterned as a catalyst for carbon nanotube growth [175]. Gold nanoparticles of 1–3 nm size are ink-jet printed into micropillar arrays, helices, zigzag, and microbridge [176, 177].

Indium-doped tin oxide (ITO) nanoparticle suspensions are used for ink-jet printing. The inks are coated on a glass substrate by a spin-coating process and patterned by the ink-jet printing technique using a $50\ \mu\text{m}$ diameter ink-jet nozzle [178]. A reverse microemulsion method is used to produce ZrO_2 ink with 4–6 nm particle size, but the solids loading must be $<1\ \text{vol}\%$ to be of practical use [179]. Ceramic stains are applied onto a ceramic ware using ink-jet printing. Even though the particle size is unknown, it is believed to be from a few to tens of nanometers range [180]. This is a rare case that nanoparticle digital processing is applied to the traditional ceramic field, even though nanoparticle applications in conventional materials have been in existence for many centuries without our realization. A drop on-demand IBM ink-jet printer is used to build a three-dimensional ZrO_2 structure with cavities and overhangs. Carbon ink serves as the support structures and is removed after pyrolysis of the organic vehicle but before sintering [181].

So far ceramic nanoparticle ink-jet printing is not much further advanced than metal nanoparticle systems. The inactive nature of many ceramic systems plays a role in this lag.

5.6 BIO-DERIVED PROCESSES

Biomaterials are an active research area in the materials community. Because of the diverse nature of biomaterials, the forming techniques also encompass a wide range. Here, we introduce two bio-derived processes: bioactive materials and biomimetic materials.

5.6.1 Bioactive Materials

For bioactive materials, microorganisms like bacteria, fungi, cells, or cell-derived subunits (e.g., proteins and enzymes) are used to create specific structures of nanoparticle-based materials. The formed structures are often small. Preparation of such nanocomposites needs to be accomplished at moderate temperatures and physiological conditions, which allow the use of sensitive proteins and even living cells as bioactive agents [182]. By avoiding harsh preparation conditions (high temperature, organic solvents) that could lead to denaturation, bacteria, fungi, and yeast cells can be incorporated while maintaining their viability. Metal oxide nanoparticles are solidified by gelling at room temperature in the presence of admixed cellular systems. SiO_2 and TiO_2 can be polymerized with a flexible polymer, such as PDMS or polytetramethyloxide, at the molecular level to form an inorganic–organic nanohybrid. During the gel formation, the biocomponent is

immobilized within the inorganic network. The immobilization of the biocomponents can be controlled by the biocomponent to oxide ratio or by the addition of pore-forming agents. After drying of the lyogel and removal of the solvent, xerogels are formed as bulk products. For TiO_2 nanoparticles, the polymers are subjected to hot HCl solution treatment to form anatase and eventually nano-sized bone-like apatites. Depending on the organic residue groups, the chemical and structural properties of the composites can be varied over a wide range. Even a direct covalent linkage of biological residues to the oxide matrix can be realized.

5.6.2 Biomimetic Materials

Biomimetic materials are materials and composites that exhibit organizational and functional specificity exemplified by biological minerals such as bones, shells, and teeth. Building three-dimensional structures by the biomimetic approach is to construct a structure inside or on a scaffold using building blocks that represent a significant volume fraction of the intended structure. The biomimetic shaping of nanoparticle-based materials represents the use of nanoparticle building blocks in forming higher order architectures [183]. Approaches such as shape-directed assembly [184] and programmed assembly [185] are either only suitable for two-dimensional assembly or too immature for meaningful three-dimensional structure construction. Only template-directed methods with nanoparticles spatially confined within the organized interiors of organic matrices, such as bacterial superstructures or polymer sponges, or on the surfaces of organic substrates, such as coated polymer beads or bacterial membranes, have good potentials to produce three-dimensional nanostructures.

One example of biomimetic materials is macroscopic threads of organized bacterial superstructures. A typical bacterial thread can contain in excess of 10^{10} cells and 50,000 filaments arranged as a cell [183]. The reversible swelling of unmineralized threads in the presence of inorganic nanoparticles (SiO_2 , Fe_3O_4 , and CdS) has been exploited in the fabrication of organized bacterial mineral composites. Negatively charged SiO_2 and Fe_3O_4 nanoparticle suspensions give good infiltration and replication of the bacterial superstructure. The mineralized and air-dried fibers consist of a close-packed array of 0.5 μm diameter multicellular bacterial filaments coated with a 30–70 nm thick layer of aggregated nanoparticles. For both SiO_2 and Fe_3O_4 , the repulsive forces between the nanoparticles and cell membranes (which are also negatively charged due to the predominance of carboxylic acid groups) facilitate infiltration throughout the swollen organic superstructure. When the thread is redrawn from the nanoparticle suspension, nanoparticles trapped between or adhering to the bacterial filaments are retained and consolidated within the interfilament spaces on drying. In contrast, neutral ligand-capped CdS nanoparticles, although internalized to some extent, are preferentially localized on the surface of the thread, and positively charged TiO_2 nanoparticles do not penetrate the swollen fiber at all. Instead, TiO_2 nanoparticles are deposited on the external surface of the bacterial thread to produce a

coherent surface coating with uniform thickness. One key requirement for the formation of a continuous wall structure from the entrapped nanoparticles is that the nanoparticles bond into an extended network and that the nanostructure does not collapse upon removal of the organic matrix. This is achieved for amorphous SiO_2 nanoparticles, which produce intact inorganic fibers with ordered macroporous channels after the bacterial template is removed by calcination. In contrast, bacterial threads infiltrated with crystalline Fe_3O_4 nanoparticles do not produce stable porous inorganic replicas of the multicellular superstructure. The nanoparticles remain only loosely associated after calcination. The biomimetic process has been used to deposit nano-sized bone-like apatite on fine polymer fibers, which are textured into a three-dimensional knit framework (Fig. 5.28) [186].

For nanostructures, the biomimetic approach generally works well, provided that there is sufficient chemical and interfacial complementarity between the organic and inorganic components. However, inorganic mineralization of ordered structures extending beyond 100 nm can be difficult to achieve at high volume fractions because the supersaturation level attainable within the template is too

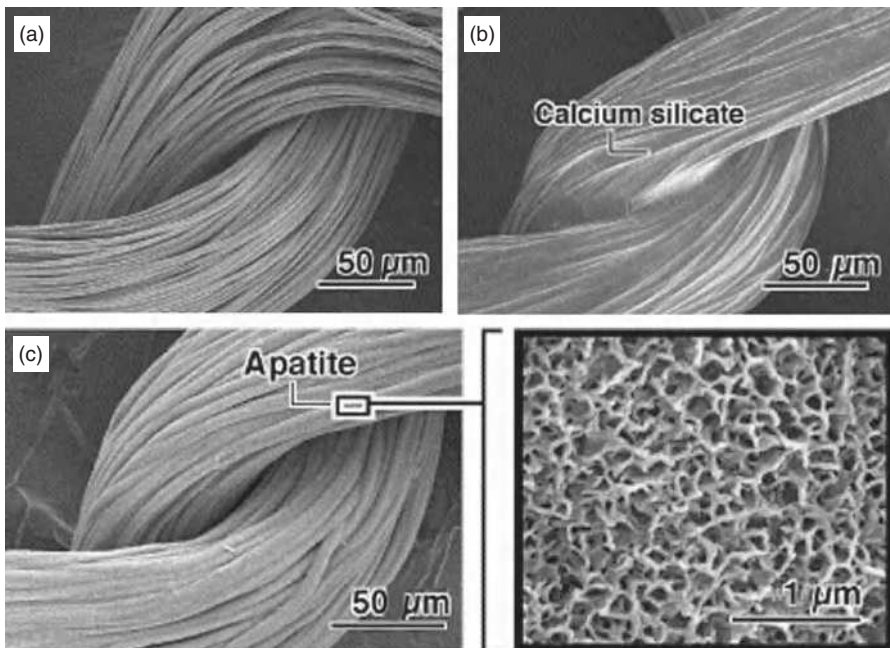


FIGURE 5.28 Scanning electron photographs of the surface of a woven yarn of ethylene–vinyl alcohol copolymer fibers before (a), after calcium silicate coating (b), and after subsequent soaking in a simulated body fluid for 2 days (c) [186]. (Reprinted with permission from Kokubo T, Kim H-M, Kawashita M. Novel bioactive materials with different mechanical properties. *Biomaterials* 2003;24:2161–2175, Elsevier.)

low to produce a stable replica of the void space. One possibility is to use continuous flow of precursor solutions rather than batch processing. Another major limitation is that the nanoparticles are randomly arranged with respect to each other within the organized spaces of the template and show no registry with the template itself. This is not unexpected given that the particles are isotropic and repulsive interactions are used predominantly for space filling. Thus, although complicated macro-organized templates can be replicated, at the local scale the ordering is random.

5.7 SUMMARY

Shaping of nanoparticles into three-dimensional components is a very diverse process. It ranges from dry compaction, which deals with particles up to a few hundred grams at a time, to wet forming processes involving very dilute suspensions that manipulate particles one at a time. The characteristics of different forming techniques are summarized in Table 5.1. Each technique has its own strengths as well as limitations to meet the specific demands of the task on hand. However, the characteristics of an optimal processing method are universal. The technique should offer high reliability and repeatability on the three-dimensional structure properties and minimize processing steps. Although some of these specifications are obvious, the maximization of a component's properties might be in opposition to the efficiency of the process. The best practice is to achieve the maximum performance within the constraints of the processing cost.

Dry forming and semidry forming processes mainly stem from conventional powder processing techniques and hold the greatest potential for large-scale production of nanoparticle materials. The existing tools and knowledge can be quickly extended to address specific nanoparticle issues. These relatively mature approaches are ideally suited for making high-density and modest homogeneity components. The applications are often found in structural or functional applications that require dense components.

Wet processing holds the greatest potential for solving nanoparticle agglomeration issues and providing uniform microstructures. This general category includes pressure casting, tape casting, freeze casting, gel casting, and electrophoretic deposition. For all the wet forming processes except for electrophoretic deposition, the ability to achieve a high solids loading suspension is the key for the application of the techniques. Even though specific colloidal processing issues can be challenging, the potential for offering uniform nanostructures and homogeneous distributions of multiple compositions at the individual particle level is very attractive.

As an extension of the conventional forming techniques, one emerging class of methods is digital processing, which includes direct writing, stereolithography, and ink-jet printing. These forming methods yield complex-shaped objects directly from a computer-created three-dimensional representation through

TABLE 5.1 Comparison of Different Shaping Techniques

| | Types | Advantages | Disadvantages | Component size |
|--------------------|-------------------------------|---|--|---|
| Dry processing | Uniaxial pressing | Simple, low cost, high efficiency | Simple shape, density gradient | Centimeter to millimeter |
| | Cold isostatic pressing | Improved uniformity, increased part complexity | Complex equipment, limited peak pressure | Centimeter to millimeter |
| | Superhigh pressure compaction | High efficiency, high density | Cracking, complex and specialized equipment and tooling, mechanism not well understood | Centimeter to millimeter |
| | Dynamic compaction | High efficiency, high density | Cracking, complex and specialized equipment and tooling, mechanism not well understood | Centimeter to millimeter |
| Semidry processing | Molding | Complex shape, high efficiency, uniform density | High organic content, complex organic particle system | Centimeter to millimeter |
| | Extrusion | Complex cross section, high efficiency, textured microstructure | High organic content, defects | Centimeter to millimeter |
| Wet processing | Casting | Complex shapes, purposely designed graded structure | Low efficiency, complex drying process, preferential orientation | Decimeter to millimeter |
| | Tape casting | Thin sheet, high efficiency | High organic content, defects, problematic drying, preferential orientation | 5–1000 μm thickness, decimeter width, meter long |

(Continued)

TABLE 5.1 (Continued)

| | Types | Advantages | Disadvantages | Component size |
|------------------------|----------------------------|--|--|--------------------------|
| | Freeze casting | Uniform microstructure, complex shape, low organic content | Low viscosity and high solids loading suspension, limited size | Centimeter to millimeter |
| | Gel casting | Complex shape, uniform microstructure | Cracking, low green strength | Centimeter to millimeter |
| | Electrophoretic deposition | Density independent of particle size, complex shape, low solids loading suspension | Gas bubble-induced pores | Centimeter to millimeter |
| Digital processing | Robocasting | Complex three-dimensional shape | High organic content, low efficiency | Centimeter to millimeter |
| | Stereolithography | Complex three-dimensional shape | Special polymer, large shrinkage, low resolution | Centimeter to submicron |
| | Ink-jet printing | Complex two-dimensional structure, high resolution | Narrow particle size distribution | Centimeter to micron |
| Bio-derived processing | Bioactive materials | Unique microstructure, wide range of property variation | Limited to special nanoparticles | Submicron to micron |
| | Biomimetic materials | Higher order architecture | Nanoparticle arrangement has no registry | Submicron to micron |

controlled deposition of nanoparticles. The focus of these new techniques is for complex but near-net-shaped prototypes. When the component quantity is low but the shape is complex, digital processing offers an ideal alternative in three-dimensional component forming. Some of these techniques remain in the research labs for improvement; others have become available in the manufacturing sector for large quantity production. These techniques hold the key to producing complex three-dimensional nanostructures, and improvements can be expected to meet the needs of very special applications.

The increasing demand for the ability to manipulate nanoparticles at the individual particle or molecule level has motivated research in bio-derived processes. During the past decade, many researchers have participated in this quest and generated a multitude of new methods. Although these efforts open up a whole new array of nanoparticle processing techniques, most of the methods remain at the conceptual stage, either due to processing difficulties or low efficiency. With the certainty that new discoveries will continue to be made in this area, the commercialization of these techniques still has a long way to go. Nevertheless, these are exciting fields that determine our ultimate ability to manipulate nanoparticles. The efforts will also lead nanoparticle processing into a more controlled and design-focused stage by intelligently utilizing the surface properties of nanoparticle packings. Many unique properties are expected to come from this refined shaping paradigm.

QUESTIONS

1. For 1 g 50 nm particles and 1 g 5 μm particles, based on random packing principle and assuming spherical shapes, calculate the contact points among the particles and the surface area for each material. Assume the materials density is 4.0 g cm^{-3} .
2. Why do nanoparticles agglomerate more easily than micron-sized particles?
3. What are the potential strategies to increase the green density during dry forming process? Explain how each of them works.
4. For semidry forming process, do you expect the green sample after the binder removal to have higher or lower density than the micron-size counterparts? Why?
5. In a solution, how does the surface charge of a particle arise?
6. Schematically describe the electrical double-layer structure and the electrical potential of a particle in a polar solvent.
7. Describe DLVO theory in detail.
8. During wet forming processes, which ones have an external field/force to increase the nanoparticle packing density? Which ones don't? How do these affect the sample densities?
9. Give two examples of digital processing techniques for nanoparticle-based systems and explain how each of the processes work.
10. What are the unique attributes of bio-derived forming processes?

REFERENCES

1. Mayo MJ, Hagne DC, Chen DJ. Processing nanocrystalline ceramics for applications in superplasticity. *Mater Sci Eng A* 1993;166:145–159.
2. German RM. *Powder Metallurgy and Particulate Materials Processing*. Princeton, NJ: Metal Powder Industries Federation; 2005.
3. Rahaman MN. *Ceramic Processing and Sintering*. 2nd ed. New York, NY: Marcel Dekker, Inc.; 2003.
4. Reed JS. *Principles of Ceramic Processing*. New York, NY: John Wiley & Sons, Inc.; 1995.
5. German RM. *Particle Packing Characteristics*. Princeton, NJ: Metal Powder Industries Federation; 1989. pp. 219–246.
6. Ahn J-P, Park J-K, Huh M-Y. Effect of green density on the subsequent densification and grain growth of ultrafine SnO₂ powder during isochronal sintering. *J Am Ceram Soc* 1997;80:2165–2167.
7. Kim J, Lee HW. New opportunity for nanopowder forming processes. *Adv Ceram Compos Key Eng Mater* 2003;247:35–38.
8. Lee JS, Kang YS, Kwon SK, Cha BH, Qin XY. A new processing route for net-shaped nanoparticulate materials. *Adv Powder Technol* 2004;15:639–655.
9. Teng M-H, Tsai S-W, Chiou W-A. Magnetic packing of graphite encapsulated nickel nanoparticles. *J Alloys Compd* 2010;495:488–490.
10. Ruys AJ, Mai Y-W. The nanoparticle-coating process: a potential sol-gel route to homogeneous nanocomposites. *Mater Sci Eng A* 1999;265:202–207.
11. Li W, Lannutti JJ. Cold isostatic compaction of nano-size powders: surface densification and dimensional asymmetry. *J Mater Res* 2002;17:2794–2801.
12. Trunec M, Maca K. Compaction and pressureless sintering of zirconia nanoparticles. *J Am Ceram Soc* 2007;90:2735–2740.
13. Mayo MJ. Processing of nanocrystalline ceramics from ultrafine particles. *Int Mater Rev* 1996;41:85–115.
14. Raming TP, Winnubst AJA, van Zyl WE, Verweij H. Densification of zirconia-hematite nanopowders. *J Eur Ceram Soc* 2003;23:1053–1060.
15. Shi JL, Gao JH, Li BS, Yen TS. Processing of nano-Y-TZP/Al₂O₃ composites. II: compaction and sintering behavior of nano-Y-TZP/Al₂O₃ composite powders. *J Eur Ceram Soc* 1995;15:967–913.
16. Gonzalez EJ, Hockey B, Piermarini GJ. High pressure compaction and sintering of nano-size gamma-Al₂O₃ powder. *Mater Manuf Processes* 1996;11:951–967.
17. Gao L, Li W, Wang HZ, Zhou JX, Chao ZJ, Zai QZ. Fabrication of nano Y-TZP materials by superhigh pressure compaction. *J Eur Ceram Soc* 2001;21:135–138.
18. Serdyuk GG, Sakhnenko AV, Svistun LI. Manufacturing of powdered metals, and product organization, industrial use of the high-rate (impact) pressing of metallic powders. *Powder Metall Met Ceram* 2000;39:514–519.
19. Raminga TP, van Zyl WE, Carton EP, Verweij H. Sintering, sinter forging and explosive compaction to densify the dual phase nanocomposite system Y₂O₃-doped ZrO₂ and RuO₂. *Ceram Int* 2004;30:629–634.
20. Jaramillo D, Hinojosa G, Hallen JM, Balmori H, Inal OT. Mechanical and microstructural characterization of Al-SiC composite material obtained by dynamic compaction. *Key Eng Mater* 1997;127:977–984.
21. Venz GJ, Killen PD, Page NW. Hot shock compaction of nanocrystalline alumina. *J Mater Sci* 2003;38:2935–2944.

22. Rabe T, Prummer R, Wasche R. Explosive compaction of nanosized tin-powders. *Mater Sci Forum* 1997;235–238:285–290.
23. Nagarathnam K, Trostle D, Kruczynski D, Massey D. Materials behavior and manufacturing aspects of high pressure combustion driven compaction P/M components. In: *Advances in Powder Metallurgy & Particulate Materials—2004, Proceedings of the 2004 International Conference on Powder Metallurgy & Particulate Materials, June 13–17, Chicago, Illinois; 2004*. Part 9, 9–2 15pp.
24. Gallas MR, Hockey B, Pechenik A, Piermarini GJ. Fabrication of transparent gamma-Al₂O₃ from nanosize particles. *J Am Ceram Soc* 1994;77:2107–2112.
25. Kondo K, Sawai S. Fabricating nanocrystalline diamond ceramics by a shock compaction method. *J Am Ceram Soc* 1990;73:1983–1991.
26. Gallas MR, Rosa AR, Costa TH, da Jornada JAH. High pressure compaction of nanosize ceramic powders. *J Mater Res* 1997;12:764–768.
27. Costa TMH, Gallas MR, Benvenuti EV, da Jornada JAH. Study of nanocrystalline gamma-Al₂O₃ produced by high-pressure compaction. *J Phys Chem B* 1999;103:4278–4284.
28. Dimitrov H, Blazquez JS, Latuch J, Kulik T. Microstructure and mechanical properties of bulk nanocrystalline Al₈₈Mm₅Ni₅Fe₂ alloy consolidated at a high pressure. *Intermetallics* 2007;15:891–900.
29. Yan ZQ, Chen F, Cai YX, Cui L. High velocity compaction and characteristics of Ti powder. *Acta Metall Sinica* 2010;46:227–232.
30. Sadangi RK, Shukla V, Kear BH. Processing and properties of ZrO₂(3Y₂O₃)-Al₂O₃ nanocomposites. *Int J Refract Met Hard Mater* 2005;23:363–368.
31. Glade SC, Thadhani NN. Shock consolidation of mechanically alloyed amorphous Ti-Si powders. *Metall Mater Trans A* 1995;26:2565–2569.
32. Sadangi RK, Shukla V, Kear BH. Processing and properties of ZrO₂(3Y(2)O(3))-Al₂O₃ nanocomposites. *Int J Refract Met Hard Mater* 2005;23:363–368.
33. Sethi G, Myers NS, German RM. An overview of dynamic compaction in powder metallurgy. *Int Mater Rev* 2008;53:219–234.
34. Zhao Z, Li X-J, Tao G. Manufacturing nano-alumina particle-reinforced copper alloy by explosive compaction. *J Alloys Compd* 2009;478:237–239.
35. Dai C, Thadhani NN. Shock-compression response of magnetic Fe₃O₄ nanoparticles. *Acta Mater* 2011;59:785–796.
36. Sachan M, Majetich SA. Combustion-driven compactions of nanostructured Sm–Co and Fe mixtures. *IEEE Trans Magn* 2005;41:3874–3876.
37. German R, Bose A. *Injection Molding of Metals and Ceramics*. Princeton, NJ: Metal Powder Industries Federation; 1997.
38. German RM. *Powder Injection Molding – Design and Applications*. State College, PA: Innovation Materials Solutions; 2003.
39. Gadow R, Kern F. Pressureless sintering of injection molded zirconia toughened alumina nanocomposites. *J Ceram Soc Jpn* 2006;114:958–962.
40. Merz L, Rath S, Piotter V, Ruprecht R, Ritzhaupt-Kleissl J, Hausselt J. Feedstock development for micro powder injection molding. *Microsyst Technol* 2002;8:129–132.
41. Merz L, Rath S, Piotter V, Ruprecht R, Hausselt J. Powder injection molding of metallic and ceramic microparts. *Microsyst Technol* 2004;10:202–204.
42. Yu PC, Li QF, Fuh JYH, Li T, Ho PW. Microinjection molding of micro gear using nano-sized zirconia powder. *Microsyst Technol* 2009;15:401–406.
43. Imasu J, Sakka Y. Large-scale patterning of TiO₂ nano powders using micro molds. *J Ceram Soc Jpn* 2007;115:697–700.

44. Radha B, Kulkarni GU. Micro- and nanostripes of self-assembled Au nanocrystal superlattices by direct micromolding. *Nano Res* 2010;3:537–544.
45. Hua Z, Zhou DM, Greenberg R, Thundat T. Nanopowder molding method for creating implantable high-aspect-ratio electrodes on thin flexible substrate. *Biomaterials* 2006;27:2009–2017.
46. Kaya C, Butler EG. Zirconia-toughened alumina ceramics of helical spring shape with improved properties from extruded sol-derived pastes. *Scr Mater* 2003;48:359–364.
47. Kaya C, Blackburn S. Extrusion of ceramic tubes with complex structures of non-uniform curvatures made from nano-powders. *J Eur Ceram Soc* 2004;24:3663–3670.
48. Karaman I, Haouaoui M, Maier HJ. Nanoparticle consolidation using equal channel angular extrusion. *J Mater Sci* 2007;42:1561–1576.
49. Kaya C, Butler EG. Near net-shape manufacturing of alumina/zirconia high temperature ceramics with fine scale aligned multiphase microstructures using co-extrusion. *J Mater Process Technol* 2003;135:137–143.
50. Fan H-T, Xu X-J, Ma X-K, Zhang T. Preparation of LaFeO₃ nanofibers by electrospinning for gas sensors with fast response and recovery. *Nanotechnology* 2011;22:115502 7pp.
51. Huang J, Wang D, Hou H, You T. Electrospun palladium nanoparticle-loaded carbon nanofibers and their electrocatalytic activities towards hydrogen peroxide and NADH. *Adv Funct Mater* 2008;18:441–448.
52. Chuangchote S, Sagawa T, Yoshikawa S. Efficient dye-sensitized solar cells using electrospun TiO₂ nanofibers as a light harvesting layer. *Appl Phys Lett* 2008;93:033310 3pp.
53. Liu H, Yang J, Liang J, Huang Y, Tang C. ZnO nanofiber and nanoparticle synthesized through electrospinning and their photocatalytic activity under visible light. *J Am Ceram Soc* 2008;91:1287–1291.
54. Erisken C, Kalyon DM, Wang H. A hybrid twin-screw extrusion/electrospinning method to process nanoparticle-incorporated electron spun nanofibres. *Nanotechnology* 2008;19:165302 8pp.
55. Ozkan S, Gevgilili H, Kalyon DM, Kowalczyk J, Mezger M. Twin-screw extrusion of nano-alumina-based simulants of energetic formulations involving gel-based binders. *J Energetic Mater* 2007;25:173–201.
56. Cesarano JIII, Aksay IA. Processing of highly concentrated aqueous alpha-alumina suspensions stabilized with poly-electrolytes. *J Am Ceram Soc* 1988;71:1062–1067.
57. Lewis JA. Colloidal processing of ceramics. *J Am Ceram Soc* 2000;83:2341–2359.
58. Cesarano JIII, Aksay IA, Bleier A. Stability of aqueous alpha-alumina suspensions with poly(methacrylic acid) polyelectrolyte. *J Am Ceram Soc* 1988;71:250–255.
59. Napper D. *Polymeric Stabilization of Colloidal Dispersions*. London: Academic Press; 1983. p. 8.
60. Bohn JJ, Ben-Moshe M, Tikhonov A, Qu D, Lamont DN, Asher SA. Charge stabilized crystalline colloidal arrays as templates for fabrication of non-close-packed inverted photonic crystals. *J Colloid Interface Sci* 2010;344:298–307.
61. Iijima M, Kamiya H. Surface modification for improving the stability of nanoparticles in liquid media. *KONA Powder Part J* 2009;27:119–129.
62. Lu K, Kessler CS, Davis RM. Optimization of a nanoparticle suspension for freeze casting. *J Am Ceram Soc* 2006;89:2459–2465.
63. Lu K. Theoretical analysis of colloidal interaction energy in nanoparticle suspensions. *Ceram Int* 2008;34:1353–1360.
64. Vincent B, Luckham PF, Waite FA. Effect of free polymer on the stability of sterically stabilized dispersions. *J Colloid Interface Sci* 1980;73:508–521.

65. Vincent B, Edwards J, Emmett S, Jones A. Depletion flocculation in dispersions of sterically-stabilized particles (soft spheres). *Colloids Surf* 1986;18:261–281.
66. Sigmund W, Bell N, Bergstrom L. Novel powder processing methods for advanced ceramics. *J Am Ceram Soc* 2000;83:1557.
67. Cho J, Dogan F. Colloidal processing of load lanthanum zirconate titanate ceramic. *J Mat Sci* 2001;36:2397–2403.
68. Tallon C, Limacher M, Franks GV. Effect of particle size on the shaping of ceramics by slip casting. *J Eur Ceram Soc* 2010;30:2819–2826.
69. Singh B, Bhattacharjee S, Besra L, Sengupta DK. Evaluation of dispersibility of aqueous alumina suspension in presence of Darvan. *Ceram Int* 2004;30:939–946.
70. Lu K, Kessler CS. Colloidal dispersion and rheology study of nanoparticles. *J Mater Sci* 2006;41:5613–5618.
71. Wagner NJ, Bender JW. The role of nanoscale forces in colloid dispersion rheology. *MRS Bull* 2004;29:100–106.
72. Krieger IM, Dougherty M. A mechanism for non-newtonian flow in suspensions of rigid spheres. *Trans Soc Rheol* 1959;3:137–152.
73. Dietrich A, Neubrand A. Effects of particle size and molecular weight of polyethylenimine on properties of nanoparticulate silicon dispersions. *J Am Ceram Soc* 2001;84:806–812.
74. German RM. *Particle Packing Characteristics*. Princeton, NJ: Metal Powder Industries Federation; 1989. pp. 89–119.
75. Liu D. Particle packing and rheological property of highly-concentrated ceramic suspensions: Φ_m determination and viscosity prediction. *J Mat Sci* 2000;35:5503–5507.
76. Atkinson A, Segal DL. Some recent developments in aqueous sol-gel processing. *J Sol-Gel Sci Technol* 1998;13:133–139.
77. Vasylykiv O, Sakka Y. Synthesis and sintering of zirconia nano-powder by non-isothermal decomposition from hydroxide. *J Ceram Soc Jpn* 2001;109:500–505.
78. Morsi K, Keshavan H, Bal S. Processing of grain-size functionally gradient bioceramics for implant applications. *J Mater Sci* 2004;15:191–197.
79. Kaya C, Butler EG. Plastic forming and microstructural development of α -alumina ceramics from highly compacted green bodies using extrusion. *J Eur Ceram Soc* 2002;22:1917–1926.
80. Huisman W, Graule T, Gauckler LJ. Centrifugal slip casting of zirconia (TZP). *J Eur Ceram Soc* 1994;13:33–39.
81. Shevchenko AV, Dudnik EV, Ruban AK, Zaitseva ZA, Lopato LM. Functional graded materials based on ZrO_2 and Al_2O_3 . *Powder Metall Met Ceram* 2003;42:145–153.
82. Leo G, Chushkin Y, Luby S, Majkova E, Kostic I, Ulmeanu M, Luches A, Giersig M, Hilgendorff M. Ordering of free-standing Co nanoparticles. *Mater Sci Eng C* 2003;23:949–952.
83. Mistler RE, Twinn ER. *Tape Casting: Theory and Practice*. Westerville, OH: The American Ceramic Society; 2000.
84. Lee J-H, Yonathan P, Yoon D-H, Kim W-J, Park J-Y. Dispersion stability and its effect on tape casting on solvent-based SiC slurries. *J Ceram Process Res* 2009;10:301–307.
85. Zuo KH, Jiang DL, Zhang JX, Lin QL. Forming nanometer TiO_2 sheets by nonaqueous tape casting. *Ceram Int* 2007;33:477–481.
86. Vinothini V, Singh P, Balasubramanian M. Optimization of barium titanate nanopowder slip for tape casting. *J Mater Sci* 2006;41:7082–7087.
87. Luo LH, Tok AIY, Boey FYC. Aqueous tape casting of 10 mol%- Gd_2O_3 -doped CeO_2 nano-particles. *Mater Sci Eng A* 2006;429:266–271.

88. Reddy SB, Singh PP, Raghu N, Kumar V. Effect of type of solvent and dispersant on nano PZT powder dispersion for tape casting slurry. *J Mater Sci* 2002;37:929–934.
89. Lim D-S, You D-H, Choi H-J, Lim S-H, Jang H. Effect of CNT distribution on tribological behavior of alumina-CNT composites. *Wear* 2005;259:539–544.
90. Vozdecky P, Roosen A, Knieke C, Peukert W. Direct tape casting of nanosized Al_2O_3 slurries derived from autogenous nanomilling. *J Am Ceram Soc* 2010;93:1313–1319.
91. Bodnarchuk M, Kovalenko MV, Pichler S, Fritz-Popovski G, Hesser G, Heiss W. Large-area ordered superlattices from magnetic wustite/cobalt ferrite core/shell nanocrystals by doctor blade casting. *ACS Nano* 2010;4:423–431.
92. Koch D, Andresen L, Schmedders T, Grathwohl G. Evolution of porosity by freeze casting and sintering of sol-gel derived ceramics. *J Sol-Gel Sci Tech* 2003;26:149–152.
93. Jones RW. Near net shape ceramics by freeze casting. *Ind Ceram* 2000;20:117–120.
94. Laurie J, Bagnall CM, Harris B, Jones RW, Cooke RG, Russell-Floyd RS, Wang TH, Hammett FW. Colloidal suspensions for the preparation of ceramics by a freeze casting route. *J Non-Cryst Solids* 1992;147–148:320–325.
95. Bollman H. Unique new forming technique. *Ceram Age* 1957;791:36–38.
96. Novich BE, Sundback CA, Adams RW. Quickset injection molding of high-performance ceramics. In: Cima MJ, editor. *Forming Science and Technology for Ceramics: Ceramic Transactions*. Westerville, OH: American Ceramic Society; 1992. Vol 26, pp. 157–164.
97. Bergstrom L, Schilling CH, Aksay IN. Consolidation behavior of flocculated alumina suspensions. *J Am Ceram Soc* 1992;75:3305–3314.
98. Chang JC, Velamakanni BV, Lange FF, Pearson DS. Centrifugal consolidation of $\text{Al}_2\text{O}_3/\text{ZrO}_2$ composite slurries vs. interparticle potentials: particle packing and mass segregation. *J Am Ceram Soc* 1992;74:2201–2204.
99. Li W, Lu K, Walz JY. Freeze casting of porous materials-A review of critical factors in microstructure evolution. *Int Mater Rev* 2012;57:37–60.
100. Tynova E, Gregorova E, Demjan J, Pabst W. Alumina ceramics prepared by enzyme-free direct coagulation casting. *Key Eng Mater* 2004;264–268:229–232.
101. Koch D, Andresen L, Schmedders T, Grathwohl G. Evolution of porosity by freeze casting and sintering of sol-gel derived ceramics. *J Sol-Gel Sci Technol* 2003;26:149–152.
102. Sofie SW, Dogan F. Freeze casting of aqueous alumina slurries with glycerol. *J Am Ceram Soc* 2001;84:1459–1464.
103. Deville S. Freeze-casting of porous ceramics: a review of current achievements and issues. *Adv Eng Mater* 2008;10:155–169.
104. Dogan F, Sofie SW. Microstructural control of complex-shaped ceramics processed by freeze casting. *CFI-Ceram Forum Int* 2002;79:E35–E38.
105. Rak ZS. Advanced shaping techniques in advanced ceramics. *CFI-Ceram Forum Int* 2000;77:E25–E26.
106. Araki K, Halloran JW. New freeze-casting technique for ceramics with sublimable vehicles. *J Am Ceram Soc* 2004;87:1859–1863.
107. Araki K, Halloran JW. Room-temperature freeze casting for ceramics with nonaqueous sublimable vehicles. *J Am Ceram Soc* 2004;87:2014–2019.
108. Tang J, Chen YF, Wang H, Liu HL, Fan QS. Preparation of orientated porous silicon carbide bodies by freeze-casting process. *Key Eng Mater* 2005;280–283:1287–1290.
109. Lu K, Kessler CS. Nanoparticle colloidal suspension optimization and freeze-cast forming. *Ceram Eng Sci Proc* 2006;27:1–10.
110. Mukai SR, Nishihara H, Tamon H. Formation of monolithic silica gel microhoneycombs (SMHs) using pseudosteady state growth of microstructural ice crystals. *Chem Commun* 2004;7:874–875.

111. Mukai SR, Nishihara H, Tamon H. Porous properties of silica gels with controlled morphology synthesized by unidirectional freeze-gelation. *Microporous Mesoporous Mater* 2003;63:43–51.
112. Deville S, Saiz E, Nalla RK, Tomsia AP. Freezing as a path to build complex composites. *Science* 2006;311:515–518.
113. Deville S, Maire E, Lasalle A, Bogner A, Gauthier C, Leloup J, Guizard C. In situ X-ray radiography and tomography observations of the solidification of aqueous alumina particle suspensions-part I: initial instants. *J Am Ceram Soc* 2009;92:2489–2496.
114. Deville S, Maire E, Lasalle A, Bogner A, Gauthier C, Leloup J, Guizard C. In situ X-ray radiography and tomography observations of the solidification of aqueous alumina particle suspensions-part II: steady state. *J Am Ceram Soc* 2009;92:2497–2503.
115. Landi E, Valentini F, Tampieri A. Porous hydroxyapatite/gelatine scaffolds with ice-designed channel-like porosity for biomedical applications. *Acta Biomater* 2008;4:1620–1626.
116. Gannon P, Sofie S, Deibert M, Smith R, Gorokhovskiy V. Thin film YSZ coatings on functionally graded freeze cast NiO/YSZ SOFC anode supports. *J Appl Electrochem* 2009;39:497–502.
117. Zhang YM, Hu LY, Han JC, Jiang ZH. Freeze casting of aqueous alumina slurries with glycerol for porous ceramics. *Ceram Int* 2010;36:617–621.
118. Rahaman MN, Fu Q. Manipulation of porous bioceramic microstructures by freezing of suspensions containing binary mixtures of solvents. *J Am Ceram Soc* 2008;91:4137–4140.
119. Zuo KH, Zeng YP, Jiang DL. Effect of polyvinyl alcohol additive on the pore structure and morphology of the freeze-cast hydroxyapatite ceramics. *Mater Sci Eng C* 2010;30:283–287.
120. Pekor CM, Kisa P, Nettleship I. Effect of polyethylene glycol on the microstructure of freeze-cast alumina. *J Am Ceram Soc* 2008;91:3185–3190.
121. Sofie SW. Fabrication of functionally graded and aligned porosity in thin ceramic substrates with the novel freeze-tape-casting process. *J Am Ceram Soc* 2007;90:2024–2031.
122. Statham MJ, Hammett E, Harris B, Cooke RG, Jordan RM, Roche A. Net-shape manufacture of low-cost ceramic shapes by freeze-gelation. *J Sol-Gel Sci Technol* 1998;13:171–175.
123. Deville S, Saiz E, Tomsia AP. Ice-templated porous alumina structures. *Acta Mater* 2007;55:1965–1974.
124. Waschki T, Oberacker R, Hoffmann MJ. Control of lamellae spacing during freeze casting of ceramics using double-side cooling as a novel processing route. *J Am Ceram Soc* 2009;92:S79–S84.
125. Cooney MJ, Lau C, Windmeisser M, Liaw BY, Klotzbach T, Minter SD. Design of chitosan gel pore structure: towards enzyme catalyzed flow-through electrodes. *J Mater Chem* 2008;18:667–674.
126. Parks WM, Guo YB. A casting based process to fabricate 3D alginate scaffolds and to investigate the influence of heat transfer on pore architecture during fabrication. *Mater Sci Eng C* 2008;28:1435–1440.
127. Liu G, Zhang D, Meggs C, Button TW. Porous Al₂O₃-ZrO₂ composites fabricated by an ice template method. *Scripta Mater* 2010;62:466–468.
128. Fu Q, Rahaman MN, Dogan F, Bal BS. Freeze casting of porous hydroxyapatite scaffolds-I. processing and general microstructure. *J Biomed Mater Res B* 2008;86B:514–522.
129. Ren LL, Zeng YP, Jiang DL. Fabrication of gradient pore TiO₂ sheets by a novel freeze-tape-casting process. *J Am Ceram Soc* 2007;90:3001–3004.

130. Deville S, Maire E, Lasalle A, Bogner A, Gauthier C, Leloup J, Guizard C. Influence of particle size on ice nucleation and growth during the ice-templating process. *J Am Ceram Soc* 2010;93:2507–2510.
131. Zhang YM, Hu LY, Han JC. Preparation of a dense/porous bilayered ceramic by applying an electric field during freeze casting. *J Am Ceram Soc* 2009;92:1874–1876.
132. Omatete OO, Young AC, Janney MA. Dilute gelcasting alumina suspensions. *Ceram Trans* 1990;12:537–544.
133. Ramay HRR, Zhang M. Biphasic calcium phosphate nanocomposite porous scaffolds for load-bearing bone tissue engineering. *Biomaterials* 2004;25:5171–5180.
134. Liu YQ, Gao LA. Dispersion of aqueous alumina suspensions using copolymers with synergistic functional groups. *Mater Chem Phys* 2003;82:362–369.
135. Ananthakumar S, Prabhakaran K, Hareesh US, Manohar P, Warriar KGK. Gel casting process for Al_2O_3 -SiC nanocomposites and its creep characteristics. *Mater Chem Phys* 2004;85:151–157.
136. Wang HT, Huang LM, Wang ZB, Mitra A, Yan YS. Hierarchical zeolite structures with designed shape by gel-casting of colloidal nanocrystal suspensions. *Chem Commun* 2001;15:1364–1365.
137. Chan CM, Cao GZ, Stoebe TG. Net shape ceramic microcomponents by modified sol-gel casting. *Microsyst Technol* 2000;6:200–204.
138. Santacruz I, Nieto MI, Binner J, Moreno R. Gel casting of aqueous suspensions of BaTiO_3 nanopowders. *Ceram Inter* 2009;35:321–326.
139. Sarkar P, Nicholson PSJ. Electrophoretic deposition (EPD): mechanisms, kinetics, and applications to ceramics. *J Am Ceram Soc* 1996;79:1987–2002.
140. Hamaker HC, Verwey EJW. Colloid stability. The role of the forces between the particles in electrodeposition and other phenomena. *Trans Faraday Soc* 1940;36:180–185.
141. Koelmans H, Overbeek JThG. Stability and electrophoretic deposition of suspensions in non-aqueous media. *Discuss Faraday Soc* 1954;18:52–63.
142. Clasen R, Tabellion J. Electric-field-assisted processing of ceramics-Part I: perspectives and applications. *CFI-Ceram Forum Int* 2003;80:E40–E45.
143. Tabellion J, Clasen R. Electrophoretic deposition from aqueous suspensions for near-shape manufacturing of advanced ceramics and glasses-applications. *J Mater Sci* 2004;39:803–811.
144. Kaya C, Kaya F, Boccaccini AR, Chawla KK. Fabrication and characterization of Ni-coated carbon fibre-reinforced alumina ceramic matrix composites using electrophoretic deposition. *Acta Mater* 2001;49:1189–1197.
145. Chung Y-W, Leu I-C, Lee J-H, Hon M-H. Filling behavior of ZnO nanoparticles into opal template via electrophoretic deposition and the fabrication of inverse opal. *Electrochim Acta* 2009;54:3677–3682.
146. Ghorbani M, Afshar MR. Electrophoretic deposition of titanium dioxide nano-powders films in isopropanol as a solvent. *Int J Mod Phys B* 2008;22:2989–2994.
147. Fu Y-F, Fan H-Q, Deng Y-L, Chen J. Preparation and electrical properties of BST thick film deposited by electrophoretic deposition method. *J Inorg Mater* 2008;23:687–690.
148. Oetzel C, Clasen R. Preparation of zirconia dental crowns via electrophoretic deposition. *J Mater Sci* 2006;41:8130–8137.
149. Kaya C. Al_2O_3 -Y-TZP/ Al_2O_3 functionally graded composites of tubular shape from nano-sols using double-step electrophoretic deposition. *J Eur Ceram Soc* 2003;23:1655–1660.

150. Koura N, Tsukamoto T, Shoji H, Hotta T. Preparation of various oxide films by an electrophoretic deposition method: a study of the mechanism. *Jpn J Appl Phys* 1995;34:1643–1647.
151. Sharma AD, Sen A, Maiti HS. Effectiveness of various suspension media for electrophoretic deposition of YBCO superconductor powder. *Ceram Int* 1993;19:65–70.
152. Heule M, Vuillemin S, Gauckler LJ. Powder-based ceramic meso- and microscale fabrication processes. *Adv Mater* 2003;15:1237–1245.
153. Kai CC. Three-dimensional rapid prototyping technologies and key development areas. *Comput Control Eng J* 1994;5:200–206.
154. Upcraft S, Fletcher R. The rapid prototyping technologies. *Assembly Autom* 2003;23:318–330.
155. Tay BY, Evans JRG, Edirisinghe MJ. Solid freeform fabrication of ceramics. *Int Mater Rev* 2003;48:341–370.
156. Heule M, Vuillemin S, Gauckler LJ. Powder-based ceramic meso- and microscale fabrication processes. *Adv Mater* 2003;15:1237–1245.
157. Pham DT, Gault RS. A comparison of rapid prototyping technologies. *Int J Mach Tools Manuf* 1998;38:1257–1287.
158. Cesarano J, Segalman R, Calvert P. ‘Robocasting’: direct fabrication of ceramics and composites. *Ceram Ind* 1998;148:94–102.
159. Stuecker JN, Miller JE, Ferrizz RE, Mudd JE, Cesarano JIII. Advanced support structures for enhanced catalytic activity. *Ind Eng Chem Res* 2004;43:51–55.
160. Stuecker JN, Cesarano J, Hirschfeld DA. Control of the viscous behavior of highly concentrated mullite suspensions for robocasting. *J Mater Process Technol* 2003;142:318–325.
161. Munch E, Franco J, Deville S, Hunger P, Saiz E, Tomsia AP. Porous ceramic scaffolds with complex architectures. *JOM* 2008;60:54–58.
162. Li Q, Lewis JA. Nanoparticle inks for directed assembly of three dimensional periodic structures. *Adv Mater* 2003;15:1639–1643.
163. Bocanegra-Bernal MH, Matovic B. Dense and near-net-shape fabrication of Si_3N_4 ceramics. *Mater Sci Eng A* 2009;500:130–149.
164. Miranda M, Fernandez A, Saiz E, Tomsia A, Torrecillas R. Application of new forming and sintering techniques to obtain hydroxyapatite and beta-TCP nanostructured composites. *Int J Mater Res* 2010;101:117–121.
165. Ahn BY, Duoss EB, Motala MJ, Guo X, Park S-I, Xiong Y, Yoon J, Nuzzo RG, Rogers JA, Lewis JA. Omnidirectional printing of flexible, stretchable, and spanning silver microelectrodes. *Science* 2009;323:1590–1593.
166. Cai K, Sun J, Li Q, Wang R, Li B, Zhou J. Direct-writing construction of layered meshes from nanoparticles-vaseline composite inks: rheological properties and structures. *Appl Phys A* 2011;102:501–507.
167. Tay BY, Evans JRG, Edirisinghe MJ. Solid freeform fabrication of ceramics. *Int Mater Rev* 2003;48:341–370.
168. Bertsch A, Jiguet S, Renaud P. Microfabrication of ceramic components by microstereolithography. *J Micromech Microeng* 2004;14:197–203.
169. Lee JW, Ahn GS, Kim DS, Cho D-W. Development of nano- and microscale composite 3D scaffolds using PPF/DEF-HA and microstereolithography. *Microelectron Eng* 2009;86:1465–1467.
170. Passinger S, Saifullah MSM, Reinhardt C, Subramanian KRV, Chichkov BN, Welland ME. Direct 3D patterning of TiO_2 using femtosecond laser pulses. *Adv Mater* 2007;19:1218–1221.

171. Le HP. Progress and trends in ink-jet printing technology. *J Imaging Sci Technol* 1998;42:49–62.
172. Noguera R, Lejeune M, Chartier T. 3D fine scale ceramic components formed by ink-jet prototyping process. *J Eur Ceram Soc* 2005;25:2055–2059.
173. Jeong S, Woo K, Kim D, Lim S, Kim JS, Shin H, Xia Y, Moon J. Controlling the thickness of the surface oxide layer on Cu nanoparticles for the fabrication of conductive structures by ink-jet printing. *Adv Funct Mater* 2008;18:679–686.
174. Fuller SB, Wilhelm EJ, Jacobson JM. Ink-jet printed nanoparticle microelectromechanical systems. *J Microelectromech Syst* 2002;11:54–60.
175. Ago H, Murata K, Yumura M, Yotani J, Uemurac S. Ink-jet printing nanoparticle catalyst for site-selective carbon nanotube growth. *Appl Phys Lett* 2003;82:811–813.
176. Ko SH, Chung J, Hotz N, Nam KH, Grigoropoulos CP. Metal nanoparticle direct inkjet printing for low-temperature 3D micro metal structure fabrication. *J Micromech Microeng* 2010;20:125010, 7pp.
177. Ko SH, Pan H, Grigoropoulos CP, Luscombe CK, Frechet JMJ, Poulikakos D. All-inkjet-printed flexible electronics fabrication on a polymer substrate by low-temperature high-resolution selective laser sintering of metal nanoparticles. *Nanotechnology* 2007;18:345202 8pp.
178. Yu J, Lee S, Lim E, Kim T, Lee KK. Preparation of indium tin oxide inks for electrically conductive transparent oxide film with ink-jet-printing method. *Mol Cryst Liq Cryst* 2010;519:134–140.
179. Guo RS, Qi HT, Yang ZF, Chen YR. Preparation and properties of the AEO9/ alcohol/alkane/water reverse microemulsion ceramic inks. *Ceram Int* 2004;30:2259–2267.
180. Atkinson A, Segal DL. Some recent developments in aqueous sol-gel processing. *J Sol-Gel Sci Technol* 1998;13:133–139.
181. Mott M, Song JH, Evans JRG. Microengineering of ceramics by direct ink-jet printing. *J Am Ceram Soc* 1999;82:1653–1658.
182. Bottcher H, Soltmann U, Mertig M, Pompe W. Biocers: ceramics with incorporated microorganisms for biocatalytic, biosorptive and functional materials development. *J Mater Chem* 2004;14:2176–2188.
183. Davis SA, Breulmann M, Rhodes KH, Zhang BJ, Mann S. Template-directed assembly using nanoparticle building blocks: a nanotectonic approach to organized materials. *Chem Mater* 2001;13:3218–3226.
184. Li M, Schnablegger H, Mann S. Coupled synthesis and self-assembly of nanoparticles to give structures with controlled organization. *Nature* 1999;402:393–395.
185. Li M, Wong KKW, Mann S. Organization of inorganic nanoparticles using biotin-streptavidin connects. *Chem Mater* 1999;11:23–26.
186. Kokubo T, Kim H-M, Kawashita M. Novel bioactive materials with different mechanical properties. *Biomaterials* 2003;24:2161–2175.

CHAPTER 6

SINTERING

6.1 INTRODUCTION

Sintering is defined as the bonding of particle packing into a coherent, predominantly solid structure by the application of heat to enable one or more mechanisms of atomic movement to the particle contact interface to occur [1, 2]. On a macroscopic scale, the process is accompanied by strengthening and dimensional decrease (shrinkage). On a microstructural scale, bonding occurs as necks grow at the points of contact between particles, and the free surface decreases. As the bonds between contacting particles enlarge and merge, grain growth proceeds.

Active nanomaterial research has brought new excitement as well as challenges to sintering. Depending on the needs of the specific application in discussion, two possibilities exist. One is to strengthen and stabilize the nanoparticle packing/arrangement while maintaining the high surface area, porosity, and the unique arrangement of particle-based materials at nanoscale. This can be categorized as porous nanoparticle material sintering. The other is to achieve high or full density while keeping the grains at <100 nm. This can be categorized as dense nanoparticle material sintering. Porous nanoparticle material sintering is more achievable but also less studied. Most of the sintering efforts have been devoted to achieving full density and maintaining nano-sized grains. Innovative sintering approaches become a must in order to meet some of the specific requirements of nanoparticle-based materials.

6.2 THEORIES

6.2.1 Sintering Stages

At the microscopic level, sintering addresses the diffusion process of a particle collection. Classical sintering studies are focused on rigorously defined geometric models such as the simplified two-sphere model or the tetrakaidecahedron model [3–6]. From a mechanistic point of view, sintering proceeds by evaporation–condensation, surface diffusion, grain boundary diffusion, volume diffusion, plastic deformation, or creep (the latter two cases apply if a pressure is used). Volume diffusion includes the diffusion process from the particle/grain surface to the neck that leads to coarsening (volume diffusion coarsening) and the diffusion process from the grain boundary to the neck that leads to densification (volume diffusion densification). Only grain boundary diffusion, volume diffusion densification, and plastic deformation/creep lead to densification. The other diffusion processes lead to microstructural coarsening. Lowering the surface energy by the elimination of particle (grain)–pore interfaces is the driving force for sintering. At the microstructural level, particles/grains change their shapes by rounding off sharp corners or developing facets at low surface energy orientations. Even though there is no sharp morphological transition during sintering, classical sintering theories almost always divide the process into three stages (initial, intermediate, and final), mostly for discussion convenience. With the designation that the grain size is G and the grain–grain neck size is X , the initial stage of sintering refers to the state when the neck size ratio X/G is <0.3 ; during this sintering stage, the porous structure is open and fully interconnected, and the porosity is only slightly lower than that of the green state. The intermediate stage of sintering refers to the state when X/G is >0.3 but the porosity is 10% or more; during this sintering stage, pores are much smoother and have an interconnected, cylindrical structure. Extensive grain growth and pore isolation occur in the latter portion of the intermediate stage of sintering. At around 8–10% porosity, sintering proceeds into the final stage; cylindrical pores collapse into spherical pores; densification substantially slows down; and extensive grain growth is most likely to occur. Based on this understanding, porous nanoparticle material sintering can also be viewed as the sintering process that only involves initial and/or intermediate stages of sintering, while dense nanoparticle material sintering involves all three stages.

Conventional sintering has been well analyzed mechanism by mechanism based on simplified grain shapes. Extensive discussion on the contributions of the diffusion processes to shrinkage and grain growth is available. However, understanding and effective control of nanoparticle material sintering require a holistic view on all the factors that influence shrinkage and grain growth.

6.2.2 Shrinkage

At free sintering conditions, diffusion occurs locally based on chemical potential difference; plastic deformation and creep are generally absent since the sintering

stress is too low. Only grain boundary diffusion and volume diffusion densification lead to densification (shrinkage). Based on the definition of diffusion flux for a formula unit of grains, diffusion flux j can be expressed as

$$j = \frac{\alpha_{GB}}{\sqrt{2\pi M_w \cdot R \cdot T}} \cdot \frac{\Omega P_{\text{flat}} \gamma_{GB}}{kT} \cdot H, \quad (6.1)$$

where α_{GB} is grain boundary diffusion coefficient, M_w is molecular weight, R is gas constant, T is absolute temperature, Ω is atomic volume of a formula unit of grains, P_{flat} is partial pressure of a flat grain surface, γ_{GB} is grain boundary energy, and k is Boltzmann's constant. The absolute volumetric change rate due to grain boundary diffusion for two grains, $\frac{dV}{dt} |_{GB,2}$, can be described as [7, 8]

$$\frac{dV}{dt} |_{GB,2} = A_{GB,2} \cdot \frac{\alpha_{GB}}{\sqrt{2\pi M_w \cdot R \cdot T}} \cdot \frac{\Omega P_{\text{flat}} \gamma_{GB}}{kT} \cdot H, \quad (6.2)$$

where $A_{GB,2}$ is grain boundary area between the two grains. The overall absolute volumetric change rate by grain boundary diffusion, $\frac{dV}{dt} |_{GB}$, can be summed for all grain-grain-pore triple junctions in different directions as

$$\frac{dV}{dt} |_{GB} = A_{GB} \cdot \frac{\alpha_{GB}}{\sqrt{2\pi M_w \cdot R \cdot T}} \cdot \frac{\Omega P_{\text{flat}} \gamma_{GB}}{kT} \cdot \Sigma H, \quad (6.3)$$

where A_{GB} is total grain boundary area, ΣH is vector sum of the mean curvature H with the consideration of the relative orientation of the grain boundaries in the sample. For the volumetric change rate, $\frac{dV}{dt} |_V$, due to volume diffusion densification, an equation similar to Equation (6.3) can be derived. The total absolute shrinkage rate for a sintering body is [7, 8]:

$$\begin{aligned} \frac{dV}{V \cdot dt} |_d &= \frac{dV}{V \cdot dt} |_{GB} + \frac{dV}{V \cdot dt} |_V \\ &= \frac{A_{GB}}{V} \cdot \frac{1}{\sqrt{2\pi M_w \cdot R \cdot T}} \cdot \frac{\Omega \cdot P_{\text{flat}} (\alpha_{GB} \cdot \gamma_{GB} + \alpha_V \cdot \gamma_V)}{kT} \Sigma H, \quad (6.4) \\ &= C' \cdot \frac{A_{GB}}{V} \cdot \Sigma H = C' \cdot A \cdot \Sigma H \end{aligned}$$

where α_V is volume diffusion coefficient, γ_V is volume energy, C' is a system and temperature related constant, and A is volumetric grain boundary area. H is mean curvature and can be expressed as

$$H = \frac{1}{2} \cdot \frac{\iint \left(\frac{1}{r_1} + \frac{1}{r_2} \right) da}{\iint da}, \quad (6.5)$$

where r_1, r_2 are principal curvatures at grain–grain–pore triple junctions, da is area element at grain–grain–pore triple junctions [9]. r_1 and r_2 can be positive, negative, or zero. For very small shrinkage, Equation (6.4) can be further expressed as

$$\frac{d\rho}{\rho \cdot dt} = C' \cdot A \cdot \Sigma H. \quad (6.6)$$

For a given material under a specific temperature (given C'), Equation (6.6) shows that A and ΣH comprehensively represent the densification rate. A represents grain packing density, contact, and the available grain boundary area for densification. ΣH represents grain size, shape, and intergrain neck geometry. ΣH also represents pore size and shape. C' , A , and ΣH collectively represent the spontaneous densification tendency of a sintering system. With a temperature change, C' varies based on intrinsic material properties such as diffusion coefficients and interfacial energies.

For densification, the grain size effect is reflected in ΣH , which is dictated by nanoparticle packing. ΣH may or may not have a significant effect on densification due to the vector sum effect over the entire sintering body. On the other hand, A is strongly dependent on nanoparticle packing (Eq. (6.6)). If nanoparticle packing is poor, A will be small. To improve densification, A should be increased during the forming process by achieving the highest green density possible. Equation (6.6), albeit useful, involves consideration of all the grains and their packing geometries in a system. As a result, it is intuitively instructive to be used to understand the effects of different factors, but cumbersome to be applied to real systems.

6.2.3 Grain Growth

Different from shrinkage, grain growth is more a local event for a given grain. Its behavior mainly hinges on its neighbors and their interactions (except for the evaporation–condensation mechanism). Nonetheless, the grain growth process can be understood by starting with chemical potential difference and then examining the Gibbs–Thomson equation. For the evaporation–condensation grain growth mechanism, the chemical potential difference between atoms per formula unit on a flat surface and on a grain surface of curvature H is

$$\Delta\mu = \mu_{\text{curv}} - \mu_{\text{flat}} = \gamma_{\text{GV}}\Omega H, \quad (6.7)$$

where μ_{curv} is the chemical potential on the grain surface, μ_{flat} is the chemical potential on a flat surface, and γ_{GV} is the grain–pore interfacial energy. At equilibrium, the chemical potential difference is related to the partial pressure above the curved grain surface:

$$\Delta\mu = kT \ln \frac{P_{\text{curv}}}{P_{\text{flat}}}, \quad (6.8)$$

where P_{curv} is the partial pressure on the grain surface, and P_{flat} is the partial pressure on the flat surface. Combining Equations (6.7) and (6.8) yields

$$\ln \frac{P_{\text{curv}}}{P_{\text{flat}}} = H \frac{\Omega \gamma_{\text{SV}}}{kT} \approx \frac{P_{\text{curv}} - P_{\text{flat}}}{P_{\text{flat}}}. \quad (6.9)$$

When the pressure difference between the curved grain surface and the flat surface is assumed to be small. Equation (6.9) can be rewritten as

$$P_{\text{curv}} = P_{\text{flat}} \left(1 + H \frac{\Omega \gamma_{\text{GV}}}{kT} \right). \quad (6.10)$$

For grain growth through the evaporation–condensation mechanism, the grain growth rate can be expressed as

$$\begin{aligned} \left. \frac{dG}{dt} \right|_{\text{E-C}} &= K_{\text{E-C}}(P_{\text{curv}} - P_{\text{flat}}) = K_{\text{E-C}} \cdot P_{\text{flat}} \frac{\Omega \gamma_{\text{GV}}}{kT} H \\ &= K_{\text{E-C}} \cdot S_{\text{E-C}} \cdot H, \end{aligned} \quad (6.11)$$

$$S_{\text{E-C}} = P_{\text{flat}} \frac{\Omega \gamma_{\text{GV}}}{kT}, \quad (6.12)$$

where $K_{\text{E-C}}$ is a constant representing grain boundary mobility due to the evaporation–condensation diffusion mechanism, and $S_{\text{E-C}}$ is a constant representing the intrinsic material properties at a given temperature. When the grain growth is contributed from the surface diffusion mechanism, the grain growth rate can be expressed as

$$\left. \frac{dG}{dt} \right|_S = K_S \cdot S_S \cdot H, \quad (6.13)$$

where S_S is a system-related constant, and K_S is a constant representing grain surface mobility due to the surface diffusion mechanism. Similarly, the grain growth rate due to volume diffusion coarsening can be expressed as

$$\left. \frac{dG}{dt} \right|_V = K_V \cdot S_V \cdot H, \quad (6.14)$$

Again, S_V is a system-related constant and K_V is a constant representing grain surface mobility due to the volume diffusion coarsening mechanism. The overall grain growth rate can be expressed as

$$\frac{dG}{dt} = (K_{\text{E-C}} \cdot S_{\text{E-C}} + K_S \cdot S_S + K_V \cdot S_V)H. \quad (6.15)$$

Clearly, the intrinsic properties of the material to be sintered play essential roles in grain growth rate, reflected by K_{E-C} , K_S , K_V , S_{E-C} , S_S , S_V in Equation (6.15). Composition and sintering temperature can be modified to adjust these values. For nanoparticles, particle/grain radii r_1 and r_2 are small and thus H is large. This means fast grain growth is an intrinsic characteristic of nanoparticle sintering based on Equation (6.15). In addition to the grain growth rate, the mean grain size r usually increases with sintering time t according to

$$G^3 = G_0^3 + Kt, \quad (6.16)$$

where G_0 is the initial grain size, and K is a thermally activated parameter that includes grain boundary mobility.

6.3 CHARACTERISTICS OF NANOPARTICLE SINTERING

Sintering of nanoparticle-based materials shares many of the common principles with micron- and submicron-sized particulate systems. This includes the fundamental diffusion mechanisms, grain growth rules, and intrinsic material property effects such as interfacial energy. However, nanoparticle sintering has its own unique characteristics. For example, it has been proposed that nonlinear diffusion leads to different kinetic rates of diffusion for nanoparticle sintering, which in turn results in different kinetic rates of sintering [10]. Compared to conventional micron-sized or submicron-sized particles, the behavior of nanoparticles during sintering is notably different with respect to the rate of densification and the temperature range at which densification occurs. The densification of nanoparticles is strongly affected by the excessive surface area of nanoparticles, agglomeration of nanoparticles, and smaller pores. Although many of these factors also impact the sintering of conventional micron-sized and submicron-sized particles, the effects are more dramatic and magnified in the sintering of nano-sized particles. In addition, conventional sintering includes solid-state sintering and liquid phase sintering in the broad sense; most nanoparticle sintering, however, focuses on solid-state sintering. Liquid phase sintering is very limited for nanoparticle-based materials. This mainly stems from the fact that liquid phase sintering induces dramatic grain growth, which is seldom desired for nanoparticle sintering. Understandably, nanoparticle-based material sintering is associated with both advantages and disadvantages. The advantages include shorter diffusion paths and enhanced diffusion by increased curvature of surfaces. The disadvantages include higher agglomeration, packing inhomogeneity, and more adsorbed foreign species on particle surfaces.

6.3.1 Designer Systems

Different from conventional micron-sized particles, nanoparticles are often synthesized by carefully controlled processes with high-purity raw materials. As a

result, the starting materials for sintering are often of very high purities. Impurity effects on sintering are drastically reduced. Moreover, for nanoparticle-based material sintering, there is usually a high motivation to keep the grain size < 100 nm in order to achieve improved or novel properties. In addition, nanoparticles have a much higher content of surface species. These surface species are more active than the bulk species because of the broken bonds and defects on the surface. The interfacial reaction and interface chemistry of nanoparticles play a more important role in sintering.

For the sintering systems that involve more than one kind of nanoparticles, the incentive is often to achieve nanostructures and enhanced properties, not to lower sintering temperatures or facilitate densification. Mixing homogeneity between different compositions is theoretically better than the submicron- and micron-sized counterparts. This is because the spatial distribution of different species is much shorter. Since different species only need to diffuse < 100 nm to interact, the reaction rate for nanocomposites is much faster, and sintering can thus be accelerated.

In addition to random mixing of different species, composite nanoparticles often involve very specific distributions/arrangements of compositions. A typical example is the core/shell structure. Different species are arranged in an ideal pattern such that the shell thickness (composition ratio) becomes the dominant factor in controlling the sintering process. If the shell is thick enough, then sintering proceeds as if it were pure shell material. If the shell is thin enough, then the reaction and diffusion of the core and shell species become important and must be considered.

6.3.2 Particle Size Distribution and Packing Characteristics

For nanoparticles, a huge amount of specific surface area is available. The specific surface area of nanoparticles with an average size below 10 nm can rise to several hundred square meters per gram. This high surface area is accompanied by a large amount of surface energy that needs to be effectively controlled, and better yet, utilized to its advantage. Otherwise, very undesirable nanoparticle agglomeration is spontaneous and sintering defects set in. On one hand, agglomeration consumes the surface energy that should be expended on densification. On the other hand, large interagglomerate pores have to be removed during subsequent sintering in order to achieve homogeneous or full densification; nanoparticle agglomerate size (and hence interagglomerate pore size), rather than the nanoparticle size, governs the densification of the samples. When agglomeration causes a loss of contacts or a reduction in coordination numbers in a particle packing before sintering, the poorly packed region can mature into a critical defect if it is prevented from healing.

For templated and assembled samples that show regularity in nanoparticle packing, the sintering behavior is different from the randomly arranged nanoparticles of bulk samples. This stems from the fact that each particle in the latter case has a different neighboring environment and thus different diffusion

paths. Interestingly, the sintering behavior of these more controlled nanoparticle arrangements aligns better with the classic sintering modeling predictions as the sintering theories often assume ideal particle geometries and packing structures.

Particle size distribution also plays an important role in nanoparticle material sintering. For nanoparticles, it is a challenging task to obtain a narrow size distribution during synthesis. This is because the high thermal and chemical stabilities of nanoparticles (mostly oxides) after nucleation and growth inhibit narrowing in size by the well-known Ostwald ripening process. Small grains are stable against dissolution back into the solution, and controlled release of reactant(s) is not effective in controlling the growth of large particles. Particle size separation for nanoparticles in large quantities also does not exist. As a result, a wide particle size distribution is common for nanoparticles, and some particles can extend to submicron size. Because of the usually small population of large-sized particles in a nanoparticle collection, they do not increase the packing density substantially, but will act as the seeds for abnormal grain growth during sintering. Even if a nanoparticle size distribution is desirably narrow, (random) particle packing efficiency is low because of the high frictional forces between nanoparticles; it is difficult to achieve homogeneous and/or high green density samples, which is desired for sintering densification.

6.3.3 Complex Systems

Nanoparticle sintering can encounter more complex systems than conventional sintering processes. For example, because of the low sintering temperature of metal nanoparticles, the sintering of metal-polymer systems may become a reality. Intermetallic compound sintering may become reactive. In addition, sintering of nanoparticles into a bulk, fully dense component may not be the norm of the requirements anymore. Nanoparticle sintering may involve constrained sintering on films or substrates; or, the sintering process may involve sintering nanoparticles into clusters. Also, nanoparticles may be sandwiched in-between two substrates or their distribution may vary greatly, etc. Nanoparticles can also act as a second phase in nanocomposite sintering [11–13]; they can disperse in a matrix, inhibit the grain growth, and adjust the grain size and mechanical properties [14–18]. For example, 5 vol% β -SiC nanoparticles with a size <300 nm are added into 200 nm α -Al₂O₃ particles and sintered with a pulse electric current under an applied pressure of 5.5 MPa and a vacuum of 6 Pa to obtain a porous nanocomposite [14]. The starting particle mixture is ball milled and sintered at 1000°C for 15 minutes. The nano-sized SiC particles disperse at the boundaries of Al₂O₃ grains. In comparison, pure α -Al₂O₃ particles are sintered at 950°C for 15 minutes. Both samples have sintered porosity around 20%. However, obvious neck growth appears in the pure Al₂O₃ sample, and the grain size of Al₂O₃ in the composites is smaller than that of the pure Al₂O₃ sample. This phenomenon indicates that the SiC nanoparticles located at the grain

boundaries of the Al_2O_3 matrix restrict the growth of the Al_2O_3 grains. With SiC nanoparticle addition, the mass transport by evaporation–condensation and surface diffusion is also inhibited by the second phase, which creates an extra diffusion barrier. The refined microstructure reinforces the strength of the sintered nanocomposites.

6.3.4 Phase Transformation

Nanoparticles are often synthesized at low temperatures or from nonequilibrium processes. This produces nanoparticles at the metastable state or consisting of polymorphic mixtures, precursors, or amorphous phases of the desired material. For successful sintering, organic removal and nanoparticle phase transformation to stable crystal structures are necessary. However, when these transitions do occur, they are usually accompanied by significant microstructural changes that have to be controlled. Otherwise, decomposition or phase transformation-induced volume change can introduce a substantial amount of porosity/defects during sintering. When prolonged sintering is used to remove pores for full densification, coarsening will inevitably set in.

Al_2O_3 -based porous ceramics with high surface areas are fabricated from the mixture of Al_2O_3 and $\text{Al}(\text{OH})_3$ powders by free sintering at $>1100^\circ\text{C}$ [19–21]. The green body is obtained by cold isostatic pressing under a pressure of ~ 30 MPa. Sintering is conducted in an air atmosphere with a heating rate of 1°C min^{-1} at $<1000^\circ\text{C}$ and a heating rate of $10^\circ\text{C min}^{-1}$ at $>1000^\circ\text{C}$. The sample is held at the sintering temperature for 30 minutes and then cooled down to room temperature at a rate of $10^\circ\text{C min}^{-1}$. The pore size distribution of the porous Al_2O_3 sample is bimodal, with one peak at ~ 100 nm and the other at ~ 10 nm. The porosity is 40–60%. The Al_2O_3 grains produced by the decomposition of $\text{Al}(\text{OH})_3$ are several tens of nanometers in size. The fine pores (~ 10 nm) are located between these fine particles, and the large pores (~ 100 nm) are the channels between the large particles. The fine pores are formed due to the incomplete phase transformation of θ - Al_2O_3 (produced by decomposition of $\text{Al}(\text{OH})_3$) to α - Al_2O_3 . When the sintering temperature increases to $>1200^\circ\text{C}$, the fine pores disappear because of the complete phase transformation of θ - Al_2O_3 . Due to the 60 vol% decrease during the decomposition of $\text{Al}(\text{OH})_3$, the large pores in the specimen prepared from the particles with $\text{Al}(\text{OH})_3$ are stable and grow when the sintering temperature increases.

6.3.5 Lower Sintering Temperature

Generally, the sintering temperatures for nanoparticle-based materials are much lower than that of their micron- or submicron-sized counterparts. This results from the much smaller particle size and thus dramatically increased surface area/energy. Sintering between nanoparticles can even occur during nanoparticle synthesis, which is usually undesirable but will not be the topic of this chapter.

During use, nanoparticle-based materials should be stable and further sintering should be avoided. For example, sintering should be avoided for nanoparticle-based sensors, catalysts, and hot gas filters. For the intended nanoparticle material sintering processes, the high surface area that is partly consumed as the driving force should be properly preserved because many applications also require this characteristic to perform their functions. In other words, sintering itself should not exhaust too much of the surface area.

Particle surfaces are known to have a higher concentration of defects and dangling bonds than the interior of particles. As a result, the atomic mobility on the particle surfaces is higher. Nanoparticle surfaces take up a much larger volume fraction of the total sintering system than micron-sized systems. Collectively, nanoparticles demonstrate a more activated sintering behavior and have a much earlier onset of sintering temperatures. For many nanoparticles, the sintering onset temperature is in the range of $0.2\text{--}0.3 T_m$ (where T_m is the melting point of the sintering species in Kelvin), as compared with the much delayed onset of sintering temperature in micron-sized particulate systems, normally $0.5\text{--}0.8 T_m$ [22–24]. Several studies on the sintering of Y_2O_3 stabilized ZrO_2 nanoparticles have shown that sintering initiates at a temperature 200°C lower than that of the micron-sized particles [25–27]. An even greater temperature difference in sintering, 400°C , is reported for TiO_2 nanoparticles compared to commercial micron-sized TiO_2 particles [28]. Similar results are observed for CeO_2 [29] and TiN nanoparticles [30]. Sintering of tungsten carbide and cobalt (WC-Co) nanoparticle mixtures shows that the entire sintering temperature decreases steadily as the initial average particle size decreases from $30\ \mu\text{m}$ to $10\ \text{nm}$ [31]. Rapid densification of iron and copper nanoparticles starts at $\sim 200^\circ\text{C}$ lower temperatures [32]. A reduction of the sintering temperature is also reported for tungsten nanoparticles [33, 34]. Nano-sized tungsten particles produced by high-energy mechanical milling dramatically decrease the sintering temperature from 2500°C to 1700°C . Tungsten with initial sizes of $\sim 20\ \text{nm}$ can be sintered to $>98\%$ relative density without any pressure at 1100°C in a hydrogen atmosphere [35].

Nanoparticle-based sintering systems also have much lower sintering activation energies. This is often reflected by the lower sintering temperatures discussed above. The activation energy for ZrO_2 nanoparticles is $<50\%$ of that for submicron ZrO_2 particles [36]. ZnO nanoparticle grain growth activation energy is $<10\%$ of that of the micron-sized ZnO particles [37]. In fact, these energies can only be labeled as apparent activation energy. Multiple sintering mechanisms may be operating simultaneously. This is especially true during the early stage of sintering when no one clearly dominant mechanism can be identified; the results calculated using the kinetic data give apparent activation energy values, which are the combined contribution of multiple mechanisms. A majority of studies point toward lower activation energies for the early stage of sintering. This is reasonable due to the huge surface energy and the expected high sintering activity of nanoparticles. From a different perspective, low sintering temperature and activation energy of nanoparticles provide the added ability to manipulate and tailor sintering that has not been possible before. For example,

a high concentration of vacancies at the grain boundaries is beneficial for grain boundary diffusion and pore removal.

Surface diffusion is one of the most cited mechanisms that contribute to the sintering of nano-sized particles. However, its main contribution is grain coarsening. When the grain coordination number reaches a critical value, some pores may become stable and resist being removed. The shrinkage of a pore cannot progress until the equilibrium condition is tipped in favor of sintering by grain growth. Thus, surface diffusion can contribute to densification but indirectly by disturbing the geometrical constraint for pores. However, excessive surface diffusion means excessive coarsening and loss of desired fine microstructure, which should be avoided.

Other interparticle diffusion mechanisms, other than surface diffusion, could also contribute to coarsening of particles. In particular, there is a relaxation period for migration, redistribution, and annihilation of defects due to the fact that nanoparticles are usually at nonequilibrium states and likely contain excess amounts of defects that are created during the synthesis of nanoparticles. Owing to the nonequilibrium structure of nanoparticles, diffusivity is dramatically enhanced during the relaxation process, which may contribute to the grain growth at the beginning of sintering (so-called dynamic grain growth). Dynamic grain growth usually dominates during the heat-up stage and for the first few minutes after reaching a preset isothermal holding temperature. Therefore, rapid dynamic grain growth accounts for the experimental observation that the first grain size data point during isothermal holding is several times of the initial particle size. The relaxation time depends on material, nanoparticle synthesis method, and temperature.

6.3.6 Larger Sintering Driving Force

A review paper by Fang et al. provides a good treatment of the sintering driving force [10]. The thermodynamic driving force for sintering particles of any size is the reduction of surface energy. Based on conventional sintering theories, the driving force of sintering ρ' is given by

$$\rho' = \gamma\kappa = \gamma \left(\frac{1}{R_1} + \frac{1}{R_2} \right), \quad (6.17)$$

where γ is the surface energy of the material, κ is the curvature of the surface, and R_1 and R_2 are the principal radii of the curvature. The driving force for the sintering of nano-sized particles is, therefore, inversely proportional to the size of the particles. This relationship leads to a much higher driving force for the sintering of nano-sized particles compared to micron-sized particles. For example, based on Equation (6.17), the driving force for 10 nm size particles is two orders of magnitudes higher than that for 1 μm size particles.

The driving force for nanoparticle sintering can be even higher than the result from Equation (6.17) if the nonlinear dependency of vacancy concentrations on

the particle size is considered. During sintering, mass transport, usually mediated by vacancies, is driven by the difference in vacancy concentration:

$$\Delta C_V = C_V - C_{V0}, \quad (6.18)$$

where C_V is the vacancy concentration for a surface with curvature k , and C_{V0} is the vacancy concentration for a flat surface. Based on the Gibbs–Thomson equation, the vacancy concentration for a curved surface is

$$C_V = C_{V0} \exp\left(-\frac{\gamma\kappa\Omega}{kT}\right), \quad (6.19)$$

where Ω is the atomic volume, κ is Boltzmann's constant, and T is the absolute temperature. For micron-sized particles, the term $\frac{\gamma\kappa\Omega}{kT}$ is much smaller than 1, so Equation (6.19) becomes linear:

$$C_V \approx -C_{V0} \frac{\gamma\kappa\Omega}{kT}. \quad (6.20)$$

However, when the particle size approaches nanoscale, the linear approximation is no longer valid. The correct expression for the driving force of mass transport should be given as

$$C_V = C_{V0} \exp\left(-\frac{\gamma\kappa\Omega}{kT}\right) - C_{V0}. \quad (6.21)$$

Equation (6.21) shows that the driving force for mass transport during sintering is a nonlinear function of the surface curvature, and it increases exponentially when particle size decreases to nanoscale. This nonlinear relationship of the driving force for nanoparticle sintering is expected to have a dramatic effect on the sintering kinetics.

In the final stage of nanoparticle sintering, isolated spherical pores are situated at the grain boundaries and, in particular, at triple junctions; grain growth is affected by the remaining pores that pin the grain boundaries, which reduce the kinetic rate of grain growth. Pores are considered to be a second phase with an inhibiting force against grain boundary movement. Owing to the presence of a large number of pores in the system at the beginning of the final stage of nanoparticle sintering, the grain boundaries are at first dragged by the pores and the rate of grain growth is slow. But as sintering proceeds, both the number and the size of the pores decrease as a result of densification. When the density reaches the specific value at which a grain boundary is able to break away from the inhibition of the pores (i.e., pore/boundary separation occurs), grain growth accelerates dramatically. So, the desirable scenario would be to allow the pores to attach to the grain boundaries and be sufficiently removed before they become trapped inside individual grains.

6.4 POROUS NANOPARTICLE MATERIAL SINTERING

A variety of porous microstructures can be created by controlled sintering of particles. The degree of sintering depends on sintering temperature, time, atmosphere, pressure, and the type and amount of sintering additives. Porous nanoparticle-based materials are generally made with a large surface area, a high porosity, and unique functional or structural properties [38–42]. For nanoparticle-based superstructures, assemblies, and thin films, partial sintering is also more common than full density sintering in order to maintain the unique attributes of the created structures. These materials are of scientific and technological importance because of their vast abilities to adsorb and interact with atoms, ions, and molecules on their large surfaces (interior and exterior) and in the nanometer- to micron-sized pores. Bulk nanoparticle-based porous materials have important uses in various fields such as ion exchange membranes, separation filters, catalysts, insulators, bone implants, sensors, and biological molecular isolations and purifications [43–45]. They also offer new opportunities in guest–host synthesis and molecular manipulation and reaction at the nanoscale.

While the solid phase needs to be continuous, the pore phase may be continuous or discrete. If the pore phase is continuous, the pores are often open. If the pore phase is discrete, the pores are often elongated and closed. The accessibility of the pores and the internal surface area are important considerations in the sintering process. For superstructures and assemblies, stabilization of the nanoparticle packing can often be the leading reason for sintering. There is no strict definition on the amount of porosity for nanoparticle-based porous materials. However, the consideration generally excludes the particulate materials with only a couple of percent residual porosity that cannot be removed by sintering. The highest amount of porosity can be as high as 95%. The final products should have grain sizes <100 nm. However, this aspect is often relaxed to include materials with grains as large as 200 nm. In addition, there have been no strict limits on pore sizes, which can range from nanometers to microns. While porous green samples can be created through many different methods and at drastically different scales, the fundamental aspects during sintering are basically the same as discussed in Section 6.2 of this chapter.

Partial sintering has the desirable characteristics of simple equipment requirements, ability to sinter complex shapes, and low cost. However, how to tailor sintering densification and grain growth is critical, as both proceed by lowering the nanoparticle surface energy through chemical potential difference. Because of this, other techniques have been developed to sinter porous materials by using nanoparticles as initial materials, and they can be classified into three main methods: (a) partial sintering of green state nanoparticle-based assemblies or packings, (b) pore forming sintering that relies on the gas reaction product(s) to generate or tailor pores and porosity, and (c) template-directed sintering that relies on a template to control the pore size, shape, distribution, and the sintering diffusion paths.

6.4.1 Partial Sintering

Porous nanoparticle-based materials can be obtained by maintaining the residual porosity through partial sintering. For nanoparticle superstructures and assemblies, porous structures are achieved by sintering at low temperatures. For very small particles, sintering can even occur at room temperatures [46]. For bulk nanoparticle-based materials, partial sintering is mostly performed at elevated temperatures to create porous materials. For example, in the classical sintering approach, a two-step sintering method (a high temperature sintering step followed by a prolonged isothermal holding at a low temperature) is often used to obtain dense nanoparticle-based materials [47–49] (to be discussed in Section 6.5.1.2 of this chapter) while one-step partial sintering can fabricate porous materials with small grain sizes and low densities.

Silver nanoparticles exhibit sintering at room or slightly higher temperatures when their surfaces are clean and without protective organic dispersants [50]. The initial microstructures of the silver nanoparticles and the microstructures after sintering at various temperatures for 30 minutes are compared in Figure 6.1 for inkjet-printed lines. The initial silver nanoparticles of the printed lines exhibit a self-aligned close-packed arrangement. The nanoparticles sintered at 60°C maintain the initial state, as shown in Figures 6.1a and b. Thus, a temperature below 60°C is too low to remove the dispersant from the silver nanoparticles, and sintering of the nanoparticles does not occur in this temperature range. On the other hand, the microstructure of the silver nanoparticles substantially changes with sintering at $\geq 80^\circ\text{C}$. Nanoparticles of 10–30 nm size can be seen in the sample sintered at 80°C. With increasing temperature, grain coarsening becomes more drastic. The particle size distribution widens in Figures 6.1c–e. In addition to large grains of a few tens of nanometers to 100 nm in size, fine silver nanoparticles with ~ 10 nm size remain. Thus, sintering of the silver nanoparticles is nonuniform. This bimodal distribution of nanoparticles indicates that some silver nanoparticles grow quickly by absorbing surrounding smaller nanoparticles, which have a higher surface energy.

FePt and (FePt)₉₅Au₅ nanoparticles with an average size of ~ 4 nm are sintered at temperatures ranging from 250°C to 500°C for 30 minutes. The nanoparticle arrays shrink and agglomerate during sintering, leading to a loss of positional order with increasing temperature. Gold additives contribute significantly to the sintering of the FePt nanoparticles. Since gold atoms have a low surface energy that favors surface segregation, the (FePt)₉₅Au₅ nanoparticle arrays have a tendency to lose their positional order at lower sintering temperatures [51]. Copper nanoparticles of 5 nm size are inkjet printed and sintered at 250°C under a reducing atmosphere [52]. After sintering, a mixture of small and large grains exists in the microstructure. The large grains are ~ 500 nm, which is roughly two orders of magnitude larger than the initial particle size. A crystalline silicon wafer with (111) orientation is extensively ball milled for up to 72 hours, leading to a decrease in the average grain size to 15 nm. After pressing at 400 MPa and sintering at 900°C for 60 minutes in a high-purity

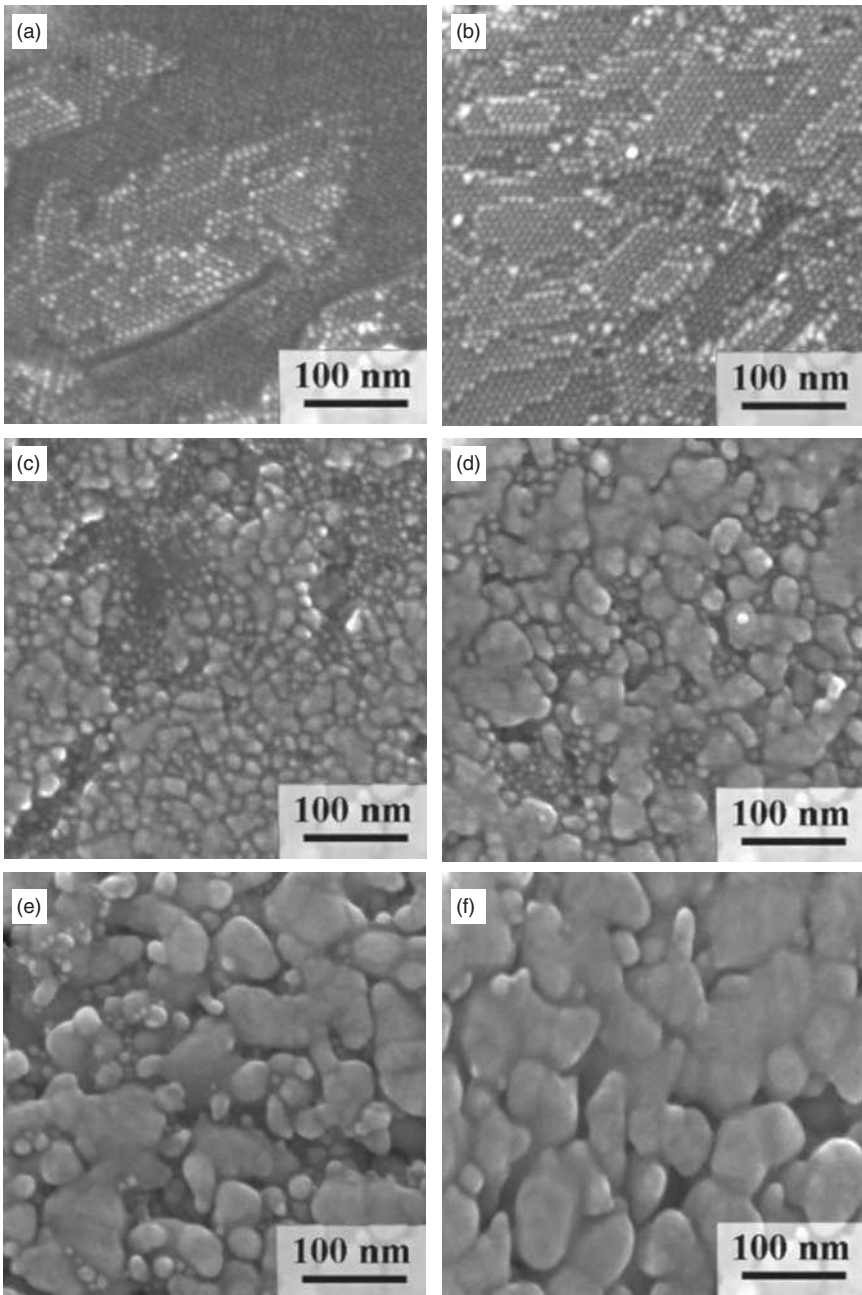


FIGURE 6.1 Microstructural changes of the silver nanoparticles observed by scanning electron microscopy: (a) Initial state, sintered for 30 minutes at (b) 60°C, (c) 80°C, (d) 100°C, (e) 150°C, and (f) 200°C [50]. (Reprinted with permission from Wakuda D, Kim K-S, Suganuma K. Room-temperature sintering process of Ag nanoparticle paste. *IEEE Trans Compon Packag Technol* 2009;32:627–632, Copyright 2009, IEEE.)

argon atmosphere, a porous silicon structure with a uniform microstructure is obtained [53].

For ceramics, bulk porous nanoparticle-based material sintering is more common. Porous nanocrystalline Gd-doped CeO_2 is prepared by a one-step sintering process from commercial 10 mol% Gd-doped CeO_2 nanoparticles of ~ 5 nm size and $176.5 \text{ m}^2 \text{ g}^{-1}$ specific surface area [54]. After being mixed through ball milling and compacted through cold isostatic pressing, the green body is sintered at 800°C for 30 minutes with a heating rate of 5°C min^{-1} ; this suppresses the grain growth and results in porous nanostructured Gd-doped CeO_2 . The grain size is limited to 30 nm and the porosity is 26%. Porous ZrO_2 is fabricated by compacting ZrO_2 nanoparticles and partial sintering in air at 1100 – 1450°C for 30 minutes with a heating and cooling rate of $10^\circ\text{C min}^{-1}$ [55,56]. The average size of the initial ZrO_2 nanoparticles is 28 nm. The porosity ranges between 12% and 60% based on different compaction and sintering conditions. Since ZrO_2 nanoparticles have the inherent tendency for agglomeration, which cannot be eliminated by ball milling, the green body of compacted ZrO_2 nanoparticles is composed of numerous ZrO_2 agglomerates. During the sintering process, the densely packed regions sinter faster than the loosely packed regions. Therefore, nonuniform shrinkage occurs, which causes strains, voids, and crack-like flaws, and results in degraded mechanical properties. An increase in the compaction pressure of the green body can efficiently reduce these voids and flaws because of the collapse and breakup of the ZrO_2 agglomerates (Fig. 6.2). Addition of $\text{Zr}(\text{OH})_4$ is another way to obtain uniform microstructures in the green compacts, due to the space constraint of large $\text{Zr}(\text{OH})_4$ particles and an internal friction between $\text{Zr}(\text{OH})_4$ hard agglomerates [56]. $\text{Zr}(\text{OH})_4$ decomposes into ZrO_2 during sintering, and porous ZrO_2 ceramics with 400–800 MPa fracture strength are

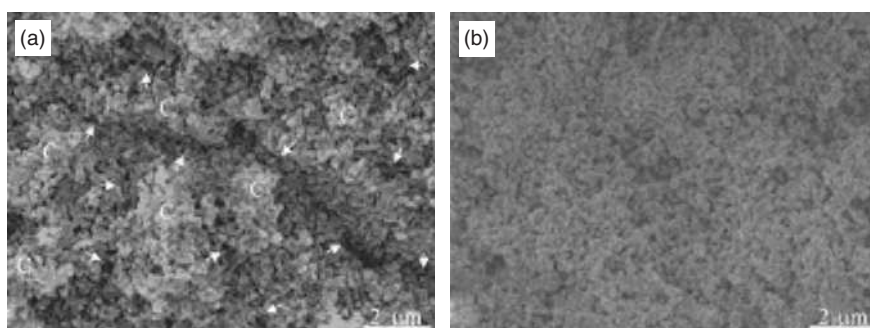


FIGURE 6.2 Scanning electron images of the surface structure of porous ZrO_2 materials after being sintered at 1200°C for 30 minutes from (a) a green body compacted at 30 MPa pressure, and (b) a green body compacted at 75 MPa pressure. The porosity of (a) is 47.4%, and the porosity of (b) is 44.5% [56]. (Reprinted with permission from Deng ZY, Zhou Y, Inagaki Y, Ando M, Ohji T. Role of $\text{Zr}(\text{OH})_4$ hard agglomerates in fabricating porous ZrO_2 ceramics and the reinforcing mechanisms. *Acta Mater* 2003;51:731–739, Copyright 2003, Elsevier.)

formed. There is no significant difference in pore coordination number throughout the specimen, and the shrinkage is homogeneous.

As discussed, one challenge for nanoparticle-based material sintering is maintaining nano-sized grains since nanoparticles experience extremely rapid grain growth during the sintering process due to their high surface energy and large sintering driving force [57, 58]. Sintering of nanoparticle-based composites possesses the advantage of efficiently controlling the grain size by either prohibiting nanoparticle agglomeration and grain growth or by inducing chemical reactions between different species. The porosity of the sintered nanocomposites can also be tailored by using volume expansion from the reactions during the sintering process [59]. For nanocomposite sintering, there can be one species [60] or multiple species [59, 61] with nano-sized initial particles.

High-energy ball milling of powder precursors has been employed for the fabrication of porous materials [62, 63]. For example, applying high-energy ball milling to an equimolar mixture of TiO_2 (76 nm crystallite size) and ZrO_2 (63 nm crystallite size) decreases the sintering temperature of ZrTiO_4 ceramics. The crystallite sizes from the oxides ball milled for 7 hours are between 5 and 7 nm. Before sintering, the ball-milled powder is compacted at 180 MPa. After that, sintering is carried out in air for 8 hours at 1100–1400°C with a heating rate of $23^\circ\text{C min}^{-1}$. Sintered morphology and porosity are dependent on the sintering temperature. The nano-sized precursors allow the solid-state reaction of the oxides to form ZrTiO_4 at a temperature 200°C lower than that of the conventional solid-state syntheses. This facilitates the formation of small grain sizes and small pores.

Sintering of $\text{SiO}_2\text{-Al}_2\text{O}_3$ nanocomposite is conducted. In this system, SiO_2 particles are 22 nm in size, while Al_2O_3 particles are 37.5 nm in size. The SiO_2 and Al_2O_3 nanoparticles are first mixed in water. With the introduction of NaCl, the suspension experiences a gel formation process. The prepared gel is then freeze cast and sintered at 1300°C. The microstructure of the sintered $\text{SiO}_2\text{-Al}_2\text{O}_3$ nanocomposite is shown in Figure 6.3. The porous microstructure is fabricated by the sublimation of ice crystals during freeze drying and then partial

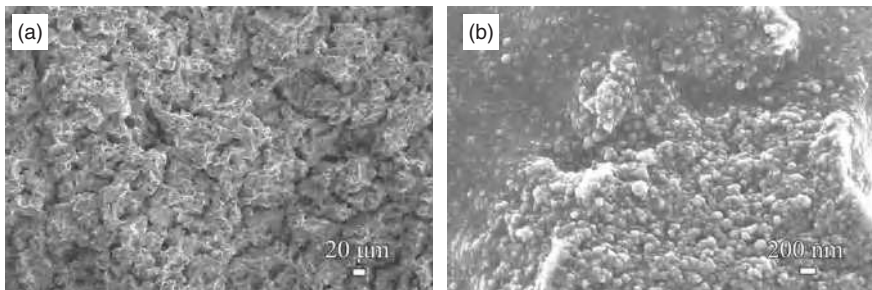


FIGURE 6.3 Microstructures of $\text{SiO}_2\text{-Al}_2\text{O}_3$ nanocomposite sintered at 1300°C: (a) low magnification and (b) high magnification.

sintering. The sintering process leads to the densification of the pore walls while maintaining the nano-sized grains. Diffusion between SiO_2 nanoparticles and Al_2O_3 particles occurs and leads to pseudo-mullite formation. Compared to the freeze cast green sample, the strength of the sintered $\text{SiO}_2\text{-Al}_2\text{O}_3$ nanocomposite is greatly improved without a certain loss of porosity.

6.4.2 Pore Forming Sintering

Higher porosities can be achieved by adding so-called pore formers. These pore formers occupy some space during the shape forming process and are burned off in the early stage of sintering. SiO_2 nanoparticles (40 wt%) with a cationic surfactant, tetradecyltrimethylammonium bromide, are made into a homogeneous dispersion in an aqueous medium at pH 9. A foam is generated by using a continuous bubbling of perfluorohexane-saturated nitrogen through a porous glass disk. After 10 hours of drying under ambient conditions and free drainage, a macroporous hybrid material is obtained in a monolithic state, while further sintering at 650°C leads to a pure inorganic monolith. Either polygonal (Fig. 6.4a) or spherical (Figs. 6.4b and c) SiO_2 macroscopic cell morphologies are obtained [64].

Nanoparticles can also act as a second phase and inhibit grain growth by chemical reaction. Nano-sized $\text{La}_{0.6}\text{Sr}_{0.4}\text{Co}_{0.2}\text{Fe}_{0.8}\text{O}_{3-\delta}$ (LSCF) and $\text{La}_{0.8}\text{Sr}_{0.2}\text{MnO}_{3-\delta}$ (LSM) oxides are synthesized by an *in situ* carbon-templating process with a grain size of 20–30 nm. The LSCF-containing precursor is first calcined under an oxygen deficient atmosphere at 900°C for 160 minutes; the obtained powder is then pressed into pellets, which are then sintered in air at 1000°C for 5 hours. The obtained composites have nano-sized pure phase perovskite with a crystalline size as small as 14 nm. Carbon has a suppressing effect on the grain growth of perovskite. Furthermore, when the *in situ* created carbon is applied as a template for pore formation, a sintered perovskite is obtained [65]. A porosity as high as 75%

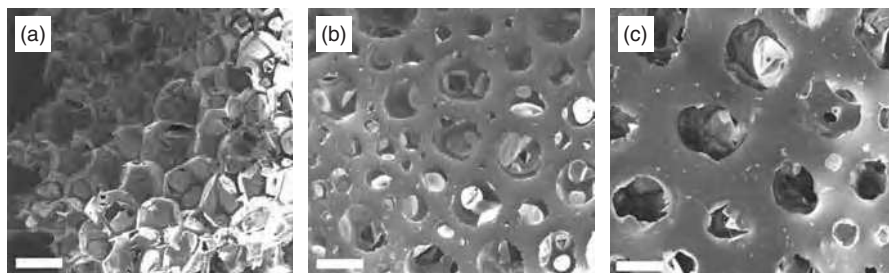


FIGURE 6.4 Scanning electron images of SiO_2 porous materials at three different SiO_2 nanoparticle suspension flux values at the foam's top: (a) 0 g s^{-1} , (b) 0.07 g s^{-1} , and (c) 0.15 g s^{-1} . The scale bars represent $100 \mu\text{m}$ [64]. (Reprinted with permission from Carn F, Saadaoui H, Masse P, Ravaine S, Julian-Lopez B, Sanchez C, Deleuze H, Talham DR, Backov R. Three-dimensional opal-like silica foams. *Langmuir* 2006;22:5469–5475, Copyright 2006, American Chemical Society.)

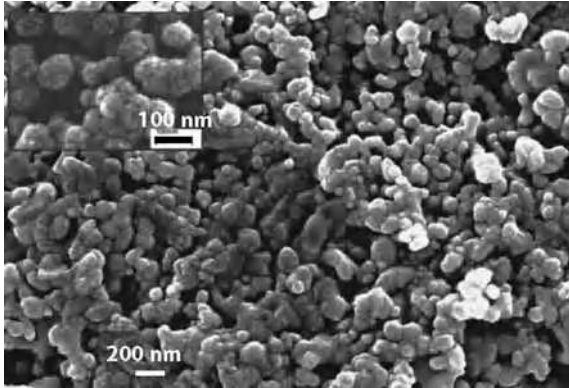
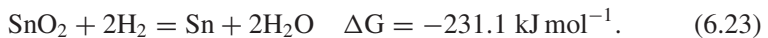


FIGURE 6.5 Scanning electron surface morphologies of the porous LSCF sample by *in situ* carbon templating and sintering at 1000°C in air for 5 hours [65]. (Reprinted with permission from Zhou W, Ran R, Shao Z, Jin W, Xu N. Synthesis of nanoparticle and highly porous conducting perovskites from simple *in situ* sol-gel derived carbon templating process. *Bull Mater Sci* 2010;33:371–376, Springer Science + Business Media, Fig. 8.)

is obtained, which is much higher than that prepared by the conventional process (30–40%). By altering the oxygen concentration and dwelling time during the sintering of the solid precursor under oxygen-deficient conditions, the amount of carbon in the composite can be controlled. The porosity is then determined by the amount of carbon in the carbon–perovskite composite. Figure 6.5 shows the scanning electron surface morphologies of the sintered sample, which is highly porous, with irregular pores varying from several microns to submicrons, and to nanometers. The sintered porous sample has a high surface area for oxygen surface activation during fuel cell use.

CeO₂ is a stable ceramic even at high temperatures under a reducing atmosphere. In contrast, SnO₂ can easily be reduced to elemental tin and evaporated since the melting point of tin is only 231.93°C. The Gibbs free energies for CeO₂, SnO₂, and H₂O at 1000 K are –1186.13, –666.26, and 448.69 kJ mol^{–1}, respectively. Thus, CeO₂ cannot be reduced to cerium in hydrogen, while the reduction of SnO₂ to tin metal is thermodynamically favored:



Based on this understanding, CeO₂ and SnO₂ are mixed. The SnO₂ phase is then evaporated during high temperature sintering, leaving behind an open porous matrix of CeO₂ [66].

Porous nanocomposites can also be obtained by taking advantage of unique starting powders. During the sintering process, reaction might occur and can be used to tailor the porosity of porous materials [67]. The shrinkage of the

nanoparticles due to the reaction within the green body can lead to pores in the sample. The distribution and size of the pores can be controlled by the amount of the initial nanoparticles and the sintering conditions. Copper-coated SiC nanoparticles (average diameter 120 nm) are sintered in ammonia or nitrogen atmosphere, and porous or dense nanocomposites are obtained, respectively [68]. In the ammonia atmosphere, ammonia decomposes at high temperatures, and the resulting hydrogen reduces Cu_2O :



Copper melts at 1050°C in this system and coagulates to form large blocks. Since the copper/SiC interface is nonwetting, segregation between SiC clusters and copper blocks occurs and results in porous microstructures. In contrast, when sintering is carried out in the nitrogen atmosphere, Cu_2O remains in the system, promotes the wetting behaviors between copper and SiC, and leads to the formation of dense nanocomposites. The porosity of the resulting porous nanocomposites can be effectively controlled by modifying the sintering atmosphere.

Porous $\text{TiO}_2/\text{SiO}_2$ and $\text{TiO}_2/\text{ZrO}_2$ nanocomposites are fabricated using a surfactant [69]. After hydrolysis of titanium isopropoxide ($\text{Ti}(\text{OPri})_4$) and zirconium propoxide (or tetraethyl orthosilicate ($\text{Si}(\text{OC}_2\text{H}_5)_4$)) with a surfactant, decaoxyethylene cetyl ether ($\text{C}_{16}(\text{EO})_{10}$), the precursor is sintered at different temperatures from 350°C to 800°C . The well-dispersed silicon or zirconium in the titanium matrix enhances the mechanical properties and thermal stability of the porous nanocomposites (SiO_2 or ZrO_2 prohibits the phase transformation of TiO_2 from anatase to rutile). The second phases are also able to inhibit the grain growth and allow TiO_2 to maintain <10 nm size until 800°C . As a result, the surface area of the nanocomposite is much higher than that of pure TiO_2 sample.

Porous nanocomposites can also be made by a reduction reaction during sintering [70]. Tetragonal spinel CuFe_2O_4 , formed by calcining CuO and $\alpha\text{-Fe}_2\text{O}_3$ at 1000°C in air, is sintered at 360°C in a hydrogen atmosphere. Copper nanoparticles are synthesized by the reduction of CuFe_2O_4 and are well dispersed in the fine Fe_2O_3 matrix:



Because of the immiscibility between copper and Fe_3O_4 , the sintering of copper nanograins is inhibited and the copper nanostructures are conserved. One possible explanation for the formation of porous structure is the removal of oxygen. Pores form in the Fe_3O_4 matrix as a result of loss of oxygen [70].

Macroporous 4 mol% Y_2O_3 -stabilized nanocrystalline ZrO_2 is fabricated by colloidal processing using a commercially available nanopowder and polymethylmethacrylate (PMMA) sacrificial spheres as starting materials. Monolithic bodies

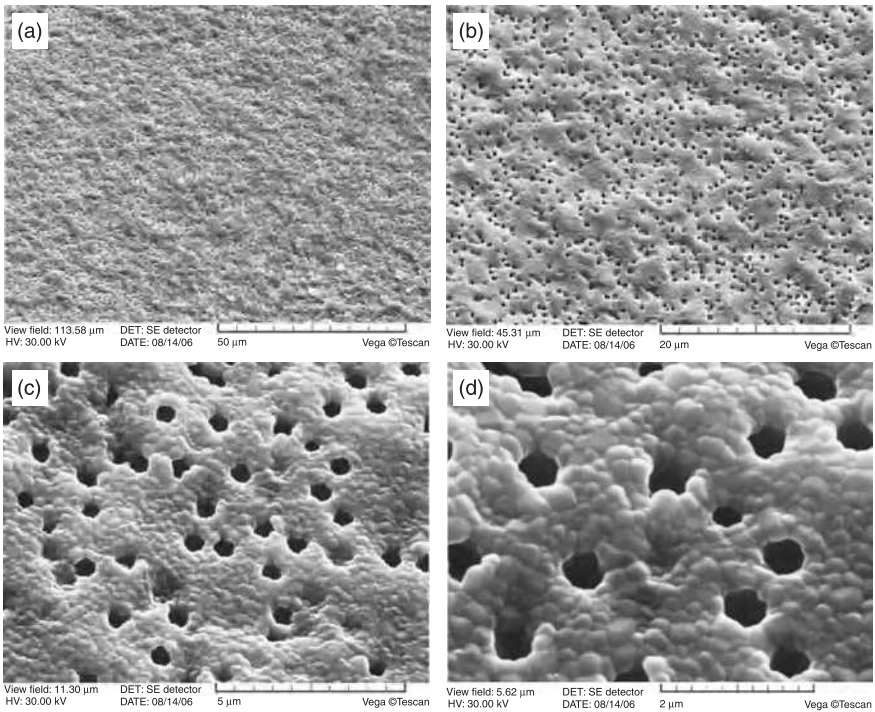


FIGURE 6.6 Fracture surfaces of a sintered body fabricated by gel-casting with 1 μm PMMA spheres after sintering at 1320°C for 1 hour. The average grain size is 200 nm, the average pore size is 460 nm, and the porosity is $\sim 10\%$ [71]. (Reprinted with permission from Cruz HS, Spino J, Grathwohl G. Nanocrystalline ZrO_2 ceramics with idealized macropores. *J Eur Ceram Soc* 2008;28:1783–1791, Copyright 2008, Elsevier.)

obtained by gel-casting of ZrO_2/PMMA suspensions have homogeneous microstructures. After sintering, the grain size is <200 nm with a macropore diameter at ~ 1 μm and closed porosity varying between 10% and 20%. In Figure 6.6, the microstructures (fracture surfaces) obtained from a porous sample sintered at 1320°C for 1 hour is shown at different magnifications. The microstructure is characterized by 200 nm grains and pore sizes around 500 nm, with a total porosity of $\sim 10\%$. The pores are perfectly closed, surrounded by 10–14 grains (two-dimensional image) and immersed in a fully dense matrix [71].

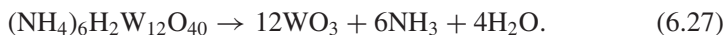
6.4.3 Template-Directed Sintering

Different strategies have been adopted to control morphology, pore size, pore size distribution, porosity, and connectivity of the pores in porous materials. Template method is one of the most effective approaches for creating pores with desired size, distribution, and geometry. It has been successfully used to produce

uniform porous nanostructures (e.g., nanotubes and honeycombs). Nanocrystalline materials with well-controlled macropores are fabricated via colloidal processing using mono-sized polymer particles as sacrificial templates [71–73]. Obtaining oppositely charged particle suspensions at similar pH values is the key for the fabrication of such macroporous materials. After sintering, polymer particles are removed, and the porosity can be controlled by modifying the volume ratio of nanoparticles to polymer particles.

During the preparation of polymer and nanoparticle suspensions, the nanoparticles should be surface modified to adjust the absolute zeta potential of the suspension to higher than 40 mV, which can be achieved by using short-chain organic compound 3,6,9-trioxadecanoic acid for ZrO₂ nanoparticles and polyethylenimine for Al₂O₃ and TiO₂ nanoparticles. The sacrificial polymer particles, such as poly(methyl methacrylate) (PMMA), need to have opposite surface charge and large zeta potential versus the corresponding nanoparticles under the same pH condition. The electrostatic attraction of nanoparticles and PMMA enables the formation of stable core/shell composites of polymer/nanoparticles. The green body is then formed by vacuum filtration of the suspensions and humidity-controlled drying. The first step of the sintering process is to burn out the polymer template. A high volume fraction of the decomposed organic gas might produce macro-cracks because the diffusion rate of the generated gas molecules toward the bulk surface is slower than their formation rate. Therefore, the burnout process should be performed in air at very low heating rates (<0.2°C min⁻¹). For a PMMA–Al₂O₃ nanoparticle system, after the PMMA removal, the Al₂O₃ (34 nm) green body is sintered at 1100°C for 2 hours with a heating rate of 1°C min⁻¹; the pore size is 280 nm and the porosity is 75.5%, which is very close to the theoretical porosity of close-packed spheres [72]. The total and closed porosities decrease slightly with sintering temperatures. For ZrO₂ nanoparticle suspension (with 12 nm mean particle size) and 2 μm PMMA sphere sacrificial template, the synthesized porous material has around 20% porosity after sintering at 1200°C for 4 hours [71]. The self-assembly of the polymer spheres enables the creation of ordered and uniform three-dimensional porous materials [74, 75]. An ordered three-dimensional TiO₂ porous structure with ~70% porosity is fabricated by sintering a polystyrene (160 nm–1 μm) template with TiO₂ nanoparticles (50 nm). The pore size, wall thickness, and porosity of the materials can be controlled by adjusting the size of the polymer and the ratio of polymer to nanoparticles.

TiO₂ membranes with an average pore size of 3.3 nm are fabricated via a template assisted sol–gel process, during which a triblock polymer is used as a template to modify the properties of the sols and finally improve the separation performance of the membranes [76]. Three-dimensionally ordered macroporous (3DOM) tungsten(VI) oxide (WO₃) is obtained with a high pore fraction using ammonium metatungstate ((NH₄)₆H₂W₁₂O₄₀) as a tungsten precursor:



In the presence of a colloidal crystal template of PMMA spheres, WO₃ crystals grow in the nanometer-sized voids between the PMMA spheres, and the specific

surface area increases up to ~ 30 times compared to nonporous WO_3 . The surface area is tunable by changing the PMMA sphere diameter up to 500°C . Higher temperature sintering of the 3DOM WO_3 produces WO_3 nanocrystalline particles by sintering-induced disassembly [77].

Mesoporous CeO_2 nanoparticles (5–10 nm in diameter) are synthesized through a hard-template approach using MCM-48 (an ordered, mesoporous SiO_2 host structure). After removal of SiO_2 by hot NaOH solution, the obtained mesoporous CeO_2 is a reverse-replica of the porous structures of MCM-48 with a pore diameter ranging from 2.5 to 4 nm [78].

A sandwich-vacuum method is used to fabricate TiO_2 binary inverse opals with an open, porous structure [79]. Figures 6.7a, d, and g illustrate the detailed microstructure of the resultant TiO_2 binary inverse opals at number ratios of small to large microspheres of 2, 4, and 8, respectively. These TiO_2 binary inverse opals exhibit highly ordered structure over large domains ($>10\ \mu\text{m} \times 10\ \mu\text{m}$) with few defects. Figures 6.7b, e, and h reveal two sets of pore structures with defined sizes of ~ 670 and ~ 115 nm, respectively. In addition, an increase in the number ratio of small polystyrene microspheres leads to three-dimensional-ordered macroporous TiO_2 structures with a higher porosity. The pores are formed at the sites originally taken by the large and small polystyrene microspheres, and the trilayer solid phase regions are the contact points of large polystyrene microspheres. For all of the binary inverse opals, the average diameter of the macropores is ~ 670 nm, indicating an $\sim 33\%$ contraction of the TiO_2 binary inverse opals. This shrinkage may be caused by both the melting of the polystyrene microspheres and the sintering of the produced particles. The smaller, randomly distributed solid phases are formed at the touch points of the small microspheres with the large ones. The ordered large regions and random small regions indicate that the large polystyrene microspheres are packed in face-centered cubic form, but the small ones are not packed in a highly ordered fashion. By examining the distribution of the large and small regions presented in the cross-sectional images (Fig. 6.7c and f), it can be inferred that the general distribution of the small microspheres is in the body-centered cubic structure and uniform. However, the arrangement of the small microspheres in the interstitial spaces among the large microspheres is not as highly ordered as those on the top layer. Figure 6.7f also demonstrates an ordered structure along the $\langle 100 \rangle$ direction with 12 layers of pores. The cross-sectional image of three-dimensional-ordered macroporous TiO_2 at a lower magnification (Fig. 6.7i) shows that TiO_2 binary inverse opals over relatively large areas can be obtained via this method. The average pore wall thickness is ~ 50 nm and is mechanically robust enough to maintain the integrity of the three-dimensional-ordered macroporous structure. In comparison with the fabrication of TiO_2 unary inverse opals, the fabrication of TiO_2 binary inverse opals is more complicated, with a number of interactions and smaller interstices to be filled.

6.4.4 Special Sintering Processes

6.4.4.1 Microwave Sintering

Microwave sintering uses electromagnetic radiation with wavelengths ranging from 1 mm to 30 cm (frequencies of 300 GHz

to 1 GHz) [80] to sinter nanoparticle-based superstructures and bulk materials. The sintering process is different from electric resistance heating since heat is generated in the bulk of the material through electromagnetic radiation absorption such as ionic conduction, dipole relaxation, and photon–phonon interaction rather than from an external source [81]. The use of microwaves allows the energy to be

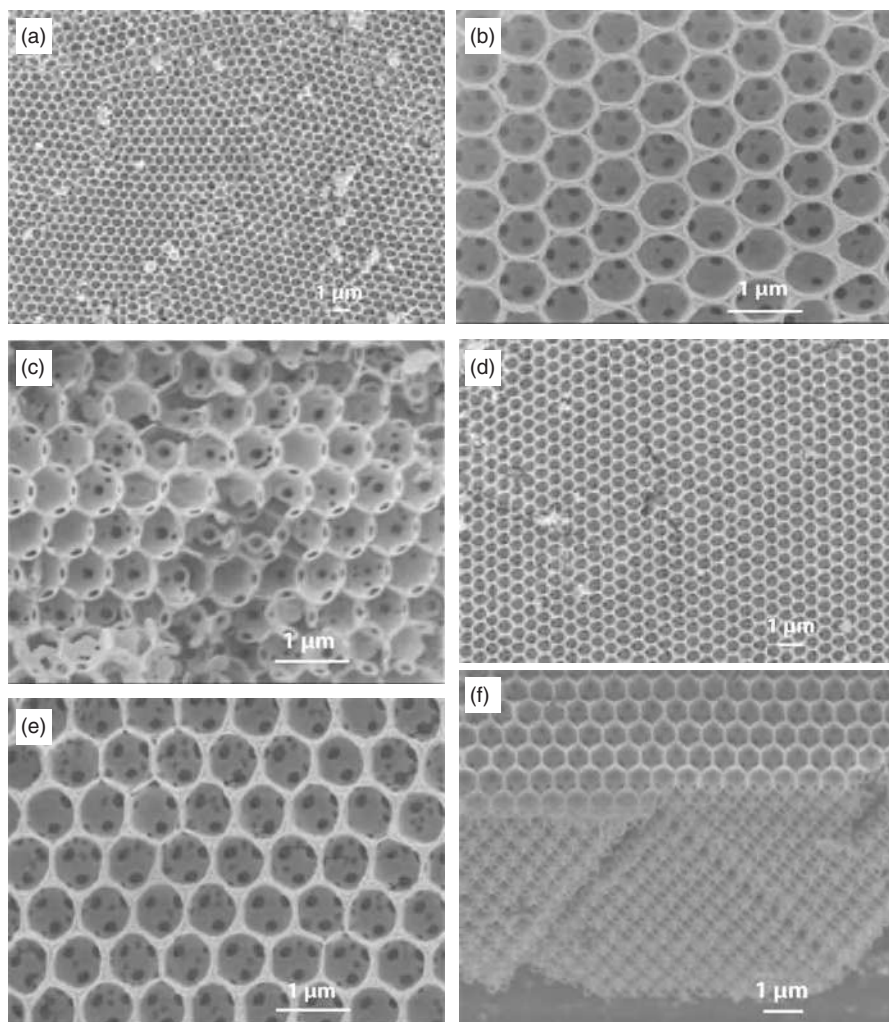


FIGURE 6.7 Top and cross-sectional views of TiO₂ binary inverse opals fabricated using a sandwich-vacuum infiltration technique. The number ratios of small to large microspheres are (a–c) 2, (d–f) 4, and (g–i) 8 [79]. (Reprinted with permission from Cai Z, Teng J, Xiong Z, Li Y, Li Q, Lu X, Zhao XS. Fabrication of TiO₂ binary inverse opals without overlayers via the sandwich-vacuum infiltration of precursor. *Langmuir* 2011;27:5157–5164, Copyright 2011, American Chemical Society.)

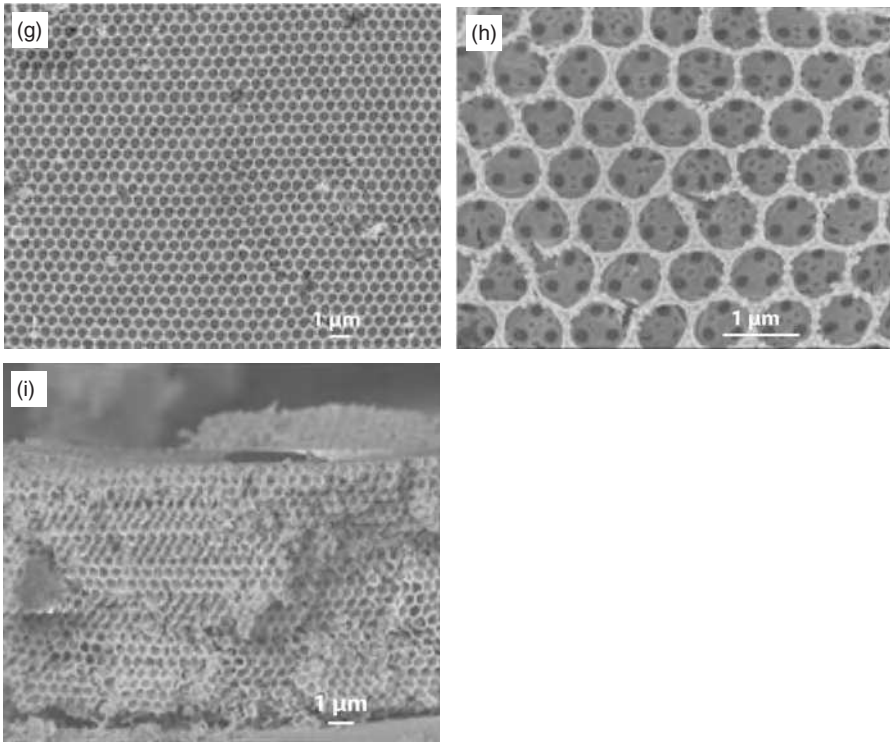


FIGURE 6.7 (Continued)

transferred directly into the materials without being consumed by the surrounding environment. Similar to micron-sized counterparts, microwave sinterability depends on how much and how fast that microwave energy can be absorbed by the material. The rate of energy absorption $W_{\text{microwave}}$ can be expressed in terms of watts per unit volume as [80]

$$W_{\text{microwave}} = \omega \cdot \varepsilon_0 \cdot \varepsilon''_{\text{eff}} \cdot E_{\text{rms}}^2 + \omega \cdot \mu, \quad (6.28)$$

where ω is angular frequency and equals $2\pi f$ (f is microwave frequency in hertz), ε_0 is permittivity of free space (8.85×10^{-12} farads m^{-1}), $\varepsilon''_{\text{eff}}$ is effective dielectric loss (dissipation) factor (unitless), E_{rms} is root-mean-square of internal electric field (volts/m), and H_{rms} is root-mean-square of magnetic field (A m^{-1}). The terms on the right side of Equation (6.28) refer to electric and magnetic losses, respectively. Generally, the magnetic losses are negligible and only the electric losses contribute to the absorbed power, which is proportional to the microwave frequency and the dielectric loss factor. Furthermore, the dielectric loss factor $\varepsilon''_{\text{eff}}$ increases with temperature and frequency for many low-loss materials. Theoretically, higher microwave power frequency is desired for more

efficient power absorption [82–84]. However, this advantage has not been widely realized so far; the majority of microwave sintering is carried out at 2.45 GHz because of the widespread availability of this microwave length for radar and food processing.

Because microwave radiation heats nanoparticles by coupling with electric dipoles and a primary location for such dipoles is grain boundaries, microwave sintering is particularly effective in rapidly heating nanoparticle-based materials, which have enormous surface areas and, subsequently, grain boundaries. Heating rates in excess of $1000^{\circ}\text{C min}^{-1}$ can be achieved. This makes it a desirable technique to sinter porous materials without compromising grain sizes since the rapid heating rate suppresses the surface diffusion and thereby minimizes the grain growth. Due to volumetric heating and enhanced sintering kinetics, sintering can occur at much lower temperatures with shorter processing time and reduced energy consumption. Microwave sintering can be 6–12 times faster and requires only 5% of the energy used by conventional sintering processes [85]. Even low dielectric loss factor hydroxyapatite nanoparticles of 35 nm size with 38% green density have been sintered to $>95\%$ by exposure to microwave radiation for only 5 minutes. The sintered grain size is 200–300 nm [86]. Using dielectric loss specificity, selective sintering has been applied to a ZrO_2 and Al_2O_3 nanocomposite; ZrO_2 preferentially absorbs microwave energy, which leads to localized heating. The resulting composite shows higher fracture strength under the same density and indicates the accelerated neck growth of the ZrO_2 phase [87]. Silver nanoparticles of 30–50 nm size are microwave sintered on polymer substrates for electronic applications [88]. The conductance of the sample substantially increases (10–34% of the theoretical value of bulk silver) compared to that from conventional heating methods.

In cases where the material to be sintered does not itself couple well to microwaves, the compact can be embedded in a good susceptor such as SiC or ZrO_2 for heating. The susceptors are materials that have high dielectric loss factors at low temperatures. This technique has been used to process TiO_2 and Al_2O_3 nanoparticles, which have low dielectric loss factors at $<500^{\circ}\text{C}$. A heating rate greater than $250^{\circ}\text{C min}^{-1}$ is achieved in these cases [89]. Microwave sintering can also involve both microwave heating and radiation heating (microwave hybrid heating) for improved efficiency. Microwave sintering of TiO_2 nanoparticles shows promising results compared with conventional sintering in terms of surface area, crystalline phase, optical property, and morphology [90].

Another system fabricated by microwave sintering is $\text{Al}_2\text{O}_3/\text{ZrO}_2$ nanocomposite [87]. The initial mean particle sizes of Al_2O_3 and ZrO_2 are 150 nm and 50 nm, respectively. Since the microwave absorbency is sensitively dependent on the change of dielectric loss factors of materials with heat, ZrO_2 absorbs significant microwave energy due to its great increase in dielectric loss factor from 25°C to 1000°C [61]. Therefore, localized heating at Al_2O_3 boundaries (where ZrO_2 is situated) can be realized by microwave sintering. The preferential neck growth between grains is promoted by this selective heating, and the sintering temperature is lower than that of conventional sintering for the same sintered density.

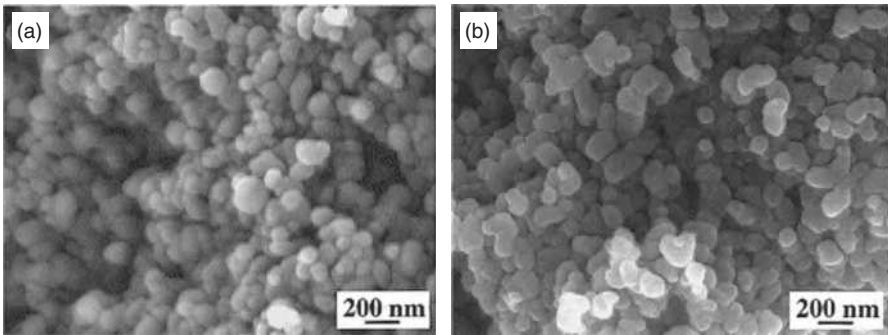


FIGURE 6.8 Typical fracture surfaces of the $\text{Al}_2\text{O}_3/10 \text{ wt}\% \text{ ZrO}_2$ composite with a relative density of 55%: (a) conventional sintering at 1100°C and (b) microwave sintering at 1000°C for 15 minutes [87]. (Reprinted with permission from Oh ST, Tajima K, Ando M, Ohji T. Fabrication of porous Al_2O_3 by microwave sintering and its properties. *Mater Lett* 2001;48:215–218, Copyright 2001, Elsevier.)

Figure 6.8 shows representative micrographs of the fracture surfaces of two composites with a relative density of 55%; one is sintered at 1100°C in the conventional furnace, and the other is sintered at 1000°C in the microwave furnace. In the case of the conventional sintering (Fig. 6.8a), the grain size appears to be nearly identical to that of the initial particles. On the other hand, the microstructure of the composite fabricated by microwave sintering (Fig. 6.8b) is characterized by the enhanced neck growth between the initially touching particles. This neck growth is very likely attributed by the selective heating effect due to the difference in the absorbency of microwaves between the matrix and the second phase. A porous nanocomposite of 55% density is obtained by microwave sintering at 1000°C for 15 minutes, whereas 1100°C is required for the same sintered density for conventional sintering. In addition, the microwave-sintered nanocomposite possesses higher elastic modulus and fracture strength due to the growth of grain necks through surface diffusion.

Since microwave sintering involves no pressure or die constraint, it can sinter complex geometries. Other advantages of microwave sintering include retention of lower temperature crystalline phases and achievement of stronger bonds between adjacent grains [91]. However, microwave sintering is not suitable for large samples. This is due to the nonuniform heating profile occurring inside the microwave cavity. Microwaves can generate “hot spots” where heating is much more rapid. Inhomogeneous heating can lead to inhomogeneous, unpredictable microstructures as well as warping and cracking. These shortcomings are reminiscent of the problems encountered in the rapid-rate sintering using conventional radiation sources, only with the reverse of density gradient direction. Another undesired possibility is the uncontrollable local heating due to the temperature sensitivity of the microwave absorption coefficient, causing melting or cracking of the sample. Variable frequency microwaves can reduce the severity of hot

spots and create multiple new hot spots, resulting in a much more homogeneous heating profile; however, variable frequency microwave sintering is not widely practiced because of the added cost of the technique. In addition to hot spots, the heating rate by microwaves differs based on the sample geometry, specifically the surface area to volume ratio. More heat is lost in the regions with a greater surface area. Conversely, thicker samples heat up more quickly than thin samples [92]. A multimode cavity with adjustable power is beneficial for uniform electromagnetic field distribution and large sample densification [93]. Nevertheless, the different heating rates based on sample geometries make microwave heating difficult to model. An additional problem for microwave sintering is the difficulty of measuring and controlling the sintering temperatures. This is due to the difficulty in placing a contact thermocouple inside the microwave cavity while sintering is in progress. Noncontact temperature measurement, such as fiber optic pyrometer, is not well accepted in accuracy. It has been reported that microwave sintering requires lower sintering temperature [93,94]. Without good temperature control, this proclaimed advantage often goes unproved. Also, uncontrolled excessive heating can cause liquid phase formation and thus excessive grain growth.

6.4.4.2 Electrical Sintering Many sintering processes relying on an electrical current as an aid for densification have evolved. The electric current applied may be pulsed or continuous. If the electric current is pulsed, pulses are often repeated over a period of time. A pulse duration can be as short as milliseconds. The current can range from 2 to 60 kA. Spark plasma sintering is the most widely used electrically assisted sintering technique. Variations of spark plasma sintering include plasma-activated sintering [95,96], pulse electric current sintering [97], and pulse discharge pressure sintering [98]. Traditionally, spark plasma sintering has been used to sinter dense materials. In recent years, pressureless or low pressure spark plasma sintering of nanoparticle-based porous materials has emerged. The objective is to partially densify the materials.

During sintering, the particles are heated as the current or electromagnetic wave passes through them. Direct heating occurs by Joule effect or conduction, depending on the material and the heating stage. Particle surface activation and increased diffusion rates in the contact zones are achieved by the applied current or electromagnetic radiation. Current or electromagnetic wave generated heating facilitates good interparticle bonding [99]. The debate about plasma existence is still ongoing. It is widely believed that a pulsed current creates favorable conditions for impurity removal and activation of particle surfaces. On a local scale, electrical discharge, sparks, plasma, and electrical current concentration may occur. Rapid heating results in bypassing of low temperature regions where surface diffusion controlled sintering is dominant. This preserves the available surface area to temperatures where densification diffusion is significant and the corresponding mass transport is enhanced. Because of these desirable characteristics, electrically assisted sintering enables fast sintering while maintaining nanostructures.

Electrical sintering is used to sinter silver nanoparticles of 10–20 nm size [100]. Identical samples are also thermally sintered in an oven at 120°C for 20 minutes. Scanning electron images show that the oven-sintered samples have very small structural changes from the unsintered state, whereas the electrically sintered sample exhibits significant neck formation and grain growth.

For conventional sintering with an electric current and an applied pressure, it will be labeled as spark plasma sintering in this chapter, without going into the details about the presence of plasma or not. High strength porous Al₂O₃ is fabricated by spark plasma sintering using nanocrystalline Al(OH)₃ (~20 nm) as the starting powder [101]. After the spark plasma sintering between 1000°C and 1200°C with a uniaxial pressure of 10 MPa and a heating rate of 175°C min⁻¹, the volumetric decrease due to the decomposition of Al(OH)₃ and the further shrinkage due to the θ -Al₂O₃ to α -Al₂O₃ phase transformation lead to vacant space near the decomposed particles. Thus, porous Al₂O₃ with porosity ranging between 20% and 60% is fabricated after sintering. The low sintering temperature and short holding time during the spark plasma sintering help to retain the fine pores and narrow pore size distribution in the Al₂O₃ matrix [102, 103]. At 1000°C and 1050°C, the pore size distribution is extremely narrow and varies between 3 and 50 nm. At $\geq 1100^\circ\text{C}$, the pore size distribution becomes wider and is around 100 nm. An increase in the pore size distribution has also been observed with increasing pressure at a constant temperature of 1050°C. Overall, the pore size distribution becomes wider with an increase in sintering temperature or pressure. This is contrary to the normally observed phenomenon that the pore size distribution becomes smaller with increasing sintering temperature. The explanation is likely related to the more active grain neck sintering for the spark plasma sintering process. Due to the relatively low spark plasma sintering temperature and pressure, the average grain size is retained around 50–150 nm. The dominance of the neck growth of grains during spark plasma sintering also leads to high fracture strength (150–300 MPa).

Al₂O₃/Al₂TiO₅ porous composites are produced by spark plasma sintering using 20–45 nm Al₂O₃ and 20–50 nm TiO₂ as raw materials [5]. Above 1280°C, excess TiO₂ reacts with Al₂O₃ with an 11 vol% per mole expansion:



Pores with an average size of 15 μm (ranging from 1 to 35 μm) are homogeneously dispersed in the composite matrix. Due to the use of nano-sized initial particles and the spark plasma sintering technique, the composite possesses both a porous structure and strong dense walls since necking between particles occurs at relatively low temperatures under the electric current and pressure. The resulting porous composites possess good mechanical properties, such as high flexural strength, fracture toughness, Vickers hardness, and elastic modulus [59]. These improvements are attributed to the combination of homogeneous Al₂O₃ and TiO₂ grains, the uniformly distributed pores, the stronger pore walls, the more extensive necks between grains, and strengthened grain boundaries.

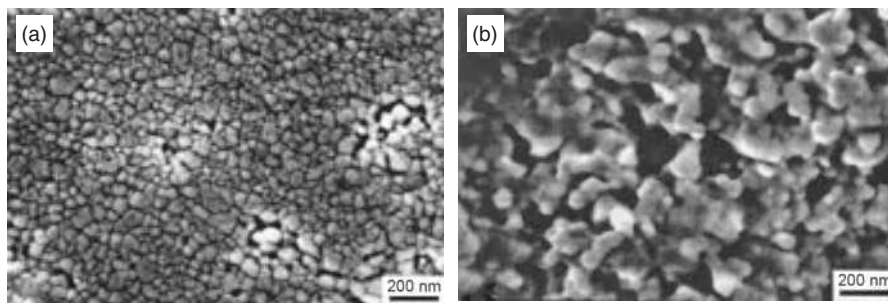


FIGURE 6.9 Scanning electron micrographs of the $3\text{Y-ZrO}_2 = 10 \text{ mol\% Al}_2\text{O}_3$, sintered at 1100°C with a heating rate of (a) $200^\circ\text{C min}^{-1}$ and (b) $30^\circ\text{C min}^{-1}$ [104]. (Reprinted with permission from Yoshimura M, Ohji T, Sando M, Niihara K. Rapid rate sintering of nanograined ZrO_2 -based composites using pulse electric current sintering method. *J Mater Sci Lett* 1988;17:1389–1391, Springer Science + Business Media, Fig. 4.)

ZrO_2 (containing 3 mol% Y_2O_3 , denoted by 3Y-ZrO_2) and 10 mol% Al_2O_3 dispersed 3Y-ZrO_2 (denoted by $3\text{Y-ZrO}_2 = 10 \text{ mol\% Al}_2\text{O}_3$) nanocomposite particles are prepared using a sol-gel synthesis approach and sintered by a pulsed electric current sintering method at 1100°C for 5 minutes in a vacuum under an applied pressure of 50 MPa. The heating rates are varied from $30^\circ\text{C min}^{-1}$ to $200^\circ\text{C min}^{-1}$. Figure 6.9 shows the microstructures of the $3\text{Y-ZrO}_2 = 10 \text{ mol\% Al}_2\text{O}_3$ composites sintered at the two rates to 1100°C , and then rapidly cooled down. The grain size of the composite sintered at $200^\circ\text{C min}^{-1}$ is significantly smaller than that at $30^\circ\text{C min}^{-1}$, supporting the advantage of rapid rate sintering [104].

The sintering behaviors of nanoparticles can also be modified by other secondary phases [15]. Al_2O_3 (200 ppm MgO)/3 vol% ZrO_2 composites are sintered at 1000°C , 1200°C , and 1300°C by pulse electric current sintering. ZrO_2 grains locate at the Al_2O_3 grain boundaries and constrain the Al_2O_3 grain growth. Similarly, MgO and TiO_2 dopants inhibit the grain growth and affect the grain boundary mobility of Al_2O_3 according to the solute drag mechanism [16]. The strength of the resulting sintered nanocomposites is greatly improved without a significant porosity loss due to the neck formation and the enhanced contacts between the grains during the sintering process.

The key advantages of the electrical sintering method include: (i) improved heating, (ii) short sintering time, and (iii) ability to obtain a predetermined final conductivity as an indication of sintering degree [100].

6.4.4.3 Laser Sintering Laser sintering uses a high power laser (e.g., a CO_2 laser) to “fuse” nanoparticles into solid structures. The sintered material density depends more on the laser peak power than on the laser duration. Since the lasers have finite penetration depth into the nanoparticle-based materials, the technique is most suited for thin films or layer-by-layer sintering processes. In addition,

since the lasers have a limited temperature range, they cannot sinter very high melting temperature materials. Composites with polymer contents are commonly used to facilitate the sintering and bonding. Nonetheless, laser sintering can sinter large surface areas quickly, or selectively sinter local areas on a large surface. This can be much desired for nanoparticle-based superstructures or thin film systems.

Porous scaffolds are made using nanoparticles as secondary phases during the sintering process. Selective laser sintering is effective in producing porous nanocomposite scaffolds since sintering conditions such as laser power, scan spacing, and part bed temperature can be adjusted [17, 18]. Carbonated hydroxyapatite (CHAp) of 20 nm size is added into poly(L-lactide) (PLLA) at 10 wt% and sintered by a Sinerstation 2000 SLS machine to fabricate nanocomposite microspheres [17]. Both pure PLLA and PLLA/CHAp composite samples show a porous microstructure with a combination of macropores that are purposely designed and micropores that are formed by partial sintering. In comparison, the PLLA/CHAp nanocomposite scaffold has much smaller grain sizes, while the PLLA scaffold displays a higher degree of fusion within the particles. This is because the added CHAp nanoparticles locate on the boundaries of the PLLA and produce an extra barrier against fusion and diffusion during the sintering process. Calcium phosphate/poly(hydroxybutyrate-co-hydroxyvalerate) nanocomposite scaffolds (with calcium phosphate grain size in the range of 10–30 nm) fabricated by the selective laser sintering process show similar results regarding microstructure evolution [18].

6.5 DENSE NANOPARTICLE-BASED MATERIAL SINTERING

The paramount challenge in fully densifying nanoparticle-based materials is maintaining the sintered grains at <100 nm size. In this regard, free sintering has mainly evolved around improving nanoparticle packing characteristics, using additives to tailor the diffusion rates, and modifying sintering schedules (customized sintering cycles).

6.5.1 Free Sintering

6.5.1.1 Customized Nanoparticle Systems For nanoparticle-based systems that have been sintered to full density by free sintering, a strong correlation between densification and starting particle characteristics, such as small particle size and narrow particle size distribution, has been observed. Y_2O_3 - ZrO_2 particles of 10 nm size can be sintered at 1100°C to >99% density with grain size below 80 nm [105]. Separately, ZrO_2 particles of 4–14 nm size are sintered to full density [106]. The sintering success for both ZrO_2 materials can be partly attributed to the small starting nanoparticle sizes. Grain growth factor for ZrO_2 is around 10 under the free sintering conditions. For many nanoparticle-based materials that start with >20 nm particle size, such high grain growth factor will undoubtedly push the sintered grain size into the micron range. For example, free sintering of ZnO cannot maintain the grains at nanosize [107].

In addition to the starting nanoparticle size and size distribution, high nanoparticle packing (green density) before sintering is another critical factor to consider. Due to the rapid grain growth tendency of nanoparticle-based materials, one natural approach to maintain nano-sized grains is to reduce the necessary sintering densification by starting with a high green density. Based on Equation (6.6), this means increasing the densification rate by increasing volumetric grain boundary area A without accelerating and even possibly suppressing the grain growth rate by eliminating the grain-pore interfacial area. This theoretical predication has been verified by independent work on TiN and SnO₂ nanoparticles [108, 109]. The low green density samples formed under conventional compaction show rapid densification but at the expense of rapid grain growth. For the high green density samples compacted under superhigh pressures, there is no excessive grain growth. More importantly, the final-sintered densities are always higher for the higher green density samples. As another example, a 60% dense Y₂O₃-ZrO₂ sample compacted under 3 GPa pressure is sintered at 1050°C for 5 hours to full density while maintaining the grain size at ~80 nm [110]. The desired densification and grain growth behaviors are believed to be from the increase in contact points and coordination numbers between the grains and the decrease in pore size from the high green density. When phase transformation is involved during sintering, Al₂O₃ serves as a good example to illustrate the green density effect. When γ -Al₂O₃ nanoparticles are compacted at <3 GPa pressure, a microstructure containing a significant porosity sets in at all sintering temperatures due to the development of a highly porous or vermicular structure during γ to α phase transformation. When γ -Al₂O₃ nanoparticles are compacted at >3 GPa pressure, there is no formation of the vermicular structure and nearly full density is obtained with the grain size at 150 nm [111]. A different study shows that extruded γ -Al₂O₃ can transform into α -Al₂O₃ after sintering at 1100°C for 2 hours; α -Al₂O₃ of 99.4% density with a very fine microstructure is produced at low sintering temperatures if the green density is optimized by improving particle packing to 68% density [112]. With high-pressure compaction, the sintering temperature can also be lowered such that the phase transformation unavoidable in micron-sized Al₂O₃ particle sintering can be eliminated. A pressure up to 3.0 GPa and liquid nitrogen lubrication have been used to achieve dense and transparent γ -Al₂O₃ green compacts [113]. The transparent green compacts are further sintered in vacuum at 800°C for 10 hours, and bulk nanostructured γ -Al₂O₃ is obtained.

One approach to modify the grain boundary characteristics is to add a second phase. The desired outcome is that the second phase will reduce the grain boundary mobility while facilitating grain boundary diffusion. Dopants or lower melting temperature species that form a liquid phase at sintering temperatures are often used. Depending on the concentration of the doping element, fully dense and nanostructured materials can be obtained. Y₂O₃ and Al₂O₃ are used in the sintering of Y₂O₃-ZrO₂ and Al₂O₃-ZrO₂. The Al₂O₃ particles have 10 nm size and the Y₂O₃ particles have <20 nm size. The ZrO₂ matrix particles also have 10 nm size. After 1100°C sintering, the ZrO₂-based composites have 30 nm grain size with a full density. Such small grain size is believed to result from

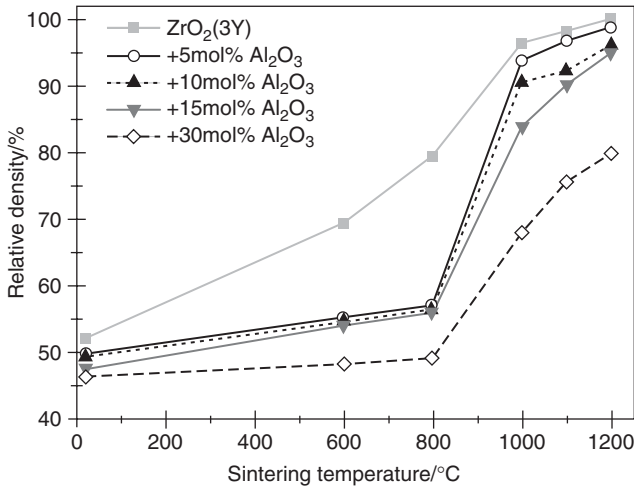


FIGURE 6.10 Relative density change as a function of sintering temperature for different $\text{ZrO}_2(3\text{Y})/\text{Al}_2\text{O}_3$ nanocomposites [117]. (Reprinted with permission from Zhang Y, Chen J, Hu L, Liu W. Pressureless-sintering behavior of nanocrystalline $\text{ZrO}_2\text{-Y}_2\text{O}_3\text{-Al}_2\text{O}_3$ system. *Mater Lett* 2006;60:2302–2305, Copyright 2006, Elsevier.)

a homogeneous distribution of Y_2O_3 and Al_2O_3 particles, hindering ZrO_2 grain boundary mobility and thus grain growth by pinning the grain boundaries [114]. Y_2O_3 is also used in nano-sized TiO_2 to control grain growth [115]. Empirically, the suppression of grain growth during sintering by pinning the grain boundaries with second phase grains is successful when the starting particle size does not exceed 30 nm. Also, weakly agglomerated or nonagglomerated nanoparticles are an essential prerequisite for the homogeneous dispersion of the matrix nanoparticles and the pinning phase. The desired condition for controlled grain growth is that the secondary phase is well separated but not percolative [116].

$\text{ZrO}_2\text{-Y}_2\text{O}_3\text{-Al}_2\text{O}_3$ nanoparticles are synthesized using a chemical coprecipitation method, compacted uniaxially, and sintered. A fully dense sample of 3 mol% Y_2O_3 stabilized ZrO_2 ($\text{ZrO}_2(3\text{Y})$) and a 99% relative density sample of 5 mol% Al_2O_3 doped $\text{ZrO}_2(3\text{Y})$ are obtained after sintering at 1200°C. The presence of Al_2O_3 inhibits ZrO_2 grain growth and suppresses the densification process. Full densification is achieved for the $\text{ZrO}_2(3\text{Y})/5$ mol% Al_2O_3 composites sintered at 1250°C. Figure 6.10 shows the variations of the relative density of the $\text{ZrO}_2(3\text{Y})/\text{Al}_2\text{O}_3$ nanoceramics with the sintering temperature. The relative density increases with sintering temperature and is strongly dependent on the Al_2O_3 content. In the samples without Al_2O_3 , densification starts at $\sim 600^\circ\text{C}$ and increases continuously. A fully dense $\text{ZrO}_2(3\text{Y})$ sample is obtained after sintering at 1200°C; under the same sintering conditions, a relative density of 99% is attained for the 5 mol% Al_2O_3 doped sample. Figure 6.10 shows that the densification is much slower in the samples with higher Al_2O_3 contents (10, 15,

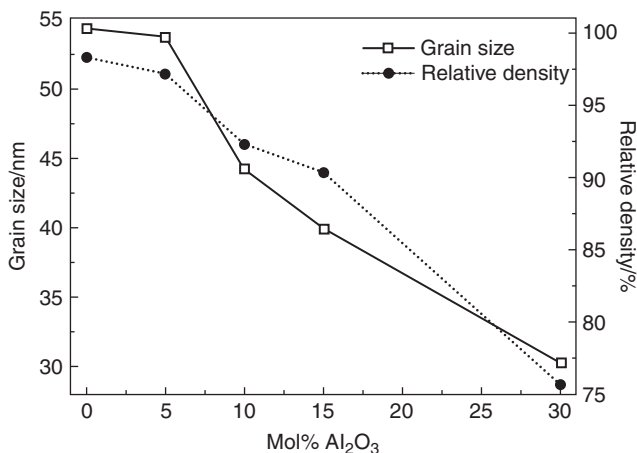


FIGURE 6.11 Effect of Al₂O₃ content on the density and grain size of ZrO₂(3Y)/Al₂O₃ nanocomposites sintered at 1100°C [117]. (Reprinted with permission from Zhang Y, Chen J, Hu L, Liu W. Pressureless-sintering behavior of nanocrystalline ZrO₂-Y₂O₃-Al₂O₃ system. *Mater Lett* 2006;60:2302–2305, Copyright 2006, Elsevier.)

and 30 mol%). Even after sintering at 1200°C, only relatively low densities of 96.3%, 95.2%, and 80% are obtained for the samples doped with 10, 15, and 30 mol% Al₂O₃, respectively. The effect of Al₂O₃ content on the density and grain size of ZrO₂(3Y) samples sintered at 1100°C is presented in Figure 6.11. The ZrO₂(3Y)/30 mol% Al₂O₃ sample after sintering at 1100°C has a very small grain size (30 nm), but at the cost of a relatively low density (75.7%) [117].

ZrO₂(3Y) and CuO nanoparticles are prepared by coprecipitation and copper oxalate complexation–precipitation techniques, respectively. During the sintering of 8 mol% CuO-doped ZrO₂(3Y) sample, several solid-state reactions influence densification behaviors. A strong dissolution of CuO in the ZrO₂(3Y) matrix occurs below 600°C, resulting in significant enrichment of CuO in the ZrO₂(3Y) grain boundary layer with several nanometers thickness. This “transient” liquid phase strongly enhances densification. Around 860°C, a solid-state reaction occurs, forming Y₂Cu₂O₅. This solid-state reaction induces the formation of thermodynamically stable monoclinic ZrO₂ phase and retards densification. Using this microstructural development knowledge during sintering, it is possible to obtain a dense nano–nano composite with a grain size of 120 nm after sintering at 960°C for 20 hours (heating rate 20°C min⁻¹) (Fig. 6.12b). After sintering at 1130°C for 2 hours (heating rate 15 C min⁻¹), the sample shows a nonuniform microstructure with irregularly shaped grains of ~200 nm. Also, some pure CuO grains are observed (e.g., the grain indicated by an arrow in Fig. 6.12a) [118].

In parallel to solid-state sintering that relies on dopants for grain growth suppression, some hard-to-sinter nanomaterials, especially carbides and nitrides, have been sintered by introducing a liquid phase. For example, two eutectic

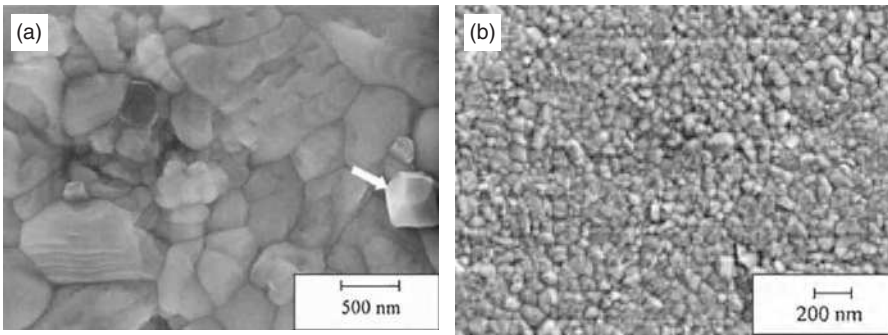


FIGURE 6.12 Scanning electron images of 8 mol% CuO-doped 3 mol% Y_2O_3 - ZrO_2 composites: (a) after sintering for 2 hours at $1130^\circ C$ (heating rate $15^\circ C \text{ min}^{-1}$) and (b) after sintering for 20 hours at $960^\circ C$ (heating rate $20^\circ C \text{ min}^{-1}$) [118]. (Reprinted with permission from Winubst L, Ranb S, Speets EA, Blank DHA. Analysis of reactions during sintering of CuO-doped 3Y-TZP nano-powder composites. *J Eur Ceram Soc* 2009;29:2549–2557, Copyright 2009, Elsevier.)

additives, MnO_2 , SiO_2 and CaO , ZnO , SiO_2 , are added into 5 wt% SiC/Al_2O_3 nanocomposite; densities up to 99% are achieved at $1300^\circ C$ [119]. Scanning electron and transmission electron analyses show the presence of a residual glassy phase along the grain boundaries. However, grain growth control has been a difficult problem for liquid phase sintering. For the above SiC/Al_2O_3 system, average grain size drastically increases to microns when compared to the same matrix nanocomposite processed without additives. Even for the Si_3N_4 - Si_2N_2O transient liquid phase sintering system that is aimed to reduce liquid phase presence time, the grain size still quickly grows to as large as 300 nm [120]. SiC/Si_3N_4 nanocomposites are processed by liquid phase sintering, but the Si_3N_4 matrix grain is micron-sized. Densification of Si_3N_4 with nano-sized Al_2O_3 and Y_2O_3 incorporated *in situ* by a combustion process strongly accelerates the densification [121]. The microstructure of the as-sintered components seems dense and homogeneous; but again, the Si_3N_4 matrix grain is micron-sized. So far, the main focuses of nanoparticle liquid phase sintering studies are to avoid pressure sintering and lower sintering temperatures. Often times, only the secondary phases are nano-sized and the grain growth cannot be effectively suppressed. Densification and coarsening occur concurrently and cannot be effectively separated.

6.5.1.2 Customized Sintering Cycles Substantial efforts have been devoted to devising different sintering schedules in order to fully densify nanoparticle-based materials. The theoretical foundation can be traced back to the constant C' in Equation (6.6) and the constants K_{E-C} , K_s , K_V , S_{E-C} , S_S , and S_V in Equation (6.15). These constants represent intrinsic sintering material properties that change with temperature. By devising different sintering schedules, grain boundary diffusion and volume diffusion densification mechanisms can be

enhanced while evaporation–condensation, surface diffusion, and volume diffusion coarsening mechanisms can be suppressed. Among different sintering schedules studied are rapid-rate sintering, controlled-rate sintering, two-step sintering, and combined stage sintering.

For many nanoparticle-based materials at high sintering temperatures, the activation energy for densification is lower than that for coarsening; grain boundary diffusion or volume diffusion densification becomes dominant and leads to more effective densification. Based on this consideration, rapid heating to high temperatures should be adopted in order to favor densification. If nanoparticles can quickly pass the temperature range where surface diffusion controlled coarsening prevails over densification, then densification should dominate the sintering process. For 100 nm starting Al_2O_3 particles, the sintered grain size decreases from 875 nm to 443 nm when the heating rate increases from 2°C min^{-1} to $25^\circ\text{C min}^{-1}$ while other parameters are kept the same [122].

To obtain high density or full density samples, the use of rapid-rate sintering alone is limited, partly because densification and grain growth simultaneously increase at peak temperatures. More frequently, rapid heating is used as the first step in more complicated sintering schedules. Also, rapid-rate sintering processes are only suitable for small or thin-walled articles. When this method is applied to large size samples, a thermal gradient inevitably develops between the surface and the core of the samples and subsequently retards the bulk of the sample from being densified. For 3 mol% $\text{Y}_2\text{O}_3\text{--ZrO}_2$ nanoparticle samples, a fast heating rate (such as $200^\circ\text{C min}^{-1}$) severely retards densification in comparison to a slow heating rate of 2°C min^{-1} [123]. Microstructural evidence suggests that densification rate greatly exceeds heat transfer rate in this material; consequently, the sample interior is not able to densify before being geometrically constrained by a fully dense shell which forms at the sample exterior [123]. Rapid-rate sintering is also observed to severely retard the densification of indium doped tin oxide [124]. Similarly, it is postulated that the heat transfer rate in indium doped tin oxide is much slower than the densification rate. Due to the differential densification, the outermost region of the sample is well densified, while many large pores are observed inside the densified ring.

Controlled-rate sintering uses densification as a monitoring parameter for heating rate control. The main strategy is to maintain the open pore channels by extending the intermediate stage of sintering so that the grain boundary can be effectively impeded and pore removal through the grain boundary can continue well into the $>90\%$ density range. Controlled-rate sintering is a theoretically sound but practically difficult approach in controlling nano-sized grain growth while encouraging densification. It requires extensive benchmark data on grain growth and densification rate correlation in order to have a suitably prescribed densification rate, and thus an optimal sintering schedule. Also, grain growth has to be carefully controlled during long time high temperature sintering. So far, the approach is limited to only a few systems without well-recognized success. It is common to find that in controlled-rate sintering, the first stage usually involves rapid-rate sintering.

The third approach in nanoparticle-based material sintering by manipulating sintering schedule is two-step sintering. The success of this process is first demonstrated by Y_2O_3 nanoparticle sintering. With nano-sized starting Y_2O_3 particles, the grain size is 60 nm for magnesium-doped Y_2O_3 and 115 nm for pure Y_2O_3 after full densification [47, 48]. During sintering, Y_2O_3 is heated to 1310°C at $10^\circ\text{C min}^{-1}$ and cooled at $50^\circ\text{C min}^{-1}$ to 1150°C with no dwell. Full density is achieved after holding at 1150°C for 20 hours, during which there is no grain growth. This approach is further corroborated by $BaTiO_3$ and Ni–Cu–Zn ferrite systems [49]. To succeed in the two-step sintering, a sufficiently high density (at least 70%) should be obtained during the first step of the sintering process, the high temperature step. The pore morphology achieved during the first step, prior to the second step low temperature sintering, is very important. The key is to effectively utilize the kinetic difference between grain boundary diffusion and grain-boundary migration. The $>70\%$ density achieved during the first step sintering preserves the pore-grain triple junctions and retards grain boundary migration. During the second step sintering, the grain junctions and grain boundary-pore junctions have a higher activation energy to prevent grain boundary migration, but the temperature is high enough for grain boundary diffusion. When the pores are subcritical and unstable against shrinkage at the appropriate second step sintering temperature, grain boundary migration is much slower compared to grain boundary diffusion, and sintering densification can proceed up to 100% without excessive grain growth. The end result is enhancement of grain boundary diffusion and suppression of grain boundary mobility. This approach reveals again the importance of high particle packing density (this time achieved by the first step sintering). Even though it has not been explicitly discussed, the results are clearly consistent with the high coordination number and large grain boundary area that Equation (6.6) calls for.

3 mol% Y_2O_3 -stabilized ZrO_2 nanoparticles of ~ 16 nm size are two-step sintered to $\sim 99\%$ dense with an average grain sizes as fine as ~ 65 nm. Sintering is performed using a hybrid microwave/radiation sintering furnace that can be operated in either pure radiation or hybrid microwave/radiation mode. The microwave frequency is 2.45 GHz, and a fixed microwave energy of 600 W is used throughout the sintering cycle, with the amount of radiation power being varied to yield the desired temperature–time profile. The two-step sintered samples are heated at the same 7°C min^{-1} rate to an initial temperature, but after only 0.1 minute immediately cooled back down to a lower temperature as rapidly as possible before holding for periods of up to 30 hours. For the single-step sintered samples, the sintering temperature is from 900°C to 1150°C , while for the two-step sintered samples the initial high temperature is 1150°C and the lower sintering temperature after the prolonged holding is varied between 1000°C and 1050°C . With radiation heating, there is a steady increase in grain size up to 90–95% of full density when there is a sharp increase in grain size. This fits with the closing of the porosity, at which point grain growth generally becomes significant. The use of two-step sintering, however, clearly reduces grain growth while allowing densification to continue. As explained before, to succeed in two-step sintering, a

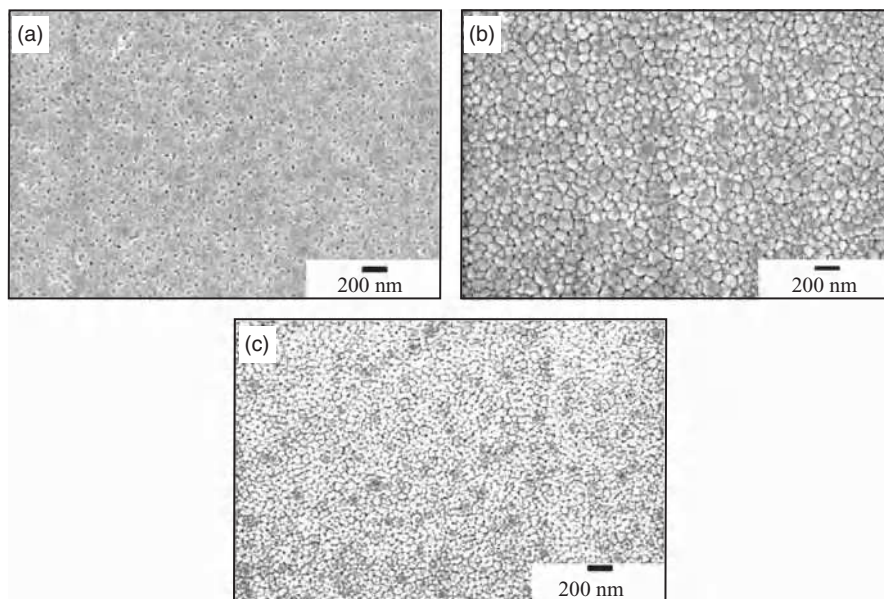


FIGURE 6.13 Nanostructures for the 3 mol% Y_2O_3 -stabilized ZrO_2 samples sintered by hybrid microwave/radiation sintering. (a) End of first step sintering, (b) end of single-step sintering, and (c) end of two-step sintering [125]. (Reprinted with permission from Binner J, Vaidhyanathan B. Processing of bulk nanostructured ceramics. *J Eur Ceram Soc* 2008;28: 1329–1339, Copyright 2008, Elsevier.)

density $\geq 70\%$ of the theoretical density should be obtained during the first step; the benefits arising from this level of densification are related to the pores, which become subcritical and unstable against shrinkage, rather than the density value itself. For the radiantly heated samples, the rapid increase in grain growth begins at densities of 90–95%, achieving full density with an average grain size ≥ 160 nm. However, the combination of hybrid heating with the two-step sintering technique results in the final grain size in the range of 60–80 nm while achieving densities in excess of 99% [125]. Figure 6.13 shows the nanostructures for the 3 mol% Y_2O_3 -stabilized ZrO_2 samples sintered by hybrid microwave/radiation sintering.

The two-step sintering approach is also used to enhance densification with minimum grain growth for bulk nano- Si_3N_4 ceramics. Addition of Y_2O_3 changes the primary phase, giving rise to β - Si_3N_4 with nanoscale grain size and near full density without the Si_2N_2O phase. During the single-step sintering conducted at 1650–1800°C with no holding, sintered densities between 76% and 98% theoretical are achieved. Grain size data suggest that grain growth is not significant for single-step sintering up to 1750°C due to the rapid heating rate and very short holding time. With regard to the second sintering step, sintering for 20 hours at 1450°C does not yield significant grain growth, while sintering at 1500°C for 20 hours shows grain growth. The combination of a first step sintering at a

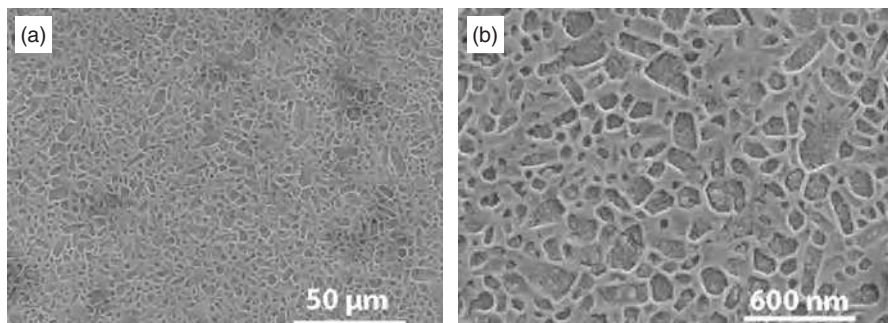


FIGURE 6.14 Scanning electron micrographs showing uniform Si_3N_4 microstructures with 12 wt% Y_2O_3 and 3 wt% Al_2O_3 additives. (a) Low magnification and (b) high magnification [126]. (Reprinted with permission from Kim H-D, Park Y-J, Han B-D, Park M-W, Bae W-T, Kim Y-W, Lin H-T, Becher PF. Fabrication of dense bulk nano- Si_3N_4 ceramics without secondary crystalline phase. *Scr Mater* 2006;54:615–619, Copyright 2006, Elsevier.)

peak temperature of 1750°C with no holding and a second step at 1450°C with a 20 hour holding yields 97% theoretical density with ~ 67 nm grain sizes. The microstructure of the sample sintered at 1650°C , followed by sintering at 1425°C for 15 hours, is homogeneous (Fig. 6.14). Clearly, the two-step sintering cycle does not lead to significant grain growth in the final stage sintering [126].

To utilize the full advantage of sintering schedules in encouraging sintering densification and suppressing grain growth, a combination of rapid-rate sintering, controlled-rate sintering, and two-step sintering (also called combined stage sintering) has been studied for the BaTiO_3 system [127]. The process starts with rapid-rate sintering to a certain temperature followed by controlled-rate sintering to a high temperature. Then, the sintering system is quickly lowered to another low temperature for extended thermal holding. This combined stage sintering method is believed to facilitate the control of grain size and pore morphology. The application of this sintering approach to pure BaTiO_3 nanoparticles enables suppression of grain growth during the intermediate and final stages of sintering, achieving fully dense BaTiO_3 with 108 nm grain size. The grain growth rate increases drastically during isothermal sintering from 1.9 nm h^{-1} at 1050°C to 18 nm h^{-1} at 1150°C . There is a narrow temperature window that should be carefully controlled to avoid excessive grain growth. Still, the grain growth control is a daunting task. The final sintered density can only reach 97.6% while maintaining ≤ 100 nm grain size. If the sintered density is to increase to more than 98%, the grain size drastically increases to 250 nm.

6.5.1.3 Remarks on Free Sintering By any measure, free sintering of dense nanoparticle-based materials requires careful control of nanoparticle size, nanoparticle packing, sintering additives, and sintering schedules in order to enhance sintering densification while suppressing grain growth. Even with the best

efforts, pressureless sintering of dense nanoparticle-based materials remains a challenging task. For nanoparticles, the starting nanoparticle size should be as small as possible, preferably 10 nm or less. Also, the particle size distribution should be as narrow as possible, almost definitely mono-dispersed. Otherwise, coarsening can easily occur. Green density should be as high as possible, preferably higher than 60%. Also, the nanoparticles should be free from agglomeration, which can create large defects and prevent full densification. Dopants are effective in suppressing grain growth. Efforts in studying dopants should be continued with the premise that the additives do not introduce detrimental effects to the other aspects of dense nanoparticle-based materials. However, liquid phase sintering should be avoided if fast grain growth is unacceptable. For sintering schedule control, two-step sintering and combined stage sintering are the most effective. Rapid-rate sintering cannot effectively address the grain growth issues that are active at all temperatures, especially at high temperatures.

6.5.2 Pressure Sintering

Since free sintering of dense nanoparticle-based materials is very challenging, different strategies with external sintering driving forces have been evaluated. Supplying additional sintering driving force is often viewed as an effective strategy in densification to counter the rapid grain growth. Pressure sintering, which includes hot pressing, hot isostatic pressing, sinter forging, and pressure spark plasma sintering, can effectively achieve full densification for nanostructured materials by providing external sintering driving forces. Lower sintering temperature and shorter sintering time can be used while achieving full densification. However, microstructural inhomogeneity and sintered shape limitation are difficult to overcome. Pressure sintering also incurs more cost, and the densified microstructures may be anisotropic. Creep and contact flattening have been widely believed to be responsible for densification.

6.5.2.1 Hot Pressing Hot pressing is the sintering process in a rigid die by applying heat and a uniaxial pressure to loose or precompacted nanoparticles. The radial direction experiences a smaller shear stress than the applied axial compressive pressure, P_{applied} . The radial stress can be estimated as νP_{applied} , where ν is Poisson's ratio. For the densification rate in the axial direction, Equations (6.4) and (6.6) can be modified to account for the externally applied pressure by assuming no plastic deformation or creep:

$$\left. \frac{dV}{V \cdot dt} \right|_{\text{d,HP}} = \frac{A_{\text{GB}}}{V} \cdot \frac{1}{\sqrt{2\pi M_w \cdot R \cdot T}} \cdot \frac{\Omega \cdot P_{\text{flat}}}{kT} ((\alpha_{\text{GB}} \cdot \gamma_{\text{GB}} + \alpha_{\nu} \cdot \gamma_{\nu}) \Sigma \mathbf{H} + \alpha_{\text{HP}} \cdot P_{\text{applied}} \cdot \phi'), \quad (6.30)$$

$$\left. \frac{d\rho}{\rho \cdot dt} \right|_{\text{d,HP}} = C' \cdot A \cdot \Sigma \mathbf{H} + C_{\text{HP}} \cdot A \cdot P_{\text{applied}} \cdot \phi', \quad (6.31)$$

$\alpha_{\text{HP}} \cdot P_{\text{applied}} \cdot \phi'$ in Equation (6.30) represents the sintering driving force from the externally applied pressure, α_{HP} is the diffusion coefficient of the sintering process due to hot pressing pressure, ϕ' is stress intensification factor due to the particle–particle neck geometry, and C_{HP} is a system-related constant determined by hot pressing stress and temperature. Since the compact undergoing sintering often experiences plastic deformation or creep and is constrained in the radial direction, the shrinkage rates are often not represented by Equation (6.30) or (6.31), and the net shrinkage of the compact is often reflected in the axial dimensional decrease only. Because of the anisotropic shrinkage, microstructural evolution is nonuniform. Grain size increase tends to be more extensive in the radial direction than in the axial direction.

For micron-sized particles, the typical hot pressing temperature and pressure are up to 2000°C and hundreds of megapascals. For nanoparticle-based materials, the sintering temperature is generally a few hundred degrees centigrade lower than that of the micron-sized counterparts, but the sintering pressure is much higher because of the much higher frictional forces from nanoparticles. Hot pressing can yield dense compacts with nanostructures [128]. However, a pressure as high as gigapascals can be necessary to maintain the nano-sized grains. Nanoparticles of nickel and ZrO₂ (11 nm and 90 nm, respectively) are synthesized from NiO and zirconium by high-energy ball milling. A highly dense nanostructured 2Ni–ZrO₂ (mol%) composite is consolidated at 650°C by high-frequency induction heat sintering within 2 minutes of the mechanical synthesis of the powders (Ni–ZrO₂) under 500 MPa pressure. This process allows quick densification to near theoretical density and prohibits grain growth. The average grain sizes of ZrO₂ and nickel are about 12 nm and 31 nm, respectively [129]. MgO of 10 nm particle size is hot pressed to 99.5% at 790°C and 150 MPa, and <74 nm grain size is obtained. An interesting finding is that not only the magnitude of the applied pressure but also the temperature at which the pressure is applied is critical for effective MgO densification. Higher shrinkage and shrinkage rate are obtained when the pressure is applied at 550°C rather than at room temperature [130]. It is believed that at room temperature MgO nanoparticles have higher frictional forces; if the gigapascal level pressure is applied at this point, it can lead to plastic deformation induced pores and strain hardening. At elevated temperatures, frictional forces may be overcome by surface diffusion; grain sliding is enabled and equiaxed grains can be maintained without strain hardening. However, such pressure sensitivity is closely related to the nanoparticle hardness and the magnitude of the pressure applied. For nanoparticles with a high hardness, this phenomenon may not be observed.

A high temperature and high pressure sintering method is adopted to fabricate dense nanostructured BaTiO₃. For the direct procedure sintering (pressed at 7 MPa and sintered at 6 GPa, 1000°C for 5 minutes), there exist many “beams” in nanostructured BaTiO₃. The “beams” are composed of barium, titanium, and oxygen. Using the three-step sintering method, that is, two times cold pressing (pressing at 7 MPa followed by cold isostatic pressing at 3 GPa, grinding the pellet into a powder and repressing it into a pellet at 7 MPa) followed by the

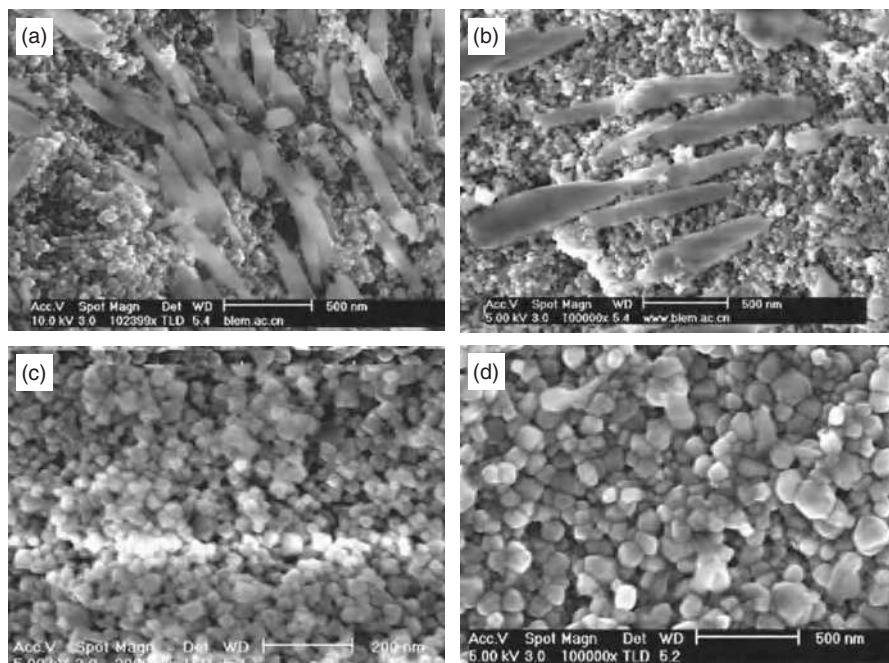


FIGURE 6.15 Scanning electron images of nanostructured BaTiO_3 ceramics. (a) 30 nm grain size prepared by the direct procedure sintering with 10 nm starting particles, (b) 60 nm grain size prepared by the direct procedure sintering with 50 nm starting particle size, (c) 30 nm grain size prepared by three-step sintering method with 10 nm starting particle size, and (d) 60 nm grain size prepared by three-step sintering method with 50 nm starting particle size [131]. (Reprinted with permission from Xiao CJ, Jin CQ, Wang XH. The fabrication of nanocrystalline BaTiO_3 ceramics under high temperature and high pressure. *J Mater Process Technol* 2009;209:2033–2037, Copyright 2009, Elsevier.)

high pressure and high temperature sintering at 6 GPa, 1000°C for 5 minutes, all the “beams” disappear. Moreover, dense nanostructured BaTiO_3 with uniform grain sizes is obtained. The three-step sintering process is believed to be effective in removing nanoparticle agglomerates and thus beam formation. The scanning electron image of the sintered samples with 10 nm starting particle size, fabricated by the direct procedure sintering, are shown in Figure 6.15a. Without the cold isostatic pressing step, the grain size is about 30 nm. The dimensions of the “beams” are about 250–400 nm in length and 60–120 nm in diameter, which are far larger than that of the grains. The average density of the sintered samples is 94.5%. For the direct procedure sintering with BaTiO_3 nanoparticles of 50 nm size (Fig. 6.15b), there also exist many “beams” in the sintered nanostructured samples. The BaTiO_3 grain size is 60 nm. The dimensions of the “beams” are 600–1000 nm in length and 120–400 nm in diameter. The scanning electron images of the BaTiO_3 samples sintered by the three-step

method are shown in Figures 6.15c and d for 10 nm and 50 nm starting particle sizes. The samples exhibit homogeneous grain size distributions, and the grain sizes are about 30 and 60 nm, respectively. The densities are about 96.1% and 97.2%, respectively. Moreover, the “beams” in the nanostructured BaTiO₃ matrix disappear [131].

As discussed earlier, phase transformation is common during sintering of nanoparticle-based materials and presents challenges for densification. This problem applies equally to the hot pressing process. The well-known example is Al₂O₃. Even with MgO addition (0.1 wt%) to suppress Al₂O₃ grain growth, the Al₂O₃ phase transformation from $\gamma \rightarrow \alpha$ increases grain size from 23 to 75 nm, and hot pressing (1450°C, 60 MPa) fails to maintain nano-sized grains [132]. In a different study, Al₂O₃ is fabricated without additives under high pressures (2–7 GPa) at different temperatures (600–1200°C) using 20 nm γ -Al₂O₃ nanoparticles as the starting material. High pressure increases the nucleation rate while reducing the growth rate of the transformed α phase so that Al₂O₃ grain size decreases and nano-sized grains in the sintered structure are achieved. Grain size of ~200 nm and density of 98.0% are obtained under the sintering condition of 1000°C at 7 GPa with a holding time of 1 minute.

Even though the problematic aspect of phase transformation in hindering full densification of nanoparticle materials is known, one special type of hot pressing can desirably utilize phase transformation to assist densification. The necessary pressure is usually very high (on the order of a few gigapascals); however, to minimize diffusion, the densification temperature is desirably moderate (around $1/3 T_m$). This technique is called transformation-assisted sintering and only applies to materials undergoing a phase transformation during the sintering process. The transformation to the new phase must necessarily experience a significant volume reduction. During sintering, the initial phase becomes metastable. By controlling the nucleation and growth of the new phase at high temperature and pressure, a nanostructure can be achieved after complete phase transformation. High pressure is the necessary condition for fast nucleation and slow diffusion, thus, slow new phase grain growth. Pressure on the order of 8 GPa can be applied to maximize the formation of nuclei of the stable phase. This combination of pressure and temperature can produce sintered grain sizes even smaller than those of the starting nanoparticles, contrary to the well-known sintering processes that often result in increased grain sizes. Anatase TiO₂ has been sintered via pressure induced phase transformation at 445°C and 1.5 GPa for 1 hour; the sintered sample is 98% dense rutile phase with a grain size of 36 nm [133]. The anatase to rutile phase transformation that begins at about 650°C can be progressively lowered as the pressure is raised. With increasing pressure during the phase transformation assisted sintering process, a continued grain refinement of the rutile phase is observed [134]. Phase transformation-assisted sintering of γ -Al₂O₃ nanoparticles has been carried out in a similar manner to obtain 98% dense α -Al₂O₃. The grain size of the consolidated α -Al₂O₃ is <50 nm after sintering at 8 GPa and 800°C for 15 minutes, which stands as the smallest grain size for α -Al₂O₃ so far [135].

Liquid phase sintering in combination with pressure sintering is another approach used to maintain nano-sized grains. For example, 30 nm SiC nanoparticles are densified through combined hot pressing (30 MPa) and liquid phase sintering; Al₂O₃ and Y₂O₃ are used as sintering aids. Dense SiC materials with a mean grain size <100 nm are obtained after 20 minutes of sintering [136]. However, the amount of the liquid phase needs to be carefully adjusted in order to combine liquid phase sintering and hot pressing. The optimal liquid phase for the SiC matrix is 10 wt%. For Si₃N₄ hot pressing at 1850°C and 2 MPa, Y₂O₃ liquid phase content of 9 wt% induces extensive grain growth. The SiO₂ surface layer on the Si₃N₄ nanoparticles is believed to contribute to the undesirable glassy phase in addition to the Y₂O₃ liquid phase added [137]. In another case, dense 20 vol% TiN-Si₃N₄ composites are obtained by hot pressing at 1550–1800°C and 30 MPa for 1 hour with 3 vol% addition of Al₂O₃ and 5 vol% addition of Y₂O₃ as liquid phases. The average TiN nanoparticle size is about 40 nm, but the Si₃N₄ matrix is in the micron range [138]. Clearly, the most desirable approach is still to hot press nanoparticles without additives. Amorphous Si₃N₄ of 18 nm size compacted to 87% density can be densified without additives under high pressures (1.0–5.0 GPa) and at 1600°C [139]. A sintered density of 95–98% is obtained at temperatures slightly below the onset of crystallization (1000–1100°C) followed by a slow density increase at higher temperatures, indicating significantly enhanced densification of the amorphous Si₃N₄ at relatively low temperatures under a high pressure. The clear distinction between these three Si₃N₄ studies is the higher isostatic pressure used for the last one, resulting in a smaller grain size with high densification.

For a different system, similar strategies apply. The densification of TiC-10 vol% metal (cobalt, nickel, and iron) materials is accomplished within 2 minutes using a high-frequency induction heated sintering method under 80 MPa pressure. Highly dense TiC-metal (cobalt, nickel, and iron) composites with a relative density up to 99.9% are obtained. The average grain size of TiC in the TiC-10 vol% nickel composite is approximately 44 nm [140]. Also, material purity is critical for nanoparticle-based material sintering. The extremely high free carbon content and low green density of the commercially available SiC nanoparticles are responsible for their poor sinterability. Reduction in the free carbon content by oxidation and control of the SiO₂ content by acid treatment are beneficial for enhancing the sinterability of the SiC nanoparticles during liquid phase sintering. A grain size of ~100 nm and a density of 95% are achieved for the treated SiC particles containing Al₂O₃-Y₂O₃-CaO as the sintering additive at 1750°C and 25 MPa pressure [141].

Overall, hot pressing is a well-accepted nanoparticle material sintering technique. It requires equipment of moderate complexity while providing sintered components with a high density and limited grain growth. Also, samples with moderately complex cross sections can be sintered. However, hot pressing produces anisotropic microstructures, which has been well documented in the literature. The radial direction usually has larger grain size than the axial direction as a result of the applied pressure in the axial direction.

6.5.2.2 Hot Isostatic Pressing Hot isostatic pressing uses flexible dies and hydrostatic pressure for densification. The sintering pressure is usually generated by a pressurized inert gas, such as argon, nitrogen, or helium. The compaction is applied to all surfaces of the sample in comparison to only two opposite surfaces for hot pressing. Sintering densification rate can be expressed, again under the assumption of no plastic deformation or creep, as

$$\frac{dV}{V \cdot dt} \Big|_{d,HIP} = \frac{A_{GB}}{V} \cdot \frac{1}{\sqrt{2\pi M_w \cdot R \cdot T}} \cdot \frac{\Omega \cdot P_{flat}}{kT} ((\alpha_{GB} \cdot \gamma_{GB} + \alpha_V \cdot \gamma_V) \times \Sigma H + \alpha_{HIP} \cdot P_{applied} \cdot \phi'), \quad (6.32)$$

$$\frac{d\rho}{\rho \cdot dt} \Big|_{d,HIP} = C' \cdot A \cdot \Sigma H + C_{HIP} \cdot A \cdot P_{applied} \cdot \phi', \quad (6.33)$$

$\alpha_{HIP} \cdot P_{applied} \cdot \phi'$ in Equation (6.32) represents the sintering driving force from the isostatically applied pressure, α_{HIP} is the diffusion coefficient due to hot isostatic pressing stress, and C_{HIP} is a system-related constant determined by hot isostatic pressing stress and temperature. Higher hot isostatic pressing pressure enables faster densification. When the applied pressure is high enough to cause plastic deformation or creep, the densification rate will be higher than those represented by these equations.

A review paper has detailed the engineering aspect of hot isostatic pressing [142]. With the understanding that hot isostatic pressing was developed and has been mainly used for hard-to-sinter materials, it is still reasonable to say that its applications to nano-sized materials are not as common as they should be. Hot isostatic pressing of nanostructured oxides is best demonstrated by a 10 vol% ZrO_2 - Al_2O_3 nanocomposite with the intent of using ZrO_2 nanoparticles to reduce Al_2O_3 grain growth. The nanoparticle mixture is cold isostatically compacted at 495 MPa and presintered at 1200°C for 2 hours before it is hot isostatically pressed at 1200°C and 247 MPa. The sintered sample is 99% dense with <100 nm grain size [143]. For the oxides that experience phase transformation, hot isostatic pressing in general cannot provide the gigapascal level pressure required for phase transformation-assisted densification. For example, hot isostatic pressing (1400°C, 200 MPa) of Al_2O_3 - ZrO_2 nanocomposite (27–50 vol% Al_2O_3) is studied [144]. The intent is to use the metastable to stable phase transformation of ZrO_2 for nanocomposite formation. Even though the sintered grains are mostly smaller than 200 nm, grain growth is still obvious. Moreover, densification of other oxides is not as successful as the Al_2O_3 - ZrO_2 composites. For example, a TiO_2 compact with 14 nm particle size is cold isostatically compacted at 2 GPa to 75% density and then hot isostatically pressed at 2 GPa and 1000°C. Densification is enhanced to 95% at 900°C, but rapid grain growth to micron sizes sets in after 900°C [145]. For 5.0 vol% nano-SiC/ Al_2O_3 composite hot isostatically pressed at 7–8 MPa, the average Al_2O_3 matrix grain size is in the micron range and only the dispersed SiC is nano-sized [146]. Again, the relatively low pressure cannot

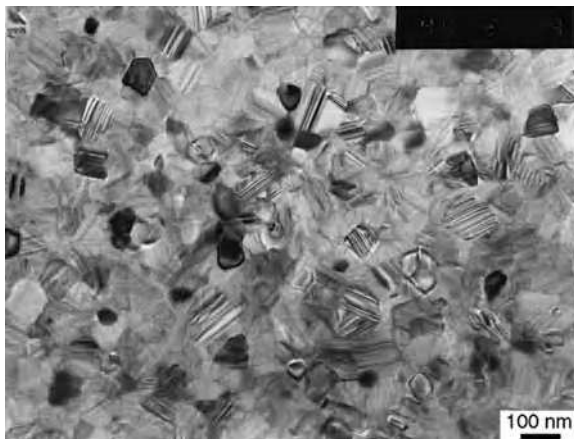


FIGURE 6.16 Transmission electron micrograph of monolithic SiC sample created by hot isostatic pressing [147]. (Reprinted with permission from Dong SM, Jiang DL, Tan SH, Guo JK. Preparation and characterization of nanostructured monolithic SiC and Si₃N₄-SiC composite by hot isostatic pressing. *J Mater Sci Lett* 1997;16:1080–1083, Springer Science + Business Media, Fig. 2.)

provide a sufficient sintering driving force for grain growth control. Nano-sized SiC is maintained by keeping the content below the percolation threshold for SiC grain contact. Overall, hot isostatic pressing is not as widely applied to oxide nanomaterials as it can potentially be, and this trend shows no indication to change.

For nonoxides, hot isostatic pressing has been applied to both carbide and nitride nanomaterials, as well as their composites. The relatively more active research activities for these materials are likely facilitated by the knowledge accumulated from the micron-sized counterparts. Nanostructured SiC is prepared by hot isostatic pressing. A dense and homogeneous nanostructure with ~ 100 nm grain size is obtained at 1850°C and 200 MPa pressure after sintering for 1 hour [147]. The glassy SiO₂ layer on the SiC grains plays an important role in obtaining the nanostructure shown in Figure 6.16. For Si₃N₄ hot isostatically pressed at 1850°C and 40 MPa, grain growth of two orders of magnitude occurs due to the low pressure used [137]. High pressure hot isostatic pressing can potentially maintain Si₃N₄ grains at nanoscale but has not been reported. Si₃N₄/SiC nanocomposite is prepared using pretreated Si₃N₄ and SiC nanoparticles; a dense and homogeneous nanostructure with an average grain size of 50 nm is obtained at 1750°C and 150 MPa for 1 hour. The limited grain growth is attributed to the heterophase compositions during hot isostatic pressing. The existence of carbon in the nanoparticles benefits the removal of SiO₂ along the grain boundaries.

Hot isostatic pressing has the advantage of uniform densification in all directions and can thus offer homogenous microstructures. The process can also form components within precise tolerances and allows the formation of complex

geometries while suppressing grain growth. These advantages are inherent in the process itself and apply to materials of nano to micron starting particle sizes. However, hot isostatic pressing has its own limitations. The well-known factors are the complexity and high cost of hot isostatic pressing equipment. In addition, there is a lack of container materials that have a softening temperature in the range of 600–1100°C, which is the sintering temperature range for many nanoparticles [148]. Also, hot isostatic pressing is limited in achieving high pressures, mostly only up to 200 MPa. This pressure level is far less than that of hot pressing (usually up to gigapascal level) and is often not high enough to achieve densification while controlling grain growth. Another important factor that should be considered in hot isostatic pressing of nonoxides is the stoichiometry of the nanoparticles. For example, the glassy SiO₂ layer on SiC greatly facilitates SiC densification, which has its pros and cons [147]. When lower melting temperature oxides exist, they accelerate densification with glassy phase formation in-between the grain boundaries. However, these species may also form a liquid, accelerate grain growth, and deteriorate material properties even though the overall densification is improved.

6.5.2.3 Sinter Forging Sinter forging is a combined superplastic deformation and sintering process. The technique is mainly used for ductile materials such as metals. Since nanoparticles exhibit superplasticity at higher temperatures, sinter forging has been applied to nanoparticle-based material sintering. In comparison to other sintering techniques, sinter forging is not a mainstream sintering process for nanomaterials. The external sintering driving force is similar to that of hot pressing except that sinter forging may or may not have die constraint. When there is no die constraint, nanoparticles need to be precompacted and/or presintered into a coherent shape. During sinter forging, the compact can deform extensively and impart a large shear stress. The axial stress causes shear creep and a hydrostatic pressure. The hydrostatic pressure increases the sintering rate while the shear creep reduces flaws, aligns grains, and produces a fine structure. The radial dimension can increase instead of decrease when there is no die constraint. The large shear strains in the densifying body play important roles in closing pores; the sliding between nanograins aids densification by filling pores with grains and pore fragmentation. In other words, the large, “unsinterable” pores can be filled by internal superplastic flow of the surrounding matrix under the right temperature, pressure, and strain rate. Also, sinter forging without die constraint eliminates pressure loss due to particle-die wall friction and creates a state of shear stress that favors not only pore closure but also particle bonding along collapsed pore interfaces, allowing more effective densification. As a result, sinter forging solves one of the major problems for nanoparticles—poor sintering behavior associated with agglomeration.

Early studies of sinter forging are mainly focused on simple oxides. Sinter forging of ZrO₂ nanoparticles at 950°C and 300 MPa achieves 45 nm grain size and full density [106]. Sinter forging of TiO₂ from 550°C to 750°C and <100 MPa can maintain grain size at 60 nm while achieving 97% density [115]. Such small grain sizes are remarkable in light of the tendency of nanoparticles for

grain growth, even though part of the success can be ascribed to the nano-sized starting particle size.

In addition to single-phase oxides, sinter forging also demonstrates its densification capability for composites. One example is 3 mol% Y_2O_3 - ZrO_2 nanoparticles of 8 nm size. Sinter forging can achieve 99% density and 85 nm grain size at 1100°C for only 30 minutes [149]. The prerequisite is that the nanoparticles are compacted at 400 MPa to “squash” the large pores. For ZrO_2 - Fe_2O_3 nanocomposite of 46–52% green density, sinter forging can achieve 80–85 nm grain size at 1000°C and 100 MPa pressure [150]. For free sintering densification, the same composite compacted to ~60% density still experiences excessive grain growth to submicron size. For nonoxides, sinter forging of presintered Si_3N_4 - Si_2N_2O at 1550°C and 30 MPa for 1 hour is carried out and >98% density is achieved [120]. However, sinter-forging studies of other nonoxides are not widely reported.

In comparison to hot pressing, most sinter-forging studies are carried out at lower pressures, generally at <300 MPa pressure. In the meantime, sinter forging can achieve faster densification. However, there is little theoretical understanding about the microstructural evolution during sinter forging. The main focus has been on demonstrations of sintering densification feasibility. The disadvantages of sinter forging are that the microstructure tends to be anisotropic, the technique is not very effective for <20 nm nanoparticles because the required threshold stress is very high, and too high a shear strain can damage the sample. The microstructural shortcomings as well as the complexity of the sinter-forging process limit its widespread application in nanoparticle-based material sintering.

6.5.2.4 Pressure Spark Plasma Sintering Pressure spark plasma sintering is realized by subjecting the green compact to arc discharges generated by a pulsed electric current and a simultaneous pressure. An electric discharge process takes place on a microscopic level, increases local temperature, and accelerates material diffusion. Sintering densification proceeds under a uniaxial pressure and a high-intensity electrical discharge (from 2000 to 60,000 A in a few milliseconds). The exact role of the current has been proposed by many but has been doubted by others for lack of unambiguous experimental evidence. The possible effects from the electric current include electron wind modification of the diffusion flux (i.e., electromigration), increase in point defect concentration, and reduction in the mobility activation energy for defects. Electric current can also offer cleaner grain boundaries. With these in mind, spark plasma sintering has improved characteristics compared with conventional pressure-assisted sintering processes, potentially because of the effects of spark plasma, spark impact pressure, Joule heating, electromagnetic field, electromigration, surface current, and rapid heating. The factors that influence spark plasma sintering include pulse duration (on-time/off-time), peak current value, applied voltage, repetition frequency, waveform, energy density, heating and cooling rates, and vacuum/atmosphere control. When a spark discharge appears in a gap or at the contact point between two particles, a local high temperature state of several to tens of thousands of degrees centigrade is generated momentarily. This causes

evaporation and melting on the surface of particles; “neck” is formed around the area of contact between particles. The externally applied pressure is generally 30–200 MPa. The heating rate is 100–1000°C min⁻¹, which is much faster than that of electric resistance rapid heating [123, 151]. High heating rates reduce the duration of surface diffusion, this favors the sinterability of nanoparticle-based materials and the densification is intensified by grain-boundary diffusion while the grain growth is hindered [152]. Sintering environments can be vacuum, argon, hydrogen, or air. Since no current or only a very weak current passes through nonconducting samples, the discharge originates from the electric field of the pulsed direct current used. The intensity of this discharge is not only dependent on the intensity of the applied pulses but also on factors such as particle size, pore size, and the density of the compact. Superplasticity and bonding quality of the nanoparticles remarkably increase while experiencing Joule heating from the current passing through them. This method has attracted considerable attention as a rapid sintering method that has excellent energy density control. It is also capable of producing highly dense and homogeneous, nanostructured sintered components. Power consumption of the spark plasma sintering method is about one-third to one-fifth of that of traditional sintering techniques, including classic pressureless sintering, hot pressing, and hot isostatic pressing. A constitutive model for spark plasma sintering of conductive materials is developed by considering the contributions of sintering stress (surface tension), external load, and electromigration to sintering shrinkage. It is shown that electromigration-related material flux can be a significant component of the electric current-accelerated diffusion [153].

An excellent review on spark plasma sintering is available [154]. Compared to hot pressing densification Equations (6.30) and (6.31), an additional sintering driving force is provided by the high electric current, which can be evaluated from the electromigration theory:

$$\frac{dV}{V \cdot dt} \Big|_{d,SPS} = \frac{A_{GB}}{V} \cdot \frac{1}{\sqrt{2\pi M_w \cdot R \cdot T}} \cdot \frac{\Omega \cdot P_{flat}}{kT} ((\alpha_{GB} \cdot \gamma_{GB} + \alpha_V \cdot \gamma_V) \times \Sigma \mathbf{H} + \alpha_{SPS} \cdot P_{applied} \cdot \phi' + \alpha_e \cdot F \cdot z \cdot E), \quad (6.34)$$

$$\frac{d\rho}{\rho \cdot dt} \Big|_{d,SPS} = C' \cdot A \cdot \Sigma \mathbf{H} + C_{SPS} \cdot A \cdot P_{applied} \cdot \phi' + C_E \cdot A \cdot F \cdot z \cdot E, \quad (6.35)$$

where $\alpha_{SPS} \cdot P_{applied} \cdot \phi'$ in Equation (6.34) represents the sintering driving force from the axially applied pressure, α_{SPS} is the diffusion coefficient of the sintering species due to the external stress, α_e is the diffusion coefficient due to the electric field, F is Faraday's constant, z is the effective charge on the diffusing species, E is the electrical field, C_{SPS} is a system-related constant under the spark plasma sintering stress, and C_E is a system-related constant under the applied electrical field. Similar to pressure sintering, the above densification rate prediction

becomes invalid when plastic flow occurs. Also, the radial shrinkage can be zero because of the stress applied and the die constraint.

Transparent hydroxyapatite is sintered at a pressure up to 500 MPa. Achieving full densification at the minimized sintering temperature allows for the preparation of transparent hydroxyapatite with stoichiometric composition, avoiding the loss of structural water that commonly takes place during the conventional sintering methods [155]. Fully dense hetero-nanostructured (i.e., containing intermixed nano and micron grains) metallic (FeAl) materials are successfully produced by spark plasma sintering when mechanically milled nanostructured powders are used. This is due to the large temperature differences generated during the spark plasma sintering, which locally modifies the recrystallization response of the heavily deformed structure during sintering. Y_2O_3 addition delays the onset of recrystallization and, thereby, produces microstructures containing more than 80% of sub-500 nm grains [156]. One of the most distinct features of spark plasma sintering is the much shorter sintering time. For example, SnO_2 can be sintered to 92% density by spark plasma sintering in 10 minutes at 890°C versus 61% density in 3 hours at 1000°C by conventional sintering. Since grain growth takes time, the sintered grain size can be retained at nanoscale. Because of this, materials such as AlN and hydroxyapatite can be sintered to transparent state [157].

For oxides, both equiaxed and elongated nanoparticles have been successfully densified while maintaining nano-sized grains. ZrO_2 is sintered to full density while maintaining the grain size at <100 nm [158, 159]. MgO nanoparticle densification is achieved between 700°C and 825°C under applied pressures of 100–150 MPa. Fully dense and transparent MgO with 52 nm average grain size is fabricated [160]. Hydroxyapatite particles of rod-like shape, with an average size of 84 nm × 33 nm, are consolidated by spark plasma sintering to full density at 825°C for 3 minutes. The process yields hydroxyapatite nanograins with an average size of 130 nm × 98 nm. The morphology of the nanorods changes to a more equiaxed shape during sintering [161]. NiO with 20 nm particle size is spark plasma sintered for 5 minutes at 100 MPa between 600°C and 900°C and for different durations at 800°C. Fully dense nanocrystalline compacts are obtained after 20 minutes at 800°C [162]. Nanocrystalline Y_2O_3 with 18 nm crystallite size is sintered using spark plasma sintering at 1100°C and 100 MPa for different durations. Specimens with 98% density and 106 ± 33 nm grain size are formed after 20 minutes. The grain size at the final stage of sintering first increases and then stagnates with the spark plasma sintering duration. The nanostructure consists of convex tetrahedron shaped nanopores at some of the grain boundary junctions. Nanopore drag in Y_2O_3 leads to grain growth stagnation. Extended spark plasma sintering duration up to 40 minutes leads to sudden grain coarsening and loss of the nanograin character.

Fully dense β - Si_3N_4 is consolidated by spark plasma sintering. A commercially available β - Si_3N_4 nanopowder is used as the starting material. Sintering is carried out with a heating rate of 90°C min⁻¹ by varying sintering temperature from 1550°C to 1700°C. Figure 6.17 shows the typical microstructure for each

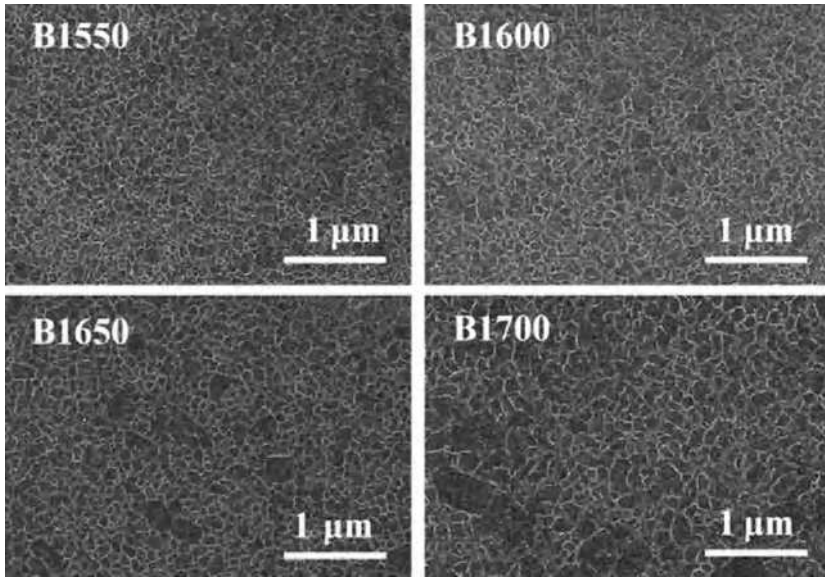


FIGURE 6.17 Scanning electron micrographs of Si_3N_4 specimen sintered at (a) 1550°C, (b) 1600°C, (c) 1650°C, and (d) 1700°C for 4 minutes with a heating rate of $90^\circ\text{C min}^{-1}$ in vacuum by spark plasma sintering [163]. (Reprinted with permission from Lee C-H, Lu H-H, Wang C-A, Lo W-T, Nayak PK, Huang J-L. Microstructure and fracture behavior of $\beta\text{-Si}_3\text{N}_4$ based nanoceramics. *Ceram Int* 2011;37:641–645, Copyright 2011, Elsevier.)

specimen sintered at various temperatures for 4 minutes in vacuum by spark plasma sintering. No significantly elongated grains are observed in these final microstructures. Hence, $\beta\text{-Si}_3\text{N}_4$ with a lower aspect ratio is achieved. The frequency distributions of grain length, grain diameter, and aspect ratio of $\beta\text{-Si}_3\text{N}_4$ grains for each specimen are evaluated by image analysis. In Figure 6.17a, the average grain length is 101.7 nm and the average grain diameter is 49.2 nm with an aspect ratio of 3.04. In Figure 6.17b, the average grain length is 110.6 nm and the average grain diameter is 50.9 nm with an aspect ratio of 3.18. In Figure 6.17c, the average grain length is 125.7 nm and the average grain diameter is 58.6 nm with an aspect ratio of 3.19. In Figure 6.17d, the average grain length is 164.5 nm and the average grain diameter is 70.2 nm with an aspect ratio of 3.36 [163]. Increase in sintering temperature leads to not only grain size increase but also aspect ratio increase.

For nitrides such as Si_3N_4 , nanoparticles of 10 nm size are spark plasma sintered at 1600°C for 5 minutes at a heating rate of $300^\circ\text{C min}^{-1}$. The sample is fully densified with homogeneous Si_3N_4 nanograins of ~ 70 nm size [164]. Even with the consideration of the Y_2O_3 and Al_2O_3 dopants used, such small Si_3N_4 grain size is uncommon for other sintering processes. Another example of nonoxides by spark plasma sintering is carbide. Nanostructured $\beta\text{-SiC}$, with

primary particle size in the range of 5–20 nm, is consolidated to 98% density at 1700°C and 40 MPa without additives [165]. The common theme for the above Si₃N₄ and SiC studies is that high-energy mechanical milling is used to produce nano-sized starting particles. This is consistent with computer simulation prediction, which shows that at 800°C and 150 MPa, MgO of 20 nm size may be densified within 1 minute, compared to 8 minutes for 40 nm, and 10 minutes for 50 nm particle sizes [166]. These results are also consistent with the observations made for pressureless sintering. Even for the well-pursued spark plasma sintering, a grain growth factor of a few folds is common. Obtaining small particle size to start with is a key factor in achieving nano-sized grains.

In addition to the single-phase nanomaterials discussed above, spark plasma sintering is applied to nanocomposites and demonstrates microstructure refinement capability. For hydroxyapatite-3 mol% Y₂O₃-ZrO₂ composite sintered by spark plasma sintering at 1150°C and 50 MPa by heating the sample at 200°C min⁻¹ to the peak temperature, the ZrO₂ grains are only about 50 nm, the hydroxyapatite grains are ~100 nm [167]. ZrO₂ and hydroxyapatite grains distribute homogeneously. Because of the relatively low sintering temperature and short dwelling time (3 minutes), the reaction between hydroxyapatite and ZrO₂ that almost always occurs by other methods can be avoided. For nonoxide matrix nanocomposite, Si₃N₄/SiC with grain size below 100 nm is obtained by using amorphous Si-C-N particles and controlling the Y₂O₃ amount. With decreasing Y₂O₃ content, the ratio of SiC to Si₃N₄ increases and the grain size decreases from 150 nm to as small as 38 nm. The hindered grain growth is attributed to the decreased involvement of the liquid phase [168]. For Ni-Co dispersed Al₂O₃ nanocomposites, marked refinement of Al₂O₃ grain size and homogeneous distribution of 90 nm Ni-Co are realized even though the Al₂O₃ matrix grain size is at the micron level [169]. TiN/Si₃N₄ and TiC-SiC nanocomposites are also made using similar approaches [170, 171].

From a different perspective, dense nanostructured materials are obtained from micron-sized particles by spark plasma sintering. Dense Pb(Mg_{1/3}Nb_{2/3})O₃-PbTiO₃ with grain sizes of 20–100 nm is obtained from a starting powder of 1–10 μm in size. The significant microstructural refinement is attributed to a pulsed electric field-induced thermo-mechanical fatigue process, which *in situ* “shatters” the large particles into nano-sized grains during sintering. An advantage of this technique over the previous ones is that it avoids the usage of nanoparticles [172].

Densification maps of spark plasma sintering for MgO nanoparticles are constructed using a hot isostatic pressing model [166]. Plastic flow and diffusion are believed to be the dominating mechanisms at the first and final stages of densification, respectively, whereas power-law creep does not contribute to densification. Spark plasma sintering is mostly effective before pores become isolated. After pores are closed, grain boundary diffusion and grain boundary migration become the rate-determining processes. There are cases in which full densification of nanomaterials is not achieved, such as the hydroxyapatite-3 mol% Y₂O₃-ZrO₂ composite mentioned previously, which only achieves 97.3% density [167]. The other exception reported is antimony-doped SnO₂ of 10–15 nm

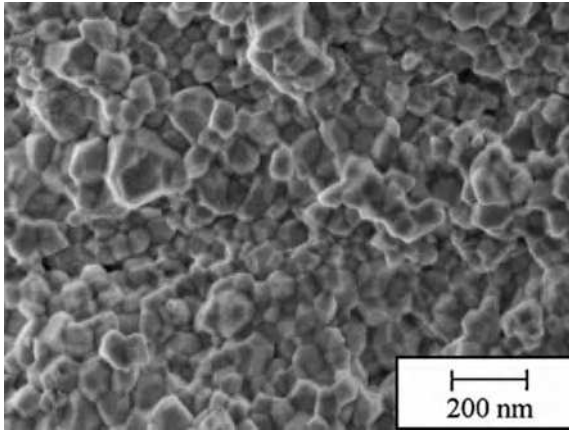


FIGURE 6.18 Scanning electron image of the fractured surface of a 3 mol% Y_2O_3 - ZrO_2 sample doped with 8 mol% CuO after spark plasma sintering at 1100°C and 100 MPa for 1 minute [174]. (Reprinted with permission from Rana S, Vleugels J, Huang S, Vanmeensel K, Blank DHA, Winnubst L. Manipulating microstructure and mechanical properties of CuO doped 3Y-TZP nano-ceramics using spark-plasma sintering. *J Eur Ceram Soc* 2010;30:899–904, Copyright 2010, with permission from Elsevier.)

particle size, which is spark plasma sintered to 97% density but excessive grain growth to micron size occurs during the final stage of sintering [173]. Surface diffusion and evaporation–condensation mechanisms are known to be dominant in SnO_2 sintering, which can be the contributing factors for the above observation.

Nanostructured composites of 3 mol% Y_2O_3 - ZrO_2 doped with 8 mol% CuO are processed by spark plasma sintering. A 96% dense composite with an average grain size of 70 nm is obtained at 1100°C and 100 MPa for 1 minute. In contrast to free sintering, the reactions between CuO and Y_2O_3 - ZrO_2 are suppressed and the CuO phase is reduced to metallic copper, while the Y_2O_3 - ZrO_2 phase remains almost purely tetragonal. Figure 6.18 exhibits a dense microstructure and an average grain size of ~ 70 nm. This value is significantly smaller than that of the composite prepared by pressureless sintering (120 nm and several microns for 960°C and 1130°C sintered samples, respectively). The inhibition of grain growth is believed to be associated with the extremely fast heating rate and short sintering time in combination with a high external pressure [174].

Summing the nanoparticle-based material spark plasma sintering studies so far, there are several advantages that accrue from this process. First, the rapid heat transfer and resistance heating of particles significantly shorten the high temperature exposure of nanoparticles, which is essential for preserving the nanostructures. The rapid heating (100 – $1000^\circ C\ min^{-1}$) in spark plasma sintering enhances the densification process, which usually occurs at high temperatures. Apart from a very fast heating rate, it also allows for fast cooling rates, very short holding times

(as short as 1 minute), and the possibility to obtain fully dense nanostructures at comparatively low sintering temperatures, typically a few hundred degrees centigrade lower than in the conventional pressure sintering. The sintering pressure for spark plasma sintering is lower than that of hot pressing and close to that of hot isostatic pressing, typically ≤ 200 MPa, which might be limited by the uppermost strength of the best available graphite molds. It is also applicable to densifying a large variety of powder materials (conductive and nonconductive). The materials include oxides, carbides, nitrides, and composites. These combined advantages offer very limited grain growth. The grain size of the dense compact is almost definitely smaller than that from other densification techniques. Another advantage of spark plasma sintering technique is less sintering additives. This mainly stems from the accelerated interparticle bonding by the electric pulses, which make the reduction/elimination of additives possible. Spark plasma sintering is the most effective densification technique for nanomaterials, whereas other techniques might fail. One of the most remarkable features of spark plasma sintering is the small grain size the process can maintain while achieving full densification. However, spark plasma sintering also has its limitations. Because of the rapid densification process and the existence of multiple sintering driving forces, it is difficult to decouple the diffusion mechanisms and trace the exact sintering processes. Most efforts are focused on achieving fully dense nanostructures without in-depth discussion of atomic diffusion or deformation processes. Also, the vast majority of spark plasma sintering is based on samples with simple shapes and small sizes, even though a continuous production of components of complex geometries and > 150 mm diameter pieces has been demonstrated, at least partly for proof-of-concept and partly to demonstrate the untapped capabilities of spark plasma sintering. Spark plasma sintering is not applicable to every material. Sintering efficiency depends on the electrical properties of the material being sintered [175]. The required electrical current, current source, and current discharge rate are all system-specific and have to be studied for each material. Another disadvantage is the expensive equipment involved, such as the sintering setup and the special dies capable of imparting a high current to the compact at elevated temperatures and pressures. Also, temperature gradient is inevitable in the samples. Under certain conditions, the difference may reach 450°C or more [176, 177]. This can result in differential densification and subsequent microstructural inhomogeneities [178].

6.5.2.5 Other Sintering Techniques There are a few other techniques that densify nanoparticles into bulk compacts but involve drastically different factors than the sintering processes discussed so far. A typical example is plasma spray forming. The sintering temperature, sintering driving force, and atomic diffusion processes for these processes are not well characterized or understood. Here, we only provide a brief description of the plasma spray technique to be inclusive. Also, the research activities in these areas are very limited.

Plasma spray forming is a process in which particles are heated to plasma temperatures and then propelled at a rapid speed towards a much cooler substrate. On

contact with the substrate, the plasma is effectively quenched and fully sintered. Forming and sintering are carried out in one step by melting, blending, and consolidation. Densification of the spray deposit is dominated by both solidification and solid-state sintering. The densification maps for plasma spray forming have been modeled after hot isostatic pressing and show that plastic flow is most prevalent in the first stage of sintering, while diffusion is most prevalent in the final stage of sintering. The model also shows that power-law creep, which is sometimes present in hot isostatic pressing, has little or no effect on plasma spray forming. $\text{Al}_2\text{O}_3\text{-ZrO}_2\text{-TiO}_2$, $\text{Al}_2\text{O}_3\text{-ZrO}_2\text{-SiO}_2$, and $\text{ZrO}_2\text{-CaO-MgO-SiO}_2$ layered structures or composites are produced by plasma spray forming, but the particle sizes are in the micron range [179]. A substrate cooling technique has been developed to retain nano-sized Al_2O_3 in the spray deposit. Al_2O_3 nanoparticles are partially melted and trapped between the fully melted, micron-sized Al_2O_3 grains. Net shape and freestanding Al_2O_3 is fabricated [180, 181]. Near-net-shape bulk $\text{MoSi}_2\text{-Si}_3\text{N}_4\text{-SiC}$ nanocomposite has also been consolidated using plasma spray forming [182].

One of the advantages of plasma spray forming is the ability to sinter a part while forming it. Since the material must go through a high temperature before being sprayed, the structure of the material has the possibility to be homogenized. The technique can be applied to multiphase materials by creating supersaturated solutions that will precipitate out upon cooling of the plasma. This process also allows for shorter sintering temperatures and suppression of grain growth by extremely fast translation of particles through the high temperature zone (plasma flame). However, plasma parameters need to be carefully controlled to avoid melting of nano-sized particles. One of the biggest drawbacks of this method is that it results in pancake-shaped grains. It may also be difficult to produce complex shapes or thick samples.

6.6 SUMMARY

Nanoparticle-based material sintering has been the driving force for the advancement of different sintering techniques. The challenges in densifying nanoparticle-based materials while controlling grain growth have pushed the efforts to closely examine the critical sintering factors and design effective sintering processes. Each technique has its own strengths as well as limitations to meet the specific needs of nanoparticle-based material sintering. One of the most obvious limitations is the small sample size that nanoparticle-based material sintering can densify due to the challenge of achieving uniform temperature and pressure, especially when fast heating is involved. Also, nanoparticle-based material sintering needs to improve the processing efficiency with low complexity and cost.

At the fundamental level, there is a need to decouple densification and coarsening diffusion mechanisms. The relative contribution of each diffusion mechanism should be assessed. The activation energy change of each diffusion mechanism with temperature should be quantified. Efforts are desired to understand and

control the evolution of nano-sized grains. Fundamental understanding of the connection between nanoscopic evolution and macroscopic shrinkage needs to be developed.

For porous nanoparticle-based material sintering, the discussion is broadly divided into partial sintering, pore forming sintering, template-directed sintering, and special sintering processes. Partial sintering simply sinters materials to a density lower than the theoretical density and then terminates the process, sometimes with purposeful control of sintering rate. Pore forming sintering utilizes pore-forming reactions to generate pores. For template-directed sintering, pores are created during the forming process by sacrificial species. Special sintering processes include microwave sintering, electric field-assisted sintering, and laser sintering.

Dense nanoparticle-based material sintering may be carried out without pressure (free sintering) or with pressure (hot pressing, hot isostatic pressing, sinter forging, spark plasma sintering, and other special techniques). For free sintering, either nanoparticle systems or sintering cycles can be specifically customized. For pressure sintering, hot pressing, hot isostatic pressing, and sinter forging are the extensions of conventional techniques to nanoparticle-based sintering systems. Spark plasma sintering is a more recent development and has been very successful in producing fully dense nanostructured materials.

There is much work ahead in the field of nanoparticle-based material sintering. The prospects for further growth are evident with the expanding base of nanoparticle-based materials and sintering techniques. The quantification of the microstructure-processing-property links for increasingly complex nanoparticle-based materials will remain a research focus. The beneficial impacts of the new processing options include shorter processing times, unique nanostructures, and, in the long run, improved properties.

QUESTIONS

1. During sintering, how can the large surface area for nanoparticles be utilized to their advantages? If not properly utilized, what are the potential detriments to sintering?
2. Based on the intrinsic characteristics of nanoparticles, explain the corresponding strategies that can be devised to facilitate sintering densification.
3. How many sintering stages does porous material sintering generally involve? Explain three strategies to maintain the porosity desired.
4. To obtain homogeneous, sintered three-dimensional nanostructures from nanoparticles, what are the necessary conditions during forming and during sintering?
5. Explain three ways that one can utilize for fully dense nanoparticle-based material sintering.
6. What are the fundamental driving forces that accelerate spark plasma sintering? Explain in detail.

REFERENCES

1. McColm IJ. *Dictionary of Ceramic Science and Engineering*. 2nd ed. New York, NY: Plenum Press; 1994. p. 292.
2. German RM. *Sintering Theory and Practice*. New York, NY: John Wiley & Sons, Inc.; 1996. pp. 1–22.
3. Kuczynski GC. Self-diffusion in sintering of metallic particles. *Metals Trans* 1949;185:169–178.
4. Kingery WD, Berg M. Study of initial stages of sintering solids by viscous flow, evaporation-condensation, and self-diffusion. *J Appl Phys* 1955;26:1205–1212.
5. Coble RL. Initial sintering of alumina and hematite. *J Am Ceram Soc* 1958;41:55–62.
6. Johnson DL. New method of obtaining volume, grain-boundary, and surface diffusion coefficients from sintering data. *J Appl Phys* 1969;40:192–200.
7. German RM. *Sintering Theory and Practice*. New York, NY: John Wiley & Sons, Inc.; 1996. pp. 67–141.
8. Barsoum MW. *Fundamentals of Ceramics*. New York, NY: The McGraw-Hill Companies, Inc.; 1997. pp. 331–390.
9. Nishikawa Y, Jinnai H, Koga T, Hashimoto T, Hyde ST. Measurements of interfacial curvatures of bicontinuous structure from three-dimensional digital images. 1. a parallel surface method. *Langmuir* 1998;14:1242–1249.
10. Fang ZZ, Wang H. Densification and grain growth during sintering of nanosized particles. *Int Mater Rev* 2008;53:326–352.
11. Tuan WH, Huang YC. High percolative BaTiO₃-Ni nanocomposites. *Mater Chem Phys* 2009;118:187–190.
12. Cao MR, Wang SB, Han WB. Influence of nanosized SiC particle on the fracture toughness of ZrB₂-based nanocomposite ceramic. *Mater Sci Eng A* 2010;527:2925–2928.
13. Pee JH, Park JC, Hwang KT, Kim S, Cho WS. Synthesis of an aluminum nitride-yttria (AlN-Y₂O₃) composite from nano-sized porous AlN and YCl₃. *Res Chem Intermed* 2010;36:801–809.
14. Oh ST, Tajima K, Ando M, Ohji T. Strengthening of porous alumina by pulse electric current sintering and nanocomposite processing. *J Am Ceram Soc* 2000;83:1314–1316.
15. Jayaseelan DD, Kondo N, Brito ME, Ohji T. High-strength porous alumina ceramics by the pulse electric current sintering technique. *J Am Ceram Soc* 2002;85:267–269.
16. Bennison SJ, Harmer MP. Grain-growth kinetics for alumina in the absence of a liquid-phase. *J Am Ceram Soc* 1985;68:C22–C24.
17. Zhou WY, Lee SH, Wang M, Cheung WL, Ip WY. Selective laser sintering of porous tissue engineering scaffolds from poly(L)/carbonated hydroxyapatite nanocomposite microspheres. *J Mater Sci* 2008;19:2535–2540.
18. Duan B, Wang M. Encapsulation and release of biomolecules from Ca-P/PHBV nanocomposite microspheres and three-dimensional scaffolds fabricated by selective laser sintering. *Polym Degrad Stab* 2010;95:1655–1664.
19. Deng ZY, Fukasawa T, Ando M, Zhang GJ, Ohji T. Microstructure and mechanical properties of porous alumina ceramics fabricated by the decomposition of aluminum hydroxide. *J Am Ceram Soc* 2001;84:2638–2644.
20. Deng ZY, Fukasawa T, Ando M, Zhang GJ, Ohji T. High-surface-area alumina ceramics fabricated by the decomposition of Al(OH)₃. *J Am Ceram Soc* 2001;84:485–491.
21. Deng ZY, Fukasawa T, Ando M, Zhang GJ, Ohji T. Bulk alumina support with high tolerant strain and its reinforcing mechanisms. *Acta Mater* 2001;49:1939–1946.

22. Mayo MJ, Hague DC, Chen DJ. Processing nanocrystalline ceramics for applications in superplasticity. *Mater Sci Eng A* 1993;166:145–159.
23. Skandan G, Hahn H, Kear BH, Roddy M, Cannon WR. The effect of applied stress on densification of nanostructured zirconia during sinter-forging. *Mater Lett* 1994;20:305–309.
24. Risbud SH, Shan CH, Mukherjee AK, Kim MJ, Bow JS, Holl RA. Retention of nanostructure in aluminum-oxide by very rapid sintering at 1150°C. *J Mater Res* 1995;10:237–239.
25. Lee HY, Riehemann W, Mordike BL. Sintering of nanocrystalline ZrO₂ and zirconia toughened alumina (ZTA). *J Eur Ceram Soc* 1992;10:245–253.
26. Hahn H. Microstructure and properties of nanostructured oxides. *Nanostruct Mater* 1993;2:251–265.
27. Skandan G. Processing of nanostructured zirconia ceramics. *Nanostruct Mater* 1995;5:111–126.
28. Mayo MJ. Synthesis and applications of nanocrystalline ceramics. *Mater Des* 1993;14:323–329.
29. Zhou YC, Rahaman MN. Hydrothermal synthesis and sintering of ultrafine CeO₂ powders. *J Mater Res* 1993;8:1680–1686.
30. Rabe T, Waesche R. Sintering behaviour of nanocrystalline titanium nitride powders. *Nanostruct Mater* 1995;6:357–360.
31. Maheshwari P, Fang ZGZ, Sohn HY. Early-stage sintering densification and grain growth of nanosized WC-Co powders. *Int J Powder Metall* 2007;43:41–47.
32. Dominguez O, Champion Y, Bigot J. Liquid like sintering behavior of nanometric Fe and Cu powders: experimental approach. *Metall Mater Trans A* 1998;29A:2941–2949.
33. Malewar R, Kumar KS, Murty BS, Sarma B, Pabi SK. On sinterability of nanostructured W produced by high-energy ball milling. *J Mater Res* 2007;22:1200–1206.
34. Oda E, Ameyama K, Yamaguchi S. Fabrication of nano grain tungsten compact by mechanical milling process and its high temperature properties. *Mater Sci Forum* 2006;503–504:573–578.
35. Wang H, Fang ZZ. Study of size-dependent sintering behavior of Tungsten powders. *Proceeding of 2008 International Conference on Tungsten, Refractory and Hard Materials VII*; 2008 June 8–12; Washington, DC: Metal Powder Industries Federation; 2008. pp. 05.72–05.77.
36. Maca K, Trunec M, Dobsak P. Bulk zirconia nanoceramics prepared by cold isostatic pressing and pressureless sintering. *Rev Adv Mater Sci* 2005;10:84–88.
37. Hynes AP, Doremus RH, Siegel RW. Sintering and characterization of nanophase zinc oxide. *J Am Ceram Soc* 2002;85:1979–1987.
38. Kumar BVM, Kim YW. Processing of polysiloxane-derived porous ceramics: a review. *Sci Technol Adv Mater* 2010;11:044303 16pp.
39. Lefebvre LP, Banhart J, Dunand DC. Porous metals and metallic foams: current status and recent developments. *Adv Eng Mater* 2008;10:775–787.
40. Polarz S, Smarsly B. Nanoporous materials. *J Nanosci Nanotechnol* 2002;2:581–612.
41. Frenzer G, Maier WF. Amorphous porous mixed oxides: sol-gel ways to a highly versatile class of materials and catalysts. *Annu Rev Mater Res* 2006;36:281–331.
42. Rowsell JLC, Yaghi OM. Metal-organic frameworks: a new class of porous materials. *Microporous Mesoporous Mater* 2004;73:3–14.
43. Schuth F. Engineered porous catalytic materials. *Annu Rev Mater Res* 2005;35:209–238.
44. Levine B. A new era in porous metals: applications in orthopaedics. *Adv Eng Mater* 2008;10:788–792.

45. Simske SJ, Ayers RA, Bateman TA. Porous materials for bone engineering. *Mater Sci Forum* 1997;250:151–182.
46. Wakuda D, Kim K-S, Suganuma K. Room temperature sintering of Ag nanoparticles by drying solvent. *Scr Mater* 2008;59:649–652.
47. Chen IW, Wang XH. Sintering dense nanocrystalline ceramics without final-stage grain growth. *Nature* 2000;404:168–171.
48. Wang XH, Chen PL, Chen IW. Two-step sintering of ceramics with constant grain-size, I. Y_2O_3 . *J Am Ceram Soc* 2006;89:431–437.
49. Wang XH, Deng XY, Bai HL, Zhou H, Qu WG, Li LT, Chen IW. Two-step sintering of ceramics with constant grain-size, II: $BaTiO_3$ and Ni-Cu-Zn ferrite. *J Am Ceram Soc* 2006;89:438–443.
50. Wakuda D, Kim K-S, Suganuma K. Room-temperature sintering process of Ag nanoparticle paste. *IEEE Trans Compon Packag Technol* 2009;32:627–632.
51. Kang S, Jia Z, Zoto I, Reed D, Nikles DE, Harrell JW, Thompson G, Mankey G, Krishnamurthy VV, Porcar L. Sintering behavior of spin-coated FePt and FePtAu nanoparticles. *J Appl Phys* 2006;99:08N704 3pp.
52. Jang S, Seo Y, Choi J, Kim T, Cho J, Kim S, Kim D. Sintering of inkjet printed copper nanoparticles for flexible electronics. *Scr Mater* 2010;62:258–261.
53. Jakubowicz J, Smardz K, Smardz L. Characterization of porous silicon prepared by powder technology. *Physica E* 2007;38:139–143.
54. Jo SH, Muralidharan P, Kim DK. Electrical characterization of dense and porous nanocrystalline Gd-doped ceria electrolytes. *Solid State Ionics* 2008;178:1990–1997.
55. Deng ZY, Yang JF, Beppu Y, Ando M, Ohji T. Effect of agglomeration on mechanical properties of porous zirconia fabricated by partial sintering. *J Am Ceram Soc* 2002;85:1961–1965.
56. Deng ZY, Zhou Y, Inagaki Y, Ando M, Ohji T. Role of $Zr(OH)_4$ hard agglomerates in fabricating porous ZrO_2 ceramics and the reinforcing mechanisms. *Acta Mater* 2003;51:731–739.
57. Fang ZZ, Wang H. Densification and grain growth during sintering of nanosized particles. *Int Mater Rev* 2008;53:326–352.
58. Lu K. Sintering of nanoceramics. *Int Mater Rev* 2008;53:21–38.
59. Yang Y, Wang Y, Tian W, Wang Z, Li CG, Zhao Y, Bian HM. In situ porous alumina/aluminum titanate ceramic composite prepared by spark plasma sintering from nanostructured powders. *Scr Mater* 2009;60:578–581.
60. Fujita H, Jefferson G, McMeeking RM, Zok FW. Mullite/alumina mixtures for use as porous matrices in oxide fiber composites. *J Am Ceram Soc* 2004;87:261–267.
61. Demirskyi D, Ragulya A. Low-temperature microwave sintering of TiN–SiC nanocomposites. *J Mater Sci* 2012;47:3741–3745.
62. Gajovic A, Furic K, Music S, Djerdj I, Tonejc A, Tonejc AM, Su DS, Schlogl R. Mechanism of $ZrTiO_4$ synthesis by mechanochemical processing of TiO_2 and ZrO_2 . *J Am Ceram Soc* 2006;89:2196–2205.
63. Gajovic A, Santic A, Djerdj I, Tomasic N, Mogus-Milankovic A, Su DS. Structure and electrical conductivity of porous zirconium titanate ceramics produced by mechanochemical treatment and sintering. *J Alloy Compd* 2009;479:525–531.
64. Carn F, Saadaoui H, Masse P, Ravaine S, Julian-Lopez B, Sanchez C, Deleuze H, Talham DR, Backov R. Three-dimensional opal-like silica foams. *Langmuir* 2006;22:5469–5475.
65. Zhou W, Ran R, Shao Z, Jin W, Xu N. Synthesis of nano-particle and highly porous conducting perovskites from simple in situ sol–gel derived carbon templating process. *Bull Mater Sci* 2010;33:371–376.

66. Liu Y, Liu M. Creation of porous ceria by sublimation of tin dioxide during sintering. *Adv Eng Mater* 2006;8:89–93.
67. Yang Y, Wang Y, Tian W, Wang Z, Li CG, Zhao Y, Bian HM. In situ porous alumina/aluminum titanate ceramic composite prepared by spark plasma sintering from nanostructured powders. *Scr Mater* 2009;60:578–581.
68. Zhang R, Gao L, Guo JK. Effect of Cu_2O on the fabrication of SiC_p/Cu nanocomposites using coated particles and conventional sintering. *Composites Part A* 2004;35:1301–1305.
69. Chen XF, Wang XC, Fu XZ. Hierarchical macro/mesoporous $\text{TiO}_2/\text{SiO}_2$ and $\text{TiO}_2/\text{ZrO}_2$ nanocomposites for environmental photocatalysis. *Energy Environ Sci* 2009;2:872–877.
70. Kameoka S, Tanabe T, Tsai AP. Self-assembled porous nano-composite with high catalytic performance by reduction of tetragonal spinel CuFe_2O_4 . *Appl Catal A* 2010;375:163–171.
71. Cruz HS, Spino J, Grathwohl G. Nanocrystalline ZrO_2 ceramics with idealized macropores. *J Eur Ceram Soc* 2008;28:1783–1791.
72. Tang FQ, Fudouzi H, Uchikoshi T, Sakka Y. Preparation of porous materials with controlled pore size and porosity. *J Eur Ceram Soc* 2004;24:341–344.
73. Tang F, Fudouzi H, Uchikoshi T, Awane T, Sakka Y. Fabrication of ordered macroporous structures based on hetero-coagulation process using nanoparticle as building blocks. *Chem Lett* 2003;32:276–277.
74. Qi L, Sorge JD, Birnie DP. Dye-sensitized solar cells based on TiO_2 coatings with dual size-scale porosity. *J Am Ceram Soc* 2009;92:1921–1925.
75. Wang DY, Salgueirino-Maceira V, Liz-Marzan LW, Caruso F. Gold-silica inverse opals by colloidal crystal templating. *Adv Mater* 2002;14:908–912.
76. Dong Z, Jing W, Xing W. Triblock polymer template assisted sol-gel process for fabrication of multi-channel $\text{TiO}_2/\text{ZrO}_2$ ultrafiltration membrane. *J Membr Sci* 2011;373:167–172.
77. Sadakane M, Sasaki K, Kunioku H, Ohtani B, Abe R, Ueda W. Preparation of 3-D ordered macroporous tungsten oxides and nano-crystalline particulate tungsten oxides using a colloidal crystal template method, and their structural characterization and application as photocatalysts under visible light irradiation. *J Mater Chem* 2010;20:1811–1818.
78. Ying F, Wangb S, Au C-T, Lai S-Y. Highly active and stable mesoporous Au/CeO_2 catalysts prepared from MCM-48 hard-template. *Microporous Mesoporous Mater* 2011;142:308–315.
79. Cai Z, Teng J, Xiong Z, Li Y, Li Q, Lu X, Zhao XS. Fabrication of TiO_2 binary inverse opals without overlayers via the sandwich-vacuum infiltration of precursor. *Langmuir* 2011;27:5157–5164.
80. Clark DE, Folz DC. What is microwave processing? In: Clark DE, Folz DC, Folgar CE, Mahmoud MM, editors. *Microwave Solutions for Ceramic Engineers*. Westerville, Ohio: American Ceramic Society; 2005. pp. 1–34.
81. Bykov YV, Rybakov KI, Semenov VE. High-temperature microwave processing of materials. *J Phys D* 2001;34:R55–R75.
82. Lewis D, Rayne RJ, Bender BA, Kufihara LK, Chow G-M, Fliflet A, Kincaid A, Bruce R. Conventional and high frequency microwave processing of nanophase ceramic materials. *Nanostruct Mater* 1997;9:97–100.
83. Link G, Feher L, Thumm M, Ritzhaupt-Kleissl H-J, Bohme R, Weisenburger A. Sintering of advanced ceramics using a 30-GHz, 10-kW, CW industrial gyrotron. *IEEE Trans Plasma Sci* 1999;27:547–554.

84. Birnboim A, Carmel Y. Simulation of microwave sintering of ceramic bodies with complex geometry. *J Am Ceram Soc* 1999;82:3024–3030.
85. Harrison WB, Hanson MRB, Koepke BG. Microwave processing and sintering of PZT and PLZT ceramics. *Microwave Processing of Materials, Symposium Proceedings*. Pittsburgh, PA: Materials Research Society; 1988. Vol 124, pp. 279–286.
86. Vijayan S, Varma H. Microwave sintering of nanosized hydroxyapatite powder compacts. *Mater Lett* 2002;56:827–831.
87. Oh S-T, Tajima K-I, Ando M, Ohji T. Fabrication of porous Al₂O₃ by microwave sintering and its properties. *Mater Lett* 2001;48:215–218.
88. Perelaer J, Klokkenburg M, Hendriks CE, Schubert US. Microwave flash sintering of inkjet-printed silver tracks on polymer substrates. *Adv Mater* 2009;21:4830–4834.
89. Freim J, McKittrick KJ, Katz J, Sickafus K. Microwave sintering of nanocrystalline γ -Al₂O₃. *Nanostruct Mater* 1994;4:371–385.
90. Jung S, Kim JH. Sintering characteristics of TiO₂ nanoparticles by microwave processing. *Korean J Chem Eng* 2010;27:645–650.
91. Bykov Y, Eremeev A, Egorov S, Ivanov V, Kotov Y, Khrustov V, Sorokin A. Sintering of nanostructural titanium oxide using millimeter-wave radiation. *Nanostruct Mater* 1999;12:115–118.
92. Birnboim A, Carmel Y. Simulation of microwave sintering of ceramic bodies with complex geometry. *J Am Ceram Soc* 1999;82:3024–30.
93. Xie Z, Wang C, Fan X, Huang Y. Microwave processing and properties of Ce-Y-ZrO₂ ceramics with 2.45 GHz irradiation. *Mater Lett* 1999;38:190–196.
94. Ciacchi FT, Nightingale SA, Badwal SPS. Microwave sintering of zirconia-yttria electrolytes and measurement of their ionic conductivity. *Solid State Ionics* 1996;86–88:1167–1172.
95. Kemer EL, Johnson EL. Microwave plasma sintering of alumina. *Am Ceram Soc Bull* 1985;64:1132–1136.
96. Mishra RS, Shackelford JF, Mukherjee AK. Plasma activated sintering of nanocrystalline gamma-Al₂O₃. *Nanostruct Mater* 1995;5:525–544.
97. Wada S, Suganuma M, Kitagawa Y, Murayama N. Comparison between pulse electric current sintering and hot pressing of silicon nitride ceramics. *J Ceram Soc Jpn* 1999;107:887–890.
98. Kimura H, Hongo K. In process nanocrystalline control consolidation of the amorphous ZrO₂-20 mol% Al₂O₃ powder. *Mater Trans* 2006;47:1374–1379.
99. Groza JR, Zavaliangos A. Sintering activation by external electrical field. *Mater Sci Eng A* 2000;287:171–177.
100. Allen ML, Aronniemi M, Mattila T, Alastalo A, Ojanpera K, Suhonen M, Seppä H. Electrical sintering of nanoparticle structures. *Nanotechnology* 2008;19:175201 4pp.
101. Chakravarty D, Ramesh H, Rao TN. High strength porous alumina by spark plasma sintering. *J Eur Ceram Soc* 2009;29:1361–1369.
102. Jayaseelan DD, Kondo N, Brito ME, Ohji T. High-strength porous alumina ceramics by the pulse electric current sintering technique. *J Am Ceram Soc* 2002;85:267–269.
103. Oh ST, Tajima K, Ando M, Ohji T. Strengthening of porous alumina by pulse electric current sintering and nanocomposite processing. *J Am Ceram Soc* 2000;83:1314–1316.
104. Yoshimura M, Ohji T, Sando M, Niihara K. Rapid rate sintering of nano-grained ZrO₂-based composites using pulse electric current sintering method. *J Mater Sci Lett* 1988;17:1389–1391.
105. Maca K, Trunec M, Dobsak P. Bulk zirconia nanoceramics prepared by cold isostatic pressing and pressureless sintering. *Rev Adv Mater Sci* 2005;10:84–88.

106. Skandan G. Processing of nanostructured zirconia ceramics. *Nanostruct Mater* 1995;5:111–126.
107. Hynes AP, Doremus RH, Siegel RW. Sintering and characterization of nanophase zinc oxide. *J Am Ceram Soc* 2002;85:1979–87.
108. Rabe T, Prummer R, Wasche R. Explosive compaction of nanosized TiN-particles. *Mater Sci Forum* 1997;235–238:285–290.
109. Ahn JP, Park JK, Huh MY. Effect of green density on the subsequent densification and grain growth of ultrafine SnO₂ powder during isochronal sintering. *J Am Ceram Soc* 1997;80:2165–2167.
110. Gao L, Li W, Wang HZ, Zhou JX, Chao ZJ, Zai QZ. Fabrication of nano Y-TZP materials by superhigh pressure compaction. *J Eur Ceram Soc* 2001;21:135–138.
111. Gonzalez EJ, Hockey B, Piermarini GJ. High pressure compaction and sintering of nano-size gamma-Al₂O₃ powder. *Mater Manuf Processes* 1996;11:951–967.
112. Kaya C, Butler EG. Plastic forming and microstructural development of α -alumina ceramics from highly compacted green bodies using extrusion. *J Eur Ceram Soc* 2002;22:1917–1926.
113. Gallas MR, Hockey B, Pechenik A, Piermarini GJ. Fabrication of transparent gamma-Al₂O₃ from nanosize particles. *J Am Ceram Soc* 1994;77:2107–2112.
114. Betz U, Sturm A, Loeffler JF, Wagner W, Wiedenmann A, Hahn H. Low temperature isothermal sintering and microstructural characterization of nanocrystalline zirconia ceramics using small angle neutron scattering. *Nanostruct Mater* 1999;12:689–692.
115. Averbach RS, Hofler HJ, Tao R. Processing of nano-grained materials. *Mater Sci Eng A* 1993;166:169–177.
116. Mayo MJ. Processing of nanocrystalline ceramics from ultrafine particles. *Int Mater Rev* 1996;41:85–115.
117. Zhang Y, Chen J, Hu L, Liu W. Pressureless-sintering behavior of nanocrystalline ZrO₂–Y₂O₃–Al₂O₃ system. *Mater Lett* 2006;60:2302–2305.
118. Winnubst L, Ranb S, Speets EA, Blank DHA. Analysis of reactions during sintering of CuO-doped 3Y-TZP nano-powder composites. *J Eur Ceram Soc* 2009;29:2549–2557.
119. Borsa CE, Ferreira HS, Kiminami RHGA. Liquid phase sintering of Al₂O₃/SiC nanocomposites. *J Eur Ceram Soc* 1999;19:615–621.
120. Luo JT, Zhang KF, Wang GF, Han WB. Superplasticity and sinter-forging of fine-grained Si₃N₄-Si₂N₂O composite. *Mater Sci Forum* 2005;475–479:2987–2990.
121. Wang LW, Sigmund WM, Roy S, Aldinger F. Improved densification by nano-sized sintering aids for Si₃N₄. *J Mater Res* 1999;14:4562–4569.
122. Aminzare M, Mazaheri M, Golestani-fard E, Rezaie HR, Ajeian R. Sintering behavior of nano alumina power shaped by pressure filtration. *Ceram Int* 2011;37:9–14.
123. Chen DJ, Mayo MJ. Rapid rate sintering of nanocrystalline ZrO₂-3mol% Y₂O₃. *J Am Ceram Soc* 1996;79:906–912.
124. Kim B-C, Lee J-H, Kim J-J, Ikegami T. Rapid rate sintering of nanocrystalline indium tin oxide ceramics: particle size effect. *Mater Lett* 2002;52:114–119.
125. Binner J, Vaidhyanathan B. Processing of bulk nanostructured ceramics. *J Eur Ceram Soc* 2008;28:1329–1339.
126. Kim H-D, Park Y-J, Han B-D, Park M-W, Bae W-T, Kim Y-W, Lin H-T, Becher PF. Fabrication of dense bulk nano-Si₃N₄ ceramics without secondary crystalline phase. *Scr Mater* 2006;54:615–619.
127. Polotai A, Breece K, Dickey E, Randall C. A novel approach to sintering nanocrystalline barium titanate ceramics. *J Am Ceram Soc* 2005;88:3008–3012.

128. Wang GF, Zhang KF, Han WB. Effects of initial density of green compact on hot-press sintering and superplastic forming of nano 3Y-TZP. *Key Eng Mater* 2002;224–226:721–724.
129. Shon I-J, Kang H-S. Properties and fast low-temperature consolidation of nanocrystalline Ni–ZrO₂ composites by high-frequency induction heated sintering. *J Alloys Compd* 2011;509:2964–2969.
130. Ehre D, Gutmanas EY, Chaim R. Densification of nanocrystalline MgO ceramics by hot-pressing. *J Eur Ceram Soc* 2005;25:3579–3585.
131. Xiao CJ, Jin CQ, Wang XH. The fabrication of nanocrystalline BaTiO₃ ceramics under high temperature and high pressure. *J Mater Process Technol* 2009;209:2033–2037.
132. Chang S, Doremus RH, Schadler LS, Siegel RW. Hot-pressing of nano-size alumina powder and the resulting mechanical properties. *Int J Appl Ceram Technol* 2004;1:172–179.
133. Liao S-C, Pae KD, Mayo WE. Retention of nanoscale grain size in bulk sintered materials via a pressure-induced phase transformation. *Nanostruct Mater* 1997;8:645–656.
134. Kear BH, Mayo WE. On the processing of nanostructured ceramics. *Mater Sci Forum* 2003;437–438:399–402.
135. Kear BH, Colaizzi J, Mayo WE, Liao S-C. On the processing of nanocrystalline and nanocomposite ceramics. *Scr Mater* 2001;44:2065–2068.
136. Sciti D, Vicens J, Herlin N, Grabis J, Bellosi A. SiC nano-materials produced through liquid phase sintering: processing and properties. *J Ceram Process Res* 2004;5:40–47.
137. Paranosenkov VP, Kelina IY, Plyasunkova LA, Bykov YV. Preparation of dense ceramics based on silicon nitride nanoparticles. *Refract Ind Ceram* 2003;44:223–226.
138. Gao L, Li JG, Kusunose T, Niihara K. Preparation and properties of TiN–Si₃N₄ composites. *J Eur Ceram Soc* 2004;24:381–386.
139. Li Y-L, Liang Y, Zheng F. Sintering of nanopowders of amorphous silicon nitride under ultrahigh pressure. *J Mater Res* 2000;15:988–994.
140. Woo K-D, Kim B-R, Kwon E-P, Kang D-S, Shon I-J. Properties and rapid consolidation of nanostructured TiC-based hard materials with various binders by a high-frequency induction heated sintering. *Ceram Int* 2010;36:351–355.
141. Kim Y-K, Lee Y-I, Mitomo M. Sinterability of nano-sized silicon carbide powders. *J Ceram Soc Jpn* 2006;114:681–685.
142. Bocanegra-Bernal MH. Hot Isostatic Pressing (HIP) technology and its applications to metals and ceramics. *J Mater Sci* 2004;39:6399–6420.
143. Bhaduri S, Bhaduri SB, Zhou E. Auto ignition synthesis and consolidation of Al₂O₃–ZrO₂ nano/nano composite powders. *J Mater Res* 1998;13:156–165.
144. Sadangi RK, Shukla V, Kear BH. Processing and properties of ZrO₂(3Y₂O₃)-Al₂O₃ nanocomposites. *Int J Refract Met Hard Mater* 2005;23:363–368.
145. Hahn H, Logas J, Averback RS. Sintering characteristics of nanocrystalline TiO₂. *J Mater Res* 1990;5:609–614.
146. Hareesh UNS, Sternitzke M, Janssen R, Claussen N, Warriier KG. Processing and properties of sol-gel-derived alumina/silicon carbide nanocomposites. *J Am Ceram Soc* 2004;87:1024–1030.
147. Dong SM, Jiang DL, Tan SH, Guo JK. Preparation and characterization of nano-structured monolithic SiC and Si₃N₄-SiC composite by hot isostatic pressing. *J Mater Sci Lett* 1997;16:1080–1083.
148. Seal S, Kuiry SC, Georgieva P, Agarwal A. Manufacturing nanocomposite parts: present status and future challenges. *MRS Bull* 2004;29:16–21.

149. Li W, Gao L. Sintering of nanocrystalline $ZrO_2(3Y)$ by hot-pressing. *Mater Trans* 2001;42:1653–1656.
150. Raming TP, Winnubst AJA, Zyl WEv, Verweij H. Densification of zirconia-hematite nanoparticles. *J Eur Ceram Soc* 2003;23:1053–1060.
151. Wu SJ, De Jonghe LC, Rahaman MN. Sintering of nanophase gamma- Al_2O_3 powder. *J Am Ceram Soc* 1996;79:2207–2211.
152. Olevsky EA, Kandukuri S, Froyen L. Consolidation enhancement in spark-plasma sintering: impact of high heating rates. *J Appl Phys* 2007;102:114913, pp12.
153. Olevsky E, Froyen L. Constitutive modeling of spark-plasma sintering of conductive materials. *Scr Mater* 2006;55:1175–1178.
154. Munir ZA, Anselmi-Tamburini U, Ohyanagi M. The effect of electric field and pressure on the synthesis and consolidation of materials: a review of the spark plasma sintering method. *J Mater Sci* 2006;41:763–777.
155. Eriksson M, Liua Y, Hua J, Gaob L, Nygren M, Shen Z. Transparent hydroxyapatite ceramics with nanograin structure prepared by high pressure spark plasma sintering at the minimized sintering temperature. *J Eur Ceram Soc* 2011;31:1533–1540.
156. Grosdidier T, Jia G, Launois S. Processing dense hetero-nanostructured metallic materials by spark plasma sintering. *Scr Mater* 2007;57:525–528.
157. Chaudhry AA, Yan H, Gong K, Inam F, Viola G, Reece MJ, Goodall JBM, Rehman I, McNeil-Watson FK, Corbett JCW, Knowles JC, Darr JA. High-strength nanograined and translucent hydroxyapatite monoliths via continuous hydrothermal synthesis and optimized spark plasma sintering. *Acad Biomater* 2011;7:791–799.
158. Nygren M, Shen ZJ. On the preparation of bio-, nano- and structural ceramics and composites by spark plasma sintering. *Solid State Sci* 2003;5:125–131.
159. Morita K, Hiraga K, Kim BN, Yoshida H, Sakka Y. Fabrication and microstructural characterization of nano-crystalline ZrO_2 -based composite. *Rev Adv Mater Sci* 2005;10:39–44.
160. Chaim R, Shen ZJ, Nygren M. Transparent nanocrystalline MgO by rapid and low-temperature spark plasma sintering. *J Mater Res* 2004;19:2527–2531.
161. Guo XY, Xiao P, Liu J, Shen ZJ. Fabrication of nanostructured hydroxyapatite via hydrothermal synthesis and spark plasma sintering. *J Am Ceram Soc* 2005;88:1026–1029.
162. Chaim R, Bar-Hama OR. Densification of nanocrystalline NiO ceramics by spark plasma sintering. *Mater Sci Eng A* 2010;527:462–468.
163. Lee C-H, Lu H-H, Wang C-A, Lo W-T, Nayak PK, Huang J-L. Microstructure and fracture behavior of β - Si_3N_4 based nanoceramics. *Ceram Int* 2011;37:641–645.
164. Xu X, Nishimura T, Hirosaki N, Xie R-J, Zhu YC, Yamamoto Y, Tanaka H. New strategies for preparing nanosized silicon nitride ceramics. *J Am Ceram Soc* 2005;88:934–937.
165. Yamamoto T, Kitaura H, Kodera Y, Ishii T, Ohyanagi M, Munir ZA. Consolidation of nanostructured beta-SiC by spark plasma sintering. *J Am Ceram Soc* 2004;87:1436–1441.
166. Chaim R, Margulis M. Densification maps for spark plasma sintering of nanocrystalline MgO ceramics. *Mater Sci Eng A* 2005;407:180–187.
167. Li W, Gao L. Fabrication of HAp-ZrO₂ (3Y) nano-composite by SPS. *Biomater* 2003;24:937–940.
168. Wan J, Gasch MJ, Mukherjee AK. Silicon nitride-silicon carbide nanocomposites fabricated by electric-field-assisted sintering. *J Am Ceram Soc* 2002;86:526–528.
169. Oh S-T, Sando M, Niihara K. Mechanical and magnetic properties of Ni-Co dispersed Al_2O_3 nanocomposites. *J Mater Sci* 2001;36:1817–1821.

170. Lee C-H, Lu H-H, Wang C-A, Nayak P-K, Huang J-L. Microstructure and mechanical properties of TiN/Si₃N₄ nanocomposites by spark plasma sintering (SPS). *J Alloys Compd* 2010;508:540–545.
171. Cabrero J, Audubert F, Pailler R. Fabrication and characterization of sintered TiC-SiC composites. *J Eur Ceram Soc* 2011;31:313–320.
172. Chen K, Zhang X, Wang H, Zhang L, Zhu J, Yang F, An L. Making nanostructured ceramics from micrometer-sized powders via grain refinement during SPS sintering. *J Am Ceram Soc* 2008;91:2475–2480.
173. Zhang JR, Gao L, Chen MH. Spark plasma sintering of high-density antimony-doped tin oxide ceramics from nanoparticles. *J Am Ceram Soc* 2006;89:3874–3876.
174. Rana S, Vleugels J, Huangc S, Vanmeensel K, Blank DHA, Winnubst L. Manipulating microstructure and mechanical properties of CuO doped 3Y-TZP nano-ceramics using spark-plasma sintering. *J Eur Ceram Soc* 2010;30:899–904.
175. Schneider J, Mishra RS, Mukherjee A. Plasma activated sintering of ceramic materials. In: Logan K, editor. *Advanced Synthesis and Processing of Composites and Advanced Ceramics II, Ceramic Transactions 79*. Westerville, Ohio: American Ceramic Society; 1996.
176. Wang YC, Fu ZY. Study of temperature field in spark plasma sintering. *Mater Sci Eng B* 2002;90:34–37.
177. Anselmi-Tamburini U, Gennari S, Garay JE, Munir ZA. Fundamental investigations on the spark plasma sintering/synthesis process II. Modeling of current and temperature distributions. *Mater Sci Eng A* 2005;394:139–148.
178. Wang SW, Chen LD, Hirai T, Kang YS. Fundamental investigations on the spark plasma sintering/synthesis process - II. Modeling of current and temperature distributions. *J Mater Sci Lett* 1999;18:1119–1121.
179. Sampath S, Gansert R, Herman H. Plasma-spray forming ceramics and layered composites. *JOM* 1995;47:30–33.
180. Agarwal A, McKechnie T, Seal S. The spray forming of nanostructured aluminum oxide. *JOM* 2002;54:42–44.
181. Agarwal A, McKechnie T, Seal S. Net shape nanostructured aluminum oxide structures fabricated by plasma spray forming. *J Therm Spray Technol* 2003;12:350–359.
182. Hong SJ, Viswanathan V, Rea K, Patil S, Deshpande S, Georgieva P, McKechnie T, Seal S. Plasma spray formed near-net-shape MoSi₂-Si₃N₄ bulk nanocomposites - structure property evaluation. *Mater Sci Eng A* 2005;404:165–172.

CHAPTER 7

MANUFACTURING ISSUES AND EMERGING AREAS

7.1 INTRODUCTION

There is considerable “art” in the current state of nanoparticle-based materials synthesis, superstructure construction, shaping, and sintering, with repeatability constituting one of the greatest challenges. This is mainly because nanoparticle-based processing steps often push the limits of existing technical capabilities and current knowledge base.

One challenge dealing with nanoparticle material processing lies with material purity. Nanoparticle synthesis often requires highly pure chemicals to start with, such as 99.999%. Since one nanoparticle may contain only a few tens or a couple of hundreds of atoms, a few impurity atoms and their minor arrangement details would influence the collective behaviors and properties of nanoparticles or nanoparticle-based materials. Even with ultrapure starting materials and carefully controlled processes, it may still be difficult to eliminate a few foreign atoms and control the precise arrangement of all atoms in a nanoparticle. Slight changes in temperature or humidity can cause atomic level packing and nanoparticle variations.

Another challenge in nanoparticle-based material processing comes from the scale-up process. Nanoparticles and nanoparticle-based materials of controlled size and morphology have been made. However, materials made under real-world conditions do not necessarily correlate with those made in ideal laboratory environments. This is often caused by minute variations in composition, temperature,

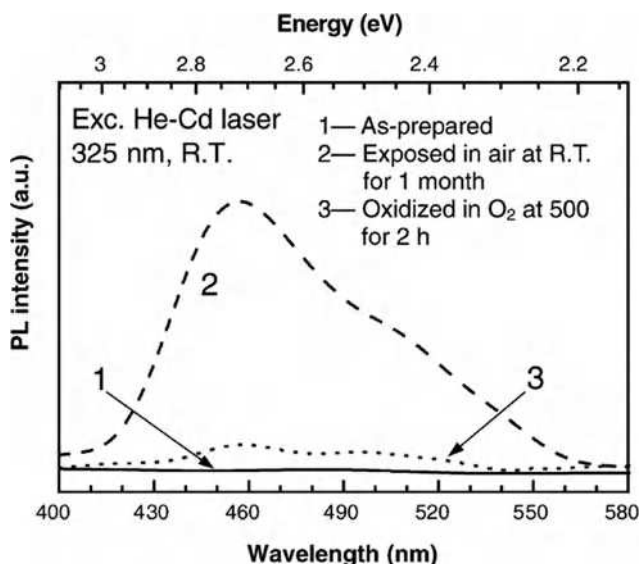


FIGURE 7.1 Room temperature photoluminescence spectra of silicon nanoparticles immediately after preparation, after being stored in air for 1 month, and after being oxidized in pure oxygen at 500°C for 2 hours [1] (Reprinted with permission from Zhu XP, Yukawa T, Hirai M, Suzuki T, Suematsu H, Jiang W, Yatsui K. Defect-related photoluminescence of silicon nanoparticles produced by pulsed ion-beam ablation in vacuum. *Appl Surf Sci* 2005;242:256–260, Copyright 2005, Elsevier).

or other environmental conditions in large, realistic systems. For nanoparticle-based superstructures and bulk components, small variations in processing, composition, or defect density and distribution can dramatically change product performance. Even storage/aging at ambient conditions can change the properties of nanoparticles and nanoparticle-based materials. Figure 7.1 shows the photoluminescence (PL) spectra of silicon nanoparticles recorded immediately after the deposition (as-prepared), after 1 month exposure to air, and after exposure to O₂ at 500°C for 2 hours. The silicon nanoparticles are made by pulsed ion beam ablation in vacuum [1]. For the as-prepared sample, photoluminescence signals are too weak to be observed but become much stronger with prolonged exposure time in air. For the samples exposed to air, the photoluminescence spectrum clearly presents an asymmetric shape, composed of a primary peak at 455 nm (blue range) and a shoulder around 510 nm (green range). For the sample thermally annealed in flowing pure O₂ at 500°C for 2 hours, the photoluminescence spectrum shows a great decrease in the emission intensity, as also shown in Figure 7.1.

The third example challenge is that complicated electronics and high vacuum capabilities are often a must for nanoparticle material processing and characterization. Instability in the noise level, power supply, and vibration are often

common causes of the randomness in the results. Advanced and more consistent instrumentation will allow more reliable and pain-free processing and measurement of physical dimensions, purity, properties, and functionality of materials. This will in turn enable the process to be scalable, controllable, predictable, and repeatable.

Based on the above understanding, measurement and quantification of nanoparticles and nanoparticle-based materials will be discussed in this chapter. Process and quality control will be analyzed in order to achieve repeatable nanoparticle-based material processing. In addition, the state of the computer modeling efforts will be assessed in the realm of verifying experiments and predicting nanoparticle-based material behaviors under new circumstances. In light of the widespread use of nanoparticle-based materials, the environmental and health implications of nanoparticles and nanoparticle-based materials will be examined.

7.2 DEFECTS AND MEASUREMENT

7.2.1 Defects

Current focus on the evaluation of nanoparticles and nanoparticle-based material is mainly on physical characterization. This includes size, shape, morphology, surface area, crystal structure, and composition of individual particles or nanoparticle-based bulk samples. However, there is little effort on measuring the defects inside nanoparticles or nanoparticle-based materials beyond the conventional pore size, porosity, and grain level characterization. This is partly because defect measurement for nanoparticle-based materials is difficult. The features to be identified are at the nanoscale and smaller, which often tests the limit of the measurement technique itself. More often than not, the nature of the defects can be altered during sample preparation. How to detect, characterize, and trace defects, which are often much smaller than nanoparticles themselves, is a matter to be discussed. Under the assumption that these issues can be resolved, there are three aspects of defects that need to be addressed: defect nature, size, and population, as illustrated in Figure 7.2.

7.2.1.1 Defect Nature When examining the defects of a given sample, the first question to be resolved is the nature of the defects. Is the defect an irregularity in atomic packing? Is it a mismatch between different phases? Is it adsorption of undesirable foreign species? Or, is it the metastable state of the material itself? The follow-up question would be what the consequence of the presence of the defects is. Will they serve as the reactive sites for interfacing with the environment? Will they cause stress/strain in the material? Or, will they change the electrical conductivity, light transmission, magnetism, or other properties of the material?

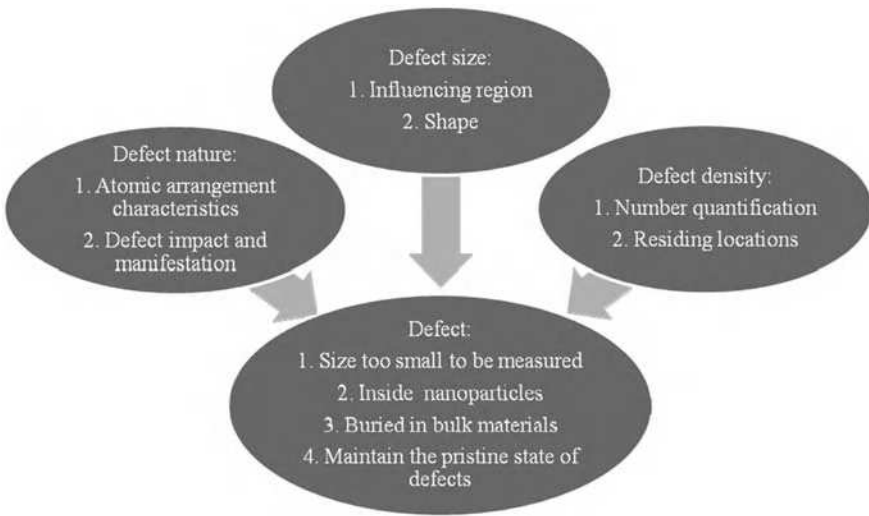


FIGURE 7.2 Different aspects of defects.

7.2.1.2 Defect Size Defect size can be understood as the scope or region of the irregularity of the species arrangement or distribution. Is it atomic in scale? Is it nanometer? Or, is it greater than nanoscale? Defect shape also needs to be considered in the realm of defect size. Do the defects have linear shape, two-dimensional shape, or three-dimensional shape? Is it circular if it is two dimensional, or is it spherical if it is in three dimensions?

7.2.1.3 Defect Density Defect density can be understood as the number of defects within a given space (either volume, area, or mass), which has a profound impact on material performance. For example, quantum yield can be substantially reduced when a quantum dot particle surface has too many defects due to surface corrosion/oxidation. Do these defects distribute randomly or in regular periodicity? Also, is the defect through the volume or simply along a surface or an interface? Also, the residing locations of the defects should be properly considered. However, the measurement of defect density is in its infancy. Counting the number of defects is cumbersome and impractical. In addition, defects may be buried inside materials and cannot be counted. There is a lack of techniques for detecting them, let alone quantifying them.

Even with all these uncertainties, defects must be reduced or at least controlled when they seriously compromise material performance. Since defects generated at nanoscale are often random, unintentional, and untraceable, mitigation of defects at the nanoscale is now almost exclusively done by trial-and-error. Because of the lack of fundamental evaluation, description, and measurement of defects, the strategies for properly controlling them have been elusive.

7.2.2 Measurement

If a product or a sample cannot be measured, it cannot be manufactured. Additionally, if that product cannot be made repeatedly, it should not be manufactured [2]. Measurements on the nanoscale often come with more uncertainty due to the difficulty of locating and manipulating species exactly, especially at length scales below ~ 10 nm. In many experiments, the device that holds or measures the nanoscale structure can also produce irreversible material changes. For example, electron microscopy can produce defects in the nanostructure being imaged due to the electron bombardment; during optical measurements, metal nanoparticles are subjected to serious heating effects that can melt or destroy the nanoparticles or nanostructures; and atomic force microscopy studies of nanoparticles or the corresponding bulk materials may lead to structural reorganization. For liquid-based samples, the necessary sample preparation steps for characterization can fundamentally change the nature of the samples themselves. The most common technique for measuring nanostructures, electron microscopy, requires that the samples be removed from their natural environments, such as from solutions, and placed on a grid under circumstances where aggregation and restructuring can occur. This can fundamentally change the validity of the measurement itself. *In situ* measurements are not available for many of the existing material systems to alleviate some of these issues. For example, there is no tested technique to measure the nanostructure of a self-assembled monolayer on a colloidal particle in solution or defect evolution in a nanoparticle-based sample undergoing sintering. In general, the measurements can be categorized into three categories, as shown in Figure 7.3.

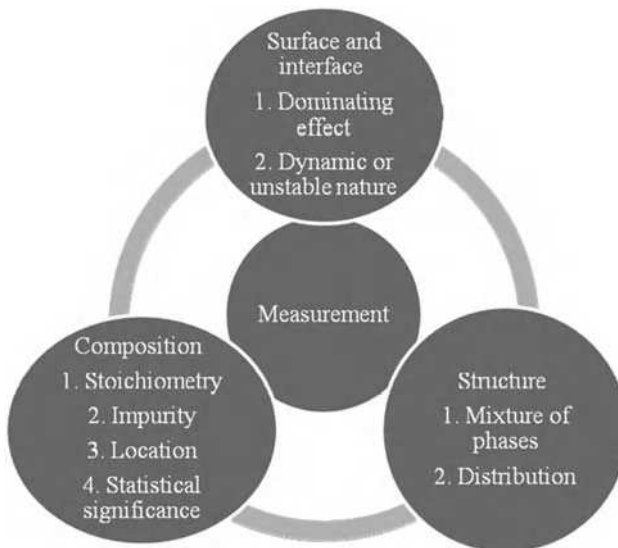


FIGURE 7.3 Interrelationship of various measurements at nanoscale.

7.2.2.1 Composition For the composition measurements of nanoparticles and nanoparticle-based materials, two levels need to be considered. One is the stoichiometry of the designed composition itself. The other is the impurities of the material system. In addition to the known composition characterization issues and more exact need for the quantification of compositions, there are some challenges at the nanoscale that are not encountered at the microlevel. For example, doping in semiconductors is a well-established process. However, random dopant concentration fluctuations become extremely important at the nanoscale since the fluctuation of dopant concentration would be no longer tolerable. Making the situation rather complicated is the location of the dopant atoms. Surface atoms behave differently from center atoms and alter material properties. With a typical doping concentration of 10^{18} cm^{-3} , there will be just one dopant atom in a device of $10 \times 10 \times 10 \text{ nm}^3$ in size. Distribution fluctuation of dopants can result in totally different functionalities of devices in such a size range. The challenge is not only to achieve reproducible and given concentrations of dopant atoms at the nanoscale but also to precisely control the location of dopant atoms [3].

Because of the important but elusive presence, nature, stability, and influence of defects and impurities, three-dimensional measurement of compositions with atomic resolution is needed. Measuring an average composition over a region (even as small as 10 nm) is not sufficient. Also, the statistical significance of the measurements needs to be redefined and validated. Nanoparticle reference materials of different medium, size, chemical composition, surface functionality, shape, and charge will enable traceability, calibration, and validation of measurements in nanomanufacturing.

7.2.2.2 Structure For crystal structure analysis at nanoscale, X-ray diffraction peak line broadening needs to be rigorously analyzed to avoid strain-induced peak shifting. A mixture of crystalline and amorphous structures can make the diffraction pattern indexing extremely challenging. For nanoparticles with an amorphous surface shell, crystal structure identification may not be possible. The same applies to heterogeneous microstructures of nanocomposites. When nanoscale composition distribution needs to be characterized, X-ray diffraction is not feasible. For electron diffraction, the region of interest needs to be carefully chosen since only very small areas are analyzed. Also, the statistical significance needs to be rigorously tested since the technique can only analyze very local regions in a sample.

7.2.2.3 Surface and Interface Different from conventional particle-based materials, large surfaces and interfaces are an indispensable part of nanoparticle-based materials. The extremely large surface/interface area of these materials dictates that the high content of species on the surface and at the interface cannot be ignored in any given nanoparticle-based system. In addition, surface structure and activity can be significantly different from those of bulk materials. Interfacial properties and wetting characteristics require development of new measurement

techniques. Buried interfaces/interphases at nanoscale can dictate the collective electronic, magnetic, and photonic behaviors of the structures and devices and need to be quantified. New approaches are also needed to measure dynamic or unstable interfaces.

When reliable gauges are established, standardization for both nanoparticle synthesis and bulk material processing is the prerequisite for reliable end products. This will lay the stepping stone for the scale-up of nanoparticle-based material manufacturing. Currently, standardized procedures are still needed even at lab-scale, and a given sample cannot be produced the same way in different labs. This hinders reliable comparison of the measurements made under real-world conditions. Current measurements need to be updated and new measurements need to be defined and developed to address these issues.

Another need at the horizon of nanoparticle-based material processing is measurement verification and validation. For example, there are only a couple of measurement techniques for composition analysis (mostly through composition analysis modules on transmission electron microscopy or specific use of atomic force microscopy), so the reliability and accuracy of the measurements need to be carefully evaluated and calibrated. Currently, typical gauge-to-gauge difference for nanoscale measurements is at the same scale as the products to be measured. Reference materials should be developed to validate new findings and understanding. Often times, very specific materials are needed for such purposes. Establishment of specific metrological capabilities and globally accepted standards for manufacturing and measurements of nanoparticle-based materials and their properties is necessary. Comparing the measurements taken by different instruments and laboratories has been problematic because reference materials are not available to ensure that different laboratories and techniques are transferable in measurements.

Measurement for nanoparticle-based products also means gauging the nanoscale structure, performance, and properties in a user-friendly manner. Instruments capable of three-dimensional chemical and structural characterization at nanoscale and platforms for simultaneously assessing multiple properties on a single sample would be extremely beneficial. Techniques that can span multiple length and time scales simultaneously are highly desired. Methods for measuring and visualizing chemical dynamics (time-resolved chemistry) remain extremely relevant. Improved resolution of measurement tools by orders of magnitude over current capabilities is needed in order to probe local behaviors on the atomic and molecular scale and correlate those behaviors with the macroscopic behaviors of larger entities [2]. *In situ* measurement is also critical for quick feedback and reliable processing. Currently, there are very limited nondestructive measurement capabilities at < 100 nm.

Besides improving the resolution and zooming in onto the nanoscale, new measurement techniques need to be developed for new property evaluation. Currently, no techniques exist for examining and quantifying the number density of dispersed nanoparticles, whether they are in a liquid solution or a gas phase. Topological description of nanoscale grains or pore networks is nonexistent.

Overall, the measurement of compositions, structures, and interactions at surfaces and interfaces with near-atomic resolution is critical. Ultimately, quantitative measurement of chemistries and structures at the nanoscale and the linkage of these measurements to processing parameters and end-use properties need to be established.

7.3 PROCESS AND QUALITY CONTROL

Many challenges exist for the scale-up production of nanoparticles and nanoparticle-based materials. Before a mass production process is implemented, a robust quality control method should be established to provide inspection methods, standards, nondestructive quality measurements, indicators of attribute thresholds, methods for failure analysis, and other measurements. The critical issues are the distribution of shape, size, surface charge/structure, and functionality within a batch and variation from batch to batch [2]. The slow advancement in this regard is partly attributed to the segmented nanomanufacturing industry. Because the applications of nanoparticle-related materials span from health care, electronics, automotive, to aerospace, it is natural that different industries have different standards and needs for different aspects of the process and quality control. High-throughput characterization techniques that can be easily adapted from one industry to another rarely exist. Linkage needs to be established first to connect key, easily controlled process parameters to nanoscale morphologies/features that define a material's performance. In this way, the understanding of nanoscale features and properties can be effectively utilized to enable the creation of robust process control parameters that ensure repeatable manufacturing processes [2].

For in-line and in-process quality checks, conventional electron microscopy is not fast enough to provide the population statistics necessary to sufficiently characterize nanoparticles or the corresponding bulk materials. Rapid, automated techniques are currently lacking for the determination of the metrics that are applicable during and after the production of nanomaterials [2]. For quality control in manufacturing, in-process tools are needed to measure such parameters such as temperature, gas flow, and pressure. Real-time tools for monitoring the liquid state of nanoparticles and nanoarchitectures as well as the self-assembly processes, including three-dimensional methods capable of probing through layer depths, are desired. Advanced instruments for characterizing nanoparticle-based material properties nondestructively at the nanoscale spatial resolution are highly needed. For a nanomanufacturing process to be repeatable, controllable, predictable, and operable at a reasonable scale, high-throughput characterization methods, off-line at the minimum and in-process at the maximum, are needed.

Nanoparticle-based materials are complex systems, and their properties are influenced by a multitude of variables that operate at different length scales. There is a lack of fundamental understanding of the important variables connecting the structure, chemistry, and physics of nanoparticle-based materials to

performance. Sometimes, it is even difficult to know what variables are important for a given performance requirement. This lack of understanding leads to developments based on trial-and-error and inhibits the timely development and commercialization of these novel materials [2]. Process and quality control for the scale-up of nanoparticle-based manufacturing should be tailored with targeted performance in mind. Critical to the realization of robust nanomanufacturing is the development of the necessary metrology and standards that can evaluate and guide the nanoparticle-based manufacturing on a daily basis. These standards are needed for consistent manufacturing and testing of nanoparticle-based materials, verifying the purity of the materials as well as the quality and consistency of the process. Integration of the instruments, their interoperability, and appropriate information management is also critical and must be considered for viable nanomanufacturing. The characterization techniques discussed in Chapter 3 can serve as a road map for establishing these protocols.

Nanoparticle-based synthesis and processing technologies need to be developed to the point where marketing and manufacturing personnel can create a simple bill of materials and warrant the items with confidence. Realizing these advances will require accelerated understanding of material-processing-property relations and the development of measurement science and standards. Developing a stable, reliable manufacturing process where all the significant variables are properly considered is a challenge even for conventional material manufacturing, let alone ones that contain various nanoscale species and structures [2].

7.4 MODELING AND SIMULATION

This book is focused heavily on the experimental aspects of nanoparticles and nanoparticle-based materials. However, modeling and simulation can be a cross-cutting and enabling tool for discovery, process design, and process control and deserve more attention.

At nanoscale, many measurement and characterization techniques become very costly or impossible. Computer simulation and modeling become ideal tools for understanding material behaviors and predicting new properties. The scale of attention fits the capabilities of many modeling efforts perfectly. The interactions not detectable experimentally can be easily revealed and measured by simulation. Modeling can represent and visualize the theoretical understanding and/or the physical mechanisms related to the interaction of nanoparticles with other materials and the effects of processing on morphology; modeling can also provide predictions of the behaviors of nanoparticle-based materials at the nanolevel.

The challenges for computer modeling and simulation are the very different nature of the processing steps and the multiscale nature of the materials themselves. Current computational methods and algorithms are not sufficient in addressing modeling across multiple length and time scales. Nanoscale structures and phenomena do not always vary with length in the same way. The quantum dot

behavior, in which the colors of semiconductor nanoparticles vary with size due to electron confinement effects, is associated with size on the few-nanometer-length scale, whereas the variation of the color of metal nanoparticles with size due to electrodynamic effects is associated with particles in the 10–200 nm regime. The formation of covalent bonds is often highly localized, so small-scale interactions have to be extrapolated to determine adsorbate binding energies that are useful for much larger particles. There is a lack of integration tools for quantum, atomistic, meso, and macro (or finite element) length and time scales. This is a field where no one type of theories can be used in all cases, and where the marriage of theories associated with different length scales is still somewhat rocky. Most of the problems are being addressed by pushing traditional theories, such as electronic structure theory and molecular dynamic theory, to systems that are much larger than they have been traditionally calibrated for, and for which serious approximations need to be introduced to make the simulation manageable. In other areas, continuum theories are pushed down to smaller length scales than they were originally developed for, and again approximations need to be introduced to make these new models produce useful results. Multiscale theories, in which the atomistic and continuum scales are meshed together, are still limited, and the application of such approaches to real systems is rare.

Computer modeling of nanoparticle synthesis and nanoparticle-based material processing serves several critical roles. First of all, it offers design tools for the formation, evolution, and interaction of nanoparticles and the corresponding materials during processing. Second, it helps to illustrate design principles and rules for nanoparticles and related bulk materials. For a simulation module, the fundamental mechanisms and guiding processing principles have to be researched and mathematically constructed. This helps to elucidate the understanding and validate the theories in the field. Third, it enables integrated and predictive structure-property and composition-performance correlations. Fourth, it validates experimental techniques and provides input for future improvement.

Since there is very little coverage of the modeling and simulation aspects of nanoparticles and nanoparticle-based materials in this book, a few brief examples are offered as follows to provide a glimpse of the topic.

A chemical vapor synthesis (CVS) process used to create nano-sized aluminum powder for various hydrogen storage materials is simulated by computational fluid dynamic modeling. The fluid flow, heat transfer, and chemical reaction phenomena taking place inside the reactor are analyzed together with particle formation and growth. Chemical reaction rate and population balance models are used to calculate the particle formation and growth. The temperature, velocity, and particle size distribution fields inside the reactor are computed. The particle size computed by the program is compared with the experimental data, and the calculated average size of the final product particles is consistent with that obtained in the experimental work [4]. The CVS of a WC nanopowder from tungsten hexachloride (WCl_6) is simulated by a two-dimensional multiphase computational fluid dynamics model. A population balance model is coupled with gas-phase equations to describe the formation and growth of WC nanoparticles.

The model is validated with experimental data in terms of average particle size and concentration of the unreacted precursor at the outlet [5]. However, the simulation is mostly macroscopic without details on individual nanoparticle formation and growth.

A mathematical model is developed to describe the dynamics of liquid-phase synthesis of nanoparticles. The model predicts the time evolution of particle size distribution and supersaturation by employing a generalized single-particle growth rate law that avoids some of the restrictive assumptions present in most classical approaches of the problem. A moving boundary algorithm is formulated using information about the mean and standard deviation of the distribution in order to update the grid. Discretization is performed at each time step only at the domain that contains a significant amount of particles, thus increasing the accuracy of the prediction. This approach is useful in simulating the fast changes in the particle size distribution characteristics occurring in the transition between the focusing and defocusing stages [6]. However, validation by experiments is still needed.

Self-assembly of superlattices of semiconducting colloidal nanorods horizontally and vertically oriented on substrates is modeled. The models include van der Waals and Coulombic coupling between nanorods with intrinsic electric dipoles and their coupling to the substrates with and without the effect of external electric fields on the self-assembly processes. The results indicate that the length to diameter aspect ratio and the number of nanorods are the most important factors that determine the type of the packing. These phase transitions can be efficiently controlled by external electric fields (Fig. 7.4) [7]. As an example, without an electric field, nanorods in the bilayer cluster with a hexagonal symmetry on the substrate. The nanorod dipoles are vertically oriented in the antiferroelectric order, which provides the lowest possible energy. With an electric field, nanorods form a bilayer cluster with a hexagonal symmetry perpendicular to the substrate. The nanorod dipoles are oriented in the ferroelectric order antiparallel to the field.

Numerous sintering models at atomistic, particle, and component scales have been published. Molecular dynamics (MD) simulations are employed to investigate the mechanism and kinetics of the solid-state sintering of two crystalline gold nanoparticles (4.4–10.0 nm) induced by low-energy laser heating. At 27°C, sintering occurs between two bare nanoparticles by elastic and plastic deformation driven by strong local potential gradients. The initial neck growth occurs very fast (150 picoseconds) and is therefore essentially insensitive to laser irradiation. The classical diffusion-based neck growth model is modified to predict the time-resolved neck growth with the diffusion coefficients and surface tension extracted from the molecular dynamics simulation. The diffusion model underestimates the neck growth rate for smaller particles (5.4 nm), while satisfactory agreement is obtained for larger particles (10 nm). The deviation is due to the ultrafine size effect for particles below 10 nm [8]. Computations over a broad range of temperatures and particle sizes have shown that particle sintering is very dependent on size and temperature when solid-like, and considerably less sensitive when liquid-like. The results have shown that solid-like particles sinter

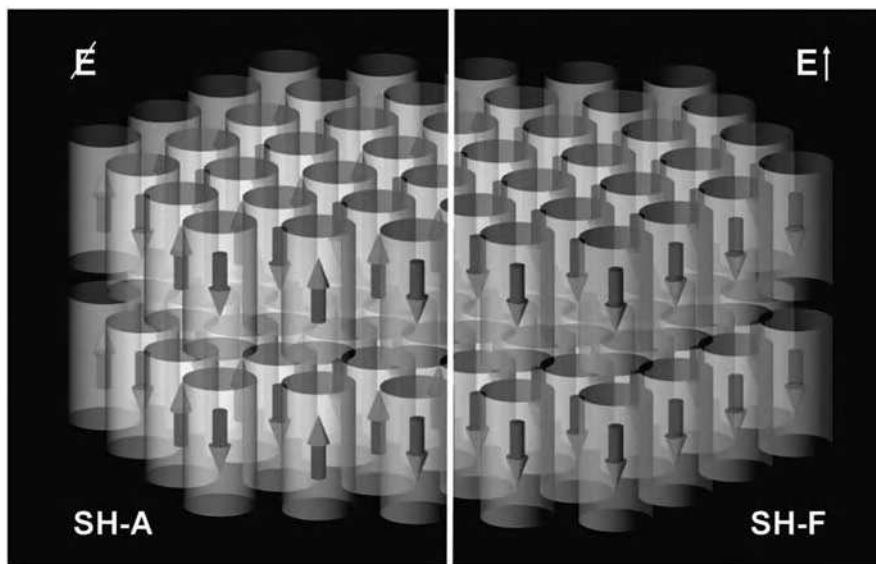


FIGURE 7.4 (left) Nanorods in the bilayer cluster with a hexagonal symmetry formed on the substrate. The nanorod dipoles are vertically oriented in the antiferroelectric order, which provides the lowest possible energy. (right) Nanorods in a bilayer cluster with a hexagonal symmetry that are formed perpendicularly to the substrate in the presence of the electric field. The nanorod dipoles are oriented in the ferroelectric order antiparallel to the field [7]. (Reprinted with permission from Titov AV, Kral P. Modeling the self-assembly of colloidal nanorod superlattices. *Nano Lett* 2008;8:3605–3612, Copyright 2008, American Chemical Society.) (For a color version of this figure, see the color plate section.)

by a solid-state diffusion mechanism while liquid-like particles sinter by a viscous flow mechanism [9]. However, there are few studies focusing specifically on nanoparticle sintering with the consideration of the unique characteristics of nanoparticle interaction and diffusion [10]. Most microstructure models are phenomenological and remain untested by comparison with experiments.

Given the current level of available computing power and resources, algorithm efficiency is a barrier to the fundamental development and maturation of computational models. Numerical methods and algorithms need to be developed to describe surface chemistry, the interfacial properties between nanoparticles and between nanoparticles and the host matrix, and the impact of functionalization on the desired properties. Numerical methods that link the design parameters with these nanoscale properties also need to be developed. The barriers for modeling can be summarized as the following:

1. Lack of databases for modeling input.
2. Absence of tools and methods to bridge multiple time and length scales.
3. Deficiency of optimally fast methods for calculation of a large number of atoms to predict structure and properties of nanoparticle-based materials.

4. Incapability of formal statistical uncertainty analysis of modeling and simulation.
5. Lack of methodology for systematic intercomparison of codes used for verification and validation.
6. Tools for modeling and simulation are often difficult to use.
7. Lack of methods to integrate and analyze large datasets.
8. Ineffective deconvolution techniques for analyzing nanoscale and atomic data.
9. Shortage of systematically generated experimental data at all relevant time and length scales for guiding and validating model development.
10. Lack of close collaboration between experts in high-precision measurement and dedicated theorists and computer modelers.

Modeling and simulation capabilities must reach a level of maturity where one can forecast processing capabilities and variations based on the nanomaterial's fundamental parameters. Reliable and accurate modeling is the necessary state for desired advancement and understanding of nanoparticle-based materials (Fig. 7.5). Precursors to such confidence will be significant advancements in

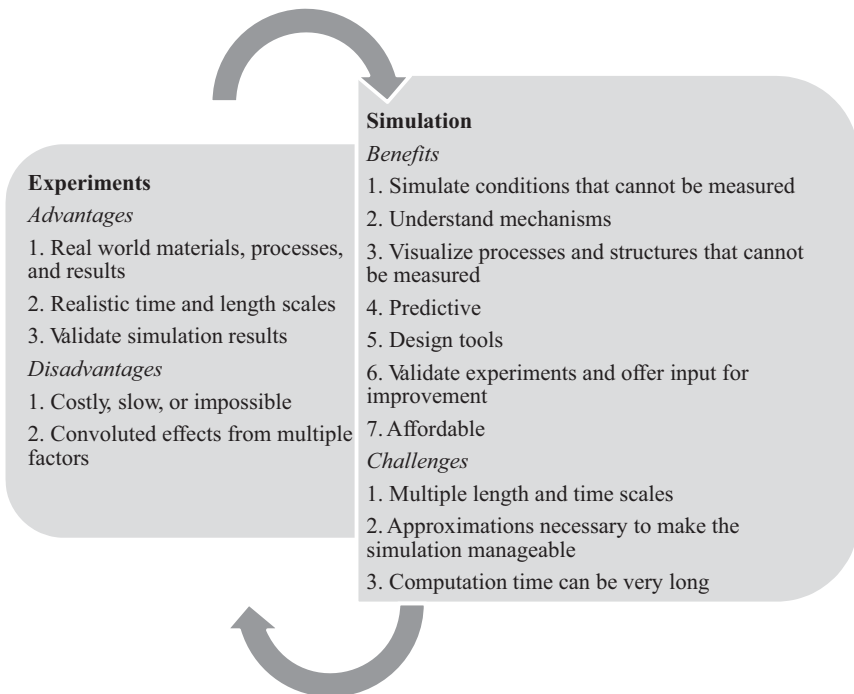


FIGURE 7.5 Comparisons between experiments and simulation for nanoparticle-based materials.

multiscale modeling, innovative algorithms to model over multiple length- and time-scales for realistic system sizes, and more fundamental long-term algorithm development. Experimentally validated models, increased access to high speed computing capabilities, and improved portability of models on existing computing platforms are catalysts for such improvements. These algorithms can be drawn from the areas of quantum physics, chemical simulation, statistical simulation, and finite-element simulation. In addition, efforts should be put toward correlating structural measures to mechanical, electrical, magnetic, thermal, and optical properties and quality metrics.

7.5 ENVIRONMENTAL AND HEALTH CONCERNS

Nanoparticles and nanoparticle-based materials have the potential to unleash innovations in numerous fields such as energy, electronics, environment, and biology and lead to powerful technological and economic benefits. These materials are being used increasingly for commercial purposes such as fillers, opacifiers, catalysts, semiconductors, microelectronics, cosmetics, and drug carriers. Nanoparticles have been incorporated in hundreds of different types of products, and the novel properties of nanomaterials offer great promise to provide new technological breakthroughs. However, materials in this size range may approach the length scale at which some specific physical or chemical interactions with their environments can occur. As a result, possible undesirable results of these capabilities, such as harmful interactions with biological systems and the environment and the potential to generate toxicity, need to be carefully evaluated and addressed. The establishment of principles and test procedures to ensure safe manufacture and use of nanoparticle-based materials in the marketplace is urgently needed.

So far, the concern has mainly evolved around nanoparticles, especially air-borne nanoparticles. There have not been many concerns related to bulk nanoparticle-based materials. The general notion is that if nanoparticles are not free to move from one place to another, then the chance of them becoming toxic in the environment or getting into the human body is low.

7.5.1 Environmental Concerns

The great diversity of nanoparticles being produced today brings not only many industrial and consumer applications (such as car tires, sunscreen, and cosmetics) but also a variety of unknown potential environmental effects. For example, nanoparticles may become air-borne after being dried from a liquid system or after being worn off from a nanoparticle-based bulk component. Due to the unique physical and chemical properties of these manufactured and released nanoscale species, they may behave very differently in the environment than their naturally occurring counterparts. While there have been no major, direct harmful consequences identified either by the manufacturer or user of these

technologies, environmental and safety issues are of concern to all industries and consumers employing or considering the use of nanoparticle-based products. For example, it is well known that as a particle shrinks in size to the nanoscale, the ratio between its surface area and mass increases. A material may exhibit markedly different reactivity in nanoscale than that demonstrated in bulk-sized equivalents. These changes in properties can be advantageous and provide results for the realization and maturation of new applications. However, they can also result in increased environmental hazards. Research is needed to assuage popular fears and demonstrate both consumer and environmental safety.

The impact of nanoparticles on the environment can take on many different forms. Often changes in the environment such as temperature and humidity can result in aggregation or a shift in the particle size distribution. Even though the process might be long or difficult to predict, nanoparticles emitted into the environment will eventually be deposited on the Earth's surface. Once coming into contact with the Earth's surface, nanoparticles have the potential to contaminate soil, enter surface water or groundwater systems, or interact with biota. Biological organisms may not have been in contact with anthropogenic nanoparticles over the course of their evolution; consequently, these organisms (fish, invertebrates, amoeba, etc.) have not faced any selection pressure imposed by the presence of nanoparticles and may be susceptible to any risks that nanoparticles may pose. Since industrial and consumer waste streams eventually lead to the natural aquatic environment, it is inevitable that manufactured nanoparticles will be introduced into surface water, and likely also groundwater systems, if this has not happened already (Fig. 7.6).

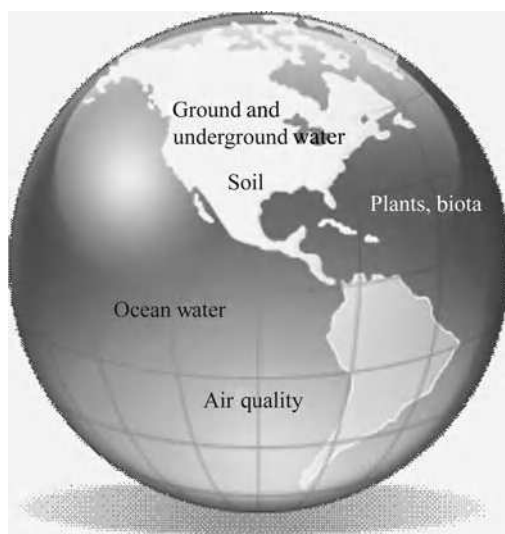


FIGURE 7.6 Unknown interactions between the environment and nanoparticles.

Nanoparticles may also undergo a series of evolutions in their life cycles. This includes the degree of agglomeration, aerodynamic size, number concentration, surface area, etc. When airborne, nanoparticles can affect air quality and get absorbed by different species. Such unexpected variations, if unaccounted for, can have a significant effect on the available nanoparticle dose and on the interpretation of any results obtained thereafter. Despite the current lack of knowledge relating to which environments, and hence which organisms, are most likely to be exposed to nanoparticles, the toxicological potential of nanoparticles on a range of organisms cannot be ignored. The impact may span the breadth of microorganisms, plants, invertebrates, and vertebrates, although relatively few publications are available within each category. The toxicity of nanoparticles to microorganisms has been widely studied in relation to the development of antimicrobial agents and devices for use in the environment, in industry, and in medical devices. However, the literature relating to the effects of nanoparticles on plants, invertebrates, and vertebrates is scarce.

Data regarding the volume of nanoparticles produced globally is sparse and sometimes contradictory. One estimate puts total production in the millions of tons worldwide. Given the growth rate of nanotechnology over recent years and the virtual lack of studies of the environmental impacts of nanoparticles, research of this nature has recently become a focus of regulatory agencies and governments. Currently, no data exist on environmental concentrations of manufactured nanoparticles. It is, however, important to proactively consider the potential environmental impacts of these pervasive nanomaterials.

7.5.2 Health Concerns

Consumer products that include nanoparticles are amongst the fastest growing lines of nanoproducts; hundreds of such products are reported to be on the market [11–14]. They are mainly used for antiseptic and odor-fighting by coating and impregnating materials, such as: (1) paints, (2) home appliances (refrigerators, laundry machines, and cooking utensils), (3) medical instruments (bandages, catheters, and pacemakers) and drug delivery, (4) water purification, (5) clothing, (6) antibacterial sprays, (7) personal care products (toothpaste, shampoo), and (8) coating of electronics, etc. Considering these uses, nanoparticles can be found indoors (in industrial and household environments) and outdoors (in the vicinity of smelters, nanomaterial industries, wastewater treatment plants, etc.). Nanoparticle-related products are an emerging area and have potential health and safety risks throughout their product life cycles (Fig. 7.7). The health risk of nanoparticles is a function of both their hazard to human health and their exposure potential. It is prudent for companies to try to mitigate the potential risks of nanoparticles during the design stage rather than downstream during manufacturing or consumer use. Typically, toxicity is measured as a function of mass, but when a material is reduced to the nanoscale, this metric is no longer valid or reliable. Nanoparticles may be ingested, inhaled, injected, or absorbed through the skin into the body. Thus, understanding the fate of these materials in

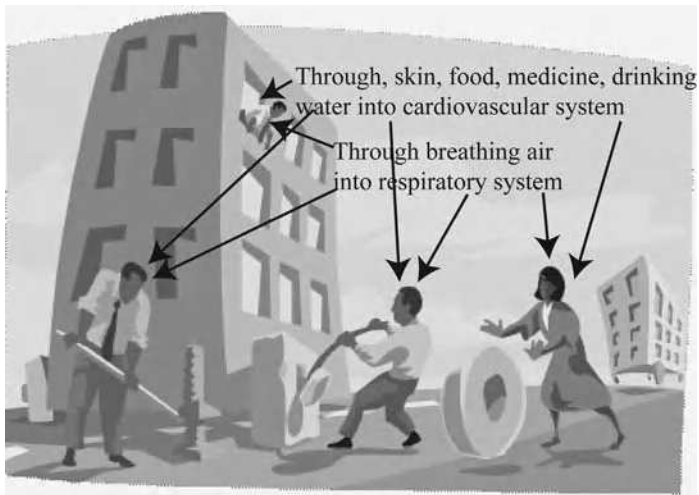


FIGURE 7.7 Nanoparticle pathways into human bodies.

the environment and their chemical stability is an important step for predicting scenarios of human exposure to nanoparticles.

Nanoparticle risks pose a new form of risk assessment challenges. Besides a lack of data, there are deep scientific uncertainties regarding a risk assessment framework: (a) particle characteristics that may affect toxicity, (b) particle fate and transport through human bodies, (c) the routes of exposure and the metrics by which exposure ought to be measured, (d) the mechanisms of translocation to different parts of the body, and (e) the mechanisms of toxicity and disease. In each of these areas, there are multiple competing models and hypotheses. These are not merely parametric uncertainties, but about the choice of the causal mechanisms themselves and the proper model variables to be used, that is, structural uncertainties.

There are still fundamental uncertainties about the specific physical and chemical properties of airborne particles that cause health risks. Specifically on the subject of air quality, it is known that inhaled airborne particles can lead to inflammation of the respiratory and cardiovascular systems. Some airborne particles, such as asbestos, have raised special concerns due to their shape, which can lead to worse health effects. It is believed that physical and chemical particularities of nanoparticles can also cause more intense health implications [15]. It is known that damages to the respiratory system increase as particle sizes decrease, notably within nanoscale [16]. Potential health effects of inhaled nanoparticles include asthma complications, chronic bronchitis, and respiratory tract infections. There is a potential for lung exposure to a wide variety of nanoparticles which have yet to be studied in terms of (1) where they would deposit within the respiratory tract and (2) the subsequent toxicity mechanisms. It is also suggested that different

sizes, structures, and compositions of nanoparticles may interfere in their toxic mechanisms [17].

Studies on carbonaceous airborne nanoparticles show that these materials have a very high potential for adsorbing semivolatile organic compounds, namely polycyclic aromatic hydrocarbons. Thus, these nanoparticles can serve as transport carriers for pollutants that would otherwise not become airborne and get into human lungs [18–20]. For other common nanoparticles such as silver, little is known in terms of adsorption or condensation of other chemicals to their surfaces. The much larger surface areas of nanoparticles can increase their chemical activity. If these products become mass produced, the impact on human health cannot be predicted yet. There are currently no official government registries or regulations for such nanoproducts [21].

Particle size and surface area have been shown to play important roles in toxicity, both due to the larger release of ions per volume and the likelihood of smaller particles penetrating into the body. *In vitro* studies with silver nanoparticles report that nanoscale particles can enter cells and cause DNA damage [22]. Some semiconductor and oxide nanoparticles enter lung epithelial cells by means of a Trojan-horse type mechanism (ions do not enter cells, but nanoparticles do and release ions once inside) [12]. Then, nanoparticles may directly or indirectly result in oxidative stress or may even interfere with metabolic activities inside the cells [23, 24]. Oxidative stress is caused by the formation of reactive oxygen species at the surface of or within cells, which may induce inflammatory processes in the human nose, lung, and cardiovascular systems [15, 25].

Currently, there are many issues to be addressed before product designers can fully apply these principles and make informed choices about nanoparticles. How should they characterize the nanoparticles used in their products? What are the key attributes that should be included in the characterization? How do the hazards found in nanoparticle research apply to the nanoparticles in products? As the field of nanotechnology progresses, better answers to these questions will emerge. Another major challenge is the lack of comprehensive data for the product performance, hazard, and exposure potential of nanoparticles with different shapes, sizes, surfaces, structures, and functionalizations. These data gaps need to be addressed by further targeted research by government and industry. Predictive models will also need to be developed to provide additional data. Ideally, these data should be housed in a centralized, open-access database available to researchers and industry. Over time, the “design for safer nanomaterials” principles could become more effective as additional performance, hazard, and exposure potential data are accumulated and made available. Ultimately, these initial design principles will need to be tested and refined over time to help guide product designers to make more informed and effective decisions for selecting nanoparticles that they incorporate into their products.

A battery of tests should be developed to uncover particularly hazardous properties. Miniature and low-cost instrumentation to monitor personal exposure to nanoparticles in the workplace will play an important role in the design and implementation of mitigation strategies. For example, a new miniature disk

electrostatic aerosol classifier has been designed and evaluated. This new miniature prototype provides a low-cost solution for miniature nanoparticle sizers, much needed in spatially distributed particle size measurement or personal exposure monitoring [26]. Over the long term, research aimed at developing a mechanistic understanding of the numerous characteristics that influence nanoparticle toxicity is essential. Predicting the potential toxicity of emerging nanoparticles will require hypothesis-driven research that elucidates how physicochemical parameters influence toxic effects on biological systems. Research needs should be determined in the context of current availability of testing methods for nanoparticles. Finally, the general policy and strategic opportunities should be created to accelerate the development and implementation of testing protocols and ensure that the information generated is translated effectively for all stakeholders.

7.6 SUMMARY

In this chapter, the emerging issues for nanoparticles and nanoparticle-based materials are evaluated. These issues can be divided into the categories of defects and measurement, process and quality control, modeling, and environmental and health aspects.

Defect measurement of nanoparticle-based materials comes with its characteristics and challenges. Defect size, structure, and density need to be properly defined at this scale before they can be statistically represented.

The measurement problem is complicated by the fact that at the nanoscale, the very act of measurement itself can greatly perturb the system. At this scale, background noise is a significant issue; environmental impacts such as vibrations and small changes in temperature can cause significant variability in a measurement. Current measurements need to be adapted, and new measurements need to be defined and developed in order to measure the composition, structure, surface/interface of nanoparticles and nanoparticle-based materials.

Efforts need to be directed toward the development of a collaborative framework/architecture that enables the integration of quantitative models and experimental data. The predictive modeling framework can enable experimentalists and theoreticians to work in parallel and streamline the creation of metrology and standards. Computer modeling and simulation present great promise in tracing species interaction throughout the life cycle of a process. Computationally efficient algorithms for nanoparticles should be developed that predict the nucleation during synthesis to ultimate application (in particle or bulk form) as a function of process variables/metrics.

There are two potential toxicity issues to be addressed for this new group of materials: the impact on the environment and on humans. For the first, the deposition and migration of nanoparticles are primary issues. For the second, the interaction of nanoparticles with and the removal from human bodies are important issues to address.

QUESTIONS

1. Devise a defect evaluation criterion for nanoparticles or nanoparticle-based materials and explain how one can measure or trace it.
2. Between practice and the state-of-the-art modeling and simulation for nanoparticles and nanoparticle-based materials, what approaches and collaborative efforts can be taken for practitioners/experimentalists and modelers to narrow/close the gap?
3. List three nanoparticle-based products and trace the potential paths that each of them can be released into the environment.
4. What potential health risks can nanoparticle pose? How can nanoparticles enter a human body and what is the fate of the nanoparticles after that?

REFERENCES

1. Zhu XP, Yukawa T, Hirai M, Suzuki T, Suematsu H, Jiang W, Yatsui K. Defect-related photoluminescence of silicon nanoparticles produced by pulsed ion-beam ablation in vacuum. *Appl Surf Sci* 2005;242:256–260.
2. Postek MT, Lyons KW, Ouimette MS, Holdridge GM. Executive Summary. Proceedings of Instrumentation, Metrology, and Standards for Nanomanufacturing Conference; 2006 October 17–19; Gaithersburg, Maryland.
3. Cao G. *Nanostructures & Nanomaterials: Synthesis, Properties, and Applications*. London: Imperial College Press; 2004.
4. Sohn HY, Perez-Fontes S, Choi JW. Computational fluid dynamic modeling of a chemical vapor synthesis process for aluminum nanopowder as a hydrogen storage precursor. *Chem Eng J* 2010;156:215–225.
5. Ryu T, Olivas-Martinez M, Sohn HY, Fang ZZ, Ring TA. Computational fluid dynamics simulation of chemical vapor synthesis of WC nano powder from tungsten hexachloride. *Chem Eng Sci* 2010;65:1773–1780.
6. Mantzaris NV. Liquid-phase synthesis of nanoparticles: particle size distribution dynamics and control. *Chem Eng Sci* 2005;60:4749–4770.
7. Titov AV, Kral P. Modeling the self-assembly of colloidal nanorod superlattices. *Nano Lett* 2008;8:3605–3612.
8. Pan H, Ko SH, Grigoropoulos CP. The solid-state neck growth mechanisms in low-energy laser sintering of gold nanoparticles: a molecular dynamics simulation study. *J Heat Transfer* 2008;130:092404 7pp.
9. Zachariah MR, Carrier MJ. Molecular dynamics computation of gas-phase nanoparticle sintering: a comparison with phenomenological models. *J Aerosol Sci* 1999;30:1139–1151.
10. Pan J. Modelling sintering at different length scales. *Int Mater Rev* 2003;48:69–85.
11. Luoma SN. *Silver Nanotechnologies and the Environment: Old Problems or New Challenges?* Project on Emerging Nanotechnologies (PEN), Woodrow Wilson International Center for Scholars, 2008.
12. Limbach LK, Wick P, Manser P, Grass RN, Bruinink A, Stark WJ. Exposure of engineered nanoparticles to human length epithelial cells: influence of chemical composition and catalytic activity on oxidative stress. *Environ Sci Technol* 2007;41:4158–4163.

13. Mueller NC, Nowack B. Exposure modeling of engineered nanoparticles in the environment. *Environ Sci Technol* 2008;42:4447–4453.
14. Ji JH, Jung JH, Kim SS, Yoon J-U, Park JD, Choi BS, Chung YH, Kwon IH, Jeong J, Han BS, Shin JH, Sung JH, Song KS, Yu IJ. Twenty-eight-day inhalation toxicity study of silver nanoparticles in Sprague-Dawley rats. *Inhalation Toxicol* 2007;19:857–871.
15. Soto K, Garza KM, Murr LE. Cytotoxic effects of aggregated nanomaterials. *Acta Biomater* 2007;3:351–8.
16. Asgharian B, Price OT. Deposition of ultrafine (NANO) particles in the human lung. *Inhalation Toxicol* 2007;19:1045–1054.
17. Park S, Lee YK, Jung M, Kim KH, Chung N, Ahn EK, Lim Y, Lee KH. Cellular toxicity of various inhalable metal nanoparticles on human alveolar epithelial cells. *Inhalation Toxicol* 2007;19:59–65.
18. Muir DCF, Cena K. Generations of ultrafine silver aerosols for inhalation studies. *Aerosol Sci Technol* 1987;6:303–306.
19. Schmid O, Moller W, Semmler-Behnke M, Ferron GA, Karg E, Lipka J, Schulz H, Kreyling WG, Stoeger T. Dosimetry and toxicology of inhaled ultrafine particles. *Biomarkers* 2009;14:67–73.
20. Marr LC, Dzepina K, Jimenez JL, Reisen F, Bethel HL, Arey J, Gaffney JS, Marley NA, Molina LT, Molina MJ. Sources and transformations of particle-bound polycyclic aromatic hydrocarbons in Mexico City. *Atmos Chem Phys* 2006;6:1733–1745.
21. Felcher EM. *The Consumer Product Safety Commission and Nanotechnology*. Project on Emerging Nanotechnologies (PEN), Woodrow Wilson International Center for Scholars, 2008.
22. Ayres JG, Borm P, Cassee FR, Castranova V, Donaldson K, Ghio A, Harrison RM, Hider R, Kelly F, Kooter IM, Marano F, Maynard RL, Mudway I, Nel A, Sioutas C, Smith S, Baeza-Squiban A, Cho A, Duggan S, Froines J. Evaluating the toxicity of airborne particulate matter and nanoparticles by measuring oxidative stress potential-A workshop report and consensus statement. *Inhalation Toxicol* 2008;20:75–99.
23. Park S, Lee YK, Jung M, Kim KH, Chung N, Ahn E-K, Lim Y, Lee K-H. Cellular toxicity of various inhalable metal nanoparticles on human alveolar epithelial cells. *Inhalation Toxicol* 2007;19:59–65.
24. Teeguarden JG, Hinderliter PM, Orr G, Thrall BD, Pounds JG. Particokinetics in vitro: Dosimetry considerations for in vitro nanoparticle toxicity assessments. *Toxicol Sci* 2007;95:300–312.
25. Oberdorster G, Oberdorster E, Oberdorster J. Concepts of nanoparticle dose metric and response metric. *Environ Health Perspect* 2007;115:A290.
26. Li L, Chen D-R, Qi C, Kulkarni PS. A miniature disk electrostatic aerosol classifier (mini-diskEAC) for personal nanoparticle sizers. *J Aerosol Sci* 2009;40:982–992.

EXPLANATION OF UNFAMILIAR NOMENCLATURES

Acoustic cavitation: The formation, growth and implosive collapse of bubbles in liquids irradiated with high-intensity ultrasound.

Adiabatic expansion: Increase in volume without heat flow, in or out.

Agglomeration: The state or process of particles gathering into a larger “lump” that is bonded by van der Waals force, capillary force, or even solid bonds.

Airy disk: The bright region in the center of the diffraction pattern resulting from a uniformly illuminated circular aperture.

Aliphatic tail: The end group of a compound that is composed of carbon and hydrogen arranged in straight or branched chains, and not containing aromatic rings.

Aliquot: A portion of a total amount of a solution.

Ammonolysis: Any reaction with ammonia, analogous to hydrolysis, in which a bond is broken and an NH₂ group is appended to one fragment.

Amoeba: A kind of large cell that has a single large tubular pseudopod at the anterior end and several secondary ones branching to the sides.

Amphiphilic surfactant: Surfactants are surface-active molecules that have the unique properties of getting adsorbed at various interfaces (e.g., air–water, oil–water, etc.) and altering the properties of the interface. Amphiphilic surfactants possess a special molecular structure—contain both a water loving polar part (hydrophilic) and a water hating nonpolar part (hydrophobic).

- Antibody*: A large Y-shaped protein used by the immune system to identify and neutralize foreign objects such as bacteria and viruses.
- Aprotic solvent*: A solvent that is not capable of hydrogen bonding. A notable example is acetone that has an oxygen and hydrogen but not an O–H bond in its structure (the oxygen is only bonded to the carbon) and is therefore incapable of hydrogen bonding and aprotic. Other common examples are ethers, dimethylformamide, dimethylsulfoxide, and acetonitrile.
- Au₅₅*: A cuboctahedral structure consisting of one central gold atom, an inner shell of 12 gold atoms, and an outer one of 42 gold atoms.
- Azeotropic mixture*: A solution of two or more liquids, the composition of which does not change upon distillation, also known as azeotrope.
- Azimuthal angle*: The angle between the line connecting the original and the point of interest and the reference line projected perpendicularly on the substrate.
- Biota*: Total collection of organisms of a geographic region or a time period, from local geographic scales and instantaneous temporal scales all the way up to the whole planet and whole timescale spatiotemporal scales.
- Blazed grating*: A special type of diffraction grating. Blazed gratings produce maximum efficiency at a specified wavelength; that is, a diffraction grating that is blazed at 250 nm will operate most efficiently when light with a wavelength of 250 nm passes through the grating. Like standard diffraction gratings, blazed gratings diffract incoming light using a series of grooves. However, in blazed gratings the grooves have been manufactured such that they form right angles with a specified blaze angle, which is the angular distance from the surface normal of the diffraction plate. The magnitude of the blaze angle determines the wavelength at which the grating will be most efficient.
- Bragg angle*: In Bragg's law, the angle θ between the wave vector of the incident plane wave and the lattice planes.
- Bragg diffraction*: At certain specific wavelengths and incident angles, the incident waves produce intense peaks of reflected radiation.
- Bragg's law*: Refers to the simple equation, $n\lambda = 2d \sin \theta$, derived by the English physicists Sir W. H. Bragg and his son Sir W. L. Bragg in 1913 to explain why the cleavage faces of crystals appear to reflect X-ray beams at certain angles of incidence. It describes the condition for a plane wave to be diffracted from a family of lattice planes.
- Brownian motion*: Random drifting of particles suspended in a fluid (a liquid or a gas) or the mathematical model used to describe such random movements.
- Capsid*: The protein coat surrounding the nucleic acid of a virus.
- Centrifugation*: A process that involves the use of a centrifugal force for the sedimentation of mixtures.
- Chelating unit*: A chemical compound in the form of a ring that contains a metal ion attached by coordinate bonds to at least two nonmetal ions.
- Coercivity*: Coercive field or coercive force of a ferromagnetic material, the intensity of the applied magnetic field required to reduce the magnetization

of that material to zero after the magnetization of the sample has been driven to saturation. Measures the resistance of a ferromagnetic material to becoming demagnetized. Usually measured in oersted or ampere/meter units.

Coordination chemistry: The study of compounds formed between metal ions and other neutral or negatively charged molecules such as $[\text{Co}(\text{NH}_2\text{CH}_2\text{CH}_2\text{NH}_2)_2\text{ClNH}_3]^{2+}\text{Cl}_2^{2-}$. In this formulation, $\text{Co}(\text{NH}_2\text{CH}_2\text{CH}_2\text{NH}_2)_2\text{ClNH}_3]^{2+}$ is known as a metal complex, which is a charged species consisting of metal ion bonded to one or more groups of molecules. The bonded molecules are called ligand.

Coulombic force: The force exerted by stationary objects bearing electric charge on other stationary objects bearing electric charge. If the charges are of the same sign, then the force is repulsive; if they are of opposite signs, the force is attractive. The strength of the force is described by Coulomb's law.

Curie temperature: The critical temperature beyond which a previously ferromagnetic material becomes paramagnetic.

Debye temperature: The temperature of a crystal's highest normal mode of vibration, that is, the highest temperature that can be achieved due to a single normal vibration. The Debye temperature is given by $\theta_D = \frac{h\nu_m}{k}$, where h is Planck's constant, k is Boltzmann's constant, and ν_m is the Debye frequency.

Denaturation: A process in which proteins or nucleic acids lose the tertiary structure and secondary structure that are present in their native state by application of some external stress or compound such as a strong acid or base, a concentrated inorganic salt, an organic solvent (e.g., alcohol or chloroform), or heat. If proteins in a living cell are denatured, it results in disruption of cell activity and possibly cell death. Denatured proteins can exhibit a wide range of characteristics, from loss of solubility to communal aggregation.

Dielectric constant: The ratio of the permittivity of a substance to the permittivity of free space. It is an expression of the extent to which a material concentrates electric flux, and is the electrical equivalent of relative magnetic permeability.

Electrodynamic effect: The effect of electric charge and electric and magnetic fields, along with the forces and motions those fields induce.

Electromigration: Migration (as of ions or colloidal particles) in an electric field.

Electron mean free path: Average distance covered by a moving electron between successive impacts (collisions), which modify its direction or energy or other electron properties.

Electron scattering: The process whereby an electron is deflected from its original trajectory.

Electron wave function: A probability amplitude in quantum mechanics describing the quantum state of an electron and how it behaves. Typically, its values are complex numbers and, for a single electron, it is a function of space and time.

Electronic structure: Arrangement of electrons of an atom, a molecule, or other physical structure. It concerns the way electrons can be distributed in the orbitals of the given system (atomic or molecular for instance).

Electrophoresis: Motion of dispersed particles relative to a fluid under the influence of a spatially uniform electric field.

Excimer laser: A form of ultraviolet laser that is commonly used in the production of microelectronic devices, eye surgery, and micromachining.

Excluded-volume force: Excluded-volume is the volume that is inaccessible to molecular motion or other molecules in a system as a result of the presence of the first molecule. The interaction (force) arising from this effect is called excluded-volume force.

Femtosecond laser: An electromagnetic pulse whose time duration is in the order of a femtosecond (10^{-15} second).

Ferromagnetic: Pertaining to a substance, such as iron that below a certain temperature, can possess magnetization in the absence of an external magnetic field; pertaining to a substance in which the magnetic moments of the atoms are aligned.

Ferritin: A ubiquitous intracellular protein that stores iron and releases it in a controlled fashion.

Ferroelectricity: Of or relating to a crystalline dielectric that can be given a permanent electric polarization by application of an electric field.

Field emission: Emission of electrons induced by an electrostatic field.

Fluorescence quantum yield: The ratio of the number of photons emitted to the number of photons absorbed.

Förster resonant energy transfer: Nonradiative excitation transfer between two molecular entities separated by distances considerably exceeding the sum of their van der Waals radii. It describes the transfer in terms of the interaction between the transition (dipole) moments of the entities in the very weak dipole–dipole coupling limit.

Galvanic displacement: The process of spontaneous reduction of the ions of a metal by another metal above it in the electromotive series. For example, a piece of iron immersed in a copper sulfate solution will be immediately covered by a thin film of copper.

Gene transfection: The process by which a bacterial cell is infected with purified DNA or RNA isolated from a virus after a specific pretreatment.

Grazing angle: When dealing with a beam that is nearly parallel to a surface, the angle between the beam and the surface.

Grazing incidence SAXS: A scattering technique used to study nanostructured surfaces and thin films. It combines the accessible length scales of small-angle X-ray scattering and the surface sensitivity of grazing incidence diffraction.

Hard-sphere force: In colloidal chemistry, the interaction force between particles when they are idealized as hard spheres.

High-angle annular dark field scanning transmission electron image: Scanning transmission electron image is the reversed optical system of conventional transmission electron image; the electron path in bright field scanning transmission electron image is the same as when the ray path direction is reversed

in conventional transmission electron image. High-angle annular dark field scanning transmission electron microscope is based on imaging incoherent scattering, and the contrast of the image is not reversed by defocusing above and below the point of “just focus.”

Hydrodynamic size: The effective radius of a particle in a solution measured by assuming that it is a body moving through the solution and resisted by the solution's viscosity. If the solvent is water, the hydrodynamic radius includes all the water molecules attracted to the particles. As a result, the measured particle size may be larger than the dry particle size (a hypothetical hard sphere that diffuses with the same speed as the particle under examination, apparent size of the dynamic hydrated/solvated particle).

In-plane coherence length parameter: A characteristic length in superconductor, a length scale on which superconducting order parameter changes considerably.

Inverse opal: Inverse replicas of opals. Instead of consisting of a regular arrangement of uniform spherical particles (as in opals), inverse opals consist of a regular arrangement of spherical void spaces surrounded by solid walls.

Langmuir monolayer adsorption: An adsorption model developed by Irving Langmuir in 1916. It is a semiempirical isotherm derived from a proposed kinetic mechanism. It is based on four assumptions:

1. The surface of the adsorbent is uniform, that is, all the adsorption sites are equivalent.
2. Adsorbed molecules do not interact.
3. All adsorption occurs through the same mechanism.
4. At the maximum adsorption, only a monolayer is formed: molecules of adsorbate do not deposit on other, already adsorbed, molecules of adsorbate, only on the free surface of the adsorbent.

Langmuir–Blodgett technique: A Langmuir–Blodgett film contains one or more monolayers of an organic material, deposited from the surface of a liquid onto a solid by immersing (or emersing) the solid substrate into (or from) the liquid. A monolayer is adsorbed homogeneously with each immersion or emersion step, thus films with very accurate thickness can be formed. This thickness is accurate because the thickness of each monolayer is known and can therefore be added to find the total thickness of a Langmuir–Blodgett film. The monolayers are assembled vertically and usually composed of amphiphilic molecules with a hydrophilic head and a hydrophobic tail (e.g., fatty acids).

Langmuir–Schaefer technique: Similar to Langmuir–Blodgett technique (in the case of vertical deposition) but applies to the case of horizontal deposition.

Lattice fringe: An electron microscope image with lattice information such as phase, lattice parameters, crystal shape, and/or the relationship between adjacent crystals.

Light-emitting diode: A semiconductor device that emits visible light when an electric current passes through it. The light is mostly monochromatic, occurring at a single wavelength. The output from a light-emitting diode can range from red (at a wavelength of approximately 700 nm) to blue-violet (about 400 nm). Some light-emitting diodes emit infrared energy (830 nm or longer); such a device is known as an infrared-emitting diode.

Lyogel: A gel containing much liquid, opposite of xerogel.

Lyosphere: Charged particle with its surrounding double layer of counter ions.

Magnetization: The vector field that expresses the density of permanent or induced magnetic dipole moments in a magnetic material.

Mean free path length: Average distance covered by a moving species between successive impacts (collisions) that modify its direction or energy or other properties.

Mercury porosimetry: An analytical technique used to determine various quantifiable aspects of a material's porous nature, such as pore diameter, total pore volume, surface area, and bulk and absolute densities. The technique involves the intrusion of a nonwetting liquid (often mercury) at high pressure into a material through the use of a porosimeter. The pore size can be determined based on the external pressure needed to force the liquid into a pore against the opposing force of the liquid's surface tension.

Microwave absorption cross section: The actual area that absorbs the microwaves from the source, it governs how much of the incident power is captured and sent back.

Modal particle size: The size that occurs most frequently in the particle size frequency distribution.

Morphosynthesis: Chemical construction and patterning of inorganic materials with unusual and complex architectures at different length scales.

Nucleophilic substitution: The reaction of an electron pair donor (the nucleophile) with an electron pair acceptor (the electrophile). An sp^3 -hybridized electrophile must have a leaving group in order for the reaction to take place.

Oriental order: Measure of the tendency of molecules to align along a direction on a long-range basis.

Paramagnetic: A form of magnetism whereby the paramagnetic material is only attracted when in the presence of an externally applied magnetic field.

Perpendicular coherence length parameter: A characteristic length in superconductor, a length scale on which superconducting order parameter changes considerably.

Photoluminescence: A process in which a substance absorbs photons (electromagnetic radiation) and then re-radiates photons. From quantum mechanics point of view, this can be described as an excitation to a higher energy state and then a return to a lower energy state accompanied by the emission of a photon.

Photoresist: A light-sensitive polymeric material. It may become soluble or insoluble after exposure to light.

Plasmon band blue shift: Plasmon band decrease in wavelength (increase in frequency).

Plasmon excitation: An oscillation of free electron density with respect to the fixed positive ions in a metal.

Plasmon resonance: A biosensing technique in which biomolecules capable of binding to specific analytes or ligands are first immobilized on one side of a metallic film. Light is then focused on the opposite side of the film to excite the surface plasmons, that is, the oscillations of free electrons propagating along the film's surface. The refractive index of light reflecting off this surface is measured. When the immobilized biomolecules are bound by their ligands, an alteration in surface plasmons on the opposite side of the film is created which is directly proportional to the change in bound, or adsorbed, mass. Binding is measured by changes in the refractive index. The technique is used to study biomolecular interactions, such as antigen–antibody binding.

Plasmonic lithography: Using plasmon as a source to pattern different features or arrangements.

Plasmonics: Study of plasmon. A plasmon is a quantum of plasma oscillation, a quasiparticle resulting from the quantization of plasma oscillations just as photons and phonons are quantizations of light and mechanical vibrations, respectively (though the photon is an elementary particle, not a quasiparticle).

Polyol method: The synthesis of metal-containing compounds in poly(ethylene glycol)s.

Power-law creep: Creep is the tendency of a solid material to slowly move or deform permanently under the influence of stresses. A model is discussed that gives rise to the widely used power law for creep under constant load, namely, well-known Andrade creep law $dl/dt = \Omega t^{-n}$ where l is the strain, t the time, Ω is a factor dependent on temperature and load, and n is an exponent that may have any value between 0 and 1.

Pseudoplasticity: Also called shear thinning, viscosity reduction of non-Newtonian fluids (e.g., polymers and their solutions, most slurries, and suspensions) that undergo viscosity reductions under conditions of shear stress (i.e., viscometric flow).

Pyrometer: Noncontacting device that intercepts and measures thermal radiation, a process known as pyrometry. This device can be used to determine the temperature of an object's surface.

Quantum confinement: For an object in a conservative field of force, a region in which the object has a lower potential energy than in all the surrounding regions.

Quantum size effect: Unusual properties of extremely small crystals that arise from confinement of electrons to small regions of space in one, two, or three dimensions.

Quantum tunneling: Quantum mechanical phenomenon where an electron tunnels through a barrier that it classically could not surmount.

Redox reaction: Reduction–oxidation reactions, describing all chemical reactions in which atoms have their oxidation state changed.

Rietveld refinement: A technique in the characterization of crystalline materials. Neutron and X-ray diffraction of powder samples results in a pattern characterized by reflections (peaks in intensity) at certain positions. The process uses height, width, and position of these reflections to determine many aspects of the materials structure.

Silk fibroin: A type of protein created by silkworms in the production of silk.

Small-angle neutron scattering: A technique used for investigations of structure of various substances, with spatial sensitivity of about 1–1000 nm. A beam of neutrons is directed at a sample, which can be an aqueous solution, a solid, a powder, or a crystal. The neutrons are elastically scattered by changes of refractive index on a nanometer scale inside the sample through the interaction with the nuclei of the atoms present in the sample. Because the nuclei of all atoms are compact and of comparable size, neutrons are capable of interacting strongly with all atoms.

Solute drag mechanism: A mechanism in sintering that explains the hindrance effect from a solute in slowing or stopping the movement of grain boundaries.

Spallation source: A source in which fragments of material (spall) are ejected from a body due to impact or stress.

Spin polarization: The degree to which spin, that is, the intrinsic angular momentum of elementary particles, is aligned with a given direction. This property may pertain to the spin, hence to the magnetic moment, of conduction electrons in ferromagnetic metals, such as iron, giving rise to spin-polarized currents.

Stern and Helmholtz double layer: A structure that appears on the surface of an object when it is placed into a liquid. The first layer, the surface charge (either positive or negative), comprises ions adsorbed directly onto the object due to a host of chemical interactions. The second layer is composed of ions attracted to the surface charge via the Coulomb force, electrically screening the first layer. This second layer is loosely associated with the object, because it is made of free ions that move in the fluid under the influence of electric attraction and thermal motion rather than being firmly anchored. It is thus called the diffuse layer.

Supercritical drying: A process by which the liquid in a substance is transformed into gas in the absence of surface tension and capillary stress and is the most common process to transform gels into aerogels. It is performed to replace the liquid in a material with a gas without destroying the delicate nanostructured pore network.

Superlattice: A periodic structure of layers of two (or more) materials.

- Superparamagnetism:* A phenomenon by which magnetic materials may exhibit a behavior similar to paramagnetism even when at temperatures below the Curie or the Néel temperature. This is a small length-scale phenomenon, where the energy required to change the direction of the magnetic moment of a particle is comparable to the ambient thermal energy.
- Superplasticity:* The unusual ability of some materials (such as nanomaterials) to elongate uniformly by thousands of percent at elevated temperatures, much like hot polymers or glasses.
- Surface plasmon effect:* Coherent electron oscillations that exist at the interface between any two materials where the real part of the dielectric function changes sign across the interface (e.g., a metal-dielectric interface, such as a metal sheet in air).
- Synchrotron X-ray source:* X-ray source originated from a synchrotron electromagnetic radiation source. A synchrotron is a particular type of cyclic particle accelerator in which the magnetic field (to turn the particles so they circulate) and the electric field (to accelerate the particles) are carefully synchronized with the traveling particle beam.
- Thermal diffusion length:* The average distance traveled by a particle, such as a minority carrier in a semiconductor or a thermal neutron in a nuclear reactor, from the point at which it is formed to the point at which it is absorbed.
- Thermal scattering:* Scattering of electrons, neutrons, or X-rays passing through a solid due to the thermal motion of atoms in the crystal lattice.
- Thermionic emission:* Heat-induced flow of charge carriers from a surface or over a potential-energy barrier.
- Thermophoresis:* A phenomenon observed when a mixture of two or more types of mobile particles are subjected to the force of a temperature gradient and different types of particles respond to it differently.
- Translational order:* A condition when molecules have some arrangement in space. Crystals have three degrees of translational order (each molecule is fixed in space with an x, y, and z coordinate) and liquids have no translational order.
- Translocation:* Capture, transport, and release, or introduction/reintroduction of plants, animals, or habitat from one location to another.
- UV laser:* Lasers (or other laser-based light sources) generating ultraviolet light.
- Wave-particle duality:* A theory explaining that all particles exhibit both wave and particle properties. As a central concept of quantum mechanics, this duality addresses the inability of classical concepts like “particle” and “wave” to fully describe the behavior of quantum-scale objects.
- X-ray absorption spectroscopy:* A widely used technique for determining the local geometric and/or electronic structure of matter. The experiment is usually performed at synchrotron radiation sources, which provide intense and tunable X-ray beams. Samples can be in fluids or as condensed matter.

YAG laser: Nd:YAG (neodymium-doped yttrium aluminum garnet, $\text{Nd:Y}_3\text{Al}_5\text{O}_{12}$) is a crystal that is used as a lasing medium for solid-state lasers. Generally, the crystalline host is doped with around 1% neodymium by atomic percent. Nd:YAG lasers are optically pumped using a flashtube or laser diodes. These are one of the most common types of laser, and are used for many different applications. Nd:YAG lasers typically emit light with a wavelength of 1064 nm, in the infrared.

APPENDIX 2

PREFIXES IN THE INTERNATIONAL SYSTEM OF UNITS

| Prefix | Symbol | 10^n | Decimal | Short scale | Long scale |
|--------|--------|------------|----------------------------|---------------|---------------|
| yotta | Y | 10^{24} | 1000000000000000000000000 | Septillion | Quadrillion |
| zetta | Z | 10^{21} | 100000000000000000000000 | Sextillion | Trilliard |
| exa | E | 10^{18} | 100000000000000000000000 | Quintillion | Trillion |
| peta | P | 10^{15} | 100000000000000000000000 | Quadrillion | Billiard |
| tera | T | 10^{12} | 100000000000000000000000 | Trillion | Billion |
| giga | G | 10^9 | 1000000000 | Billion | Milliard |
| mega | M | 10^6 | 1000000 | Million | |
| kilo | k | 10^3 | 1000 | Thousand | |
| hecto | h | 10^2 | 100 | Hundred | |
| deca | da | 10^1 | 10 | Ten | |
| | | 10^0 | 1 | One | |
| deci | d | 10^{-1} | 0.1 | Tenth | |
| centi | c | 10^{-2} | 0.01 | Hundredth | |
| milli | m | 10^{-3} | 0.001 | Thousandth | |
| micro | μ | 10^{-6} | 0.000001 | Millionth | |
| nano | n | 10^{-9} | 0.000000001 | Billionth | Milliardth |
| pico | p | 10^{-12} | 0.000000000001 | Trillionth | Billionth |
| femto | f | 10^{-15} | 0.000000000000001 | Quadrillionth | Billiardth |
| atto | a | 10^{-18} | 0.000000000000000001 | Quintillionth | Trillionth |
| zepto | z | 10^{-21} | 0.000000000000000000001 | Sextillionth | Trilliardth |
| yocto | y | 10^{-24} | 0.000000000000000000000001 | Septillionth | Quadrillionth |

INDEX

Note: Page numbers with italicized *f*'s and *t*'s refer to figures and tables, respectively.

- absolute temperature, 6, 27, 136, 331, 340
- acoustic cavitation, 100, 415
- activation energy, 27, 338, 364-365, 376, 383
- adiabatic expansion, 43, 44, 415
- agglomeration, 49-51, 59-61, 107-109, 130-131, 286-287, 334-335
- aggregate, 41, 51, 103, 157, 220, 290
- aggregation, 31, 61, 110, 232, 408
- airy disk, 197, 415
- aliphatic tail, 82, 415
- aliquot, 157, 415
- ammonolysis, 75, 415
- amoeba, 408, 415
- amorphization, 105, 126
- amphiphilic surfactant, 81, 415
- angle-resolved nanosphere lithography, 205, 206*f*, 257
- antibody, 243, 416, 421
- apparent activation energy, 338
- aprotic solvent, 64, 416
- arrested precipitation, 54, 169
- atomic absorption, 168-169
- atomic emission, 168
- atomic force microscopy, 129, 133, 135*f*, 152, 398, 400
- atomic mobility, 338
- atomic volume, 6, 331, 340
- atomization, 50
- Au55, 244, 261, 416
- auger electron, 129*t*, 161, 162*f*, 170, 186*t*, 209
 - spectroscopy, 129*t*, 161, 186*t*, 189, 192, 209
- Avogadro's number, 147
- azeotropic mixture, 292, 416
- azimuthal angle, 205, 416
- ball milling, 103-105, 107, 156*f*, 344-345, 369
- band gap, 7, 10, 245, 306
- Beer's Law, 178

- BET, 129*t*, 146-148, 150, 189
 binary nanoparticle superlattice, 234
 bioactive material, 20, 313, 315*f*, 318*t*, 328
 bio-derived processing, 20, 264, 318*t*
 biomimetic material, 20, 313-314, 318*t*
 biota, 408, 416
 Boltzmann constant, 6. *See also*
 Boltzmann's constant
 Boltzmann's constant, 27, 136, 284, 331,
 340, 417
 bottom-up, 20, 195, 217-218, 236, 256
 Bragg angle, 138, 157, 160, 416
 Bragg diffraction, 138, 416
 Bragg's law, 138, 160, 186*t*, 416
 Brownian motion, 17, 39, 136, 229, 416
 bulk composition, 129*t*, 161, 168, 186-187*t*,
 189
 bulk structure, 129*t*, 150-151, 155

 calcination, 54, 65, 100, 245-246, 249, 252,
 280-281
 calibration, 399
 calorimetry, 129*t*, 145
 cantilever, 134-135, 153
 capillary force, 20, 65, 134, 217, 230-232,
 256
 capping agent, 66, 77, 86, 205-206, 244
 capsid, 243, 416
 casting, 20, 246, 263-264, 282, 288-300,
 304-306, 316-318, 349
 catalysis, 8, 91, 110, 146, 248
 centrifugal force, 290, 416
 centrifugation, 54, 243, 245, 416
 chelating unit, 84, 416
 chemical activity, 7, 203, 411
 chemical potential, 26, 296, 330, 332, 341
 chemical vapor deposition, 42, 117, 214
 chemical vapor synthesis, 10, 39, 41-43, 403
 citrate reduction method, 59
 coagulation, 17, 32, 39, 108, 300
 coalescence, 32, 34, 36-37, 39, 41, 70, 73
 coarsening, 330, 333, 339, 363-364, 368,
 378, 383
 coercivity, 54, 60, 103, 126, 251, 272, 416
 coextrusion, 278
 cold isostatic pressing, 266-268, 317*t*, 337,
 344, 369-370
 colloidal suspension, 20, 132, 251-252, 264,
 282, 288, 290

 combined stage sintering, 364, 367-368
 combustion-driven compaction, 268,
 270-272, 321
 computer-aided design, 304
 constant current mode, 134
 constant height, 134
 contact angle, 28, 149
 controlled-rate sintering, 364, 367
 coordination chemistry, 175, 417
 coordination number, 65, 265, 335, 339,
 345, 360, 365
 co-precipitation, 53-54, 60, 62, 67, 71
 Coulombic force, 136, 417
 covalent bonding, 20, 218, 225-226, 256
 creep, 9, 330, 368-369, 373, 375, 380, 383,
 421
 critical energy barrier, 27
 cryochemical synthesis, 53, 70-72, 112*t*,
 121
 crystallinity, 42-43, 54-56, 65, 68, 73,
 98-100, 111
 Curie temperature, 10, 54, 417

 D₉₀, 312
 De Broglie relation, 151
 Debye length, 283
 Debye temperature, 8, 417
 defect scattering, 10
 denaturation, 313, 417
 dense nanoparticle material sintering, 20,
 329-330
 densification, 269, 271, 330-332, 334-341,
 356, 359-369, 371-378, 380-384
 rate, 332, 360, 364, 368, 373, 377
 depletion flocculation, 286, 323
 depth profiling, 161, 164-165, 186*t*
 dielectric constant, 95, 223, 263, 283-284,
 417
 dielectric loss factor, 353-354
 diffusion coefficient, 29, 41, 136, 331-332,
 369, 373, 377, 404
 diffusion flux, 331, 376
 diffusivity, 339
 digital processing, 20, 264, 304, 313, 316,
 318*t*, 319
 digital writing, 20
 dipole moment, 20, 217, 218*t*, 222-223,
 225, 230, 256
 direct patterning, 311

- direct writing, 304, 307, 309*f*; 316, 327
 directed assembly, 195, 221, 229-230, 252, 256, 314
 dislocation, 9-10
 dispersant, 17, 100, 184, 220, 285-287, 291-292, 302, 342
 DLVO theory, 282-283, 300, 319
 doctor blade casting, 291, 294*f*, 324
 dry compaction, 264-265, 267, 272, 316
 dry forming, 20, 264, 269, 282, 316, 319
 dry processing, 292, 317*t*
 drying-mediated assembly, 221
 dynamic compaction, 20, 264, 268, 270-271, 317*t*
 dynamic grain growth, 339
 dynamic laser light scattering, 129*t*, 130

 elastic scattering, 145, 155, 162, 181
 electric field-assisted sintering, 384, 392
 electrical conduction, 10
 electrical conductivity, 7, 10, 387, 396
 electrical double layer, 283-284, 319
 electrical sintering, 356-358, 389
 electrodynamic effect, 403, 417
 electroless coating, 83
 electroless deposition, 83, 123
 electromagnetic spectrum, 144, 178
 electromigration, 376-377, 417
 electron beam lithography, 20, 206-208, 209*f*, 211, 212*f*, 256
 electron diffraction, 129*t*, 151, 156-160, 186*t*, 234, 399
 pattern, 61-62, 151, 157, 158*f*, 159*f*, 160, 235*f*
 electron energy-loss spectroscopy, 129*t*, 161
 electron mean free path, 3, 417
 electron scattering, 10, 417
 electron spectroscopy, 129*t*, 161, 174, 186*t*, 192, 209
 electron wave function, 7, 417
 electronegativity, 225
 electronic structure, 7, 10, 144, 175-176, 187*t*, 417, 423
 electrophoresis, 300-301, 302*f*, 418
 electrophoretic deposition, 20, 264, 282, 300-304, 316, 318*t*
 electrospinning, 64, 120, 279-282, 322
 electrospray, 75, 211

 electrostatic interaction, 177, 217, 223, 225, 252, 283-284
 electrostatic lithography patterning, 211
 electrostatic stabilization, 282-283, 285
 electrosteric stabilization, 282-283
 energetics, 20, 128, 129*t*, 144-146, 184, 191
 energy dispersive spectroscopy, 80, 81*f*, 94*f*, 171*f*, 187*t*, 276*f*
 energy dispersive X-ray spectroscopy, 129*t*, 161
 epitaxy, 203, 256
 equilibrium pressure, 6
 evaporation-condensation, 330, 332-333, 337, 364, 381, 385
 evaporation-induced assembly, 252
 excimer laser, 44, 48, 197, 418
 excluded volume, 136, 286, 418
 excluded-volume force, 418
 explosive compaction, 268, 270-271, 321, 390
 extrusion, 20, 264, 272, 277-279, 282, 307, 317*t*

 failure strain, 9
 feedstock, 50, 273-274, 321
 femtosecond laser, 44, 48-49, 118, 310-311, 327, 418
 ferrimagnetic, 54
 ferritin, 87-88, 124, 418
 ferroelectricity, 160, 418
 ferromagnetic, 11, 38, 54, 59, 103, 416-418, 422
 Fick's first law, 29
 field emission, 130, 206*f*, 418
 field-directed assembly, 229
 flame aerosol synthesis, 49-51
 flame atomic absorption spectrometry, 169
 flexural strength, 9, 357
 flocculation, 4, 220, 246*f*; 285-286, 323
 flowability, 274, 286
 fluorescence quantum yield, 82, 418
 focusing in size, 29
 Fourier transform infrared spectroscopy, 129*t*, 161, 176, 187*t*, 189, 228
 fracture toughness, 9, 357, 385
 free sintering, 20, 330, 337, 359, 367-368, 376, 381, 384
 freeze casting, 20, 282, 293, 295-297, 316, 318*t*

- frictional force, 265-266, 268-269, 272, 336, 369
- functional group, 167-168, 176, 181, 225-226, 238, 251
- galvanic displacement, 200, 418
- gas adsorption, 129*t*, 146-50, 191
isotherm, 150
- gas constant, 6, 33, 149, 331
- gas phase synthesis, 25*f*, 32, 96, 109-110
- gel casting, 20, 282, 293, 295, 297-300, 316, 318*t*
- gelation, 63, 70, 297, 325
- gene transfection, 87, 418
- Gibbs–Thomson equation, 332, 340
- global thermodynamics, 20, 128-129, 144-145, 184
- grain boundary, 330-334, 339-340, 358, 360-365, 377-378, 380, 385
area, 331-332, 360, 365
diffusion, 330-331, 339, 360, 363-365, 377, 380
mobility, 333-334, 358, 360-361, 365
scattering, 10
- grain growth, 329-330, 332-334, 338-341, 344-346, 356-369, 371-378, 380-383
rate, 333-334, 360, 367
- grain sliding, 9, 369
- grain surface mobility, 333
- grazing angle, 213, 214*f*, 418
- grazing incidence SAXS, 141, 418
- Hall–Petch equation, 9
- hard-sphere force, 136, 418
- heat capacity, 17, 145
- heterocoagulation, 64, 79, 245, 246*f*
- heterogeneous nucleation, 24, 26-28, 42, 79, 83, 87, 91, 297
site, 28
- high pressure compaction, 268-269, 320-321, 360, 390
- high-angle annular dark field scanning transmission electron image, 209, 418
- highly blazed grating, 248
- homogeneous nucleation, 19, 26, 34, 79, 85
- hot isostatic pressing, 13, 20, 277, 368, 373-375, 377, 380, 382-384
- hot pressing, 20, 368-369, 371-373, 375-377, 382, 384
- hydrodynamic size, 132, 136, 419
- hydrogen bonding, 15, 20, 218, 225, 227-229, 256, 416
- hydrolysis, 53, 61-66, 75, 79-80, 90-91, 98
- immobilization, 86, 199, 261, 314
- impurity scattering, 10
- inductively coupled plasma, 169
- inelastic scattering, 145, 162, 181
- inert gas condensation, 32-37, 116-117
- initial stage of sintering, 330
- ink-jet printing, 20, 304, 312-313, 316, 318*t*, 328
- in-plane coherence length parameter, 144, 419
- interfacial energy, 6, 332, 334
- intermediate stage of sintering, 330, 364
- inverse opal, 247*f*, 301, 302*f*, 351, 352*f*, 419
- ion beam lithography, 20, 212, 256
- ionic liquid, 66, 68, 70, 78
- isoelectric point, 203, 241, 282, 286
- isothermal holding, 339, 342
- Kelvin equation, 6, 149
- Krieger–Dougherty equation, 286
- Langmuir monolayer adsorption, 146, 419
- Langmuir–Blodgett technique, 23, 124, 220, 419
- Langmuir–Schaefer technique, 220, 258, 419
- laser ablation, 37, 43-49, 92-94, 207
- laser fluence, 46
- laser irradiation, 45, 51-52, 92, 179, 404
- laser photolysis, 93, 125, 179, 193
- laser sintering, 328, 358-359, 384-385, 413
- laser-assisted synthesis, 89, 92, 114*t*, 169
- lattice defect scattering, 10
- lattice fringe, 80, 97, 419
- layer-by-layer assembly, 228, 252
- Lennard–Jones potential, 219
- light-emitting diodes, 17, 420
- liquid phase sintering, 334, 363, 368, 372, 390-391
- low-energy electron diffraction, 129*t*, 151
- luminescence, 97

- lyogel, 314, 420
 lyosphere, 301, 420
- macropore, 148, 246, 249, 349*f*, 350-351, 359
- magnetic field strength, 223
 magnetic susceptibility, 7, 12
 magnetization, 11-12, 416-418, 420
- mask, 16, 196-197, 205
- mass transport, 37, 337, 340, 356
- mean free path length, 32, 420
- mechanical alloying, 103, 105, 106*f*, 126-127
- mechanochemical milling, 104
- mercury porosimetry, 148, 420
- mesopore, 148, 150, 249
- metal salt reduction, 53, 58-60, 111*t*
- micelle synthesis, 31, 81, 89, 91, 114*t*
- microcontact printing, 200*f*, 236, 238
- microextrusion, 277
- micromolding, 273-275, 276*f*, 277, 322
- micropore, 148, 150, 359
- microscopy, 129-135, 152-153, 183-185, 398, 400-401
- microstereolithography, 310, 327
- microwave, 89, 94-98, 114*t*, 351-356, 365-366, 384, 420
 absorption cross section, 95, 420
 radiation, 354
 sintering, 351, 354-356, 384, 387, 389
- microwave-assisted synthesis, 95, 114*t*
- milling, 102-107, 109-110, 214, 338, 344-345, 369, 380
- modal particle size, 36, 420
- modeling, 15, 336, 392-393, 396, 402-403, 405-407, 412-414
- molding, 20, 264, 272-278, 298*f*, 317*t*
- monodispersity, 36, 55, 111*t*, 218, 220-221
- monolayer, 38, 82-85, 146-147, 200, 214, 225, 230-244, 253-256
- monomer, 68, 144, 245, 297, 298*f*, 308-309
- morphosynthesis, 85, 420
- nanoimprint lithography, 215, 236, 238-239, 240*f*
- nanoparticle growth, 25-31, 52, 59, 89-90, 97, 103, 244
- nanoparticle packing, 264, 268, 319, 329, 332, 359-360
- nanosphere lithography, 205, 206*f*
- neutron scattering, 129*t*, 130, 140-141, 143*f*, 149
- nitrogen adsorption, 150
- nucleation rate, 27-28, 33, 65, 91, 371
- nucleophilic substitution, 226, 420
- oligomer, 144, 308-309
- omnidirectional printing, 307, 308*f*, 327
- optical atomic spectroscopy, 129*t*, 161, 168, 170-171
- optical spectroscopy, 129*t*, 144, 190
- orientational order, 230, 420
- Ostwald ripening, 28, 30-31, 56, 59, 234, 336
- oxide melt solution, 129*t*, 145
 calorimetry, 129*t*, 145
- paramagnetic, 54, 417, 420
- partial sintering, 341-342, 344, 359, 384
- particle radius, 6, 29, 136
- particulate gel casting, 297
- patterning, 205-208, 211, 213, 242, 275, 277, 311
- peak broadening, 138, 155, 166*f*
- peptizing agent, 65
- periodicity, 181, 196, 199, 241, 244, 311, 397
- permeability, 18, 288, 417
- perpendicular coherence length parameter, 144, 420
- phase shifting photolithography, 197, 198*f*
- phase transformation, 65, 76, 135, 145, 337, 371, 373
- photo correlation spectroscopy, 135
- photoelectron, 129*t*, 152*f*, 161, 164-166, 187*t*, 209, 255
- photolithography, 20, 197-204, 207, 236, 241-242, 256
- photoluminescence, 55, 144, 395, 413, 420
- photomask, 197, 201, 203, 241
- photonic crystal, 311, 322
- photopolymerization, 307
- photoresist, 197, 199, 203, 207-209, 241, 242*f*, 421
- physical vapor deposition, 37-38, 40
- physical vapor synthesis, 32, 39-40, 115
- Planck constant, 151, 164
- plasma spray forming, 382-383, 393

- plasma-assisted synthesis, 94, 114*t*
 plasmon band blue shift, 13, 421
 plasmon excitation, 7, 12, 421
 plasmon resonance, 210, 241, 421
 plasmonic lithography, 241, 421
 plasmonics, 210, 421
 plastic deformation, 105-106, 270-271, 330,
 368-369, 373, 375, 404
 plastic forming, 272-273, 323, 390-391
 plasticity, 271-272, 279
 plasticizer, 291-292
 polydimethylsiloxane, 274
 polydispersity, 74, 218
 polymeric gel casting, 297
 polymerization, 63, 76, 85, 168, 297-299,
 307, 310
 polymorph, 105, 145-146, 337
 polyol method, 131*f*, 157, 189, 421
 pore former, 346
 pore forming sintering, 341, 346, 384
 pore shape, 148
 pore size distribution, 148-150, 272, 290,
 301, 337, 349, 357
 pore volume, 148-150, 420
 porous nanoparticle material sintering, 20,
 329-330, 341-359
 powder injection molding, 273-274, 277,
 321
 power-law creep, 380, 383, 421
 precipitation, 53-56, 58-59, 64-66, 111*t*,
 148, 362
 pressure casting, 20, 282, 288-291, 295,
 316
 pressure sintering, 20, 356, 363, 368-369,
 372, 382, 384
 pressure spark plasma sintering, 356, 368,
 376, 392
 programmed assembly, 314
 pseudoplasticity, 421
 pulsed laser ablation, 44, 47, 118, 207
 pyrolysis, 30, 41, 50, 72-76, 112*t*, 311, 313
 pyrometer, 356, 421
- quantum confinement, 7, 421
 quantum dot, 13, 17, 54, 144, 199, 205-206,
 220
 quantum size effect, 7, 421
 quantum tunneling, 11, 153, 422
 quasimelting, 145
- radiation heating, 354, 365
 Raman effect, 181
 Raman scattering, 182, 215
 Raman spectra, 181-183
 Raman spectroscopy, 129*t*, 161, 181, 183,
 188*t*
 rapid-rate sintering, 355, 364, 367-368
 Rayleigh criterion, 197
 reaction-controlled growth, 29
 recrystallization, 71, 145, 378
 redox reaction, 59-60, 251, 422
 reducing agent, 43, 54, 60, 83, 157, 200
 reverse micelle, 80-82, 89-90, 109
 Rietveld refinement, 118, 160, 422
 robocasting, 304-306, 318*t*, 327
- saturation concentration, 29
 scanning electron microscopy, 129*t*, 130,
 209, 343*f*
 scanning probe microscopy, 129*t*, 130, 133,
 185*t*
 scanning transmission electron microscope,
 172, 419
 scanning tunneling microscopy, 40*f*, 129*t*,
 133, 152*f*, 153, 186*t*, 215
 Scherrer constant, 138
 Scherrer equation, 138, 140, 156
 secondary ion mass spectroscopy, 129*t*,
 161, 165, 167*f*, 186*t*
 sedimentation, 220, 245, 416
 segregation, 274, 288-289, 291, 293, 295,
 299
 selected area electron diffraction, 55*f*, 57*f*,
 157, 159-160, 234-235
 selective laser sintering, 328, 359, 385
 self-assembled monolayer, 84, 214, 225,
 238-240, 244, 256, 398
 semidry forming, 20, 264, 272, 316, 319
 semidry processing, 317*t*
 shape-directed assembly, 314
 shock wave compaction, 268-270
 shrinkage, 329-332, 344-345, 365-366, 369,
 377-378, 384
 silk fibroin, 86, 124, 422
 simulation, 15, 20, 37, 380, 402-404,
 406-407, 412-413
 sinter forging, 20, 368, 375-376, 384, 386,
 390
 sintering activity, 338

- sintering driving force, 339, 345, 368-369, 373-375, 377, 382
- slip casting, 246, 288-289, 295, 299, 323
- small angle neutron scattering, 140, 143*f*, 149, 422
- small angle scattering, 129*t*, 140, 185*t*
- small angle X-ray scattering, 140, 142*f*, 190, 418
- soft lithographic molding, 274
- sol-gel method, 120, 141, 150, 192, 281
- solid state reaction, 104, 107, 110, 345, 362
- solid state sintering, 334, 362, 383, 404
- solids loading, 274-275, 286-288, 291-292, 296-297, 304-306, 310-313, 318*t*
- solubility, 5-6, 30, 53, 65, 157, 220
- solute drag mechanism, 358, 422
- solution calorimetry, 129*t*, 145
- solventless synthesis, 76-78, 113*t*
- solvothermal synthesis, 25, 53, 65-66, 68, 112*t*
- sonication, 54, 89, 97-100, 114*t*, 240
- sonication-assisted synthesis, 97, 114*t*
- spallation source, 141, 422
- spark plasma sintering, 20, 356-357, 368, 376-382, 384
- specific surface area, 4, 145-148, 184, 264-265, 287, 335, 344
- specific surface energy, 26, 33-34
- spin casting, 209, 290
- spin polarization, 12, 422
- spin-coating, 216*f*, 221, 313
- sporosarcina ureae, 243
- spray pyrolysis, 31, 50, 72-73, 75-76, 112*t*
- springback, 269, 272, 289
- stabilizer, 58, 79, 83, 86, 101-102, 222-223, 230, 293
- steady state diffusion, 29
- stereolithography, 20, 304, 307-308, 310, 316, 318*t*
- steric stabilization, 77, 282-284
- stern and Helmholtz double layer, 422
- stoichiometry, 35, 44, 64, 72, 159, 375, 399
- Stokes-Einstein equation, 136
- strain hardening, 272, 369
- supercritical drying, 65, 422
- superhigh pressure compaction, 20, 263, 268-270, 272, 317*t*
- superlattice, 7, 159*f*, 234-237, 276*f*, 293-294, 404-405, 422
- superparamagnetic, 12, 37, 54, 60, 93
- superparamagnetism, 97, 423
- superplasticity, 9, 375, 377, 423
- supersaturation, 26-28, 30, 33-34, 44, 53, 65
- superwide pressure range adsorption, 149
- surface activity, 4, 184
- surface behavior, 3, 4
- surface composition, 129*t*, 161-162, 165, 186-187*t*
- surface diffusion, 330, 333, 337, 339, 354-356, 364
- surface energy, 5, 31-34, 145-146, 157, 330, 338-345
- surface enthalpy, 145
- surface plasmon effect, 13, 423
- surface scattering, 10
- surface structure, 110, 129*t*, 150-151, 154-155, 243, 344*f*, 399
- synchrotron X-ray source, 165, 423
- T4 virion, 243
- tape casting, 20, 263, 282, 291-293, 295, 316, 317*t*
- template-assisted assembly, 242, 255
- template-directed sintering, 341, 349, 384
- templating, 20, 28, 83-85, 195, 242, 248-249, 251-252
- tensile strength, 9, 277, 278
- thermal diffusion length, 3, 423
- thermal scattering, 10, 423
- thermionic emission, 130, 423
- thermophoresis, 34, 423
- time of flight mass spectrometry, 167
- top-down, 20, 195-197, 218, 236, 256, 293
- topography, 134, 302
- toxicity, 87, 407, 409-412, 414
- translational order, 230, 423
- translocation, 410, 423
- transmission electron microscopy, 129*t*, 130, 132, 185*t*, 193
- tunneling current, 133-134, 153, 186*t*, 189
- two-step sintering, 342, 364-368, 387
- ultrasound, 97-100, 125, 415
- uniaxial compaction, 20, 264-267
- uniaxial pressure casting, 289
- UV laser, 44, 46, 423
- UV-vis spectroscopy, 129*t*, 161, 178-179, 181, 189

- vacancy concentration, 339-340
- validation, 183, 399-400, 404, 406
- van der Waals force, 17, 20, 220, 265, 282, 300, 415
- vapor pressure, 3, 5, 6, 32, 34, 36
- verification, 400, 406
- viscosity, 274, 277, 282, 286-289, 291-292, 301, 310
- volume diffusion, 330-331, 333, 363-364
 - coarsening mechanism, 333, 364

- water adsorption calorimetry, 129*t*, 145
- wavelength dispersive spectroscopy, 187*t*
- wave-particle duality, 151, 423
- wet forming, 20, 282, 287-290, 316, 319
- wet processing, 264, 316, 317*t*
- wettability, 203

- xerogel, 65, 75, 191, 314, 420
- X-ray absorption spectroscopy, 149, 423
- X-ray diffraction, 99-100, 105, 129*t*, 138, 155, 228, 399
 - line broadening, 129*t*, 138
- X-ray fluorescence spectroscopy, 129*t*, 161, 170*f*
- X-ray photoelectron spectroscopy, 129*t*, 161, 164, 187*t*, 209
- X-ray scattering, 129*t*, 140-141, 142*f*, 190, 418

- YAG laser, 44-45, 205, 424
- yield strength, 9

- zeta potential, 246, 301, 350